8th edition

Copernicus Publications
The Innovative Open Access Publisher

STATE OF THE PLANET

COPERNICUS

OCEAN STATE REPORT

8th edition of the Copernicus
Ocean State Report | 2024

PROGRAMME OF
THE EUROPEAN UNION

Copernicus
Europe's eyes on Earth

Copernicus
Marine Service

Implemented by
MERCATOR OCEAN
INTERNATIONAL

About the Copernicus Ocean State Report

As part of the Copernicus Marine Service, the annual Copernicus Ocean State Report (OSR) launched in 2015 is the key tool of its ocean reporting framework. The OSR reports on the state, variability, and ongoing changes in the marine environment of the global ocean and the European regional seas over the past decades up to close to real time. Using observation-based (remote sensing, in situ) and ocean reanalysis data, the OSR provides a comprehensive 4-dimensional (latitude, longitude, depth, and time) analysis of the Blue, Green, and White Ocean. The OSR is intended to act as a reference, providing a unique ocean monitoring dashboard for the scientific community and for policy makers and others with decision making responsibilities.

Copernicus
Marine Service

PROGRAMME OF
THE EUROPEAN UNION

Copernicus
Europe's eyes on Earth

Implemented by
MERCATOR
OCEAN
INTERNATIONAL

STATE OF THE
PLANET

About State of the Planet

State of the Planet (SP) is a journal dedicated to the publication of scientific synthesis reports and assessments on all subjects of the Earth and environmental sciences. In a rapidly changing world, expert-based assessments of academic findings curated for a wider audience to support decision making, science communication, education, and funder mandates are becoming more and more widespread. Such reports are extensive science community efforts offering timely, state-of-the-art insight into a specific field of the Earth sciences. State of the Planet is open to any reporting and assessment initiative by (inter-) governmental agencies, environmental services, learned societies or associations of researchers that aim to publish on a regular basis.

Copernicus Publications
The Innovative Open Access Publisher

publications@copernicus.org
http://publications.copernicus.org

This document was produced with funding by the European Union. Views and opinions expressed are however those of the author(s) only and the European Commission cannot be held responsible for any use which may be made of the information contained therein.

Cover photo by Rod Long on Unsplash

von Schuckmann, K., Moreira, L., Grégoire, M., Marcos, M., Staneva, J., Brasseur, P., Garric, G., Lionello, P., Karstensen, J., and Neukermans, G. (Eds.): 8th edition of the Copernicus Ocean State Report (OSR8), Copernicus Publications, State Planet, 4-osr8, https://doi.org/10.5194/sp-4-osr8, 2024.

State Planet, 4-osr8, 1, 2024
https://doi.org/10.5194/sp-4-osr8-1-2024

The state of the global ocean

Karina von Schuckmann[1], Lorena Moreira[1], Mathilde Cancet[2], Flora Gues[3], Emmanuelle Autret[4], Jonathan Baker[5], Clément Bricaud[1], Romain Bourdalle-Badie[1], Lluis Castrillo[6], Lijing Cheng[7], Frederic Chevallier[8], Daniele Ciani[9], Alvaro de Pascual-Collar[6], Vincenzo De Toma[9], Marie Drevillon[1], Claudia Fanelli[9], Gilles Garric[1], Marion Gehlen[8], Rianne Giesen[10], Kevin Hodges[11], Doroteaciro Iovino[12], Simon Jandt-Scheelke[13], Eric Jansen[12], Melanie Juza[14], Ioanna Karagali[15], Thomas Lavergne[16], Simona Masina[12], Ronan McAdam[12], Audrey Minière[1], Helen Morrison[13], Tabea Rebekka Panteleit[13], Andrea Pisano[9], Marie-Isabelle Pujol[17], Ad Stoffelen[10], Sulian Thual[1], Simon Van Gennip[1], Pierre Veillard[17], Chunxue Yang[9], and Hao Zuo[18]

[1]Mercator Ocean international, Toulouse, France
[2]CNRS/LEGOS, Toulouse, France
[3]CELAD, Mercator Ocean international, Toulouse, France
[4]Ifremer, Brest, France
[5]Met Office, Exeter, UK
[6]Nologin Oceanic Weather Systems, Madrid, Spain
[7]IAP, Chinese Academy of Sciences, Beijing, China
[8]LSCE, IPSL, Gif-sur-Yvette, France
[9]Consiglio Nazionale delle Ricerche, Istituto di Scienze Marine (CNR-ISMAR), Rome, Italy
[10]Royal Netherlands Meteorological Institute, Utrecht, the Netherlands
[11]University of Reading, Reading, UK
[12]CMCC Foundation – Euro-Mediterranean Center on Climate Change, Bologna, Italy
[13]Federal Maritime and Hydrographic Agency (BSH), Hamburg, Germany
[14]SOCIB, Palma, Spain
[15]National Centre for Climate Research, Danish Meteorological Institute, Copenhagen, Denmark
[16]Norwegian Meteorological Institute, Bergen, Norway
[17]Collecte Localisation Satellites (CLS), Ramonville St Agne, France
[18]European Centre for Medium-range Weather Forecasts (ECMWF), Reading, UK

Correspondence: Karina von Schuckmann (karina.von.schuckmann@mercator-ocean.fr)

Published: 30 September 2024

Abstract. Here, the Copernicus Ocean State Report offers detailed scientific analysis of the ocean under climate change, ocean variability, and ocean extremes. This evidence-based reporting is based on a set of key ocean indicators such as sea surface temperature, sea level rise, ocean heat content, ocean acidification, and sea ice extent. Moreover, key indicators for ocean variability such as the El Niño–Southern Oscillation and major ocean current systems such as the Atlantic Meridional Overturning Circulation are tackled. Major results show that the global ocean's sea surface temperature continues to steadily increase, particularly in the Northern Hemisphere, with a global warming rate of 0.13 ± 0.01 °C per decade from 1982 to 2023. Since around the 1970s, the ocean warming trend has intensified, doubling its rate over the past 2 decades. Concurrently, global mean sea level has risen significantly at intensifying rates from $2.1\,\mathrm{mm\,yr^{-1}}$ in the 1990s to $4.3\,\mathrm{mm\,yr^{-1}}$ in recent years, with regional disparities. The Arctic Ocean has faced unprecedented sea ice loss and warming, while Antarctic sea ice has reached record lows. Ocean acidification has progressed, decreasing pH at a rate of -0.017 per decade. Marine heatwaves have become more frequent, intense, and extensive, affecting up to 80 % of the global ocean surface annually. Despite significant variability, extreme ocean surface wind speeds have been prevalent, particularly in the North Atlantic, North Pacific, and Southern Ocean. The Atlantic Meridional Overturning Circulation shows no significant decline but varies substantially. In 2023, La Niña conditions have transitioned to El Niño conditions in the Pacific Ocean.

Executive summary

The sea surface temperature (SST) of the global ocean continues to warm, and this warming is not uniform across ocean basins and particularly pronounced in the Northern Hemisphere. Global mean sea surface temperature is warming at a rate of $0.13 \pm 0.01\,^{\circ}\mathrm{C}$ *per decade over the period 1982–2023.* Apart from areas of major ocean current systems in the Pacific, Atlantic, and Southern Ocean, the ocean surface is warming. In particular, 75 % of the Northern Hemisphere ocean surface is warming faster than the global average, compared to 35 % of the Southern Hemisphere ocean.

Ocean warming continues to increase globally, and since the 1960s, rates of change have doubled in the past 2 decades. Over the period 1960–2023, the global ocean heat content increased at a rate of $0.58 \pm 0.1\,\mathrm{W\,m^{-2}}$*. Since 2005, this global rate has increased to* $1.05 \pm 0.2\,\mathrm{W\,m^{-2}}$*.* Regionally, ocean warming is evolving differently in various areas of the global ocean, while since 1960, the strongest upper 2000 m ocean warming has occurred in the Southern Ocean (60–35° S), the North Atlantic (20–50° N), and the South Atlantic (60° S–0°).

Global mean sea level observed by satellite altimetry has risen more than 10 cm, at a rate of $3.4 \pm 0.3\,\mathrm{mm\,yr^{-1}}$*, and accelerated by* $0.11 \pm 0.05\,\mathrm{mm\,yr^{-2}}$ *over the past 30 years. Global mean sea level rose from* $2.1 \pm 0.3\,\mathrm{mm\,yr^{-1}}$ *over the period 1993–2002 to* $4.3 \pm 0.3\,\mathrm{mm\,yr^{-1}}$ *over 2013–2023.* Regional sea level rise is not uniform, and almost 50 % of the ocean is rising faster than the global average. The regions with faster rates are the major western boundary currents (in the Kuroshio current in the western North Pacific and in the Gulf Stream and the Brazil and Malvinas currents in the Atlantic Ocean), large parts of the western Pacific Ocean and Indian Ocean, and some areas in the Atlantic Ocean.

The Arctic Ocean has been exposed to unprecedented sea ice loss and surface ocean warming of 4.37 °C since the 1980s, and in 2016, Antarctic sea ice entered a new state of low sea ice, reaching the lowest levels on record in 2023. Over the period 1979–2023, the Northern Hemisphere sea ice extent decreased by −4.33 % per decade on annual average, by −12.64 % per decade in September (Summer), and by −2.55 % per decade in March (Winter). Record summer sea ice loss is reported during the years 2012 and 2020. The trend in surface temperature in the Arctic Ocean amounts to $0.104 \pm 0.005\,^{\circ}\mathrm{C\,yr^{-1}}$ between 1982 and 2023. Most of the Arctic Ocean basin is experiencing surface warming, particularly in the northern Barents Sea, the Kara Sea, the Beaufort Sea, and the Eurasian part of the Arctic Ocean. Antarctic sea ice extent does not show a long-term trend on average due to high variability and contrasting regional trends over the period 1982–2023. In 2016, Antarctic sea ice showed a rapid decrease, entering a new low state of sea ice, and 2023 became by far the lowest year on record. Global mean sea ice extent in the polar regions was at its lowest point in 2023 as compared to the 1993–2010 reference period.

Global ocean acidification has continuously increased over the past 37 years (1985–2022), with an observed rate of decrease in ocean pH of −0.017 pH unit per decade. Regionally, ocean acidification is not increasing uniformly. About 47 % of the sampled ocean is getting more acidic at a faster rate than the global average, particularly in the Indian Ocean, the Southern Ocean, the eastern equatorial Pacific Ocean, the northern tropical Pacific, and some regions in the Atlantic Ocean.

The year 2022 was the third consecutive year of El Niño–Southern Oscillation (ENSO) La Niña conditions, and the year 2023 was marked by developing El Niño conditions. The tropical Pacific Ocean experienced multi-year La Niña conditions persisting during 2020, 2021, and 2022. This phase of ENSO reverted afterwards, transitioning to neutral conditions in boreal spring 2023 and then to a warm El Niño phase in the second half of 2023.

The Atlantic Meridional Overturning Circulation (AMOC) strength does not show a statistically significant decline over the period 1993–2023. Since 1993, the strength of AMOC has undergone stark variations in both the reanalyses and observations, superposing any long-term change. Scientific controversy prevails in the published literature, and several studies estimate low AMOC strength or even predict a near-term collapse, while other studies elevate fluctuations of AMOC.

Since 1982, the frequency, duration, intensity, and regional extension of marine heatwaves of strong and extreme categories have increased, and during the years 2022 and 2023, large areas of the surface ocean were affected. Over the period 1982–2023, the fraction of the global ocean surface that experienced a marine heatwave (MHW) event over 1 year increased from 50 % to 80 %. The spatial extension of strong MHW events and the yearly averaged maximum duration of MHW events in recent years have doubled since 2008 from about 20 % to 40 % and from 20 to 40 d, respectively, while they were relatively stable before the mid-2000s. In 2022, 12 % of the global ocean surface experienced at least one marine heatwave event of severe to extreme category, with most persistent events lasting 6 months or longer occurring in the Coral Sea, affecting waters off northeast Australia and the Melanesian Pacific Island states. In 2023, 22 % of the global ocean surface experienced at least one severe to extreme marine heatwave event. The most prominent events, lasting 6 months or longer, occurred in the tropical central and eastern Pacific, associated with the emerging 2023–2024 El Niño and the coastal Niño off the coast of Peru, and in the northern tropical Atlantic and the Southern Ocean south of 40° S.

Globally, most extreme ocean surface wind speeds exceeding 20 m s^{-1} over the past 16 years prevail in the central and subpolar North Atlantic, the North Pacific, and the Southern Ocean. The detection of long-term trends in extreme wind speeds is hampered by their large variability in space and time, such as being triggered by the El Niño–Southern Oscillation. Over the period 2007–2023, ocean surface extreme wind speeds in the North Atlantic exceeding more than 22 m s^{-1} were particularly pronounced along the southern coast of Greenland. Extreme winds also reach more than 20 m s^{-1} in the North Pacific and Southern Ocean. Extreme wind speeds in the tropical bands (10–30° of latitude) amount typically to about 13 m s^{-1} and around or below 10 m s^{-1} in the equatorial band (0–10° of latitude). Wind speed extremes in the western tropical Pacific are closely correlated with the El Niño–Southern Oscillation index, with more extreme wind speeds and longer-lived tropical cyclones during El Niño years.

1 Ocean and climate

1.1 Sea surface temperature

The surface of the ocean is in permanent dialogue with the overlying atmosphere, and every change in this complex interaction governed by air–sea processes transferring energy, momentum, and gases between them is reflected in changes of sea surface temperature. Hence, regular monitoring of sea surface temperature is a fundamental component of climate variability assessment. Also, sea surface temperature is identified as an essential ocean variable in weather prediction and atmospheric model simulation, and it has a profound role in the study of marine ecosystems, ocean dynamics, and ocean health (Centurioni et al., 2019). Global targets of political ambitions are aligned along the global climate indicator of Earth surface temperature (UN, 2015) from which the ocean surface constitutes the major fraction covering nearly 70 % of the Earth's surface. The most recent assessment of available scientific knowledge under the sixth assessment cycle of the IPCC has reported that each of the last 4 decades has been successively warmer than any decade that preceded it since 1850. Global surface temperature was 1.09 [0.95 to 1.20] °C higher in 2011–2020 than 1850–1900, with larger increases over land (1.59 [1.34 to 1.83] °C) than over the ocean (0.88 [0.68 to 1.01] °C), IPCC, 2021). While the global mean sea surface temperature is increasing, there is variability around this average, with different regions and locations experiencing different responses, both in terms of trend and variance on different timescales and which are linked to climate modes (such as the El Niño–Southern Oscillation) and/or ocean dynamics.

In 2023, the global mean temperature was the highest on record (Fig. 1). Since 1982, global mean surface temperature has risen at a rate of 0.13 ± 0.01 °C. Superposed on the long-term trend, the global mean sea surface temperature also shows large variations around the average, which is known to be dominated by internal variations from the El Niño–Southern Oscillation (ENSO; Fig. 1, red and blue shading). Except for the area poleward of about 50° S, the eastern tropical Pacific where upwelling takes place, the central subtropical South Atlantic, and the area of the so-called "cold blob" in the subtropical North Atlantic (Fan et al., 2023; Sanders et al., 2022), which show no statistically significant trend, the rest of the ocean surface is warming. The spatial pattern of the global SST trend also evidences that nearly 14 % of the ocean surface is warming more slowly compared to the global mean surface warming rate (Fig. 2b, Table 1), and 40 % of the ocean surface is even observed to warm at a rate equal to or exceeding 2 times or more (12 %) the global mean surface warming (Fig. 2b, Table 1). Higher warming rates characterize the Northern Hemisphere in all ocean basins, particularly north of 30° N.

1.2 Ocean heat content

The global ocean is warming, and this human-driven warming is irreversible over centuries to millennia (IPCC, 2021). The ocean is warming because today the Earth is out of energy balance with anthropogenic climate forcing (Forster et al., 2021; Hansen et al., 2011; von Schuckmann et al., 2016). This Earth energy imbalance leads to an accumulation of heat in the Earth system, from which the majority – about 90 % – is stored in the global ocean. The rest is warming the continents, melting the ice in the frozen parts of the world, and warming the atmosphere (von Schuckmann et al., 2020). In other words: the ocean is our sentinel for monitoring the current state and future perspectives of planetary warming and is hence the fundamental indicator of high policy relevance (Cheng et al., 2024; von Schuckmann et al., 2023). In accordance with climate models, this indicator also reveals that Earth system heating is accelerating (Minière et al., 2023; Storto and Yang, 2024; Cheng et al., 2024).

Ocean warming has wide-reaching implications (Cheng et al., 2022). For example, ocean warming contributes to about 40 % of the observed global mean sea level rise and alters ocean currents (Gulev et al., 2021). It also indirectly alters storm tracks (IPCC, 2018), increases ocean stratification (Li et al., 2022), and can lead to changes in marine ecosystems (Bindoff et al., 2019). Particularly, and together with ocean acidification and deoxygenation, ocean warming can lead to dramatic changes in ecosystem assemblages, biodiversity impacts, population extinction, coral bleaching, infectious diseases, and changes in animal behaviour (including reproduc-

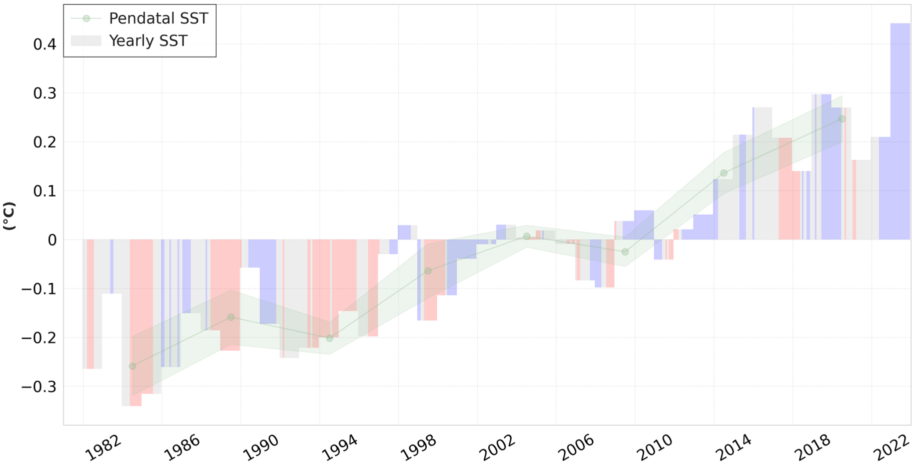

Figure 1. Annual global (90° N–90° S) mean sea surface temperature (bars) anomalies (relative to the 1991–2020 baseline) together with pentadal (green line) values over the satellite record as derived from product ref. SST.3 in the Supplement over the period 1982–2023. The green shaded envelope represents the 2σ ensemble spread of pentadal values for three products (product ref. SST.1–SST.4). Colours on bars indicate the positive (red, El Niño), negative (blue, La Niña), and neutral (grey) phases of the multivariate ENSO index (product ref. SST.5).

Table 1. Percentage of ocean surface affected by different sea surface temperature trends, for the whole considered areas, and when considering only the shallow waters (depth between 0 and 200 m) in the regions.

Region	Selection of trend: surface temperature trend as compared to the global mean trend	Percentage of ocean surface (related to the considered region) concerned by the selected trend	Percentage of ocean surface for the shelf regions (depth 0 to 200 m deep) in the considered area
Global ocean	Negative trend	5 %	1 %
Global ocean	Positive trend, lower than global mean	14 %	24 %
Global ocean	Trend equal to or lower than 2 times the global mean	40 %	40 %
Global ocean	Trend larger than 2 times the global mean	12 %	25 %
Northern Hemisphere ocean	Trend larger than the global mean	75 %	78 %
Southern Hemisphere ocean	Trend larger than the global mean	35 %	32 %

tion), as well as the redistribution of habitats (Garcia Molinos et al., 2015; Gattuso et al., 2015; Ramírez et al., 2017).

Different research groups have developed products for evaluating ocean heat content, which rely on different data processing methods and bias corrections (Gulev et al., 2021; Cheng et al., 2022). Albeit these different approaches, those estimates agree on the fact that the global ocean has been warming since about 1960 onwards (Fig. 3a). The rate of ocean warming for the period 1960–2023 amounts to $0.58 \pm 0.1\,\mathrm{W\,m^{-2}}$ (Fig. 3a). For the most recent 2 decades (2005–2023), the global mean ocean warming rate has increased as compared to the long-term change ($1.05 \pm 0.2\,\mathrm{W\,m^{-2}}$, Fig. 3a). This doubling of the global ocean warming rate has been discussed in the recent literature (Cheng et al., 2022; Loeb et al., 2021; von Schuckmann et al., 2023), also in the light of ocean warming acceleration (Minière et al., 2023). The steady increase in ocean warming rates is consistent for different types of products, including direct estimates from ocean in situ observations, indirect estimates from remote sensing, the direct estimate of net flux

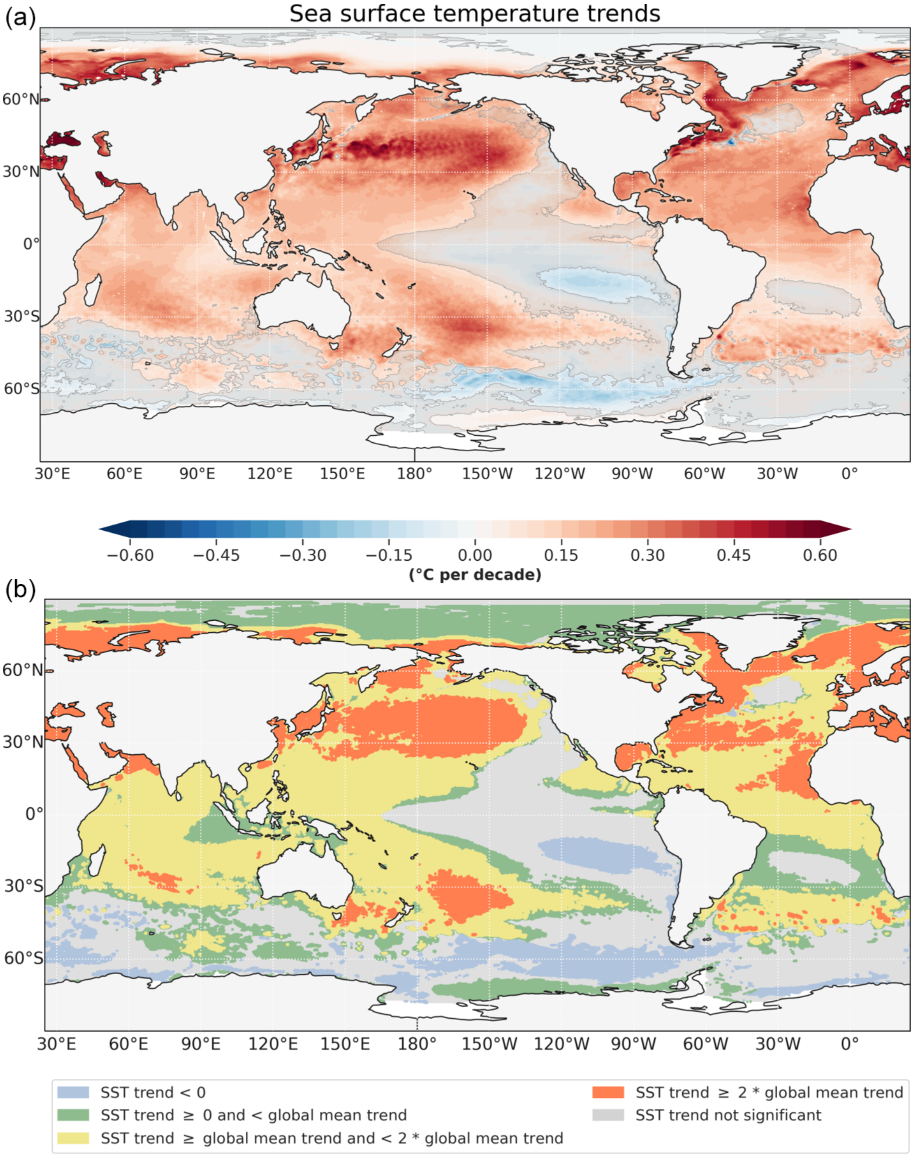

Figure 2. **(a)** Regional trend of sea surface temperature anomalies (rel. to the 1991–2020 baseline) over the period 1982–2023 as derived from product ref. SST.3. **(b)** Same as **(a)** but representing areas where the regional trend is negative (blue), positive and lower (green) than the global mean sea surface warming trend, equal to or exceeding up to 2 times (yellow) or exceeding 2 times the global mean sea surface warming trend (see Fig. 1). The grey shading represents areas where the trend is statistically not significant.

at the top of the atmosphere from satellite data, and CMIP6 climate models (Cheng et al., 2024). Different drivers of this change are discussed in the literature, including an attribution to a change in anthropogenic climate forcing (Hansen et al., 2023; Kramer et al., 2021; Raghuraman et al., 2021), or natural variability (Loeb et al., 2021).

Although ocean heat content (OHC) has increased dramatically at the surface, at depth, and over the entire water column, the pattern of ocean warming has been non-uniform (Cheng et al., 2022). The strongest upper 2000 m ocean warming occurs in the Southern Ocean (60–35° S), North Atlantic (20–50° N), and South Atlantic (60° S–0°) (Fig. 3b). The Southern Ocean domain (78–35° S) has been the largest heat reservoir since 1960, accounting for ∼ 36 % of the global upper 2000 m OHC increase. This strong warming is associated with the absorption of anthropogenic heat by the cold upwelling waters, which is then exported to the northern flank of the Antarctic Circumpolar Current (ACC) by the background overturning circulation. While the Atlantic Ocean (35° S–64° N), Pacific Ocean (35° S–60° N), Indian Ocean (35° S–30° N), and Arctic Ocean (65° N–90° N) account for ∼ 33 %, ∼ 20 %, ∼ 9 %, and ∼ 2.5 % of the global 0–2000 m OHC increase, respectively, the percentages change with time and ocean area. If considering the

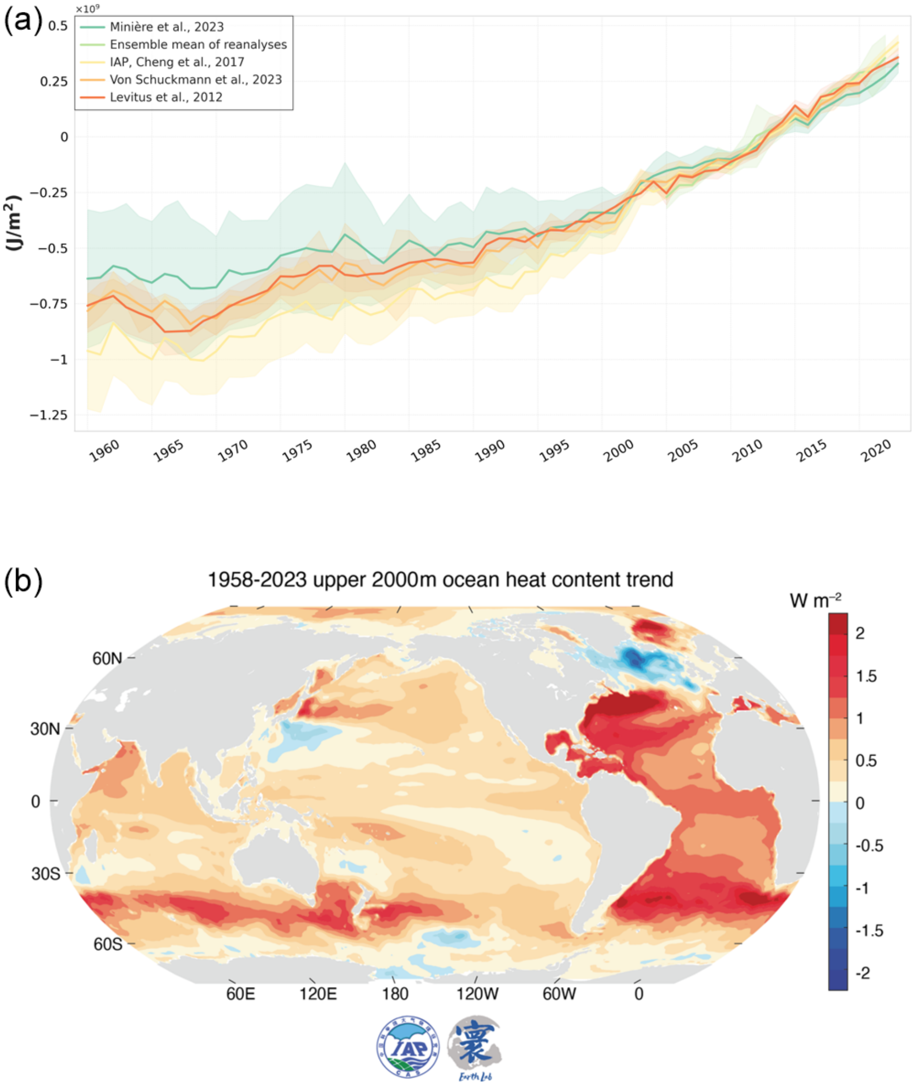

Figure 3. **(a)** Global mean ocean heat content (60° S–60° N) integrated from the surface down to 2000 m depth based on different products, i.e. IAP (Cheng et al., 2017 (product ref. OHC.1); Levitus et al., 2012 (product ref. OHC.2); Minière et al., 2023 (product ref. OHC.5), GCOS (von Schuckmann et al., 2023) product ref. OHC.6) and the Copernicus Marine Ocean Monitoring Indicators (product ref. OHC.7 ensemble mean of reanalyses based on product ref. OHC.8). Shaded areas indicate the uncertainty for each method respectively. The trend is estimated from product ref. 1–8 using a locally weighted scatterplot smoothing approach and amounts to $0.58 \pm 0.13\,\mathrm{W\,m^{-2}}$ over the period 1960–2023 and $1.05 \pm 0.17\,\mathrm{W\,m^{-2}}$ over the period 2005–2023. **(b)** Regional trend over 1960–2023 for ocean heat content in the upper 2000 m depth, in $\mathrm{W\,m^{-2}}$. Data updated from Cheng et al. (2017), product ref. OHC.1.

difference of ocean area, area-averaged warming is larger in the Southern Ocean, Atlantic Ocean, and Mediterranean Sea (ranging from $1.11\text{–}1.42 \times 10^9\,\mathrm{J\,m^{-2}}$) compared to the other basins ($0.49\text{–}0.70 \times 10^9\,\mathrm{J\,m^{-2}}$), indicating very intensive warming mainly associated with the ocean circulations. Some regions are cooling, in particular the subpolar Atlantic Ocean extending from the near surface down to >800 m depth (Fig. 3b). The contrasting pattern of cooling (∼ 50–70° N) and warming (20–50° N) in the North Atlantic has been associated with both circulation changes and local air–sea interactions (Cheng et al., 2022). Other cooling regions include the northwest Pacific, southwest Pacific, and southwest Indian oceans (Fig. 3b).

1.3 Sea level

Sea level is a global climate indicator of major interest (GCOS/WMO) as its long-term change encompasses different components of the Earth climate system in response to anthropogenic and natural forcing (Cazenave and Moreira, 2022). According to IPCC (2019), global mean sea level is rising, with acceleration in recent decades due to increasing rates of ice loss from the Greenland and Antarctic ice sheets, as well as continued glacier mass loss and ocean thermal expansion. Global mean sea level increased by 0.20 m between 1901 and 2018, with an increasing rate of rise for which human influence has very likely been the main driver since at least 1971 (IPCC, 2023).

The rise in sea levels has increased the adverse effects of coastal floods, storms, and tropical cyclones and, hence, the consequent losses and damages, increasing inhabitants' and infrastructure vulnerability and food security risk, in particular in low-lying areas and island states (IPCC, 2022a). Adaptation and mitigation measures, such as the restoration of mangroves and coastal wetlands, reduce the risks from sea level rise (IPCC, 2022b). Part of the present-day global mean sea level rise is driven by human-induced global warming, which impacts oceans' mass and volume. The ocean mass change (also known as barystatic sea level change) refers to the sea level change due to water mass redistribution between the ocean and land due to Greenland and Antarctica ice sheets' mass loss, the melting of glaciers and ice caps, and changes in terrestrial water storage (Oppenheimer et al., 2019). Change in ocean volume or density (also known as steric sea level change) is due to temperature and salinity changes regionally and, at global scale, to thermal expansion of the ocean in response to warming (Oppenheimer et al., 2019).

Assessment of the global mean sea level budget is key to disentangling the causes of sea level change. The sea level budget between 1993 and 2016 was been reported to have been closed within uncertainties (e.g., WCRP Global Sea Level Budget Group, 2018). Horwath et al. (2022) estimated the closure of the sea level budget over two periods 1993–2016 and 2003–2016. For the period 1993–2016, the thermal expansion contributes with 38 % and the ocean mass component with 57 % to the global mean sea level trend. During the second period, 2003–2016, ocean mass contributions increased, mostly due to the contribution from the Greenland ice sheet, accounting now for 66 % of global mean sea level rise. The recent literature has reported the non-closure of the sea level budget since 2016 (Chen et al., 2020); however, efforts have been made to identify the reasons. Barnoud et al. (2021) identified that errors in Argo salinity measurements are responsible for about 40 % of the non-closure; however, part of the non-closure remains unexplained.

Since the early 1990s, sea level has been routinely monitored by precision radar altimeters on board the still-growing satellite constellation. Historically, sea level has also been monitored by tide gauges installed along coastlines that measure relative sea level, which is the height of the water relative to the height of the land. Relative sea level change as measured by tide gauges describes the variation in ocean height in relation to the land at a specific location. Absolute sea level as measured by satellites change refers to the variation in the ocean's height relative to the Earth's centre, irrespective of any changes in the adjacent land's elevation.

The Copernicus Marine Service altimetry-based global mean sea level (GMSL) has been rising at a rate of $3.4\,\mathrm{mm\,yr^{-1}}$ with an uncertainty that amounts to $\pm 0.3\,\mathrm{mm\,yr^{-1}}$ with a confidence level of 90 % (Guérou et al., 2023) over the last 30 years (Fig. 4). The Copernicus Marine Service sea level data have been adjusted for the modelled glacial isostatic adjustment from Spada and Melini (2019), with a global mean correction on the order of $-0.3\,\mathrm{mm\,yr^{-1}}$. The altimetry-based sea level data are affected by the TOPEX-A instrumental drift over the period 1993–1998 (e.g., WCRP Global Sea Level Budget Group, 2018). The correction applied is based on Ablain et al. (2017). This empirical correction is based on a comparison with tide gauges, and it led to a drift correction of about $-1.0\,\mathrm{mm\,yr^{-1}}$ between January 1993 and July 1995 and $+3.0\,\mathrm{mm\,yr^{-1}}$ between August 1995 and February 1999, with an uncertainty of $1.0\,\mathrm{mm\,yr^{-1}}$ (WCRP Global Sea Level Budget Group, 2018). Even though this correction was initially intended for the GMSL, Legeais et al. (2020) stated that the anomaly of the onboard calibration correction is not expected to have any spatial signature on the regional sea level trends since it affects all measurements equally; as a consequence, here we correct the regional sea level data.

Over 1993–2023, the GMSL has increased by more than 10 cm (Fig. 4). The rate of rise for the first 10 years (1993–2002) of the altimetry era is estimated to be $2.1\,\mathrm{mm\,yr^{-1}}$, whereas the rate of rise for the last 10 years (2013–2023) is estimated to be $4.3\,\mathrm{mm\,yr^{-1}}$, indicating an acceleration that is broadly reported in the recent literature (e.g., Hamlington et al., 2020). The acceleration is estimated to have been $0.11 \pm 0.06\,\mathrm{mm\,yr^{-2}}$ over the last 30 years (e.g., Guérou et al., 2023).

At regional scale, the sea level rise is not uniform. Whereas a positive trend is observed in most regions, spots of negative trends can also be observed (Fasullo and Nerem, 2018). As shown in Fig. 5, 49 % of the altimetry-based observed ocean is rising at a faster rate as compared to the global average rate ($3.4\,\mathrm{mm\,yr^{-1}}$ over 1993–2023). This is the case in the Indian Ocean and in some regions of the Pacific and Atlantic Ocean (yellow areas in Fig. 5b). A total of 23 % of the ocean level has been rising faster than the rate over the last 10 years ($4.3\,\mathrm{mm\,yr^{-1}}$ over mid-2013 to mid-2023), as for instance in the eddy-rich regions in the North Atlantic and North Pacific Ocean basins, in the western Pacific Ocean and Pacific islands, and also in the Gulf of Mexico and some areas in the South Atlantic and Indian Ocean basins (orange regions in Fig. 5). Overall, most regions display positive trends over the period 1993–2023 except in the eastern Pacific Ocean and, for some spots, near the major Northern Hemisphere western boundary currents (e.g. the Kuroshio current) (green areas in Fig. 5b). In any case, internal variability has a significant impact on global and regional sea level trend estimates (e.g., Moreira et al., 2021; Hamlington et al., 2019), and hence, these spatial patterns are affected by the natural variability, for example, the El Niño–Southern Oscillation (ENSO).

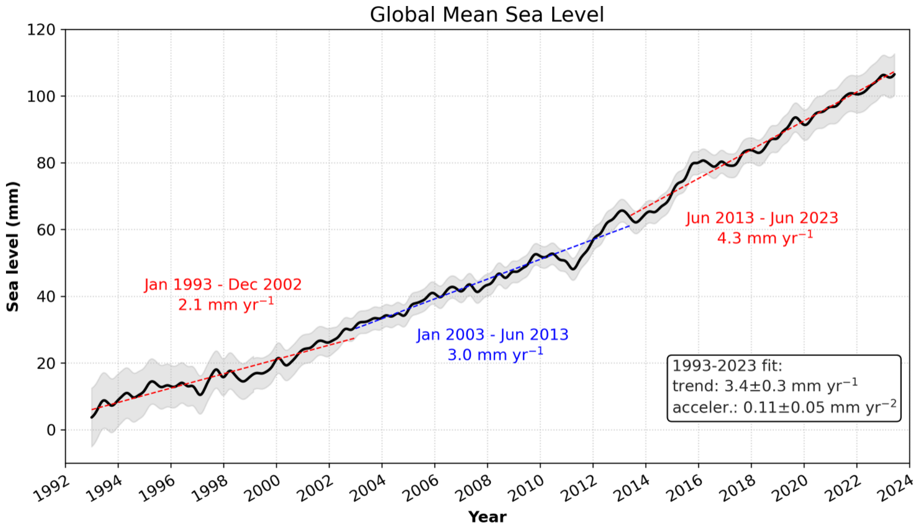

Figure 4. Global mean sea level (product ref. SL.1) time series from January 1993 to June 2023 (black curve) and its uncertainty envelope (shaded). The seasonal cycle has been removed, and the data are low-pass-filtered (175 d cut-off) and adjusted for global GIA correction of $-0.3\,\mathrm{mm\,yr^{-1}}$ (Spada and Melini, 2019) and TOPEX-A instrumental drift (1993–1998, Ablain et al., 2017). The trend and acceleration estimates for the whole altimetry era (1993–2023) are presented in the black box, trends for the first decade (1993–2002) and last decade (June 2013–June 2023) in red, and trends for the middle period (2003–June 2013) in blue.

Regionally, the mechanisms responsible for the variations in sea level trends are dominated by ocean temperature and salinity changes linked to steric effects and other processes such as ocean mass redistribution by the ocean circulation, atmospheric loading and changes in Earth gravity, Earth rotation, and viscoelastic solid-Earth deformation (GRD; Stammer et al., 2012). The latter is due to ongoing changes in the solid Earth caused by past changes in land ice (glacial isostatic adjustment, GIA) and by contemporary changes in the mass of water stored on land as ice sheets, glaciers, and land water storage (GRD sea level fingerprints) (Gregory et al., 2019). While at regional scale, sea level trends are still dominated by steric changes (Stammer et al., 2012), theoretical studies predict that with accelerated land ice melt, GRD fingerprints will become detectable (Tamisiea, 2011). An example of sea level fingerprint is the area encircling the Greenland ice sheet, which shows negative trends observed quite well for the period 2002–2019, as a consequence of ice mass melting (Coulson et al., 2022). Over 1993–2019, Prandi et al. (2021) estimated the average local sea level trend uncertainty to be $0.83\,\mathrm{mm\,yr^{-1}}$, with values ranging from 0.78 to $1.22\,\mathrm{mm\,yr^{-1}}$.

1.4 The ocean in the cryosphere

The cryosphere (that is the frozen parts of the world) and ocean are tightly interlinked, such as through major Earth system global cycles (energy, water, carbon), sea level change, or climate feedback processes (IPCC, 2019). For example, evaporation from the ocean contributes to snowfall that builds and sustains ice sheets and glaciers (Abram et al., 2019). A major fraction of global sea level rise is driven by the mass loss from melting land ice (WCRP Global Sea Level Budget Group, 2018), and ice sheets in Antarctica and Greenland currently hold about 66 m of potential global sea level rise (Fretwell et al., 2013). Ocean warming affects sea ice, ice sheet, glacier, and ice-shelf stability in areas of direct contact (Cai et al., 2023; Harrison et al., 2022; Naughten et al., 2022; Turney et al., 2020; Ciracì et al., 2023; de Steur et al., 2023; Wood et al., 2021). The injection of less dense water into the ocean from melting processes in turn affects ocean processes, hydrography, and circulation (Armitage et al., 2020; Gunn et al., 2023; Rahmstorf et al., 2015; Golledge et al., 2019). Also, ocean productivity in the polar areas is triggered – amongst others – through biogeochemical processes, such as through seasonal nutrient exchange from sea ice and glaciers' melt (Arrigo et al., 2017; Tagliabue et al., 2017).

A major player for the ocean–cryosphere nexus is sea ice, which is a thin and active system that triggers fluxes of heat, water, and carbon and is hence a fundamental actor in physical and biogeochemical processes (IPCC, 2019). Besides its role in affecting ocean circulation and processes (e.g., stratification) as mentioned above, sea ice plays a prominent role within the so called "ice–ocean–albedo feedback", which is a central process controlling high-latitude climate change: as ice cover melts from unusual warming, the underlying ocean is exposed to increasing absorption of shortwave radiation, which results in amplified ocean warming (Jenkins and Dai, 2022, 2021; Kashiwase et al., 2017; Goosse et al., 2018). Together with biogeochemical tracers, sea ice also harbours various species at the base of the food chain, which plays a

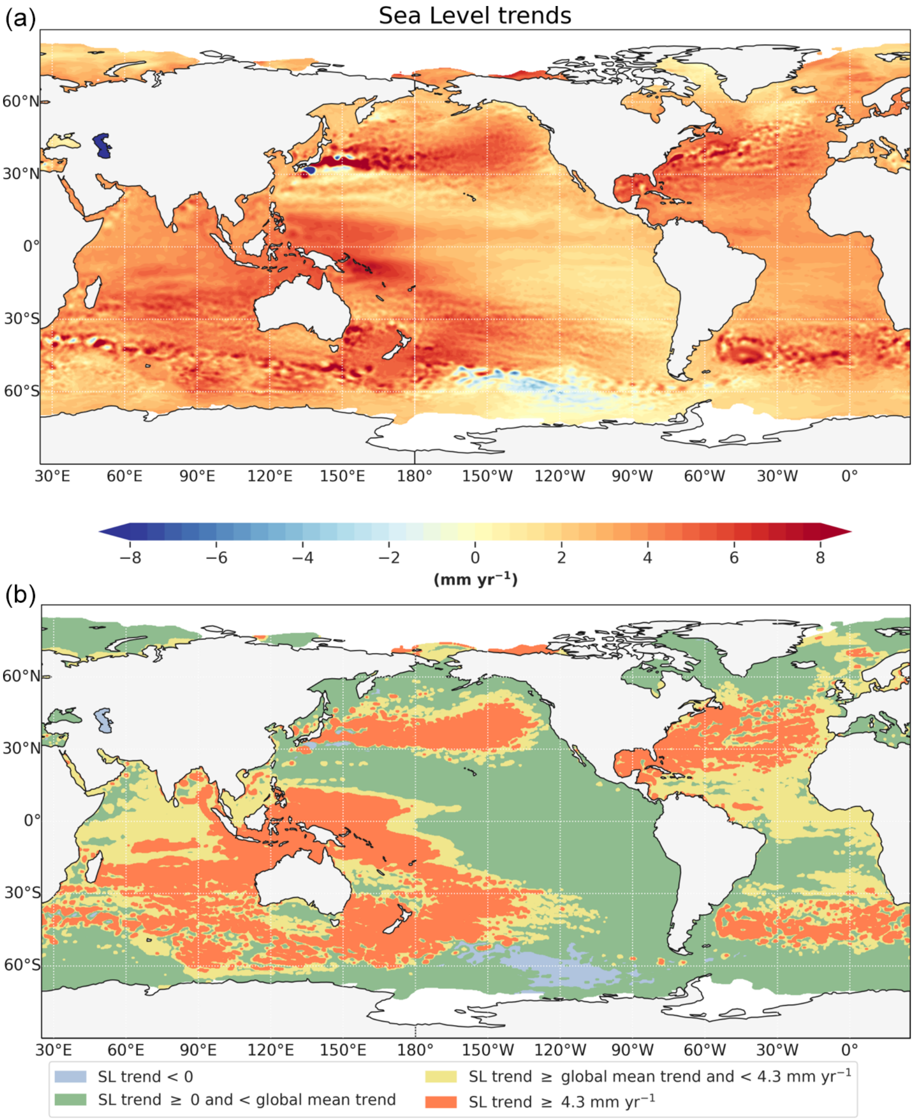

Figure 5. **(a)** Regional sea level trends from January 1993 to June 2023 (product ref. SL.2). **(b)** Shading map indicating the magnitude of the rates of sea level rise, where blue depicts regions with negative sea level trends, green indicates areas where sea level is rising more slowly than the altimetry-era global mean sea level rate of rise of 3.4 mm yr^{-1}, yellow indicates locations where sea level is increasing at a range between the global mean trend and 4.3 mm yr^{-1}, and orange indicates regions where sea level is rising at a rate faster than 4.3 mm yr^{-1}, which is the global mean sea level trend estimate over the last 10 years (June 2013–June 2023). The data used are corrected for GIA (Spada and Melini, 2019) and TOPEX-A drift (Ablain et al., 2017).

central role in the biological carbon pump and supports key foraging species such as Arctic cod (Lannuzel et al., 2020). Since about the 1980s, Arctic Sea ice area has decreased by about 40 % (10 %) in September (March) from anthropogenic warming, and in 2011–2020, annual average Arctic sea ice area reached its lowest level since at least 1850 (IPCC, 2021). The Arctic is likely to be practically sea ice-free in September at least once before 2050 under all scenarios considered in the recent IPCC report (IPCC, 2021), with sea ice losses projected to begin in the European Arctic and proceed to the Pacific and western Arctic and then the central Arctic (Jahn et al., 2024).

Sea ice is frozen seawater that floats on the ocean surface. The sea ice extent indicator is defined as the area where at least 15 % of the surface area is frozen (Fig. 6). Knowing how the sea ice cover is changing is essential for monitoring Arctic climate and has critical relevance for ecosystem health; Arctic communities; and economy such as fisheries, tourism, and transport (Meredith et al., 2019).

Since 1979, the Northern Hemisphere sea ice extent has decreased at an annual rate of $-0.50 \pm 0.02 \times 10^6$ km^2 per

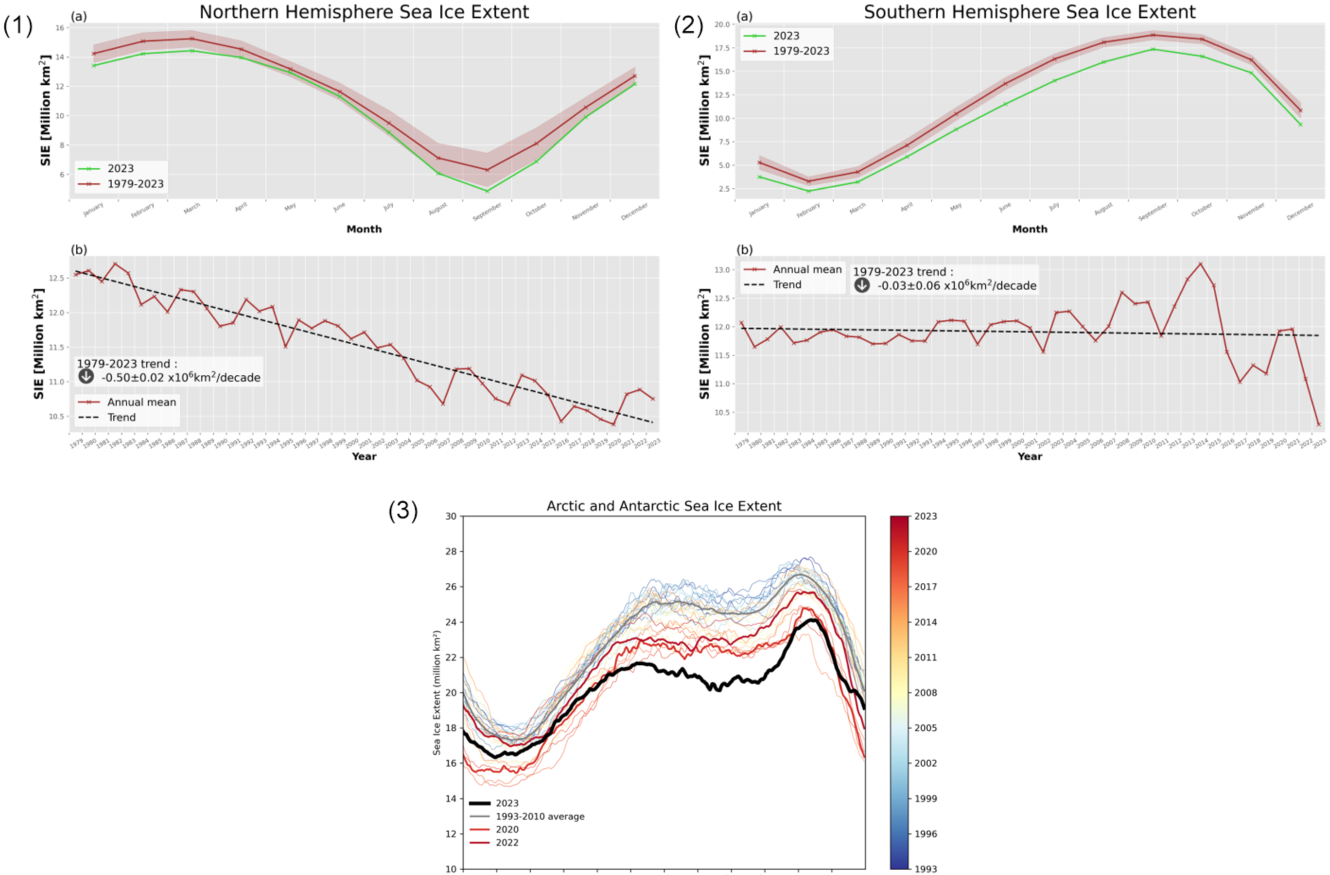

Figure 6. Panel **(1)**: **(a)** Seasonal Northern Hemisphere sea ice extent expressed in millions of square kilometres averaged over the period 1979–2023 (red), shown together for the seasonal cycle in the year 2023 (green), and **(b)** time series of yearly average Northern Hemisphere Sea ice extent. The change of sea ice extent over the period 1979–2023 is expressed as a trend in millions of square kilometres per decade and is plotted with a dashed line in panel **(b)**. Time series are based on satellite observations (SMMR, SSM/I, SSMIS) by EUMETSAT OSI SAF with R&D input from ESA CCI (product ref. SI.1). Panel **(2)**: **(a)** Seasonal Southern Hemisphere sea ice extent expressed in millions of square kilometres averaged over the period 1979–2023 (red), shown together for the seasonal cycle in the year 2023 (green), and **(b)** time series of yearly averaged Southern Hemisphere sea ice extent. The change of sea ice extent over the period 1979–2023 is expressed as a trend in millions of square kilometres per decade and is plotted with a dashed line in panel **(b)**. Time series are based on satellite observations SMMR, SSM/I, SSMIS by EUMETSAT OSI SAF with R&D input from ESA CCI (product ref. SI.2). Panel **(3)**: Arctic and Antarctic sea ice extent between 1993 to 2023. The black line represents the year 2023. Time series estimated using GLORYS12V1 and GLO12 (product ref. SI.3–4).

decade ($-4.33\,\%$ per decade) (Fig. 6). Loss of sea ice extent during summer exceeds the loss observed during winter periods: summer (September) sea ice extent loss amounts to $-0.80 \pm 0.06 \times 10^6\,\mathrm{km}^2$ per decade ($-12.64\,\%$ per decade), and winter (March) sea ice extent loss amounts to $-0.39 \pm 0.03 \times 10^6\,\mathrm{km}^2$ per decade ($-2.55\,\%$ per decade). These values agree with those assessed in the IPCC Special Report on the Ocean and Cryosphere in a Changing Climate (SROCC) (Meredith et al., 2019). Sea ice extent in September 2012 saw to date a record minimum Northern Hemisphere value since the beginning of the satellite record, followed by September 2020. January and February 2023 had the third-lowest values on record for these months, and September 2023 had the fifth-lowest values.

Sea surface temperature and sea ice surface temperatures play a crucial role in the heat exchange between the ocean and atmosphere and the sea ice growth and melt processes in the Arctic and are important for forecast and predictions (Meredith et al., 2019; Rasmussen et al., 2018). Combining sea surface temperature and sea ice surface temperature is identified as the most appropriate method for determining the surface temperature of the Arctic while challenged by the presence of complex interactions between water and sea ice at different space scales and timescales (Minnett et al., 2020; Nielsen-Englyst et al., 2023) (Fig. 7). Over the period 1982–2023, the cumulative trends exceed 2 °C for the greatest part of the Arctic Ocean, with the largest trends to occur in the northern Barents Sea, Kara Sea, Beaufort Sea, and the

Eurasian part of the Arctic Ocean (Fig. 7b). Zero to slightly negative trends are found in the North Atlantic part of the Arctic Ocean. The combined sea and sea ice surface temperature trend is $0.104 \pm 0.005\,^{\circ}\mathrm{C\,yr^{-1}}$, which corresponds to an increase of around 4.37 °C between 1982 and 2023.

For many years, i.e. from the beginning of the record up to the year 2016, Antarctic sea ice increased (Parkinson, 2019) (Fig. 6), despite continued global warming (IPCC, 2021) and the projected decline by climate models (Fox-Kemper et al., 2021). This overall increase in Antarctic sea ice could be allocated to increasing regional sea ice concentrations in the Ross and Weddell seas, which are on average only partly compensated for by a decrease in ice concentrations in the Bellingshausen Sea (Parkinson and Cavalieri, 2012; Lecomte et al., 2017). These regional patterns of sea ice increase over the period 1979–2016 have been linked to air–sea interactions (i.e. wind, precipitation) (Holland and Kwok, 2012; Haumann et al., 2014; Purich et al., 2016; Marsland and Wolff, 2001; Liu et al., 2004; Liu and Curry, 2010), sea ice advection or other internal ice–ocean processes (Haumann et al., 2016; Abernathey et al., 2016; Polvani and Smith, 2013; Zunz et al., 2013; Meehl et al., 2016), and the influence of freshwater discharge from Antarctic meltwater at the ocean and cryosphere nexus (Bintanja et al., 2013a; Pauling et al., 2017; Bintanja et al., 2013b; Swart and Fyfe, 2013). In autumn 2016, however, Antarctic sea ice experienced an unprecedented rapid loss, and since then, it has remained in a state of low sea ice, reaching record low levels in the years 2022 and 2023 (Gilbert and Holmes, 2024) (Fig. 6). Recent studies highlight that ocean warming has played a role in pushing Antarctic sea ice into this new low-extent state (Zhang et al., 2023; Purich and Doddridge, 2023). Values in 2023 are the lowest on record and amount to more than $1.5 \times 10^6\,\mathrm{km}^2$ below the pre-2000 levels (Fig. 6).

Monitoring change in sea ice extent globally allows for identifying changes in Earth's albedo sea ice feedback. The Earth's albedo, or its ability to reflect sunlight, is heavily influenced by the extent of ice cover on the planet's surface. And ice, with its high reflectivity, has a significant cooling effect on the Earth's climate by bouncing a substantial portion of incoming solar radiation back into space. As global ice cover decreases due to climate change, more sunlight is absorbed by darker surfaces like water and land, potentially leading to increased warming and altered weather patterns and exacerbating global climate change (Abram et al., 2019). Global sea ice extent in the polar regions – considering both the Arctic and Antarctic areas together – was on average at its lowest point in 2023 (Fig. 6), well below the 2020 and 2022 values. The drastic drop in global mean sea ice extent in 2023 is caused by a combination of strong Arctic sea ice melting during the Northern Hemisphere spring and the concurrent lack of Antarctic sea ice growth during the Southern Hemisphere autumn. This global historical low sea ice extent started in May and lasted until end of October, with total sea ice cover between 20 and $22 \times 10^6\,\mathrm{km}^2$ over the entire period.

1.5 Ocean acidification

The ocean plays a major role in the global carbon cycle, and it is an important sink for anthropogenic $\mathrm{CO_2}$, moderating climate change (Gruber et al., 2019). According to the recent IPCC report, the ocean has taken up between 20 %–30 % of total anthropogenic carbon dioxide emissions since the 1980s (IPCC, 2019). Every year, the ocean absorbs about 25 % of the carbon dioxide released to the atmosphere (Canadell et al., 2021) by fossil fuel consumption, cement manufacturing, and land use change. The ongoing uptake of $\mathrm{CO_2}$ alters the ocean carbonate system (i.e. lowers ocean pH) and threatens marine ecosystems, as well as reliant human communities (Doney et al., 2020). The decrease in ocean pH is referred to as ocean acidification (e.g., Canadell et al., 2021).

Ocean acidification is one of the 10 targets of the Sustainable Development Goal 14: Life Below Water (SG14.3 – minimize and address the impacts of ocean acidification, including through enhanced scientific cooperation at all levels) of the United Nation's 2030 Agenda for Sustainable Development (UN, 2015). The Intergovernmental Oceanographic Commission (IOC) of UNESCO is the custodian agency of SDG 14 Target 3, gathering together average marine acidity (pH) measured at an agreed suite of representative sampling stations. It provides guidance on how to establish the monitoring of ocean acidification by detailing which measurements to take. The methodology follows the best practices established by the scientific community. It supports the design of the most appropriate sampling strategy for a particular location and presents tools for the collection, quality control, and reporting of the data (UN, 2023).

IPCC (2019) states that open-ocean surface pH has declined by a very likely range of 0.017 to 0.027 pH units per decade since the late 1980s, with the decline in surface ocean pH very likely to have already emerged from background natural variability for more than 95 % of the ocean surface area. Ocean acidification has spread deeper in the ocean, surpassing 2000 m depth in the northern North Atlantic and in the Southern Ocean (Canadell et al., 2021). At regional scale, ocean acidification is not increasing uniformly: 47 % of the sampled ocean is getting more acidic at a rate faster than the global average, particularly in the Indian Ocean, the Southern Ocean, the eastern equatorial and northern tropical Pacific Ocean, and some regions in the Atlantic Ocean (Fig. 8). At global scales, the trends have shown a decrease of about 0.06 pH units (from 8.11 to 8.05) since 1985, corresponding to an approximately 30 % increase in acidity (Fig. 9), a rate of -0.017 ± 0.002 pH units per decade.

2 Ocean variability

2.1 El Niño–Southern Oscillation

The El Niño–Southern Oscillation (ENSO) is one of the most important and well-studied natural climate variability phe-

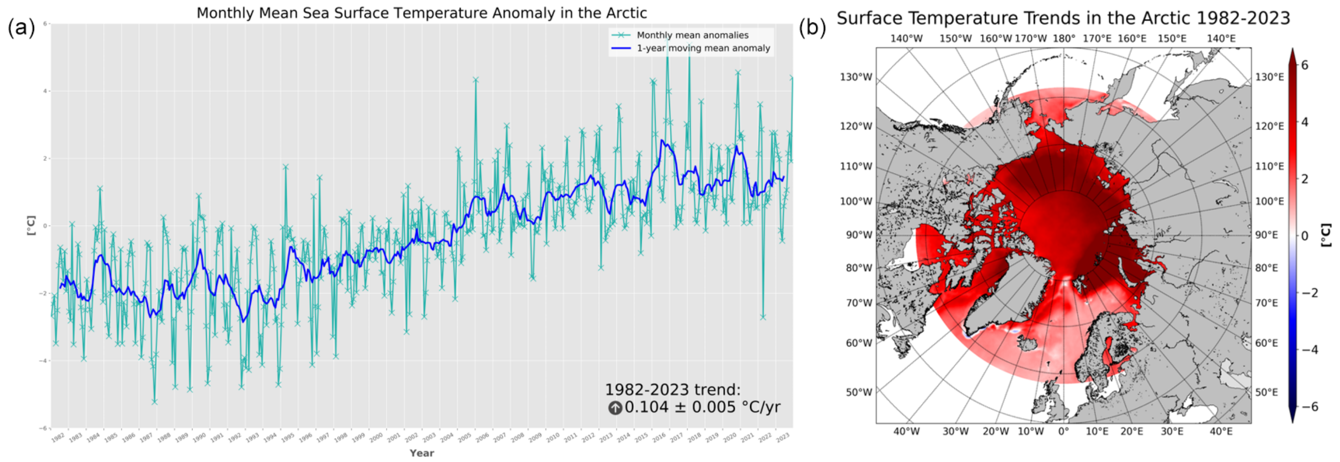

Figure 7. **(a)** Time series of monthly mean (turquoise line) and annual mean (blue line) of sea and sea ice surface temperature anomalies for January 1982 to December 2023, relative to the 1991–2020 mean (product ref. SI.5). **(b)** Cumulative trends (i.e. the rate of change, °C yr^{-1}, scaled by the number of years, 42 years) in combined sea and sea ice surface temperature anomalies calculated from 1982 to 2023 for the Arctic Ocean (product ref. SI.6).

nomena, originating from coupled ocean atmosphere interactions in the Pacific Ocean and impacting Earth's climate globally through complex interaction between oceanic and atmospheric processes (McPhaden et al., 2006; Timmermann et al., 2018). ENSO is the dominant source of climate on seasonal to multi-year timescales that originates in the tropical Pacific Ocean, with alternating warming and cooling phases – El Niño and La Niña, as well as neutral conditions. It has major worldwide social and economic consequences through its global-scale effects on atmospheric and oceanic circulation, marine and terrestrial ecosystems, and other natural systems (McPhaden et al., 2020). For example, ENSO-driven ocean temperature extremes, including marine heatwaves, have been shown to result in coral bleaching, loss of kelp forests, mass mortality of marine invertebrates, and geographical shifts of species due to heat stress (Holbrook et al., 2020; Oliver et al., 2017, 2018; Cavole et al., 2016; Garrabou et al., 2009). The recent IPCC assessment has concluded that since the late 19th century, major modes of climate variability such as ENSO have shown no sustained trends (Gulev et al., 2021), as the detectability of a projected increase of ENSO variability by climate models is hampered by the strong influence of internal variability (Cai et al., 2021).

Several indices are used to monitor the state of ENSO variability in the tropical Pacific. For instance, the Niño 3.4 index (Trenberth and Stepaniak, 2001) measures sea surface temperature anomalies averaged in the east-central tropical Pacific (5° N–5° S, 170–120° W). An El Niño (La Niña) event is declared when Niño 3.4 SST remains above +0.4 °C (below −0.4 °C) for several months, while the tropical Pacific also exhibits commonly associated atmospheric change (Houghton and Wilson, 2020; Trenberth, 1997). Since 1998, five out of six La Niña events lasted 2 to 3 years (Wang et al., 2023) (Fig. 10). Recently, multi-year La Niña conditions persisted during 3 consecutive years, 2020, 2021 and 2022 (Fig. 10). This cold phase of ENSO reverted in 2023, transitioning to neutral conditions during boreal spring 2023 and then to El Niño conditions in boreal summer 2023 (WMO, 2023) (Fig. 10). During the year 2023, intense ocean surface warming was also observed along the coasts of Ecuador and Peru. Sea surface temperature anomalies averaged in the coastal region Niño 1 + 2 (10–0° S, 90–80° W) remained above +2 °C for most of the year (https://www.mercator-ocean.eu/actualites/record-high-sea-surface-temperatures-north-atlantic-drop-in-phytoplankton-el-nino-costal-el-nino/, last access: 11 September 2024). Such coastal warming is referred to as a "coastal El Niño" that usually overlaps with El Niño but can sometimes occur independently (Hu et al., 2019; Gasparin et al., 2019). The 2023 coastal El Niño surface warming in fact started a few months before the start of the 2023 El Niño.

2.2 Atlantic Meridional Overturning Circulation

The Meridional Overturning Circulation (MOC) plays a central role in Earth's climate because it ultimately transports heat, freshwater, carbon, oxygen, and nutrients around the globe. The MOC is driven by a complex interplay of ocean currents, driven by the wind and water density differences, by surface buoyancy and momentum (wind) fluxes, and by interior ocean mixing (Rhein et al., 2011). The upper and lower branches of the MOC are connected via intense water mass transformation processes through air–sea exchange mainly in the subpolar and polar oceans. The recent literature has presented significant changes in the Southern Ocean since the mid-1970s, with a broadening and strengthening of the upper overturning cell and a contraction and weakening of the lower cell (Lee et al., 2023).

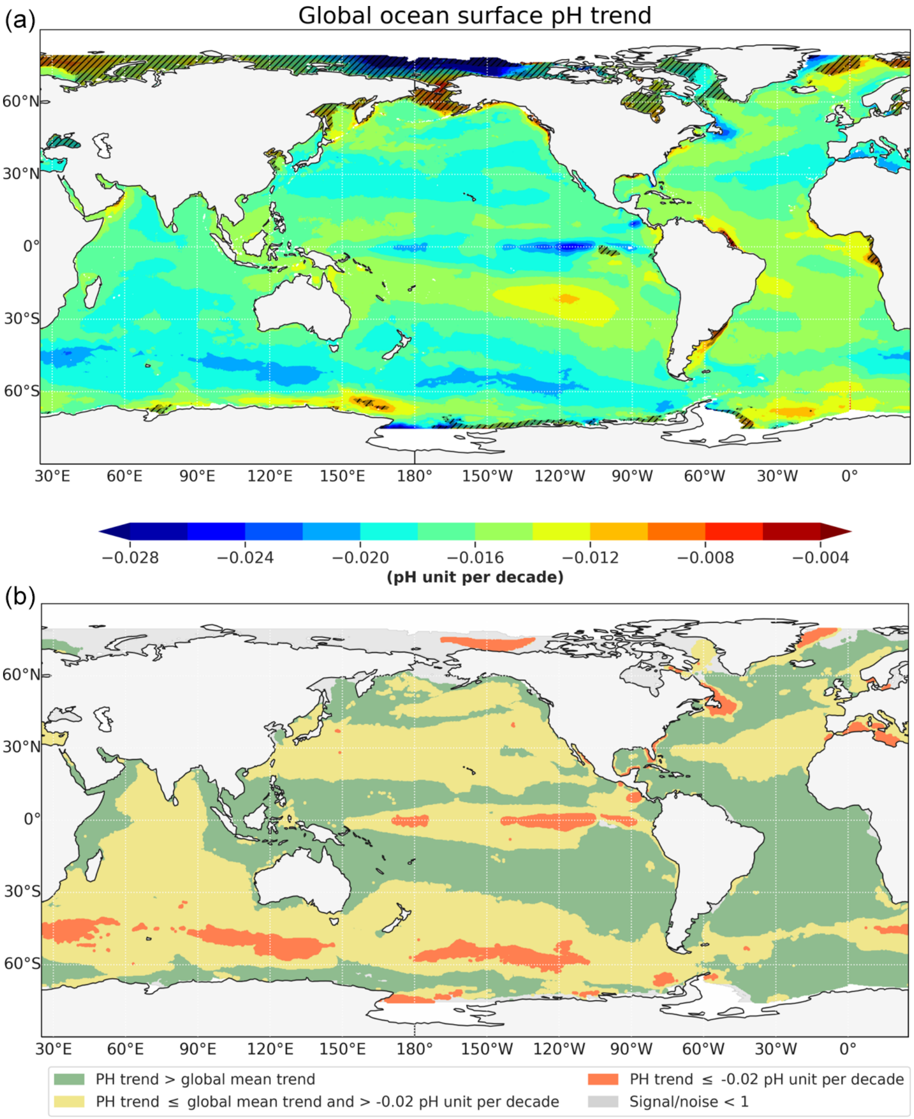

Figure 8. **(a)** Global ocean surface pH trend (in pH unit per decade) computed over the period 1985–2022 (product ref. OA.1). Black hatching shows the regions where pH trends are associated with the highest uncertainty estimates σ ($\sigma > 10\,\% \mid \mu \mid$, i.e. σ-to-μ ratio greater than 10 %). The 10 % threshold is chosen at the 90th confidence level of all ratio values computed across the global ocean. **(b)** Shading map indicating the magnitude of the pH decrease rates from product ref. OA.1, where green indicates areas where pH is decreasing more slowly than the global mean pH trend of −0.017 pH unit per decade, yellow indicates locations where pH is decreasing at a rate between the global mean trend and −0.02 pH unit per decade, and orange indicates regions where pH is decreasing at rate faster than −0.02 pH unit per decade.

The Atlantic Meridional Overturning Circulation (AMOC) is a major circulation system in the Atlantic Ocean and plays a key role for the North Atlantic and global climate (Volkov et al., 2023; Jackson et al., 2015). The northward flow of high-salinity waters in the upper North Atlantic Ocean and heat loss to the atmosphere are essential for the formation of deep, dense waters at high latitudes (Holliday et al., 2020). In the Northern Hemisphere the northward transport is mainly via the Gulf Stream and North Atlantic Current system, while the southward transport of cold and dense water is via the Deep Western Boundary Current System. The AMOC components are monitored at a number of latitudes across the Atlantic (Frajka-Williams et al., 2019), with basin-wide arrays being the South Atlantic Meridional Overturning Circulation (SAMOC) array at 34.5° S (subtropical South Atlantic), which ran in a pilot phase from 2009 to 2010 and has routinely been run since 2013; the RAPID array (McCarthy et al., 2015; Smeed et al., 2014) at 26.5° N (subtropical North Atlantic), in operation since 2004; and the OSNAP array (OSNAP, 2023; Lozier et al., 2019) at nominal 60° N (subpolar North Atlantic) and operational since 2014. The AMOC estimates from the

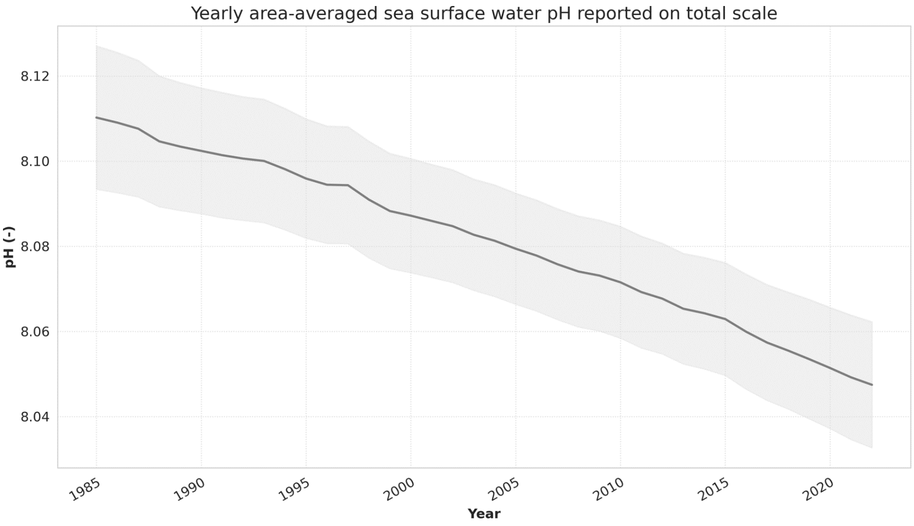

Figure 9. Time series of annual global mean surface sea water pH reported on a total scale over the period 1985–2022 and associated uncertainties (range). Product ref. OA.2.

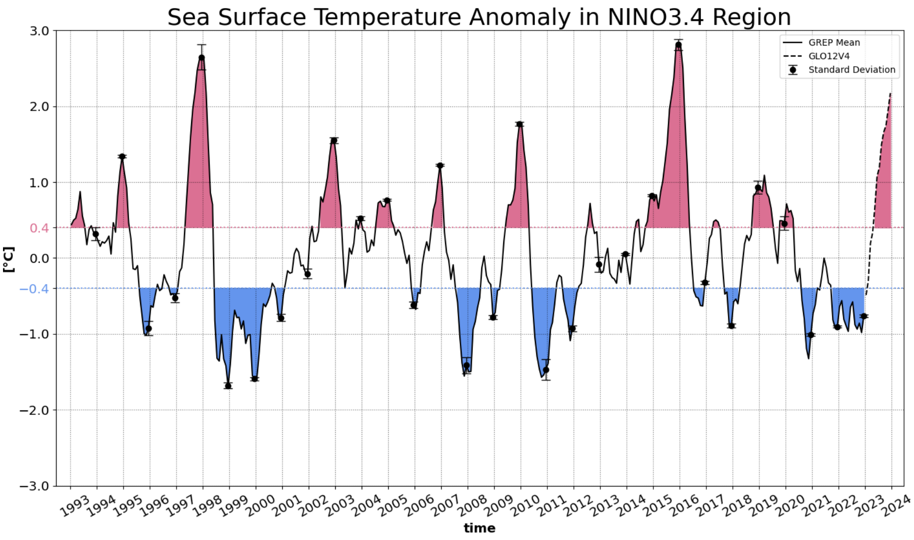

Figure 10. Monthly ensemble mean (solid line) and spread (bars) of sea surface temperature anomalies (relative to the 1993–2014 climatology) averaged over the NINO box 3.4 (5° S–5° N, 170–120° W). Product ref. OV.1 based on product ref. OHC.8 for the period 1993–2022 and extended up to December 2023 using product ref. SI.4 (using GLORYS2V4 (product ref. OHC.8) 1993–2014 as climatology).

arrays make use of moored instruments, ship and float data, and data from satellites. Variability in the AMOC influences global ocean heat content (OHC) and heat/freshwater transport, global ocean carbon uptake, nutrient redistribution, and sea level change (Fox-Kemper et al., 2021).

The 2014–2020 OSNAP observational period in the subpolar North Atlantic reveals robust seasonal variability driven by the wintertime formation and export of dense water and by the seasonally varying Ekman transport amplified by the positive phase of the North Atlantic Oscillation (Fu et al., 2023). While combining records from ocean reanalyses (Jackson et al., 2018; Baker et al., 2022, 2023) and direct observations from the RAPID array (Moat et al., 2023) monitoring of the AMOC can be established from 1993 onwards (Fig. 11). The results clearly visualize the challenge of detecting any long-term change of AMOC as discussed in Box 1, as records show large uncertainties and are dominated by large interannual to decadal-scale variations over a period that is too short to capture any eventual slowdown in the AMOC strength.

The AMOC has been identified as one of the tipping elements in the climate system with various implications for Earth's climate (Lenton et al., 2008; Boers, 2021; McKay et al., 2022; Chen and Tung, 2023; Westen et al., 2024; Rahmstorf, S., 2024). According to the most recent IPCC assessment, there is low confidence that the AMOC has declined during the 20th century (Gulev et al., 2021), but it is projected to very likely weaken over the 21st century for all emissions scenarios (IPCC, 2021). The assessment further states that an abrupt collapse of the AMOC cannot be ruled out, which would very likely cause abrupt shifts in regional weather patterns and water cycle, such as a southward shift in the tropical rain belt, weakening of the African and Asian monsoons and strengthening of Southern Hemisphere monsoons, and drying in Europe (IPCC, 2021).

However, scientific controversy prevails in published literature as it is difficult to quantify the impact of anthropogenic warming on the AMOC due to its strong interannual to multi-decadal fluctuations and short observational records that complicates the long-term trend detection (Jackson et al., 2022; Zhu et al., 2023). For example, assessments show that there is low confidence in reconstructed and modelled AMOC changes for the 20th century because of their low agreement in quantitative trends (Fox-Kemper et al., 2021). Some studies have found that the AMOC is slowing down, such as for example the analysis of proxy records revealing that during recent decades, the AMOC reached its weakest point for more than a thousand years (Caesar et al., 2021) - a result which is contradicted by the recent study of (Chen and Tung, 2023). A more recent statistical-based study estimates a collapse of the AMOC to occur around mid-century under the current scenario of future emissions (Ditlevsen and Ditlevsen, 2023), as well as a recent study which discusses based on model results that AMOC is on tipping course (Westen et al., 2024).

Box 1. Did AMOC change?

3 Ocean extremes

3.1 Marine heatwaves

A marine heatwave (MHW) is commonly defined as a period of at least 5 consecutive days of anomalously warm sea surface temperatures exceeding the 90th climatological percentile threshold (Hobday et al., 2016). In other words, it is seen as an extreme event during which a given region heats way past its regular range of temperature variations. The regular range of variations is defined in practice over a reference period (here 1993–2016), which is discussed as a sensible choice (Amaya et al., 2023). Marine heatwaves are globally observed and are emerging as important stressors to marine ecosystems at the individual, collective, and community levels, also including coral reefs and seagrass beds (Welch et al., 2023; Smith et al., 2023; Wakelin et al., 2021; Marba and Duarte, 2010). They can trigger the migration of species and mass extinctions and lead to significant economic losses in fisheries and aquaculture (Garrabou et al., 2022; Smith et al., 2023; Oliver et al., 2019; Holbrook et al., 2022).

The frequency, duration, and intensity of marine heatwaves have increased over the past decades under global warming (Peal et al., 2023; Yao et al., 2022; Oliver et al., 2019; IPCC, 2021). The fraction of the global ocean surface that did not experience any MHW event over the year has increased from about 50 % in the 1980s to about 80 % in the most recent years (Fig. 12). The ocean surface fraction affected by strong MHW events has doubled since 2008, from about 20 % to 40 % in recent years, and severe and extreme marine heatwave events also show positive trends in terms of surface extent over the same period. However, the positive trend of extreme marine heatwave events is dampened when excluding sea-ice-covered regions from the computation (Fig. 12), while the impact on other marine heatwave categories is minor (not shown). In these regions, the marine heatwave detections may be less optimal and may require further scientific evaluations and refinements both in terms of sea surface temperature data (Vazquez-Cuervo et al., 2022; Castro et al., 2023) and marine heatwave detection methodology (Hu et al., 2020; Huang et al., 2021). The yearly averaged maximum duration of marine heatwave events doubled between 2008 and 2023 (from 20 to about 40 d), while it was relatively stable from 1982 to the mid-2000s (Fig. 12). The global ocean surface fraction affected by marine heatwave events lasting more than 1 month experienced a 5-fold increase between the mid-2000s (about 12 %) and 2023 (55 %). Similar results are obtained for the marine heatwave durations when excluding the sea-ice-covered regions.

These results also highlight the interannual variability of marine heatwave events and the major role of climate drivers such as ENSO, as larger fractions of the global ocean tend to experience marine heatwave events during El Niño years and smaller regions during La Niña periods (Oliver et al., 2019) (Fig. 13). Larger fractions of the ocean were affected by strong and severe marine heatwave events during the strong El Niño years (1982–1983, 1997–1998, 2010, 2015–2016), and the yearly averaged maximum marine heatwave duration was also larger for these years (Fig. 12).

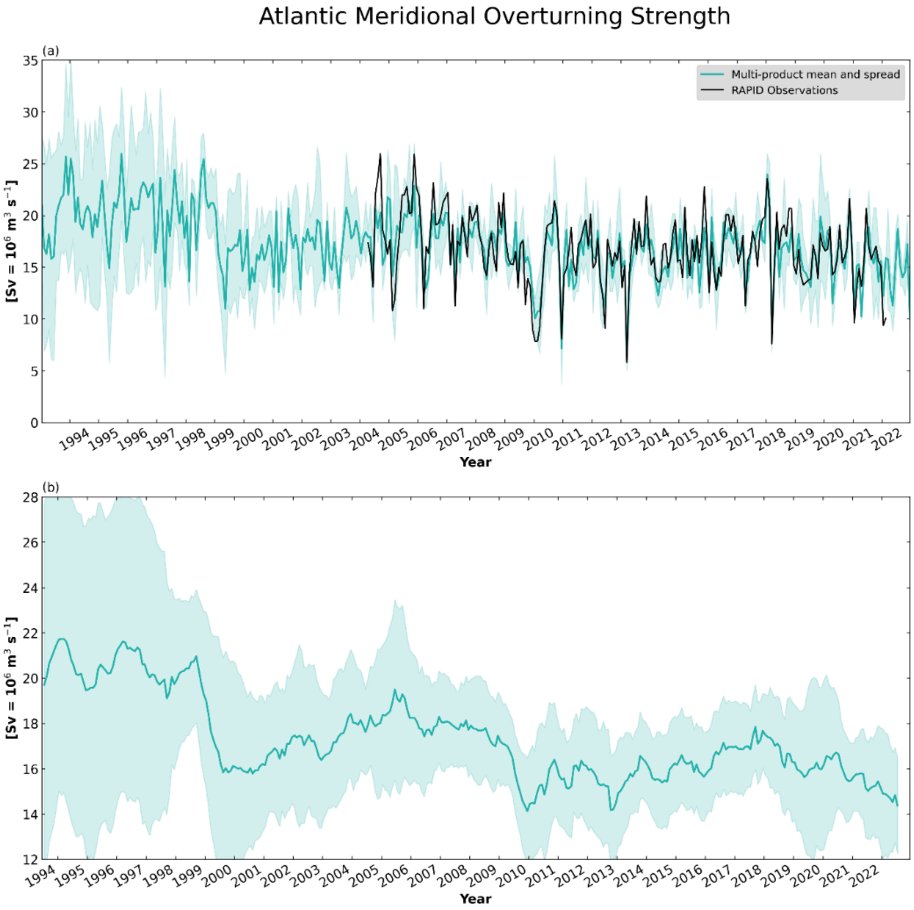

Figure 11. Temporal evolution of the Atlantic Meridional Overturning Circulation (AMOC) strength at 26.5° N obtained by integrating the meridional transport at 26.5° N across the Atlantic basin (zonally) and then cumulatively integrating over depth. Its maximum value in depth is then taken as the strength in Sverdrups ($\mathrm{Sv} = 1 \times 10^6\,\mathrm{m}^3\,\mathrm{s}^{-1}$). The green line and shading (2 times the standard deviation) are based on product ref. OV.2 computed from product ref. OHC.8. The black line shows the observational record from the RAPID array (Moat et al., 2023). Panel **(a)** shows monthly mean values, and panel **(b)** shows interannual variations by applying a 12-month running mean.

In 2022, 74 % of the global ocean experienced a marine heatwave, whatever its category, and large areas were affected by strong (34 %) or even severe (7 %) and extreme (5 %) marine heatwaves (Table 2). For 28 % of the ocean surface, the maximum marine heatwave category detected in 2022 was moderate. These numbers are on the order of those obtained by Peal et al. (2023). The most persistent and most prominent feature for marine heatwaves, lasting over a period of 6 months and longer, temporarily related to severe and extreme categories, occurred in the Coral Sea, also affecting waters off northeast Australia and the Melanesian Pacific island states (Fig. 14). Marine heatwaves lasting more than 4 months in 2022 and reaching up to severe and extreme categories are reported for the central subtropical Pacific, the South Atlantic, and the western Mediterranean Sea.

In 2023, 90 % of the global ocean surface was hit by at least one marine heatwave event. This increase compared to 2022 is mainly due to evolving El Niño conditions in winter 2023 and to particularly warm surface waters in the North Atlantic Ocean. For 26 % of the ocean surface, the maximum marine heatwave category detected was moderate. Larger areas were affected by strong (43 %), severe (14 %), and extreme (8 %) marine heatwaves. The regions that experienced the most prominent marine heatwave events in 2023, lasting more than 6 months and reaching up to severe and extreme categories, include (Fig. 15) the following:

- the tropical Pacific, driven by the emerging 2023–2024 El Niño event;
- off the coast of Peru and linked to the so-called “coastal El Niño”;
- the northern tropical Atlantic Ocean;
- the Southern Ocean poleward of 40° S, with large areas of extreme category in the Atlantic and Pacific.

Areas where most prominent marine heatwaves lasted 3 to 6 months and reached up to extreme and severe categories include the following:

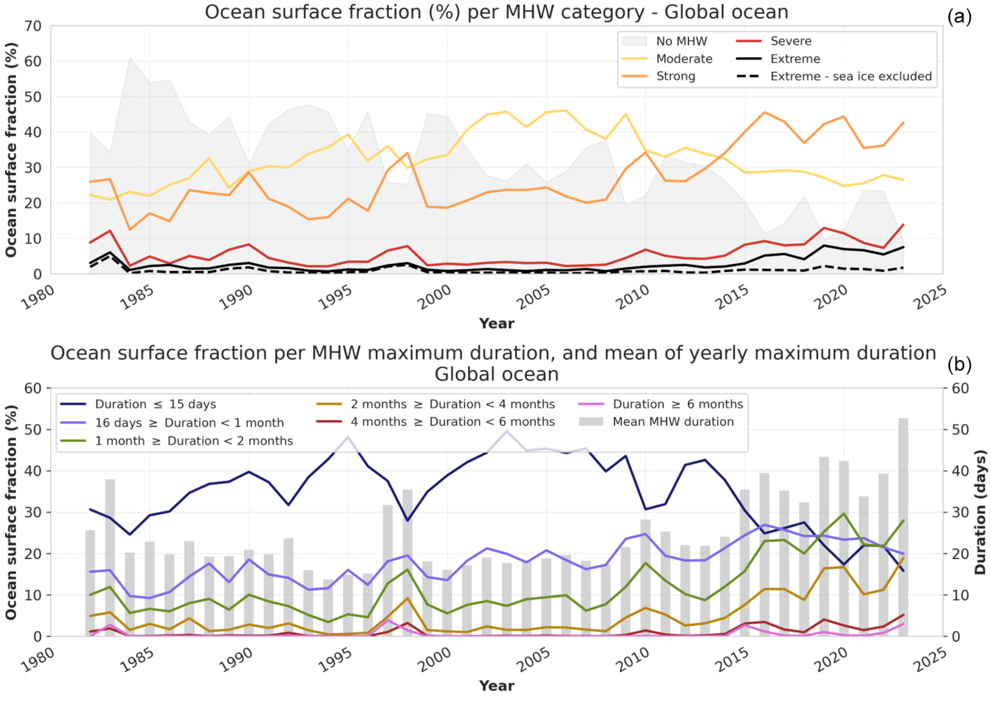

Figure 12. **(a)** Percentage of global ocean surface where the maximum MHW category detected was moderate, strong, severe, or extreme (Hobday et al., 2016), or there was no MHW. The dashed black line shows the same information for extreme categories when excluding sea ice regions from the computation (see Fig. 14 for sea ice mask applied, minor impact for the other categories). These ocean fraction estimates are done following the same method as Hobday et al. (2018). **(b)** Percentage of global ocean surface where the maximum MHW duration was within a given period (lines) and yearly mean of maximum MHW durations (bars). The method of Hobday et al. (2016) is used and is derived from the products ref. SST.1 and SST.2.

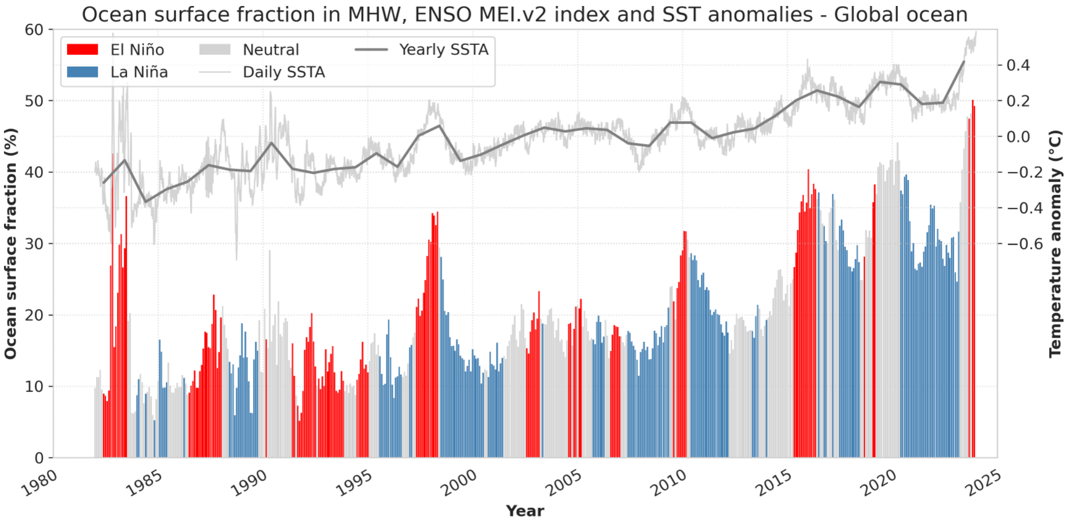

Figure 13. Upper plot: globally averaged daily (light line) and annual (bold line) SST anomalies (reference period 1993–2016) from products ref. SST.1 and SST.2. Bottom plot: the amplitude of the bars shows the percentage of global ocean surface where MHW were detected. The colours of the bars correspond to the ENSO MEI.v2 (multivariate) index values (red for El Niño conditions when MEI ≥ 0.5, blue for La Niña conditions when MEI ≤ -0.5, and grey for neutral conditions when MEI is between -0.5 and 0.5 (product ref. SST.5)). The evaluation of this MHW indicator is done following the method of Hobday et al. (2016) and is derived from the products ref. SST.1 and SST.2.

Table 2. Percentage of global ocean surface hit by a MHW event in 2022 and 2023, depending on the category. The second column provides the same information but considering the global ocean without the sea-ice-covered regions (see Fig. 14 for sea ice mask applied). These ocean fraction estimates are done following the same method as Hobday et al. (2018).

Percentage of ocean surface hit by a MHW	Global		Global – sea ice excluded	
	2022	2023	2022	2023
All categories	74 %	90 %	73 %	92 %
Max category 1 (moderate)	28 %	26 %	30 %	29 %
Max category 2 (strong)	34 %	43 %	36 %	46 %
Max category 3 (severe)	7 %	14 %	6 %	14 %
Max category 4 or higher (extreme)	5 %	8 %	1 %	2 %

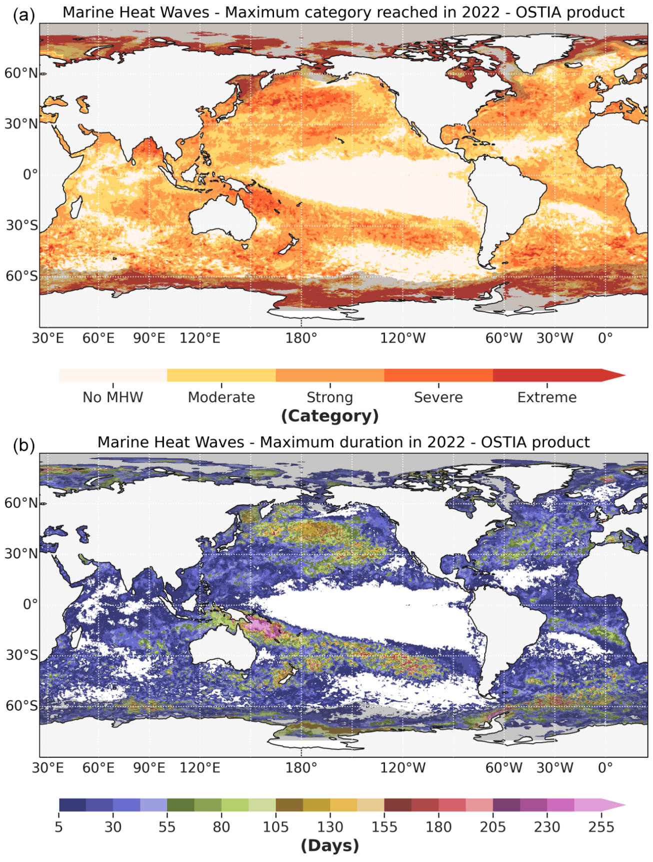

Figure 14. (a) Maximum category of marine heatwave reached in 2022 and **(b)** maximum duration of marine heatwave events in 2022. The evaluation of this indicator is done following the method of Hobday et al. (2016) and is derived from the products ref. SST.1 and SST.2. The areas shaded in grey correspond to regions where there was at least 1 d of sea ice (sea ice concentration larger than 0.15 in the product ref. SST.1) during the climatological reference period (1993–2016), implying potentially less accurate marine heatwave detections (see text for more details).

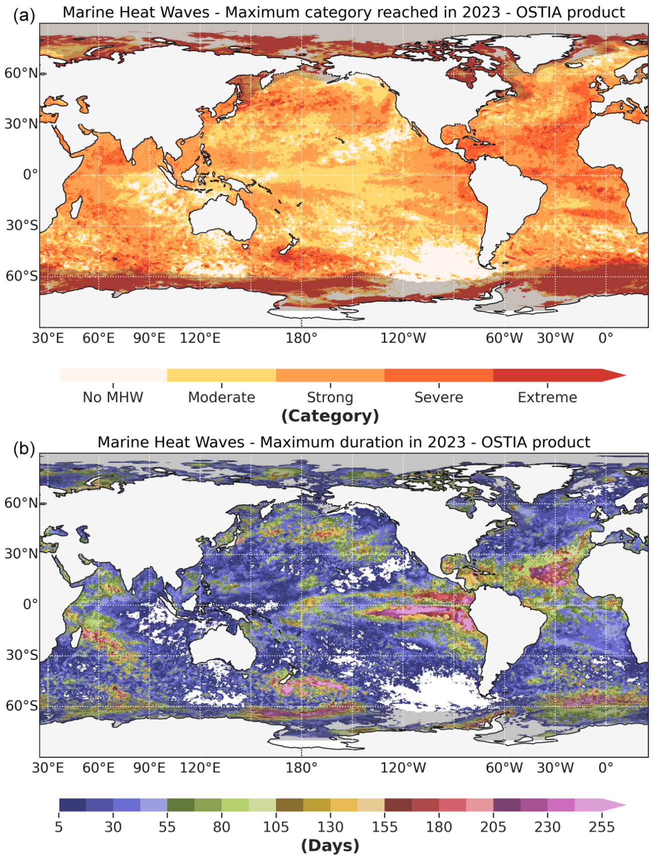

Figure 15. Same as Fig. 14 but for the year 2023.

- the southern tropical Indian Ocean;
- the northern tropical Atlantic up to the coast of Europe and central America;
- the central northern subpolar Pacific;
- the Arctic Ocean, particularly in the Kara, Beaufort, Lincoln, and East Siberian seas.

3.2 Wind extremes over the ocean

Extreme wind speeds over the ocean surface and associated stormy weather and rough surface ocean conditions are particularly destructive natural hazards. In coastal regions, the combination of high waves and storm surges can lead to

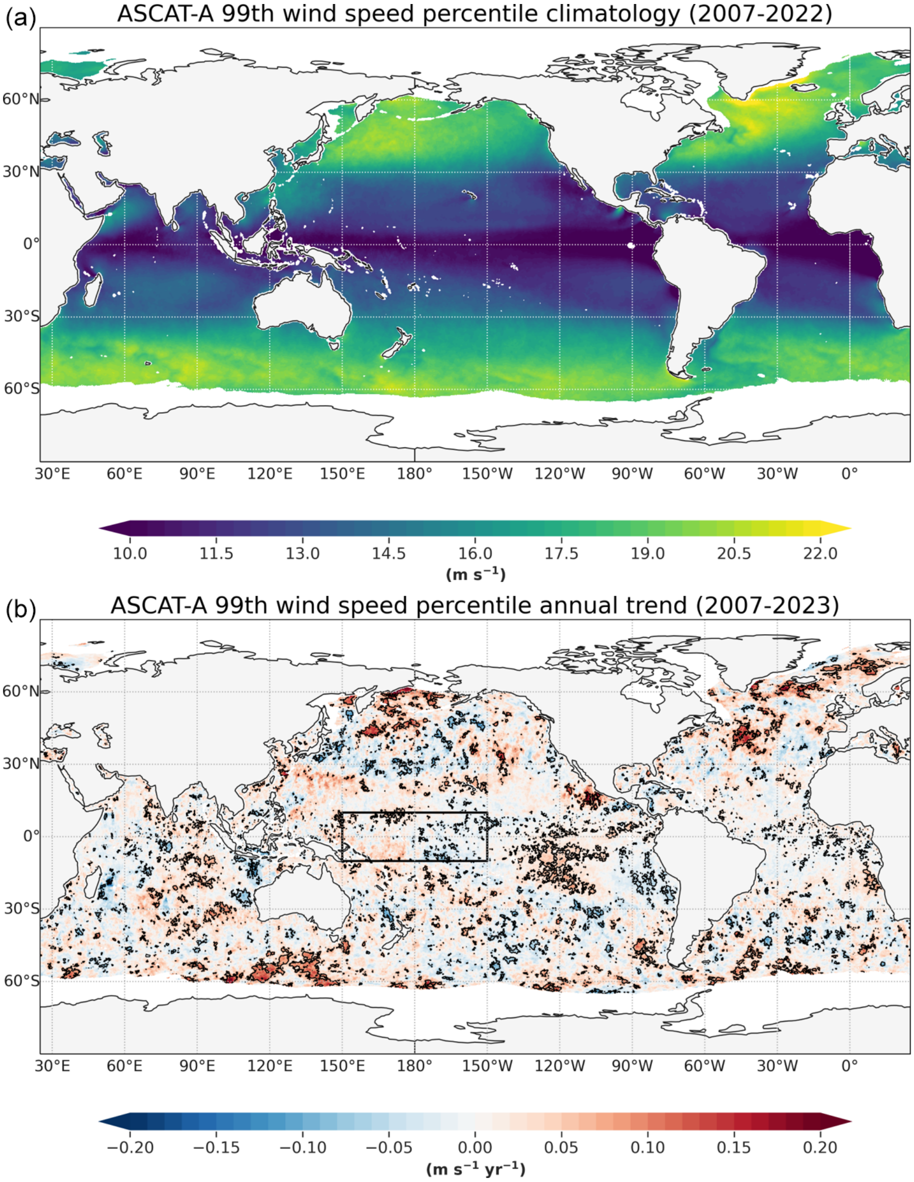

Figure 16. The 99th wind speed percentile. **(a)** Climatology (2007–2022) and **(b)** annual trend (2007–2023). Areas with trends significant above the 90 % confidence level are outlined in black. Computation at 0.25° resolution from product ref. Wind.1 (ASCAT-A) following the method of Giesen and Stoffelen (2022). The black box shows the region used in Fig. 17.

flooding, coastline erosion, coastal water quality degradation, and ecosystem destructions (Sopkin et al., 2014; Harley et al., 2017; Amores et al., 2020; Wetz and Yoskowitz, 2013; González-De Zayas et al., 2021; Bonnington et al., 2023; Patrick et al., 2022; Alvarez-Fanjul et al., 2022; Giesen et al., 2021). Massive rainfall associated with storms can result in inundation and landslides (Negri et al., 2005). The increasing demographic pressure in coastal regions can increase the risks and vulnerability of populations if disaster risk mitigation and reduction practices (e.g. shelters, early-warning systems) are not adopted (Peduzzi et al., 2012; Alvarez-Fanjul et al., 2022; She and Nielsen, 2019; de Alfonso et al., 2020; Giesen et al., 2021). Many economic sectors such as tourism, ports, and fishing can be impacted by extreme coastal events (Verschuur et al., 2023; Kunze, 2021; de Alfonso et al., 2020). In the open ocean, storms and associated high winds and waves can affect offshore infrastructures as well as marine traffic (Mattu et al., 2022; Lam and Lassa, 2016; Staneva et al., 2020).

Regions that have been affected by the most extreme ocean surface wind speeds (>22 $\mathrm{m\,s^{-1}}$) over the 2007–2022 period (Fig. 16) (Sampe and Xie, 2007; Giesen and Stoffelen, 2022) include the central and subpolar parts of the North Atlantic Ocean, especially the southern tip and eastern coast of Green-

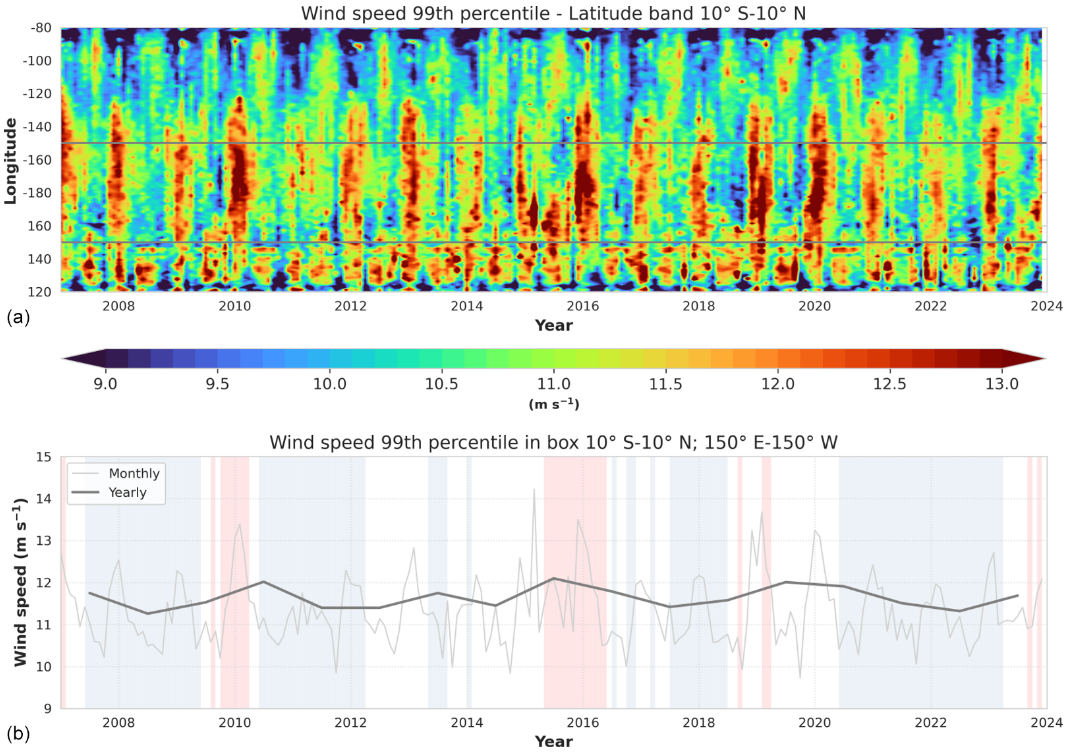

Figure 17. **(a)** Monthly wind speed 99th percentile from product ref. Wind.1 (ASCAT-A) between latitudes 10° S and 10° N in the western tropical Ocean (see box in Fig. 16), presented as a function of longitude and time. The horizontal grey lines show the longitudes 150° E and 150° W. **(b)** Time series of monthly and yearly wind speed 99th percentile from product ref. Wind.1 (ASCAT-A) for the box shown in Fig. 16. The shading corresponds to the ENSO MEI.v2 index values: red for El Niño conditions when MEI ≥ 0.5, blue for La Niña conditions when MEI ≤ -0.5, and white for neutral conditions (product ref. SST.5).

land. It should be noted that the values given here are representative of the 1 % highest ocean surface wind speeds (i.e. reported at 99th percentiles). The North Pacific Ocean and the Southern Ocean are the other regions with the strongest extreme wind speeds ($>20\,\mathrm{m\,s^{-1}}$) in the long-term climatology. Extreme wind speeds reach about $13\,\mathrm{m\,s^{-1}}$ in the tropical bands (10–30° of latitude), while they are low (around or below $10\,\mathrm{m\,s^{-1}}$) in the equatorial band (0–10° of latitude).

Typically, tropical cyclones are too short-lived and small to be reflected in these numbers. Further analyses are required to address the role of tropical cyclones in affecting the climatological extreme wind speeds, particularly with respect to the percentile method used, and the sensitivity to the spatial resolution of the wind products. Local patterns of extreme wind speeds can also be noted, such as in the Gulf of Tehuantepec, off Mexico in the Pacific Ocean (e.g., Zamudio et al., 2006; Romero-Centeno et al., 2003).

Results from the recent IPCC sixth assessment report reflect the challenge of attributing long-term change in wind extremes explained by the interplay with natural variability, the length of the time series, and uncertainties in the estimates. For example, past changes of maximum wind speeds and other measures of dynamical intensity of extratropical cyclones have been assessed with low confidence (Seneviratne et al., 2021). The report also assessed that tropical and extra-tropical cyclone tracks tend to migrate poleward as the tropical climate zones expand with global warming. However, while none of the observed changes of Category 3–5 tropical cyclone instances can be explained by natural variability alone, their observed increase is assessed as likely. With respect to future evolution, there is high confidence that the proportion of intense tropical cyclones, average peak tropical cyclones wind speeds, and peak wind speeds of the most intense tropical cyclones will increase on the global scale with increasing global warming (Seneviratne et al., 2021).

Due to their spatial and temporal abundance, satellite instruments excel in the monitoring of long-term trends in ocean surface wind extremes (Fig. 16). Analysing long-term trends of extreme wind speeds has revealed several areas of significant increase in extreme wind speeds over the past 16 years (2007–2023) (Fig. 16). However, results are identified to be highly sensitive to methodological approaches and trend periods, challenging the attribution of long-term change and the interplay of natural variability (Giesen and Stoffelen, 2022). The main regions where positive trend features remain stable when addressing different timescales (2007–2020 versus 2007–2023) are the central North Atlantic Ocean Gulf Stream region (30–35° N, 30–50° W), the subpolar Atlantic region between Greenland and south of Iceland, the Bering Sea and the northwest Pacific Ocean, the subtropical Indian Ocean, and the sector of Southern Ocean located south of Australia (Fig. 16b). Decreases in wind speed extremes are also stable in the Tasman Front. However, further analysis, specific detection, and attribution studies, as well as longer time series, are needed in the future for the identification of long-term trends in observed extreme wind speeds.

In some areas, interannual variability such as large-scale climate-mode teleconnections (El Niño–Southern Oscillation/ENSO, North Atlantic Oscillation, Pacific Decadal Oscillation, Indian Ocean Dipole, etc.) are known to affect extreme winds and storminess regimes (Krueger et al., 2019; Roose et al., 2023; Yuan and Cao, 2013; and Lin et al., 2020), as well as their consecutive impacts on the ocean (waves, storm surges) (Holbrook et al., 2020). For example, wind speed extremes in the western tropical Pacific are closely correlated with the ENSO index (Fig. 17), with more extreme wind speeds and longer-lived tropical cyclones during El Niño years (Hu et al., 2017; Eusebi Borzelli and Carniel, 2023; Camargo and Sobel, 2005). A positive trend is detected in this region for the period 2007–2020 in Giesen and Stoffelen (2022) because ENSO was negative (La Niña) in the early years (2007-2008) and positive (El Niño) in 2015–2016 and 2019 (Fig. 17). La Niña conditions in 2020–2022 almost entirely dampened the positive trend in the region when adding the years 2021–2023 to the extreme wind speed trend estimation (Fig. 16b).

In summary, our results indicate that extreme wind speeds over the ocean show regional patterns but likewise are highly variable in space and time. Satellite-based wind observations are the major source for analysis and statistics of extreme wind events over the ocean. In particular, for extreme winds, however, the satellite-based estimates are questionable, and, hence, regular and state-of-the-art in situ monitoring of winds is and will be essential to inform national meteorological and oceanographic services and feed their early-warning systems with accurate and robust information (see for example the WMO Regional Climate Centers: CSIS, 2024).

Code availability. All codes are available upon request.

Data availability. All data used are available, and their sources are listed in the Supplement.

Supplement. The supplement related to this article is available online at: https://doi.org/10.5194/sp-4-osr8-1-2024-supplement.

Author contributions. KvS, LM, MC, FG: conceptualization, methodology, writing (original draft), investigation, supervision, and formal analysis. All authors: writing (review and editing) and data curation.

Competing interests. At least one of the (co-)authors is a member of the editorial board of *State of the Planet*. The peer-review process was guided by an independent editor, and the authors also have no other competing interests to declare.

Disclaimer. Please note that this article has undergone editorial review only.

References

Abernathey, R. P., Cerovecki, I., Holland, P. R., Newsom, E., Mazloff, M., and Talley, L. D.: Water-mass transformation by sea ice in the upper branch of the Southern Ocean overturning, Nat. Geosci., 9, 596–601, https://doi.org/10.1038/ngeo2749, 2016.

Ablain, M., Jugier, R., Zawadki, L., Taburet, N., Cazenave, A., and Meyssignac, B.: The TOPEX-A drift and impacts on GMSL time series, AVISO Website, https://meetings.aviso.altimetry.fr/fileadmin/user_upload/tx_ausyclsseminar/files/Poster_OSTST17_GMSL_Drift_TOPEX-A.pdf (last access: 11 September 2024), 2017.

Abram, N., Gattuso, J.-P., Prakash, A., Cheng, L., Chidichimo, M. P., Crate, S., Enomoto, H., Garschagen, M., Gruber, N., Harper, S., Holland, E., Kudela, R. M., Rice, J., Steffen, K., and von Schuckmann, K.: Framing and Context of the Report, in: IPCC Special Report on the Ocean and Cryosphere in a Changing Climate, edited by: Pörtner, H.-O., Roberts, D. C., Masson-Delmotte, V., Zhai, P., Tignor, M., Poloczanska, E., Mintenbeck, K., Alegria, A., Nicolai, M., Okem, A., Petzold, J., Rama, B., and Weyer, N. M., Cambridge University Press, Cambridge, UK and New York, NY, USA, 73–129, https://doi.org/10.1017/9781009157964.003, 2019.

Alvarez-Fanjul, E., Pérez Gomez, B., de Alfonso Alonso-Muñoyerro, M., Lorente, P., Garcia Sotillo, M., Lin-Ye, J., Aznar Lecocq, R., Ruiz Gil de la Serna, M., Perez Rubio, S., Clementi, E., Coppini, G., Garcia-Leon, M., Fernandes, M., Garcia Valdecasas, J., Garcia Valdecasas, J. M., Santos Muñoz, D., Luna Rico, M. Y., Mestres, M., Molina, R., Tintoré, J., Mourre, B., Masina, S., Mosso, C., Reyes, E., and Santana, A.: Western Mediterranean record-breaking storm Gloria: An integrated assessment based on models and observations, in: Copernicus Ocean State Report, Issue 6, J. Oper. Oceanogr., 15, s151–s159, https://doi.org/10.1080/1755876X.2022.2095169, 2022.

Amaya, D., Jacox, M. G., Fewings, M. R., Saba, V. S., Stuecker, M. F., Rykaczewski, R. R., Ross, A. C., Stock, C. A., Capotondi, A., Petrik, C. M., Bograd, S. J., Alexander, M. A., Cheng, W., Hermann, A. J., Kearney, K. A., and Powell, B. S.: Marine heatwaves need clear definitions so coastal communities can adapt, Nature, 616, 29–32, https://doi.org/10.1038/d41586-023-00924-2, 2023.

Amores, A., Marcos, M., Carrió, D. S., and Gómez-Pujol, L.: Coastal impacts of Storm Gloria (January 2020) over the north-western Mediterranean, Nat. Hazards Earth Syst. Sci., 20, 1955–1968, https://doi.org/10.5194/nhess-20-1955-2020, 2020.

Armitage, T. W. K., Manucharyan, G. E., Petty, A. A., Kwok, R., and Thompson, A. F.: Enhanced eddy activity in the Beaufort Gyre in response to sea ice loss, Nat. Commun., 11, 761, https://doi.org/10.1038/s41467-020-14449-z, 2020.

Arrigo, K. R., van Dijken, G. L., Castelao, R. M., Luo, H., Rennermalm, Å. K., Tedesco, M., Mote, T. L., Oliver, H., and Yager, P. L.: Melting glaciers stimulate large summer phytoplankton blooms in southwest Greenland waters, Geophys. Res. Lett., 44, 6278–6285, https://doi.org/10.1002/2017GL073583, 2017.

Baker, J., Renshaw, R., Jackson, L., Dubois, C., Iovino, D., and Zuo, H.: Overturning variations in the subpolar North Atlantic in an ocean reanalyses ensemble, in: Copernicus Ocean State Report, Issue 6, J. Oper. Oceanogr., 15, s16–s20, https://doi.org/10.1080/1755876X.2022.2095169, 2022.

Baker, J. A., Renshaw, R., Jackson, L. C., Dubois, C., Iovino, D., Zuo, H., Perez, R. C., Dong, S., Kersalé, M., Mayer, M., Mayer, J., Speich, S., and Lamont, T.: South Atlantic overturning and heat transport variations in ocean reanalyses and observation-based estimates, in: 7th edition of the Copernicus Ocean State Report (OSR7), edited by: von Schuckmann, K., Moreira, L., Le Traon, P.-Y., Grégoire, M., Marcos, M., Staneva, J., Brasseur, P., Garric, G., Lionello, P., Karstensen, J., and Neukermans, G., Copernicus Publications, State Planet, 1-osr7, 4, https://doi.org/10.5194/sp-1-osr7-4-2023, 2023.

Barnoud, A., Pfeffer, J., Guérou, A., Frery, M. L., Siméon, M., Cazenave, A., Chen, J., Llovel, W., Thierry, V., Legeais, J. F., and Ablain, M.: Contributions of Altimetry and Argo to Non-Closure of the Global Mean Sea Level Budget Since 2016, Geophys. Res. Lett., 48, e2021GL092824, https://doi.org/10.1029/2021GL092824, 2021.

Bindoff, N. L., Cheung, W. W. L., Kairo, J. G., Aristegui, J., Guinder, V. A., Hallberg, R., Hilmi, N., Jiao, N., Karim, M. S., Levin, L., O'Donoghue, S., Purca Cuicapusa, S. R., Rinkevich, B., Suga, T., Tagliabue, A., and Williamson, P.: Changing Ocean, Marine Ecosystems, and Dependent Communities, in: IPCC Special Report on the Ocean and Cryosphere in a Changing Climate, edited by: Pörtner, H.-O., Roberts, D. C., Masson-Delmotte, V., Zhai, P., Tignor, M., Poloczanska, E., Mintenbeck, K., Alegria, A., Nicolai, M., Okem, A., Petzold, J., Rama, B., and Weyer, N. M., Cambridge University Press, Cambridge, UK and New York, NY, USA, 447–587, https://doi.org/10.1017/9781009157964.007, 2019.

Bintanja, R., Van Oldenborgh, G. J., Drijfhout, S. S., Wouters, B., and Katsman, C. A.: Important role for ocean warming and increased ice-shelf melt in Antarctic sea-ice expansion, Nat. Geosci., 6, 376–379, https://doi.org/10.1038/ngeo1767, 2013a.

Bintanja, R., Van Oldenborgh, G. J., Drijfhout, S. S., Wouters, B., and Katsman, C. A.: Important role for ocean warming and increased ice-shelf melt in Antarctic sea-ice expansion, Nat. Geosci., 6, 376–379, https://doi.org/10.1038/ngeo1767, 2013b.

Boers, N.: Observation-based early-warning signals for a collapse of the Atlantic Meridional Overturning Circulation, Nat. Clim. Change, 11, 680–688, https://doi.org/10.1038/s41558-021-01097-4, 2021.

Bonnington, A. C., Jamieson, R. C., Smith, K. A., Oliver, A., Johnston, L. H., LeRoux, N. K., Somers, L. D., and Kurylyk, B. L.: Impacts of Extratropical Cyclone Fiona on a sensitive coastal lagoon ecosystem, Limnol. Oceanogr., 68, 2703–2715, https://doi.org/10.1002/LNO.12452, 2023.

Caesar, L., McCarthy, G. D., Thornalley, D. J. R., Cahill, N., and Rahmstorf, S.: Current Atlantic Meridional Overturning Circulation weakest in last millennium, Nat. Geosci., 14, 118–120, https://doi.org/10.1038/s41561-021-00699-z, 2021.

Cai, W., Santoso, A., Collins, M., Dewitte, B., Karamperidou, C., Kug, J. S., Lengaigne, M., McPhaden, M. J., Stuecker, M. F., Taschetto, A. S., Timmermann, A., Wu, L., Yeh, S. W., Wang, G., Ng, B., Jia, F., Yang, Y., Ying, J., Zheng, X. T., Bayr, T., Brown, J. R., Capotondi, A., Cobb, K. M., Gan, B., Geng, T., Ham, Y. G., Jin, F. F., Jo, H. S., Li, X., Lin, X., McGregor, S., Park, J. H., Stein, K., Yang, K., Zhang, L., and Zhong, W.: Changing El Niño–Southern Oscillation in a warming climate, Nat. Rev. Earth Environ.,, 2, 628–644, https://doi.org/10.1038/s43017-021-00199-z, 2021.

Cai, W., Gao, L., Luo, Y., Li, X., Zheng, X., Zhang, X., Cheng, X., Jia, F., Purich, A., Santoso, A., Du, Y., Holland, D. M., Shi, J. R., Xiang, B., and Xie, S. P.: Southern Ocean warming and its climatic impacts, Sci. Bull. (Beijing), 68, 946–960, https://doi.org/10.1016/J.SCIB.2023.03.049, 2023.

Camargo, S. J. and Sobel, A. H.: Western North Pacific Tropical Cyclone Intensity and ENSO, J. Climate, 18, 2996–3006, https://doi.org/10.1175/JCLI3457.1, 2005.

Canadell, J. G., Monteiro, P. M. S., Costa, M. H., da Cunha, L., Cox, P. M., Eliseev, A. V, Henson, S., Ishii, M., Jaccard, S., Koven, C., Lohila, A., Patra, P. K., Piao, S., Rogelj, J., Syampungani, S., Zaehle, S., and Zickfeld, K.: Global Carbon and other Biogeochemical Cycles and Feedbacks, in: Climate Change 2021: The Physical Science Basis. Contribution of Working Group I to the Sixth Assessment Report of the Intergovernmental Panel on Climate Change, edited by: Masson-Delmotte, V., Zhai, P., Pirani, A., Connors, S. L., Péan, C., Berger, S., Caud, N., Chen, Y., Goldfarb, L., Gomis, M. I., Huang, M., Leitzell, K., Lonnoy, E., Matthews, J. B. R., Maycock, T. K., Waterfield, T., Yelekçi, O., Yu, R., and Zhou, B., Cambridge University Press, Cambridge, United Kingdom and New York, NY, USA, 673–816, https://doi.org/10.1017/9781009157896.007, 2021.

Castro, S. L., Wick, G. A., Eastwood, S., Steele, M. A., and Tonboe, R. T.: Examining the Consistency of Sea Surface Temperature and Sea Ice Concentration in Arctic Satellite Products, Remote Sensing, 15, 2908, https://doi.org/10.3390/RS15112908, 2023.

Cavole, L. M., Demko, A. M., Diner, R. E., Giddings, A., Koester, I., Pagniello, C. M. L. S., Paulsen, M. L., Ramirez-Valdez, A., Schwenck, S. M., Yen, N. K., Zill, M. E., and Franks, P. J. S.: Biological impacts of the 2013–2015 warm-water anomaly in the northeast Pacific: Winners, Losers, and the Future, Oceanography, 29, 273–285, https://doi.org/10.5670/OCEANOG.2016.32, 2016.

Cazenave, A. and Moreira, L.: Contemporary sea-level changes from global to local scales: A review, P. Roy. Soc. A-Math. Phy., 478, 20220049, https://doi.org/10.1098/RSPA.2022.0049, 2022.

Centurioni, L. R., Turton, J. D., Lumpkin, R., Braasch, L., Brassington, G., Chao, Y., Charpentier, E., Chen, Z., Corlett, G., Dohan, K., Donlon, C., Gallage, C., Hormann, V., Ignatov, A., Ingleby, B., Jensen, R., Kelly-Gerreyn, B. A., Koszalka, I. M., Lin, X., Lindstrom, E., Maximenko, N., Merchant, C. J., Minnett, P., O'Carroll, A. G., Paluszkiewicz, T., Poli, P., Poulain, P., Reverdin, G., Sun, X., Swail, V., Thurston, S., Wu, L., Yu, L., Wang, B., and Zhang, D.: Global in-situ observations of essential climate and ocean variables at the air-sea interface, Front. Mar. Sci., 6, 433760, https://doi.org/10.3389/FMARS.2019.00419, 2019.

Chen, J., Tapley, B., Wilson, C., Cazenave, A., Seo, K. W., and Kim, J. S.: Global Ocean Mass Change From GRACE and GRACE Follow-On and Altimeter and Argo Measurements, Geophys. Res. Lett., 47, e2020GL090656, https://doi.org/10.1029/2020GL090656, 2020.

Chen, X. and Tung, K. K.: Evidence lacking for a pending collapse of the Atlantic Meridional Overturning Circulation, Nat. Clim. Change, 14, 40–42, https://doi.org/10.1038/s41558-023-01877-0, 2023.

Cheng, L., Trenberth, K. E., Fasullo, J., Boyer, T., Abraham, J., and Zhu, J.: Improved estimates of ocean heat content from 1960 to 2015, Sci. Adv., 3, e1601545, https://doi.org/10.1126/SCIADV.1601545, 2017.

Cheng, L., von Schuckmann, K., Abraham, J. P., Trenberth, K. E., Mann, M. E., Zanna, L., England, M. H., Zika, J. D., Fasullo, J. T., Yu, Y., Pan, Y., Zhu, J., Newsom, E. R., Bronselaer, B., and Lin, X.: Past and future ocean warming, Nat. Rev. Earth Environ., 3, 776–794, https://doi.org/10.1038/s43017-022-00345-1, 2022.

Cheng, L., von Schuckmann, K., Miniére, A., Hakuba, M. Z., Purkey, S., Schmidt, G. A., and Pan, Y.: Ocean heat content in 2023, Nat. Rev. Earth Environ., 5, 232–234, https://doi.org/10.1038/s43017-024-00539-9, 2024.

Ciracì, E., Rignot, E., Scheuchl, B., Tolpekin, V., Wollersheim, M., An, L., Milillo, P., Bueso-Bello, J. L., Rizzoli, P., and Dini, L.: Melt rates in the kilometer-size grounding zone of Petermann Glacier, Greenland, before and during a retreat, P. Natl. Acad. Sci. USA, 120, e2220924120, https://doi.org/10.1073/PNAS.2220924120, 2023.

Coulson, S., Dangendorf, S., Mitrovica, J. X., Tamisiea, M. E., Pan, L., and Sandwell, D. T.: A detection of the sea level fingerprint of Greenland Ice Sheet melt, Science, 377, 1550–1554, https://doi.org/10.1126/SCIENCE.ABO0926, 2022.

CSIS: Climate Services Information System, https://wmo.int/activities/climate-services-information-system, last access: 25 March 2024.

de Alfonso, M., Garcia-Valdecasas, J. M., Aznar, R., Perez-Gomez, B., Rodriguez, P., de los Santos, F. J., and Alvarez-Fanjul, E.: Record wave storm in the Gulf of Cadiz over the past 20 years and its impact on harbours, in: Copernicus Marine Service Ocean State Report, Issue 4, J. Oper. Oceanogr., 13, s137–s144, https://doi.org/10.1080/1755876X.2020.1785097, 2020.

de Steur, L., Sumata, H., Divine, D. V., Granskog, M. A., and Pavlova, O.: Upper ocean warming and sea ice reduction in the East Greenland Current from 2003 to 2019, Communications Earth & Environment, 4, 261, https://doi.org/10.1038/s43247-023-00913-3, 2023.

Ditlevsen, P. and Ditlevsen, S.: Warning of a forthcoming collapse of the Atlantic meridional overturning circulation, Nat. Commun., 14, 4254, https://doi.org/10.1038/s41467-023-39810-w, 2023.

Doney, S. C., Busch, D. S., Cooley, S. R., and Kroeker, K. J.: The Impacts of Ocean Acidification on Marine Ecosystems and Reliant Human Communities, Annual Review of Environment and Resources, 45, 83–112, https://doi.org/10.1146/ANNUREV-ENVIRON-012320-083019, 2020.

Eusebi Borzelli, G. L. and Carniel, S.: Where the winds clash: what is really triggering El Niño initiation?, npj Climate and Atmospheric Science, 6, 119, https://doi.org/10.1038/s41612-023-00445-9, 2023.

Fan, Y., Liu, W., Zhang, P., Chen, R., and Li, L.: North Atlantic Oscillation contributes to the subpolar North Atlantic cooling in the past century, Clim. Dynam., 61, 5199–5215, https://doi.org/10.1007/S00382-023-06847-Y, 2023.

Fasullo, J. T. and Nerem, R. S.: Altimeter-era emergence of the patterns of forced sea-level rise in climate models and implications for the future, P. Natl. Acad. Sci. USA, 115, 12944–12949. https://doi.org/10.1073/pnas.1813233115, 2018.

Forster, P., Storelvmo, T., Armour, K., Collins, W., Dufresne, J.-L., Frame, D., Lunt, D. J., Mauritsen, T., Palmer, M. D., Watanabe, M., Wild, M., and Zhang, H.: The Earth's Energy Budget, Climate Feedbacks and Climate Sensitivity, in: Climate Change 2021: The Physical Science Basis. Contribution of Working Group I to the Sixth Assessment Report of the Intergovernmental Panel on Climate Change, edited by: Masson-Delmotte, V., Zhai, P., Pirani, A., Connors, S. L., Péan, C., Berger, S., Caud, N., Chen, Y., Goldfarb, L., Gomis, M. I., Huang, M., Leitzell, K., Lonnoy, E., Matthews, J. B. R., Maycock, T. K., Waterfield, T., Yelekçi, O., Yu, R., and Zhou, B., Cambridge University Press, Cambridge, United Kingdom and New York, NY, USA, Cambridge, United Kingdom and New York, NY, USA, 923–1054, https://doi.org/10.1017/9781009157896.009, 2021.

Fox-Kemper, B., Hewitt, H. T., Xiao, C., Aðalgeirsdóttir, G., Drijfhout, S. S., Edwards, T. L., Golledge, N. R., Hemer, M., Kopp, R. E., Krinner, G., Mix, A., Notz, D., Nowicki, S., Nurhati, I. S., Ruiz, L., Sallée, J.-B., Slangen, A. B. A., and Yu, Y.: Ocean, Cryosphere and Sea Level Change, in: Climate Change 2021: The Physical Science Basis. Contribution of Working Group I to the Sixth Assessment Report of the Intergovernmental Panel on Climate Change, edited by: Masson-Delmotte, V., Zhai, P., Pirani, A., Connors, S. L., Péan, C., Berger, S., Caud, N., Chen, Y., Goldfarb, L., Gomis, M. I., Huang, M., Leitzell, K., Lonnoy, E., Matthews, J. B. R., Maycock, T. K., Waterfield, T., Yelekçi, O., Yu, R., and Zhou, B., Cambridge University Press, Cambridge, United Kingdom and New York, NY, USA, 1211–1362, https://doi.org/10.1017/9781009157896.011, 2021.

Frajka-Williams, E., Ansorge, I. J., Baehr, J., Bryden, H. L., Chidichimo, M. P., Cunningham, S. A., Danabasoglu, G., Dong, S., Donohue, K. A., Elipot, S., Heimbach, P., Holliday, N. P., Hummels, R., Jackson, L. C., Karstensen, J., Lankhorst, M., Le Bras, I. A., Susan Lozier, M., McDonagh, E. L., Meinen, C. S., Mercier, H., Moat, B. I., Perez, R. C., Piecuch, C. G., Rhein, M., Srokosz, M. A., Trenberth, K. E., Bacon, S., Forget, G., Goni, G., Kieke, D., Koelling, J., Lamont, T., McCarthy, G. D., Mertens, C., Send, U., Smeed, D. A., Speich, S., van den Berg, M., Volkov, D., and Wilson, C.: Atlantic meridional overturning circulation: Observed transport and variability, Front. Mar. Sci., 6, 436930, https://doi.org/10.3389/FMARS.2019.00260, 2019.

Fretwell, P., Pritchard, H. D., Vaughan, D. G., Bamber, J. L., Barrand, N. E., Bell, R., Bianchi, C., Bingham, R. G., Blankenship, D. D., Casassa, G., Catania, G., Callens, D., Conway, H., Cook, A. J., Corr, H. F. J., Damaske, D., Damm, V., Ferraccioli, F., Forsberg, R., Fujita, S., Gim, Y., Gogineni, P., Griggs, J. A., Hindmarsh, R. C. A., Holmlund, P., Holt, J. W., Jacobel, R. W., Jenkins, A., Jokat, W., Jordan, T., King, E. C., Kohler, J., Krabill, W., Riger-Kusk, M., Langley, K. A., Leitchenkov, G., Leuschen, C., Luyendyk, B. P., Matsuoka, K., Mouginot, J., Nitsche, F. O., Nogi, Y., Nost, O. A., Popov, S. V., Rignot, E., Rippin, D. M., Rivera, A., Roberts, J., Ross, N., Siegert, M. J., Smith, A. M., Steinhage, D., Studinger, M., Sun, B., Tinto, B. K., Welch, B. C., Wilson, D., Young, D. A., Xiangbin, C., and Zirizzotti, A.: Bedmap2: improved ice bed, surface and thickness datasets for Antarctica, The Cryosphere, 7, 375–393, https://doi.org/10.5194/tc-7-375-2013, 2013.

Fu, Y., Lozier, M. S., Biló, T. C., Bower, A. S., Cunningham, S. A., Cyr, F., de Jong, M. F., deYoung, B., Drysdale, L., Fraser, N., Fried, N., Furey, H. H., Han, G., Handmann, P., Holliday, N. P., Holte, J., Inall, M. E., Johns, W. E., Jones, S., Karstensen, J., Li, F., Pacini, A., Pickart, R. S., Rayner, D., Straneo, F., and Yashayaev, I.: Seasonality of the Meridional Overturning Circulation in the subpolar North Atlantic, Communications Earth & Environment, 4, 181, https://doi.org/10.1038/s43247-023-00848-9, 2023.

Garcia Molinos, J., Halpern, B. S., Schoeman, D. S., Brown, C. J., Kiessling, W., Moore, P. J., Pandolfi, J. M., Poloczanska, E. S., Richardson, A. J., and Burrows, M. T.: Climate velocity and the future global redistribution of marine biodiversity, Nat. Clim. Change, 6, 83–88, https://doi.org/10.1038/nclimate2769, 2015.

Garrabou, J., Coma, R., Bensoussan, N., Bally, M., Chevaldonné, P., Cigliano, M., Diaz, D., Harmelin, J. G., Gambi, M. C., Kersting, D. K., Ledoux, J. B., Lejeusne, C., Linares, C., Marschal, C., Pérez, T., Ribes, M., Romano, J. C., Serrano, E., Teixido, N., Torrents, O., Zabala, M., Zuberer, F., and Cerrano, C.: Mass mortality in Northwestern Mediterranean rocky benthic communities: effects of the 2003 heat wave, Glob. Change Biol., 15, 1090–1103, https://doi.org/10.1111/j.1365-2486.2008.01823.x, 2009.

Garrabou, J., Gómez-Gras, D., Medrano, A., Cerrano, C., Ponti, M., Schlegel, R., Bensoussan, N., Turicchia, E., Sini, M., Gerovasileiou, V., Teixido, N., Mirasole, A., Tamburello, L., Cebrian, E., Rilov, G., Ledoux, J. B., Souissi, J. Ben, Khamassi, F., Ghanem, R., Benabdi, M., Grimes, S., Ocaña, O., Bazairi, H., Hereu, B., Linares, C., Kersting, D. K., la Rovira, G., Ortega, J., Casals, D., Pagès-Escolà, M., Margarit, N., Capdevila, P., Verdura, J., Ramos, A., Izquierdo, A., Barbera, C., Rubio-Portillo, E., Anton, I., López-Sendino, P., Díaz, D., Vázquez-Luis, M., Duarte, C., Marbà, N., Aspillaga, E., Espinosa, F., Grech, D., Guala, I., Azzurro, E., Farina, S., Cristina Gambi, M., Chimienti, G., Montefalcone, M., Azzola, A., Mantas, T. P., Fraschetti, S., Ceccherelli, G., Kipson, S., Bakran-Petricioli, T., Petricioli, D., Jimenez, C., Katsanevakis, S., Kizilkaya, I. T., Kizilkaya, Z., Sartoretto, S., Elodie, R., Ruitton, S., Comeau, S., Gattuso, J. P., and Harmelin, J. G.: Marine heatwaves drive recurrent mass mortalities in the Mediterranean Sea, Glob. Change Biol., 28, 5708–5725, https://doi.org/10.1111/GCB.16301, 2022.

Gasparin, F., Echevin, V., Mignot, A., Perruche, C., and Drévillon, M.: The 2017 coastal El Niño, in: Copernicus MarineService Ocean State Report, Issue 3, J. Oper. Oceanogr., 12, s117–s119, https://doi.org/10.1080/1755876X.2019.1633075, 2019.

Gattuso, J. P., Magnan, A., Billé, R., Cheung, W. W. L., Howes, E. L., Joos, F., Allemand, D., Bopp, L., Cooley, S. R., Eakin, C. M., Hoegh-Guldberg, O., Kelly, R. P., Pörtner, H. O., Rogers, A. D., Baxter, J. M., Laffoley, D., Osborn, D., Rankovic, A., Rochette, J., Sumaila, U. R., Treyer, S., and Turley, C.: Contrasting futures for ocean and society from different anthropogenic CO_2 emissions scenarios, Science, 349, aac4722, https://doi.org/10.1126/SCIENCE.AAC4722, 2015.

Giesen, R. and Stoffelen, A.: Changes in extreme wind speeds over the global ocean, in: Copernicus Ocean State Report, Issue 6, J. Oper. Oceanogr., 15, s8–s15, https://doi.org/10.1080/1755876X.2022.2095169, 2022.

Giesen, R., Clementi, E., Bajo, M., Federico, I., Stoffelen, A., and Santoreli, R.: The November 2019 record high water levels in Venice, Italy, in: Copernicus Marine Service Ocean State Report, Issue 5, J. Oper. Oceanogr., 14, s156–s162, https://doi.org/10.1080/1755876X.2021.1946240, 2021.

Gilbert, E. and Holmes, C.: 2023's Antarctic sea ice extent is the lowest on record, Weather, 79, 46–51, https://doi.org/10.1002/WEA.4518, 2024.

Golledge, N. R., Keller, E. D., Gomez, N., Naughten, K. A., Bernales, J., Trusel, L. D., and Edwards, T. L.: Global environmental consequences of twenty-first-century ice-sheet melt, Nature,, 566, 65–72, https://doi.org/10.1038/s41586-019-0889-9, 2019.

González-De Zayas, R., Merino-Ibarra, M., Lestayo González, J. A., Chaviano-Fernández, Y., Alatorre Mendieta, M. A., Pupo, F. M., and Castillo-Sandoval, F. S.: Biogeochemical responses of a highly polluted tropical coastal lagoon after the passage of a strong hurricane (Hurricane Irma), J. Water Clim. Change, 13, 1089–1105, https://doi.org/10.2166/wcc.2021.178, 2021.

Goosse, H., Kay, J. E., Armour, K. C., Bodas-Salcedo, A., Chepfer, H., Docquier, D., Jonko, A., Kushner, P. J., Lecomte, O., Massonnet, F., Park, H. S., Pithan, F., Svensson, G., and Vancoppenolle, M.: Quantifying climate feedbacks in polar regions, Nat. Commun., 9, 1919, https://doi.org/10.1038/s41467-018-04173-0, 2018.

Gregory, J. M., Griffies, S. M., Hughes, C. W., Lowe, J. A., Church, J. A., Fukimori, I., Gomez, N., Kopp, R. E., Landerer, F., Cozannet, G. Le, Ponte, R. M., Stammer, D., Tamisiea, M. E., and van de Wal, R. S. W.: Concepts and Terminology for Sea Level: Mean, Variability and Change, Both Local and Global, Surv. Geophys., 40, 1251–1289, https://doi.org/10.1007/S10712-019-09525-Z, 2019.

Gruber, N., Clement, D., Carter, B. R., Feely, R. A., van Heuven, S., Hoppema, M., Ishii, M., Key, R. M., Kozyr, A., Lauvset, S. K., Monaco, C. Lo, Mathis, J. T., Murata, A., Olsen, A., Perez, F. F., Sabine, C. L., Tanhua, T., and Wanninkhof, R.: The oceanic sink for anthropogenic CO_2 from 1994 to 2007, Science, 363, 1193–1199, https://doi.org/10.1126/SCIENCE.AAU5153, 2019.

Guérou, A., Meyssignac, B., Prandi, P., Ablain, M., Ribes, A., and Bignalet-Cazalet, F.: Current observed global mean sea level rise and acceleration estimated from satellite altimetry and the associated measurement uncertainty, Ocean Sci., 19, 431–451, https://doi.org/10.5194/os-19-431-2023, 2023.

Gulev, S. K., Thorne, P. W., Ahn, J., Dentener, F. J., Domingues, C. M., Gerland, S., Gong, D., Kaufman, D. S., Nnamchi, H.

C., Quaas, J., Rivera, J. A., Sathyendranath, S., Smith, S. L., Trewin, B., von Schuckmann, K., and Vose, R. S.: Changing State of the Climate System, in: Climate Change 2021: The Physical Science Basis. Contribution of Working Group I to the Sixth Assessment Report of the Intergovernmental Panel on Climate Change, edited by: Masson-Delmotte, V., Zhai, P., Pirani, A., Connors, S. L., Péan, C., Berger, S., Caud, N., Chen, Y., Goldfarb, L., Gomis, M. I., Huang, M., Leitzell, K., Lonnoy, E., Matthews, J. B. R., Maycock, T. K., Waterfield, T., Yelekçi, O., Yu, R., and Zhou, B., Cambridge University Press, Cambridge, United Kingdom and New York, NY, USA, 287–422, https://doi.org/10.1017/9781009157896.004, 2021.

Gunn, K. L., Rintoul, S. R., England, M. H., and Bowen, M. M.: Recent reduced abyssal overturning and ventilation in the Australian Antarctic Basin, Nat. Clim. Change, 13, 537–544, https://doi.org/10.1038/s41558-023-01667-8, 2023.

Hamlington, B. D., Cheon, S. H., Piecuch, C. G., Karnauskas, K. B., Thompson, P. R., Kim, K. Y., Reager, J. T., Landerer, F. W., and Frederikse, T.: The Dominant Global Modes of Recent Internal Sea Level Variability, J. Geophys. Res.-Oceans, 124, 2750–2768, https://doi.org/10.1029/2018JC014635, 2019.

Hamlington, B. D., Frederikse, T., Nerem, R. S., Fasullo, J. T., and Adhikari, S.: Investigating the Acceleration of Regional Sea Level Rise During the Satellite Altimeter Era, Geophys. Res. Lett., 47, e2019GL086528, https://doi.org/10.1029/2019GL086528, 2020.

Hansen, J., Sato, M., Kharecha, P., and von Schuckmann, K.: Earth's energy imbalance and implications, Atmos. Chem. Phys., 11, 13421–13449, https://doi.org/10.5194/acp-11-13421-2011, 2011.

Hansen, J. E., Sato, M., Simons, L., Nazarenko, L. S., Sangha, I., Kharecha, P., Zachos, J. C., von Schuckmann, K., Loeb, N. G., Osman, M. B., Jin, Q., Tselioudis, G., Jeong, E., Lacis, A., Ruedy, R., Russell, G., Cao, J., and Li, J.: Global warming in the pipeline, Oxford Open Climate Change, 3, kgad008, https://doi.org/10.1093/OXFCLM/KGAD008, 2023.

Harley, M. D., Turner, I. L., Kinsela, M. A., Middleton, J. H., Mumford, P. J., Splinter, K. D., Phillips, M. S., Simmons, J. A., Hanslow, D. J., and Short, A. D.: Extreme coastal erosion enhanced by anomalous extratropical storm wave direction, Scientific Reports, 7, 6033, https://doi.org/10.1038/s41598-017-05792-1, 2017.

Harrison, L. C., Holland, P. R., Heywood, K. J., Nicholls, K. W., and Brisbourne, A. M.: Sensitivity of Melting, Freezing and Marine Ice Beneath Larsen C Ice Shelf to Changes in Ocean Forcing, Geophys. Res. Lett., 49, e2021GL096914, https://doi.org/10.1029/2021GL096914, 2022.

Haumann, F. A., Notz, D., Schmidt, H., Haumann, F. A., Notz, D., and Schmidt, H.: Anthropogenic influence on recent circulation-driven Antarctic sea ice changes, Geophys. Res. Lett., 41, 8429–8437, https://doi.org/10.1002/2014GL061659, 2014.

Haumann, F. A., Gruber, N., Münnich, M., Frenger, I., and Kern, S.: Sea-ice transport driving Southern Ocean salinity and its recent trends, Nature, 537, 89–92, https://doi.org/10.1038/nature19101, 2016.

Hobday, A. J., Alexander, L. V., Perkins, S. E., Smale, D. A., Straub, S. C., Oliver, E. C. J., Benthuysen, J. A., Burrows, M. T., Donat, M. G., Feng, M., Holbrook, N. J., Moore, P. J., Scannell, H. A., Sen Gupta, A., and Wernberg, T.: A hierarchical approach to defining marine heatwaves, Prog. Oceanogr., 141, 227–238, https://doi.org/10.1016/J.POCEAN.2015.12.014, 2016.

Hobday, A. J., Oliver, E. C. J., Gupta, A. Sen, Benthuysen, J. A., Burrows, M. T., Donat, M. G., Holbrook, N. J., Moore, P. J., Thomsen, M. S., Wernberg, T., and Smale, D. A.: Categorizing and naming marine heatwaves, Oceanography, 31, 162–173, https://doi.org/10.5670/OCEANOG.2018.205, 2018.

Holbrook, N. J., Claar, D. C., Hobday, A. J., McInnes, K. L., Oliver, E. C. J., Gupta, A. Sen, Widlansky, M. J., and Zhang, X.: ENSO-Driven Ocean Extremes and Their Ecosystem Impacts, Geoph. Monog. Series, 253, 409–428, https://doi.org/10.1002/9781119548164.CH18, 2020.

Holbrook, N. J., Hernaman, V., Koshiba, S., Lako, J., Kajtar, J. B., Amosa, P., and Singh, A.: Impacts of marine heatwaves on tropical western and central Pacific Island nations and their communities, Glob. Planet. Change, 208, 103680, https://doi.org/10.1016/J.GLOPLACHA.2021.103680, 2022.

Holland, P. R. and Kwok, R.: Wind-driven trends in Antarctic sea-ice drift, Nat. Geosci., 5, 872–875, https://doi.org/10.1038/ngeo1627, 2012.

Holliday, N. P., Bersch, M., Berx, B., Chafik, L., Cunningham, S., Florindo-López, C., Hátún, H., Johns, W., Josey, S. A., Larsen, K. M. H., Mulet, S., Oltmanns, M., Reverdin, G., Rossby, T., Thierry, V., Valdimarsson, H., and Yashayaev, I.: Ocean circulation causes the largest freshening event for 120 years in eastern subpolar North Atlantic, Nat. Commun., 11, 585, https://doi.org/10.1038/s41467-020-14474-y, 2020.

Horwath, M., Gutknecht, B. D., Cazenave, A., Palanisamy, H. K., Marti, F., Marzeion, B., Paul, F., Le Bris, R., Hogg, A. E., Otosaka, I., Shepherd, A., Döll, P., Cáceres, D., Müller Schmied, H., Johannessen, J. A., Nilsen, J. E. Ø., Raj, R. P., Forsberg, R., Sandberg Sørensen, L., Barletta, V. R., Simonsen, S. B., Knudsen, P., Andersen, O. B., Ranndal, H., Rose, S. K., Merchant, C. J., Macintosh, C. R., von Schuckmann, K., Novotny, K., Groh, A., Restano, M., and Benveniste, J.: Global sea-level budget and ocean-mass budget, with a focus on advanced data products and uncertainty characterisation, Earth Syst. Sci. Data, 14, 411–447, https://doi.org/10.5194/essd-14-411-2022, 2022.

Houghton, I. A. and Wilson, J. D.: El Niño Detection Via Unsupervised Clustering of Argo Temperature Profiles, J. Geophys. Res.-Oceans, 125, e2019JC015947, https://doi.org/10.1029/2019JC015947, 2020.

Hu, S., Hu, D., Guan, C., Xing, N., Li, J., and Feng, J.: Variability of the western Pacific warm pool structure associated with El Niño, Clim. Dynam., 49, 2431–2449, https://doi.org/10.1007/S00382-016-3459-Y, 2017.

Hu, S., Zhang, L., and Qian, S.: Marine Heatwaves in the Arctic Region: Variation in Different Ice Covers, Geophys. Res. Lett., 47, e2020GL089329, https://doi.org/10.1029/2020GL089329, 2020.

Hu, Z. Z., Huang, B., Zhu, J., Kumar, A., and McPhaden, M. J.: On the variety of coastal El Niño events, Clim. Dynam., 52, 7537–7552, https://doi.org/10.1007/S00382-018-4290-4, 2019.

Huang, B., Wang, Z., Yin, X., Arguez, A., Graham, G., Liu, C., Smith, T., and Zhang, H. M.: Prolonged Marine Heatwaves in the Arctic: 1982–2020, Geophys. Res. Lett., 48, e2021GL095590, https://doi.org/10.1029/2021GL095590, 2021.

IPCC: Global Warming of 1.5 °C. An IPCC Special Report on the impacts of global warming of 1.5 °C above pre-industrial levels and related global greenhouse gas emission pathways, in the context of strengthening the global response to the threat of climate change, sustainable development, and efforts to eradicate poverty, edited by: Masson-Delmotte, V., Zhai, P., Pörtner, H.-O., Roberts, D., Skea, J., Shukla, P. R., Pirani, A., Moufouma-Okia, W., Péan, C., Pidcock, R., Connors, S., Matthews, J. B. R., Chen, Y., Zhou, X., Gomis, M. I., Lonnoy, E., Maycock, T., Tignor, M., and Waterfield, T., Cambridge University Press, Cambridge, UK and New York, NY, USA, 616 pp., https://doi.org/10.1017/9781009157940, 2018.

IPCC: Summary for Policymakers, in: IPCC Special Report on the Ocean and Cryosphere in a Changing Climate, edited by: Pörtner, H.-O., Roberts, D. C., Masson-Delmotte, V., Zhai, P., Tignor, M., Poloczanska, E., Mintenbeck, K., Alegría, A., Nicolai, M., Okem, A., Petzold, J., Rama, B., and Weyer, N. M., Cambridge University Press, 755 pp., https://doi.org/10.1017/9781009157964, 2019

IPCC: Climate Change 2021: The Physical Science Basis. Contribution of Working Group I to the Sixth Assessment Report of the Intergovernmental Panel on Climate Change, Cambridge University Press, Cambridge, United Kingdom and New York, NY, USA, https://doi.org/10.1017/9781009157896, 2021.

IPCC: Summary for Policymakers, in: Climate Change 2022: Impacts, Adaptation, and Vulnerability. Contribution of Working Group II to the Sixth Assessment Report of the Intergovernmental Panel on Climate Change, edited by: Pörtner, H.-O., Roberts, D. C., Tignor, M., Poloczanska, E. S., Mintenbeck, K., Alegria, A., Craig, M., Langsdorf, S., Löschke, S., Möller, V., Okem, A., and Rama, B., Cambridge University Press, Cambridge, UK and New York, NY, USA, 3–33, https://doi.org/10.1017/9781009325844.001, 2022a.

IPCC: Summary for Policymakers [P.R. Shukla, J. Skea, A. Reisinger, R. Slade, R. Fradera, M. Pathak, A. Al Khourdajie, M. Belkacemi, R. van Diemen, A. Hasija, G. Lisboa, S. Luz, J. Malley, D. McCollum, S. Some, P. Vyas, (eds.)], in: Climate Change 2022: Mitigation of Climate Change. Contribution of Working Group III to the Sixth Assessment Report of the Intergovernmental Panel on Climate Change, edited by: Shuka, P. R., Skea, J., Slade, R., Al Khourdajie, A., van Diemen, R., McCollum, D., Pathak, M., Some, S., Vyas, P., Fradera, R., Belkacemo, M., Hasija, A., Lisboa, G., Luz, S., and Malley, J., Cambridge University Press, Cambridge, UK and New York, NY, USA, 3–48, https://doi.org/10.1017/9781009157926.001, 2022b.

IPCC: Summary for Policymakers, in: Climate Change 2023: Synthesis Report. Contribution of Working Groups I, II and III to the Sixth Assessment Report of the Intergovernmental Panel on Climate Change, edited by: Core Writing Team, Lee, H., and Romero, J., IPCC, Geneva, Switzerland, 1–34, https://doi.org/10.59327/IPCC/AR6-9789291691647.001, 2023.

Jackson, L. C., Kahana, R., Graham, T., Ringer, M. A., Woollings, T., Mecking, J. V., and Wood, R. A.: Global and European climate impacts of a slowdown of the AMOC in a high resolution GCM, Clim. Dynam., 45, 3299–3316, https://doi.org/10.1007/S00382-015-2540-2, 2015.

Jackson, L., Dubois, C., Masina, S., Storto, A., and Zuo, H.: Atlantic Meridional Overturning Circulation, in: Copernicus Marine Service Ocean State Report, Issue 2, J. Oper. Oceanogr., 11, s65–s66, https://doi.org/10.1080/1755876X.2018.1489208, 2018.

Jackson, L. C., Biastoch, A., Buckley, M. W., Desbruyères, D. G., Frajka-Williams, E., Moat, B., and Robson, J.: The evolution of the North Atlantic Meridional Overturning Circulation since 1980, Nat. Rev. Earth Environ., 3, 241–254, https://doi.org/10.1038/s43017-022-00263-2, 2022.

Jahn, A., Holland, M. M., and Kay, J. E.: Projections of an ice-free Arctic Ocean, Nat. Rev. Earth Environ., 5, 164–176, https://doi.org/10.1038/s43017-023-00515-9, 2024.

Jenkins, M. and Dai, A.: The Impact of Sea-Ice Loss on Arctic Climate Feedbacks and Their Role for Arctic Amplification, Geophys. Res. Lett., 48, e2021GL094599, https://doi.org/10.1029/2021GL094599, 2021.

Jenkins, M. T. and Dai, A.: Arctic Climate Feedbacks in ERA5 Reanalysis: Seasonal and Spatial Variations and the Impact of Sea-Ice Loss, Geophys. Res. Lett., 49, e2022GL099263, https://doi.org/10.1029/2022GL099263, 2022.

Kashiwase, H., Ohshima, K. I., Nihashi, S., and Eicken, H.: Evidence for ice-ocean albedo feedback in the Arctic Ocean shifting to a seasonal ice zone, Scientific Reports, 7, 8170, https://doi.org/10.1038/s41598-017-08467-z, 2017.

Kramer, R. J., He, H., Soden, B. J., Oreopoulos, L., Myhre, G., Forster, P. M., and Smith, C. J.: Observational Evidence of Increasing Global Radiative Forcing, Geophys. Res. Lett., 48, e2020GL091585, https://doi.org/10.1029/2020GL091585, 2021.

Krueger, O., Feser, F., and Weisse, R.: Northeast Atlantic Storm Activity and Its Uncertainty from the Late Nineteenth to the Twenty-First Century, J. Climate, 32, 1919–1931, https://doi.org/10.1175/JCLI-D-18-0505.1, 2019.

Kunze, S.: Unraveling the Effects of Tropical Cyclones on Economic Sectors Worldwide: Direct and Indirect Impacts, Environ. Resour. Econ., 78, 545–569, https://doi.org/10.1007/S10640-021-00541-5, 2021.

Lam, J. S. L. and Lassa, J. A.: Risk assessment framework for exposure of cargo and ports to natural hazards and climate extremes, Marit. Policy Manag., 44, 1–15, https://doi.org/10.1080/03088839.2016.1245877, 2016.

Lannuzel, D., Tedesco, L., van Leeuwe, M., Campbell, K., Flores, H., Delille, B., Miller, L., Stefels, J., Assmy, P., Bowman, J., Brown, K., Castellani, G., Chierici, M., Crabeck, O., Damm, E., Else, B., Fransson, A., Fripiat, F., Geilfus, N. X., Jacques, C., Jones, E., Kaartokallio, H., Kotovitch, M., Meiners, K., Moreau, S., Nomura, D., Peeken, I., Rintala, J. M., Steiner, N., Tison, J. L., Vancoppenolle, M., Van der Linden, F., Vichi, M., and Wongpan, P.: The future of Arctic sea-ice biogeochemistry and ice-associated ecosystems, Nat. Clim. Change, 10, 983–992, https://doi.org/10.1038/s41558-020-00940-4, 2020.

Lecomte, O., Goosse, H., Fichefet, T., De Lavergne, C., Barthélemy, A., and Zunz, V.: Vertical ocean heat redistribution sustaining sea-ice concentration trends in the Ross Sea, Nat. Commun., 8, 258, https://doi.org/10.1038/s41467-017-00347-4, 2017.

Lee, S.-K., Lumpkin, R., Gomez, F., Yeager, S., Lopez, H., Takglis, F., Dong, S., Aguiar, W., Kim, D., and Baringer, M.: Human-induced changes in the global meridional overturning circulation are emerging from the Southern Ocean, Commun. Earth Environ., 4, 69, https://doi.org/10.1038/s43247-023-00727-3, 2023.

Legeais, J.-F., Llovel, W., Melet, A., and Meyssignac, B.: Evidence of the TOPEX-A Altimeter Instrumental Anomaly and Acceleration of the Global Mean Sea Level, in: Copernicus Marine Service Ocean State Report, Issue 4, J. Oper. Oceanogr., s77–s82, https://doi.org/10.1080/1755876X.2020.1785097, 2020.

Lenton, T. M., Held, H., Kriegler, E., Hall, J. W., Lucht, W., Rahmstorf, S., and Schellnhuber, H. J.: Tipping elements in the Earth's climate system, P. Natl. Acad. Sci. USA, 105, 1786–1793, https://doi.org/10.1073/PNAS.0705414105, 2008.

Levitus, S., Antonov, J. I., Boyer, T. P., Baranova, O. K., Garcia, H. E., Locarnini, R. A., Mishonov, A. V., Reagan, J. R., Seidov, D., Yarosh, E. S., and Zweng, M. M.: World ocean heat content and thermosteric sea level change (0–2000 m), 1955–2010, Geophys. Res. Lett., 39, 10603, https://doi.org/10.1029/2012GL051106, 2012.

Li, L., Lozier, M. S., and Li, F.: Century-long cooling trend in subpolar North Atlantic forced by atmosphere: an alternative explanation, Clim. Dynam., 58, 2249–2267, https://doi.org/10.1007/S00382-021-06003-4, 2022.

Lin, I. I., Camargo, S. J., Patricola, C. M., Boucharel, J., Chand, S., Klotzbach, P., Chan, J. C. L., Wang, B., Chang, P., Li, T., and Jin, F. F.: ENSO and Tropical Cyclones, Geoph. Monog. Series, 253, 377–408, https://doi.org/10.1002/9781119548164.CH17, 2020.

Liu, J. and Curry, J. A.: Accelerated warming of the Southern Ocean and its impacts on the hydrological cycle and sea ice, P. Natl. Acad. Sci. USA, 107, 14987–14992, https://doi.org/10.1073/PNAS.1003336107, 2010.

Liu, J., Curry, J. A., and Martinson, D. G.: Interpretation of recent Antarctic sea ice variability, Geophys. Res. Lett., 31, 2205, https://doi.org/10.1029/2003GL018732, 2004.

Loeb, N. G., Johnson, G. C., Thorsen, T. J., Lyman, J. M., Rose, F. G., and Kato, S.: Satellite and Ocean Data Reveal Marked Increase in Earth's Heating Rate, Geophys. Res. Lett., 48, e2021GL093047, https://doi.org/10.1029/2021GL093047, 2021.

Lozier, M. S., Li, F., Bacon, S., Bahr, F., Bower, A. S., Cunningham, S. A., de Jong, M. F., de Steur, L., deYoung, B., Fischer, J., Gary, S. F., Greenan, B. J. W., Holliday, N. P., Houk, A., Houpert, L., Inall, M. E., Johns, W. E., Johnson, H. L., Johnson, C., Karstensen, J., Koman, G., Le Bras, I. A., Lin, X., Mackay, N., Marshall, D. P., Mercier, H., Oltmanns, M., Pickart, R. S., Ramsey, A. L., Rayner, D., Straneo, F., Thierry, V., Torres, D. J., Williams, R. G., Wilson, C., Yang, J., Yashayaev, I., and Zhao, J.: A sea change in our view of overturning in the subpolar North Atlantic, Science, 363, 516–521, https://doi.org/10.1126/science.aau6592, 2019.

Marbà, N. and Duarte, C.M.: Mediterranean warming triggers seagrass (*Posidonia oceanica*) shoot mortality, Glob. Change Biol., 16, 2366–2375, https://doi.org/10.1111/j.1365-2486.2009.02130.x, 2010.

Marsland, S. J. and Wolff, J. O.: On the sensitivity of Southern Ocean sea ice to the surface freshwater flux: A model study, J. Geophys. Res.-Oceans, 106, 2723–2741, https://doi.org/10.1029/2000JC900086, 2001.

Mattu, K. L., Bloomfield, H. C., Thomas, S., Martínez-Alvarado, O., and Rodríguez-Hernández, O.: The impact of tropical cyclones on potential offshore wind farms, Energy Sustain. Dev., 68, 29–39, https://doi.org/10.1016/J.ESD.2022.02.005, 2022.

McCarthy, G. D., Smeed, D. A., Johns, W. E., Frajka-Williams, E., Moat, B. I., Rayner, D., Baringer, M. O., Meinen, C. S., Collins, J., and Bryden, H. L.: Measuring the Atlantic Meridional Overturning Circulation at 26° N, Prog. Oceanogr., 130, 91–111, https://doi.org/10.1016/j.pocean.2014.10.006, 2015.

McKay, D. I. A., Staal, A., Abrams, J. F., Winkelmann, R., Sakschewski, B., Loriani, S., Fetzer, I., Cornell, S. E., Rockström, J., and Lenton, T. M.: Exceeding 1.5 °C global warming could trigger multiple climate tipping points, Science, 377, eabn7950, https://doi.org/10.1126/SCIENCE.ABN7950, 2022.

McPhaden, M. J., Zebiak, S. E., and Glantz, M. H.: ENSO as an Integrating Concept in Earth Science, Science, 314, 1740–1745, https://doi.org/10.1126/SCIENCE.1132588, 2006.

McPhaden, M. J., Santoso, A., and Cai, W.: Introduction to El Niño Southern Oscillation in a Changing Climate, Geoph. Monog. Series, 253, 1–19, https://doi.org/10.1002/9781119548164.CH1, 2020.

Meehl, G. A., Arblaster, J. M., Bitz, C. M., Chung, C. T. Y., and Teng, H.: Antarctic sea-ice expansion between 2000 and 2014 driven by tropical Pacific decadal climate variability, Nat. Geosci., 9, 590–595, https://doi.org/10.1038/ngeo2751, 2016.

Meredith, M., Sommerkorn, M., Cassotta, S., Derksen, C., Ekaykin, A., Hollowed, A., Kofinas, G., Mackintosh, A., Melbourne-Thomas, J., Muelbert, M. M. C., Ottersen, G., Pritchard, H., and Schuur, E. A. G.: Polar Regions Supplementary Material, in: IPCC Special Report on the Ocean and Cryosphere in a Changing Climate, edited by: Pörtner, H.-O., Roberts, D. C., Masson-Delmotte, V., Zhai, P., Tignor, M., Poloczanska, E., Mintenbeck, K., Alegria, A., Nicolai, M., Okem, A., Petzold, J., Rama, B., and Weyer, N. M., https://www.ipcc.ch/srocc/ (last access: 11 September 2024), 2019.

Minière, A., von Schuckmann, K., Sallée, J. B., and Vogt, L.: Robust acceleration of Earth system heating observed over the past six decades, Scientific Reports, 13, 22975, https://doi.org/10.1038/s41598-023-49353-1, 2023.

Minnett, P. J., Kilpatrick, K. A., Podestá, G. P., Evans, R. H., Szczodrak, M. D., Izaguirre, M. A., Williams, E. J., Walsh, S., Reynolds, R. M., Bailey, S. W., Armstrong, E. M., and Vazquez-cuervo, J.: Skin Sea-Surface Temperature from VIIRS on Suomi-NPP–NASA Continuity Retrievals, Remote Sensing, 12, 3369, https://doi.org/10.3390/RS12203369, 2020.

Moat, B. I., Smeed, D. A., Rayner, D., Johns, W. E., Smith, R., Volkov, D., Baringer, M. O., and Collins, J.: Atlantic meridional overturning circulation observed by the RAPID-MOCHA-WBTS (RAPID-Meridional Overturning Circulation and Heatflux Array-Western Boundary Time Series) array at 26N from 2004 to 2022 (v2022.1), British Oceanographic Data Centre – Natural Environment Research Council, UK [data set], https://doi.org/10.5285/04c79ece-3186-349a-e063-6c86abc0158c, 2023.

Moreira, L., Cazenave, A., and Palanisamy, H.: Influence of interannual variability in estimating the rate and acceleration of present-day global mean sea level, Global Planet. Change, 199, 103450, https://doi.org/10.1016/J.GLOPLACHA.2021.103450, 2021.

Naughten, K. A., Holland, P. R., Dutrieux, P., Kimura, S., Bett, D. T., and Jenkins, A.: Simulated Twentieth-Century Ocean Warming in the Amundsen Sea, West Antarctica, Geophys. Res. Lett., 49, e2021GL094566, https://doi.org/10.1029/2021GL094566, 2022.

Negri, A. J., Burkardt, N., Golden, J. H., Halverson, J. B., Huffman, G. J., Larsen, M. C., McGinley, J. A., Updike, R. G., Verdin, J. P., and Wieczorek, G. F.: The Hurricane–Flood–Landslide Continuum, B. Am. Meteorol. Soc., 86, 1241–1247, 2005.

Nielsen-Englyst, P., Høyer, J. L., Kolbe, W. M., Dybkjær, G., Lavergne, T., Tonboe, R. T., Skarpalezos, S., and Karagali, I.: A combined sea and sea-ice surface temperature climate dataset of the Arctic, 1982–2021, Remote Sens. Environ., 284, 113331, https://doi.org/10.1016/J.RSE.2022.113331, 2023.

Oliver, E. C. J., Benthuysen, J. A., Bindoff, N. L., Hobday, A. J., Holbrook, N. J., Mundy, C. N., and Perkins-Kirkpatrick, S. E.: The unprecedented 2015/16 Tasman Sea marine heatwave, Nat. Commun., 8, 16101, https://doi.org/10.1038/ncomms16101, 2017.

Oliver, E. C. J., Donat, M. G., Burrows, M. T., Moore, P. J., Smale, D. A., Alexander, L. V., Benthuysen, J. A., Feng, M., Sen Gupta, A., Hobday, A. J., Holbrook, N. J., Perkins-Kirkpatrick, S. E., Scannell, H. A., Straub, S. C., and Wernberg, T.: Longer and more frequent marine heatwaves over the past century, Nat. Commun., 9, 1324, https://doi.org/10.1038/s41467-018-03732-9, 2018.

Oliver, E. C. J., Burrows, M. T., Donat, M. G., Sen Gupta, A., Alexander, L. V., Perkins-Kirkpatrick, S. E., Benthuysen, J. A., Hobday, A. J., Holbrook, N. J., Moore, P. J., Thomsen, M. S., Wernberg, T., and Smale, D. A.: Projected Marine Heatwaves in the 21st Century and the Potential for Ecological Impact, Front. Mar. Sci., 6, 481127, https://doi.org/10.3389/FMARS.2019.00734, 2019.

Oppenheimer, M., Glavovic, B., Hinkel, J., Roderik, van, Magnan, A., Abd-Elgawad, A., Rongshu, C., Cifuentes, M., Robert, D., Ghosh, T., Hay, J., Ben, M., Meyssignac, B., Sebesvari, Z., A.J., S., Dangendorf, S., and Frederikse, T.: Sea Level Rise and Implications for Low Lying Islands, Coasts and Communities, in: IPCC Special Report on the Ocean and Cryosphere in a Changing Climate, edited by: Pörtner, H.-O., Roberts, D. C., Masson-Delmotte, V., Zhai, P., Tignor, M., Poloczanska, E., Mintenbeck, K., Alegria, A., Nicolai, M., Okem, A., Petzold, J., Rama, B., and Weyer, N. M., Cambridge University Press, Cambridge, UK and New York, NY, USA, 321–445, https://doi.org/10.1017/9781009157964.006, 2019.

OSNAP | Overturning in the Subpolar North Atlantic Program: A Subpolar Measure of the Atlantic Meridional Overturning Circulation, https://www.o-snap.org/, last access: 21 December 2023.

Parkinson, C. L.: A 40-y record reveals gradual Antarctic sea ice increases followed by decreases at rates far exceeding the rates seen in the Arctic, P. Natl. Acad. Sci. USA, 116, 14414–14423, https://doi.org/10.1073/PNAS.1906556116, 2019.

Parkinson, C. L. and Cavalieri, D. J.: Antarctic sea ice variability and trends, 1979–2010, The Cryosphere, 6, 871–880, https://doi.org/10.5194/tc-6-871-2012, 2012.

Patrick, C. J., Kominoski, J. S., McDowell, W. H., Branoff, B., Lagomasino, D., Leon, M., Hensel, E., Hensel, M. J. S., Strickland, B. A., Aide, T. M., Armitage, A., Campos-Cerqueira, M., Congdon, V. M., Crowl, T. A., Devlin, D. J., Douglas, S., Erisman, B. E., Feagin, R. A., Geist, S. J., Hall, N. S., Hardison, A. K., Heithaus, M. R., Hogan, J. A., Hogan, J. D., Kinard, S., Kiszka, J. J., Lin, T. C., Lu, K., Madden, C. J., Montagna, P. A., O'Connell, C. S., Proffitt, C. E., Reese, B. K., Reustle, J. W., Robinson, K. L., Rush, S. A., Santos, R. O., Schnetzer, A., Smee, D. L., Smith, R. S., Starr, G., Stauffer, B. A., Walker, L. M., Weaver, C. A., Wetz, M. S., Whitman, E. R., Wilson, S. S., Xue, J., and Zou, X.: A general pattern of trade-offs between ecosystem resistance and resilience to tropical cyclones, Sci. Adv., 8, 9155, https://doi.org/10.1126/SCIADV.ABL9155, 2022.

Pauling, A. G., Smith, I. J., Langhorne, P. J., and Bitz, C. M.: Time-Dependent Freshwater Input From Ice Shelves: Impacts on Antarctic Sea Ice and the Southern Ocean in an Earth System Model, Geophys. Res. Lett., 44, 10454–10461, https://doi.org/10.1002/2017GL075017, 2017.

Peal, R., Worsfold, M., and Good, S.: Comparing global trends in marine cold spells and marine heatwaves using reprocessed satellite data, in: 7th edition of the Copernicus Ocean State Report (OSR7), edited by: von Schuckmann, K., Moreira, L., Le Traon, P.-Y., Grégoire, M., Marcos, M., Staneva, J., Brasseur, P., Garric, G., Lionello, P., Karstensen, J., and Neukermans, G., Copernicus Publications, State Planet, 1-osr7, 3, https://doi.org/10.5194/sp-1-osr7-3-2023, 2023.

Peduzzi, P., Chatenoux, B., Dao, H., De Bono, A., Herold, C., Kossin, J., Mouton, F., and Nordbeck, O.: Global trends in tropical cyclone risk, Nat. Clim. Change, 2, 289–294, https://doi.org/10.1038/nclimate1410, 2012.

Polvani, L. M. and Smith, K. L.: Can natural variability explain observed Antarctic sea ice trends? New modeling evidence from CMIP5, Geophys. Res. Lett., 40, 3195–3199, https://doi.org/10.1002/GRL.50578, 2013.

Prandi, P., Meyssignac, B., Ablain, M., Spada, G., Ribes, A., and Benveniste, J.: Local sea level trends, accelerations and uncertainties over 1993–2019, Scientific Data, 8, 1, https://doi.org/10.1038/s41597-020-00786-7, 2021.

Purich, A. and Doddridge, E. W.: Record low Antarctic sea ice coverage indicates a new sea ice state, Communications Earth & Environment, 4, 314, https://doi.org/10.1038/s43247-023-00961-9, 2023.

Purich, A., Cai, W., England, M. H., and Cowan, T.: Evidence for link between modelled trends in Antarctic sea ice and underestimated westerly wind changes, Nat. Commun., 7, 10409, https://doi.org/10.1038/ncomms10409, 2016.

Raghuraman, S. P., Paynter, D., and Ramaswamy, V.: Anthropogenic forcing and response yield observed positive trend in Earth's energy imbalance, Nat. Commun., 12, 4577, https://doi.org/10.1038/s41467-021-24544-4, 2021.

Rahmstorf, S.: Is the Atlantic overturning circulation approaching a tipping point?, Oceanography, 37, https://doi.org/10.5670/oceanog.2024.501, 2024.

Rahmstorf, S., Box, J. E., Feulner, G., Mann, M. E., Robinson, A., Rutherford, S., and Schaffernicht, E. J.: Exceptional twentieth-century slowdown in Atlantic Ocean overturning circulation, Nat. Clim. Change, 5, 475–480, https://doi.org/10.1038/nclimate2554, 2015.

Ramírez, F., Afán, I., Davis, L. S., and Chiaradia, A.: Climate impacts on global hot spots of marine biodiversity, Sci. Adv., 3, e1601198, https://doi.org/10.1126/SCIADV.1601198, 2017.

Rasmussen, T. A. S., Høyer, J. L., Ghent, D., Bulgin, C. E., Dybkjær, G., Ribergaard, M. H., Nielsen-Englyst, P., and Madsen, K. S.: Impact of Assimilation of Sea-Ice Surface Temperatures on a Coupled Ocean and Sea-Ice Model, J. Geophys. Res.-Oceans, 123, 2440–2460, https://doi.org/10.1002/2017JC013481, 2018.

Rhein, M., Kieke, D., Hüttl-Kabus, S., Roessler, A., Mertens, C., Meissner, R., Klein, B., Böning, C. W., and Yashayaev, I.: Deep water formation, the subpolar gyre, and the meridional overturning circulation in the subpolar North Atlantic, Deep-Sea Res. Pt. II, 58, 1819–1832, https://doi.org/10.1016/J.DSR2.2010.10.061, 2011.

Romero-Centeno, R., Zavala-Hidalgo, J., Gallegos, A., and O'Brien, J. J.: Isthmus of Tehuantepec Wind Climatology and ENSO Signal, J. Climate, 16, 2628–2639, https://doi.org/10.1175/1520-0442(2003)016<2628:IOTWCA>2.0.CO;2, 2003.

Roose, S., Ajayamohan, R. S., Ray, P., Xie, S. P., Sabeerali, C. T., Mohapatra, M., Taraphdar, S., Mohanakumar, K., and Rajeevan, M.: Pacific decadal oscillation causes fewer near-equatorial cyclones in the North Indian Ocean, Nat. Commun., 14, 5099, https://doi.org/10.1038/s41467-023-40642-x, 2023.

Sampe, T., and Xie, S.: Mapping High Sea Winds from Space: A Global Climatology, B. Am. Meteorol. Soc., 88, 1965–1978, https://doi.org/10.1175/BAMS-88-12-1965, 2007.

Sanders, R. N. C., Jones, D. C., Josey, S. A., Sinha, B., and Forget, G.: Causes of the 2015 North Atlantic cold anomaly in a global state estimate, Ocean Sci., 18, 953–978, https://doi.org/10.5194/os-18-953-2022, 2022.

Seneviratne, S. I., Zhang, X., Adnan, M., Badi, W., Dereczynski, C., Di Luca, A., Ghosh, S., Iskandar, I., Kossin, J., Lewis, S., Otto, F., Pinto, I., Satoh, M., Vicente-Serrano, S. M., Wehner, M., and Zhou, B.: Weather and Climate Extreme Events in a Changing Climate, in: Climate Change 2021: The Physical Science Basis. Contribution of Working Group I to the Sixth Assessment Report of the Intergovernmental Panel on Climate Change, edited by: Masson-Delmotte, V., Zhai, P., Pirani, A., Connors, S. L., Péan, C., Berger, S., Caud, N., Chen, Y., Goldfarb, L., Gomis, M. I., Huang, M., Leitzell, K., Lonnoy, E., Matthews, J. B. R., Maycock, T. K., Waterfield, T., Yelekçi, O., Yu, R., and Zhou, B., Cambridge University Press, Cambridge, United Kingdom and New York, NY, USA, 1513–1766, https://doi.org/10.1017/9781009157896.013, 2021.

She, J. and Nielsen, J. W.: "Silent" storm surge extremes in the western Baltic Sea on 4 January 2017, in: Copernicus Marine Service Ocean State Report, Issue3, J. Oper. Oceanogr., 12, s111–s117, https://doi.org/10.1080/1755876X.2019.1633075, 2019.

Smeed, D. A., McCarthy, G. D., Cunningham, S. A., Frajka-Williams, E., Rayner, D., Johns, W. E., Meinen, C. S., Baringer, M. O., Moat, B. I., Duchez, A., and Bryden, H. L.: Observed decline of the Atlantic meridional overturning circulation 2004–2012, Ocean Sci., 10, 29–38, https://doi.org/10.5194/os-10-29-2014, 2014.

Smith, K. E., Burrows, M. T., Hobday, A. J., King, N. G., Moore, P. J., Sen Gupta, A., Thomsen, M. S., Wernberg, T., and Smale, D. A.: Biological Impacts of Marine Heatwaves, Annu. Rev. Mar. Sci., 15, 119–145, https://doi.org/10.1146/annurev-marine-032122-121437, 15, 119–145, 2023.

Sopkin, K. L., Stockdon, H. F., Doran, K. S., Plant, N. G., Morgan, K. L. M., Guy, K. K., and Smith, K. E. L.: Hurricane Sandy: observations and analysis of coastal change, U.S. Geological Survey Open-File Report, 54, https://doi.org/10.3133/OFR20141088, 2014.

Spada, G. and Melini, D.: SELEN^4 (SELEN version 4.0): a Fortran program for solving the gravitationally and topographically self-consistent sea-level equation in glacial isostatic adjustment modeling, Geosci. Model Dev., 12, 5055–5075, https://doi.org/10.5194/gmd-12-5055-2019, 2019.

Stammer, D., Cazenave, A., Ponte, R. M., and Tamisiea, M. E.: Causes for Contemporary Regional Sea Level Changes, Annu. Rev. Mar. Sci., 5, 21–46, https://doi.org/10.1146/annurev-marine-121211-172406, 2012

Staneva, J., Behrens, A., and Gayer, G.: Predictability of large wave heights in the western Black Sea during the 2018 winter storms, in: Copernicus Marine Service Ocean State Report, Issue 4, J. Oper. Oceanogr., 13, s144–s149, https://doi.org/10.1080/1755876X.2020.1785097, 2020.

Storto, A. and Yang, C.: Acceleration of the ocean warming from 1961 to 2022 unveiled by large-ensemble reanalyses, Nat. Commun., 15, 545, https://doi.org/10.1038/s41467-024-44749-7, 2024.

Swart, N. C. and Fyfe, J. C.: The influence of recent Antarctic ice sheet retreat on simulated sea ice area trends, Geophys. Res. Lett., 40, 4328–4332, https://doi.org/10.1002/GRL.50820, 2013.

Tagliabue, A., Bowie, A. R., Boyd, P. W., Buck, K. N., Johnson, K. S., and Saito, M. A.: The integral role of iron in ocean biogeochemistry, Nature, 543, 51–59, https://doi.org/10.1038/NATURE21058, 2017.

Tamisiea, M. E.: Ongoing glacial isostatic contributions to observations of sea level change, Geophys. J. Int., 186, 1036–1044, https://doi.org/10.1111/J.1365-246X.2011.05116.X, 2011.

Timmermann, A., An, S. Il, Kug, J. S., Jin, F. F., Cai, W., Capotondi, A., Cobb, K., Lengaigne, M., McPhaden, M. J., Stuecker, M. F., Stein, K., Wittenberg, A. T., Yun, K. S., Bayr, T., Chen, H. C., Chikamoto, Y., Dewitte, B., Dommenget, D., Grothe, P., Guilyardi, E., Ham, Y. G., Hayashi, M., Ineson, S., Kang, D., Kim, S., Kim, W. M., Lee, J. Y., Li, T., Luo, J. J., McGregor, S., Planton, Y., Power, S., Rashid, H., Ren, H. L., Santoso, A., Takahashi, K., Todd, A., Wang, G., Wang, G., Xie, R., Yang, W. H., Yeh, S. W., Yoon, J., Zeller, E., and Zhang, X.: El Niño–Southern Oscillation complexity, Nature, 559, 535–545, https://doi.org/10.1038/s41586-018-0252-6, 2018.

Trenberth, K. E.: The Definition of El Niño, B. Am. Meteorol. Soc., 78, 2771–2778, https://doi.org/10.1175/1520-0477(1997)078<2771:TDOENO>2.0.CO;2, 1997.

Trenberth, K. E. and Stepaniak, D. P.: Indices of El Niño Evolution, J. Climate, 14, 1697–1701, https://doi.org/10.1175/1520-0442(2001)014<1697:LIOENO>2.0.CO;2, 2001.

Turney, C. S. M., Fogwill, C. J., Golledge, N. R., McKay, N. P., van Sebille, E., Jones, R. T., Etheridge, D., Rubino, M., Thornton, D. P., Davies, S. M., Ramsey, C. B., Thomas, Z. A., Bird, M. I., Munksgaard, N. C., Kohno, M., Woodward, J., Winter, K., Weyrich, L. S., Rootes, C. M., Millman, H., Albert, P. G., Rivera, A., van Ommen, T., Curran, M., Moy, A., Rahmstorf, S., Kawamura, K., Hillenbrand, C. D., Weber, M. E., Manning, C. J., Young, J., and Cooper, A.: Early Last Interglacial ocean warming drove substantial ice mass loss from Antarctica, P. Natl. Acad. Sci. USA, 117, 3996–4006, https://doi.org/10.1073/PNAS.1902469117, 2020.

UN: United Nations Environment Programme (12/1), Paris Agreement, https://wedocs.unep.org/20.500.11822/20830 (last access: 11 September 2024), 2015.

UN: Measure and Report Ocean Acidification – Sustainable Development Goal 14.3.1 Indicator Methodology, Department of Economic and Social Affairs: https://sdgs.un.org/partnerships/measure-and-report-ocean-acidification-sustainable-development-goal-1431-indicator, last access: 27 November 2023.

Vazquez-Cuervo, J., Castro, S. L., Steele, M., Gentemann, C., Gomez-Valdes, J., and Tang, W.: Comparison of GHRSST SST Analysis in the Arctic Ocean and Alaskan Coastal Waters Using Saildrones, Remote Sensing, 14, 692, https://doi.org/10.3390/RS14030692, 2022.

Verschuur, J., Koks, E. E., Li, S., and Hall, J. W.: Multi-hazard risk to global port infrastructure and resulting trade and logistics losses, Communications Earth & Environment, 4, 5, https://doi.org/10.1038/s43247-022-00656-7, 2023.

Volkov, D. L., Zhang, K., Johns, W. E., Willis, J. K., Hobbs, W., Goes, M., Zhang, H., and Menemenlis, D.: Atlantic meridional overturning circulation increases flood risk along the United States southeast coast, Nat. Commun., 14, 5095, https://doi.org/10.1038/s41467-023-40848-z, 2023.

von Schuckmann, K., Palmer, M. D., Trenberth, K. E., Cazenave, A., Chambers, D., Champollion, N., Hansen, J., Josey, S. A., Loeb, N., Mathieu, P. P., Meyssignac, B., and Wild, M.: An imperative to monitor Earth's energy imbalance, Nat. Clim. Change, 6, 138–144, https://doi.org/10.1038/nclimate2876, 2016.

von Schuckmann, K., Cheng, L., Palmer, M. D., Hansen, J., Tassone, C., Aich, V., Adusumilli, S., Beltrami, H., Boyer, T., Cuesta-Valero, F. J., Desbruyères, D., Domingues, C., García-García, A., Gentine, P., Gilson, J., Gorfer, M., Haimberger, L., Ishii, M., Johnson, G. C., Killick, R., King, B. A., Kirchengast, G., Kolodziejczyk, N., Lyman, J., Marzeion, B., Mayer, M., Monier, M., Monselesan, D. P., Purkey, S., Roemmich, D., Schweiger, A., Seneviratne, S. I., Shepherd, A., Slater, D. A., Steiner, A. K., Straneo, F., Timmermans, M.-L., and Wijffels, S. E.: Heat stored in the Earth system: where does the energy go?, Earth Syst. Sci. Data, 12, 2013–2041, https://doi.org/10.5194/essd-12-2013-2020, 2020.

von Schuckmann, K., Minière, A., Gues, F., Cuesta-Valero, F. J., Kirchengast, G., Adusumilli, S., Straneo, F., Ablain, M., Allan, R. P., Barker, P. M., Beltrami, H., Blazquez, A., Boyer, T., Cheng, L., Church, J., Desbruyeres, D., Dolman, H., Domingues, C. M., García-García, A., Giglio, D., Gilson, J. E., Gorfer, M., Haimberger, L., Hakuba, M. Z., Hendricks, S., Hosoda, S., Johnson, G. C., Killick, R., King, B., Kolodziejczyk, N., Korosov, A., Krinner, G., Kuusela, M., Landerer, F. W., Langer, M., Lavergne, T., Lawrence, I., Li, Y., Lyman, J., Marti, F., Marzeion, B., Mayer, M., MacDougall, A. H., McDougall, T., Monselesan, D. P., Nitzbon, J., Otosaka, I., Peng, J., Purkey, S., Roemmich, D., Sato, K., Sato, K., Savita, A., Schweiger, A., Shepherd, A., Seneviratne, S. I., Simons, L., Slater, D. A., Slater, T., Steiner, A. K., Suga, T., Szekely, T., Thiery, W., Timmermans, M.-L., Vanderkelen, I., Wjiffels, S. E., Wu, T., and Zemp, M.: Heat stored in the Earth system 1960–2020: where does the energy go?, Earth Syst. Sci. Data, 15, 1675–1709, https://doi.org/10.5194/essd-15-1675-2023, 2023.

Wakelin, S., Townhill, B., Engelhard, G., Holt, J., and Renshaw, R.: Marine heatwaves and cold-spells, and their impact on fisheries in the North Sea, in: Copernicus Marine Service Ocean State Report, Issue 5, J. Oper. Oceanogr., 14, s91–s96, https://doi.org/10.1080/1755876X.2021.1946240, 2021.

Wang, B., Sun, W., Jin, C., Luo, X., Yang, Y. M., Li, T., Xiang, B., McPhaden, M. J., Cane, M. A., Jin, F., Liu, F., and Liu, J.: Understanding the recent increase in multiyear La Niñas, Nat. Clim. Change, 13, 1075–1081, https://doi.org/10.1038/s41558-023-01801-6, 2023.

WCRP Global Sea Level Budget Group: Global sea-level budget 1993–present, Earth Syst. Sci. Data, 10, 1551–1590, https://doi.org/10.5194/essd-10-1551-2018, 2018.

Welch, H., Savoca, M. S., Brodie, S., Jacox, M. G., Muhling, B. A., Clay, T. A., Cimino, M. A., Benson, S. R., Block, B. A., Conners, M. G., Costa, D. P., Jordan, F. D., Leising, A. W., Mikles, C. S., Palacios, D. M., Shaffer, S. A., Thorne, L. H., Watson, J. T., Holser, R. R., Dewitt, L., Bograd, S. J., and Hazen, E. L.: Impacts of marine heatwaves on top predator distributions are variable but predictable, Nat. Commun., 14, 5188, https://doi.org/10.1038/s41467-023-40849-y, 2023.

Westen, R. M. van, Kliphuis, M., and Dijkstra, H. A.: Physics-based early warning signal shows that AMOC is on tipping course, Sci. Adv., 10, 1189, https://doi.org/10.1126/SCIADV.ADK1189, 2024.

Wetz, M. S. and Yoskowitz, D. W.: An "extreme" future for estuaries? Effects of extreme climatic events on estuarine water quality and ecology, Mar. Pollut. Bull., 69, 7–18, https://doi.org/10.1016/J.MARPOLBUL.2013.01.020, 2013.

WMO: WMO El Niño/La Niña Updates, World Meteorological Organization, https://community.wmo.int/en/activity-areas/climate/wmo-el-ninola-nina-updates, last access: 21 December 2023.

Wood, M., Rignot, E., Fenty, I., An, L., Bjørk, A., van den Broeke, M., Cai, C., Kane, E., Menemenlis, D., Millan, R., Morlighem, M., Mouginot, J., Noël, B., Scheuchl, B., Velicogna, I., Willis, J. K., and Zhang, H.: Ocean forcing drives glacier retreat in Greenland, Sci. Adv., 7, eaba7282, https://doi.org/10.1126/SCIADV.ABA7282, 2021.

Yao, Y., Wang, C., and Fu, Y.: Global Marine Heatwaves and Cold-Spells in Present Climate to Future Projections, Earth's Future, 10, e2022EF002787, https://doi.org/10.1029/2022EF002787, 2022.

Yuan, J. P. and Cao, J.: North Indian Ocean tropical cyclone activities influenced by the Indian Ocean Dipole mode, Sci. China Earth Sci., 56, 855–865, https://doi.org/10.1007/S11430-012-4559-0, 2013.

Zamudio, L., Hurlburt, H. E., Metzger, E. J., Morey, S. L., O'brien, J. J., Tilburg, C., Zavala-Hidalgo, J., Zamudio, C. :, Hurlburt, H. E., Metzger, E. J., Morey, S. L., O'brien, J. J., Tilburg, C. E., and Zavala-Hidalgo, J.: Interannual variability of Tehuantepec eddies, J. Geophys. Res.-Oceans, 111, C05001, https://doi.org/10.1029/2005JC003182, 2006.

Zhang, L., Delworth, T. L., Yang, X., Zeng, F., Lu, F., Morioka, Y., and Bushuk, M.: The relative role of the subsurface Southern Ocean in driving negative Antarctic Sea ice extent anomalies in 2016–2021, Communications Earth & Environment, 3, 302, https://doi.org/10.1038/s43247-022-00624-1, 2023.

Zhu, C., Liu, Z., Zhang, S., and Wu, L.: Likely accelerated weakening of Atlantic overturning circulation emerges in optimal salinity fingerprint, Nat. Commun., 14, 1245, https://doi.org/10.1038/s41467-023-36288-4, 2023.

Zunz, V., Goosse, H., and Massonnet, F.: How does internal variability influence the ability of CMIP5 models to reproduce the recent trend in Southern Ocean sea ice extent?, The Cryosphere, 7, 451–468, https://doi.org/10.5194/tc-7-451-2013, 2013.

State Planet, 4-osr8, 2, 2024
https://doi.org/10.5194/sp-4-osr8-2-2024

The state of the ocean in the northeastern Atlantic and adjacent seas

Karina von Schuckmann[1], **Lorena Moreira**[1], **Mathilde Cancet**[2], **Flora Gues**[3], **Emmanuelle Autret**[4], **Ali Aydogdu**[5], **Lluis Castrillo**[6], **Daniele Ciani**[7], **Andrea Cipollone**[5], **Emanuela Clementi**[5], **Gianpiero Cossarini**[8], **Alvaro de Pascual-Collar**[6], **Vincenzo De Toma**[7], **Marion Gehlen**[9], **Rianne Giesen**[10], **Marie Drevillon**[1], **Claudia Fanelli**[7], **Kevin Hodges**[11], **Simon Jandt-Scheelke**[12], **Eric Jansen**[5], **Melanie Juza**[13], **Ioanna Karagali**[14], **Priidik Lagemaa**[15], **Vidar Lien**[16], **Leonardo Lima**[5], **Vladyslav Lyubartsev**[5], **Ilja Maljutenko**[15], **Simona Masina**[5], **Ronan McAdam**[5], **Pietro Miraglio**[5], **Helen Morrison**[12], **Tabea Rebekka Panteleit**[12], **Andrea Pisano**[7], **Marie-Isabelle Pujol**[17], **Urmas Raudsepp**[15], **Roshin Raj**[18,19], **Ad Stoffelen**[10], **Simon Van Gennip**[1], **Pierre Veillard**[17], and **Chunxue Yang**[7]

[1]Mercator Ocean international, Toulouse, France
[2]CNRS/LEGOS, Toulouse, France
[3]CELAD, Mercator Ocean international, Toulouse, France
[4]Ifremer, Brest, France
[5]CMCC Foundation – Euro-Mediterranean Center on Climate Change, Bologna, Italy
[6]Nologin Oceanic Weather Systems, Madrid, Spain
[7]Consiglio Nazionale delle Ricerche, Istituto di Scienze Marine (CNR-ISMAR), Bologna, Italy
[8]National Institute of Oceanography and Applied Geophysics, Sgonico (TS), Trieste, Italy
[9]LSCE, IPSL, Gif-sur-Yvette, France
[10]Royal Netherlands Meteorological Institute, Utrecht, the Netherlands
[11]University of Reading, Reading, UK
[12]Federal Maritime and Hydrographic Agency (BSH), Hamburg, Germany
[13]SOCIB, Palma, Spain
[14]National Centre for Climate Research, Danish Meteorological Institute, Copenhagen, Denmark
[15]Tallinn University of Technology, Tallinn, Estonia
[16]IMR, Bergen, Norway
[17]Collecte Localisation Satellites (CLS), Ramonville St-Agne, France
[18]Nansen Environmental and Remote Sensing Center, Bergen, Norway
[19]Bjerknes Center for Climate Research, Bergen, Norway

Correspondence: Karina von Schuckmann (karina.von.schuckmann@mercator-ocean.fr)

Published: 30 September 2024

Abstract. In this paper, the Copernicus Ocean State Report offers detailed scientific analysis of the ocean under climate change, ocean variability, and ocean extremes in the northeastern Atlantic and adjacent seas. Major results show that the northeastern Atlantic Ocean and adjacent seas have experienced consistent warming, with sea surface temperatures increasing at a rate of 0.25 ± 0.03 °C per decade since 1982, doubling the global average trend. This warming is most pronounced in the Black Sea, Mediterranean Sea, and Baltic Sea. Sea levels have risen significantly over the past 30 years, particularly in the Baltic and Mediterranean seas. Ocean acidification has also increased, with pH decreasing at a rate of -0.017 ± 0.001 units per decade. Marine heatwaves have intensified and expanded, affecting over 60 % of the region in 2022 and 2023. Over the past 16 years, most extreme wind speeds exceeding $22\,\mathrm{m\,s^{-1}}$ prevailed in the central and subpolar North Atlantic and northern Mediterranean Sea. The region has also seen significant variability in ocean climate indicators and circulation

Published by Copernicus Publications.

patterns, including increased Atlantic Water transport to the Arctic Ocean through the Fram Strait and notable variations in the Mediterranean Sea's meridional overturning circulation. No major Baltic inflow occurred in winter 2022/23.

1 Introduction

The area of the northeastern Atlantic Ocean and adjacent seas begins in the North Atlantic Ocean from the point at 24.58° N, extends east to 68.5° E, and continues due north to the geographical North Pole along the meridian 44° W, including the regional sea areas such as the Mediterranean Sea, the Black Sea, the North Sea, and the Baltic Sea (Fig. 1). The criteria for the choice of this area rely on both oceanic and policy relevant criteria. Specifically, the northeastern Atlantic Ocean and adjacent seas contain all Copernicus Marine areas and cover all European waters. In addition, the area includes the regional seas areas under the UNEP regional seas conventions (https://www.unep.org/explore-topics/oceans-seas/what-we-do/working-regional-seas/regional-seas-programmes/regional-seas, last access: 11 September 2024) (e.g. OSPAR, https://www.ospar.org/, last access: 11 September 2024). The GOOS regional alliances (https://goosocean.org/who-we-are/goos-regional-alliances/, last access: 11 September 2024), such as EuroGOOS (https://eurogoos.eu, last access: 11 September 2024), MONGOOS (https://mongoos.eurogoos.eu/, last access: 11 September 2024), and Black Sea GOOS (https://goosocean.org/who-we-are/goos-regional-alliances/gra-black-sea-goos/, last access: 11 September 2024), are considered as well. The northeastern Atlantic Ocean and adjacent seas also cover the FAO 27 major fishing area (https://www.fao.org/fishery/en/area/27/en, last access: 11 September 2024), as well as the WMO region VI-Europe (https://wmo.int/about-us/regions/europe#:~:text=The%20WMO%20Regional%20Office%20for,on%20society%20and%20the%20environment, last access: 11 September 2024). On the one hand, this choice allows us to consider the ocean dynamics and processes (e.g. to consider full basin approaches for the regional seas). On the other hand, it aligns with various European and international actors at the science–policy interface.

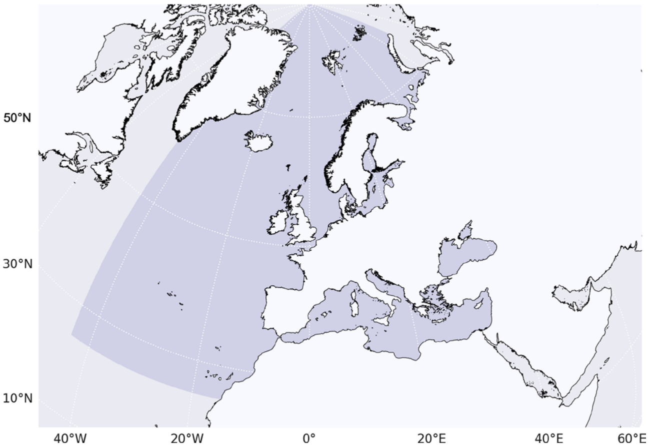

Figure 1. Northeastern Atlantic Ocean and adjacent seas region highlighted in blue grey.

Executive summary

Sea surface temperature of the northeastern Atlantic Ocean and adjacent seas shows consistent warming across all ocean subbasins that doubles the global average trend and is most pronounced in the eastern part of the region. Since 1982, the area-averaged sea surface temperature in the northeastern Atlantic Ocean and adjacent seas has been rising at a rate of 0.25 ± 0.03 °C per decade, with the Black Sea, Mediterranean Sea, and Baltic Sea experiencing the most intense warming rates. Overall, nearly the entire western part of the region is warming at least 2 times faster than the global average, while rates gradually decrease when approaching the adjacent large-scale patterns linked to the North Atlantic warming hole in the western part of the region.

The interplay of long-term change and natural variations determine stark variations in ocean warming in the northeastern Atlantic, while the ocean warming trend dominates in the adjacent seas. Large multi-annual- to decadal-scale variations dominate ocean warming in the area-average of the northeastern Atlantic and adjacent seas, as well as in the Iberia–Biscay–Irish area. In the Mediterranean Sea, the Black Sea, and the Baltic Sea, ocean warming dominates at rates exceeding the global mean warming rate.

All ocean areas in the northeastern Atlantic Ocean and adjacent seas have been experiencing sea level rise over the past 30 years as obtained from absolute sea level measurements, particularly in the Baltic Sea and the Mediterranean Sea. Rates of area-averaged sea level rise during the period 1993–2023 in the northeastern Atlantic Ocean and adjacent seas range from $1\pm0.8\,\mathrm{mm\,yr^{-1}}$ in the Black Sea, $2.5\pm0.8\,\mathrm{mm\,yr^{-1}}$ in the Mediterranean Sea, to $4.1\pm0.8\,\mathrm{mm\,yr^{-1}}$ in the Baltic Sea. Regionally, the sea level in 46 % of the ocean area in the northeastern Atlantic Ocean and adjacent seas is rising at a rate larger than the global mean average rate ($3.4\,\mathrm{mm\,yr^{-1}}$ over 1993–2023). Areas of fast sea level rise above the global rate of rise for the last 10 years (mid-2013–mid-2023), estimated to be $4.3\,\mathrm{mm\,yr^{-1}}$, are observed in the North Atlantic Ocean and in 9 % of the Baltic Sea.

Sea ice coverage in the Baltic Sea does not show a significant trend over the period 1993–2023, and in winter 2022/23 the Baltic Sea experienced a moderate ice season, with 15 % sea ice coverage. The moderate ice season 2022/23 in the Baltic Sea reached a maximum area of about 65 000 km^2, which amounts to 15 % of total Baltic Sea ice coverage. Usually, the maximum sea ice extent is reached at the end of February, but in 2023 the maximum ice cover was observed in the second week of March. Although records show a decrease in sea ice extent over the period 1993–2023, the linear trend is not statistically significant.

Regional mean ocean acidification in the northeastern Atlantic Ocean and adjacent seas has continuously increased over the past 37 years (1985–2022), with an observed rate of decrease in ocean pH of -0.017 ± 0.001 *pH units per decade.* Regional rates of change of ocean pH are not homogenously distributed. About 51 % of the sampled ocean surface in the northeastern Atlantic Ocean and adjacent sea areas is becoming more acidic at a rate of -0.017 pH units per decade. The largest rates of pH decrease are reported in the Mediterranean Sea. In the Baltic Sea and Black Sea, the reporting on ocean acidification is challenged by large uncertainties.

Indicators of ocean climate variability and circulation in the northeastern Atlantic Ocean and adjacent seas all show large variations at interannual to decadal scales, and there is an increase reported in Atlantic Water transport to the Arctic Ocean through the Fram Strait. The meridional overturning circulation in the Mediterranean Sea is stronger in the eastern basin as compared to the western basin, showing stark interannual to decadal change since the late 1980s. The Atlantic Water volume transport in the Nordic Seas show large variations at interannual and decadal timescales. In the Fram Strait, the model data indicates an increase in the Atlantic Water transport to the Arctic Ocean. Major Baltic inflows that determine variations in hydrographic and biogeochemical conditions in the Baltic Sea basin were identified in 1993, 2002, and 2014. There was no major Baltic inflow in winter 2022/23, and in 2023 oxygen was completely consumed below the depth of 75 m.

Since 1982, the frequency, duration, intensity, and regional extension of marine heatwave (MHW) events in the northeastern Atlantic Ocean and adjacent seas have increased, and more than 60 % of the region has experienced at least one strong, severe, or extreme marine heatwave in 2022 and 2023, including areas of European aquaculture activities. From 1982 to 2023, the fraction of the ocean surface in this area that experienced marine heatwave events over the year increased from 20 % to more than 90 %, and since 2013 the cumulative ocean surface fraction affected by strong, severe, and extreme marine heatwave events has been larger than that experiencing moderate events. The duration of the events has also increased, with marine heatwave events of more than 1 month prevailing in the area since 2017. In 2022, about 12 % of the northeastern Atlantic Ocean and adjacent seas have experienced at least one severe to extreme marine heatwave, increasing to about 32 % in 2023. In 2022, the most prominent marine heatwaves lasting for at least 4 months and reaching categories up to severe or extreme are reported for the English Channel and the western Mediterranean Sea. In 2023, the most persistent marine heatwaves are observed in the North Atlantic, lasting 4 months and longer, and in the Adriatic, Ionian, and western Black seas, lasting about 3 months. Severe to extreme categories were reached in all these regions.

In the northeastern Atlantic Ocean and adjacent seas, most extreme ocean surface wind speeds exceeding 22 $\mathrm{m\,s^{-1}}$ *over the past 16 years prevail in the central and subpolar North Atlantic and in the northern Mediterranean Sea.* The detection of long-term trends in extreme wind speeds is hampered by their large variability in space and time. Over the period 2007–2023, extreme ocean surface wind speeds in the North Atlantic that exceed more than 22 $\mathrm{m\,s^{-1}}$ are particularly pronounced along the southern coast of Greenland. Extreme wind speeds also reach about 20 $\mathrm{m\,s^{-1}}$ in the northwestern Mediterranean Sea. In September 2023, Storm Daniel, which occurred in the Mediterranean Sea, was designated as a Medicane (Mediterranean hurricane) and had devastating impacts on the Greek and Libyan coasts, causing an overwhelming amount of loss and damage in Libya. During the autumn to winter season, larger areas of higher storm density are reported as compared to the spring to summer seasons, such as in the North Atlantic across 40° N from the Canadian coast to the coast of Europe and in all adjacent seas.

2 Ocean and climate

2.1 Sea surface temperature

Monitoring changes in regional sea surface temperature is essential for evaluating climate variability and its regional impacts. Over more than the past quarter of a century, a major fraction of the surface ocean in the northeastern Atlantic Ocean and adjacent seas has been warming at rates that are equal to or higher than the global rate (WMO, 2023).

Over the past 4 decades (1982–2023), the Mediterranean Sea surface temperature warmed at a rate of 0.41 ± 0.01 °C per decade, corresponding to a mean surface temperature warming of about 1.7 °C. The spatial pattern of the Mediterranean Sea surface temperature trend shows a general uneven warming tendency following an eastward increased tendency. The strongest surface warming is reported in the eastern Mediterranean Sea, such as in the Adriatic, Aegean, Levantine, and Ionian seas (MedECC, 2020b). Between 2022 and 2023, the Mediterranean Sea experienced an exceptionally long-lasting and intense marine heatwave that hit the whole basin. This marine heatwave started in

May 2022, when the mean anomaly increased abruptly from −0.1 ± 0.2 °C (April) to 0.8 ± 0.1 °C (May), reaching the highest values during June (1.7 ± 0.1 °C) and July (1.45 ± 0.07 °C) and persisting until spring 2023 (Marullo et al., 2023).

The Baltic Sea sea surface temperature is rising at a rate of 0.38 ± 0.04 °C per decade (over the period 1982–2023), which represents an average warming of about 1.60 °C. Sea surface warming in the Baltic Sea is characterized by a distinct north–south gradient, and the largest increase in sea surface temperature has been reported for the northern part of the Gulf of Bothnia, the Gulf of Finland, the Gulf of Riga, and the northern part of the Baltic Proper (Meier et al., 2022; von Storch et al., 2015). A long-term increase in surface ocean temperature has also been detected in the North Sea at rates exceeding the global mean values (Huthnance et al., 2016). The rise in sea surface temperature in areas of so-called Large Marine Ecosystems has even been classified within a "superfast warming category", such as for those located in the Norwegian Sea, North Sea, and along the Celtic-Biscay Shelf (Kessler et al., 2022).

The Black Sea is experiencing the most intense sea surface temperature trend among the European seas, estimated at 0.65 ± 0.02 °C per decade (period: 1982–2023), which corresponds to an average increase of about 2.7 °C during the last 42 years. Together with the Baltic and the Mediterranean seas, the Black Sea represents a hot spot of global warming, where the surface warming trend largely exceeds both the northeastern Atlantic Ocean and adjacent seas and the global mean sea surface temperature trend (0.25 ± 0.03 and 0.13 ± 0.01 °C per decade, respectively).

The Iberia–Biscay–Irish (IBI) and the European North West Shelf (NWS) seas are characterized by milder warming rates estimated at 0.24 ± 0.02 and 0.22 ± 0.02 °C per decade, respectively. These trends are strongly affected by decadal variability superposed on the long-term trend (Fig. 2).

Variations from interannual to decadal scales play a critical role in shaping the evolution of regional sea surface temperature. Major climate modes affect northeastern Atlantic Ocean and adjacent seas sea surface temperature, such as the Atlantic Multidecadal Oscillation (AMO) or the North Atlantic Oscillation (NAO) (Pisano et al., 2020; Yan and Tang, 2021; Valcheva and Slabakova, 2020; Kniebusch et al., 2019), and can, together with ocean processes and cryosphere–ocean interactions, challenge the detection of long-term trends from global warming. For example, in the Baltic Sea, changes in the interplay of atmospheric circulation and ocean processes (e.g. changes in the frequency of coastal upwelling) have resulted in regional patterns of lower-than-average surface warming, which is manifested northeast of Bornholm up to and along the Swedish coast (von Storch et al., 2015). In the North Sea, changes in sea surface temperature are largely affected by decadal variations driven by water mass exchange from the adjacent northeastern Atlantic, superposing any long-term surface warming trend (Huthnance et al., 2016). In the North Atlantic, the so-called "warming hole" – a large pattern of unusual cold sea surface temperature – is discussed as being driven by ocean processes (e.g. circulation change), air–sea interactions, cryosphere–ocean interactions, and changes in anthropogenic forcing (Li et al., 2022; Allan and Allan, 2019; Caesar et al., 2018; Hu and Fedorov, 2020; Qasmi, 2023; Gutiérrez et al., 2021).

Good knowledge of sea surface temperature spatial patterns and trends is also critical to correctly assess European climate trends and projections, as they determine variations in regional weather and climate at a variety of scales that have societal implications (O'Carroll et al., 2019). For example, knowledge of the temporal evolution of sea surface temperature can provide important handles to increase the predictability of certain events, such as wet and dry extremes in Europe (Ionita et al., 2012, 2015; Volosciuk et al., 2016).

The rise in sea surface temperature is not homogeneous, and the rate of regional surface ocean warming is largest in the eastern part of the European zone and decreases further towards the western part (Fig. 3). The latter is also affected by the extension of the so-called North Atlantic warming hole. However, nearly the entire northeastern Atlantic Ocean and adjacent seas area is affected by an increase in sea surface temperature, and about 43 % of the area is warming at a rate 2 times faster than the global mean warming rate, i.e. in the Mediterranean Sea, North Sea, Baltic Sea, and Black Sea areas (Fig. 4, Table 1).

2.2 Ocean heat content

Regional ocean warming is not homogeneous, and the North Atlantic area between 20–50° N has been identified as one of the regions that is affected by unusual strong warming rates as compared to the rest of the global ocean (Cheng et al., 2022, Fig. 5). However, subsurface water temperature changes at various timescales in the subpolar North Atlantic as triggered by several factors, such as anthropogenic warming (Cheng et al., 2022), heat redistribution (Messias and Mercier, 2022), climate variability (e.g. the North Atlantic Oscillation; Hurrell and Deser, 2010), and dynamical processes linked to gyre dynamics and large-scale ocean circulation (Yeager, 2020). In the central subpolar North Atlantic, a decadal-scale cooling of the surface ocean has been reported, also known as the so-called "North Atlantic cold blob" or North Atlantic warming hole (Hansen et al., 2010; Drijfhout et al., 2012; Li et al., 2022; Fan et al., 2023), which impacts North Atlantic storm track activities and weather patterns in Europe (Gervais et al., 2019, 2020; Woollings et al., 2018). The cold blob has been also associated with variations in ocean heat content down to about 1000 m depth (Dubois et al., 2018). Several drivers of the cold blob have been hypothesized, such as evidence for an Atlantic Meridional Overturning Circulation (AMOC) slowdown (Drijfhout et al., 2012; Menary and Wood, 2018; Rahmstorf et al., 2015; Caesar et al., 2018; Chemke et al., 2020), variations in the subpolar

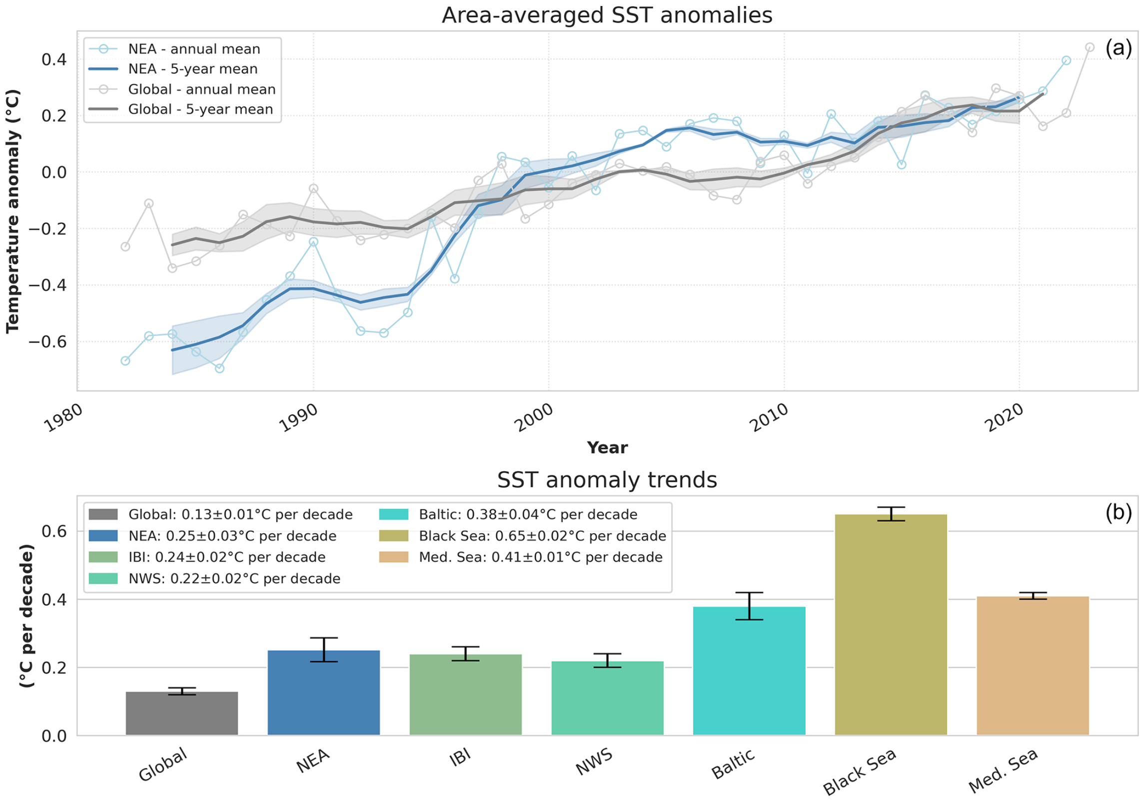

Figure 2. (a) Annual (light) and pentadal (bold) data of global (grey) and northeastern Atlantic Ocean and adjacent seas (blue) mean sea surface temperature anomalies (relative to the 1991–2020 baseline) as derived from the product ref. SST.3 (see Supplement). The shaded areas indicate the 2σ envelope using three different products (product refs. SST.1–SST.4) to indicate the agreement between different products. **(b)** Linear trends (in °C per decade) of area-averaged sea surface temperature over the period 1982–2023 in the global ocean, the northeastern Atlantic Ocean and adjacent seas (designated here as "NEA"), the Iberia–Biscay–Irish (IBI) area, the European North West Shelf (NWS), the Baltic Sea (Baltic), the Black Sea, and the Mediterranean Sea (Med. Sea). Black bars indicate the 2σ uncertainty. Trends and associated uncertainties are estimated by using the X-11 seasonal adjustment procedure (Pezzulli et al., 2005), except for the northeastern Atlantic Ocean and adjacent seas ("NEA") region (see Fig. 1), which uses linear least-squares regression. The product used for the global and northeastern Atlantic Ocean and adjacent seas averages is similar to panel **(a)**, and for IBI product ref. SST.7 is used, for the Baltic Sea product ref. SST.8 is used, for the Mediterranean Sea product ref. SST.9 is used, for the NWS product ref. SST.6 is used, and for the Black Sea product ref. SST.10 is used.

Table 1. Percentage of ocean surface affected by different sea surface temperature trends in the northeastern Atlantic Ocean and adjacent seas and when considering only the shallow waters (depth between 0 and 200 m) in the area.

Selection on trend	Percentage of ocean surface for the whole area	Percentage of ocean surface for the shelf regions (depth 0 to 200 m deep)
Negative trend	0.1 %	0.2 %
Positive trend, lower than global mean	5 %	6 %
Trend equal or lower than 2 times the global mean	40 %	27 %
Trend larger than 2 times the global mean	43 %	64 %

gyre circulation (Hu and Fedorov, 2020; Keil et al., 2020; Ma et al., 2020), and changing process at the air–sea interface (Fan et al., 2023; Sanders et al., 2022).

The strong interplay of natural and anthropogenic warming is reflected during the regionalization approach for the ocean warming indicator. Over the period 1960–2023, the area-averaged results for the northeastern Atlantic Ocean and adjacent seas indicate ocean warming at a rate of $0.3 \pm 0.1\,\mathrm{W\,m^{-2}}$ (Fig. 6, ensemble 1). However, temporal changes in ocean warming are strongly affected by natural

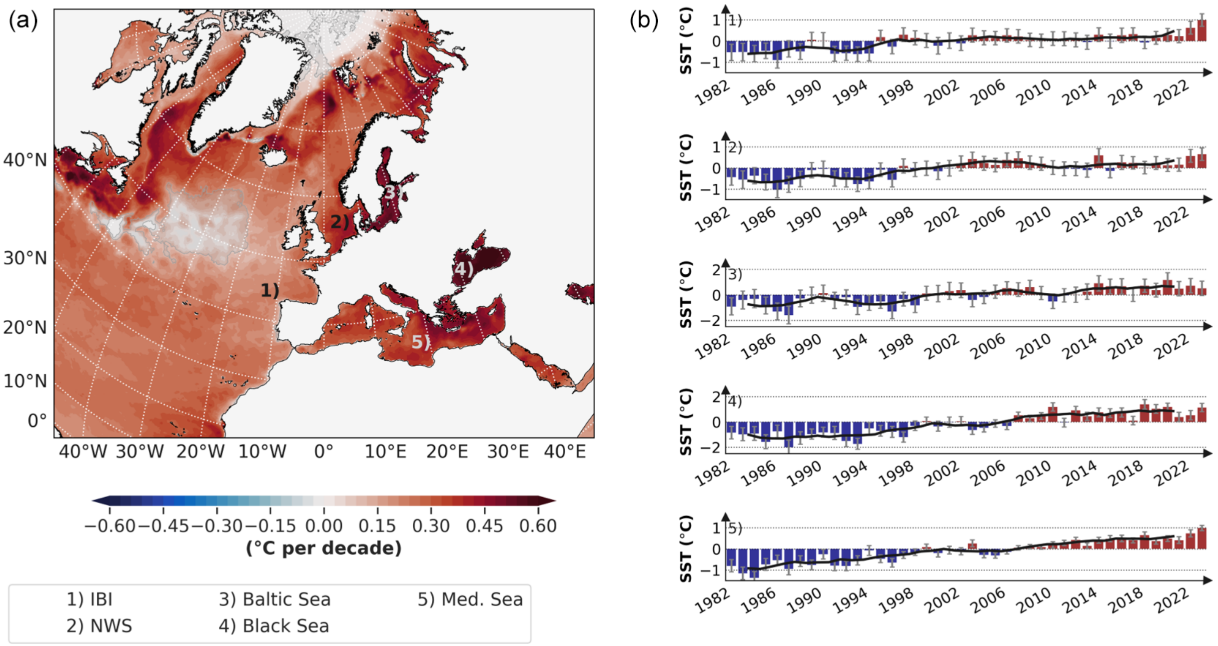

Figure 3. (a) Trend of sea surface temperature anomalies (relative to the 1991–2020 baseline) (in °C per decade) for the European regional seas and the North Atlantic over the period 1982–2023 as derived from product ref. SST.3. Grey shading indicates the areas where the trend is not statistically significant. **(b)** Regional time series of area-averaged sea surface temperature anomalies (relative to the 1991–2020 baseline) for the different regions, i.e. (1) IBI, (2) NWS, (3) Baltic Sea, (4) Black Sea, and (5) Mediterranean Sea (product refs. SST.6–SST.10). Products used for the regional time series are similar to Fig. 4. The black curves show the 5-yearly mean of the sea surface temperature anomalies. The grey ticks on the yearly anomaly bars show the associated uncertainty range.

variations (Fig. 5), and consequently warming rates quantified since the year 2005 are not statistically significant in the northeastern Atlantic and adjacent seas ($-0.1 \pm 0.4\,\mathrm{W\,m^{-2}}$, Fig. 6, ensemble 1). The dominant role of large natural variations is also again reflected in the high sensitivity of the ocean warming trend evaluation in this region when considering different time periods (de Pascual-Collar et al., 2023) (Fig. 6).

In the adjacent seas, ocean warming emerges more clearly in the time series. The sea surface of the Black Sea is experiencing the most intense warming since about the 1980s, leading to an average increase of 2.7 °C over the past 42 years (see results on the indicator sea surface temperature in this issue), and basin-wide ocean warming of the upper 300 m shows the highest warming level in the study area over the period 2005–2023 (Fig. 6). Whether this high level is the result of both the ongoing warming trend and natural variability, which is known to play a central role (Lima et al., 2020, 2021), remains a matter of research (Cheng et al., 2024), with a marked increase over the past few decades (Pinardi et al., 2015; Simoncelli et al., 2018; von Schuckmann et al., 2016; Fig. 6).

2.3 Sea level

At a regional scale, the sea level trends show spatial patterns, with regions rising at a faster or slower rate than the global mean rates or even dropping in some areas. The regional sea level trends depart from the global mean sea level rise as a result of the superposition of geographical trend patterns caused by different processes (Cazenave and Moreira, 2022). For example, the sea level trends in the Mediterranean Sea differ from global mean trends as a result of the semi-enclosed conditions of the Mediterranean Sea (Pinardi et al., 2014). The process contributing to the regional variability in sea level trends are regional changes in ocean circulation, temperature, and salinity (stereodynamic changes); redistribution of ocean water mass by the ocean circulation (manometric changes); atmospheric loading; and changes in Earth gravity, Earth rotation, and viscoelastic solid Earth deformation (GRD) due to ongoing changes in the solid Earth caused by past changes in land ice (GIA) and contemporary changes in the mass of water stored on land as ice sheets, glaciers, and land water storage (GRD sea level fingerprints) (Gregory et al., 2019).

Depending on the measurement technique used, different information on sea level change can be obtained. For example, relative sea level as obtained from tide gauges is referred to the height of the sea surface relative to the sea floor, and

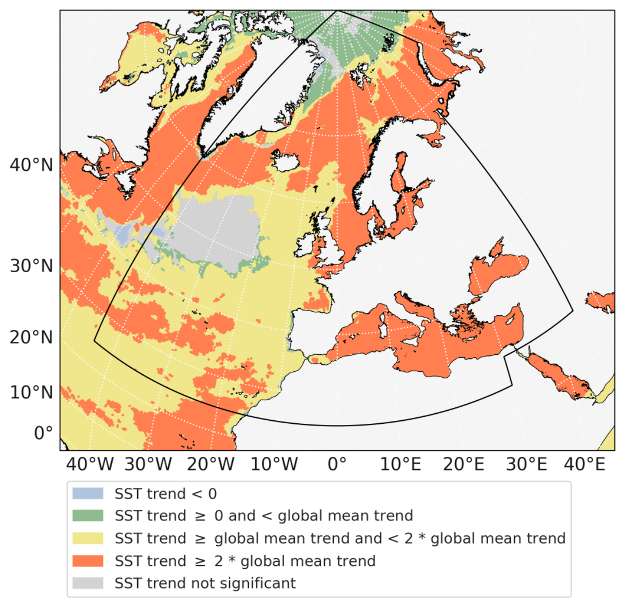

Figure 4. Areas where the regional trend is negative (blue), is positive and lower than the global mean sea surface warming trend (green), is equal or less than 2 times the global mean sea surface warming trend (yellow), or exceeds 2 times the global mean sea surface warming trend (orange) as derived from the product ref. SST.3. The grey shading represents areas where the trend is not statistically significant. The black box indicates the northeastern Atlantic Ocean and adjacent seas zone used.

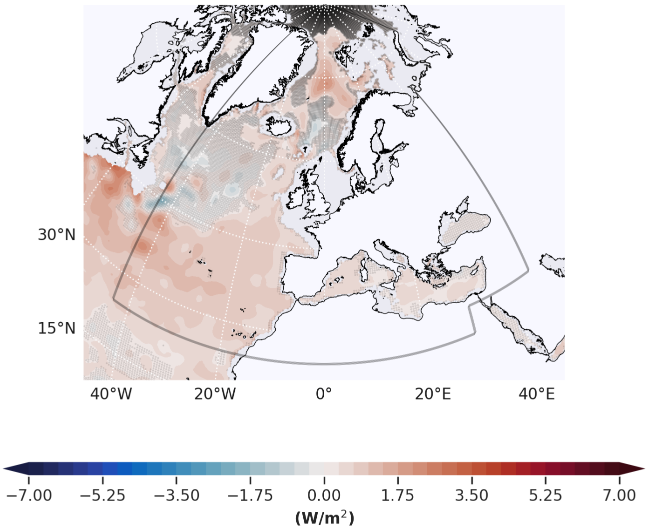

Figure 5. Ocean warming regional trends over the period 1960–2023 and integrated over the upper 700 m depth based on the product ref. OHC.3. The shaded grey zones indicate the regions where the noise exceeds the signal of the ensemble product refs. OHC.1–4, indicating the level of disagreement of regional trends in the different products. The bold grey line indicates the study area, i.e. the northeastern Atlantic Ocean and adjacent seas.

thus to land, at a given location. Sea level from the satellite is linked to the so-called absolute sea level, which is the height of the sea surface at a given location relative to the reference ellipsoid. At a regional scale, these are important concepts allowing for further understanding on the causes of sea level change. For example, in the Baltic Sea the rise in absolute sea level has been assessed to a rate of 1.3 to 1.8 mm yr^{-1} over the period 1993–2010 (Hünicke et al., 2015; The BACC II Author Team, 2015), whereas relative sea level in the Baltic Sea shows the lowest increase as compared to other ocean areas in Europe due to land uplift (Ranasinghe et al., 2021; Vousdoukas et al., 2017). The Baltic Sea is strongly affected by vertical land motion, especially due to the GIA caused by the melting of past ice sheets (Ludwigsen et al., 2020), and relative sea level trends have been shown to be strongly negative (Passaro et al., 2021). Accordingly, the IPCC (2021a) projected that relative sea level will rise in all European areas except for the Baltic Sea. However, absolute sea level trends show statistically significant positive trends (Fig. 7) (Passaro et al., 2021).

A recent assessment report for the Mediterranean climate has reported a mean sea level rise of 6 cm over the past 20 years, and this trend is likely to accelerate (with regional differences) by the global rate of 43 to 84 cm until 2100 (MedECC, 2020c). In the North Sea, an absolute mean sea level trend of 2.61 ± 0.95 mm yr^{-1} has been reported over the period 1995–2019, which varies regionally between 1.5 and 3.5 mm yr^{-1} over the region, with the highest trends in the German Bight and around Denmark and lower trends around the southern part of Great Britain (Dettmering et al., 2021). Sea level change in the northeastern Atlantic up to the European shelf area is known to be largely affected by variations driven by ocean dynamics and processes at the air–sea interface, which have induced large sea level variations at decadal and smaller timescales, superposing the long-term trend in this area (Chafik et al., 2019). In the Black Sea, a recent study has reported a mean rate of total sea level rise of 2.5 ± 0.5 mm yr^{-1} over the entire basin (Avşar and Kutoglu, 2020), with large interannual- to decadal-scale variations driven by climate variability, freshwater fluxes from land, and sea level fluctuations in the Mediterranean Sea (Volkov and Wilson, 2019).

The Copernicus Marine Service sea level data for the European regional seas have been adjusted for the TOPEX-A instrumental drift based on Ablain et al. (2017) and adjusted for the GIA using latitude and coastal weighting on the map of GIA trend from Spada and Melini (2019). Therefore, the European weighted-mean GIA corrections amount to -0.49 mm yr^{-1}. At basin level, the correction amounts to 0.21 mm yr^{-1} in the Baltic Sea, whereas in the Mediterranean Sea it is on the order of -0.21 mm yr^{-1}. On the other hand, in the Black Sea the correction is estimated to 0.08 mm yr^{-1}, and it ranges between -0.5 and -0.69 mm yr^{-1} in the North West shelf and Iberia–Biscay–Irish regions, respectively.

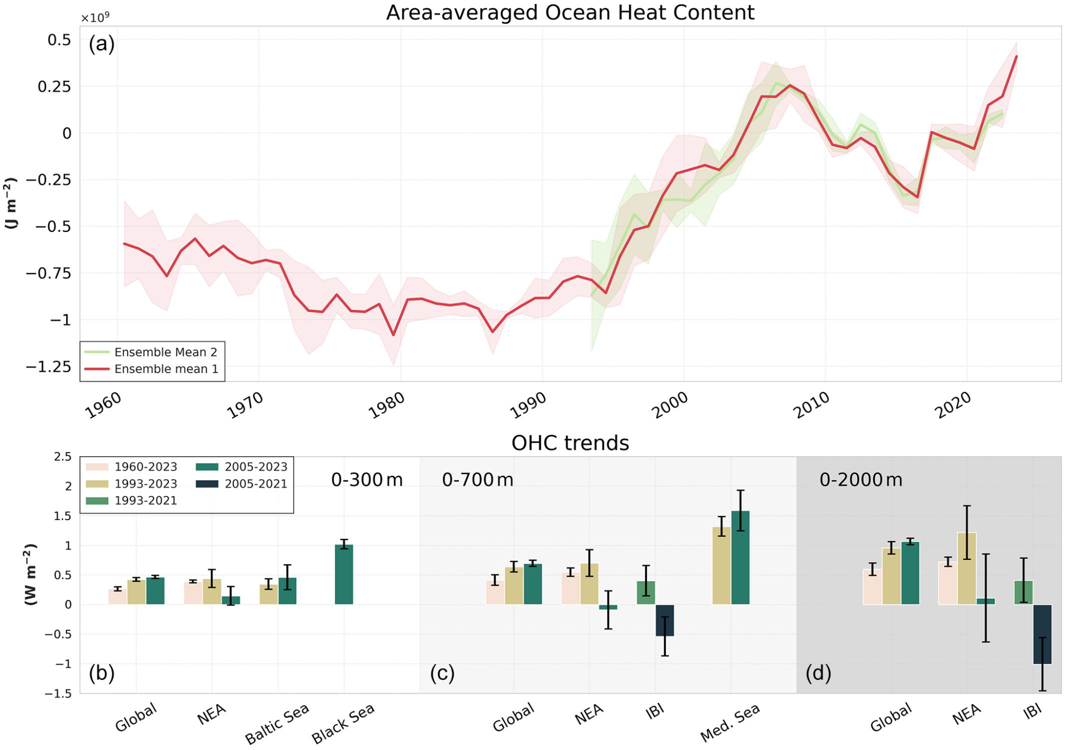

Figure 6. (a) Area-averaged ocean heat content in the northeastern Atlantic Ocean and adjacent seas (area indicated in Fig. 5) integrated over the upper 700 m depth based on an observation-based multi-product approach for ensemble 1 (product refs. OHC.1–4) and for the reanalysis-based ensemble 2 (product ref. OHC.8). The shaded areas indicate the ensemble spread. **(b–c)** Ocean warming trends derived over different periods (long-term: 1960–2023; mid-term: 1993–2023; recent decades: from 2005 onwards) and for different ocean layers (0–300, 0–700, 0–2000 m). Products for the northeastern Atlantic Ocean and adjacent seas area (NEA) include product refs. OHC.1–4; for the Baltic Sea product ref. OHC.9 is used; for the Black Sea product ref. OHC.10 is used; for the Mediterranean Sea product ref. OHC.11 is used; and for the Iberia–Biscay–Irish area product ref. OHC.12 is used. Trends of the global average (ensemble of product refs. OHC.1–2) are added for comparison, and an ordinary least-squares regression is used.

Most recent Ocean State Report estimates of absolute sea level recorded by altimeters onboard satellites show sea level rise over all the European seas ranging from 1.04 to 4.11 mm yr^{-1} with uncertainties on the order of 0.8 mm yr^{-1}. However, space-based radar altimetry does not provide reliable sea level data within 20 km of the coast, and the amount of valid data strongly decreases due to land contamination within the radar echo in the vicinity of the coast (Cazenave et al., 2022; The Climate Change Initiative Coastal Sea Level Team, 2020; Vignudelli et al., 2019). The sea level rise presents spatial variations with differences across basins, with the Baltic Sea absolute sea level rising at a faster rate and the Black Sea at a comparably slower pace (Fig. 7).

The northeastern Atlantic Ocean and adjacent seas area-averaged sea level time series (Fig. 7a) presents dominant interannual variability that in this region is dominated by the North Atlantic Oscillation (NAO) (Calafat et al., 2022; Chafik et al., 2019; Meli et al., 2023; Passaro et al., 2021; Volkov and Landerer, 2015). Karimi et al. (2022) showed that the NAO dominates the interannual variations of barystatic sea level in the Baltic Sea, whereas steric sea level plays a key role in decadal variations. Additionally, Chafik et al. (2019) proposed that the decadal sea level changes are driven by steric variability in the subpolar North Atlantic. Masina et al. (2022) presented an anticorrelation between the Mediterranean mean sea level and the upper branch of the Atlantic Meridional Overturning Circulation at 26.5° N.

Over the January 1993–June 2023 period, the regional rates of rise are positive across the northeastern Atlantic and adjacent seas region, except for some eddy-scale areas in the eastern Mediterranean Sea (Fig. 8a), where negative trends are observed. The rate of sea level rise in the Mediterranean Sea shows spatial variations that reflect changes at basin-scale circulation. Based on data over the altimetry era, Meli et al. (2023) showed that the mass component is the dominant driver in this area, except for in the Levantine and Aegean subbasins, where the steric component is the major contributor to the sea level trends.

In the Black Sea, the major drivers of change have been attributed to steric variability, water mass changes related to the Mediterranean inflow, and freshwater fluxes (precipitation, evaporation, and river discharge) (Tsimplis et al., 2004;

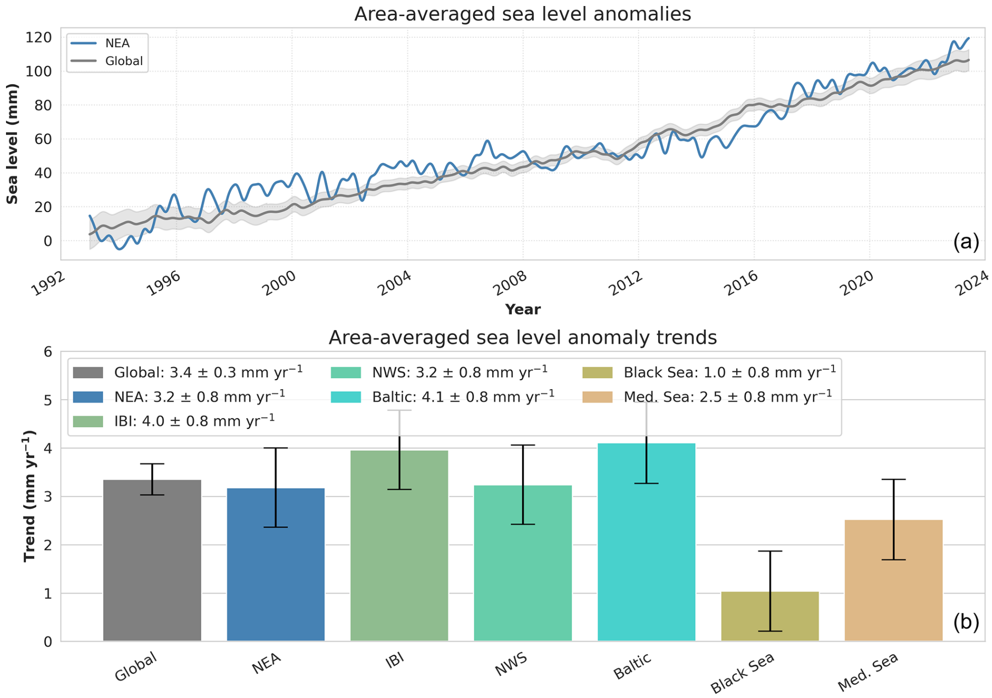

Figure 7. **(a)** Global (product ref. SL.1, grey curve) and northeastern Atlantic Ocean and adjacent seas (blue curve) mean sea level time series from January 1993 to June 2023. The shaded grey envelope shows the uncertainty of the global mean sea level time series. The time series have been adjusted from the seasonal cycle, low-pass-filtered (175 d cut-off), and corrected for GIA (Spada and Melini, 2019) and Topex-A drift (Ablain et al., 2017). The area average for the northeastern Atlantic Ocean and adjacent seas region (NEA) is indicated in Fig. 5 (black box). **(b)** Linear trends (in mm yr^{-1}) and associated uncertainties (black bars) for the global ocean, northeastern Atlantic Ocean and adjacent seas (NEA), the Iberia–Biscay–Irish (IBI), the North West Shelf (NWS), Baltic Sea, Black Sea, and Mediterranean Sea, shown as area-averaged sea level (product ref. SL.3-SL.7) time series from January 1993 to June 2023.

Volkov and Landerer, 2015). Most of the Mediterranean Sea and Black Sea are rising a slower rate than the global mean sea level (Fig. 8b). On the other hand, the entire Baltic Sea is rising faster than the global mean sea level trend, estimated to be 3.4 mm yr^{-1} over 1993–2023. Large areas of the Iberia–Biscay–Irish regional seas and the Gulf Stream region show sea level trends larger than the 4.3 mm yr^{-1} observed at global level for the last 10 years (June 2013–June 2023; Fig. 8b).

2.4 The Baltic Sea cryosphere

In addition to the polar seas, there are several marine regions around the world where sea ice occurs, such as the Baltic Sea. Sea ice occurs in a wide range of types and forms and significantly and directly affects marine transport and navigation. Specifically, the presence of sea ice cover sets special requirements for navigation, both for the construction of the ships and their behaviour in ice, as in many cases merchant ships need icebreaker assistance (JCOMM Expert Team on Sea Ice, 2017). Variations in sea ice conditions at different timescales in the Baltic Sea can also have implications for regional weather and climate as sea ice influences the way the ocean and atmosphere interact via fluxes of heat, water, or carbon. There is a tight link between surface air temperature and sea ice loss in the Baltic Sea that makes sea ice monitoring a critical climate indicator for this region (Granskog et al., 2006). Changes in sea ice are also known to affect the ecosystem in the Baltic Sea (Pärn et al., 2022; Granskog et al., 2006; Climate Change in the Baltic Sea, 2021; Meier et al., 2022; Eilola et al., 2013). For example, extreme events at the land–sea ice interface that adversely affect infrastructure at the coast happened several times between 2010 and 2019 (Girjatowicz and Łabuz, 2020). They are usually linked to onshore riding up of sea ice from shore to land, i.e. ice ridges, through a combination of specific sea ice conditions, storms, currents, and sea level variations (Leppäranta, 2013).

The importance of sea ice is reflected in the fact that sea ice variations have been monitored regularly in the Baltic Sea since the late 19th century (Meier et al., 2022). Basin-wide assessments have revealed that sea ice in the Baltic Sea undergoes large seasonal and interannual variations, and a long-term trend in sea ice loss has also been observed for this part of the world ocean (Meier et al., 2022; The BACC II Author Team, 2015). In the past, the entire Baltic Sea was covered in ice, as it was in the 1940s (Vihma and Haapala, 2009), whereas in most recent periods only the northern areas of the Baltic Sea are mostly covered in ice (Raudsepp et al., 2020).

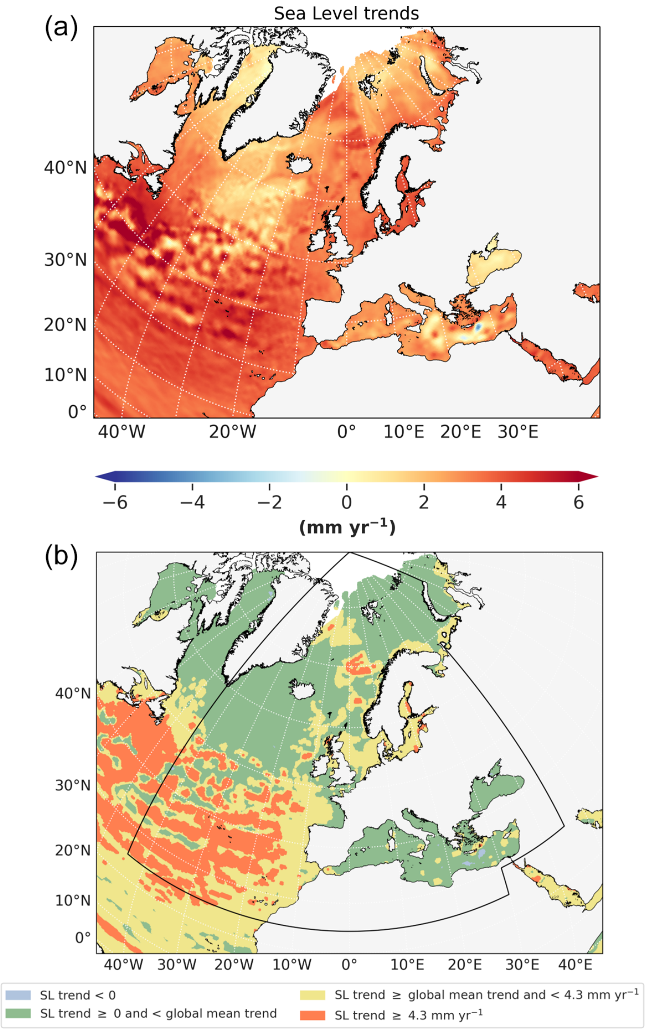

Figure 8. **(a)** Northeastern Atlantic Ocean and adjacent seas sector sea level trends from January 1993 to June 2023 (product ref. SL.2). **(b)** Shading map indicating the magnitude of the sea level rise rates: blue colour depicts regions with negative sea level trends, green colour indicates areas where sea level is rising slower than the altimetry era global mean sea level rate of rise of 3.4 mm yr^{-1}, yellow colour indicates locations where sea level is increasing at a range between the global mean trend and 4.3 mm yr^{-1}, and orange colour indicates regions where sea level is rising at faster rate than 4.3 mm yr^{-1}, which is the global mean sea level trend estimate over the last 10 years (June 2013–June 2023). The black box indicates the northeastern Atlantic Ocean and adjacent seas zone used. The data used are corrected for GIA (Spada and Melini, 2019) and TOPEX-A drift (Ablain et al., 2017).

Sea ice coverage in the Baltic Sea is strongly seasonal, and sea ice starts to form in October and may last until June of the following year. The ice season 2022/23 had the moderate maximum ice extent in the Baltic Sea and reached a maximum area of about 65 000 km^2, which amounts to 15 % of total Baltic Sea ice coverage. Usually, the maximum sea ice extent is reached at the end of February, but in 2023 maximum ice cover was recorded a couple of weeks later (Fig. 9). Although results indicate a decrease in sea ice extent over the period 1993–2023, the linear trend is not statistically significant.

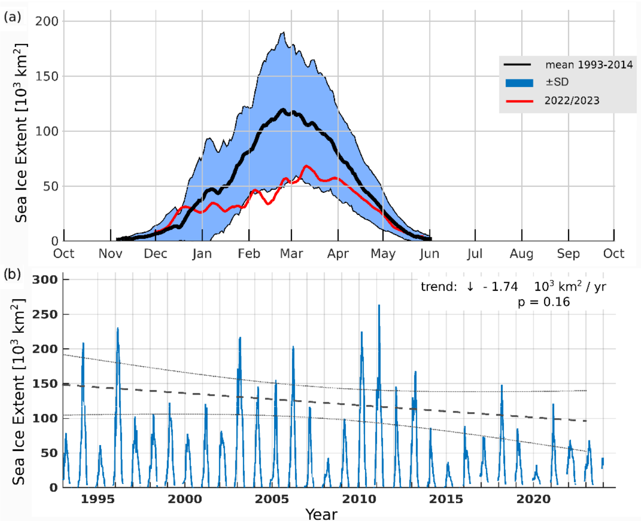

Figure 9. **(a)** Time series of day-of-year averaged sea ice extent derived from remote sensing and in situ observations (product ref. SI.7; Uiboupin et al., 2008; Havsis | SMHI, 2023). Long-term mean (black line) and 1 standard deviation (blue shading) are calculated over the period October 1992–September 2014. Daily sea ice extent is for the 2022/2023 ice season (red line). **(b)** Time series of the area-integrated daily sea ice extent for the Baltic Sea in 1993–2023. Initial data that consist of remote sensing and in situ observations (product ref. SI.7; Uiboupin et al., 2008; Havsis | SMHI, 2023) are smoothed using 7 d window moving-average filter.

3 Ocean acidification

On average, ocean acidification in the northeastern Atlantic Ocean and adjacent seas follows the same path as observed at the global scale, showing a steady decrease in surface pH since 1985 at an average rate on the order of the global mean trend of -0.017 ± 0.001 pH units per decade (Fig. 10). At a regional scale, the map of regional trends of sea surface pH in the northeastern Atlantic Ocean and adjacent seas is not homogeneous and presents geographically varying patterns (Fig. 11). In the open ocean, the main driver of regional ocean surface pH change is predominantly attributed to atmospheric CO_2 concentrations (Gehlen et al., 2020). When approaching the coast, additional stressors of industrial or agricultural origin and natural fluctuations from ocean processes (e.g. circulation, coastal upwelling) contribute to variations in ocean pH. For example, nutrient runoff by rivers leads to eutrophication of coastal waters, which can enhance pH variations, particularly in stratified coastal water systems through CO_2 uptake (primary production) and release (bacterial respiration) (Carstensen and Duarte, 2019).

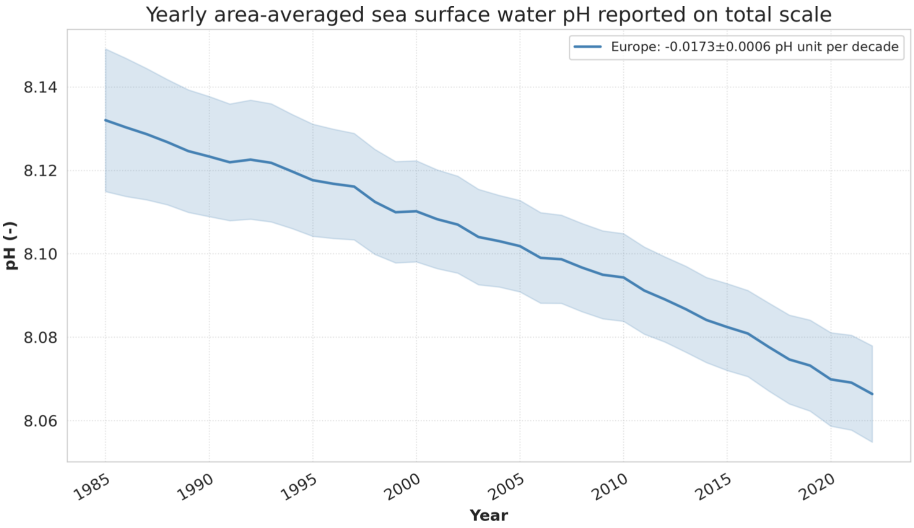

Figure 10. Annual mean sea surface water pH reported on a total scale averaged over the northeastern Atlantic Ocean and adjacent seas (black polygon in Fig. 8). The regions of high uncertainty in the regional trend estimates have been excluded from the regional averaging (areas shaded in grey in Fig. 11). The shaded area around the curve indicates the uncertainty envelope computed as a quadratic regional mean of the monthly pH uncertainty estimates, which is then averaged over time to obtain yearly estimates. The northeastern Atlantic Ocean and adjacent seas area-averaged time series is derived from product ref. OA.3.

In the northeastern Atlantic Ocean, regional patterns of pH decrease range from about −0.020 to −0.012 pH units, i.e. at comparable or higher rates than the global average (Fig. 11). The North Atlantic Ocean is one of the most important anthropogenic CO_2 sinks of the global ocean, storing about 25 % of the global oceanic anthropogenic CO_2 despite it only covering 15 % of the global ocean surface (Sabine et al., 2004). This is mainly due to the Atlantic Meridional Overturning Circulation (AMOC) that transports ocean surface waters laden with anthropogenic CO_2 from the equatorial Atlantic Ocean to the subpolar North Atlantic Ocean, which enters the deep ocean through deep-water mass formation and then flow equatorwards (Bopp et al., 2015; Gruber et al., 2019; Khatiwala et al., 2013; Sabine et al., 2004).

In the Mediterranean Sea, reported rates of pH decrease range from about −0.016 pH units in the northern parts of the basin to more than 0.022 pH units in the southern parts (Fig. 11). Available estimates of pH trend from local in situ observations provide a sparse and quite heterogeneous range of values (Luchetta et al., 2010; Marcellin Yao et al., 2016; Kapsenberg et al., 2017; Merlivat et al., 2018; Hassoun et al., 2019; Wimart-Rousseau et al., 2021; Hassoun et al., 2022), while estimates based on the Copernicus Mediterranean Sea Biogeochemistry Reanalysis (Cossarini et al., 2021) reports a lower range (from −0.012 to −0.006 pH units per decade). The Mediterranean Sea has a very rich and specific biodiversity, and changes in the pH and carbonate chemistry over the long term may have significant impacts on calcifying organisms, such as plankton, corals, and shells, and the whole dependent food web, as well as on aquaculture and fisheries activities (e.g. Cramer et al., 2018; Bednarsek et al., 2023). The Mediterranean Sea has a specifically large capacity to absorb and buffer atmospheric CO_2 due to the following features.

1. The Mediterranean Sea has a higher alkalinity from river discharges and Black Sea inflow combined with evaporation, which in turn increases the capacity to neutralize acid and favour dissolution of CO_2 (e.g. Middelburg et al., 2020; Schneider et al., 2010; Cossarini et al., 2015).

2. The Mediterranean Sea has a ventilation of deep waters on shorter timescales from a fast overturning circulation (i.e. a few decades to 200 years), which leads to fast transfer of anthropogenic CO_2 into deep ocean layers (e.g. Schneider et al., 2010; Hassoun et al., 2015).

The highest alkalinity levels are reported in the eastern Mediterranean Sea, such as in the Aegean and Levantine basins, which are triggered by inflow from the Black Sea, stronger evaporation, and larger salinity than in the western basin (Schneider et al., 2007; Hassoun et al., 2015). Deep water mass formation – generally evolving during winter months – is located in the Gulf of Lion, the Adriatic Sea, and the Aegean basin (Hassoun et al., 2015; Ingrosso et al., 2017). These intermediate and deep-water masses then flow westward until they enter the Atlantic Ocean through the Strait of Gibraltar (Flecha et al., 2019).

In the Black Sea, uncertainties are too large to determine estimates of ocean pH trends, which is predominantly explained by a lack of observations in this area (Fig. 11). In addition, specific hydrographic conditions and dynamics pre-

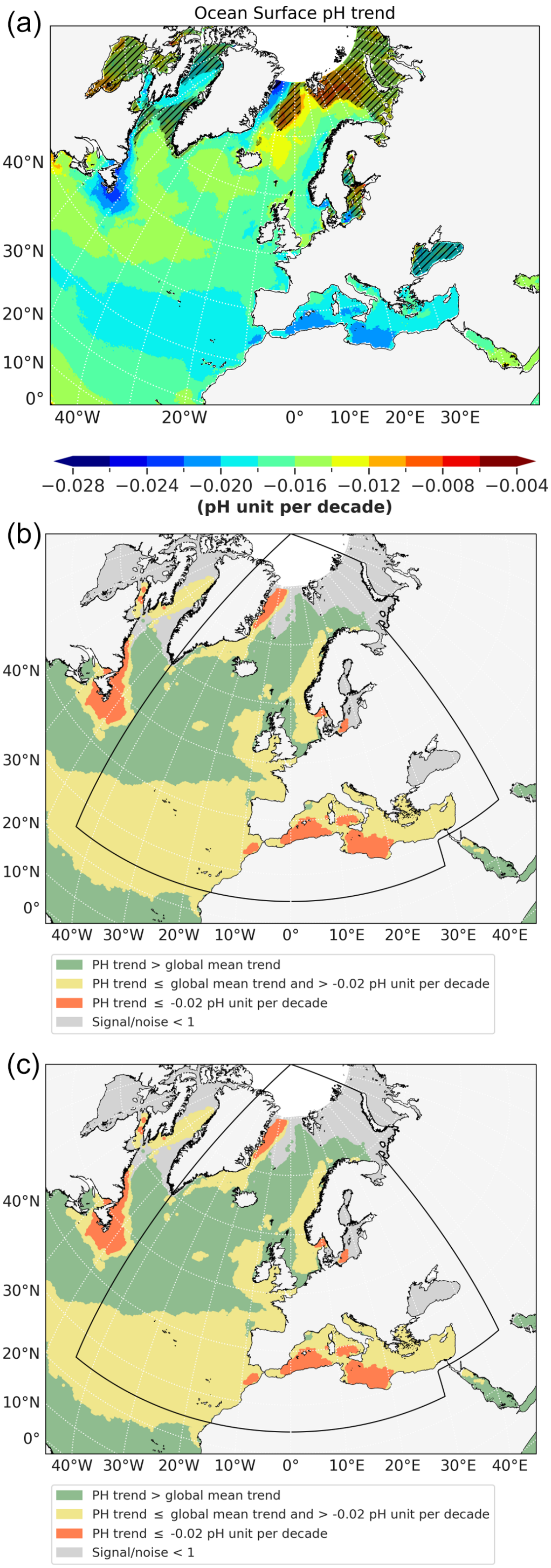

Figure 11. **(a)** Regional trend of sea surface pH (in pH units per decade) over the period 1985–2022 from product ref. OA.1. The black hatches represent areas where the noise exceeds the signal. **(b)** The same as panel **(a)** but representing areas where the regional pH is decreasing slower than the global mean sea surface pH trend of −0.017 pH units per decade (green), at a rate between the global mean sea surface pH trend and −0.02 pH units per decade (yellow), or at faster rate than −0.02 pH units per decade (orange). The grey shading represents areas where the noise exceeds the signal. The black box indicates the northeastern Atlantic Ocean and adjacent seas zone used.

vail, adding further complexity to the quantification of long-term pH change in this area. For example, the Black Sea is a very stratified system and is a semi-enclosed basin influenced by water exchange with the Sea of Marmara and the Mediterranean Sea (BSC, 2019). The Black Sea is also characterized by a permanent anoxic layer below 100 to 150 m with significant concentrations of hydrogen sulfide, which prevents benthic life beyond the continental shelf. In addition, major inflows from rivers with high alkalinity such as the Danube, the Dnipro, and the Dniester enter the Black Sea, resulting in greater alkalinity as compared to the open-ocean average (Hiscock and Millero, 2006), affecting acidification (Middelburg et al., 2020). During the 1960–1990s, the Black Sea has faced urban and industrial development along its coasts, which brought major chemical and waste pollution, together with overfishing of largest species and an introduction of invasive comb jelly, which strongly disrupted the food web. In addition, large agricultural fertilizer runoff has led to dramatic eutrophication events in the 1980–1990s (Kideys, 2002). In 1992, the Bucharest Convention for the Protection of the Black Sea Against Pollution was signed with the aim, amongst others, of controlling land-based sources of pollution (BSC, 2023). Since then, pollutants have been reduced (BSC, 2019, 2008, 2002), and the Black Sea is now considered in a post-eutrophication state (Mee et al., 2005). The Black Sea is also exposed to ocean warming (see Sect. 2), affecting the atmospheric CO_2 uptake in the Black Sea. However, today there is no clear scientific consensus regarding long-term pH decrease (acidification) in the Black Sea, as observations and studies on the subject are rare, and the emergence of a significant climate signal may be dampened by seasonal and interannual pH variations due to the processes and events mentioned above (Polonsky and Grebneva, 2019; Elge, 2021; Polonsky, 2012).

Large uncertainties also hamper the study of ocean acidification in the Baltic Sea (Fig. 11), which is particularly challenged by different terrestrial drivers of pH change (Duarte et al., 2013; Carstensen and Duarte, 2019). In addition, specific geographic and hydrographic conditions induce further complexity. The Baltic Sea is a semi-enclosed sea where ocean waters from the North Sea mix with riverine freshwaters. Low-salinity waters are generally associated with low alkalinity, which provides buffer capacity to ocean acidification (Middelburg et al., 2020; Meier et al., 2022). The waters are brackish with an average salinity of 7 psu in the surface layers and almost fresh waters (0–2 psu) in the northernmost (Gulf of Bothnia) and easternmost (Gulf of Finland) parts of the basin (HELCOM, 2023b). The alkalinity of the Baltic Sea is also affected by river runoff, draining weathered carbonate minerals from rocks in river catchment areas (Müller et al., 2016; Gustafsson and Gustafsson, 2020; Gustafsson et al., 2023). Generally, alkalinity tends to increase on the long-term in the Baltic Sea, due to several drivers that have evolved over the last decades, such as through weathering in the drainage basins, acidic rain, agricultural liming, increase in precipitations, and ocean primary production (Müller et al., 2016; Meier et al., 2022; Gustafsson et al., 2023). In addition to changes in alkalinity, the Baltic Sea also faces ocean warming (Meier et al., 2022) and anthropogenic eutrophication (HELCOM, 2023b; Gustafsson et al., 2012; Andersen et al., 2017; Murray et al., 2019; Gustafsson et al., 2023), affecting regional patterns of ocean pH. Since the 1990s, major efforts have been made by the countries bordering the Baltic to reduce the nutrient inputs into the Baltic Sea and hence to limit eutrophication. Still, there is no clear sign of general recovery of the system (Andersen et al., 2017; HELCOM, 2023a, b), and models project that several decades will be needed to reach good eutrophication status in most of the Baltic Sea (Murray et al., 2019). Moreover, shorter cold seasons, longer mild seasons driven by global warming, and resulting changes in primary production and associated carbonate cycle can in turn impact the evolution of the pH conditions. Some areas alternate roles of CO_2 sink and source across the year, and seasonal variations can locally reach more than 0.8 pH units (HELCOM, 2023b). Because of the strong interannual and seasonal variations of these natural and human-induced interlinked processes and some associated mitigation or counteracting effects like the increase in alkalinity, there is currently no significant signal of long-term ocean acidification observed in the Baltic Sea, except in a few regions, such as in the Danish Straits (Carstensen et al., 2018).

4 Ocean variability

4.1 Mediterranean meridional overturning circulation

The Mediterranean Sea is a semi-enclosed basin characterized by peculiar thermohaline circulations consisting of a basin-scale zonal overturning connected to the Atlantic through the Strait of Gibraltar and two internal meridional cells, one for the west and another for the eastern basin, driven by deep-water formation in the Gulf of Lion and the Adriatic Sea, respectively (see Tsimplis et al., 2006; Schroeder et al., 2012; Pinardi et al., 2023 for general information). The latter experienced a major shift in the early 1990s with deep-water formation temporarily occurring in the southern Aegean Sea (the so-called Eastern Mediterranean transient; Roether et al., 2014). A recent investigation of the dynamics of intermediate and deep-water formation can be found in Waldman et al. (2018).

Masina et al. (2022) presented changes in the Gibraltar inflow transport from the Atlantic Ocean into the Mediterranean Sea that trigger basin-mean sea surface height variability, which is anti-correlated with variations in the Atlantic Meridional Overturning circulation (AMOC). They show that during years of weaker (stronger) AMOC and higher (lower) sea surface height in the Mediterranean Sea, a stronger (weaker) Azores Current results in stronger (weaker) Gibraltar inflow transport.

The zonal overturning cell enables the connection between the inflow transport at the Gibraltar Strait and remote areas of the eastern Mediterranean basin. The wide and shallow Strait of Sicily sill divides the western Mediterranean basin from the eastern Mediterranean basin (Pinardi et al., 2019). The western sub-basin clockwise meridional overturning circulation is associated with the deep-water formation area of the Gulf of Lion, while the eastern clockwise meridional overturning circulation is composed of multiple cells associated with different intermediate- and deep-water sources in the Levantine, Aegean, and Adriatic seas (Lyubartsev et al., 2020).

Based on these characteristics, the Mediterranean meridional overturning circulation can be monitored by the western Mediterranean overturning index (WMOI) and eastern Mediterranean overturning index (EMOI) (Lyubartsev et al., 2020) (Fig. 12). These indices are useful for monitoring the health of the Mediterranean Sea in terms of stratification and deep-water formation, as these factors mediate the exchange of oxygen and other tracers between the surface and the deep ocean, fostering the establishment of early warming indices for the Mediterranean Sea to support the Sustainable Development Goal (SDG) 13 Target 13.3 (Lyubartsev et al., 2020).

Both the EMOI and the WMOI show no long-term trend, and both records are characterized by large interannual- to decadal-scale change (Fig. 12). Overall, the overturning circulation in the eastern Mediterranean Sea is stronger as compared to the western basin. This is demonstrated by the generally higher values of EMOI as compared to WMOI (Fig. 12). The difference in both indices is most prominent during the major climatic event in the circulation and water mass properties of the Mediterranean Sea in the last century, i.e. the so-called Eastern Mediterranean Transient (EMT; Roether et al., 2014; Incarbona et al., 2016). The pronounced peak in EMOI in the year 1992 is driven by the EMT. In 1999, the difference between EMOI and WMOI started to decrease because EMT water masses reached the Strait of Sicily flowing into the western Mediterranean Sea (Lyubartsev et al., 2020).

During the past 2 decades, WMOI reached another maximum in the year 2006, potentially linked to anomalous deep-water formation during the Western Mediterranean Transition (Lyubartsev et al., 2020). In 2019, the EMOI reached another high value, which is discussed as being triggered by subduction of the Levantine Intermediate Water along the Cretan Sea and the Rhodes Cyclonic Gyre (Taillandier et al., 2022). In 2022, the EMOI peaked again, possibly linked to deep-water formation events that took place in the northern and central Aegean Sea during the winter of 2021–2022 (Potiris et al., 2024).

4.2 Nordic Seas volume transport

The circulation of the water masses and distribution of heat and salinity between the North Atlantic and the Arctic and in the Arctic Ocean are governed by the northward flow of relatively warm and saline Atlantic Water through the Nordic Seas across the Iceland–Faroe–Scotland Ridge and into the Arctic, balanced by outflow of cold Arctic Water masses through the western Nordic Seas (Lien and Raj, 2018; Mauritzen et al., 2011; Rudels, 2012). Moreover, the exchanges between the North Atlantic and the Arctic have broad effects on sea ice, ecology, biogeochemistry, and atmospheric climate (Smedsrud et al., 2013; Polyakov et al., 2023; Gerland et al., 2023; Lundesgaard et al., 2022). Specifically, the Atlantic Water flow plays an integral part in defining both the physical and biological border between the boreal and Arctic realms. Variability of Atlantic Water flow to the Barents Sea has been found to move the position of the ice edge and influences the sea ice cover in the Barents Sea (Onarheim et al., 2015; Lien et al., 2017) and habitats of various species in the Barents Sea ecosystem (Fossheim et al., 2015; Jørgensen et al., 2022).

The northward flow of Atlantic water into the Arctic through the Faroe–Shetland Channel amounts to 2.5 Sv ($1\,\mathrm{Sv} = 10^6\,\mathrm{m^3\,s^{-1}}$) over the period 1993–2022 (Fig. 13), which is in within the uncertainty range of observation-based estimates of 2.7 ± 0.5 Sv (1993–2015) (Berx et al., 2013). In addition, a small but significant negative trend of -0.17 Sv per decade is reported for the period 1993–2022 (Fig. 13). This is in comparison to a reported non-significant trend of $-0.006\,\mathrm{Sv\,yr^{-1}}$ based on observations during the period 1993–2015 (Østerhus et al., 2019). The modelled transport in the most recent year did not differ from the historical values. The hydrographic properties of the inflowing Atlantic Water affects the hydrographic properties in the downstream Norwegian and Barents seas, and these areas are currently recovering from record low salinity levels advected from the North Atlantic (Holliday et al., 2020). Moreover, such changes may also be a precursor for different water mass composition and hence nutrients, phytoplankton, and zooplankton communities being advected into the Nordic Seas (Hátún et al., 2017). However, the strength of the inflow itself has also been shown to impact the hydrographic properties downstream in the Norwegian and Barents seas, where stronger inflow causes increased salinity and temperature (Sundby and Drinkwater, 2007) in addition to regional ocean–atmosphere interaction (Segtnan et al., 2011; Mork et al., 2019).

In the Barents Sea Opening, the model indicates a long-term average net Atlantic water inflow of 2.2 Sv compared to an observation-based estimate of 1.8 Sv (Smedsrud et al., 2013). Note the different time window used for averaging. The model results indicate a small, non-significant negative trend of -0.04 Sv per decade, which is in agreement with observations indicating no trend over the 1998–2020 period (ICES, 2022). According to Østerhus et al. (2019), a positive, significant trend of $0.016\,\mathrm{Sv\,yr^{-1}}$ was found for the period 1998–2013. Note, however, the different time window used for the calculation. The modelled transport in the most recent year did not differ from historical values. In the Fram Strait, the model data indicate a positive trend in the Atlantic Water

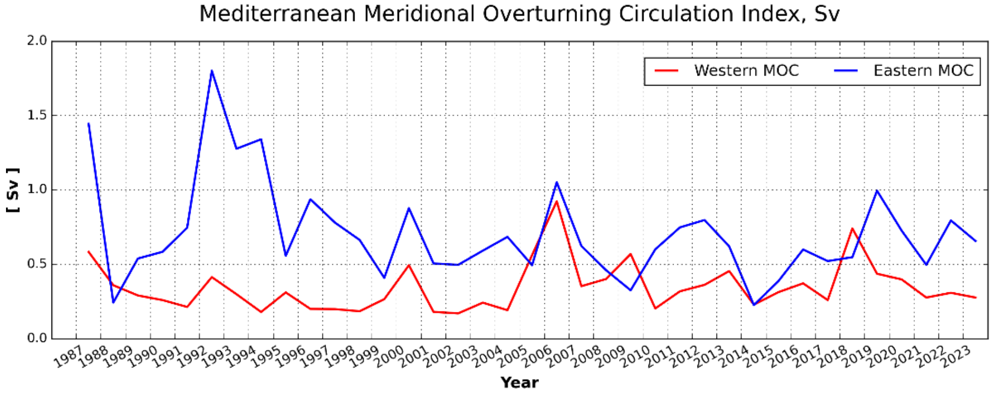

Figure 12. Time series of Mediterranean overturning indices (Sverdrup) calculated from the annual average of the meridional stream function based on product ref. OV.3., computed using the reanalysis dataset from January 1987 to July 2022 and the interim dataset August 2022 to December 2024 of product ref. OV.4. Blue represents the eastern Mediterranean overturning index ($< 36.5°$ N), and red represents the western Mediterranean overturning index ($\geq 40°$ N, $z > 300$ m).

transport to the Arctic of 0.45 Sv per decade for the period 1993–2022. This trend is partly explained by increased temperature in the West Spitsbergen Current during the period 2005–2010 (e.g. Walczowski et al., 2012), which caused a larger fraction of the water mass to be characterized as Atlantic Water ($T > 2$ °C). Moreover, the strong recirculation in the Fram Strait area further complicates the interpretation of the results.

4.3 Major Baltic inflows

In the Baltic Sea, the salinity and its changes are key factors in determining the overall stratification conditions, which strongly influence different ecosystem processes and play an important role in the energy and water cycles in this area (Lehmann et al., 2022). The long-term change in water salinity of the Baltic Sea is determined by the inflow of saline water from the North Sea and its encounter with freshwater originating from numerous rivers across the Baltic coast and from the net precipitation (Lehmann et al., 2022). A major Baltic inflow (MBI) is an event that transports large amounts of saline water into the Baltic Sea through the Danish Straits (Mohrholz, 2018), shaping the stratification and oxygen conditions and hence influencing the marine ecology of the Baltic Sea. MBIs occur sporadically, usually many years apart, and are usually of barotropic origin, initiated by a special sequence of large-scale meteorological events in winter and spring. Since 1996, summer inflows of baroclinic origin have been observed. These summer inflows inject more highly saline water with higher temperatures and low oxygen content into the halocline of the Baltic Sea (Lehmann et al., 2022).

MBI can be detected and monitored in the bottom-layer salinity of the Arkona Basin and the Bornholm Basin and through the vertical distribution of temperature, salinity, and dissolved oxygen concentration in the Gotland Basin. Temperature, salinity, and dissolved oxygen profiles in the Gotland Basin enable the estimation of the amount of the major Baltic inflow water that has reached the central Baltic, the depth interval that has been the most affected, and how much the oxygen conditions have been improved. Major Baltic inflows were identified in 1993, 2002, and 2014, showing salinity peaks in the three basins (Figs. 14, 15) and displaying a very clear signal in the Gotland Basin with water salinity, temperature, and dissolved oxygen conditions up to 100 m depth (Raudsepp et al., 2018). The bottom salinity has decreased since 2017 when the effect of the last MBI in 2014 has receded (Fig. 15). There was no MBI in winter 2022/23 and in 2023 salinity continued to decrease and oxygen was completely consumed below the depth of 75 m in the Gotland Basin.

5 Ocean extremes

5.1 Marine heatwaves

Marine heatwaves can have dramatic impacts on marine ecosystems, such as reduction of primary production, migration or reduction of endemic species, emergence of species coming from other regions, and mass mortality of organisms (Smith et al., 2023; Oliver et al., 2019; Garrabou et al., 2022), which in turn can have adverse impacts on human systems like fisheries and aquaculture (Cheung and Frölicher, 2020; IPCC, 2022; Wakelin et al., 2021). Like in the global ocean, the frequency, intensity, and duration of MHW events have increased in recent years in the northeastern Atlantic Ocean and adjacent seas and are particularly increased in the semi-enclosed seas like the Mediterranean and Black seas (Peal et al., 2023; Yao et al., 2022; Oliver et al., 2018; IPCC, 2021b; Darmaraki et al., 2019; Dayan et al., 2023; Juza et al., 2022). These events are expected to continue to increase in the future (Yao et al., 2022; Oliver et al., 2019).

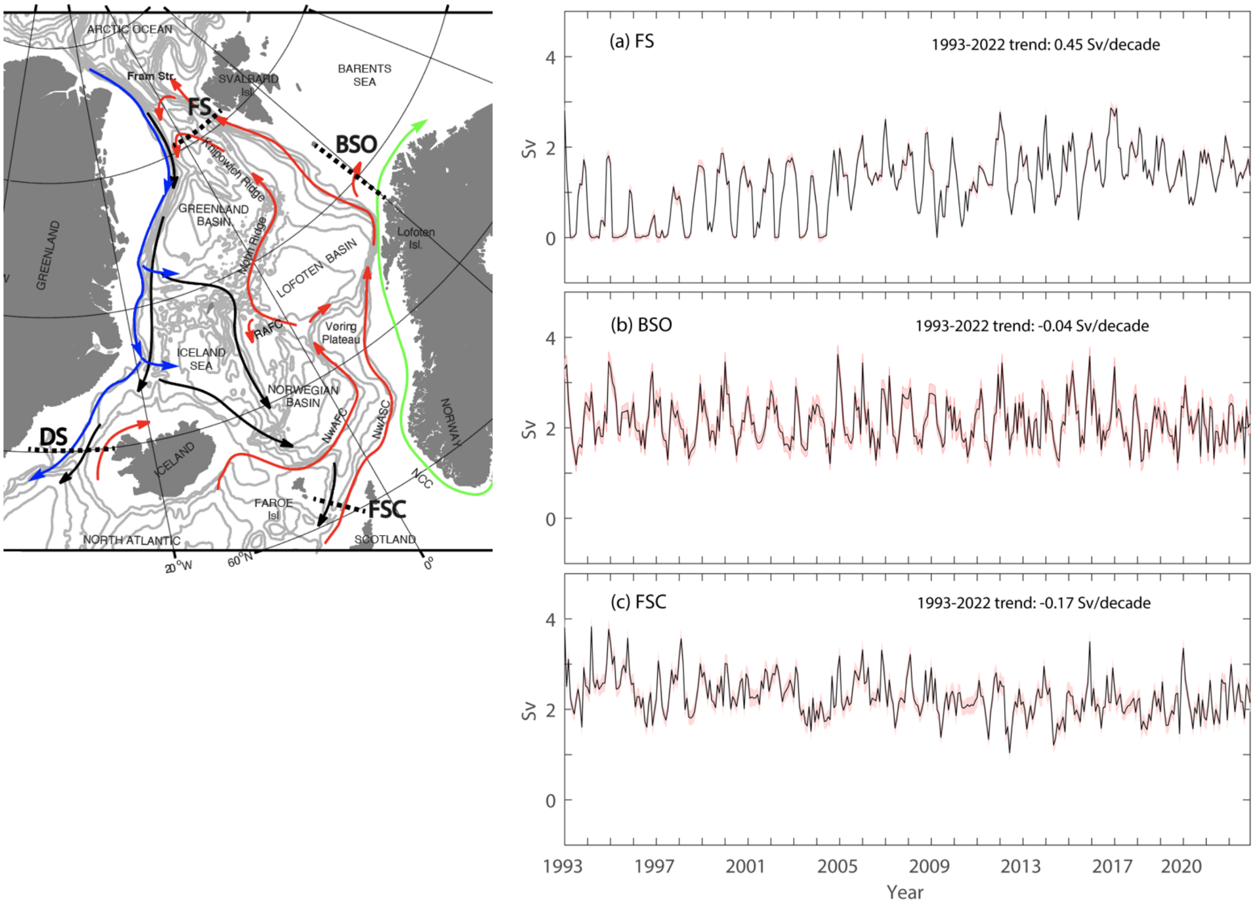

Figure 13. The left panel shows schematic water pathways in the Nordic Seas showing the overturning circulation of northward-flowing Atlantic Water (red) to southward-flowing transformed waters at depth (black). The two branches of the Norwegian Atlantic Current, the Norwegian Atlantic slope current (NwASC), and Norwegian Atlantic front current (NwAFC) are represented by red arrows. The fresh Norwegian Coastal Current (NCC) is indicated in green, while the Greenland Current is marked in blue; see Raj and Halo (2016) for details. Grey isobaths are drawn at 600 m depth levels. The dashed lines provide the locations of the sections: Faroe Shetland Channel (FSC), Barents Sea opening (BSO), Fram Strait (FS), and Denmark Strait (DS). The right-hand column shows product ref. OV.5 modelled volume transport of Atlantic Water to the Arctic via the Fram Strait **(a)**, to the Barents Sea via the Barents Sea Opening **(b)**, and to the Nordic Seas via the Faroe Shetland Channel **(c)**. Positive values indicate northward flow. The shaded region indicates the error associated with the monthly mean transport estimates.

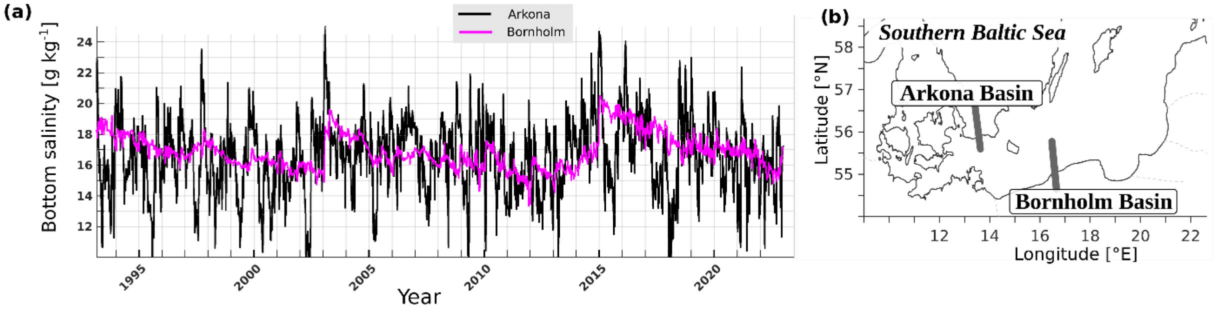

Figure 14. Time series of bottom salinity in the Arkona (black line) and Bornholm basins (magenta line) for the period of 1993–2022 (product ref. OV.6 derived from regional Copernicus Marine Service reanalysis) **(a)**. The locations of the Arkona and Bornholm basins are shown in panel **(b)**.

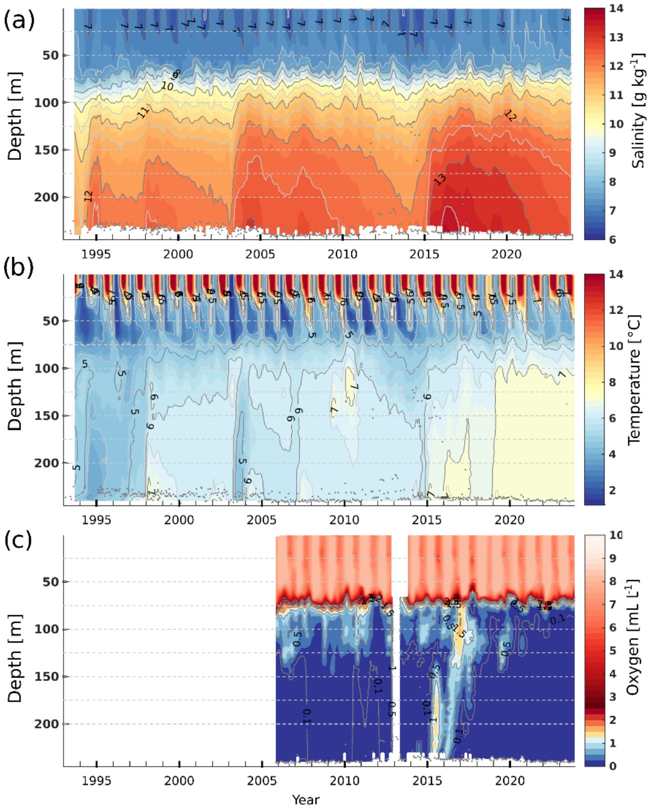

Figure 15. Profiles of salinity **(a)**, temperature **(b)**, and dissolved oxygen concentration **(c)** for the period 1993–2023 in the Gotland Basin in the Baltic Sea (product ref. OV.7) based on in situ near-real-time observations.

From 1982 to 2023, the fraction of the ocean surface that did not experience any MHW event over the year in the northeastern Atlantic Ocean and adjacent seas (black polygon in Fig. 11) dramatically dropped, from more than 80 % in 1982 to less than 10 % in 2023 (Fig. 11). The major drop occurred between 1982 and the early 2000s. Since then, the yearly fraction of ocean surface without any MHW event has remained relatively stable at around 20 % ± 10 % (i.e. 80 % ± 10 % of the region is affected by MHW events every year). The fraction of ocean surface that was affected by moderate MHW events increased from about 10 % to about 45 % between 1982 and 2001. It remained relatively stable between 2000 and 2010 and then started to drop in 2010 down to less than 20 % in 2023. The fraction of the ocean surface experiencing strong MHW events has been continuously increasing over the whole period, from less than 5 % in 1982 to more than 45 % in 2023. Severe and extreme MHW events also show a positive trend over the last decade. However, the trend of extreme category events is strongly dampened when excluding sea-ice-covered regions (Fig. 11), as is the case for the global estimates. In addition, similar to the global estimates, the impact is minor for the other categories (not shown). Since 2013, the cumulative fraction of ocean surface affected by strong, severe, and extreme MHW events has been almost systematically larger than that affected by moderate MHW events. As we consider a fixed baseline for the climatology, these results are consistent with the fact that this part of the ocean is one of those that have been warming at the fastest rates due to global warming.

Regarding the marine heatwave durations (Fig. 16), the yearly averaged maximum continuously increased from 1982 (less than 10 d) to 2023 (about 40 d). Until the mid-2010s, most of the longest MHW events lasted less than 15 d. Since then, the ocean surface fraction affected by short events at most has dropped, down to about 12 % in 2023. The ocean surface fraction affected by events lasting between 2 weeks and 1 month has increased from 1982 (less than 5 %) to the early 2000s, when it stabilized around 25 %. The ocean surface fraction affected by events lasting between 1 and 2 months has continuously increased from almost no occurrence in 1982 to more than 30 % in 2023, and these events now prevail on other MHW durations in the region. Similarly, the ocean surface fraction experiencing MHW events lasting between two and four months started to rise in the 1990s and reached more than 20 % in 2023. Events lasting more than four months remain at a low level but have also been more observed since 2015. Similar results are obtained when excluding sea-ice covered regions from the computation (not shown).

In 2022 and 2023, 91 % and 93 %, respectively, of the ocean surface in the northeastern Atlantic Ocean and adjacent seas were affected by at least one moderate marine heatwave (Table 2). These numbers rise to about 95 % when considering only the European shelf seas, i.e. regions at depths between 0 and 200 m. In 2022, about 60 % of the northeastern Atlantic Ocean and adjacent seas were affected by strong (49 %) or even severe (7 %) and extreme (5 %, mostly in the Arctic region) marine heatwaves. Some marine heatwave events prevailed for a long period of about 4 to 5 months, such as in the western Mediterranean Sea, the English Channel, and the southern Arctic. Other areas affected by strong to extreme marine heatwaves and events lasting about 1 to 2 months include the central Mediterranean Sea, the North Sea, and large parts of the Iberia–Biscay–Irish areas (Fig. 11).

In 2023, almost 80 % of the ocean surface in the northeastern Atlantic Ocean and adjacent seas experienced MHW of at least strong (45 %), severe (24 %), or extreme (8 %) categories (Table 2). Compared to 2022, the Bay of Biscay and the northeastern Atlantic region off the Iberian coast were particularly affected by marine heatwaves in 2023 (Fig. 17), with events lasting more than 5 months (Fig. 17). This corresponds to the anomalously warm surface waters that have been observed in the tropical North Atlantic Ocean since March 2023. Other regions hit by MHW events lasting 2 to 3 months in 2023 include the English Channel and the Irish Sea, the Alboran Sea, the Adriatic Sea, the Levantine basin, and the western part of the Black Sea (Fig. 17). All of these

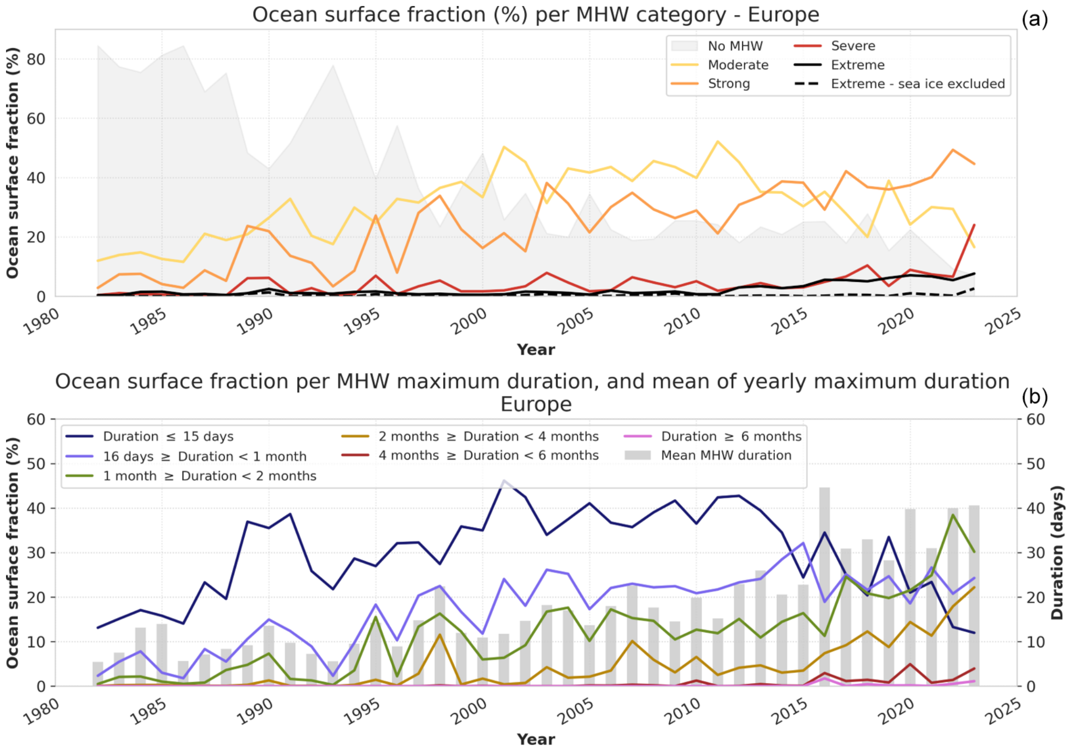

Figure 16. **(a)** Percentage of ocean surface where the maximum marine heatwave category detected was moderate, strong, severe, extreme, or no marine heatwave in the northeastern Atlantic Ocean and adjacent seas zone. The dashed black line shows the same information for extreme categories when excluding sea ice regions from the computation (see Fig. 11 for the sea ice mask applied, with a minor impact for the other categories). These ocean fraction estimates are done following the same method as Hobday et al. (2018). **(b)** Percentage of global ocean surface where the maximum MHW duration was within a given period (lines) and the yearly mean of maximum MHW durations (bars) in the northeastern Atlantic Ocean and adjacent seas zone (black polygon in Fig. 11). The evaluation of these MHW indicators is done following the method of Hobday et al. (2016) and is derived from product refs. SST.1 and SST.2.

Table 2. Percentage of ocean surface affected by a MHW event in 2022 and 2023, depending on the category, in the northeastern Atlantic Ocean and adjacent seas and when considering only the shallow waters (depth between 0 and 200 m) of the area. The information is also provided when excluding the sea-ice-covered regions from the computation (see Fig. 17 for the sea ice mask applied). These ocean fraction estimates are done following the same method as Hobday et al. (2018).

Percentage of ocean surface hit by a MHW	Northeastern Atlantic Ocean and adjacent seas				Northeastern Atlantic Ocean and adjacent seas – shelf (0–200 m deep)			
	Whole area		Sea ice excluded		Whole area		Sea ice excluded	
	2022	2023	2022	2023	2022	2023	2022	2023
All categories	91 %	93 %	93 %	97 %	94 %	95 %	95 %	96 %
Max category 1 (moderate)	29 %	17 %	33 %	17 %	24 %	8 %	28 %	8 %
Max category 2 (strong)	49 %	45 %	53 %	49 %	49 %	53 %	58 %	62 %
Max category 3 (severe)	7 %	24 %	7 %	28 %	8 %	17 %	8 %	24 %
Max category 4 or higher (extreme)	5 %	8 %	< 0.5 %	3 %	13 %	17 %	< 0.5 %	2 %

regions also experienced strong to severe MHW events over the year 2023 (Fig. 17).

The Mediterranean Sea is an area where also a multi-decadal increase in the frequency and intensity of marine heatwaves has been reported (Juza et al., 2022; Dayan et al., 2022). This basin experienced an exceptionally long-lasting and intense series of marine heatwave events between 2022 and 2023 (Fig. 17), as MHWs have been continuously detected since June 2022 until the end of 2023, particularly in the western basin (Marullo et al., 2023). In 2022, the

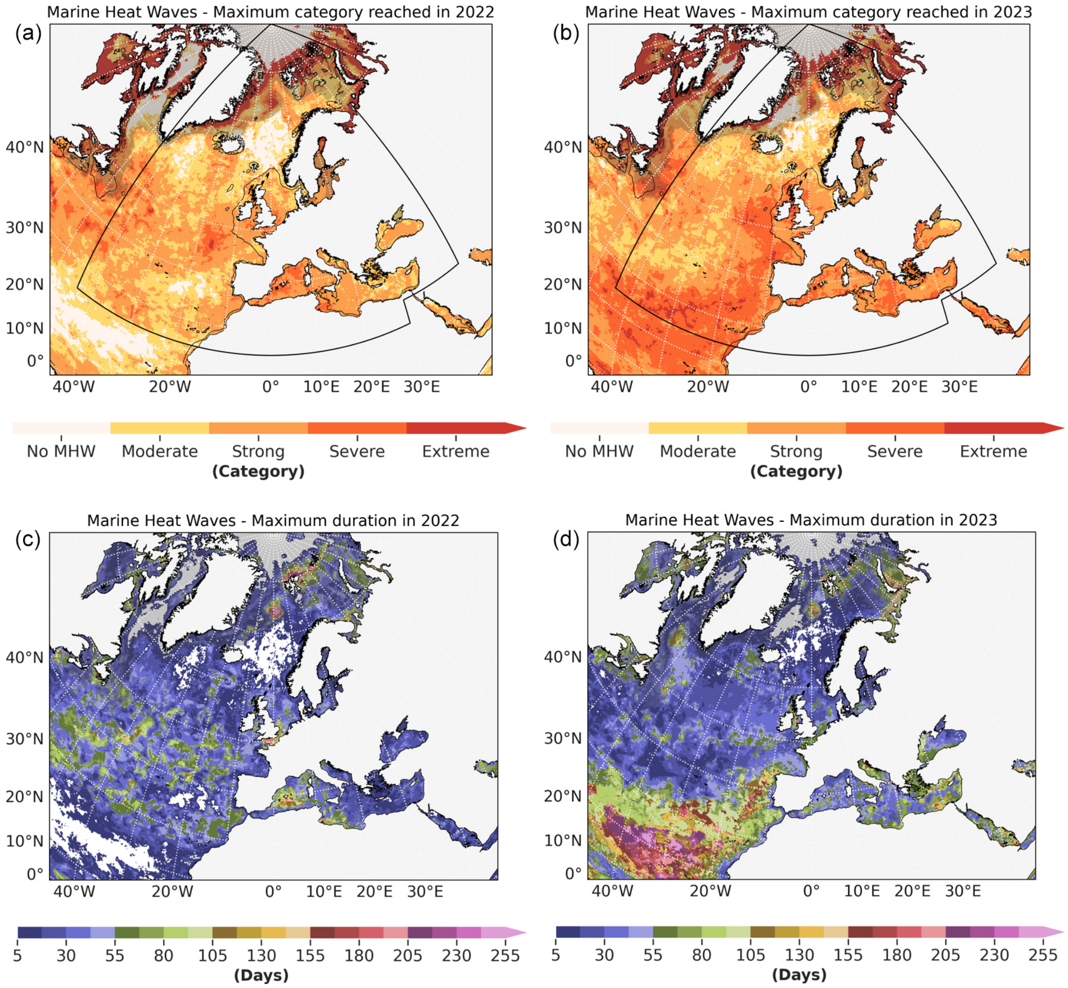

Figure 17. Maximum category of marine heatwave reached in 2022 **(a)** and 2023 **(b)** in the northeastern Atlantic Ocean and adjacent seas, as derived from product refs. SST.1 and SST.2. The thin black line shows the 200 m isobath for product ref. MHW.1. The black polygon shows the northeastern Atlantic Ocean and adjacent seas region considered in this marine heatwave section. Maximum duration of marine heatwave events in 2022 **(c)** and 2023 **(d)** in the northeastern Atlantic Ocean and adjacent seas, as derived from the same sea surface temperature products. The areas shaded in grey correspond to regions where there was at least 1 d of sea ice (sea ice concentration larger than 0.15 in the product ref. SST.1) during the climatological reference period (1993–2016), implying potentially less accurate marine heatwave detections.

Table 3. Beaufort wind scale (ignoring calm conditions from 0 to 3), other commonly used wind speed units, associated probable wave heights in the open ocean, and descriptive terms for wind and waves conditions (WMO, 2019).

Beaufort	Wind descriptive	Average wind speed			Probable wave	Sea state descriptive
number	terms	[knots]	[m s^{-1}]	[km h^{-1}]	height [m]	terms
4	Moderate breeze	11–16	5.5–7.9	20–28	1.0–1.5	Slight–moderate
5	Fresh breeze	17–21	8.0–10.7	29–38	2.0–2.5	Moderate
6	Strong breeze	22–27	10.8–13.8	39–49	3.0–4.0	Rough
7	Near gale	28–33	13.9–17.1	50–61	4.0–5.5	Rough–very rough
8	Gale	34–40	17.2–20.7	62–74	5.5–7.5	Very rough–high
9	Strong gale	41–47	20.8–24.4	75–88	7.0–10.0	High
10	Storm	48–55	24.5–28.4	89–102	9.0–12.5	Very high
11	Violent storm	56–63	28.5–32.6	103–117	11.5–16.0	Exceptionally high
12	Hurricane	> 63	> 32.6	> 117	> 14.0	Phenomenal

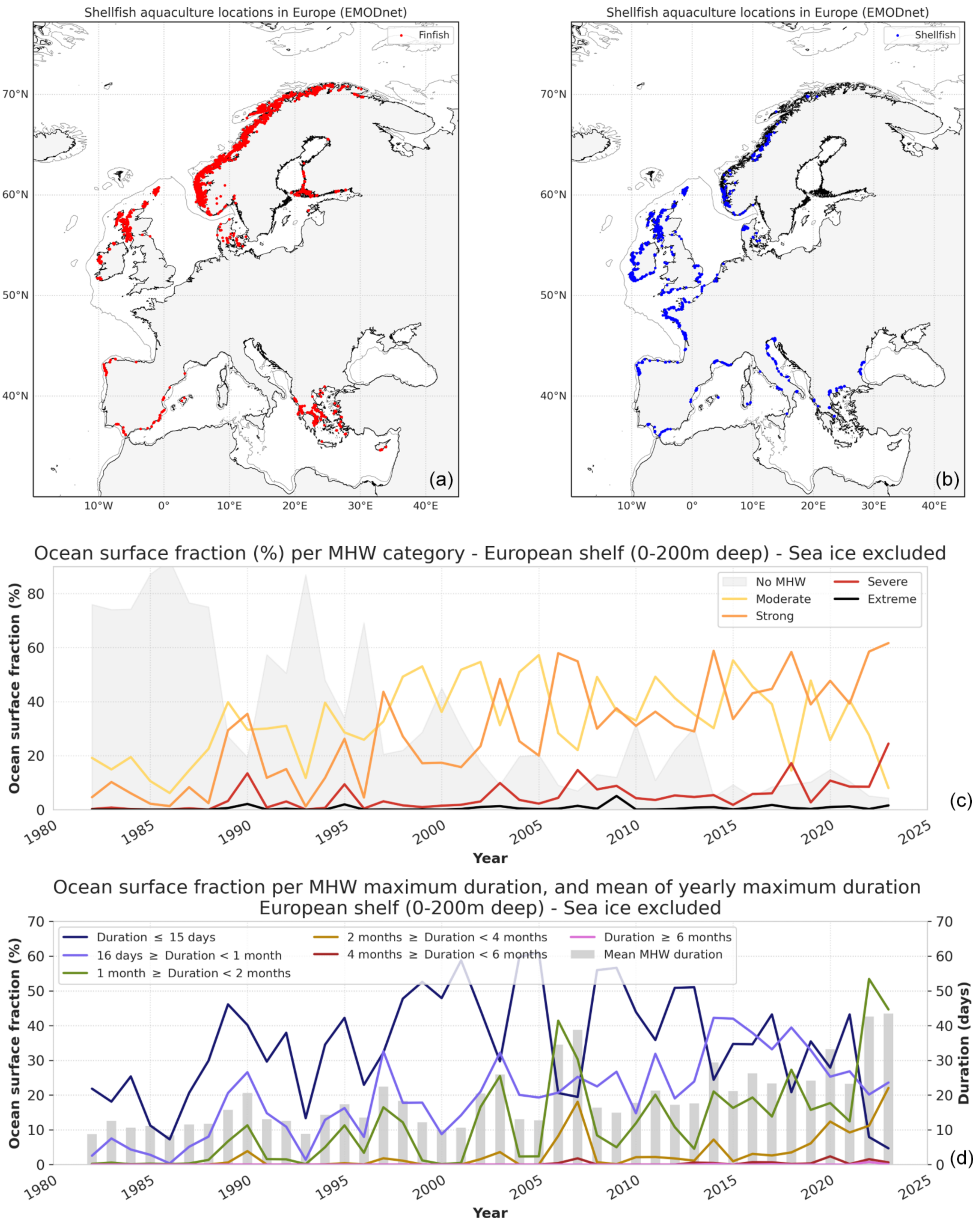

Figure 18. **(a, b)** Aquaculture sites of production in Europe for marine finfish **(a)** from product ref. MHW.2 and shellfish **(b)** from product ref. MHW.3. The thin grey line shows the 200 m isobath for product ref. MHW.1. **(c)** Percentage of ocean surface where the maximum MHW category detected was moderate, strong, severe, extreme, or no showed MHW on the continental shelves of the northeastern Atlantic Ocean and adjacent seas zone (areas within the black polygon in Fig. 17a, with a depth between 0 and 200 m) and excluding sea-ice covered regions (see Fig. 17a for the sea ice mask). These ocean fraction estimates are done following the same method as Hobday et al. (2018). **(d)** Percentage of global ocean surface where the maximum MHW duration was within a given period (lines) and the yearly mean of maximum MHW durations (bars) for the same continental shelf areas, excluding sea-ice-covered regions (see Fig. 17a for the sea ice mask). The evaluation of the MHW indicators is done following the method of Hobday et al. (2016) and is derived from product refs. SST.1 and SST.2.

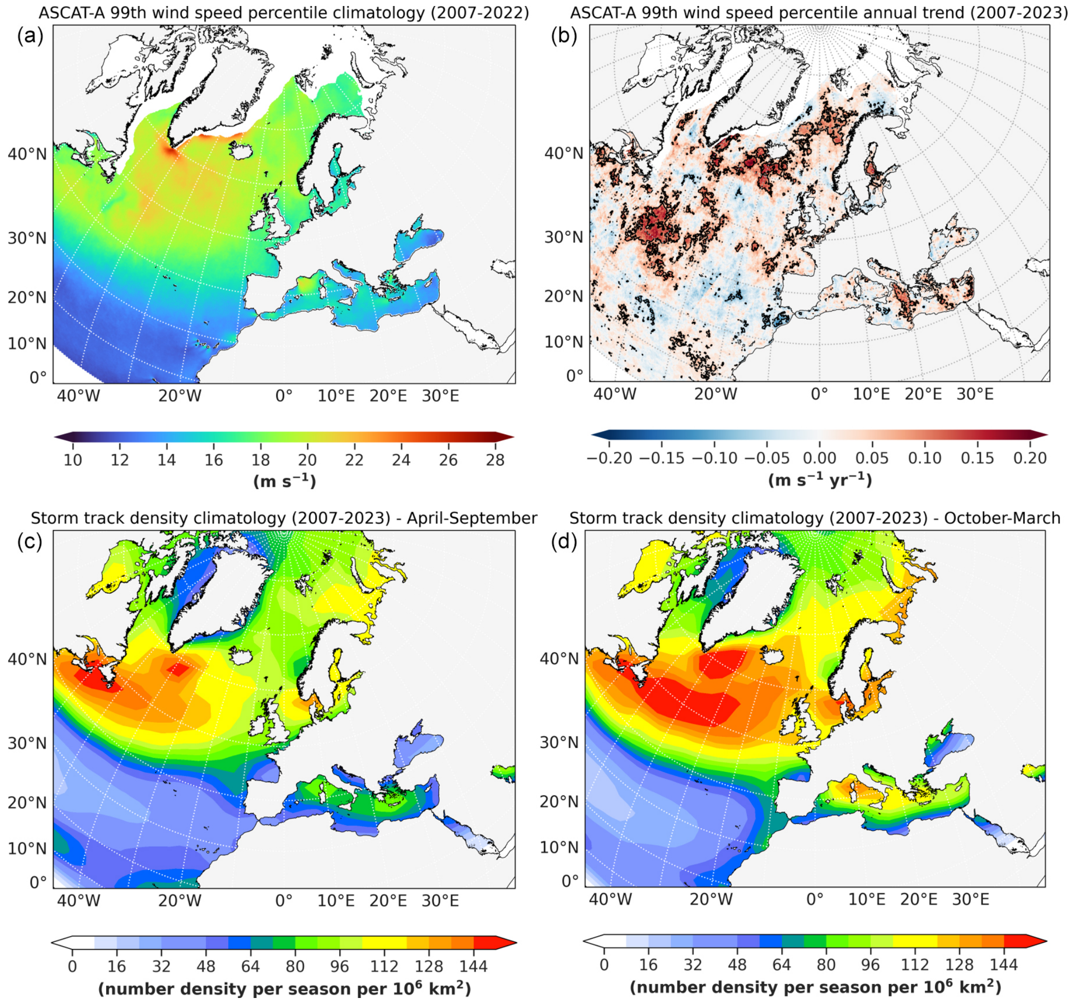

Figure 19. The 99th wind speed percentile **(a)** climatology (2007–2022) and **(b)** annual trend (2007–2023). Areas with trends significant above the 90 % confidence level are outlined in black. Computation at 0.125° resolution from product ref. Wind.1 (ASCAT-A) following the method of Giesen and Stoffelen (2022). **(c, d)** Seasonal storm track density climatology over the period 2007–2023, for spring–summer (April to September **c**) and autumn–winter (October to March, **d**), in units of number density per season per unit area, where the unit area is a 5° radius spherical cap (i.e. about 10^6 km^2), based on the storm tracks detected from product ref. Wind.2 with a threshold of 10^{-5} s^{-1} for the 850 hPa relative vorticity at T63 resolution, considering systems that last longer than 1 d and travel more than 500 km, following Hodges (1999, 1995) and Hoskins and Hodges (2002).

heatwave intensity was highest in the northern parts of the western Mediterranean, decreasing to the south and to the east. In 2023, almost the entire Mediterranean Sea experienced at least one marine heatwave of strong category, and the strongest events happened in the Ionian Sea basin (severe category) (Fig. 17).

Thermal stress on marine organisms can lead to a decrease in production (Islam et al., 2022; Smith et al., 2023), and in the worst cases unusual warming of the waters can lead to lower seawater dissolved oxygen quantities, which can cause asphyxia (Keeling et al., 2009; Roman et al., 2019) and/or foster the development of toxic algae or parasites that can prevent the consumption of farmed shellfish and finfish (Cavole et al., 2016; Boudouresque et al., 2024). Some regions of high production of shellfish and/or finfish (Fig. 12) were affected by strong to severe marine heatwaves in 2022 and 2023 (Baltic Sea, Irish Sea, English Channel, northwestern Mediterranean Sea, Adriatic Sea) or by marine heatwave events that sometimes lasted more than 2 or 3 months in a row (English Channel, Irish Sea, Balearic Sea, Adriatic Sea) (Fig. 17).

In 2022, more than 66 % of the shelf ocean surface (regions with depth between 0 and 200 m) in the northeastern Atlantic Ocean and adjacent seas experienced strong (58 %) and severe or extreme (8 %) marine heatwave events. Here we exclude sea-ice-covered regions as they represent 40 % of the considered shelf area and the marine heatwave detections may be less accurate there; see Table 2 and Fig. 17. In

2023, 88 % of these shelf regions were affected by strong (62 %), severe (24 %), or extreme (2 %) marine heatwave events. There is a clear ascending trend in the ocean surface fraction affected by marine heatwave events in these shelf regions over the last 40 years, with about 20 % of the area experiencing MHW events in the 1980s and more than 90 % in 2023 (Fig. 18). The areas affected by strong and severe events have increased over the whole period, while the extreme events are relatively stable and rare. The annual mean maximum duration of the marine heatwave events has also increased, from about 10 d in 1982 to about 40 d in the most recent years, with larger fractions of the ocean surface affected by longer events, in particular those lasting between 2 weeks and 4 months. In general, more interannual variability can be noted in these shelf estimates than when considering the whole northeastern Atlantic Ocean and adjacent seas region (Fig. 16), as the shelf regions are more sensitive to local oceanic and atmospheric dynamics and drivers.

5.2 Wind extremes

Monitoring extreme ocean surface winds, including their evolution and change over time, is of particular importance to ensure accurate representation of all linked ocean parameters (e.g. waves, storm surges, sea surface temperature, currents; Alvarez-Fanjul et al., 2019, 2022; de Alfonso et al., 2020; Staneva et al., 2020; Berta et al., 2020; Raudsepp et al., 2021; Mourre et al., 2023) in order to better understand the associated disaster risks (e.g. coastal flooding and impacts on offshore and coastal infrastructure, activities, and ecosystems), design marine infrastructures, and feed early warning systems and risk prevention and adaptation plans (de Alfonso et al., 2020; Drago et al., 2021), in line with the priorities identified in the United Nations Sendai Framework for Disaster Risk Reduction 2015–2030 (UNDRR, 2024).

When considering the northeastern Atlantic Ocean and adjacent seas, the regions that show the highest extreme ocean surface winds over the 2007–2022 period are the central and northern parts of the North Atlantic Ocean (more than 22 $\mathrm{m\,s^{-1}}$), especially between Greenland and Iceland and along the southern coast of Greenland (more than 26 $\mathrm{m\,s^{-1}}$, which corresponds to storms in the Beaufort wind scale; see Table 3) (Fig. 19a). The tropical North Atlantic Ocean (0 and 30° N) is characterized by lower extreme winds in the 99th percentile climatology, ranging between 12 and 14 $\mathrm{m\,s^{-1}}$.

Another area with strong extreme winds (about 20 $\mathrm{m\,s^{-1}}$) is the Gulf of Lion in the northwestern Mediterranean Sea, which is a region of strong cyclogenesis known to experience the most severe winds in the entire Mediterranean Sea (e.g. Zecchetto and De Biasio, 2007) and the highest extreme wind waves (Barbariol et al., 2021). In the Mediterranean Sea, a sub-group of cyclonic storms is called Medicanes (Mediterranean hurricanes). Although there is no official physical definition for the meteorological term Medicane, it is generally associated with systems that, despite being smaller in size and intensity (wind speed), share similarities with tropical cyclones, such as a circular shape with a warm core and low wind at the centre, surrounded by strong winds (MedECC, 2020a; Flaounas et al., 2022). As their definition may vary depending on the studies, there is still uncertainty on the statistics of the number or intensity of Medicanes, but they seem to generally occur one to three times per year (Cavicchia et al., 2014; Gaertner et al., 2018; Zhang et al., 2021).

In early September 2023, Storm Daniel was identified as the deadliest Medicane in recent history, hitting the coast of Libya with massive rainfall that led to the destruction of two dams, flooding the coastal city of Darna and causing more than 12 350 deaths in the area (EM-DAT, 2024). In comparison, for the whole year 2022, 43 deaths were reported by this dataset due to storm events in Europe. According to IPCC AR6, the number of Medicane events is likely to decrease, but their intensity is likely to increase under global warming (Seneviratne et al., 2021) as atmospheric convection and moisture are expected to be enhanced by higher sea surface temperatures (Flaounas et al., 2022).

At the regional scale, the detection of long-term changes also remains a challenge due to high variability and the limited length of the time series. Over the past 16 years (2007–2023), increasing extreme wind speeds are observed in several areas over the northeastern Atlantic Ocean and adjacent seas (Fig. 19). These include the central North Atlantic Ocean Gulf Stream region (30–35° N, 30–50° W), the subpolar Atlantic region between Greenland and south of Iceland, the Norwegian Sea, the Baltic Sea, and the eastern Mediterranean Sea (Ionian Sea and Levantine Sea). Such changes in extreme wind intensity in the North Atlantic Ocean may be associated with the poleward migration of tropical and extra-tropical cyclone tracks that is observed as the tropics expand with global warming (Seneviratne et al., 2021). However, further analysis, specific detection, and attribution studies, as well as longer time series, are needed in the future for the identification of long-term trends in observed extreme wind speeds (Gentile et al., 2023).

Another approach to spatially diagnose extreme ocean surface winds is to evaluate the storm track density (Fig. 19) (Hodges, 1999, 1995; Hoskins and Hodges, 2002). During the spring to summer season (i.e. April to September), the average storm density exceeds 140 south of Greenland and around 40° N at the Canadian coast (Fig. 19c). Areas where the storm density exceeds 100 include the North Sea, the Baltic Sea, the Barents Sea, the Kara Sea, and the northern Mediterranean Sea (Fig. 19c). During the autumn to winter season (i.e. October to March), these patterns intensify and increase in size, spanning the entire Atlantic Ocean across 40° N from the Canadian coast up to the coast of Europe, and the average storm density increases to more than 120 in the adjacent seas (Fig. 19d).

Code availability. Codes are not publicly available, but can be obtained upon request.

Data availability. Information about the availability of the datasets used in this paper is provided in the Supplement, and all products are publicly available.

Supplement. The supplement related to this article is available online at: https://doi.org/10.5194/sp-4-osr8-2-2024-supplement.

Author contributions. KvS, LM, MC, FG: conceptualization, methodology, writing – original draft, investigation, supervision, and formal analysis. All authors: writing – review and editing and data curation.

Competing interests. At least one of the (co-)authors is a member of the editorial board of *State of the Planet*. The peer-review process was guided by an independent editor, and the authors also have no other competing interests to declare.

Disclaimer. Please note that this article has undergone editorial review only.

References

Ablain, M., Jugier, R., Zawadki, L., Taburet, N., Cazenave, A., and Meyssignac, B.: The TOPEX-A drift and impacts on GMSL time series, AVISO, https://meetings.aviso.altimetry.fr/fileadmin/user_upload/tx_ausyclsseminar/files/Poster_OSTST17_GMSL_Drift_TOPEX-A.pdf (last access: 11 September 2024), 2017.

Allan, D. and Allan, R. P.: Seasonal Changes in the North Atlantic Cold Anomaly: The Influence of Cold Surface Waters From Coastal Greenland and Warming Trends Associated With Variations in Subarctic Sea Ice Cover, J. Geophys. Res.-Oceans, 124, 9040–9052, https://doi.org/10.1029/2019JC015379, 2019.

Alvarez-Fanjul, E., de Pascual Collar, A., Perez-Gomez, B., de Alfonso, M., Garcia Sotillo, M., Staneva, J., Clementi, E., Grandi, A., Zacharioudaki, A., Korres, G., Ravdas, M., Renshaw, R., Tinker, J., Raudsepp, U., Lagemaa, P., Maljutenko, I., Geyer, G., Müller, M., and Yumruktepe, V. Ç.: Sea level, sea surface temperature and SWH extreme percentiles: combined analysis from model results and in situ observations, in: Copernicus Marine Service Ocean State Report, Issue 3, J. Oper. Oceanogr., 12, s31–s43, https://doi.org/10.1080/1755876X.2019.1633075, 2019.

Alvarez-Fanjul, E., Pérez Gomez, B., de Alfonso Alonso-Muñoyerro, M., Lorente, P., Garcia Sotillo, M., Lin-Ye, J., Aznar Lecocq, R., Ruiz Gil de la Serna, M., Perez Rubio, S., Clementi, E., Coppini, G., Garcia-Leon, M., Fernandes, M., Garcia Valdecasas, J., Garcia Valdecasas, J. M., Santos Muñoz, D., Luna Rico, M. Y., Mestres, M., Molina, R., Tintoré, J., Mourre, B., Masina, S., Mosso, C., Reyes, E., and Santana, A.: Western Mediterranean record-breaking storm Gloria: An integrated assessment based on models and observations, in: Copernicus Ocean State Report, Issue 6, J. Oper. Oceanogr., 15, s151–s159, https://doi.org/10.1080/1755876X.2022.2095169, 2022.

Andersen, J. H., Carstensen, J., Conley, D. J., Dromph, K., Fleming-Lehtinen, V., Gustafsson, B. G., Josefson, A. B., Norkko, A., Villnäs, A., and Murray, C.: Long-term temporal and spatial trends in eutrophication status of the Baltic Sea, Biol. Rev., 92, 135–149, https://doi.org/10.1111/BRV.12221, 2017.

Avşar, N. B. and Kutoglu, Ş. H.: Recent Sea Level Change in the Black Sea from Satellite Altimetry and Tide Gauge Observations, ISPRS Int. J. Geo-Inf., 9, 185, https://doi.org/10.3390/IJGI9030185, 2020.

Barbariol, F., Davison, S., Falcieri, F. M., Ferretti, R., Ricchi, A., Sclavo, M., and Benetazzo, A.: Wind Waves in the Mediterranean Sea: An ERA5 Reanalysis Wind-Based Climatology, Front. Mar. Sci., 8, 760614, https://doi.org/10.3389/FMARS.2021.760614, 2021.

Bednarsek, N., Guilloux, B., Canu, D. M., Galdies, C., Guerra, R., Simoncelli, S., Feely, R. A., Pelletier, G., Gašparović, B., Godrijan, J., Malej, A., Solidoro, C., Turk, V., Zunino, S., Bednarsek, N., Guilloux, B., Canu, D. M., Zunino, S., and Guerra, R.: Ocean Acidification as a Governance Challenge in the Mediterranean Sea: Impacts from Aquaculture and Fisheries, 403–432, https://doi.org/10.1007/978-3-031-20740-2_18, 2023.

Berta, M., Corgnati, L., Magaldi, M. G., Griffa, A., Mantovani, C., Rubio, A., Reyes, E., and Mader, J.: Small scale ocean weather during an extreme wind event in the Ligurian Sea, in: Copernicus Marine Service Ocean State Report, Issue 4, J. Oper. Oceanogr., 13, s149–s155, https://doi.org/10.1080/1755876X.2020.1785097, 2020.

Berx, B., Hansen, B., Østerhus, S., Larsen, K. M., Sherwin, T., and Jochumsen, K.: Combining in situ measurements and altimetry to estimate volume, heat and salt transport variability through the Faroe–Shetland Channel, Ocean Sci., 9, 639–654, https://doi.org/10.5194/os-9-639-2013, 2013.

Bopp, L., Lévy, M., Resplandy, L., and Sallée, J. B.: Pathways of anthropogenic carbon subduction in the global ocean, Geophys. Res. Lett., 42, 6416–6423, https://doi.org/10.1002/2015GL065073, 2015.

Boudouresque, C. F., Astruch, P., André, S., Belloni, B., Blanfuné, A., Charbonnel, É., Cheminée, A., Cottalorda, J. M., Dupuy de la Grandrive, R., Marengo, M., Monnier, B., Pergent, G., Pergent-Martini, C., Perret-Boudouresque, M., Ruitton, S., Taupier-Letage, I., and Thibaut, T.: The Heatwave of Summer 2022 in the North-Western Mediterranean Sea: Some Species Were Winners, Water, 16, 219, https://doi.org/10.3390/W16020219, 2024.

BSC: State of the Environment of the Black Sea (1996–2000), Pressures and Trends, Publications of the Commission on the Protection of the Black Sea Against Pollution (BSC), Istambul, Turkey, 65 pp., http://www.blacksea-commission.org/Downloads/SOE_2002English.pdf (last access: 11 September 2024), 2002.

BSC: Commission on the Protection of the Black Sea Against Pollution, http://www.blacksea-commission.org/Official%20Documents/The%20Convention/full%20text/, last access: 1 December 2023.

BSC: State of the Environment of the Black Sea (2001–2006/7), edited by: Oguz, T., Publications of the Commission on the Protection of the Black Sea Against Pollution (BSC), Istambul, Turkey, 448 pp., ISBN 978-9944-245-33-3, 2008.

BSC: State of the Environment of the Black Sea (2009–2014/5), edited by: Krutov, A., Publications of the Commission on the Protection of the Black Sea Against Pollution (BSC), Istambul, Turkey, 811 pp., ISBN 978-605-84837-0-5, http://www.blacksea-commission.org/SoE2009-2014/SoE2009-2014.pdf (last access: 11 September 2024), 2019.

Caesar, L., Rahmstorf, S., Robinson, A., Feulner, G., and Saba, V.: Observed fingerprint of a weakening Atlantic Ocean overturning circulation, Nature, 556, 191–196, https://doi.org/10.1038/s41586-018-0006-5, 2018.

Calafat, F. M., Frederikse, T., and Horsburgh, K.: The Sources of Sea-Level Changes in the Mediterranean Sea Since 1960, J. Geophys. Res.-Oceans, 127, e2022JC019061, https://doi.org/10.1029/2022JC019061, 2022.

Carstensen, J. and Duarte, C. M.: Drivers of pH Variability in Coastal Ecosystems, Environ. Sci. Technol., 53, 4020–4029, https://doi.org/10.1021/ACS.EST.8B03655, 2019.

Carstensen, J., Chierici, M., Gustafsson, B. G., and Gustafsson, E.: Long-Term and Seasonal Trends in Estuarine and Coastal Carbonate Systems, Global Biogeochem. Cy., 32, 497–513, https://doi.org/10.1002/2017GB005781, 2018.

Cavicchia, L., von Storch, H., and Gualdi, S.: A long-term climatology of medicanes, Clim. Dynam., 43, 1183–1195, https://doi.org/10.1007/S00382-013-1893-7, 2014.

Cavole, L. M., Demko, A. M., Diner, R. E., Giddings, A., Koester, I., Pagniello, C. M. L. S., Paulsen, M. L., Ramirez-Valdez, A., Schwenck, S. M., Yen, N. K., Zill, M. E., and Franks, P. J. S.: Biological impacts of the 2013–2015 warm-water anomaly in the northeast Pacific: Winners, Losers, and the Future, Oceanography, 29, 273–285, https://doi.org/10.5670/OCEANOG.2016.32, 2016.

Cazenave, A. and Moreira, L.: Contemporary sea-level changes from global to local scales: A review, P. Roy. Soc. A-Math. Phy., 478, 20220049, https://doi.org/10.1098/RSPA.2022.0049, 2022.

Cazenave, A., Gouzenes, Y., Birol, F., Leger, F., Passaro, M., Calafat, F. M., Shaw, A., Nino, F., Legeais, J. F., Oelsmann, J., Restano, M., and Benveniste, J.: Sea level along the world's coastlines can be measured by a network of virtual altimetry stations, Communications Earth & Environment, 3, 1–9, https://doi.org/10.1038/s43247-022-00448-z, 2022.

Chafik, L., Nilsen, J. E. Ø., Dangendorf, S., Reverdin, G., and Frederikse, T.: North Atlantic Ocean Circulation and Decadal Sea Level Change During the Altimetry Era, Sci. Rep., 9, 1–9, https://doi.org/10.1038/s41598-018-37603-6, 2019.

Chemke, R., Zanna, L., and Polvani, L. M.: Identifying a human signal in the North Atlantic warming hole, Nat. Commun., 11, 1–7, https://doi.org/10.1038/s41467-020-15285-x, 2020.

Cheng, L., von Schuckmann, K., Abraham, J. P., Trenberth, K. E., Mann, M. E., Zanna, L., England, M. H., Zika, J. D., Fasullo, J. T., Yu, Y., Pan, Y., Zhu, J., Newsom, E. R., Bronselaer, B., and Lin, X.: Past and future ocean warming, Nat. Rev. Earth Environ., 3, 776–794, https://doi.org/10.1038/s43017-022-00345-1, 2022.

Cheng, L., Abraham, J., Trenberth, K. E., Boyer, T., Mann, M. E., Zhu, J., Wang, F., Yu, F., Locarnini, R., Fasullo, J., Zheng, F., Li, Y., Zhang, B., Wan, L., Chen, X., Wang, D., Feng, L., Song, X., Liu, Y., Reseghetti, F., Simoncelli, S., Gouretski, V., Chen, G., Mishonov, A., Reagan, J., Von Schuckmann, K., Pan, Y., Tan, Z., Zhu, Y., Wei, W., Li, G., Ren, Q., Cao, L., and Lu, Y.: New Record Ocean Temperatures and Related Climate Indicators in 2023, Adv. Atmos. Sci., 41, 1–15, https://doi.org/10.1007/S00376-024-3378-5, 2024.

Cheung, W. W. L. and Frölicher, T. L.: Marine heatwaves exacerbate climate change impacts for fisheries in the northeast Pacific, Sci. Rep., 10, 1–10, https://doi.org/10.1038/s41598-020-63650-z, 2020.

Climate Change in the Baltic Sea: 2021 Fact Sheet, Baltic Sea Environment Proceedings no. 180, HELCOM/Baltic Earth, https://helcom.fi/wp-content/uploads/2021/09/Baltic-Sea-Climate-Change-Fact-Sheet-2021.pdf (last access: 11 September 2024), 2021.

Cossarini, G., Lazzari, P., and Solidoro, C.: Spatiotemporal variability of alkalinity in the Mediterranean Sea, Biogeosciences, 12, 1647–1658, https://doi.org/10.5194/bg-12-1647-2015, 2015.

Cossarini, G., Feudale, L., Teruzzi, A., Bolzon, G., Coidessa, G., Solidoro, C., Di Biagio, V., Amadio, C., Lazzari, P., Brosich, A., and Salon, S.: High-Resolution Reanalysis of the Mediterranean Sea Biogeochemistry (1999–2019), Front. Mar. Sci., 8, 741486, https://doi.org/10.3389/FMARS.2021.741486, 2021.

Cramer, W., Guiot, J., Fader, M., Garrabou, J., Gattuso, J. P., Iglesias, A., Lange, M. A., Lionello, P., Llasat, M. C., Paz, S., Peñuelas, J., Snoussi, M., Toreti, A., Tsimplis, M. N., and Xoplaki, E.: Climate change and interconnected risks to sustainable development in the Mediterranean, Nat. Clim. Change, 8, 972–980, https://doi.org/10.1038/s41558-018-0299-2, 2018.

Darmaraki, S., Somot, S., Sevault, F., and Nabat, P.: Past Variability of Mediterranean Sea Marine Heatwaves, Geophys. Res. Lett., 46, 9813–9823, https://doi.org/10.1029/2019GL082933, 2019.

Dayan, H., McAdam, R., Masina, S., and Speich, S.: Diversity of marine heatwave trends across the Mediterranean Sea over the last decades, in: Copernicus Ocean State Report, Issue 6, J. Oper. Oceanogr., 15, s49–s56, https://doi.org/10.1080/1755876X.2022.2095169, 2022.

Dayan, H., McAdam, R., Juza, M., Masina, S., and Speich, S.: Marine heat waves in the Mediterranean Sea: An assessment from the surface to the subsurface to meet national needs, Front. Mar. Sci., 10, 1045138, https://doi.org/10.3389/FMARS.2023.1045138, 2023.

de Alfonso, M., Garcia-Valdecasas, J. M., Aznar, R., Perez-Gomez, B., Rodriguez, P., de los Santos, F. J., and Alvarez-Fanjul, E.: Record wave storm in the Gulf of Cadiz over the past 20 years and its impact on harbours, in: Copernicus Marine Service Ocean State Report, Issue 4, J. Oper. Oceanogr., 13, s137–s144, https://doi.org/10.1080/1755876X.2020.1785097, 2020.

de Pascual-Collar, Á., Aznar, R., Levier, B., and García-Sotillo, M.: Ocean heat content in the Iberian–Biscay–Ireland regional seas, in: 7th edition of the Copernicus Ocean State Report (OSR7), edited by: von Schuckmann, K., Moreira, L., Le Traon, P.-Y., Grégoire, M., Marcos, M., Staneva, J., Brasseur, P., Garric, G., Lionello, P., Karstensen, J., and Neukermans, G., Copernicus

Publications, State Planet, 1-osr7, 9, https://doi.org/10.5194/sp-1-osr7-9-2023, 2023.

Dettmering, D., Müller, F. L., Oelsmann, J., Passaro, M., Schwatke, C., Restano, M., Benveniste, J., and Seitz, F.: North SEAL: a new dataset of sea level changes in the North Sea from satellite altimetry, Earth Syst. Sci. Data, 13, 3733–3753, https://doi.org/10.5194/essd-13-3733-2021, 2021.

Drago, A., Gauci, A., Azzopardi, J., Sanchez, J., and Alonso-Martirena, A.: Monitoring storms by merged data sources for the Malta shelf area in 2019, in: Copernicus Marine Service Ocean State Report, Issue 5, J. Oper. Oceanogr., 14, s148–s156, https://doi.org/10.1080/1755876X.2021.1946240, 2021.

Drijfhout, S., van Oldenborgh, G. J., and Cimatoribus, A.: Is a Decline of AMOC Causing the Warming Hole above the North Atlantic in Observed and Modeled Warming Patterns?, J. Climate, 25, 8373–8379, https://doi.org/10.1175/JCLI-D-12-00490.1, 2012.

Duarte, C. M., Hendriks, I. E., Moore, T. S., Olsen, Y. S., Steckbauer, A., Ramajo, L., Carstensen, J., Trotter, J. A., Mcculloch, M., Duarte, C. M., Hendriks, I. E., Moore, T. S., Olsen, Y. S., Steckbauer, : A, Ramajo, L., Carstensen, J., Trotter, J. A., and Mcculloch, M.: Is Ocean Acidification an Open-Ocean Syndrome? Understanding Anthropogenic Impacts on Seawater pH, Estuar. Coast., 36, 221–236, https://doi.org/10.1007/S12237-013-9594-3, 2013

Dubois, C., von Schuckmann, K., Josey, S., and Ceschin, A.: Changes in the North Atlantic, in: Copernicus Marine Service Ocean State Report, Issue 2, J. Oper. Oceanogr., 11, s66–s70, https://doi.org/10.1080/1755876X.2018.1489208, 2018.

Eilola, K., Mårtensson, S., and Meier, H. E. M.: Modeling the impact of reduced sea ice cover in future climate on the Baltic Sea biogeochemistry, Geophys. Res. Lett., 40, 149–154, https://doi.org/10.1029/2012GL054375, 2013.

Elge, M.: Acidification Analysis of Black Sea, International Journal of Environment and Geoinformatics, 8, 467–474, https://doi.org/10.30897/IJEGEO.857893, 2021.

EM-DAT: Inventorying hazards & disasters worldwide since 1988, https://www.emdat.be/, last access: 11 September 2024.

Fan, Y., Liu, W., Zhang, P., Chen, R., and Li, L.: North Atlantic Oscillation contributes to the subpolar North Atlantic cooling in the past century, Clim. Dynam., 61, 1–17, https://doi.org/10.1007/S00382-023-06847-Y, 2023.

Flaounas, E., Davolio, S., Raveh-Rubin, S., Pantillon, F., Miglietta, M. M., Gaertner, M. A., Hatzaki, M., Homar, V., Khodayar, S., Korres, G., Kotroni, V., Kushta, J., Reale, M., and Ricard, D.: Mediterranean cyclones: current knowledge and open questions on dynamics, prediction, climatology and impacts, Weather Clim. Dynam., 3, 173–208, https://doi.org/10.5194/wcd-3-173-2022, 2022.

Flecha, S., Pérez, F. F., Murata, A., Makaoui, A., and Huertas, I. E.: Decadal acidification in Atlantic and Mediterranean water masses exchanging at the Strait of Gibraltar, Sci. Rep., 9, 1–11, https://doi.org/10.1038/s41598-019-52084-x, 2019.

Fossheim, M., Primicerio, R., Johannesen, E., Ingvaldsen, R. B., Aschan, M. M., and Dolgov, A. V.: Recent warming leads to a rapid borealization of fish communities in the Arctic, Nat. Clim. Change, 5, 673–677, https://doi.org/10.1038/nclimate2647, 2015.

Gaertner, M. Á., González-Alemán, J. J., Romera, R., Domínguez, M., Gil, V., Sánchez, E., Gallardo, C., Miglietta, M. M., Walsh, K. J. E., Sein, D. V., Somot, S., Dell'Aquila, A., Teichmann, C., Ahrens, B., Buonomo, E., Colette, A., Bastin, S., van Meijgaard, E., and Nikulin, G.: Simulation of medicanes over the Mediterranean Sea in a regional climate model ensemble: impact of ocean–atmosphere coupling and increased resolution, Clim. Dynam., 51, 1041–1057, https://doi.org/10.1007/S00382-016-3456-1, 2018.

Garrabou, J., Gómez-Gras, D., Medrano, A., Cerrano, C., Ponti, M., Schlegel, R., Bensoussan, N., Turicchia, E., Sini, M., Gerovasileiou, V., Teixido, N., Mirasole, A., Tamburello, L., Cebrian, E., Rilov, G., Ledoux, J. B., Souissi, J. Ben, Khamassi, F., Ghanem, R., Benabdi, M., Grimes, S., Ocaña, O., Bazairi, H., Hereu, B., Linares, C., Kersting, D. K., la Rovira, G., Ortega, J., Casals, D., Pagès-Escolà, M., Margarit, N., Capdevila, P., Verdura, J., Ramos, A., Izquierdo, A., Barbera, C., Rubio-Portillo, E., Anton, I., López-Sendino, P., Díaz, D., Vázquez-Luis, M., Duarte, C., Marbà, N., Aspillaga, E., Espinosa, F., Grech, D., Guala, I., Azzurro, E., Farina, S., Cristina Gambi, M., Chimienti, G., Montefalcone, M., Azzola, A., Mantas, T. P., Fraschetti, S., Ceccherelli, G., Kipson, S., Bakran-Petricioli, T., Petricioli, D., Jimenez, C., Katsanevakis, S., Kizilkaya, I. T., Kizilkaya, Z., Sartoretto, S., Elodie, R., Ruitton, S., Comeau, S., Gattuso, J. P., and Harmelin, J. G.: Marine heatwaves drive recurrent mass mortalities in the Mediterranean Sea, Glob. Change Biol., 28, 5708–5725, https://doi.org/10.1111/GCB.16301, 2022.

Gehlen, M., Chau, T. T. T., Conchon, A., Denvil-Sommer, A., Chevallier, F., Vrac, M., and Mejia, C.: Ocean acification, in: Copernicus Marine Service Ocean State Report, Issue 4, J. Oper. Oceanogr., 13, s64–s66, https://doi.org/10.1080/1755876X.2020.1785097, 2020.

Gentile, E. S., Zhao, M., and Hodges, K.: Poleward intensification of midlatitude extreme winds under warmer climate, npj Climate and Atmospheric Science, 6, 1–10, https://doi.org/10.1038/s41612-023-00540-x, 2023.

Gerland, S., Ingvaldsen, R. B., Reigstad, M., Sundfjord, A., Bogstad, B., Chierici, M., Hop, H., Renaud, P. E., Smedsrud, L. H., Stige, L. C., Arthun, M., Berge, J., Bluhm, B. A., Borgå, K., Bratbak, G., Divine, D. V., Eldevik, T., Eriksen, E., Fer, I., Fransson, A., Gradinger, R., Granskog, M. A., Haug, T., Husum, K., Johnsen, G., Jonassen, M. O., Jørgensen, L. L., Kristiansen, S., Larsen, A., Lien, V. S., Lind, S., Lindstrøm, U., Mauritzen, C., Melsom, A., Mernild, S. H., Müller, M., Nilsen, F., Primicerio, R., Søreide, J. E., van der Meeren, G. I., and Wassmann, P.: Still Arctic? – The changing Barents Sea, Elem. Sci. Anth., 11, 1–62, https://doi.org/10.1525/ELEMENTA.2022.00088, 2023.

Gervais, M., Shaman, J., and Kushnir, Y.: Impacts of the North Atlantic Warming Hole in Future Climate Projections: Mean Atmospheric Circulation and the North Atlantic Jet, J. Climate, 32, 2673–2689, https://doi.org/10.1175/JCLI-D-18-0647.1, 2019.

Gervais, M., Shaman, J., and Kushnir, Y.: Impact of the North Atlantic Warming Hole on Sensible Weather, J. Climate, 33, 4255–4271, https://doi.org/10.1175/JCLI-D-19-0636.1, 2020.

Girjatowicz, J. P. and Łabuz, T. A.: Forms of piled ice at the southern coast of the Baltic Sea, Estuar. Coast. Shelf Sci., 239, 106746, https://doi.org/10.1016/J.ECSS.2020.106746, 2020.

Giesen, R. and Stoffelen, A.: Changes in extreme wind speeds over the global ocean, in: Copernicus Ocean

State Report, Issue 6, J. Oper. Oceanogr., 15, s8–s15, https://doi.org/10.1080/1755876X.2022.2095169, 2022.

Granskog, M., Kaartokallio, H., Kuosa, H., Thomas, D. N., and Vainio, J.: Sea ice in the Baltic Sea – A review, Estuar. Coast. Shelf Sci., 70, 145–160, https://doi.org/10.1016/J.ECSS.2006.06.001, 2006.

Gregory, J. M., Griffies, S. M., Hughes, C. W., Lowe, J. A., Church, J. A., Fukimori, I., Gomez, N., Kopp, R. E., Landerer, F., Cozannet, G. Le, Ponte, R. M., Stammer, D., Tamisiea, M. E., and van de Wal, R. S. W.: Concepts and Terminology for Sea Level: Mean, Variability and Change, Both Local and Global, Surv. Geophys., 40, 1251–1289, https://doi.org/10.1007/S10712-019-09525-Z, 2019

Gruber, N., Clement, D., Carter, B. R., Feely, R. A., van Heuven, S., Hoppema, M., Ishii, M., Key, R. M., Kozyr, A., Lauvset, S. K., Monaco, C. Lo, Mathis, J. T., Murata, A., Olsen, A., Perez, F. F., Sabine, C. L., Tanhua, T., and Wanninkhof, R.: The oceanic sink for anthropogenic CO 2 from 1994 to 2007, Science, 363, 1193–1199, https://doi.org/10.1126/SCIENCE.AAU5153, 2019.

Gustafsson, B. G., Schenk, F., Blenckner, T., Eilola, K., Meier, H. E. M., Müller-Karulis, B., Neumann, T., Ruoho-Airola, T., Savchuk, O. P., and Zorita, E.: Reconstructing the development of baltic sea eutrophication 1850–2006, Ambio, 41, 534–548, https://doi.org/10.1007/S13280-012-0318-X, 2012.

Gustafsson, E. and Gustafsson, B. G.: Future acidification of the Baltic Sea – A sensitivity study, J. Marine Syst., 211, 103397, https://doi.org/10.1016/J.JMARSYS.2020.103397, 2020.

Gustafsson, E., Carstensen, J., Fleming, V., Gustafsson, B. G., Hoikkala, L., and Rehder, G.: Causes and consequences of acidification in the Baltic Sea: implications for monitoring and management, Sci. Rep., 13, 1–11, https://doi.org/10.1038/s41598-023-43596-8, 2023.

Gutiérrez, J. M., Jones, R. G., Narisma, G. T., Alves, L. M., Amjad, M., Gorodetskaya, I. V, Grose, M., Klutse, N. A. B., Krakovska, S., Li, J., Martínez-Castro, D., Mearns, L. O., Mernild, S. H., Ngo-Duc, T., van den Hurk, B., and Yoon, J.-H.: Atlas, in: Climate Change 2021: The Physical Science Basis. Contribution of Working Group I to the Sixth Assessment Report of the Intergovernmental Panel on Climate Change, edited by: Masson-Delmotte, V., Zhai, P., Pirani, A., Connors, S. L., Péan, C., Berger, S., Caud, N., Chen, Y., Goldfarb, L., Gomis, M. I., Huang, M., Leitzell, K., Lonnoy, E., Matthews, J. B. R., Maycock, T. K., Waterfield, T., Yelekçi, O., Yu, R., and Zhou, B., Cambridge University Press, Cambridge, United Kingdom and New York, NY, USA, 1927–2058, https://doi.org/10.1017/9781009157896.021, 2021.

Hansen, J., Ruedy, R., Sato, M., and Lo, K.: Global Surface Temperature Change, Rev. Geophys., 48, 4004, https://doi.org/10.1029/2010RG000345, 2010.

Hassoun, A. E. R., Gemayel, E., Krasakopoulou, E., Goyet, C., Abboud-Abi Saab, M., Guglielmi, V., Touratier, F., and Falco, C.: Acidification of the Mediterranean Sea from anthropogenic carbon penetration, Deep-Sea Res. Pt. I, 102, 1–15, https://doi.org/10.1016/J.DSR.2015.04.005, 2015.

Hassoun, A. E. R., Fakhri, M., Raad, N., Abboud-Abi Saab, M., Gemayel, E., and De Carlo, E. H.: The carbonate system of the Eastern-most Mediterranean Sea, Levantine Subbasin: Variations and drivers, Deep-Sea Res. Pt. II, 164, 54–73, https://doi.org/10.1016/J.DSR2.2019.03.008, 2019.

Hassoun, A. E. R., Bantelman, A., Canu, D., Comeau, S., Galdies, C., Gattuso, J. P., Giani, M., Grelaud, M., Hendriks, I. E., Ibello, V., Idrissi, M., Krasakopoulou, E., Shaltout, N., Solidoro, C., Swarzenski, P. W., and Ziveri, P.: Ocean acidification research in the Mediterranean Sea: Status, trends and next steps, Front. Mar. Sci., 9, 892670, https://doi.org/10.3389/FMARS.2022.892670, 2022.

Hátún, H., Azetsu-Scott, K., Somavilla, R., Rey, F., Johnson, C., Mathis, M., Mikolajewicz, U., Coupel, P., Tremblay, J., Hartman, S., Pacariz, S. V., Salter, I., and Ólafsson, J.: The subpolar gyre regulates silicate concentrations in the North Atlantic, Sci. Rep., 7, 1–9, https://doi.org/10.1038/s41598-017-14837-4, 2017.

Havsis | SMHI: https://www.smhi.se/data/oceanografi/havsis, last access: 5 December 2023.

HELCOM: HELCOM Thematic assessment of Eutrophication 2016–2021, Baltic Sea Environment Proceedings No. 192, https://helcom.fi/wp-content/uploads/2023/06/HELCOM-Thematic-assessment-of-eutrophication-2016-2021.pdf (last access: 11 September 2024), 2023a.

HELCOM: State of the Baltic Sea. Third HELCOM holistic assessment 2016-2021, Baltic Sea Environment Proceedings no. 194, https://helcom.fi/wp-content/uploads/2023/10/State-of-the-Baltic-Sea-2023.pdf (last access: 11 September 2024), 2023b.

Hiscock, W. T. and Millero, F. J.: Alkalinity of the anoxic waters in the Western Black Sea, Deep-Sea Res. Pt. II, 53, 1787–1801, https://doi.org/10.1016/J.DSR2.2006.05.020, 2006.

Hobday, A. J., Alexander, L. V., Perkins, S. E., Smale, D. A., Straub, S. C., Oliver, E. C. J., Benthuysen, J. A., Burrows, M. T., Donat, M. G., Feng, M., Holbrook, N. J., Moore, P. J., Scannell, H. A., Sen Gupta, A., and Wernberg, T.: A hierarchical approach to defining marine heatwaves, Prog. Oceanogr., 141, 227–238, https://doi.org/10.1016/J.POCEAN.2015.12.014, 2016.

Hobday, A. J., Oliver, E. C. J., Gupta, A. Sen, Benthuysen, J. A., Burrows, M. T., Donat, M. G., Holbrook, N. J., Moore, P. J., Thomsen, M. S., Wernberg, T., and Smale, D. A.: Categorizing and naming marine heatwaves, Oceanography, 31, 162–173, https://doi.org/10.5670/OCEANOG.2018.205, 2018.

Hodges, K. I.: Feature Tracking on the Unit Sphere, Mon. Weather Rev., 123, 3458–3465, https://doi.org/10.1175/1520-0493(1995)123<3458:FTOTUS>2.0.CO;2, 1995.

Hodges, K. I.: Adaptive Constraints for Feature Tracking, Mon. Weather Rev., 127, 1362–1373, https://doi.org/10.1175/1520-0493(1999)127<1362:ACFFT>2.0.CO;2, 1999.

Holliday, N. P., Bersch, M., Berx, B., Chafik, L., Cunningham, S., Florindo-López, C., Hátún, H., Johns, W., Josey, S. A., Larsen, K. M. H., Mulet, S., Oltmanns, M., Reverdin, G., Rossby, T., Thierry, V., Valdimarsson, H., and Yashayaev, I.: Ocean circulation causes the largest freshening event for 120 years in eastern subpolar North Atlantic, Nat. Commun., 11, 1–15, https://doi.org/10.1038/s41467-020-14474-y, 2020.

Hoskins, B. J. and Hodges, K. I.: New Perspectives on the Northern Hemisphere Winter Storm Tracks, J. Atmos. Sci., 59, 1041–1061, https://doi.org/10.1175/1520-0469(2002)059<1041:NPOTNH>2.0.CO;2, 2002.

Hu, S. and Fedorov, A. V.: Indian Ocean warming as a driver of the North Atlantic warming hole, Nat. Commun., 11, 1–11, https://doi.org/10.1038/s41467-020-18522-5, 2020.

Hünicke, B., Zorita, E., Soomere, T., Madsen, K. S., Johansson, M., and Suursaar, Ü.: Recent Change–Sea Level and Wind Waves, in: Second Assessment of Climate Change for the Baltic Sea Basin. Regional Climate Studies, edited by: The BACC II Author Team, Springer, Cham., 155–185, https://doi.org/10.1007/978-3-319-16006-1_9, 2015.

Hurrell, J. W. and Deser, C.: North Atlantic climate variability: The role of the North Atlantic Oscillation, J. Marine Syst., 79, 231–244, https://doi.org/10.1016/J.JMARSYS.2009.11.002, 2010.

Huthnance, J., Weisse, R., Wahl, T., Thomas, H., Pietrzak, J., Jose Souza, A., van Heteren, S., Schmelzer, N., van Beusekom, J., Colijn, F., Haigh, I., Hjøllo, S., Holfort, J., Kent, E. C., Kühn, W., Loewe, P., Lorkowski, I., Arne Mork, K., Pätsch, J., Quante, M., Salt, L., Siddorn, J., Smyth, T., Sterl, A., Woodworth Huthnance, P. J., Souza Á P Woodworth, Á. A., Souza, A., Woodworth, P., Weisse, R., van Beusekom Á F Colijn Á M Quante, Á. J., van Beusekom, J., Quante, M., Wahl, T., Thomas, H., Pietrzak, J., van Heteren, S., Schmelzer Á Holfort, N. J., Holfort, J., Haigh, I., Hjøllo Á Mork, S. K., Mork, K., Kent, E., Kühn Á Pätsch, W. J., Pätsch, J., Loewe Á Lorkowski, P. I., Lorkowski, I., and Salt, L.: Recent Change–North Sea, in: North Sea Region Climate Change Assessment. Regional Climate Studies, edited by: Quante, M. and Colijn, F., Springer, Cham., 85–136, https://doi.org/10.1007/978-3-319-39745-0_3, 2016.

ICES: Working Group on the Integrated Assessments of the Barents Sea (WGIBAR), edited by: Eriksen, E. and Filin, A., ICES Scientific Reports. Report, 235 pp., https://doi.org/10.17895/ices.pub.20051438, 2022.

Incarbona, A., Martrat, B., Mortyn, P. G., Sprovieri, M., Ziveri, P., Gogou, A., Jordà, G., Xoplaki, E., Luterbacher, J., Langone, L., Marino, G., Rodríguez-Sanz, L., Triantaphyllou, M., Di Stefano, E., Grimalt, J. O., Tranchida, G., Sprovieri, R., and Mazzola, S.: Mediterranean circulation perturbations over the last five centuries: Relevance to past Eastern Mediterranean Transient-type events, Sci. Rep., 6, 1–10, https://doi.org/10.1038/srep29623, 2016.

Ingrosso, G., Bensi, M., Cardin, V., and Giani, M.: Anthropogenic CO_2 in a dense water formation area of the Mediterranean Sea, Deep-Sea Res. Pt. I, 123, 118–128, https://doi.org/10.1016/J.DSR.2017.04.004, 2017.

Ionita, M., Lohmann, G., Rimbu, N., Chelcea, S., and Dima, M.: Interannual to decadal summer drought variability over Europe and its relationship to global sea surface temperature, Clim. Dynam., 38, 363–377, https://doi.org/10.1007/S00382-011-1028-Y, 2012.

Ionita, M., Boronean, C., and Chelcea, S.: Seasonal modes of dryness and wetness variability over Europe and their connections with large scale atmospheric circulation and global sea surface temperature, Clim. Dynam., 45, 2803–2829, https://doi.org/10.1007/S00382-015-2508-2, 2015.

IPCC: Climate Change 2021: The Physical Science Basis. Contribution of Working Group I to the Sixth Assessment Report of the Intergovernmental Panel on Climate Change, edited by: Masson-Delmotte, V., Zhai, P., Pirani, A., Connors, S. L., Péan, C., Berger, S., Caud, N., Chen, Y., Goldfarb, L., Gomis, M. I., Huang, M., Leitzell, K., Lonnoy, E., Matthews, J. B. R., Maycock, T. K., Waterfield, T., Yelekçi, O., Yu, R., and Zhou, B., Cambridge University Press, Cambridge, United Kingdom and New York, NY, USA, https://doi.org/10.1017/9781009157896, in press, 2021a.

IPCC: Summary for Policymakers, in: Climate Change 2021: The Physical Science Basis. Contribution of Working Group I to the Sixth Assessment Report of the Intergovernmental Panel on Climate Change, edited by: Masson-Delmotte, V., Zhai, P., Pirani, A., Connors, S. L., Péan, C., Berger, S., Caud, N., Chen, Y., Goldfarb, L., Gomis, M. I., Huang, M., Leitzell, K., Lonnoy, E., Matthews, J. B. R., Maycock, T. K., Waterfield, T., Yelekçi, O., Yu, R., and Zhou, B., Cambridge University Press, Cambridge, United Kingdom and New York, NY, USA, 3–32, https://doi.org/10.1017/9781009157896.001, 2021b.

IPCC: Summary for Policymakers, in: Climate Change 2022: Impacts, Adaptation, and Vulnerability. Contribution of Working Group II to the Sixth Assessment Report of the Intergovernmental Panel on Climate Change, edited by: Pörtner, H.-O., Roberts, D. C., Tignor, M., Poloczanska, E. S., Mintenbeck, K., Alegria, A., Craig, M., Langsdorf, S., Löschke, S., Möller, V., Okem, A., and Rama, B., Cambridge University Press, Cambridge, UK and New York, NY, USA, 3–33, https://doi.org/10.1017/9781009325844.001, 2022.

Islam, M. J., Kunzmann, A., and Slater, M. J.: Responses of aquaculture fish to climate change-induced extreme temperatures: A review, J. World Aquac. Soc., 53, 314–366, https://doi.org/10.1111/JWAS.12853, 2022.

JCOMM Expert Team on Sea Ice: Sea ice information services of the world, Edition 2017, World Meteorological Organization, Geneva, Switzerland, 103 pp., WMO-No.574, https://doi.org/10.25607/OBP-1325, 2017.

Jørgensen, L. L., Pecuchet, L., Ingvaldsen, R. B., and Primicerio, R.: Benthic transition zones in the Atlantic gateway to a changing Arctic ocean, Prog. Oceanogr., 204, 102792, https://doi.org/10.1016/J.POCEAN.2022.102792, 2022.

Juza, M., Fernández-Mora, A., and Tintoré, J.: Sub-Regional Marine Heat Waves in the Mediterranean Sea From Observations: Long-Term Surface Changes, Sub-Surface and Coastal Responses, Front. Mar. Sci., 9, 785771, https://doi.org/10.3389/FMARS.2022.785771, 2022.

Kapsenberg, L., Alliouane, S., Gazeau, F., Mousseau, L., and Gattuso, J.-P.: Coastal ocean acidification and increasing total alkalinity in the northwestern Mediterranean Sea, Ocean Sci., 13, 411–426, https://doi.org/10.5194/os-13-411-2017, 2017.

Karimi, A. A., Ghobadi-Far, K., and Passaro, M.: Barystatic and steric sea level variations in the Baltic Sea and implications of water exchange with the North Sea in the satellite era, Front. Mar. Sci., 9, 963564, https://doi.org/10.3389/FMARS.2022.963564, 2022.

Keeling, R. F., Körtzinger, A., and Gruber, N.: Ocean Deoxygenation in a Warming World, Annu. Rev. Mar. Sci., 2, 199–229, https://doi.org/10.1146/ANNUREV.MARINE.010908.163855, 2009.

Keil, P., Mauritsen, T., Jungclaus, J., Hedemann, C., Olonscheck, D., and Ghosh, R.: Multiple drivers of the North Atlantic warming hole, Nat. Clim. Change, 10, 667–671, https://doi.org/10.1038/s41558-020-0819-8, 2020.

Kessler, A., Goris, N., and Lauvset, S. K.: Observation-based Sea surface temperature trends in Atlantic large marine ecosystems, Prog. Oceanogr., 208, 102902, https://doi.org/10.1016/J.POCEAN.2022.102902, 2022.

Khatiwala, S., Tanhua, T., Mikaloff Fletcher, S., Gerber, M., Doney, S. C., Graven, H. D., Gruber, N., McKinley, G. A., Murata, A., Ríos, A. F., and Sabine, C. L.: Global ocean storage of anthropogenic carbon, Biogeosciences, 10, 2169–2191, https://doi.org/10.5194/bg-10-2169-2013, 2013.

Kideys, A. E.: Ecology: Fall and rise of the Black Sea ecosystem, Science, 297, 1482–1484, https://doi.org/10.1126/SCIENCE.1073002, 2002.

Kniebusch, M., Meier, H. E. M., Neumann, T., and Börgel, F.: Temperature Variability of the Baltic Sea Since 1850 and Attribution to Atmospheric Forcing Variables, J. Geophys. Res.-Oceans, 124, 4168–4187, https://doi.org/10.1029/2018JC013948, 2019.

Lehmann, A., Myrberg, K., Post, P., Chubarenko, I., Dailidiene, I., Hinrichsen, H.-H., Hüssy, K., Liblik, T., Meier, H. E. M., Lips, U., and Bukanova, T.: Salinity dynamics of the Baltic Sea, Earth Syst. Dynam., 13, 373–392, https://doi.org/10.5194/esd-13-373-2022, 2022.

Leppäranta, M.: Land-ice interaction in the Baltic Sea, Est. J. Earth Sci., 62, 2–14, https://doi.org/10.3176/EARTH.2013.01, 2013.

Li, L., Lozier, M. S., and Li, F.: Century-long cooling trend in subpolar North Atlantic forced by atmosphere: an alternative explanation, Clim. Dynam., 58, 2249–2267, https://doi.org/10.1007/S00382-021-06003-4, 2022.

Lien, V. and Raj, R. P.: North Atlantic – Arctic exchanges, in: Copernicus Marine Service Ocean State Report, Issue 2, J. Oper. Oceanogr., 11, s88–s91, https://doi.org/10.1080/1755876X.2018.1489208, 2018.

Lien, V. S., Schlichtholz, P., Skagseth, Ø., and Vikebø, F. B.: Wind-Driven Atlantic Water Flow as a Direct Mode for Reduced Barents Sea Ice Cover, J. Climate, 30, 803–812, https://doi.org/10.1175/JCLI-D-16-0025.1, 2017.

Lima, L., Peneva, E., Ciliberti, S., Masina, S., Lemieux, B., Storto, A., and Chtirkova, B.: Ocean heat content in the Black Sea, in: Copernicus Marine Service Ocean State Report, Issue 4, J. Oper. Oceanogr., 13, s41–s48, https://doi.org/10.1080/1755876X.2020.1785097, 2020.

Lima, L., Ciliberti, S. A., Aydoğdu, A., Masina, S., Escudier, R., Cipollone, A., Azevedo, D., Causio, S., Peneva, E., Lecci, R., Clementi, E., Jansen, E., Ilicak, M., Cretì, S., Stefanizzi, L., Palermo, F., and Coppini, G.: Climate Signals in the Black Sea From a Multidecadal Eddy-Resolving Reanalysis, Frontiers in Marine Science, 8, 710973, https://doi.org/10.3389/FMARS.2021.710973/BIBTEX, 2021.

Luchetta, A., Cantoni, C., and Catalano, G.: New observations of CO$_2$-induced acidification in the northern Adriatic Sea over the last quarter century, Chem. Ecol., 26, 1–17, https://doi.org/10.1080/02757541003627688, 2010.

Ludwigsen, C. A., Khan, S. A., Andersen, O. B., and Marzeion, B.: Vertical Land Motion From Present-Day Deglaciation in the Wider Arctic, Geophys. Res. Lett., 47, e2020GL088144, https://doi.org/10.1029/2020GL088144, 2020.

Lundesgaard, Ø., Sundfjord, A., Lind, S., Nilsen, F., and Renner, A. H. H.: Import of Atlantic Water and sea ice controls the ocean environment in the northern Barents Sea, Ocean Sci., 18, 1389–1418, https://doi.org/10.5194/os-18-1389-2022, 2022.

Lyubartsev, V., Borile, F., Clementi, E., Masina, S., Drudi, M., Coppini, G., Cessi, P., and Pinardi, N.: Interannual variability in the Eastern and Western Mediterranean Overturning Index, in: Copernicus Marine Service Ocean State Report, Issue 4, J. Oper. Oceanogr., 13, s30–s33, 2020.

Ma, X., Liu, W., Allen, R. J., Huang, G., and Li, X.: Dependence of regional ocean heat uptake on anthropogenic warming scenarios, Sci. Adv., 6, 303–309, https://doi.org/10.1126/SCIADV.ABC0303, 2020.

Marcellin Yao, K., Marcou, O., Goyet, C., Guglielmi, V., Touratier, F., and Savy, J. P.: Time variability of the north-western Mediterranean Sea pH over 1995–2011, Mar. Environ. Res., 116, 51–60, https://doi.org/10.1016/J.MARENVRES.2016.02.016, 2016.

Marullo, S., Serva, F., Iacono, R., Napolitano, E., di Sarra, A., Meloni, D., Monteleone, F., Sferlazzo, D., De Silvestri, L., de Toma, V., Pisano, A., Bellacicco, M., Landolfi, A., Organelli, E., Yang, C., and Santoleri, R.: Record-breaking persistence of the 2022/23 marine heatwave in the Mediterranean Sea, Environ. Res. Lett., 18, 114041, https://doi.org/10.1088/1748-9326/AD02AE, 2023.

Masina, S., Pinardi, N., Cipollone, A., Banerjee, D. S., Lyubartsev, V., von Schuckmann, K., Jackson, L., Escudier, R., Clementi, E., Aydogdu, A., and Iovino, D.: The Atlantic Meridional Overturning Circulation forcing the mean sea level in the Mediterranean Sea through the Gibraltar transport, in: Copernicus Ocean State Report, Issue 6, J. Oper. Oceanogr., 15, s36–s43, https://doi.org/10.1080/1755876X.2022.2095169, 2022.

Mauritzen, C., Hansen, E., Andersson, M., Berx, B., Beszczynska-Möller, A., Burud, I., Christensen, K. H., Debernard, J., de Steur, L., Dodd, P., Gerland, S., Godøy, T., Hansen, B., Hudson, S., Høydalsvik, F., Ingvaldsen, R., Isachsen, P. E., Kasajima, Y., Koszalka, I., Kovacs, K. M., Køltzow, M., LaCasce, J., Lee, C. M., Lavergne, T., Lydersen, C., Nicolaus, M., Nilsen, F., Nøst, O. A., Orvik, K. A., Reigstad, M., Schyberg, H., Seuthe, L., Skagseth, T., Skardhamar, J., Skogseth, R., Sperrevik, A., Svensen, C., Søiland, H., Teigen, S. H., Tverberg, V., and Wexels Riser, C.: Closing the loop – Approaches to monitoring the state of the Arctic Mediterranean during the International Polar Year 2007–2008, Prog. Oceanogr., 90, 62–89, https://doi.org/10.1016/J.POCEAN.2011.02.010, 2011.

MedECC: Climate and Environmental Change in the Mediterranean Basin – Current Situation and Risks for the Future. First Mediterranean Assessment Report, edited by: Cramer, W., Guiot, J., and Marini, K., Union for the Mediterranean, Plan Bleu, UNEP/MAP, Marseille, France, 632 pp., Zenodo, https://doi.org/10.5281/zenodo.7224821, 2020a.

MedECC: Climate and Environmental Change in the Mediterranean Basin – Current Situation and Risks for the Future. First Mediterranean Assessment Report, Marseille, France, 632 pp., Zenodo, https://doi.org/10.5281/zenodo.4768833, 2020b.

MedECC: Summary for Policymakers, in: Climate and Environmental Change in the Mediterranean Basin – Current Situation and Risks for the Future. First Mediterranean Assessment Report, edited by: Cramer, W., Guiot, J., and Marini, K., Union for the Mediterranean, Plan Bleu, UNEP/MAP, Marseille, France, 11–40, Zenodo, https://doi.org/10.5281/zenodo.5513887, 2020c.

Mee, L. D., Friedrich, J., and Gomoiu, M. T.: Restoring the Black Sea in times of uncertainty, Oceanography, 18, 100–111, https://doi.org/10.5670/OCEANOG.2005.45, 2005.

Meier, H. E. M., Kniebusch, M., Dieterich, C., Gröger, M., Zorita, E., Elmgren, R., Myrberg, K., Ahola, M. P., Bartosova, A., Bonsdorff, E., Börgel, F., Capell, R., Carlén, I., Carlund, T., Carstensen, J., Christensen, O. B., Dierschke, V., Frauen, C., Frederiksen, M., Gaget, E., Galatius, A., Haapala, J. J., Halkka, A., Hugelius, G., Hünicke, B., Jaagus, J., Jüssi, M., Käyhkö, J., Kirchner, N., Kjellström, E., Kulinski, K., Lehmann, A., Lindström, G., May, W., Miller, P. A., Mohrholz, V., Müller-Karulis, B., Pavón-Jordán, D., Quante, M., Reckermann, M., Rutgersson, A., Savchuk, O. P., Stendel, M., Tuomi, L., Viitasalo, M., Weisse, R., and Zhang, W.: Climate change in the Baltic Sea region: a summary, Earth Syst. Dynam., 13, 457–593, https://doi.org/10.5194/esd-13-457-2022, 2022.

Meli, M., Camargo, C. M. L., Olivieri, M., Slangen, A. B. A., and Romagnoli, C.: Sea-level trend variability in the Mediterranean during the 1993–2019 period, Front. Mar. Sci., 10, 1150488, https://doi.org/10.3389/FMARS.2023.1150488, 2023.

Menary, M. B. and Wood, R. A.: An anatomy of the projected North Atlantic warming hole in CMIP5 models, Clim. Dynam., 50, 3063–3080, https://doi.org/10.1007/S00382-017-3793-8, 2018.

Merlivat, L., Boutin, J., Antoine, D., Beaumont, L., Golbol, M., and Vellucci, V.: Increase of dissolved inorganic carbon and decrease in pH in near-surface waters in the Mediterranean Sea during the past two decades, Biogeosciences, 15, 5653–5662, https://doi.org/10.5194/bg-15-5653-2018, 2018.

Messias, M. J. and Mercier, H.: The redistribution of anthropogenic excess heat is a key driver of warming in the North Atlantic, Communications Earth & Environment, 3, 1–14, https://doi.org/10.1038/s43247-022-00443-4, 2022.

Middelburg, J. J., Soetaert, K., and Hagens, M.: Ocean Alkalinity, Buffering and Biogeochemical Processes, Rev. Geophys., 58, e2019RG000681, https://doi.org/10.1029/2019RG000681, 2020.

Mohrholz, V.: Major Baltic inflow statistics – Revised, Front. Mar. Sci., 5, 385391, https://doi.org/10.3389/FMARS.2018.00384, 2018.

Mork, K. A., Skagseth, Ø., and Søiland, H.: Recent Warming and Freshening of the Norwegian Sea Observed by Argo Data, J. Climate, 32, 3695–3705, https://doi.org/10.1175/JCLI-D-18-0591.1, 2019.

Mourre, B., Reyes, E., Lorente, P., Santana, A., Hernández-Lasheras, J., Hernández-Carrasco, I., García-Jove, M., and Zarokanellos, N. D.: Intense wind-driven coastal upwelling in the Balearic Islands in response to Storm Blas (November 2021), in: 7th edition of the Copernicus Ocean State Report (OSR7), edited by: von Schuckmann, K., Moreira, L., Le Traon, P.-Y., Grégoire, M., Marcos, M., Staneva, J., Brasseur, P., Garric, G., Lionello, P., Karstensen, J., and Neukermans, G., Copernicus Publications, State Planet, 1-osr7, 15, https://doi.org/10.5194/sp-1-osr7-15-2023, 2023.

Müller, J. D., Schneider, B., and Rehder, G.: Long-term alkalinity trends in the Baltic Sea and their implications for CO_2-induced acidification, Limnol. Oceanogr., 61, 1984–2002, https://doi.org/10.1002/LNO.10349, 2016.

Murray, C. J., Müller-Karulis, B., Carstensen, J., Conley, D. J., Gustafsson, B. G., and Andersen, J. H.: Past, present and future eutrophication status of the Baltic Sea, Front. Mar. Sci., 6, 428558, https://doi.org/10.3389/FMARS.2019.00002, 2019.

O'Carroll, A. G., Armstrong, E. M., Beggs, H. M., Bouali, M., Casey, K. S., Corlett, G. K., Dash, P., Donlon, C. J., Gentemann, C. L., Høyer, J. L., Ignatov, A., Kabobah, K., Kachi, M., Kurihara, Y., Karagali, I., Maturi, E., Merchant, C. J., Marullo, S., Minnett, P. J., Pennybacker, M., Ramakrishnan, B., Ramsankaran, R., Santoleri, R., Sunder, S., Saux Picart, S., Vázquez-Cuervo, J., and Wimmer, W.: Observational Needs of Sea Surface Temperature, Frontiers in Marine Science, 6, 420, https://doi.org/10.3389/fmars.2019.00420, 2019.

Oliver, E. C. J., Donat, M. G., Burrows, M. T., Moore, P. J., Smale, D. A., Alexander, L. V., Benthuysen, J. A., Feng, M., Sen Gupta, A., Hobday, A. J., Holbrook, N. J., Perkins-Kirkpatrick, S. E., Scannell, H. A., Straub, S. C., and Wernberg, T.: Longer and more frequent marine heatwaves over the past century, Nat. Commun., 9, 1–12, https://doi.org/10.1038/s41467-018-03732-9, 2018.

Oliver, E. C. J., Burrows, M. T., Donat, M. G., Sen Gupta, A., Alexander, L. V., Perkins-Kirkpatrick, S. E., Benthuysen, J. A., Hobday, A. J., Holbrook, N. J., Moore, P. J., Thomsen, M. S., Wernberg, T., and Smale, D. A.: Projected Marine Heatwaves in the 21st Century and the Potential for Ecological Impact, Front. Mar. Sci., 6, 481127, https://doi.org/10.3389/FMARS.2019.00734, 2019.

Onarheim, I. H., Eldevik, T., Årthun, M., Ingvaldsen, R. B., and Smedsrud, L. H.: Skillful prediction of Barents Sea ice cover, Geophys. Res. Lett., 42, 5364–5371, https://doi.org/10.1002/2015GL064359, 2015.

Østerhus, S., Woodgate, R., Valdimarsson, H., Turrell, B., de Steur, L., Quadfasel, D., Olsen, S. M., Moritz, M., Lee, C. M., Larsen, K. M. H., Jónsson, S., Johnson, C., Jochumsen, K., Hansen, B., Curry, B., Cunningham, S., and Berx, B.: Arctic Mediterranean exchanges: a consistent volume budget and trends in transports from two decades of observations, Ocean Sci., 15, 379–399, https://doi.org/10.5194/os-15-379-2019, 2019.

Pärn, O., Friedland, R., Rjazin, J., and Stips, A.: Regime shift in sea-ice characteristics and impact on the spring bloom in the Baltic Sea, Oceanologia, 64, 312–326, https://doi.org/10.1016/J.OCEANO.2021.12.004, 2022.

Passaro, M., Müller, F. L., Oelsmann, J., Rautiainen, L., Dettmering, D., Hart-Davis, M. G., Abulaitijiang, A., Andersen, O. B., Høyer, J. L., Madsen, K. S., Ringgaard, I. M., Särkkä, J., Scarrott, R., Schwatke, C., Seitz, F., Tuomi, L., Restano, M., and Benveniste, J.: Absolute Baltic Sea Level Trends in the Satellite Altimetry Era: A Revisit, Front. Mar. Sci., 8, 647607, https://doi.org/10.3389/FMARS.2021.647607, 2021.

Peal, R., Worsfold, M., and Good, S.: Comparing global trends in marine cold spells and marine heatwaves using reprocessed satellite data, in: 7th edition of the Copernicus Ocean State Report (OSR7), edited by: von Schuckmann, K., Moreira, L., Le Traon, P.-Y., Grégoire, M., Marcos, M., Staneva, J., Brasseur, P., Garric, G., Lionello, P., Karstensen, J., and Neukermans, G., Copernicus Publications, State Planet, 1-osr7, 3, https://doi.org/10.5194/sp-1-osr7-3-2023, 2023.

Pezzulli, S., Stephenson, D. B., and Hannachi, A.: The Variability of Seasonality, J. Climate, 18, 71–88, https://doi.org/10.1175/JCLI-3256.1, 2005.

Pinardi, N., Bonaduce, A., Navarra, A., Dobricic, S., and Oddo, P.: The Mean Sea Level Equation and Its Application to the Mediterranean Sea, J. Climate, 27, 442–447, https://doi.org/10.1175/JCLI-D-13-00139.1, 2014.

Pinardi, N., Zavatarelli, M., Adani, M., Coppini, G., Fratianni, C., Oddo, P., Simoncelli, S., Tonani, M., Lyubartsev, V., Dobricic, S., and Bonaduce, A.: Mediterranean Sea large-scale low-frequency ocean variability and water mass formation rates from 1987 to

2007: A retrospective analysis, Prog. Oceanogr., 132, 318–332, https://doi.org/10.1016/J.POCEAN.2013.11.003, 2015.

Pinardi, N., Cessi, P., Borile, F., and Wolfe, C. L. P.: The Mediterranean Sea Overturning Circulation, J. Phys. Oceanogr., 49, 1699–1721, https://doi.org/10.1175/JPO-D-18-0254.1, 2019.

Pinardi, N., Estournel, C., Cessi, P., Escudier, R., and Lyubartsev, V.: Chapter 7 – dense and deep water formation processes and Mediterranean overturning circulation Oceanography of the Mediterranean Sea, edited by: Schroeder, K. and Chiggiato, J., Elsevier, 209–261, https://doi.org/10.1016/B978-0-12-823692-5.00009-1, 2023.

Pisano, A., Marullo, S., Artale, V., Falcini, F., Yang, C., Leonelli, F. E., Santoleri, R., and Nardelli, B. B.: New Evidence of Mediterranean Climate Change and Variability from Sea Surface Temperature Observations, Remote Sens., 12, 132, https://doi.org/10.3390/RS12010132, 2020.

Polonsky, A.: Had Been Observing the Acidification of the Black Sea Upper Layer in XX Century?, Turk. J. Fish. Aquat. Sci., 12, 391–396, https://doi.org/10.4194/1303-2712-V12_2_27, 2012.

Polonsky, A. B. and Grebneva, E. A.: The Spatiotemporal Variability of pH in Waters of the Black Sea, Dokl. Earth Sci., 486, 669–674, https://doi.org/10.1134/S1028334X19060072, 2019.

Polyakov, I. V., Ingvaldsen, R. B., Pnyushkov, A. V., Bhatt, U. S., Francis, J. A., Janout, M., Kwok, R., and Skagseth, Ø.: Fluctuating Atlantic inflows modulate Arctic atlantification, Science, 381, 972–979, https://doi.org/10.1126/SCIENCE.ADH5158, 2023.

Potiris, M., Mamoutos, I. G., Tragou, E., Zervakis, V., Kassis, D., and Ballas, D.: Dense Water Formation in the North–Central Aegean Sea during Winter 2021–2022, Journal of Marine Science and Engineering, 12, 221, https://doi.org/10.3390/JMSE12020221, 2024.

Qasmi, S.: Past and future response of the North Atlantic warming hole to anthropogenic forcing, Earth Syst. Dynam., 14, 685–695, https://doi.org/10.5194/esd-14-685-2023, 2023.

Rahmstorf, S., Box, J. E., Feulner, G., Mann, M. E., Robinson, A., Rutherford, S., and Schaffernicht, E. J.: Exceptional twentieth-century slowdown in Atlantic Ocean overturning circulation, Nat. Clim. Change, 5, 475–480, https://doi.org/10.1038/nclimate2554, 2015.

Raj, R. P. and Halo, I.: Monitoring the mesoscale eddies of the Lofoten Basin: importance, progress, and challenges, Int. J. Remote Sens., 37, 3712–3728, https://doi.org/10.1080/01431161.2016.1201234, 2016.

Ranasinghe, R., Ruane, A. C., Vautard, R., Arnell, N., Coppola, E., Cruz, F. A., Dessai, S., Islam, A. S., Rahimi, M., Ruiz Carrascal, D., Sillmann, J., Sylla, M. B., Tebaldi, C., Wang, W., and Zaaboul, R.: Climate Change Information for Regional Impact and for Risk Assessment, in: Climate Change 2021: The Physical Science Basis. Contribution of Working Group I to the Sixth Assessment Report of the Intergovernmental Panel on Climate Change, edited by: Masson-Delmotte, V., Zhai, P., Pirani, A., Connors, S. L., Péan, C., Berger, S., Caud, N., Chen, Y., Goldfarb, L., Gomis, M. I., Huang, M., Leitzell, K., Lonnoy, E., Matthews, J. B. R., Maycock, T. K., Waterfield, T., Yelekçi, O., Yu, R., and Zhou, B., Cambridge University Press, Cambridge, United Kingdom and New York, NY, USA, 1767–1926, https://doi.org/10.1017/9781009157896.014, 2021.

Raudsepp, U., Legeais, J.-F., She, J., Maljutenko, I., and Jandt, S.: Baltic inflows, in: Copernicus Marine Service Ocean State Report, Issue 2, J. Oper. Oceanogr., 11, s106–s110, https://doi.org/10.1080/1755876X.2018.1489208, 2018.

Raudsepp, U., Uiboupin, R., Laanemäe, K., and Maljutenko, I.: Geographical and seasonal coverage of sea ice in the Baltic Sea, in: Copernicus Marine Service Ocean State Report, Issue 4, J. Oper. Oceanogr., 13, s115–s121, 2020.

Raudsepp, U., Männik, A., Maljutenko, I., Lagemaa, P., Rikka, S., Alari, V., and Uiboupin, R.: Extreme waves and low sea level during the storm in the Gulf of Bothnia, Baltic Sea, in: Copernicus Marine Service Ocean State Report, Issue 5, J. Oper. Oceanogr., 14, s162–s173, https://doi.org/10.1080/1755876X.2021.1946240, 2021.

Roether, W., Klein, B. and Hainbucher, D.: The Eastern Mediterranean Transient, in: The Mediterranean Sea, edited by: Borzelli, G. L. E., Gačić, M., Lionello, P., and Malanotte-Rizzoli, P., AGU Advancing Earth and Space Sciences, https://doi.org/10.1002/9781118847572.ch6, 2014.

Roman, M. R., Brandt, S. B., Houde, E. D., and Pierson, J. J.: Interactive effects of Hypoxia and temperature on coastal pelagic zooplankton and fish, Front. Mar. Sci., 6, 404311, https://doi.org/10.3389/FMARS.2019.00139, 2019.

Rudels, B.: Arctic Ocean circulation and variability – advection and external forcing encounter constraints and local processes, Ocean Sci., 8, 261–286, https://doi.org/10.5194/os-8-261-2012, 2012.

Sabine, C. L., Feely, R. A., Gruber, N., Key, R. M., Lee, K., Bullister, J. L., Wanninkhof, R., Wong, C. S., Wallace, D. W. R., Tilbrook, B., Millero, F. J., Peng, T. H., Kozyr, A., Ono, T., and Rios, A. F.: The oceanic sink for anthropogenic CO_2, Science, 305, 367–371, https://doi.org/10.1126/SCIENCE.1097403, 2004.

Sanders, R. N. C., Jones, D. C., Josey, S. A., Sinha, B., and Forget, G.: Causes of the 2015 North Atlantic cold anomaly in a global state estimate, Ocean Sci., 18, 953–978, https://doi.org/10.5194/os-18-953-2022, 2022.

Schneider, A., Wallace, D. W. R., and Körtzinger, A.: Alkalinity of the Mediterranean Sea, Geophys. Res. Lett., 34, 15608, https://doi.org/10.1029/2006GL028842, 2007.

Schneider, A., Tanhua, T., Körtzinger, A., and Wallace, D. W. R.: High anthropogenic carbon content in the eastern Mediterranean, J. Geophys. Res.-Oceans, 115, 12050, https://doi.org/10.1029/2010JC006171, 2010.

Schroeder, K., García-Lafuente, J., Josey, S. A., Artale, V., Buongiorno Nardelli, B., Carrillo, A., Gacic, M., Gasparini, G. P.,Herrmann, M., Lionello, P., Ludwig, W., Millot, C., Özsoy, E., Pisacane, G., Sánchez-Garrido, J. C., Sannino, G., Santoleri, R.,Somot, S., Struglia, M., Stanev, E., Taupier-Letage, I., Tsimplis,M. N., Vargas-Yáñez, M., Zervakis, V., and Zodiatis, G.: Chapter 3: Circulation of the Mediterranean Sea and its variability, in: The Climate of the Mediterranean Region, from the past to the future, edited by: Lionello, P., Elsevier Insights, Amsterdam, ISBN 9780124160422, 2012.

Segtnan, O. H., Furevik, T., and Jenkins, A. D.: Heat and freshwater budgets of the Nordic seas computed from atmospheric reanalysis and ocean observations, J. Geophys. Res.-Oceans, 116, 11003, https://doi.org/10.1029/2011JC006939, 2011.

Seneviratne, S. I., Zhang, X., Adnan, M., Badi, W., Dereczynski, C., Di Luca, A., Ghosh, S., Iskandar, I., Kossin, J., Lewis, S., Otto, F., Pinto, I., Satoh, M., Vicente-Serrano, S. M., Wehner, M., and Zhou, B.: Weather and Climate Extreme Events in a Changing Climate, in: Climate Change 2021: The Physical Science Basis. Contribution of Working Group I to the Sixth Assessment Report of the Intergovernmental Panel on Climate Change, edited by: Masson-Delmotte, V., Zhai, P., Pirani, A., Connors, S. L., Péan, C., Berger, S., Caud, N., Chen, Y., Goldfarb, L., Gomis, M. I., Huang, M., Leitzell, K., Lonnoy, E., Matthews, J. B. R., Maycock, T. K., Waterfield, T., Yelekçi, O., Yu, R., and Zhou, B., Cambridge University Press, Cambridge, United Kingdom and New York, NY, USA, 1513–1766, https://doi.org/10.1017/9781009157896.013, 2021.

Simoncelli, S., Pinardi, N., Fratianni, C., Dubois, C., and Notarstefano, G.: Water mass formation processes in the Mediterranean Sea over the past 30 years, in: Copernicus Marine Service Ocean State Report, Issue 2, J. Oper. Oceanogr., 11, s96–s101, https://doi.org/10.1080/1755876X.2018.1489208, 2018.

Smedsrud, L. H., Esau, I., Ingvaldsen, R. B., Eldevik, T., Haugan, P. M., Li, C., Lien, V. S., Olsen, A., Omar, A. M., Risebrobakken, B., Sandø, A. B., Semenov, V. A., and Sorokina, S. A.: The Role Of The Barents Sea In The Arctic Climate System, Rev. Geophys., 51, 415–449, https://doi.org/10.1002/ROG.20017, 2013.

Smith, K. E., Burrows, M. T., Hobday, A. J., King, N. G., Moore, P. J., Sen Gupta, A., Thomsen, M. S., Wernberg, T., and Smale, D. A.: Biological Impacts of Marine Heatwaves, Annu. Rev. Mar. Sci., 15, 119–145, https://doi.org/10.1146/annurev-marine-032122-121437, 2023.

Spada, G. and Melini, D.: SELEN^4 (SELEN version 4.0): a Fortran program for solving the gravitationally and topographically self-consistent sea-level equation in glacial isostatic adjustment modeling, Geosci. Model Dev., 12, 5055–5075, https://doi.org/10.5194/gmd-12-5055-2019, 2019.

Staneva, J., Behrens, A., and Gayer, G.: Predictability of large wave heights in the western Black Sea during the 2018 winter storms, in: Copernicus Marine Service Ocean State Report, Issue 4, J. Oper. Oceanogr., 13, s144–s149, https://doi.org/10.1080/1755876X.2020.1785097, 2020.

Sundby, S. and Drinkwater, K.: On the mechanisms behind salinity anomaly signals of the northern North Atlantic, Prog. Oceanogr., 73, 190–202, https://doi.org/10.1016/J.POCEAN.2007.02.002, 2007.

Taillandier, V., D'Ortenzio, F., Prieur, L., Conan, P., Coppola, L., Cornec, M., Dumas, F., Durrieu de Madron, X., Fach, B., Fourrier, M., Gentil, M., Hayes, D., Husrevoglu, S., Legoff, H., Le Ster, L., Örek, H., Ozer, T., Poulain, P. M., Pujo-Pay, M., Ribera d'Alcalà, M., Salihoglu, B., Testor, P., Velaoras, D., Wagener, T., and Wimart-Rousseau, C.: Sources of the Levantine Intermediate Water in Winter 2019, J. Geophys. Res.-Oceans, 127, e2021JC017506, https://doi.org/10.1029/2021JC017506, 2022.

The BACC II Author Team: Second Assessment of Climate Change for the Baltic Sea Basin, edited by: The BACC II Author Team, Springer International Publishing, Cham, https://doi.org/10.1007/978-3-319-16006-1, 2015.

The Climate Change Initiative Coastal Sea Level Team: Coastal sea level anomalies and associated trends from Jason satellite altimetry over 2002–2018, Scientific Data, 7, 1–17, https://doi.org/10.1038/s41597-020-00694-w, 2020.

Tsimplis, M. N., Josey, S. A., Rixen, M., and Stanev, E. V.: On the forcing of sea level in the Black Sea, J. Geophys. Res.-Oceans, 109, 8015, https://doi.org/10.1029/2003JC002185, 2004.

Tsimplis, M. N., Zervakis, V., Josey, S. A., Peneva, E. L., Struglia, M. V., Stanev, E. V., Theocharis, A., Lionello, P., Malanotte-Rizzoli, P., Artale, V., Tragou, E., and Oguz, T.: Changes in the Oceanography of the Mediterranean Sea and their Link to Climate Variability, in: Mediterranean Climate Variability, edited by: Lionello, P., Malanotte-Rizzoli, P., and Boscolo, R., Elsevier publishing, 227–282, ISBN 9780124160422, 2006.

Uiboupin, R., Axell, L., Raudsepp, U., and Sipelgas, L.: Comparison of operational ice charts with satellite based ice concentration products in the Baltic Sea, 2008 IEEE/OES US/EU-Baltic International Symposium, 27–29 May 2008, Tallinn, Estonia, https://doi.org/10.1109/BALTIC.2008.4625571, 2008.

UNDRR: Sendai Framework for Disaster Risk Reduction 2015–2030, UNDRR, https://www.undrr.org/publication/sendai-framework-disaster-risk-reduction-2015-2030, last access: 22 March 2024.

Valcheva, N. and Slabakova, V.: Winter and Summer Variability and Trends of Modis Derived Sea Surface Temperatures for the Western Black Sea, in: Proceeding of 1st International Conference on Environmental Protection and Disaster RISKs, 29–30 September 2020, Sofia, Bulgaria, 9–21, ISBN 978-619-7065-39-8, 2020.

Vignudelli, S., Birol, F., Benveniste, J., Fu, L. L., Picot, N., Raynal, M., and Roinard, H.: Satellite Altimetry Measurements of Sea Level in the Coastal Zone, Surv. Geophys., 40, 1319–1349, https://doi.org/10.1007/S10712-019-09569-1, 2019.

Vihma, T. and Haapala, J.: Geophysics of sea ice in the Baltic Sea: A review, Prog. Oceanogr., 80, 129–148, https://doi.org/10.1016/J.POCEAN.2009.02.002, 2009.

Volkov, D. L. and Landerer, F. W.: Internal and external forcing of sea level variability in the Black Sea, Clim. Dynam., 45, 2633–2646, https://doi.org/10.1007/S00382-015-2498-0, 2015.

Volkov, M. D. and Wilson, C.: Atlantic meridional overturning circulation: Observed transport and variability, Front. Mar. Sci., 6, 436930, https://doi.org/10.3389/FMARS.2019.00260, 2019.

Volosciuk, C., Maraun, D., Semenov, V. A., Tilinina, N., Gulev, S. K., and Latif, M.: Rising Mediterranean Sea Surface Temperatures Amplify Extreme Summer Precipitation in Central Europe, Sci. Rep., 6, 1–7, https://doi.org/10.1038/srep32450, 2016.

Von Schuckmann, K., Palmer, M. D., Trenberth, K. E., Cazenave, A., Chambers, D., Champollion, N., Hansen, J., Josey, S. A., Loeb, N., Mathieu, P. P., Meyssignac, B., and Wild, M.: An imperative to monitor Earth's energy imbalance, Nat. Clim. Change, 6, 138–144, https://doi.org/10.1038/nclimate2876, 2016.

von Storch, H., Omstedt, A., Pawlak, J., and Reckermann, M.: Introduction and Summary, in: Second Assessment of Climate Change for the Baltic Sea Basin. Regional Climate Studies, edited by: The BACC II Author Team, Springer, Cham., https://doi.org/10.1007/978-3-319-16006-1_1, 2015.

Vousdoukas, M. I., Mentaschi, L., Voukouvalas, E., Verlaan, M., and Feyen, L.: Extreme sea levels on the rise along Europe's coasts, Earths Future, 5, 304–323, https://doi.org/10.1002/2016EF000505, 2017.

Walczowski, W., Piechura, J., Goszczko, I., and Wieczorek, P.: Changes in Atlantic water properties: an important factor in the

European Arctic marine climate, ICES J. Mar. Sci., 69, 864–869, https://doi.org/10.1093/ICESJMS/FSS068, 2012.

Waldman, R., Brüggemann, N., Bosse, A., Spall, M., Somot, S., and Sevault, F.: Overturning the Mediterranean Thermohaline Circulation, Geophys. Res. Lett., 45, 8407–8415, https://doi.org/10.1029/2018GL078502, 2018.

Wakelin, S., Townhill, B., Engelhard, G., Holt, J., and Renshaw, R.: Marine heatwaves and cold-spells, and their impact on fisheries in the North Sea, in: Copernicus Marine Service Ocean State Report, Issue 5, J. Oper. Oceanogr., 14, s91–s96, https://doi.org/10.1080/1755876X.2021.1946240, 2021.

Wimart-Rousseau, C., Wagener, T., Álvarez, M., Moutin, T., Fourrier, M., Coppola, L., Niclas-Chirurgien, L., Raimbault, P., D'Ortenzio, F., Durrieu de Madron, X., Taillandier, V., Dumas, F., Conan, P., Pujo-Pay, M., and Lefèvre, D.: Seasonal and Interannual Variability of the CO_2 System in the Eastern Mediterranean Sea: A Case Study in the North Western Levantine Basin, Front. Mar. Sci., 8, 649246, https://doi.org/10.3389/FMARS.2021.649246, 2021.

WMO: Manual on Codes, Volume I.1 – International Codes. Annex II to the WMO Technical Regulations, Part A – Alphanumeric Codes, 2019.

WMO: Provisional State of the Global Climate 2023, WMO https://wmo.int/files/provisional-state-of-global-climate--2023 (last access: 22 February 2024), 2023.

Woollings, T., Barriopedro, D., Methven, J., Son, S. W., Martius, O., Harvey, B., Sillmann, J., Lupo, A. R., and Seneviratne, S.: Blocking and its Response to Climate Change, Current Climate Change Reports, 4, 287–300, https://doi.org/10.1007/S40641-018-0108-Z, 2018.

Yan, X. and Tang, Y.: Multidecadal Variability in Mediterranean Sea Surface Temperature and Its Sources, Geophys. Res. Lett., 48, e2020GL091814, https://doi.org/10.1029/2020GL091814, 2021.

Yao, Y., Wang, C., and Fu, Y.: Global Marine Heatwaves and Cold-Spells in Present Climate to Future Projections, Earths Future, 10, e2022EF002787, https://doi.org/10.1029/2022EF002787, 2022.

Yeager, S.: The abyssal origins of North Atlantic decadal predictability, Clim. Dynam., 55, 2253–2271, https://doi.org/10.1007/S00382-020-05382-4, 2020.

Zecchetto, S. and De Biasio, F.: Sea Surface Winds over the Mediterranean Basin from Satellite Data (2000–04): Meso- and Local-Scale Features on Annual and Seasonal Time Scales, J. Appl. Meteorol. Climatol., 46, 814–827, https://doi.org/10.1175/JAM2498.1, 2007.

Zhang, W., Villarini, G., Scoccimarro, E., and Napolitano, F.: Examining the precipitation associated with medicanes in the high-resolution ERA-5 reanalysis data, Int. J. Climatol., 41, E126–E132, https://doi.org/10.1002/JOC.6669, 2021.

State Planet, 4-osr8, 3, 2024
https://doi.org/10.5194/sp-4-osr8-3-2024

Monitoring global ocean heat content from space geodetic observations to estimate the Earth energy imbalance

Florence Marti[1], **Benoit Meyssignac**[2], **Victor Rousseau**[1], **Michaël Ablain**[1], **Robin Fraudeau**[1],
Alejandro Blazquez[2], **and Sébastien Fourest**[2]

[1]Magellium, 31520 Ramonville-Saint-Agne, France
[2]LEGOS (CNES/CNRS/IRD/UT3), Université de Toulouse, 31400 Toulouse, France

Correspondence: Florence Marti (florence.marti@magellium.fr)

Received: 1 August 2023 – Discussion started: 24 August 2023
Revised: 3 April 2024 – Accepted: 7 April 2024 – Published: 30 September 2024

Abstract. This study presents an improved space geodetic approach to estimate the global ocean heat content (GOHC) change and the Earth energy imbalance (EEI) over 1993–2022. The EEI exhibits a positive trend of 0.29 $\mathrm{W\,m^{-2}}$ per decade, significant at the 90 % confidence level, indicating accelerated ocean warming in line with independent Clouds and the Earth's Radiant Energy System (CERES) data. The study highlights the importance of comparing various estimates (e.g. in-situ-based GOHC) and their uncertainties to reliably assess EEI changes.

1 Introduction

The ocean absorbs almost all the excess energy stored by the Earth system that results from the anthropogenic greenhouse gas emission in the form of heat (∼ 91 %; von Schuckmann et al., 2023; Foster et al., 2021). As the ocean acts as a huge heat reservoir, the global ocean heat content (GOHC) is therefore a key component in the Earth's energy budget. An accurate knowledge of the GOHC change allows us to assess the Earth energy imbalance (EEI), which refers to the difference between the amount of energy the Earth receives from the Sun and the amount of energy it radiates and reflects back into space. A community effort (Meyssignac et al., 2019) depicted the various methodologies to estimate EEI from the GOHC, including the use of the ocean in situ temperature and salinity profiles (von Schuckmann et al., 2023), the measurement of the ocean thermal expansion from space geodesy (Marti et al., 2022; Hakuba et al., 2021), ocean reanalysis (Stammer et al., 2016), and surface net flux measurements (Kato et al., 2018; L'Ecuyer et al., 2015). Among these approaches, the space geodetic approach, detailed in Marti et al. (2022), leverages the maturity of satellite altimetry and gravimetry measurements to enable precise, extensive spatiotemporal coverage and full-depth estimates of ocean thermal expansion. As the EEI magnitude is small (0.5–1.0 $\mathrm{W\,m^{-2}}$; von Schuckmann et al., 2023) compared to the amount of energy entering and leaving the climate system (∼ 340 $\mathrm{W\,m^{-2}}$; L'Ecuyer et al., 2015), a high level of precision and accuracy are required to estimate the EEI mean (<0.3 $\mathrm{W\,m^{-2}}$) and its time variations at the decadal scale (<0.1 $\mathrm{W\,m^{-2}}$; Meyssignac et al., 2019). In this regard, the space geodetic approach emerges as a promising candidate capable of meeting the stringent EEI precision and accuracy requirements (Meyssignac et al., 2019; Marti et al., 2022).

In this study, our primary objective is to present the updated space geodetic GOHC and EEI estimates and the improvement since Marti et al. (2022), including several major evolutions in the input data, algorithms, and a temporal extension into the past since 1993. The secondary objective is to compare this updated space geodetic monthly GOHC product with GOHC time series derived from in situ observations. To ensure a consistent and homogeneous treatment, we apply the same processing method to estimate the EEI from the different yearly GOHC time series considered. The obtained EEI estimates are then compared to the net flux at the top of atmosphere (TOA) derived from the Clouds and

Published by Copernicus Publications.

Table 1. Data used to calculate the space geodetic ocean heat content change and Earth energy imbalance and to perform comparisons.

Product ref no.	Product ID and type	Data access	Reference
1	Sea level gridded data from satellite observations for the global ocean from 1993 to present	EU Copernicus Climate Change Service (2018)	Publication: Legeais et al. (2021)
2	LEGOS gravimetric (GRACE, GRACE-FO) ensemble of manometric sea level solutions	LEGOS FTP site: http://ftp.legos.obs-mip.fr/pub/soa/gravimetrie/grace_legos/V1.6/*	Update of Blazquez et al. (2018)
3	Estimating the Circulation and the Climate of the Ocean – Central Production Version 4 Release 4 (ECCOv4r4)	NASA ECCO group website	Dataset: ECCO Consortium et al. (2023). Publication: Forget et al. (2015); ECCO Consortium et al. (2021)
4	Mass contributions to global mean sea level – dataset of the European Space Agency Sea Level Budget Closure Climate Change Initiative (SLBC_cci)	CEDA archive	Dataset: Horwath et al. (2021). Publication: Horwath et al. (2022)
5	LEGOS–Magellium GOHC change/EEI dataset, v5.0	Centre National d’Etudes Spatiales (CNES) AVISO website	Dataset: Magellium/LEGOS (2020) Documentation: algorithm theoretical basis document and product user manual
6	Scripps Institution of Oceanography (SIO) – Roemmich–Gilson Argo Climatology	University of California San Diego SIO Argo website: https://sio-argo.ucsd.edu/RG_Climatology.html*	Publication: Roemmich and Gilson (2009)
7	JAMSTEC Argo product – Grid Point Value of the Monthly Objective Analysis using the Argo data (MOAA GPV), version 2021	Japan Agency for Marine-Earth Science and Technology website: https://www.jamstec.go.jp/argo_research/dataset/moaagpv/moaa_en.html*	Publication: Hosoda et al. (2010)
8	ISAS20 temperature and salinity gridded fields	SEANOE – Sea Scientific Open Data Publication	Dataset: Kolodziejczyk et al. (2021) Publication: Gaillard et al. (2016)
9	Met Office Hadley Centre observations datasets: EN4.2.2 (c14)	Met Office website: https://www.metoffice.gov.uk/hadobs/en4/download-en4-2-2.html*	Publications: Good et al. (2013); Cheng et al. (2014); Gouretski and Cheng (2020)
10	NOAA (National Oceanic and Atmospheric Administration) – NCEI (National Centers for Environmental Information) product	NCEI–NOAA website: https://www.ncei.noaa.gov/access/global-ocean-heat-content/*	Publication: Levitus et al. (2012); Garcia et al. (2019)
11	GLOBAL_OMI_OHC_area_averaged_anomalies_0_2000; numerical models, in situ observations, satellite observations	E.U. Copernicus Marine Service (2023)	Quality information document (QUID): von Schuckmann et al. (2021) Product user manual (PUM): Monier et al. (2021)
12	GCOS EHI experiment 1960–2020	World Data Center for Climate at German Climate Computing Centre (DKRZ) https://www.wdc-climate.de/ui/entry?acronym=GCOS_EHI_1960-2020*	Dataset: von Schuckmann et al. (2022) Publication: von Schuckmann et al. (2023)
13	Jet Propulsion Laboratory (JPL) GOHC change dataset from space data	https://zenodo.org/records/5104970*	Dataset: thomasfrederikse (2021) Publication: Hakuba et al. (2021)
14	Clouds and the Earth’s Radiant Energy System (CERES) Energy Balanced and Filled (EBAF) TOA and surface monthly means data in netCDF edition 4.2	NASA Atmospheric Science Data Center	Dataset: Doelling (2023) Publications: Loeb et al. (2018); Kato et al. (2018)
15	Met Office Hadley Centre observations datasets: EN4.2.2 (l09)	Met Office website: https://www.metoffice.gov.uk/hadobs/en4/download-en4-2-2.html*	Publications: Good et al. (2013); Levitus et al. (2009)

* Last access: 14 July 2023.

the Earth's Radiant Energy System (CERES) mission which serves as a reference for EEI time variations.

2 Data and method

The space geodetic approach consists of deriving the ocean heat content change from the steric sea level change (i.e. the ocean expansion) inferred by satellite observations. We present here an update of the technique for estimating the GOHC change and the EEI which relies on existing work (Marti et al., 2022) and also benefits from the progress made at regional scales.

The GOHC change is obtained as the sum of regional ocean heat content (OHC) estimated on a 1° × 1° grid. However, the uncertainties, their characterisation, and their propagation from the input data until the GOHC change and EEI are made at global scale in a similar manner to Marti et al. (2022).

Space geodetic observations are consistent with those used in Marti et al. (2022). The total sea level change is derived from altimetry sea level gridded products data from the Copernicus Change Climate Change service (C3S) [1] (note that all values in square brackets refer to datasets in Table 1). A correction for TOPEX-A drift is applied (Ablain et al., 2017), as well as a correction for the Jason-3 radiometer drift (Barnoud et al., 2023). The manometric sea level change is estimated from an update of the Blazquez et al. (2018) gravimetric solution ensemble (V1.6) [2]. We identified a subsample of this ensemble which relies on a single geocenter correction based on Sun et al. (2016) and whose mean is used as our best estimate of the manometric sea level change.

The space geodetic approach builds on the sea level budget to estimate the steric sea level (SSL) change. As we eventually focus on the GOHC change, we neglect the effect of the halosteric sea level change because the impact of salinity changes on SSL is very small at a global scale (see the appendix in Lowe and Gregory, 2006). The OHC change is obtained from the ratio of the SSL change and the integrated expansion efficiency of heat (IEEH) coefficient. Knowledge of the warming pattern is a prerequisite to estimate the IEEH. This knowledge relies on in situ observations. In previous versions, the IEEH was computed from in situ temperature/salinity profiles (mainly Argo floats). Here the IEEH is computed at a regional scale (1° × 1°) from temperature/salinity data from the ECCO ocean reanalysis [3]. Using ECCO to estimate the IEEH has an advantage as it allows for the expansion of the spatial area used to compute it. It enables the inclusion of coastal regions up to 100 km from the coastline and deep-ocean areas down to 6000 m. We have made the approximation that the IEEH is constant over time and equals its mean value over 2005–2015. This is justified at the global scale because the heat pattern of the ocean does not change significantly on decadal timescales (Kuhlbrodt and Gregory, 2012).

In-situ-derived global IEEH ranges from $1.36 \times 10^{-1}\,\mathrm{m\,YJ^{-1}}$ for a depth down to 2000 m to $1.57 \times 10^{-1}\,\mathrm{m\,YJ^{-1}}$ for a depth down to 6000 m. Using the ECCO ocean reanalysis [3] instead of in situ data yields very similar global IEEH values (see Table 2). Over a larger area, the ECCO reanalysis indicates an IEEH of $1.50 \times 10^{-1}\,\mathrm{m\,YJ^{-1}}$. The global IEEH uncertainty of $1 \times 10^{-3}\,\mathrm{m\,YJ^{-1}}$ ([5 %, 95 %] confidence interval level) is from Marti et al. (2022). It does not account for the IEEH variability due to the spatial domain.

In this study, we propose a temporal extension of the space geodetic estimate of GOHC and EEI into the past from January 1993 – the start of precise satellite altimetry. As space gravimetry observations are not available before 2002 (the GRACE mission was launched in March 2002), the manometric sea level component is extended into the past with the sum of its individual contributions from Greenland, Antarctica, glaciers, and from terrestrial water storage. These are derived from the ESA climate change initiative assessment of the sea level budget since 1993 [4].

After calculating the GOHC, the EEI is then obtained from the time derivative of the GOHC – by applying a central finite difference scheme – and accounting for the heat fraction that is entering the ocean (91 %), with the remaining 9 % of the energy being captured by the atmosphere, land, and cryosphere (IPCC, 2021). As described in Marti et al. (2022), the OHC change needs to be filtered out beforehand by applying a Lanczos low-pass filter at 3 years to remove signals related to ocean–atmosphere exchanges which do not correspond to any response to the top of the atmosphere radiation imbalance (Palmer and McNeall, 2014) and must therefore be removed to infer EEI variations. The following equation summarises how the EEI is derived from GOHC:

$$\mathrm{EEI}(t) = \frac{\mathrm{dGOHC}_{\mathrm{filtered,adjusted}}(t)}{\mathrm{d}t} \times \frac{1}{\alpha} \text{ with } \alpha = 0.91. \quad (1)$$

In order to assess the GOHC and EEI estimates, the estimation of their uncertainties is a key point. The method (described in Marti et al., 2022) consists of calculating the error variance–covariance matrices of the global mean sea level (GMSL) change data record and of the barystatic sea level data record and then propagating these error variance–covariance matrices to the GOHC and the EEI estimates. The characterisation of uncertainties is similar to that used by Marti et al. (2022). For the GMSL uncertainties, we use an updated altimetry uncertainty budget provided by Guérou et al. (2023), mainly extended over the Jason-3 period (until 2021). For the barystatic sea level uncertainties, we calculate the dispersion of the gravimetry ensemble [2]. This uncertainty is not centred on the barystatic best estimate (see Fig. 1). Besides, an uncertainty in the heat fraction entering the ocean is introduced ([89 %, 93 %]) as defined from the different estimates in the literature (e.g. Church et al., 2011; Levitus et al., 2012; IPCC, 2021; von Schuckmann et al., 2023). The uncertainty associated with the IEEH once

Table 2. Impact of the depth and the geographical extent considered for the global-integrated expansion efficiency of heat (IEEH) coefficient derived from ECCO reanalysis and in situ data (ISAS20 [8] over 0–2000 m and EN4.2.2.l09 [15] for the 2000–6000 m layer). The term "GCOS" in this context refers to the domain on which the Global Climate Observing System ensemble [12] described in von Schuckmann et al. (2023) is estimated. The table presents IEEH values estimated over a comparable extent, with the notable difference being the exclusion of the Mediterranean.

Geographical area and depth	Value of the IEEH coefficient at global scale over the 2005–2015 period (unit: m YJ^{-1})	
	In situ	ECCO
Spatial extent comparable to GCOS, 2000 m	0.136	0.135
Spatial extent comparable to GCOS, 6000 m	0.157	0.156
Spatial extension near coasts – LEGOS–Magellium dataset V5.0, 6000 m	Not available	0.150

propagated is negligible compared with other sources of uncertainty in the mean EEI (<0.1 %). From the covariance matrices, we are able to obtain the uncertainty associated with the means, trends, or accelerations in GOHC at any timescale based on an ordinary least squares regression.

The space geodetic GOHC and EEI estimates [5] are then compared to other estimates mostly based on in situ data. First, we introduce GOHC estimates based on gridded fields of temperature and salinity derived from in situ measurements provided by five centres: SIO (Scripps Institution of Oceanography) [6], the Japan Agency for Marine-Earth Science and Technology (JAMSTEC) version 2021 [7], and ISAS20 (In Situ Analysis System 20) – IFREMER (French National Institute for Ocean Science and Technology) [8], with all three relying on Argo network data; EN4, using two sets of corrections (Cheng et al., 2014; Gouretski and Cheng, 2020) [9], and NOAA (National Oceanic and Atmospheric Administration) [10]. We analyse two ocean monitoring indicators (OMIs) delivered by Copernicus Marine Environment Monitoring Service (CMEMS) [11], hereafter "CORA" and "CORA-2011". They are also based on in situ observations from the Coriolis Ocean database for ReAnalysis. CORA-2011 refers to the GOHC dataset processed by von Schuckmann and Le Traon (2011). It is delivered together with an uncertainty envelope. In addition, we compare the space geodetic estimate of the GOHC to the recent Global Climate Observing System (GCOS) ensemble estimate [12] composed of 16 time series based on subsurface temperature measurements and representative of the full water column. For the GCOS GOHC ensemble trend, we use the uncertainty indicated in von Schuckmann et al. (2023) for the period 2006–2020. Last, we introduce an alternative full-depth GOHC estimate derived from the space geodetic approach (Hakuba et al., 2021) [13] (hereafter "JPL" for the Jet Propulsion Laboratory), whose uncertainty is obtained from an ensemble approach.

Apart from GCOS ensemble and the space geodetic estimates, the different GOHC change estimates are extended with a deep-ocean warming estimate of $+0.068\,\mathrm{W\,m^{-2}}$ from Purkey and Johnson (2010) to encompass the entire water column and account for the deep ocean's substantial thermal influence below 2000 m. In this way, all different GOHC estimates cover the whole water column down to the bottom and are thus comparable with each other.

Both the GCOS ensemble and OMIs are made up of yearly time series, while other estimates are available on a monthly basis, which restricts comparisons to interannual timescales. Comparisons are thus led on the basis of annual time series both for the GOHC trend and EEI variability study. The GOHC change estimates are turned into EEI using the same method described above, with the only difference being that annual time series are linearly interpolated on a monthly timescale beforehand.

The CERES Energy Balanced and Filled (EBAF) product [14] is used as a reference for the EEI variability assessment because it is totally independent, and it is known to reproduce precisely the EEI variations with uncertainties of the order of a few tenths of $\mathrm{W\,m^{-2}}$. Its mean value is anchored with an in situ product (Lyman and Johnson, 2014).

Datasets used for this study are described in Table 1 both for the calculation of GOHC and EEI estimates and for their intercomparison. All uncertainties are reported in the text with a 5 %–95 % confidence level interval.

3 Results

The monthly space geodetic GOHC change from LEGOS–Magellium over January 1993–May 2022 highlights the accumulation of heat in the ocean (86 % of the total ocean

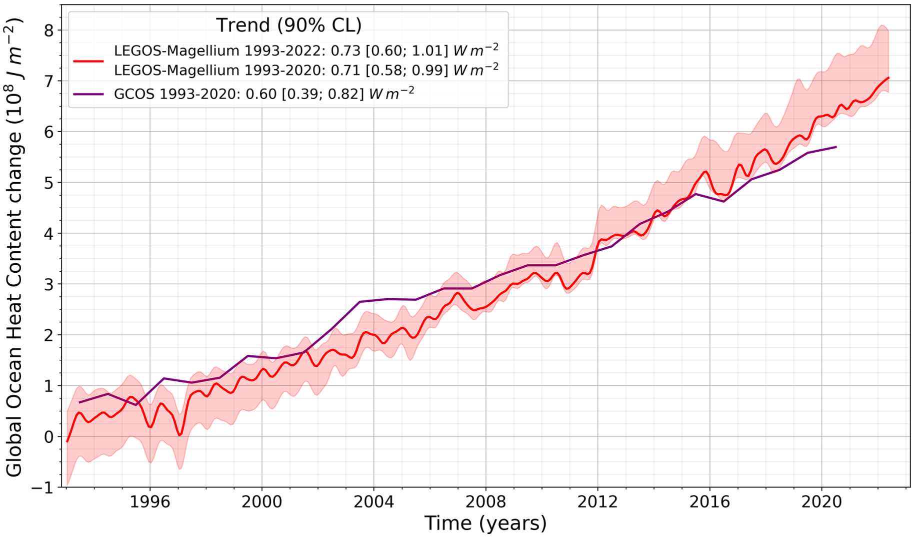

Figure 1. Global ocean heat content change over 1993–2022 depicted by the LEGOS–Magellium space geodetic dataset (red curve) and the GCOS dataset available until 2020 (purple curve). The LEGOS–Magellium dataset is characterised by its standard uncertainty envelope (68 % confidence level). The ocean surface considered for the LEGOS–Magellium dataset is comparable to that of the GCOS ensemble (von Schuckmann et al., 2023). Trends are estimated at 5 %–95 % confidence interval level and refer to the top-of-atmosphere surface.

surface, excluding the Mediterranean sea). The trend of $+0.75\,\mathrm{W\,m^{-2}}$ provides an estimate of the global ocean heat uptake (GOHU), and the uncertainty range for this accumulation rate is $[0.61;\ 1.04]\,\mathrm{W\,m^{-2}}$, meaning that the GOHU is significantly positive over 1993–2022.

A comparison is made with the annual GOHC change time series from GCOS (Fig. 1). The heat content is an extensive variable, and the GOHC is therefore highly sensitive to spatial coverage. To ensure more consistency in comparison with GCOS, we constrained the LEGOS–Magellium dataset to an ocean surface comparable to GCOS (up to 60° latitude and for areas more than 300 m deep). The impact was found to be low with a trend of $0.73\,\mathrm{W\,m^{-2}}$ over 1993–2022. Despite a higher value for the LEGOS–Magellium dataset, the trend results for 1993–2020 are in agreement within their confidence intervals with the GCOS trend of $0.60\ [0.39;\ 0.82]\,\mathrm{W\,m^{-2}}$ and the LEGOS–Magellium trend of $0.71\ [0.58,\ 0.99]\,\mathrm{W\,m^{-2}}$.

When the GOHC trends are calculated over a shorter period (2005–2019) on their respective available ocean surface (Fig. 2), the conclusions are similar to those in Fig. 1. GOHC trend results from other estimates are also shown. Note that the GCOS ensemble encompasses CORA and CORA-2011 datasets, as well as solutions based on the same in situ temperature and salinity grids that are used and mentioned in Sect. 2. In general, GOHC estimates exclusively based on in situ measurements are in agreement within their uncertainty ranges. These estimates are constructed using the same atlas of temperature and salinity profiles. Specifically, the data used to calculate the five GOHC from gridded fields covers the same ocean surface. Despite this, their trends show some discrepancies that are due to the data processing, such as the selection of valid profiles and the gridding algorithm. The comparisons confirm that the LEGOS–Magellium dataset shows a stronger trend in GOHC than datasets relying on in situ measurements but still agrees within the 90 % confidence level. The JPL space geodetic estimate supports these results and increases our confidence in our method.

Temporal variations in the EEI derived from the monthly LEGOS–Magellium space geodetic dataset agree well with the direct EEI measurements provided by CERES but less so with the EEI derived from the GCOS yearly ensemble (Fig. 3). Correlated signals are observed, particularly after 2006. These interannual variations are related to the main coupled ocean–atmosphere climate modes such as El Niño–Southern Oscillation or the Pacific Decadal Oscillation (Loeb et al., 2018; Meyssignac et al., 2023) or the atmospheric aerosol content resulting from volcanic eruptions and anthropogenic emissions. The three EEI solutions show a trend over their respective periods: $0.29\ [0.04;\ 0.56]\,\mathrm{W\,m^{-2}}$ per decade for LEGOS–Magellium over 1993–2022, $0.17\,\mathrm{W\,m^{-2}}$ per decade $[-0.25;\ 0.60]$ for GCOS over 1993–2020, and $0.44\ [0.34;\ 0.55]\,\mathrm{W\,m^{-2}}$ per decade for CERES over 2000–2022. Over the common period of 2000–2020, the LEGOS–Magellium dataset shows a positive trend of $0.37\,\mathrm{W\,m^{-2}}$ per decade, which is in agreement with CERES EEI trend of $0.44\,\mathrm{W\,m^{-2}}$ per decade, and both trends are significant at the 90 % confidence level. Given the confidence intervals and good agreement between these independent datasets, these results have provided confidence in the observed trend in EEI since 2000, indicating a very likely acceleration in global ocean warming over 2000–2020.

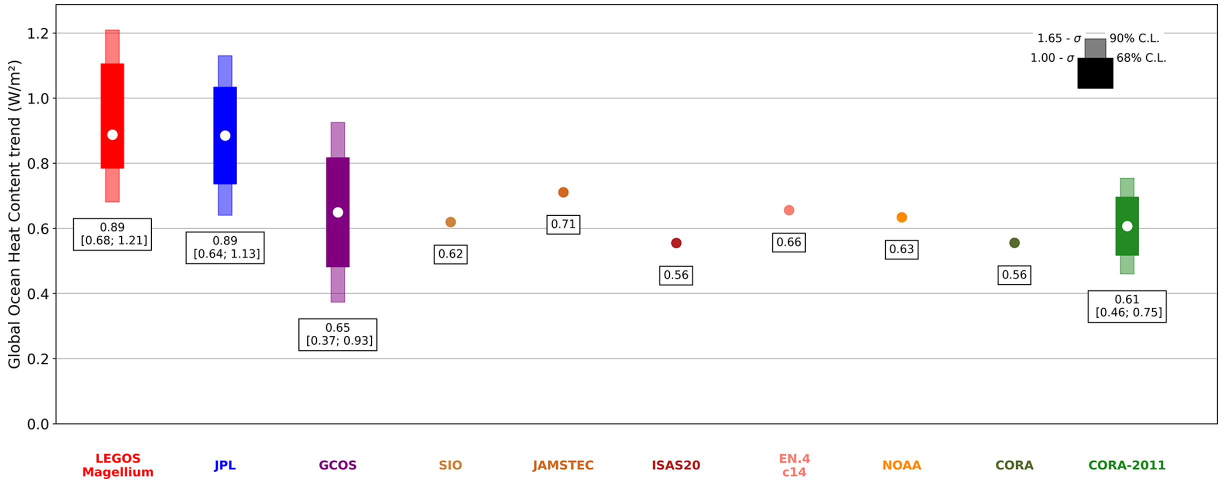

Figure 2. Global ocean heat content (GOHC) trends over the period 2005–2019 from the LEGOS–Magellium (red) and JPL (blue) space geodetic datasets, the GCOS ensemble (purple), in-situ-based GOHC change time series (brown tones), and the two CMEMS indicators (green tones). Trends are computed from annual time series and refer to the top-of-atmosphere surface, and the indicated trend intervals correspond to the [5 %–95 %] confidence interval level.

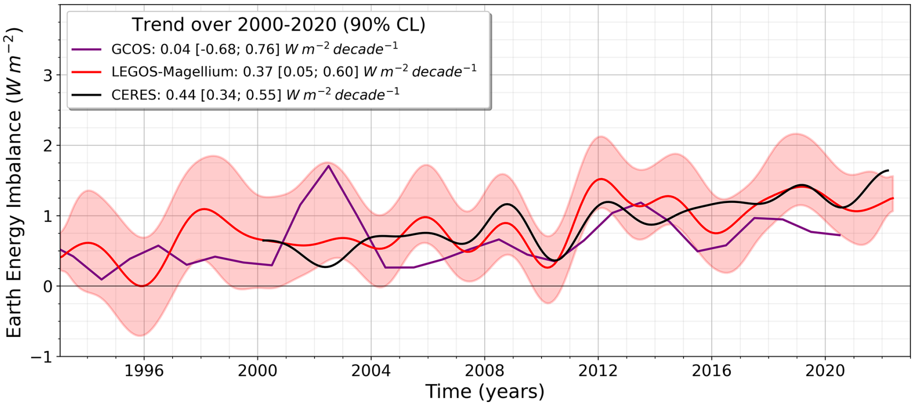

Figure 3. Earth energy imbalance (EEI) time series derived from the LEGOS–Magellium space geodetic approach (red curve), GCOS dataset (purple curve), and from satellite CERES measurements (black curve) over 1993–2022. A 3-year filter is applied to the space geodetic GOHC before derivation into EEI. The CERES time series is also filtered at 3 years for comparison. The standard uncertainty envelope (68 % confidence level) is shown for the space geodetic dataset in light red. EEI trends are given for each dataset on their common availability period 2000–2020 and refer to the top-of-atmosphere surface. Uncertainties are estimated with a [5 %–95 %] confidence interval level.

The Taylor diagram in Fig. 4 indicates the similarity in terms of temporal variability between all OHC-based EEI and the CERES reference. The dataset's proximity to the blue star determines the degree of agreement and how well it matches CERES estimate of the EEI variability. The GCOS and LEGOS–Magellium products exhibit similar time variations with a correlation of approximately 0.7, which is comparable to the results of Loeb et al. (2021). The JPL EEI has the highest correlation with CERES data (0.9) but too much variability. In-situ-based products have a correlation range of 0.25 to 0.8, indicating different levels of agreement with CERES.

4 Discussion and conclusions

This study proposes an extended estimate of the GOHC change and the EEI from 1993 onwards using the space geodetic approach. We compare this estimate with various estimates based on in situ measurements, as well as with the CERES EBAF estimate of the EEI.

Apart from the global measurement by CERES, the studied methods do not yet cover the entire ocean. However, the major advantage of the space geodetic approach is the large and homogeneous sampling of the ocean surface that has taken place since August 2002 and the integration of the whole water column. The space geodetic GOHC shows a significant trend of +0.75 [0.61; 1.04] W m^{-2} and an EEI trend

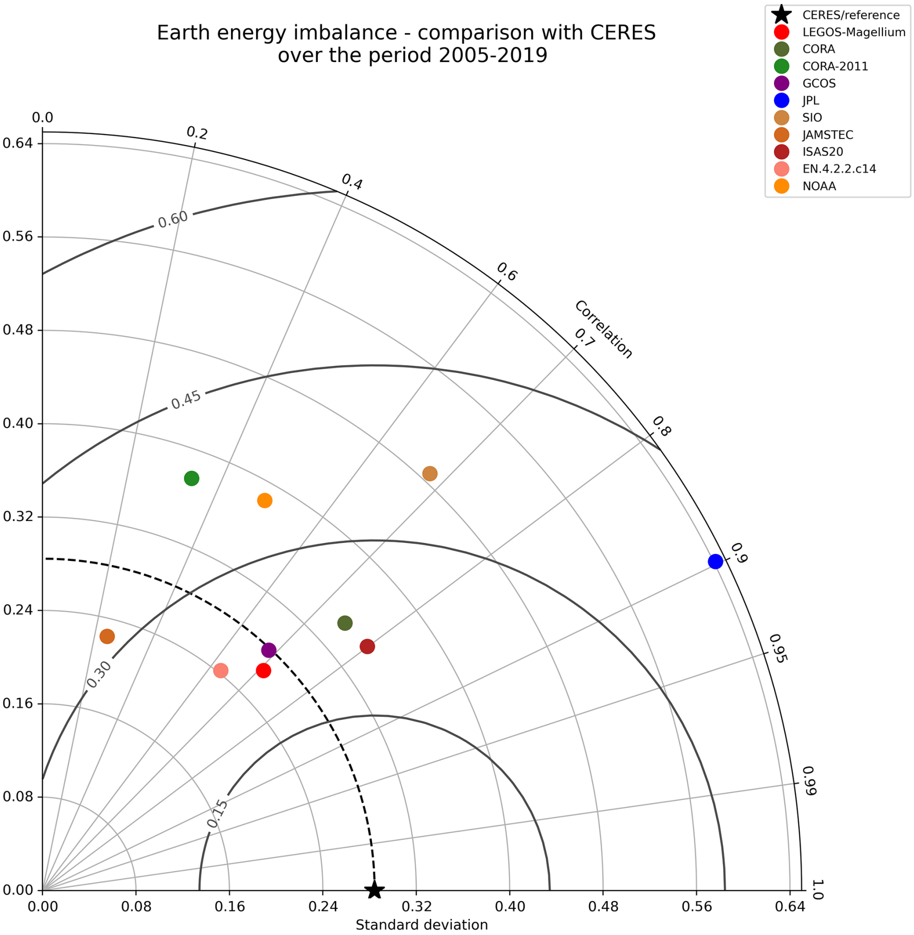

Figure 4. Comparison of Earth energy imbalance (EEI) interannual variations with respect to the CERES dataset (black star) for the 2005–2019 period. Taylor diagram gathering the correlation Pearson coefficient, with the centred root mean square ($\mathrm{W\,m^{-2}}$) and the standard deviation ($\mathrm{W\,m^{-2}}$) for the LEGOS–Magellium (red), JPL (blue), GCOS (purple), in-situ-based EEI (brown tones), and CMEMS indicators (green tones). Results refer to the top-of-atmosphere surface.

of 0.29 [0.04; 0.56] $\mathrm{W\,m^{-2}}$ per decade over the period 1993–2022.

Considering the current knowledge of the uncertainties associated with satellite gravimetry and altimetry data, the comparison of our results with other datasets allows us to cross-check the consistency of the different estimates of the ocean warming rate within a [5 %-95 %] confidence level interval. However, the higher GOHC trends observed with the space geodetic approach (LEGOS–Magellium and JPL datasets) compared to all in situ datasets could reveal limitations in the observing systems, such as the unobserved deep ocean with in situ data or systematic errors in space geodetic data, which need to be further investigated.

In addition, the comparison of our space geodetic EEI estimate with the direct EEI estimates provided by the CERES EBAF dataset provides complementary assessment information on the variability in EEI. On the one hand, we find a good temporal correlation of the EEI derived from space geodetic and CERES EBAF estimates. On the other hand, a significant EEI trend has been detected in both CERES and the space geodetic approach, suggesting a very likely acceleration in the global ocean warming over the last 20 years.

Data availability. The space geodetic GOHC change and EEI dataset (v5.0) is available online at https://doi.org/10.24400/527896/A01-2020.003 (Magellium/LEGOS, 2020), together with the complete associated documentation (product user manual and algorithm theoretical basis document).

Author contributions. FM and MA led and designed the paper, which was edited by BM, VR, and RF. VR, RF, and FM developed the processing tools and performed the computations with support from SF. AB focused on the part related to gravimetric observations. BM and MA managed and designed the study. All authors discussed the results and commented on the paper.

Competing interests. The contact author has declared that none of the authors has any competing interests.

Acknowledgements. We would like to thank Audrey Minière, Karina von Schuckmann, and Lorena Moreira Mendez for their contributions to the preparation of this paper, as well as Françoise Mertz for making the data available on the ODATIS portal and AVISO. We also thank two anonymous reviewers for their constructive comments on earlier drafts of this work.

Financial support. This work has been supported by CNES, both for its development and dissemination. The comparison with other datasets has been funded by CNRS. The ESA initially supported this work in the framework of the MOHeaCAN project (Monitoring Ocean Heat Content and Earth Energy ImbalANce from Space): https://eo4society.esa.int/projects/moheacan/ (last access: 20 December 2023).

Review statement. This paper was edited by Johannes Karstensen and reviewed by two anonymous referees.

References

Ablain, M., Jugier, R., Zawadki, L., Taburet, N., Cazenave, A., and Meyssignac, B.: The TOPEX-A Drift and Impacts on GMSL Time Series, AVISO Website, Poster, https://meetings.aviso.altimetry.fr/fileadmin/user_upload/tx_ausyclsseminar/files/Poster_OSTST17_GMSL_Drift_TOPEX-A.pdf (last access: 14 July 2023), 2017.

Barnoud, A., Picard, B., Meyssignac, B., Marti, F., Ablain, M., and Roca, R.: Reducing the Uncertainty in the Satellite Altimetry Estimates of Global Mean Sea Level Trends Using Highly Stable Water Vapor Climate Data Records, J. Geophys. Res.-Oceans, 128, e2022JC019378, https://doi.org/10.1029/2022JC019378, 2023.

Blazquez, A., Meyssignac, B., Lemoine, J., Berthier, E., Ribes, A., and Cazenave, A.: Exploring the uncertainty in GRACE estimates of the mass redistributions at the Earth surface: implications for the global water and sea level budgets, Geophys. J. Int., 215, 415–430, https://doi.org/10.1093/gji/ggy293, 2018.

Cheng, L., Zhu, J., Cowley, R., Boyer, T., and Wijffels, S.: Time, probe type, and temperature variable bias corrections to historical expendable bathythermograph observations, J. Atmos. Ocean. Tech., 31, 1793–1825, 2014.

Church, J. A., White, N. J., Konikow, L. F., Domingues, C. M., Cogley, J. G., Rignot, E., Gregory, J. M., Broeke, M. R. van den, Monaghan, A. J., and Velicogna, I.: Revisiting the Earth's sea-level and energy budgets from 1961 to 2008, Geophys. Res. Lett., 38, L18601, https://doi.org/10.1029/2011GL048794, 2011.

Doelling, D. R.: CERES Energy Balanced and Filled (EBAF) TOA and Surface Monthly means data in netCDF Edition 4.2, NASA [data set], https://doi.org/10.5067/TERRA-AQUA-NOAA20/CERES/EBAF_L3B004.2, 2023.

ECCO Consortium, Fukumori, I., Wang, O., Fenty, I., Forget, G., Heimbach, P., and Ponte, R. M.: Synopsis of the 50 ECCO Central Production Global Ocean and Sea-Ice State Estimate, Version 4 Release 4, Zenodo [data set], https://doi.org/10.5281/zenodo.4533349, 2021.

ECCO Consortium, Fukumori, I., Wang, O., Fenty, I., Forget, G., Heimbach, P., and Ponte, R. M.: ECCO Central Estimate (Version 4 Release 4), NASA [data set], https://www.ecco-group.org/products-ECCO-V4r4.htm, last access: 14 July 2023.

EU Copernicus Climate Change Service: Sea level gridded data from satellite observations for the global ocean from 1993 to present, Climate Data Store (CDS), https://doi.org/10.24381/cds.4c328c78, 2018.

E.U. Copernicus Marine Service Information (CMEMS): Global Ocean Heat Content (0–2000 m) time series and trend from Reanalysis & Multi-Observations Reprocessing, Marine Data Store (MDS) [data set], https://doi.org/10.48670/moi-00235, last accesss: 14 July 2023.

Forget, G., Campin, J.-M., Heimbach, P., Hill, C. N., Ponte, R. M., and Wunsch, C.: ECCO version 4: an integrated framework for non-linear inverse modeling and global ocean state estimation, Geosci. Model Dev., 8, 3071–3104, https://doi.org/10.5194/gmd-8-3071-2015, 2015.

Foster, J., Smallcombe, J. W., Hodder, S., Jay, O., Flouris, A. D., Nybo, L., and Havenith, G.: An advanced empirical model for quantifying the impact of heat and climate change on human physical work capacity, Int. J. Biometeorol., 65, 1215–1229, https://doi.org/10.1007/s00484-021-02105-0, 2021.

Gaillard, F., Reynaud, T., Thierry, V., Kolodziejczyk, N., and Schuckmann, K. von: In Situ–Based Reanalysis of the Global Ocean Temperature and Salinity with ISAS: Variability of the Heat Content and Steric Height, J. Climate, 29, 1305–1323, https://doi.org/10.1175/JCLI-D-15-0028.1, 2016.

Garcia, H. E., Boyer, T. P., Baranova, O. K., Locarnini, R. A., Mishonov, A. V., and Grodsky, A.: World ocean atlas 2018: Product documentation, https://www.ncei.noaa.gov/data/oceans/woa/WOA18/DOC/woa18documentation.pdf (last access: 14 July 2023), 2019.

Good, S. A., Martin, M. J., and Rayner, N. A.: EN4: Quality controlled ocean temperature and salinity profiles and monthly objective analyses with uncertainty estimates, J. Geophys. Res.-Oceans, 118, 6704–6716, https://doi.org/10.1002/2013JC009067, 2013.

Gouretski, V. and Cheng, L.: Correction for systematic errors in the global dataset of temperature profiles from mechanical bathythermographs, J. Atmos. Ocean. Tech., 37, 841–855, 2020.

Guérou, A., Meyssignac, B., Prandi, P., Ablain, M., Ribes, A., and Bignalet-Cazalet, F.: Current observed global mean sea level rise and acceleration estimated from satellite altimetry and the associated measurement uncertainty, Ocean Sci., 19, 431–451, https://doi.org/10.5194/os-19-431-2023, 2023.

Hakuba, M. Z., Frederikse, T., and Landerer, F. W.: Earth's Energy Imbalance From the Ocean Perspective

(2005–2019), Geophys. Res. Lett., 48, e2021GL093624, https://doi.org/10.1029/2021GL093624, 2021.

Horwath, M., Gutknecht, B. D., Cazenave, A., Palanisamy, H. K., Marti, F., Marzeion, B., Paul, F., Le Bris, R., Hogg, A. E., Otosaka, I., Shepherd, A., Döll, P., Cáceres, D., Müller Schmied, H., Johannessen, J. A., Nilsen, J. E. Ø., Raj, R. P., Forsberg, R., Sandberg Sørensen, L., Barletta, V. R., Simonsen, S., Knudsen, P., Andersen, O. B., Ranndal, H., Rose, S. K., Merchant, C. J., Macintosh, C. R., Von Schuckmann, K., Novotny, K., Groh, A., Restano, M., and Benveniste, J.: ESA Sea Level Budget Closure Climate Change Initiative (SLBC_cci): Time series of global mean sea level budget and ocean mass budget elements (1993–2016, at monthly resolution), version 2.2, https://doi.org/10.5285/17C2CE31784048DE93996275EE976FFF, 2021.

Horwath, M., Gutknecht, B. D., Cazenave, A., Palanisamy, H. K., Marti, F., Marzeion, B., Paul, F., Le Bris, R., Hogg, A. E., Otosaka, I., Shepherd, A., Döll, P., Cáceres, D., Müller Schmied, H., Johannessen, J. A., Nilsen, J. E. Ø., Raj, R. P., Forsberg, R., Sandberg Sørensen, L., Barletta, V. R., Simonsen, S. B., Knudsen, P., Andersen, O. B., Ranndal, H., Rose, S. K., Merchant, C. J., Macintosh, C. R., von Schuckmann, K., Novotny, K., Groh, A., Restano, M., and Benveniste, J.: Global sea-level budget and ocean-mass budget, with a focus on advanced data products and uncertainty characterisation, Earth Syst. Sci. Data, 14, 411–447, https://doi.org/10.5194/essd-14-411-2022, 2022.

Hosoda, S., Ohira, T., Sato, K., and Suga, T.: Improved description of global mixed-layer depth using Argo profiling floats, J. Oceanogr., 66, 773–787, https://doi.org/10.1007/s10872-010-0063-3, 2010.

Intergovernmental Panel on Climate Change (IPCC) (Ed.): The Earth's Energy Budget, Climate Feedbacks and Climate Sensitivity, in: Climate Change 2021 – The Physical Science Basis: Working Group I Contribution to the Sixth Assessment Report of the Intergovernmental Panel on Climate Change, Cambridge University Press, Cambridge, 923–1054, https://doi.org/10.1017/9781009157896.009, 2021.

Kato, S., Rose, F. G., Rutan, D. A., Thorsen, T. J., Loeb, N. G., Doelling, D. R., Huang, X., Smith, W. L., Su, W., and Ham, S.-H.: Surface Irradiances of Edition 4.0 Clouds and the Earth's Radiant Energy System (CERES) Energy Balanced and Filled (EBAF) Data Product, J. Climate, 31, 4501–4527, https://doi.org/10.1175/JCLI-D-17-0523.1, 2018.

Kolodziejczyk, N., Prigent-Mazella, A., and Gaillard, F.: ISAS temperature and salinity gridded fields, SEANOE [data set], https://doi.org/10.17882/52367, 2021.

Kuhlbrodt, T. and Gregory, J. M.: Ocean heat uptake and its consequences for the magnitude of sea level rise and climate change, Geophys. Res. Lett., 39, L18608, https://doi.org/10.1029/2012GL052952, 2012.

L'Ecuyer, T. S., Beaudoing, H. K., Rodell, M., Olson, W., Lin, B., Kato, S., Clayson, C. A., Wood, E., Sheffield, J., Adler, R., Huffman, G., Bosilovich, M., Gu, G., Robertson, F., Houser, P. R., Chambers, D., Famiglietti, J. S., Fetzer, E., Liu, W. T., Gao, X., Schlosser, C. A., Clark, E., Lettenmaier, D. P., and Hilburn, K.: The Observed State of the Energy Budget in the Early Twenty-First Century, J. Climate, 28, 8319–8346, https://doi.org/10.1175/JCLI-D-14-00556.1, 2015.

Legeais, J.-F., Meyssignac, B., Faugère, Y., Guerou, A., Ablain, M., Pujol, M.-I., Dufau, C., and Dibarboure, G.: Copernicus Sea Level Space Observations: A Basis for Assessing Mitigation and Developing Adaptation Strategies to Sea Level Rise, Front. Mar. Sci., 8, 704721, https://doi.org/10.3389/fmars.2021.704721, 2021.

Levitus, S., Antonov, J. I., Boyer, T. P., Locarnini, R. A., Garcia, H. E., and Mishonov, A. V.: Global ocean heat content 1955–2008 in light of recently revealed instrumentation problems, Geophys. Res. Lett., 36, L07608, https://doi.org/10.1029/2008GL037155, 2009.

Levitus, S., Antonov, J. I., Boyer, T. P., Baranova, O. K., Garcia, H. E., Locarnini, R. A., Mishonov, A. V., Reagan, J. R., Seidov, D., Yarosh, E. S., and Zweng, M. M.: World ocean heat content and thermosteric sea level change (0–2000 m), 1955–2010, Geophys. Res. Lett., 39, L10603, https://doi.org/10.1029/2012GL051106, 2012.

Loeb, N. G., Doelling, D. R., Wang, H., Su, W., Nguyen, C., Corbett, J. G., Liang, L., Mitrescu, C., Rose, F. G., and Kato, S.: Clouds and the Earth's Radiant Energy System (CERES) Energy Balanced and Filled (EBAF) Top-of-Atmosphere (TOA) Edition-4.0 Data Product, J. Climate, 31, 895–918, https://doi.org/10.1175/JCLI-D-17-0208.1, 2018.

Loeb, N. G., Johnson, G. C., Thorsen, T. J., Lyman, J. M., Rose, F. G., and Kato, S.: Satellite and Ocean Data Reveal Marked Increase in Earth's Heating Rate, Geophys. Res. Lett., 48, e2021GL093047, https://doi.org/10.1029/2021GL093047, 2021.

Lowe, J. A. and Gregory, J. M.: Understanding projections of sea level rise in a Hadley Centre coupled climate model, J. Geophys. Res.-Oceans, 111, C11014, https://doi.org/10.1029/2005JC003421, 2006.

Lyman, J. M. and Johnson, G. C.: Estimating global ocean heat content changes in upper 1800 m since 1950 and the influence of climatology choice, J. Climate, 27, 1945–1957, https://doi.org/10.1175/JCLI-D-12-00752.1, 2014.

Magellium/LEGOS: Climate indicators from space: Ocean heat content and Earth energy imbalance (V5.0), https://doi.org/10.24400/527896/A01-2020.003, 2020.

Marti, F., Blazquez, A., Meyssignac, B., Ablain, M., Barnoud, A., Fraudeau, R., Jugier, R., Chenal, J., Larnicol, G., Pfeffer, J., Restano, M., and Benveniste, J.: Monitoring the ocean heat content change and the Earth energy imbalance from space altimetry and space gravimetry, Earth Syst. Sci. Data, 14, 229–249, https://doi.org/10.5194/essd-14-229-2022, 2022.

Meyssignac, B., Boyer, T., Zhao, Z., Hakuba, M. Z., Landerer, F. W., Stammer, D., Köhl, A., Kato, S., L'Ecuyer, T., Ablain, M., Abraham, J. P., Blazquez, A., Cazenave, A., Church, J. A., Cowley, R., Cheng, L., Domingues, C. M., Giglio, D., Gouretski, V., Ishii, M., Johnson, G. C., Killick, R. E., Legler, D., Llovel, W., Lyman, J., Palmer, M. D., Piotrowicz, S., Purkey, S. G., Roemmich, D., Roca, R., Savita, A., Schuckmann, K. von, Speich, S., Stephens, G., Wang, G., Wijffels, S. E., and Zilberman, N.: Measuring Global Ocean Heat Content to Estimate the Earth Energy Imbalance, Front. Mar. Sci., 6, 432, https://doi.org/10.3389/fmars.2019.00432, 2019.

Meyssignac, B., Chenal, J., Loeb, N., Guillaume-Castel, R., and Ribes, A.: Time-variations of the climate feedback parameter λ are associated with the Pacific Decadal Oscillation, Commun. Earth Environ., 4, 241, https://doi.org/10.1038/s43247-023-00887-2, 2023.

Monier, M., Derval, C., and Fernandez, E.: EU Copernicus Marine Service Product User Manual for the Global Ocean Heat Content (0-2000m) time series and trend from Reanalysis & Multi-Observations Reprocessing, GLOBAL_OMI_OHC_area_averaged_anomalies_0_2000, Issue 4.0, Mercator Ocean International, https://catalogue.marine.copernicus.eu/documents/PUM/CMEMS-OMI-PUM-GLO-OHC.pdf (last access: 14 July 2023), 2021.

Palmer, M. D. and McNeall, D. J.: Internal variability of Earth's energy budget simulated by CMIP5 climate models, Environ. Res. Lett., 9, 034016, https://doi.org/10.1088/1748-9326/9/3/034016, 2014.

Purkey, S. G. and Johnson, G. C.: Warming of Global Abyssal and Deep Southern Ocean Waters between the 1990s and 2000s: Contributions to Global Heat and Sea Level Rise Budgets, J. Climate, 23, 6336–6351, https://doi.org/10.1175/2010JCLI3682.1, 2010.

Roemmich, D. and Gilson, J.: The 2004–2008 mean and annual cycle of temperature, salinity, and steric height in the global ocean from the Argo Program, Prog. Oceanogr., 82, 81–100, https://doi.org/10.1016/j.pocean.2009.03.004, 2009.

Stammer, D., Balmaseda, M., Heimbach, P., Köhl, A., and Weaver, A.: Ocean Data Assimilation in Support of Climate Applications: Status and Perspectives, Annu. Rev. Mar. Sci., 8, 491–518, https://doi.org/10.1146/annurev-marine-122414-034113, 2016.

Sun, Y., Riva, R., and Ditmar, P.: Optimizing estimates of annual variations and trends in geocenter motion and J_2 from a combination of GRACE data and geophysical models, J. Geophys. Res. Sol. Ea., 121, 8352–8370, https://doi.org/10.1002/2016JB013073, 2016.

thomasfrederikse: thomasfrederikse/EEI_GRACE: V1.0b, Zenodo [data set], https://doi.org/10.5281/zenodo.5104970, 2021.

von Schuckmann, K. and Le Traon, P.-Y.: How well can we derive Global Ocean Indicators from Argo data?, Ocean Sci., 7, 783–791, https://doi.org/10.5194/os-7-783-2011, 2011.

von Schuckmann, K., Monier, M., and Drevillon, M.: EU Copernicus Marine Service Quality Information Document for the Global Ocean Heat Content (0-2000m) time series and trend from Reanalysis & Multi-Observations Reprocessing, GLOBAL_OMI_OHC_area_averaged_ anomalies_0_ 2000, Issue 1.0, Mercator Ocean International, https://catalogue.marine.copernicus.eu/documents/QUID/CMEMS-OMI-QUID-GLO-OHC.pdf (last access: 14 July 2023), 2021.

von Schuckmann, K., Minière, A., Gues, F., Cuesta-Valero, F. J., Kirchengast, G., Adusumilli, S., Straneo, F., Allan, R., Barker, P. M., Beltrami, H., Boyer, T., Cheng, L., Church, J., Desbruyeres, D., Dolman, H., Domingues, C., García-García, A., Giglio, D., Gilson, J., Gorfer, M., Haimberger, L., Hendricks, S., Hosoda, S., Johnson, G. C., Killick, R., King, B. A., Kolodziejczyk, N., Korosov, A., Krinner, G., Kuusela, M., Langer, M., Lavergne, T., Li, Y., Lyman, J., Marzeion, B., Mayer, M., MacDougall, A., Lawrence, I., McDougall, T., Monselesan, D. P., Nitzbon, J., Otosaka, I., Peng, J., Purkey, S., Roemmich, D., Sato, K., Sato, K., Savita, A., Schweiger, A., Shepherd, A., Seneviratne, S. I., Simons, L., Slater, D. A., Slater, T., Smith, N., Steiner, A. K., Suga, T., Szekely, T., Thiery, W., Timmermanns, M.-L., Vanderkelen, I., Wijffels, S. E., Wu, T., and Zemp, M.: Heat stored in the Earth system 1960–2020: Where does the energy go?, https://hdl.handle.net/21.14106/279f535efb48324f4f604bb390f74deadf268812 (last access: 14 July 2023), 2022.

von Schuckmann, K., Minière, A., Gues, F., Cuesta-Valero, F. J., Kirchengast, G., Adusumilli, S., Straneo, F., Ablain, M., Allan, R. P., Barker, P. M., Beltrami, H., Blazquez, A., Boyer, T., Cheng, L., Church, J., Desbruyeres, D., Dolman, H., Domingues, C. M., García-García, A., Giglio, D., Gilson, J. E., Gorfer, M., Haimberger, L., Hakuba, M. Z., Hendricks, S., Hosoda, S., Johnson, G. C., Killick, R., King, B., Kolodziejczyk, N., Korosov, A., Krinner, G., Kuusela, M., Landerer, F. W., Langer, M., Lavergne, T., Lawrence, I., Li, Y., Lyman, J., Marti, F., Marzeion, B., Mayer, M., MacDougall, A. H., McDougall, T., Monselesan, D. P., Nitzbon, J., Otosaka, I., Peng, J., Purkey, S., Roemmich, D., Sato, K., Sato, K., Savita, A., Schweiger, A., Shepherd, A., Seneviratne, S. I., Simons, L., Slater, D. A., Slater, T., Steiner, A. K., Suga, T., Szekely, T., Thiery, W., Timmermans, M.-L., Vanderkelen, I., Wjiffels, S. E., Wu, T., and Zemp, M.: Heat stored in the Earth system 1960–2020: where does the energy go?, Earth Syst. Sci. Data, 15, 1675–1709, https://doi.org/10.5194/essd-15-1675-2023, 2023.

State Planet, 4-osr8, 4, 2024
https://doi.org/10.5194/sp-4-osr8-4-2024

Changes in the Gulf Stream path over the last 3 decades

**Antonio Sánchez-Román[1], Flora Gues[2,4], Romain Bourdalle-Badie[2], Marie-Isabelle Pujol[3],
Ananda Pascual[1], and Marie Drévillon[2]**

[1]Department of Oceanography and Global Change, Mediterranean Institute for Advanced Studies,
IMEDEA (CSIC-UIB), C/Miquel Marqués, 21, 07190 Esporles, Spain
[2]Mercator Ocean International, 2 Av. de l'Aérodrome de Montaudran, 31400 Toulouse, France
[3]Collecte Localisation Satellites, Parc Technologique du Canal, 11 rue Hermès,
31520 Ramonville-Saint-Agne, France
[4]CELAD, 48 Rte de Lavaur, 31130 Balma, France

Correspondence: Antonio Sánchez-Román (asanchez@imedea.uib-csic.es)

Received: 13 July 2023 – Discussion started: 13 September 2023
Revised: 23 February 2024 – Accepted: 20 March 2024 – Published: 30 September 2024

Abstract. The Gulf Stream transports warm waters from low to high latitudes in the North Atlantic Ocean, impacting Europe's climate. This study investigates the changing pattern of the Gulf Stream over the last 3 decades as observed in the altimetric record (1993–2022) using monthly averaged altimetry maps together with the outputs from an ocean reanalysis product. The seasonal and yearly evolution of the coordinates (destabilization point) where the Gulf Stream starts to meander and convert from a stable to an unstable detached jet is investigated. At the seasonal scale, the location of this destabilization point presents zonal shifts displacing the Gulf Stream path to the north in summer and fall and to the south in winter and spring. In addition, it presents variations at interannual scale and has varied by more than 1400 km in longitude, showing meridional shifts of 300 km over the altimetric era: it exhibits a low-frequency remarkable shift westward and southward between 1995 and 2012. From that year, the destabilization point displacement inverses, exhibiting a previously unreported migration eastward and northward that translates into a larger fraction of the stable detached jet to the detriment of the unstable meandering jet. Changes in the Gulf Stream path impact both associated mesoscale eddy kinetic energy and waters transported towards the subpolar North Atlantic. The observed shifts of the path destabilization point seem to be linked to North Atlantic Oscillation variability during winter that may play an important role: it presents a negative trend associated with a shift from a positive to a negative phase between 1995 and 2011 and an opposite behavior from a negative to a positive phase from that year until 2020 in agreement with the associated southwestward and northeastward observed migration of the destabilization point.

1 Introduction

The Gulf Stream is part of the western boundary current system. It originates in the Gulf of Mexico and flows poleward close to the North American coast from the Straits of Florida to Cape Hatteras (Fig. 1). It then leaves the continental margin and becomes a detached western boundary current flowing eastward as the Gulf Stream Extension (e.g., Joyce et al., 2009; Greatbatch et al., 2010). The Gulf Stream Extension carries near-surface warm waters from the subtropical to the subpolar North Atlantic (Guo et al., 2023) marking a transition from warm subtropical to cold subpolar waters (Joyce and Zhang, 2010; McCarthy et al., 2018) known as the Gulf Stream North Wall (GSNW). The GSNW is a sharp temperature front located to the north of the Gulf Stream that does not necessarily follows its path (Chi et al., 2019). The balance between these northward-flowing warm and shallow waters as part of the Gulf Stream and a southward cold and deep return water path describes the Atlantic Meridional Overturn-

Published by Copernicus Publications.

Table 1. Data products used.

Product ref. no.	Product ID & type	Data access	Documentation
1	SEALEVEL_GLO_PHY_L4_MY_008_047; satellite observations	EU Copernicus Marine Service Product (2023a)	Quality information Document (QUID): Pujol et al. (2023) Product User Manual (PUM): Pujol (2023)
2	GLOBAL_MULTIYEAR_PHY_001_030; numerical models	EU Copernicus Marine Service Product (2023b)	QUID: Drévillon et al. (2023a) PUM: Drévillon et al. (2023b)

ing Circulation (AMOC; e.g., Buckley and Marshall, 2016; Lozier et al., 2019; Swingedouw et al., 2022). The AMOC accounts for nearly 90 % of the total heat transport at 26.5° N in the North Atlantic (Johns et al., 2011). Thus, it is a major driver of subpolar heat content changes (McCarthy et al., 2018). This makes the Gulf Stream play a paramount role in North Atlantic climate variability and change (Frankignoul et al., 2001; Joyce and Zhang, 2010; Srokosz et al., 2012; McCarthy et al., 2015; Lozier et al., 2019). Direct estimates of the GSNW are available from 1955 (Joyce et al., 2000) and 1966 (Taylor and Stephens, 1980) onwards, allowing the analysis of the North Atlantic ocean circulation variability from decadal and multidecadal scales (McCarthy et al., 2018).

The Atlantic multidecadal variability is mainly due to internal ocean-driven variability associated with global and regional variations in precipitation and temperature, sea level fluctuations, and hurricane activity (Delworth and Mann, 2000). However, it could be also generated as a response to natural atmospheric variability (Clement et al., 2015), which is mainly associated with the North Atlantic Oscillation (NAO). The NAO is the first mode of Atlantic atmospheric forcing and describes surface sea level pressure differences between the Azores high and the subpolar low and varies at quasi-decadal and multidecadal timescales (Da Costa and Colin de Verdiere, 2002; Gray et al., 2016; Årthun et al., 2017), impacting North Atlantic sea surface temperature patterns via air–sea heat exchanges (Hurrell et al., 2003; McCarthy et al., 2018; Osman et al., 2021).

The time-varying location of the Gulf Stream can be identified using a constant sea surface height (SSH) contour from mapped absolute dynamic topography (ADT) from satellite altimetry to find snapshots of the current's path (Andres, 2016). The 25 cm SSH contour is commonly used (e.g., Lillibridge and Mariano, 2013; Rossby et al., 2014; Andres, 2016; Chi et al., 2021; Guo et al., 2023). Other methods to identify the path of the Gulf Stream are based on the location of an isotherm at a given depth. Joyce et al. (2000, 2009) used the 15 °C isotherm at 200 m depth to define the region just to the north of strong flow of the Gulf Stream that corresponds

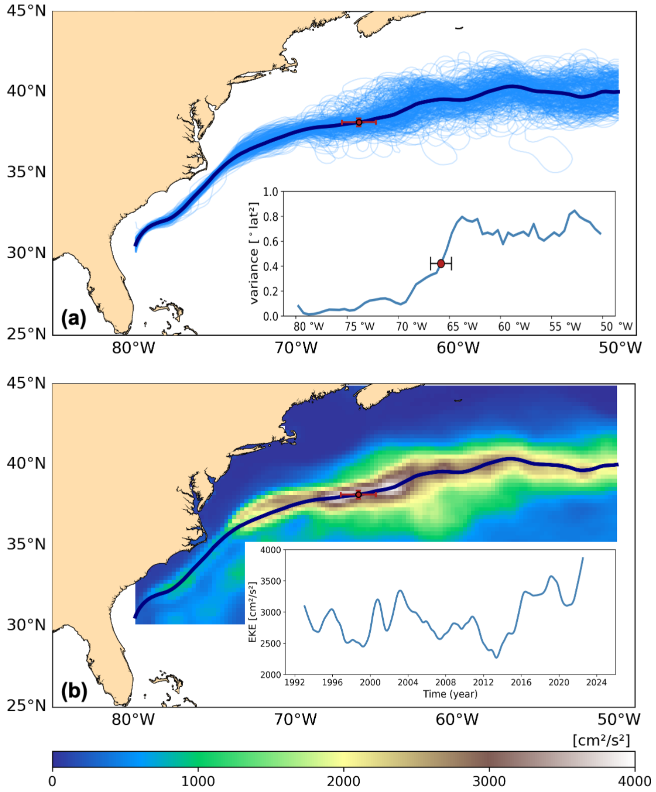

Figure 1. Panel **(a)** displays the Gulf Stream paths based on the 25 cm SSH contour from altimetry (product ref. no. 1) showing monthly mean (pale blue) and a 1993–2022 overall mean (blue). The inset displays the variance in latitudinal position of the monthly mean Gulf Stream paths (1993–2022) as a function of downstream longitude. Panel **(b)** displays the 1993–2022 overall mean EKE in the Gulf Stream region and the 1993–2022 overall Gulf Stream mean path (blue). The inset shows the aggregated EKE associated with the Gulf Stream. The red dot in panels **(a)** and **(b)** indicates the mean destabilization point (see text for more details). The confidence interval (at 95 % confidence level) of the destabilization point in both longitude and latitude is also displayed.

to the GSNW. This approach was followed by Frankignoul et al. (2001) and Seidov et al. (2019, 2021) to identify the latitude of Gulf Stream paths.

The variations in the Gulf Stream path exhibit two main modes: (i) wavelike fluctuations linked to the Gulf Stream meandering and instability and (ii) large-scale lateral shifts exhibiting seasonal and interannual changes (Frankignoul et al., 2001). In reality, western boundary currents are identified as eddy-rich regions where mean kinetic energy and available potential energy from the mean flow are converted into mesoscale eddy kinetic energy (EKE) from baroclinic and barotropic instabilities. The low-frequency interannual variability of the lateral shifts in the Gulf Stream position impacts the global climate system as a whole (Guo et al., 2023) and can be linked to changes in climate-related oceanic phenomena such as the El Niño–Southern Oscillation (Taylor et al., 1998), the AMOC (Joyce and Zhang, 2010), or the aforementioned atmospheric forcing (Wolfe et al., 2019). Taylor et al. (1998) found that the Gulf Stream shifts were correlated with the wintertime NAO during the time period spanning from 1966 to 1996, with high values of the NAO index (stronger westerlies) favoring a northerly path 2–3 years later. Joyce et al. (2000) observed northward shifts of the Gulf Stream during positive phases of the NAO with lags of 1 year between 1954 and 1990. More recently, McCarthy et al. (2018) reported shifts in the Gulf Stream path coincident with NAO variations over both quasi-decadal and multidecadal timescales, having implications for linking the Gulf Stream path and AMOC.

The Gulf Stream path variability can be seen in gridded satellite altimetry and also in derived surface velocities as meridional shifts in the path of the Gulf Stream after Cape Hatteras (McCarthy et al., 2018). In this study, altimetry maps are used together with the outputs from an ocean reanalysis to assess the changing pattern of the Gulf Stream path over the last 3 decades, impacting both associated mesoscale EKE and waters transported towards the subpolar North Atlantic. To do that, the time-varying position of the path destabilization point where the Gulf Stream Extension converts from a stable, detached jet to an unstable, meandering detached jet is investigated following the methodology described in Andres (2016). Furthermore, seasonal and interannual variability of the Gulf Stream path is assessed to investigate possible causes and consequences of observed Gulf Stream changes.

2 Methods

Daily maps of both ADT from satellite altimetry (product ref. no. 1, Table 1) and SSH from an ocean reanalysis product (product ref. no. 2, Table 1) were averaged to produce monthly maps from January 1993 to December 2022. These maps have a spatial resolution of 1/4 and 1/12°, respectively. Following this, the Gulf Stream path was identified with the 25 cm SSH contour according to, e.g., Lillibridge and Mariano (2013), Rossby et al. (2014), Andres (2016), Chi et al. (2021), and Guo et al. (2023), from detrended ADT and SSH time series (Fig. 1a). The annual and semiannual cycles were kept in the time series to allow the analysis of the seasonal signal. Also, monthly averaged geostrophic velocity fields derived from both ADT and sea level anomaly (SLA) maps (product ref. no. 1, Table 1) were used to estimate the surface velocity associated with the Gulf Stream paths. Geostrophic velocity anomalies derived from SLA maps were then used to compute the Gulf Stream surface EKE. EKE presents greater values in the vicinity of the main jets and currents such as the western boundary currents, whereas it rapidly decreases elsewhere (von Schuckmann et al., 2016). Satellite-gridded products miss part of the mesoscale variability due to coarser effective dynamical resolutions (Ballarotta et al., 2019). However, the interannual variations in EKE can still be captured (Guo et al., 2022, 2023).

Variability in Gulf Stream paths was assessed on both a seasonal and yearly basis. Following Andres (2016), the 12 monthly mean paths for a given year were separated into 0.5° longitude bins and the variance of Gulf Stream position (latitude) in each bin was calculated. It can happen that the path in a given longitude bin describes a twisted route providing two or more latitudes. To overcome this, the most northerly latitude of the 25 cm SSH contour was used in the variance calculation (Andres, 2016). This computation was also done for the Gulf Stream mean paths computed for 1993–2022 as a group (Fig. 1). The downstream distance (longitude) where the latitude's variance first reaches $0.42(°)^2$ (half of the maximum variance obtained for the aggregate) was defined as that year's path destabilization point. This is where the Gulf Stream converts from a stable, detached jet to an unstable, meandering detached jet (Fig. 1a). The confidence interval (at 95 % confidence level) of the mean destabilization point was computed from the yearly destabilization point locations. A similar analysis was conducted for the seasonal assessment. Furthermore, the aforementioned computation was repeated from daily altimetry maps to compute the confidence interval (at 95 % confidence level) of the yearly destabilization point location. To do that, the 30 daily paths for a given month were used to identify the month's path destabilization point. The 12 monthly destabilization points of a given year were then used to provide an estimation of the confidence interval for that year. Finally, a 5-year running mean filter was applied to time series of the position of the destabilization point in the yearly assessment to avoid spurious signals due to changes in higher-frequency Gulf Stream variability.

In addition, the 12 °C isotherm (iso12) at 450 m depth was identified from the product ref. no. 2 (Table 1) and used to track the path of the Gulf Stream in the water column. This isotherm was chosen because it makes it possible to both limit short-term surface variations and follow the trajectory of the Gulf Stream more at depth than previous studies based on the temperature at 200 m depth (e.g., Joyce et al., 2000, 2009).

3 Results

3.1 Transition of the Gulf Stream path to an unstable jet

The datasets and methods described above were used to characterize the mean and time-varying Gulf Stream path, and identify its transition to an unstable detached jet. Variance in Gulf Stream latitude increases abruptly around 65° W (inset in Fig. 1a) and spreads around 1600 km out along the detached jet. In addition, a local minimum in variance is found to the west at around 70° W close to a node reported by, e.g., Joyce et al. (2000).

The mean destabilization point of the monthly mean Gulf Stream paths (1993–2022) is located at coordinates close to 38° N and 66° W (Fig. 1a). West of this location (i.e., near Cape Hatteras), the path is stable, exhibiting a relatively straight, detached jet and thus low variance (inset in Fig. 1a). Downstream from the destabilization point the path becomes unstable, showing meanders that translate into high variance and associated mesoscale EKE.

The Gulf Stream is one of the regions with the strongest mesoscale energy in the global ocean (Chelton et al., 2011; Guo et al., 2023). It presents mean values larger than 2000 $\mathrm{cm^2\,s^{-2}}$ downstream from 75° W where the Gulf Stream separates from the continental margin and becomes the Gulf Stream Extension (Fig. 1b). This area has an energetic mesoscale activity exhibiting strong eddy-mean flow interaction with significant along-stream variability (Kang and Curchitser, 2015; Guo et al., 2023). The mean EKE (1993–2022) core, with values larger than 3000 $\mathrm{cm^2\,s^{-2}}$, is observed in the surroundings of the Gulf Stream mean path. In addition, the zonally maximum mean EKE exhibiting values larger than 4000 $\mathrm{cm^2\,s^{-2}}$ is located close to the destabilization point where the Gulf Stream becomes unstable. These features are consistent with previous observations both in the upstream and downstream parts of the flow (e.g., Kang and Curchitser, 2015).

The aggregated (zonally and meridionally averaged) 1-year low-pass-filtered surface geostrophic velocity associated with the Gulf Stream paths (figure not show) presents an overall negative linear trend over the period 1993–2012 with reduced speed exhibiting strong interannual variability at decadal and sub-decadal scale. This agrees with results reported by Dong et al. (2019) and Chi et al. (2021) from altimetry data for the same period. This fact translates into a recurring EKE decrease with values ranging from around 3000 $\mathrm{cm^2\,s^{-2}}$ at the beginning of the altimetric era to close to 2200 $\mathrm{cm^2\,s^{-2}}$ in 2012 (inset in Fig. 1b). From 2013 there is an inversion in the temporal evolution of the surface velocity linked to the Gulf Stream with an increasing speed until 2022 that promotes aggregated EKE values larger than 3500 $\mathrm{cm^2\,s^{-2}}$ also showing interannual variability.

Similar results were obtained from a computation using the climatological satellite product based on a steady number (two) of satellite missions (e.g., Sánchez-Román et al., 2023). Thus, this increasing EKE is not an artifact due to larger energy promoted by a larger number of satellite missions used in the all-satellite product to generate the time series.

3.2 Interannual displacement of Gulf Stream

Figure 2 shows the yearly evolution of the destabilization point in latitude (Fig. 2a) and longitude (Fig. 2b). Over the last 3 decades, the location of this destabilization point (red dots) has varied by more than 1400 km in longitude (i.e., between 57 and 70° W) showing strong interannual variability (Fig. 2b). There has been an overall evolution of the destabilization point of the Gulf Stream towards western longitudes particularly from 1995 to 2014, which agrees with the findings of Andres (2016) over the same period. However, from 2014 until 2022 an inversion in the temporal evolution of the destabilization point occurs showing a previously unreported displacement towards eastern longitudes. In addition, a meridional shift in the location of the destabilization point (Fig. 2a) of 300 km (i.e., between 37.7 and 40.6° N) is observed promoting its displacement towards southern latitudes until 2014 and towards northern latitudes from that year until 2022. These new findings expand the results reported in Andres (2016) and might have an impact on the physical properties of waters transported towards the subpolar eastern North Atlantic.

However, these results might be affected by spurious signals due to changes in higher-frequency Gulf Stream variability. To avoid this, the 5-year running mean of the position of the destabilization point was investigated (grey line in Fig. 2a and b). The low-frequency variability of the Gulf Stream path indicates a westward and southward shift of the destabilization point from 1995 to 2012 that reverses towards northward and eastward shift from that year until 2020. This pattern agrees with the temporal evolution of the standardized 5-year running mean of the annually averaged wintertime (January–March) NAO index (Fig. 2c), that shows a Pearson linear correlation with the time-varying longitude (latitude) of the destabilization point of 0.70 (0.73) significant at 95 %. In addition, the time-varying longitude of the low-frequency zonally maximum EKE associated with the Gulf Stream path presents a linear correlation with the location of the destabilization point (not shown) of 0.88, exhibiting overall differences in longitude lower than 3°. Thus, this temporal variability also matches the aforementioned time-varying surface velocities and derived mesoscale EKE associated with the Gulf Stream path, giving support to the assessment of the low-frequency variability of the Gulf Stream.

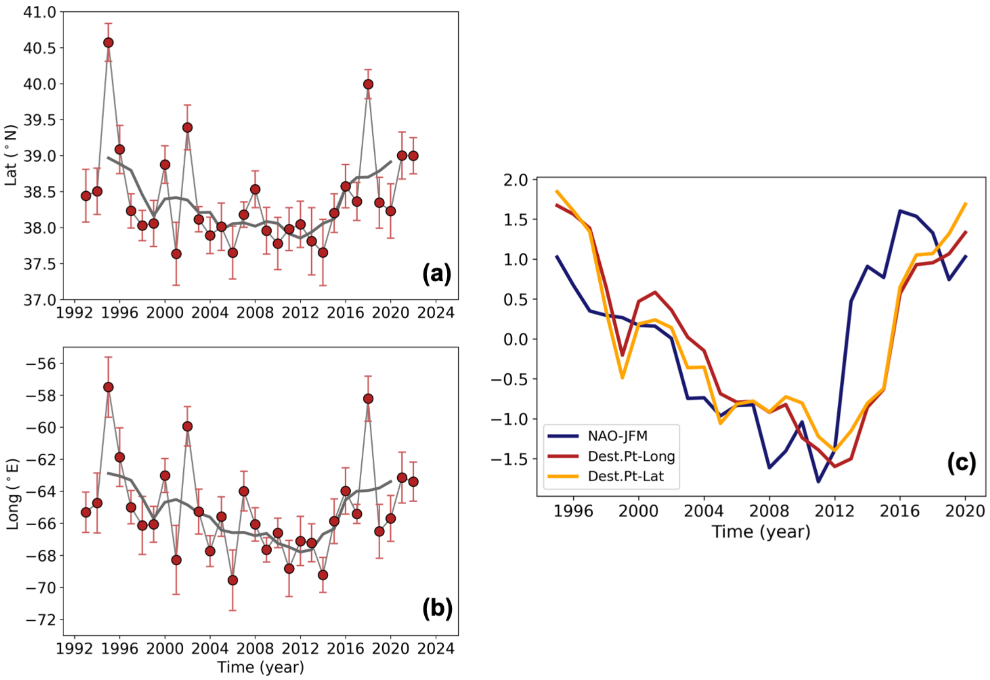

Figure 2. Yearly evolution of the destabilization point computed from altimetry data (product ref. no. 1) showing the latitude **(a)** and longitude **(b)** where the Gulf Stream becomes unstable. The solid grey line indicates the 5-year running mean of the destabilization point. The confidence interval (at 95 % confidence level) of the yearly position of the destabilization point in both longitude and latitude is also displayed. Panel **(c)** shows the standardized 5-year running mean of the position (longitude – red line; latitude – orange line) of the destabilization point and the standardized 5-year running mean of the seasonal mean NAO index during the cold season (blue line).

3.3 Temperature signature of Gulf Stream pathway

Figure 3a shows the mean Gulf Stream pathways estimated using the iso12 at 450 m depth for two representative 2-year periods before (2008–2010) and after (2014–2016) the change in trend of the destabilization point, together with Gulf Stream trajectories estimated with the method based on SSH data for the same periods. The iso12 estimate of the Gulf Stream pathway is located north of the sea level estimate because the iso12 is a signature of the GSNW rather than of the center of the pathway (Chi et al., 2019; Seidov et al., 2021). The good correspondence between mean pathways estimated with the altimeter data and with the temperature data (Fig. 3a) indicates that the signal detected at the surface is also present in the subsurface. On both diagnostics a separation of the average Gulf Stream pathway between the two periods occurs near 66° W, which corresponds to the detected mean destabilization point. Downstream the mean pathways for the two periods converge. However, in the subsurface near 450 m, this convergence seems to occur further upstream (near 62° W, purple box) on the Gulf Stream path than at the surface (east of 57° W, black box).

The meridional variability in monthly mean pathways estimated using the iso12 at 450 m depth for the 2-year periods before and after the change in the destabilization point's trend (Fig. 3b) also reflects the variation observed at the surface with the method based on SSH (Fig. 1a). The spread in latitude of the monthly mean pathways estimated for the two periods decreases in the surroundings of the mean location of the destabilization point. This signature of a more stable pathway at this longitude thus confirms that the change in the destabilization point diagnosed from altimetry also has a signature in the subsurface on the temperature field.

Furthermore, the time evolution of the temperature in the upper part of the water column (Fig. 3c) in the surroundings (downstream) of the Gulf Stream's destabilization point (purple box in Fig. 3a) exhibits a constant pattern over the first 1000 m and down to 2000 m. In addition, a strong negative hiatus was found in 2010, followed by a significant increase in temperature to become a positive anomaly in 2014. This increase may be due to both a long-term climate change and a change in the characteristics of the water masses. Thus, the analysis of the destabilization point of the Gulf Stream from SSH data could be a good indicator of the subsurface conditions (in the upper 1000 m of the water column) in the northeastern part south of the Grand Banks.

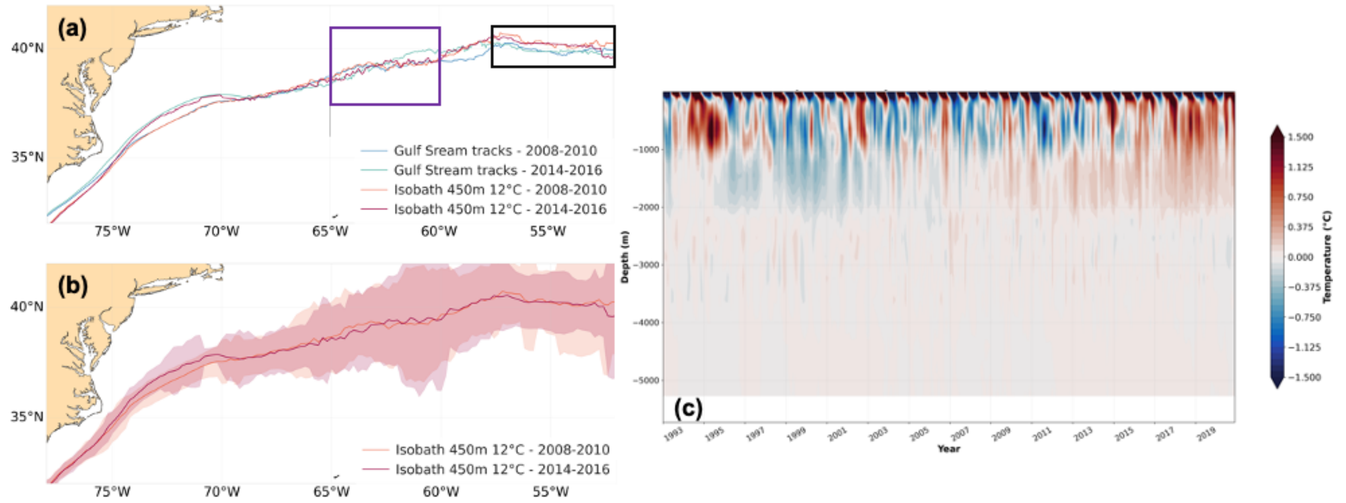

Figure 3. (a) The mean 12 °C isotherm (iso12) for 2008–2010 (orange) and 2014–2016 (red) computed from ocean reanalysis data (product ref. no. 2) superimposed to the SSH derived Gulf Stream pathway computed from altimetry data (product ref. no. 1) for the same periods (blue and green, respectively). **(b)** The mean and standard deviation (2σ) of monthly pathways estimated using the iso12 at 450 m depth computed from ocean reanalysis data (product ref. no. 2) for the periods 2008–2010 (orange) and 2014–2016 (red). Panel **(c)** displays the temporal evolution of temperature anomalies in the water column (°C) in the surroundings (downstream) of the mean Gulf Stream's destabilization point (purple box) computed for the reference period 1993–2020.

4 Discussion and conclusions

4.1 Seasonal and interannual variability of Gulf Stream paths

The Gulf Stream Extension displaces to the north in fall (exhibiting a relatively low baroclinic transport) and to the south in spring (Tracey and Watts, 1986) reaching its maximum baroclinic transport in early summer (Sato and Rossby, 1995). This seasonal pattern (Fig. 4b, d, e; product ref. no. 1 in Table 1) is extended to summer (Fig. 4a and e) and wintertime (Fig. 4c and e), respectively. This is a novelty with respect to previous estimations (e.g., Lillibridge and Mariano, 2013) having an impact on the location of the destabilization point (inset in Fig. 4e): it shifts eastwards until 65° W in winter and 65.7° W in spring, the unstable meandering detached jet being shortened and located more to the south, whereas it remains close to 66° W in summer and fall, with the unstable jet being enlarged and located more to the north. The seasonal meridional shifts of the destabilization point are negligible with values ranging from 38.1° N in spring to 38.3° N in summer. On the contrary, this seasonal displacement of the path is not observed upstream of 70° W. Thus, the seasonal meridional shifts of the detached jet are accompanied by longitudinal seasonal variability of the destabilization point. This fact has an impact on the mesoscale EKE monitored in the Gulf Stream region that shows a clear seasonal variability (von Schuckmann et al., 2016) with maximum levels in the summer period (May to September), associated with a larger unstable meandering jet located more to the north and also more mesoscale-to-sub-mesoscale activity (Ajayi et al., 2020), and minimum levels in winter (January), when the unstable jet is shorter and placed more to the south. These seasonal meridional fluctuations in the Gulf Stream path position have important consequences for regional climate because the Gulf Stream transports considerable heat from the ocean at low latitudes to the atmosphere at high latitudes (Johns et al., 2011) and contributes to the distribution of biogeochemical properties in the North Atlantic Ocean (von Schuckmann et al., 2016).

In addition to the seasonal variability of Gulf Stream paths, the destabilization point of the detached jet exhibits a remarkable low-frequency shift westward between 1995 and 2012 accompanied by a southward shift of the jet. This promotes a shorter stable detached jet with time and thus eddying flows closer to the western boundary and the Mid-Atlantic Bight (MAB) shelf that are widespread along a larger region of the North Atlantic. This proximity increases the probability of Gulf Stream–MAB interactions and has important consequences beyond a local increase in the EKE associated with the Gulf Stream (Andres, 2016). Warm core rings can spin off from the jet and bring salty and nutrient-rich deep waters to the euphotic zone at the shelf break front in the MAB, leading to enhanced primary productivity (Zhang et al., 2013; Hoarfrost et al., 2019) and ecosystem changes (Gawarkiewicz et al., 2018). Monim (2017) reported an increase of 50 % in the frequency of warm core rings formed annually in the years 2000–2016 (overall in agreement with the observed westward shift of the destabilization point) compared to 1977–1999 in the slope region south of New England, which has an important effect on biogeochemical cycling (Hoarfrost et al., 2019).

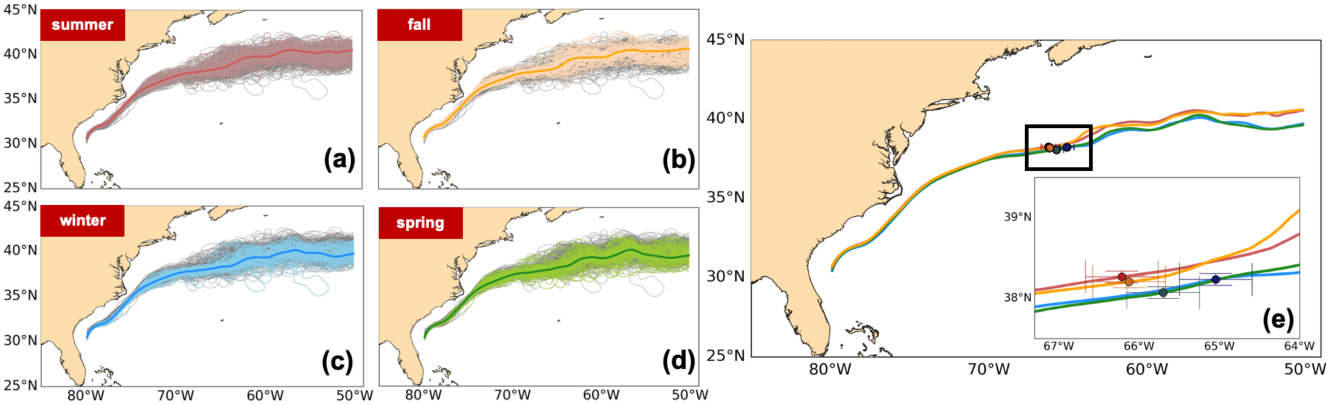

Figure 4. Gulf Stream paths based on the 25 cm SSH contour from altimetry (product ref. no. 1) showing monthly and a 1993–2022 overall seasonal mean for **(a)** summer (red, JAS), **(b)** fall (orange, OND), **(c)** winter (pale blue, JFM), and **(d)** spring (green, AMJ). Panel **(e)** displays the 1993–2022 overall seasonal means with the mean location of the seasonal destabilization point. The inset displays a zoomed-in view of the region inside the black box. The confidence interval (at 95 % confidence level) of the destabilization point in both longitude and latitude is also displayed.

In 2012, the destabilization point displacement reversal exhibits a previously unreported low-frequency migration eastward accompanied by a northward shift of the jet until 2020. This translates into a larger fraction of the stable detached jet to the detriment of the unstable meandering jet that is likely to promote the depletion of the frequency of warm core ring intrusions onto the continental shelf and the probability of Gulf Stream–MAB interactions, in contrast with the increased interactions from the westward displacement observed in the recent past.

4.2 Impact of varying Gulf Stream stability on associated EKE

Guo et al. (2023) found a dominant component in mesoscale EKE associated with the Gulf Stream that co-varies with the meridional shift of the jet. Thus, migration of the destabilization point may have an impact on both the Gulf Stream's surface velocity and associated EKE. The low-frequency southwestward shift of the destabilization point observed between 1995 and 2012 is accompanied by a weakening of the jet (not shown) and associated mesoscale surface EKE (Fig. 1b). Dong et al. (2019) attributed this velocity decrease to an increase in SSH to the north of the Gulf Stream that is mainly due to ocean warming.

The observed weakening of the jet over this period was explained by Renault et al. (2016b) in terms of energy transfers from the ocean to the atmosphere over the Gulf Stream induced by the current feedback. It attenuates the wind surface stress, inducing a positive surface stress curl opposite to the current vorticity that deflects energy from the Gulf Stream into the atmosphere and dampens eddies. It causes a mean pathway of energy from the ocean to the atmosphere (Renault et al., 2016a). Consequently, the current feedback promotes a slowdown of the jet and a drastic weakening of the EKE limiting the propagation of eddies. This mechanism could be fostered by the observed southwestward shift of the destabilization point.

On the other hand, the previously unreported low-frequency northeastward shift observed from 2013 until 2020 promotes an increasing velocity with larger associated EKE (see Fig. 1). Guo et al. (2023), based on empirical orthogonal function (EOF) analysis, found a mode that suggests an enhancement in EKE when the Gulf Stream shifts to the north. Thus, the current feedback is likely to weaken in this period, allowing energy transfers from the atmosphere to the ocean and the propagation of eddies. This would suggest a connection of the current feedback and net energy transfers between the atmosphere and the ocean with the observed meridional shifts of the jet and associated velocity rather than the variations in SSH linked to the ocean warming pointed out by Dong et al. (2019). However, the aforementioned increasing frequency of warm core ring intrusions onto the continental shelf observed during the low-frequency southwestward shift of the destabilization point can contribute to sea level rise through a steric effect (Gawarkiewicz et al., 2018) reflecting a decreased sea level difference across the Gulf Stream (Sallenger et al., 2012) and a slowdown jet. The opposite is likely to appear during the northeastward displacement of the destabilization point when a larger fraction of the stable detached jet is observed to the detriment of the unstable meandering jet. Thus, the processes related to the Gulf Stream could have an impact on sea level variability in the coastal region.

Furthermore, the global long-term change in surface mesoscale EKE found by Martinez-Moreno et al. (2021) might show that the ocean EKE has experienced an increase. These changes in EKE also show that surface mesoscale diffusivities vary on climate timescales due to a coupling between large-scale climate variability and eddy-mixing rates as a result of small amplitude changes in the large-scale flow

(Busecke and Abernathey, 2019). These authors suggested that temporal variability in mesoscale mixing could be an important climate feedback mechanism due to the relevance of lateral mesoscale mixing for the ocean uptake of heat and carbon and the distribution of oxygen and nutrients in the ocean (among other factors).

However, the underlying dynamics for the changes in the North Atlantic are not well understood, and the mechanism behind correlations between EKE variability and Gulf Stream shifts are still unclear (Guo et al., 2022; 2023), meaning that further investigation is needed.

4.3 External forcing of the Gulf Stream path destabilization

There are many factors, due to external forcing or reflecting internal variability, shaping the Gulf Stream system (Seidov et al., 2019) and thus the observed shifts of the path destabilization point. The regimes of the Gulf Stream paths described above seem to be linked to NAO variability during winter (external forcing) that may play an important role. However, the relationships found between the Gulf Stream and the NAO depend on the analysis domain, the time period considered and the index used to define the Gulf Stream path position (Lillibridge and Mariano, 2013). Andres (2016) for instance found that the NAO index was uncorrelated at zero lag with the destabilization point of the detached Gulf Stream stating that the large- and regional-scale winds may not be directly responsible for the stability of the Gulf Stream jet. However, a maximum linear correlation of 0.80 (0.76) was found here between the NAO during winter and the time-varying longitude (latitude) of the destabilization point lagging by 1 year (not shown). Thus, the Gulf Stream path seems to respond passively to the variability of the NAO during winter with a delay of a year at low frequencies. Frankignoul et al. (2001) stated that this delay is much shorter than expected from linear adjustment to wind stress changes and baroclinic Rossby wave propagation, whereas it seems consistent with the assumption that the latitude of separation of the stable Gulf Stream is controlled by the potential vorticity of the recirculation gyres in the region. In reality, the wind stress curl (WSC) is responsible for the development and maintenance (via Ekman pumping) of the dipole of the two water gyres of the Gulf Stream system (Seidov et al., 2019) and is thus coupled to the Gulf Stream dynamics (Renault et al., 2016b). WSC together with the NAO stand out as the strongest external factors impacting the low-frequency Gulf Stream path variability at the sea surface on long timescales.

The northward shift of the Gulf Stream path observed in the latest decade is likely to continue in the near future. It will probably impact the zonal displacements of the destabilization point and may promote its migration to the east, and thus there may be a larger fraction of the stable detached jet to the detriment the unstable meandering jet. Such changes in the position of the destabilization point seem to be being accompanied by a shift in the NAO index for winter. The observed time-varying Gulf Stream stability and associated ring dynamics may impact the frequency of warm core rings in the slope region south of New England and thus the upper ocean through changing events that drive the exchange of heat, nutrients, and biogeochemical properties between the continental slope and outer shelf in the coming years.

Data availability. Satellite observations and the ocean reanalysis product are available from the Copernicus Marine Service web portal (https://doi.org/10.48670/moi-00148, EU Copernicus Marine Service Product, 2023a; https://doi.org/10.48670/moi-00021, EU Copernicus Marine Service Product, 2023b). The NAO index data are available from the US National Oceanic and Atmospheric Administration, Climate Prediction Center web portal (https://www.cpc.ncep.noaa.gov/products/precip/CWlink/pna/nao.shtml, Climate Prediction Center, 2024).

Author contributions. Conceptualization: ASR, MIP, AP, MD, and RBB. Satellite data processing: ASR and MIP. Ocean reanalysis data processing: MD, RBB, and FG. Analysis and interpretation of results: ASR, MIP, RBB, AP, and MD. Writing of the paper: ASR, with input from all co-authors. All authors have read and agreed to the published version of the paper.

Competing interests. The contact author has declared that none of the authors has any competing interests.

Disclaimer. Publisher's note: Copernicus Publications remains neutral with regard to jurisdictional claims made in the text, published maps, institutional affiliations, or any other geographical representation in this paper. While Copernicus Publications makes every effort to include appropriate place names, the final responsibility lies with the authors.

Acknowledgements. This study has been conducted in the frame of Sea Level Thematic Assembly Center, as part of the Copernicus Marine Service. The Copernicus Marine Service, implemented by Mercator Ocean International, is based on a distributed model of service production, relying on the expertise of a wide network of participating European organizations involved in operational oceanography. This work represents a contribution to the CSIC Interdisciplinary Thematic Platform (PTI) Teledetección (PTI-TELEDETECT), and it was carried out within the framework of the activities of the Spanish Government through the "Maria de Maeztu Centre of Excellence" accreditation to IMEDEA (CSIC-UIB) (CEX2021-001198).

Financial support. This research has been supported by the Copernicus Marine Service, the marine component of the Copernicus Program of the European Union (contract no. 21001L01-COP-TAC-SL-2100).

Review statement. This paper was edited by Pierre Brasseur and reviewed by two anonymous referees.

References

Ajayi, A., Le Sommer, J.,Chassignet, E., Molines, J.-M.,Xu, X., Albert, A., and Cosme, E.: Spatial and temporalvariability of the North Atlantic eddyfield from two kilometric-resolutionocean models, J. Geophys. Res.-Oceans, 125, e2019JC015827, https://doi.org/10.1029/2019JC015827, 2020.

Andres, M.: On the recent destabilization of the Gulf Stream path downstream of Cape Hatteras, Geophys. Res. Lett., 43, 9836–9842, https://doi.org/10.1002/2016GL069966, 2016.

Årthun, M., Eldevik, T., Viste, E., Drange, H., Furevik, T., Johnson, H. L., and Keenlyside, N. S.: Skillful prediction of northern climate provided by the ocean, Nat. Commun., 8, 15875, https://doi.org/10.1038/ncomms15875, 2017.

Ballarotta, M., Ubelmann, C., Pujol, M.-I., Taburet, G., Fournier, F., Legeais, J.-F., Faugère, Y., Delepoulle, A., Chelton, D., Dibarboure, G., and Picot, N.: On the resolutions of ocean altimetry maps, Ocean Sci., 15, 1091–1109, https://doi.org/10.5194/os-15-1091-2019, 2019.

Buckley, M. W., and Marshall, J.: Observations, inferences, and mechanisms of the Atlantic meridional overturning circulation: A review, Rev. Geophys., 54, 5–63, https://doi.org/10.1002/2015RG000493, 2016.

Busecke, J. J. and Abernathey, R. P.: Ocean mesoscale mixing linked to climate variability, Sci. Adv., 5, eaav5014, https://doi.org/10.1126/sciadv.aav5014, 2019.

Chelton, D. B., Schlax, M. G., and Samelson, R. M.: Global observations of nonlinear mesoscale eddies, Prog. Oceanogr., 91, 167–216, https://doi.org/10.1016/j.pocean.2011.01.002, 2011.

Chi, L., Wolfe, C. L. P., and Hameed, S.: The distinction between the Gulf Stream and its North Wall, Geophys. Res. Lett., 46, 8943–8951, https://doi.org/10.1029/2019GL083775, 2019.

Chi, L., Wolfe, C. L. P., and Hameed, S.: Has the Gulf Stream slowed or shifted in the altimetry era?, Geophys. Res. Lett., 48, e2021GL093113, https://doi.org/10.1029/2021GL093113, 2021.

Clement, A., Bellomo, K., Murphy, L. N., Cane, M. A., Mauritsen, T., Rädel, G., and Stevens, B.: The Atlantic multidecadal oscillation without a role for ocean circulation. Science, 350, 320–324, https://doi.org/10.1126/science.aab3980, 2015.

Climate Prediction Center: North Atlantic Oscillation, Climate Prediction Center, National Centers for Environmental Predictions, NOAA [data set], https://www.cpc.ncep.noaa.gov/products/precip/CWlink/pna/nao.shtml (last access: 27 January 2024), 2024.

Da Costa, E. and Colin de Verdiere, A.: The 7.7-year North Atlantic Oscillation, Q. J. Roy. Meteor. Soc., 128, 797–817, https://doi.org/10.1256/0035900021643692, 2002.

Delworth, T. L. and Mann, M. E.: Observed and simulated multidecadal variability in the Northern Hemisphere, Clim. Dynam., 16, 661–676, https://doi.org/10.1007/s003820000075, 2000.

Dong, S., Baringer, M. O., and Goni, G. J.: Slow down of the Gulf stream during 1993–2016, Sci. Rep., 9, 1–10, https://doi.org/10.1038/s41598-019-42820-8, 2019.

Drévillon, M., Lellouche, J.-M., Régnier, C., Garric, G., Bricaud, C., Hernandez, H., and Bourdallé-Badie, R.: EU Copernicus Marine Service Product Quality Information Document for the Global Ocean Physics Reanalysis, GLOBAL_MULTIYEAR_PHY_001_030, Issue 1.6, Mercator Ocean International, https://catalogue.marine.copernicus.eu/documents/QUID/CMEMS-GLO-QUID-001-030.pdf (last access: 26 March 2024), 2023a.

Drévillon, M., Fernandez, E., and Lellouche, J.-M.: EU Copernicus Marine Service Product User Manual for the Global Ocean Physics Reanalysis, GLOBAL_MULTIYEAR_PHY_001_030, Issue 1.5, Mercator Ocean International, https://catalogue.marine.copernicus.eu/documents/PUM/CMEMS-GLO-PUM-001-030.pdf (last access: 26 March 2024), 2023b.

EU Copernicus Marine Service Product: Global Ocean Gridded L4 Sea Surface Heights And Derived Variables Reprocessed 1993 Ongoing, Mercator Ocean International [data set], https://doi.org/10.48670/moi-00148, 2023a.

EU Copernicus Marine Service Product: Global Ocean Physics Reanalysis, Mercator Ocean International [data set], https://doi.org/10.48670/moi-00021, 2023b.

Frankignoul, C., de Coetlogon, G., Joyce, T. M., and Dong, S.: Gulf Stream variability and ocean–atmosphere interactions, J. Phys. Oceanogr. 31, 3516–3529, https://doi.org/10.1175/1520-0485(2002)031<3516:GSVAOA>2.0.CO;2, 2001.

Gawarkiewicz, G., Todd, R. E., Zhang, W., Partida, J., Gangopadhyay, A., Monim, M.-U.-H., Fratantoni, F., Malek Mercer, A., and Dent M.: The changing nature of shelf- break exchange revealed by the OOI Pioneer Array, Oceanography, 31, 60–70, https://doi.org/10.5670/oceanog.2018.110, 2018.

Gray, L. J., Woollings, T., Andrews, M., and Knight, J.: Eleven-year solar cycle signal in the NAO and Atlantic/European blocking, Q. J. Roy. Meteor. Soc., 142, 1890–1903, https://doi.org/10.1002/qj.2782, 2016.

Greatbatch, R. J., Zhai,X., Claus, M., Czeschel, L., and Rath, W.: Transport driven by eddy momentum fluxes in the Gulf Stream Extension region, Geophys. Res. Lett., 37, L24401, https://doi.org/10.1029/2010GL045473, 2010.

Guo, Y., Bachman, S., Bryan, F., and Bishop, S.: Increasing trends in oceanic surface poleward eddy heat flux observed over the past three decades, Geophys. Res. Lett., 49, e2022GL099362, https://doi.org/10.1029/2022gl099362, 2022.

Guo, Y., Bishop, S., Bryan, F., and Bachman, S.: Mesoscale variability linked to interannual displacement of Gulf Stream, Geophys. Res. Lett., 50, e2022GL102549, https://doi.org/10.1029/2022GL102549, 2023.

Hoarfrost A., Balmonte J.P., Ghobrial S., Ziervogel K., Bane J., Gawarkiewicz G., and Arnosti C.: Gulf Stream Ring Water Intrusion on the Mid-Atlantic Bight Continental Shelf Break Affects Microbially Driven Carbon Cycling, Front. Mar. Sci., 6, 394, https://doi.org/10.3389/fmars.2019.00394, 2019.

Hurrell, J. W., Kushnir, Y., Ottersen, G., and Visbeck, M.: An overview of the North Atlantic Oscillation, Geophys. Monogr. Ser., 134, 1–35, https://doi.org/10.1029/134GM01, 2003.

Johns, W. E., Baringer, M. O., Beal, L. M., Cunningham, S. A., Kanzow, T., Bryden, H. L., Hirschi, J. J. M., Marotzke, J., Meinen, C. S., Shaw, B., and Curry, R.: Continuous, array-based estimates of Atlantic Ocean heat transport at 26.5 N, J. Climate, 24, 2429–2449, https://doi.org/10.1175/2010JCLI3997.1, 2011.

Joyce, T. M. and Zhang, R.: On the path of the Gulf Stream and the Atlantic meridional overturning circulation, J. Climate, 23, 3146–3154, https://doi.org/10.1175/2010jcli3310.1, 2010.

Joyce, T. M., Deser, C., and Spall, M. A.: The relation between decadal variability of subtropical mode water and the North Atlantic Oscillation, J. Climate, 13, 2550–2569, https://doi.org/10.1175/1520-0442(2000)013<2550:TRBDVO>2.0.CO;2, 2000.

Joyce, T. M., Kwon, Y.-O., and Yu, L.: On the relationship between synoptic wintertime atmospheric variability and path shifts in the Gulf Stream and the Kuroshio Extension, J. Climate, 22, 3177–3192, https://doi.org/10.1175/2008jcli2690.1, 2009.

Kang, D. and Curchitser, E. N.: Energetics of eddy–mean flow interactions in the gulf stream region, J. Phys. Oceanogr., 45, 1103–1120, https://doi.org/10.1175/jpo-d-14-0200.1, 2015.

Lillibridge, J. L. and Mariano, A.J.: A statistical analysis of Gulf Stream variability from 18+ years of altimetry data, Deep-Sea Res. Pt. II, 85, 127–146, https://doi.org/10.1016/j.dsr2.2012.07.034, 2013.

Lozier, M. S., Li, F., Bacon, S., Bahr, F., Bower, A. S., Cunningham, S. A., de Jong, M. F., de Steur, L., de Young, B., Fischer, J., Gary, S. F., Greenan, B. J. W., Holliday, N. P., Houk, A., Houpert, L., Inall, M. E., Johns, W. E., Johnson, H. L., Johnson, C., Karstensen, J., Koman, G., Le Bras, I. A., Lin, X., Mackay, N., Marshall, D. P., Mercier, H., Oltmanns, M., Pickart, R. S., Ramsey, A. L., Rayner, D., Straneo, F., Thierry, V., Torres, D. J., Williams, R. G., Wilson, C., Yang, J., Yashayaev, I., and Zhao, J.: A sea change in our view of overturning in the subpolar North Atlantic, Science, 363, 516–521, https://doi.org/10.1126/science.aau6592, 2019.

Martínez-Moreno, J., Hogg, A. M., England, M. H., Constantinou, N. C., Kiss, A. E., and Morrison, A. K.: Global changes in oceanic mesoscale currents over the satellite altimetry record, Nat. Clim. Change, 11, 397–403, https://doi.org/10.1038/s41558-021-01006-9, 2021.

McCarthy, G. D., Haigh, I. D., Hirschi, J. J.-M., Grist, J. P., and Smeed, D. A.: Ocean impact on decadal Atlantic climate variability revealed by sea-level observations, Nature, 521, 508–510, https://doi.org/10.1038/nature14491, 2015.

McCarthy, G. D., Joyce, T. M. M., and Josey, S. A.: Gulf Stream variability in the context of quasi-decadal and multidecadal Atlantic climate variability, Geophys. Res. Lett., 45, 11257–11264, https://doi.org/10.1029/2018GL079336, 2018.

Monim, M.: Seasonal and Inter-Annual Variability of Gulf Stream Warm Core Rings from 2000 to 2016, PhD thesis, University of Massachusetts, Dartmouth, 2017.

Osman, M., Zaitchik, B., Badr, H., and Hameed, S.: North Atlantic centers of action and seasonal to subseasonal temperature variability in Europe and eastern North America, Int. J. Climatol., 41, E1775–E1790, https://doi.org/10.1002/joc.6806, 2021.

Pujol, M.-I.: EU Copernicus Marine Service Product User Manual for the Global Ocean Gridded L4 Sea Surface Heights And Derived Variables Reprocessed 1993 Ongoing, SEALEVEL_GLO_PHY_L4_MY_008_047, Issue 8.0, Mercator Ocean International, https://catalogue.marine.copernicus.eu/documents/PUM/CMEMS-SL-PUM-008-032-068.pdf (last access: 26 March 2024), 2023.

Pujol, M.-I., Taburet G., and SL-TAC team: EU Copernicus Marine Service Product Quality Information Document for the Global Ocean Gridded L4 Sea Surface Heights And Derived Variables Reprocessed 1993 Ongoing, SEALEVEL_GLO_PHY_L4_MY_008_047, Issue 9.0, Mercator Ocean International, https://catalogue.marine.copernicus.eu/documents/QUID/CMEMS-SL-QUID-008-032-068.pdf (last access: 26 March 2024), 2023.

Renault, L., Molemaker, M. J., McWilliams, J. C., Shchepetkin, A. F., Lemarié, F., Chelton, D., Illig, S., and Hall, A.: Modulation of wind work by oceanic current interaction with the atmosphere, J. Phys. Oceanogr., 46, 1685–1704, https://doi.org/10.1175/JPO-D-15-0232.1, 2016a.

Renault, L., Molemaker, M. J., Gula, J., Masson, S., and McWilliams, J. C.: Control and stabilization of the gulf stream by oceanic current interaction with the atmosphere, J. Phys. Oceanogr., 46, 3439–3453, https://doi.org/10.1175/jpo-d-16-0115.1, 2016b.

Rossby, H., Flagg, C., Donohue, K., Sanchez-Franks, A., Lillibridge, J.: On the long-term stability of Gulf Stream transport based on 20 years of direct measurements, Geophys. Res. Lett., 41, 114–120, https://doi.org/10.1002/2013GL058636, 2014.

Sallenger Jr., A. H., Doran, K. S., and Howd, P. A.: Hotspot of accelerated sea-level rise on the Atlantic coast of North America, Nat. Clim. Change, 2, 884–888, 2012.

Sánchez-Román, A., Pujol, M. I., Faugère, Y., and Pascual, A.: DUACS DT2021 reprocessed altimetry improves sea level retrieval in the coastal band of the European seas, Ocean Sci., 19, 793–809, https://doi.org/10.5194/os-19-793-2023, 2023.

Sato, O. T. and Rossby, T.: Seasonal and low frequency variability in dynamic height anomaly and transport of the Gulf Stream, Deep-Sea Res., 42, 149–164, https://doi.org/10.1016/0967-0637(94)00034-P, 1995.

Seidov, D., Mishonov, A., Reagan, J., and Parsons, R.: Resilience of the Gulf Stream path on decadal and longer timescales, Sci. Rep., 9, 11549, doi:https://doi.org/10.1038/s41598-019-48011-9, 2019.

Seidov, D., Mishonov, A., and Parsons, R.: Recent warming and decadal variability of Gulf of Maine and Slope Water, Limnol. Oceanogr., 66, 3472–3488, https://doi.org/10.1002/lno.11892, 2021.

Srokosz, M., Baringer, M., Bryden, H., Cunningham, S., Delworth, T., Lozier, S., Marotzke, J., and Sutton, R.: Past, present, and future changes in the Atlantic meridional overturning circulation, B. Am. Meteorol. Soc., 93, 1663–1676, https://doi.org/10.1175/BAMS-D-11-00151.1, 2012.

Swingedouw, D., Houssais, M.-N., Herbaut, C., Blaizot, A.-C., Devilliers, M., and Deshayes, J.: AMOC Recent and Future Trends: A Crucial Role for Oceanic Resolution and Greenland Melting?, Front. Clim., 4, 838310, https://doi.org/10.3389/fclim.2022.838310, 2022.

Taylor, A. and Stephens, J.: Latitudinal displacements of the Gulf-Stream (1966 to 1977) and their relation to changes in temperature and zooplankton abundance in the NE Atlantic, Oceanol. Acta, 3, 145–149, https://archimer.ifremer.fr/doc/00121/23258/ (last access: 10 January 2024), 1980.

Taylor, A., Jordan, M., and Stephens, J.: Gulf Stream shifts following ENSO events, Nature, 393, 638, https://doi.org/10.1038/31380, 1998.

Tracey, K. L. and Watts, D. R.: On the Gulf Stream meander characteristics near Cape Hatteras, J. Geophys. Res., 91, 7587–7602, https://doi.org/10.1029/JC091iC06p07587, 1986.

von Schuckmann, K., Le Traon, P. Y., Alvarez-Fanjul, E., Axell, L., Balmaseda, M., Breivik, L.-A., Brewin, R. J. W., Bricaud, C., Drevillon, M., Drillet, Y., Dubois, C., Embury, O., Etienne, H., García Sotillo, M., Garric, G., Gasparin, F., Gutknecht, E., Guinehut, S., Hernandez, F., Juza, M., Karlson, B., Korres, G., Legeais, J. F., Levier, B., Lien, V. S., Morrow, R., Notarstefano, G., Parent, L., Pascual, A., Pérez-Gómez, B., Perruche, C., Pinardi, N., Pisano, A., Poulain, P. M., Pujol, I. M., Raj, R. P., Raudsepp, U., Roquet, H., Samuelsen, A., Sathyendranath, S., She, J., Simoncelli, S., Solidoro, C., Tinker, J., Tintoré, J., Viktorsson, L., Ablain, M., Almroth-Rosell, E., Bonaduce, A., Clementi, E., Cossarini, G., Dagneaux, Q., Desportes, C., Dye, S., Fratianni, C., Good, S., Greiner, S., Gourrion, J., Hamon, M., Holt, J., Hyder, P., Kennedy, J., Manzano-Muñoz, F., Melet, A., Meyssignac, B., Mulet, S., Buongiorno Nardelli, B., O'Dea, E., Olason, E., Paulmier, A., Pérez-González, I., Reid, R., Racault, M. F., Raitsos, D. E., Ramos, A., Sykes, P., Szekely, T., and Verbrugg, N.: The Copernicus Marine Environment Monitoring Service Ocean State Report, J. Oper. Oceanogr., 9, Supplement, s235–s320, https://doi.org/10.1080/1755876X.2016.1273446, 2016.

Wolfe, C. L., Hameed, S., and Chi, L.: On the drivers of decadal variability of the Gulf Stream north wall, J. Climate, 32, 1235–1249, https://doi.org/10.1175/jcli-d-18-0212.1, 2019.

Zhang, W. G., McGillicuddy, D. J., and Gawarkiewicz, G. G.: Is biological productivity enhanced at the New England shelfbreak front?, J. Geophys. Res.-Oceans, 118, 517–535, https://doi.org/10.1002/jgrc.20068, 2013.

State Planet, 4-osr8, 5, 2024
https://doi.org/10.5194/sp-4-osr8-5-2024

Monitoring main ocean currents of the Iberia–Biscay–Ireland region

Álvaro de Pascual Collar[1], Roland Aznar[1], Bruno Levier[2], and Marcos García Sotillo[1]

[1]Nologin Oceanic Weather Systems, Paseo de la Castellana 216, 8th Floor, Office 811, 28046 Madrid, Spain
[2]Mercator Ocean International, 2 Av. de l'Aérodrome de Montaudran, 31400 Toulouse, France

Correspondence: Álvaro de Pascual Collar (alvaro.depascual@nowsystems.eu)

Received: 21 July 2023 – Discussion started: 19 September 2023
Revised: 20 February 2024 – Accepted: 4 April 2024 – Published: 30 September 2024

Abstract. The Iberia–Biscay–Ireland (IBI) region is located on the eastern margin of the North Atlantic. This geographical position results in a diverse array of currents, primarily including southward surface currents (associated with the North Atlantic subtropical gyre) and poleward slope currents at intermediate depths following the continental margins of Africa and Europe. Ocean currents have significant climatic, environmental, economic, and social implications, making them a crucial parameter whose variability needs to be monitored to anticipate diagnosis and support decision-making in the face of changing scenarios.

The present study proposes a methodology that allows for systematic monitoring of ocean currents. This methodology is based on calculating volume transports within monitoring windows defined using (i) present knowledge of the ocean and (ii) delineation of the water mass to be monitored based on its density range. The proposed indicator is computed using various sources of observational and modeling data, resulting in a multi-product output. This approach provides not only an ocean monitoring indicator (OMI) of transport anomalies but also an analysis of uncertainties.

The calculation of this OMI on the currents in the IBI region shows that, despite the high uncertainties, the index is capable of detecting events of high and low transport intensity as well as significant transport trends superimposed on the interannual variability of some of the analyzed currents.

1 Introduction

The IBI (Iberia–Biscay–Ireland) region encompasses the northeastern Atlantic Ocean from the Canary Islands (latitude 28° N) to the coasts of Ireland and Great Britain (latitude 60° N). This zone is defined as one of the Marine Forecasting Centers of the Copernicus Marine Service (Fig. 1). The IBI area is a very complex region characterized by a remarkable variety of ocean processes and scales (Sotillo et al., 2015). The western, and deeper, side of the IBI domain is affected by large-scale currents, mainly the closure of the North Atlantic Drift, where it splits into two branches, the major one continuing north along the northwestern European shelves (Bower et al., 2002; Holliday et al., 2008) and the other going eastward to form the eastern boundary current of the North Atlantic subtropical gyre. This boundary current is composed of the Azores Current (Jia, 2000; Peliz et al., 2007), the Portugal equatorward current (Pérez et al., 2001), and the Canary Current (Knoll et al., 2002; Mason et al., 2011) along the European continental slope, a subsurface current flow northward following the coasts of Portugal, Spain (Mazé et al., 1997), and the Celtic–Armorican Slope (Fricourt et al., 2007). The signature of this current can be observed as far north as Porcupine Bank (52° N) (White and Bowyer, 1997; Friocourt et al., 2007; Pascual et al., 2018; de Pascual-Collar et al., 2019). The intermediate levels of the Canary basin are affected by the northward-flowing Antarctic Intermediate Water. The flow of this globally important water mass has been described in the Lanzarote Passage, located between the Canary Islands and the African coast (Knoll et al., 2002; Machín et al., 2010). The Alboran Sea, located in the western Mediterranean, is part of the IBI do-

Published by Copernicus Publications.

Table 1. List of Copernicus Marine products used for the computation of currents in the Iberia–Biscay–Ireland (IBI) region.

Product ref. no.	Product ID Acronym Type	Data access	Documentation: QUID: Quality Information Document. PUM: Product User Manual.
1	GLOBAL_MULTIYEAR_PHY_001_030 (GLO-REA) Numerical models (reanalysis)	EU Copernicus Marine Service Product (2023a)	QUID: Drévillon et al. (2023a) PUM: Drévillon et al. (2023b)
2	IBI_MULTIYEAR_PHY_005_002 (IBI-REA) Numerical models (reanalysis)	EU Copernicus Marine Service Product (2022a)	QUID: Levier et al. (2022) PUM: Amo-Baladrón et al. (2022)
3	MULTIOBS_GLO_PHY_TSUV_3D_MYNRT_015_012 (GLO-ARM) Reprocessed observations	EU Copernicus Marine Service Product (2023b)	QUID: Greiner et al. (2023) PUM: Verbrugge(2023)
4	NWSHELF_MULTIYEAR_PHY_004_009 (NWS-REA) Numerical models (reanalysis)	EU Copernicus Marine Service Product (2021)	QUID: Renshaw et al. (2021) PUM: Tonani et al. (2022)
5	MEDSEA_MULTIYEAR_PHY_006_004 (MED-REA) Numerical models (reanalysis)	EU Copernicus Marine Service Product (2022b)	QUID: Escudier et al. (2022) PUM: Lecci et al. (2022)

main. There, the Atlantic surface inflow through the Strait of Gibraltar causes an eastward flow of modified Atlantic Water, forming Western Mediterranean Water. This eastward flow is constrained near the African coast after passing the Almería–Oran front (Tintoré et al., 1988; Benzohra and Millot, 1995; Font et al., 1998), creating the Algerian Current (Font et al., 1998; Sotillo et al., 2016).

The variability of ocean currents in the IBI domain is relevant to the global thermohaline circulation and other climatic and environmental issues. For example, as discussed by Fasullo and Trenberth (2008), subtropical gyres play a crucial role in the meridional energy balance. The poleward salt transport of Mediterranean Water, driven by subsurface slope currents, has significant implications for salinity anomalies in the Rockall Trough and the Nordic Seas, as studied by Holliday (2003), Holliday et al. (2008), and Bozec et al. (2011). The Algerian current serves as the sole pathway for Atlantic Water to reach the western Mediterranean. Furthermore, the mixing processes between the Antarctic Intermediate Water and the Mediterranean Water in the African continental slope influences the salinity and nutrient concentration of the Mediterranean Water as it spreads into the North Atlantic (van Aken, 2000; Machín et al., 2010; de Pascual-Collar, 2019). Additionally, ocean currents also influence the spreading of biological populations (Daewel et al., 2008)

Since the main portion of oceanic transports occurs beneath the surface, one of the primary challenges in monitoring ocean currents is the scarcity of observational data for subsurface transport. In this context, modeling data offer a valuable alternative by providing physically consistent results in regions with sparse observations. Additionally, due to modeling data being provided in static grids, the operational computation of oceanic water mass transport is simplified. However, it is worth noting that modeling results at these intermediate and deep levels have a limited level of validation. To address this issue, ensemble approaches can be employed to estimate the uncertainties of the results, thereby improving the reliability of the findings.

In addition to climate-related regional applications, such long-term monitoring of currents in the IBI region can be of great interest for ocean-related activities for which information on regional current variability can enhance decision-making processes in the blue economy sectors (Rayner et al., 2019). This is particularly useful for maritime navigation and safety (Rayner et al., 2019), the fight against pollution, fisheries, aquaculture, marine renewable energy (Cavagnaro et al., 2020), and scientific research. By understanding the dynamics of ocean currents, stakeholders in these sectors would be able to optimize their operations, improving safety as well as planning and developing more sustainable practices. The availability of accurate and up-to-date information on regional ocean currents would contribute to the overall efficiency and effectiveness of ocean-related activities in the IBI region.

The aim of this work is to provide a pool of multi-product OMIs (ocean monitoring indicators) focused on monitoring the activity of the main currents described in the Iberia–Biscay–Ireland regional seas. To this aim, several monitoring vertical sections are proposed, and anomalies of transverse water transports are computed, providing information on the variability and trends of the monitored regional currents.

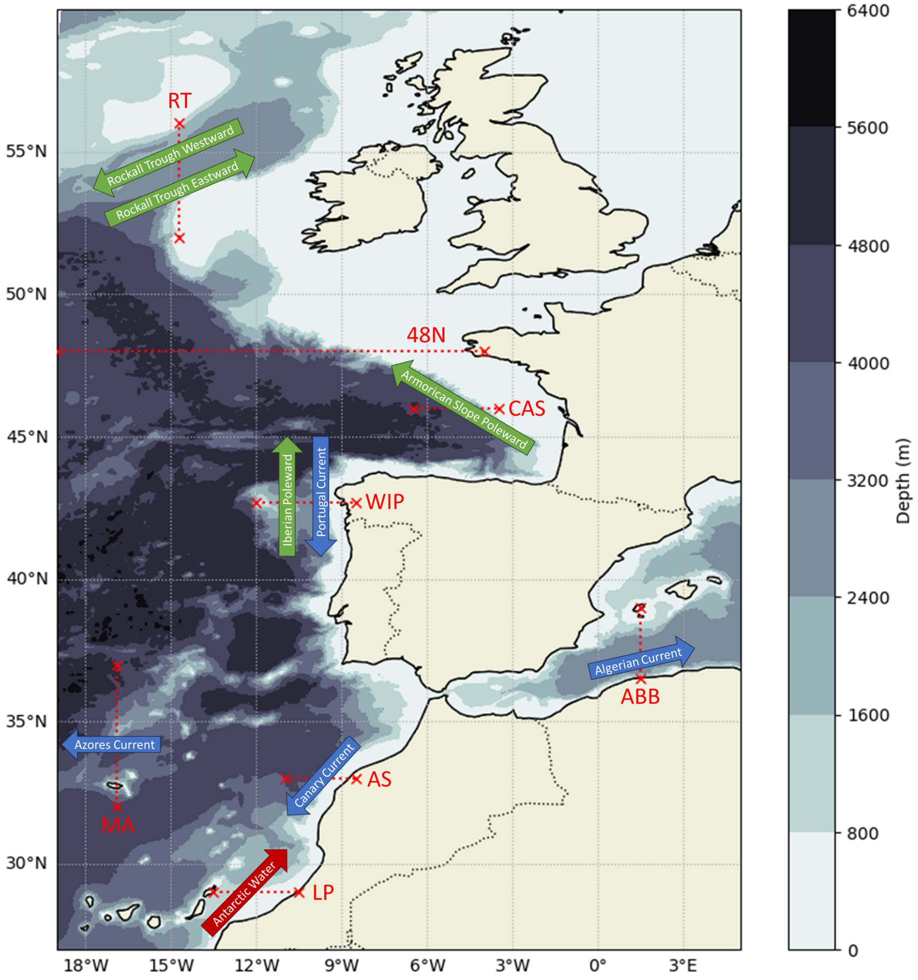

Figure 1. Bathymetry of the IBI domain. Dotted red lines indicate the location and acronyms of the sections used to calculate the mean transverse velocity: RT (Rockall Trough), 48N (48° N), CAS (Celtic–Armorican Slope), WIP (West Iberian Peninsula), ABB (Algerian–Balearic Basin), AS (African Slope), MA (Madeira), and LP (Lanzarote Passage). Arrows represent the currents monitored in each section, categorized by an arbitrary color scheme: blue arrows indicate upper levels (0–500 m), green arrows indicate intermediate depths (500–1500 m), and red arrows indicate deep levels (>1500 m).

2 Data and methods

The present study proposes a methodology to monitor the main ocean currents in the IBI region. This is achieved by analyzing the velocity field in the region and proposing representative monitoring windows where the volume transport is monitored. Since the proposed monitoring windows are defined to follow specific water masses, they are defined not only according to the spatial representativeness of the region but also defining a range of specific densities representative of the targeted water mass.

In order to provide an ensemble-based final result, five Copernicus products listed and referenced in Table 1 have been used. Among these products, there are four reanalysis products (GLO-REA, IBI-REA, NWS-REA, and MED-REA) and one product obtained from reprocessed observations (GLO-ARM).

To perform monitoring of the currents described in the Introduction, some vertical sections have been defined (see geographical locations in Fig. 1 and further details in Table 2). These sections have been proposed based on the existing bibliographic description of the main currents occurring in the IBI region. Therefore, the RT (Rockall Trough) section has been defined to monitor zonal transports of Mediterranean-origin water towards the North Sea (Holliday et al., 2008; Lozier and Stewart, 2008). The N48 section has been included to monitor total transports along the parallel 48° N; this section corresponds to another OMI operationally delivered by the Copernicus Marine Service (EU Copernicus Marine Service Product, 2019) but computed in the IBI domain. The CAS (Celtic–Armorican Slope) section has been defined to monitor northward flows along the European continental shelf (Fricourt et al., 2007). The WIP (West Iberian Peninsula) section aims to study both the northwards flow of intermediate Mediterranean Water known as the Iberian Poleward Current (Daniault et al., 1994; Mazé et al., 1997; Fricourt et al., 2007) and the southwards wind-induced surface flows along the Portuguese coast also known as the Portugal Current (Pérez et al., 2001). The ABB (Algerian–Balearic Basin) section has been defined to analyze the behavior of the Algerian Current (Tintoré et al, 1988; Benzohra and Millot, 1995; Font et al., 1998). The AS (African Slope) section has been defined to monitor surface transports induced by the trade winds along the coasts of the African continent, commonly known as the Canary Current (Knoll et al., 2002; Mason et al., 2011). Similarly, the MA (Madeira) section is intended to monitor westward zonal surface flows near the island of Madeira, commonly referred to as the Azores Current (Mason et al., 2011). Finally, the LP (Lanzarote Passage) section has been defined to monitor the flow of deep Antarctic Water between the African continental shelf and the Canary Islands (Knoll et al., 2002; Machín et al., 2010).

The OMI defined in this study aims to monitor currents by calculating volume transport anomalies in specific layers inside the previously described vertical sections. Since all the products used are in a gridded format, the vector field of transports is computed by multiplying the velocity field components by the cross-sectional area of the calculation grid cells for each product. As each product is provided on a particular grid with a specific resolution, this step is performed using the grid mesh of each product.

Within each section (i.e., RT, 48N, CAS, WIP, AAB, MA, AS, MA, and LP), the signal of each flow associated with specific water masses to be monitored has been identified. This identification is based on the oceanographic description of the region obtained from the literature. Figure 2 presents the results of transverse velocity obtained in the vertical sections defined in Fig. 1. The meridional section defined in Rockall Trough (RT) reveals two regions exhibiting intense and opposing zonal transports: the southern area (situated between approximately 53 and 54° N), characterized by the eastward transport of modified Mediterranean Water into the Nordic Seas, and the northern side, located between latitudes approximately 55.5 and 56° N, displaying subsurface westward transport emanating from Rockall Trough. This observed pattern aligns with the cyclonic circulation previously described in the trough by New and Smythe-Wright (2001). The section defined along parallel 48° N (48N) has been included to compute the same results as other OMIs computed by the Copernicus Marine Service (EU Copernicus Marine Service Product, 2019). This section has not been defined to compute the transport of a specific current but to compute the total southward transport along this latitude. The zonal section defined in the Celtic–Armorican Slope (CAS) depicts a subsurface poleward flow attached to the continental slope, with maximum intensity of the current located at 1000 m depth. The northward flow affects the complete water column, from a few hundred meters to the bottom. The zonal section proposed in the western Iberian Peninsula (WIP) displays a subsurface poleward flow with maximum speed close to the continental slope and a surface equatorward current affecting waters over the continental platform of Portugal. The meridional section between Algeria and the Balearic Islands (Algerian–Balearic Basin; ABB) shows two well-defined currents: the eastward (positive values) current attached to the Algerian coast and westward transport along the Spanish Mediterranean coast. The meridional section north of Madeira (MA) has been defined to monitor the so-called Azores Current. This current is reflected as an eastward transport seen in upper layers (up to 600 m depth), with the center part of the current being influenced (and almost split) by the presence of a sea mountain north of the Azores; below 600 m depth transports are strongly influenced by bathymetry. The zonal section defined in the African Slope (AS) displays a similar structure as the section in the western Iberian Peninsula, marked by an equatorward surface flow over the continental shelf, corresponding to the so-called Canary Current, and an opposite subsurface northward flow attached to the continental slope. The zonal section defined in the Lanzarote Passage (LP) exhibits a clear poleward transport close to the continental slope, and this transport is split into two levels; the upper–intermediate level comprises from 200 up to 550 m depth and corresponds to the slope poleward current seen in other sections (such as the African Slope, western Iberian Peninsula and Celtic–Armorican Slope). The intermediate–deeper level of the poleward current seen in the Lanzarote Passage section comprises the waters from 550 m depth up to the bottom and is associated with the flows of Antarctic Intermediate Water.

The consistency of the mean transverse velocity in vertical sections found in Fig. 1 and the described currents in the literature provide the support for proposing the lateral boundaries of the monitoring windows defined in Table 2 and marked with vertical dashed green lines in Fig. 2: Rockall Trough Eastward (RTE), Rockall Trough Westward (RTW), Armorican Slope Poleward (ASP), Iberian slope Poleward (IBP), Portugal Current (PC), Algerian Current (ALC), Azores Current (AC), Canary Current (CC), and Antarctic Water (AW). It is worth mentioning that no monitoring windows have been included in the N48 section since the generated OMI will compute the total transport along the 48° N parallel.

Since the tracked currents involve specific water masses, that the vertical boundaries of the monitoring windows are considered to exhibit vertical variability. Thus, the vertical boundaries of the monitoring windows have been defined based on the upper and lower density layers characterizing each monitored water mass. Given that the density field exhibits temporal variability within each product, the vertical boundaries of each window are dynamic, adapting to the oscillations in the ocean's density field. To find these vertical limits, T–S diagrams have been calculated for each monitoring window, temporally averaged over the period 1993–2021. Figure 3 shows the calculated T–S diagrams for each monitoring window using the IBI-REA product. The solid

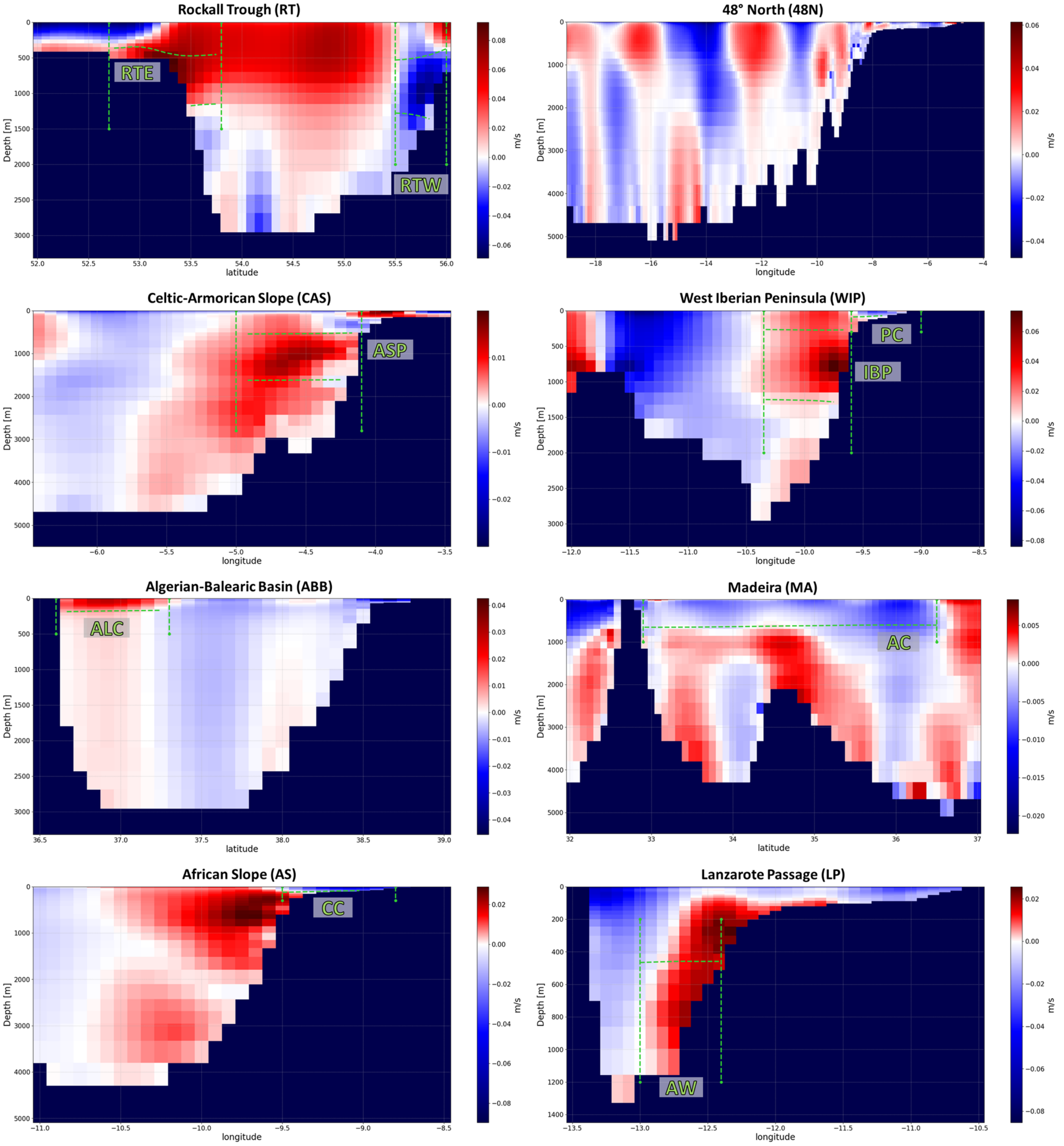

Rockall Trough (RT)

48° North (48N)

Celtic-Armorican Slope (CAS)

West Iberian Peninsula (WIP)

Algerian-Balearic Basin (ABB)

Madeira (MA)

African Slope (AS)

Lanzarote Passage (LP)

Figure 2. Mean vertical sections of transverse velocity along the transects defined in Fig. 1 computed from IBI-REA over the period 1993–2021. Green dashed lines correspond to the monitoring windows defined to describe the variability of the currents defined. RTW: Rockall Trough Westward, RTE: Rockall Trough Eastward, ASP: Armorican Slope Poleward, IBP: Iberian Poleward, PC: Portugal Current, ALC: Algerian Current, CC: Canary Current, AC: Azores Current, and AW: Antarctic Water.

Table 2. Description of the monitoring windows used to compute the ocean current OMI. Min and max values of latitude, longitude, and density anomaly are detailed (sfc used for surface, sfl for seafloor).

Section (Fig. 1)	Monitoring window (Fig. 2)	Latitude	Longitude	Density $(\mathrm{g\,m^{-3}})$	CMEMS products
Rockall Trough (RT)	Rockall Trough Westward (RTW) Rockall Trough Eastward (RTE)	55.5/56.0 52.7/53.8	−14.7 −14.7	27.32/27.7 27.25/27.65	GLO-REA IBI-REA GLO-ARM NWS-REA
Celtic–Armorican Slope (CAS)	Armorican Slope Poleward (ASP)	46.0	−5.0/−4.1	27.25/27.8	
West Iberian Peninsula (WIP)	Iberian Poleward (IBP) Portugal Current (PC)	42.7 42.7	−10.35/−9.6 −9.6/−9.0	27.1/27.75 Sfc/26.9	
Algerian–Balearic Basin (ABB)	Algerian Current (ALC)	36.6/37.3	1.5	Sfc/28.50	GLO-REA IBI-REA GLO-ARM MED-REA
Madeira (MA)	Azores Current (AC)	32.9/36.5	−16.9	Sfc/27.25	GLO-REA IBI-REA GLO-ARM
African Slope (AS)	Canary Current (CC)	33.0	−9.5/−8.8	Sfc/26.7	
Lanzarote Passage (LP)	Antarctic Water (AW)	29.0	−13/−12.4	27.1/Sfl	

density lines marked on each diagram indicate the boundaries that have been selected to define the water mass characterizing each current. Additionally, these density boundaries are also represented in Fig. 2 as horizontal dashed lines in green. Since there are some monitoring windows whose vertical boundaries may be defined by the surface (PC, CC, AC, and ALC windows) or the seafloor (AW window), some panels in Fig. 3 show a single density line. Table 2 presents the density-defined vertical boundaries used for each window, including windows with the surface or seafloor as their vertical limit.

Subsequently, the transport estimates are integrated within each defined monitoring window on a monthly basis. As explained earlier, the vertical boundaries of the monitoring windows are dynamic and defined based on specific density layers. The UNESCO equations (Fofonoff and Millard, 1983) are used to estimate the density field from the salinity and potential temperature fields of each product. Thus, each monitoring window is defined at each time step with fixed lateral boundaries (defined as static latitude–longitude locations) and variable vertical boundaries that may vary in time according to vertical oscillations of the density field (Table 2).

After spatial integration, an estimated transport time series is obtained for each product and each monitoring window. Since the proposed OMI aims to focus on interannual and longer timescales, seasonal variability is filtered out, with the data being processed as anomalies by removing the monthly mean from each value, using the climatological average of the time series in the period 1993–2021 as a reference.

Finally, outcomes from the different products are combined to produce an ensemble showing the mean of all products and the standard deviation. Since not all Copernicus products used in this study cover the entire IBI region, some products cannot be used for current monitoring in certain monitoring windows (Table 2 provides a list of the products used to monitor transports in each section).

3 Results and discussion

The anomaly of volume transports in specific monitoring windows (relative to the monthly mean transport between 1993 and 2021) is proposed as an OMI for each regional current (Fig. 4). The uncertainty is assessed by the estimation of indicators with several different Copernicus Marine products (OMIs are estimated with the more complete set of products available in each monitoring window; see Table 2); the higher the agreement of results provided by diverse systems, the higher the statistical robustness.

The interpretation of the OMI results presented in Fig. 4 should be done considering that the calculated average transports include the sign of the current velocity vector (positive for northward and eastward transports, and vice versa). Therefore, the anomalies shown in the OMI should be interpreted following the same sign convention. Thus, a positive anomaly can indicate an intensification, weakening, or even a reversal of the current. These options can be deduced from the dashed red line included in each plot. It represents the mean value of transport (with the sign reversed); thus, it aligns with the anomaly value that nullifies the transport across the monitoring window. Beyond this line, the transport reverses, indicating a transport in the opposite direction. Among the proposed monitoring windows, RTE, ASP, IBP, AW, and ALC exhibit a positive mean velocity, so positive transport anomalies imply an intensification of the current. On the other hand, the RTW, PC, CC, AC, and N48 moni-

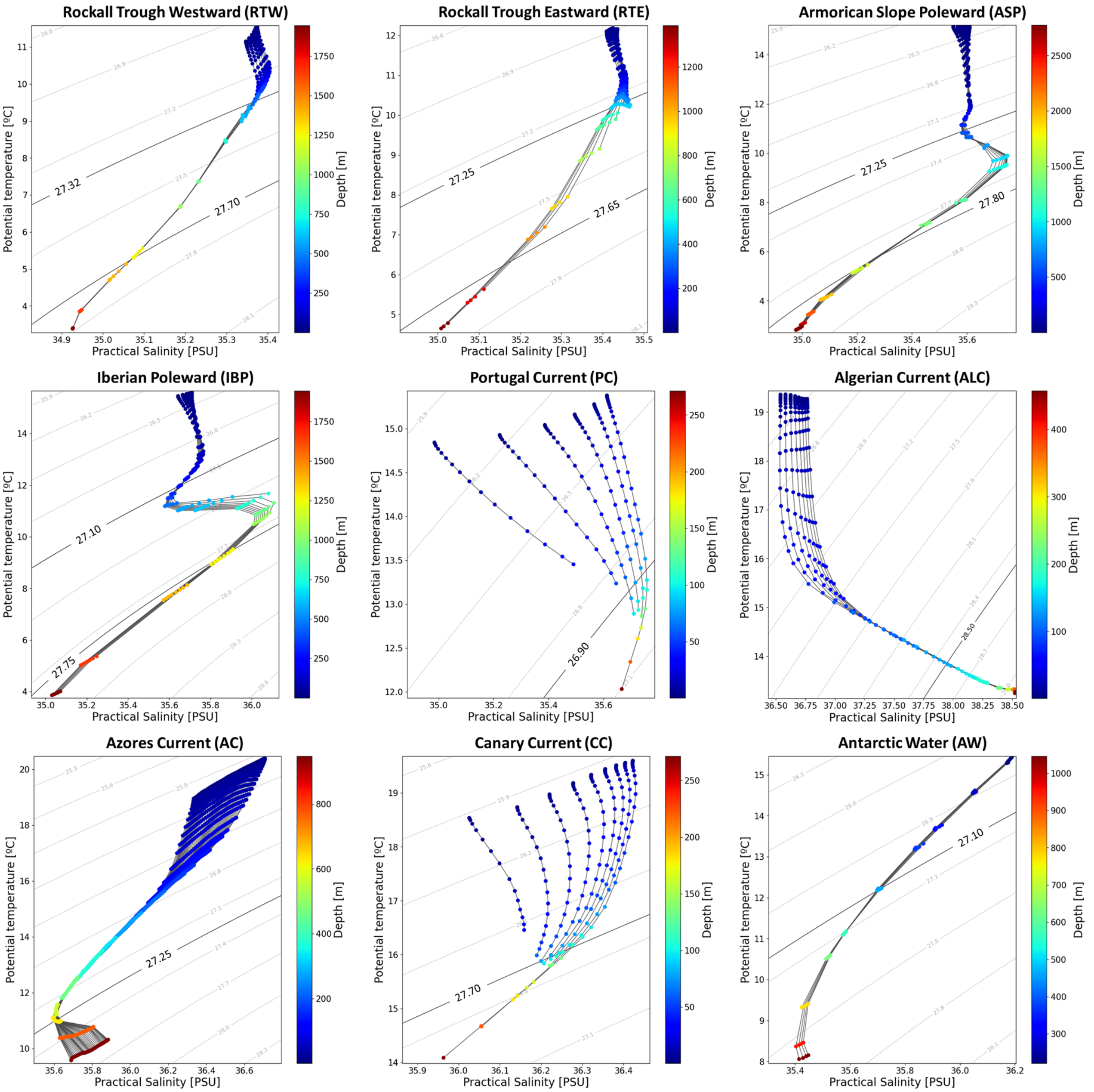

Figure 3. Averaged θ/S diagrams computed on the monitoring sections using IBI-REA product data over the period 1993–2021. Traces correspond to each vertical profile included on the corresponding monitoring window. The diagrams include the anomaly of potential density field (shown as dotted gray lines), with the vertical boundaries of each monitoring section being represented by the continuous black lines. The diagrams that have a single continuous line correspond to monitoring windows where one of the vertical levels is defined as the surface or seafloor (see Table 2).

toring windows show negative mean transport values, where intensification of the current is represented by negative transport anomalies.

Analyzing the uncertainties of the time series, it can be observed that differences among the products sometimes hinder the detection of significant anomalies. This is the case for the ASP, IBP, PC, and AW currents, for which anomalies exceeding the data dispersion are scarce. Conversely, there are other monitoring windows where a lower data dispersion allows for a more precise estimation of the overall variability. This is the case for the CC and ALC currents, where, due to being more stable and shallower currents, the uncertainties are

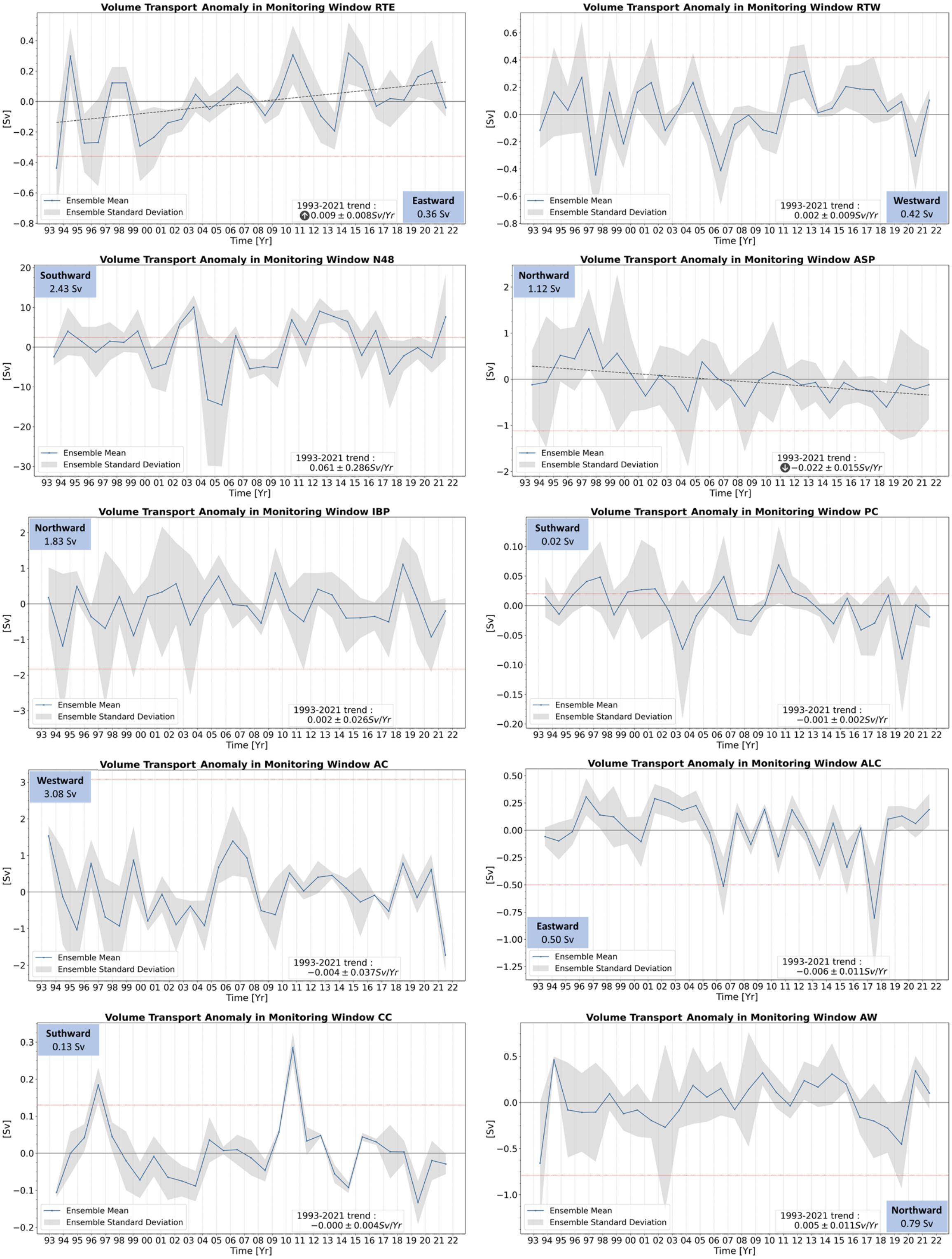

Figure 4. Annual anomalies of cross-section volume transport averaged in monitoring windows RTE, RTW, N48, ASP, IBP, PC, AC, ALC, CC, and AW. Time series are computed and averaged from different Copernicus Marine products for each window (see Table 2), providing a multi-product result. The blue line represents the ensemble mean, and shaded gray areas represent the standard deviation of the ensemble. Blue boxes include the direction of the current and mean transport computed in the period 1993–2021. Dashed red lines depict the velocity value at which the direction of the current reverses. This aligns with the average transport value (with sign reversed) and the point where absolute transport becomes zero. The analysis of trends (at 95 % confidence interval) computed in the period 1993–2021 is included (bottom right box). Trend lines (dashed gray line) are only included in the figures when a significant trend is obtained.

generally smaller than the magnitude of the anomalies. In the remaining monitoring windows (RTE, RTW, AC, and 48N), uncertainties are considerable but sufficiently low, allowing identification of specific events with pronounced variability. In this regard, examples of events of negative anomalies (1995–1996, 1999) and positive anomalies (2010 and 2014) in the RTE section, as well as the positive anomaly of the Azores Current (AC) in 2006 and the anomalous transports along the N48 section in 2003 and 2012, can be highlighted.

The uncertainty of the results also enables the detection of periods during which it can be assumed that the transport within a monitoring window is nonsignificant or null. These are periods in which the uncertainty of the data includes the threshold for null transport. Similarly, it is possible to identify periods in which the current reverses, leading to a significant reverse transport. These periods are characterized by both the ensemble mean and the range of uncertainties being greater than the zero-transport threshold. With this type of analysis, it is possible to detect currents that (i) exhibit occasional halts in transport, as seen in the cases of RTW, ASP, ALC, or AW, where there are years when the net transport is not significant; (ii) display levels of uncertainty sufficiently high to conceal the presence of the current for the majority of the study period (N48 or PC); or (iii) demonstrate significant reversals of the current in specific years, such as the case of CC in 1996 and 2010.

Analyzing the trends in the OMIs, Fig. 4 shows the absence of statistically significant trends in most of the monitoring sections. However, the sections related to the Mediterranean Water flow along the continental shelf do exhibit opposite trends, where the ASP window indicates a decrease of 0.02 $\mathrm{Sv\,yr^{-1}}$ in northward flow along the Celtic–Armorican Slope and an intensification of transport towards the Scandinavian seas of 0.01 $\mathrm{Sv\,yr^{-1}}$.

4 Conclusions

This study proposes a methodology for defining OMIs to monitor variability of the main ocean currents in the IBI region. The objective is to describe the strengths and weaknesses of the associated transports through the proposed indicator. The methodology used to define the OMI involves utilizing various Copernicus Marine products, which allows for an ensemble analysis that not only provides information on the currents, but also yields an assessment of associated uncertainties.

The proposed indicator is based on the definition of monitoring spatial windows that are representative of the overall transport of the current. These spatial windows are defined based on two criteria. Firstly, horizontal boundaries are determined using initially bibliographic criteria and by detection of the targeted currents in the averaged velocity fields. Secondly, vertical limits are defined based on the observed density of water masses. With this methodology, vertical limits of the monitoring window are not statically defined but are adaptive to the inherent vertical variability of water masses.

The results have demonstrated that the OMI is capable of monitoring the targeted regional currents with varying degrees of uncertainty. The different products used show higher agreement in shallower and more persistent currents, while the indicator exhibits more uncertainties when monitoring deep currents or those with higher temporal variability. Nevertheless, and despite the magnitude of the uncertainties, the OMI is able to detect periods of high or low activity in six of the proposed monitoring windows (RTE, RTW, CC, AC, ALC, and N48). Outstanding events, including periods of low activity in the Canary Current (in 1996 and 2010) and in the Azores Current in 2006, as well as a significant intensification of transports associated with the Azores Current in 2021, have been observed.

The OMI also allows detection of statistically significant trends in some of the monitoring spatial windows. Specifically, the RTE and ASP windows show opposite trends in water transports, while there is a transport increase towards the Nordic Seas in the Rockall Trough and a decrease in Mediterranean Water transported northward through the Celtic–Armorican continental slope.

Finally, this study highlights the utility of model data products for monitoring ocean currents. This methodology is particularly relevant for tracking deep currents where observational data availability is limited. The proposed methodology may have a further application in a variety of contexts, such as maritime navigation, fishing, aquaculture, marine renewable energy, and general scientific research. Indeed, the next steps in these fields will involve expanding the methodology to monitor not only water transports, but also the transports of other properties, such as ocean heat transport, freshwater and salt transports, or other biogeochemical properties, enhancing the interest in such OMIs for specific fields, such as the study of planetary climate variability.

Code availability. The software used for this work is the property of NOW Systems S.L. The methodology strictly describes all the steps followed to develop this code. Anyone interested in accessing this software should contact the corresponding author.

Data availability. The data used in this work have been obtained from the Copernicus Marine Service. All the mentioned databases are accessible through the Copernicus Marine Service. Their references can be found in the product tables (Table 1).

Author contributions. All authors have contributed to the completion of this work. MGS and RA participated in the conceptualization, methodology, and writing (review and editing) phases. BL contributed to the conceptualization, methodology, validation, and writing (review and editing) stages. Finally, ÁdPC coordinated

the work and also participated in the formal analysis, methodology, software development, and writing (original draft preparation).

Competing interests. The contact author has declared that none of the authors has any competing interests.

Acknowledgements. This work has been conducted under contract number 21002L6-COP-MFC IBI-5600 as part of the ongoing partnership between Nologin and Mercator Ocean International. The authors acknowledge the Copernicus Marine Service for access to the datasets used on this work. Additionally, the helpful comments of anonymous referees are gratefully acknowledged.

Financial support. This research has been supported by contract number 21002L6-COP-MFC IBI-5600 as part of the ongoing partnership between Nologin and Mercator Ocean International.

Review statement. This paper was edited by Marta Marcos and reviewed by two anonymous referees.

References

Amo-Baladrón, A., Levier, B., Aznar, R., and Sotillo, M. G.: Copernicus Marine Service Product User Manual for the Atlantic -Iberian Biscay Irish- Ocean Physics Reanalysis, IBI_MULTIYEAR_PHY_005_002, Issue 4.1, Mercator Ocean International, https://catalogue.marine.copernicus.eu/documents/PUM/CMEMS-IBI-PUM-005-002.pdf (last access: 29 April 2024), 2022.

Benzohra, M. and Millot, C.: Characteristics and circulation of the surface and intermediate water masses off Algeria, Deep-Sea Res. Pt. I, 42, 1803–1830, https://doi.org/10.1016/0967-0637(95)00043-6, 1995.

Bower, A. S., Le Cann, B., Rossby, T., Zenk, T., Gould, J., Speer, K., Richardson, P. L., Prater, M. D., and Zhang, H.-M.: Directly measured mid-depth circulation in the northeastern North Atlantic Ocean, Nature, 419, 603–607, https://doi.org/10.1038/nature01078, 2002.

Bozec, A., Lozier, M. S., Chasignet, E. P., and Halliwel, G. R.: On the variability of the Mediterranean Outflow Water in the North Atlantic from 1948 to 2006, J. Geophys. Res.-Oceans, 116, C09033, https://doi.org/10.1029/2011JC007191, 2011.

Cavagnaro, R. J., Copping, A. E., Green, R., Greene, D., Jenne, S., Rose, D., and Overhus, D.: Powering the blue economy: Progress exploring marine renewable energy integration with ocean observations, Mar. Technol. Soc. J., 54, 114–125, https://doi.org/10.4031/MTSJ.54.6.11, 2020.

Daewel, U. T. E., Peck, M. A., Kuehn, W., St. John, M. A., Alekseeva, I., and Schrum, C.: Coupling ecosystem and individual-based models to simulate the influence of environmental variability on potential growth and survival of larval sprat (*Sprattus sprattus* L.) in the North Sea, Fish. Oceanogr., 17, 333–351, https://doi.org/10.1111/j.1365-2419.2008.00482.x, 2008.

Daniault, N., Mazé, J. P., and Arhan, M.: Circulation and mixing of Mediterranean Water west of the Iberian Peninsula, Deep-Sea Res. Pt. I, 41, 1685–1714, https://doi.org/10.1016/0967-0637(94)90068-X, 1994.

de Pascual-Collar, Á., G. Sotillo, M., Levier, B., Aznar, R., Lorente, P., Amo-Baladrón, A., and Álvarez-Fanjul, E.: Regional circulation patterns of Mediterranean Outflow Water near the Iberian and African continental slopes, Ocean Sci., 15, 565–582, https://doi.org/10.5194/os-15-565-2019, 2019.

Drévillon, M., Lellouche, J.-M., Régnier, C., Garric, G., Bricaud, C., Hernandez, O., and Bourdallé-Badie, R.: EU Copernicus Marine Service Product Quality Information Document for the Global Ocean Physics Reanalysis, GLOBAL_MULTIYEAR_PHY_001_030, Issue 1.6, Mercator Ocean International, https://catalogue.marine.copernicus.eu/documents/QUID/CMEMS-GLO-QUID-001-030.pdf (last access: 29 April 2024), 2023a.

Drévillon, M., Fernandez, E., and Lellouche J. M.: Copernicus Marine Service Product User Manual for the Global Ocean Physics Reanalysis, GLOBAL_MULTIYEAR_PHY_001_030, Issue 1.5, Mercator Ocean International, https://catalogue.marine.copernicus.eu/documents/PUM/CMEMS-GLO-PUM-001-030.pdf (last access: 29 April 2024), 2023b.

Escudier, R., Clementi, E., Nigam, T., Aydogdu, A., Fini, E., Pistoia, J, Grandi, A., and Miraglio, P.: Copernicus Marine Service Product Quality Information Document for the Mediterranean Sea Physics Reanalysis, MEDSEA_MULTIYEAR_PHY_006_004, Issue 2.3, https://catalogue.marine.copernicus.eu/documents/QUID/CMEMS-MED-QUID-006-004.pdf (last access: 29 April 2024), 2022.

EU Copernicus Marine Service Product: Mean Volume Transport across sections from Reanalysis, Mercator Ocean International [data set], https://doi.org/10.48670/moi-00247, 2019.

EU Copernicus Marine Service Product: Atlantic- European North West Shelf- Ocean Physics Reanalysis, Mercator Ocean International [data set], https://doi.org/10.48670/moi-00059, 2021.

EU Copernicus Marine Service Product: Atlantic-Iberian Biscay Irish- Ocean Physics Reanalysis, Mercator Ocean International [data set], https://doi.org/10.48670/moi-00029, 2022a.

EU Copernicus Marine Service Product: Mediterranean Sea Physics Reanalysis, Mercator Ocean International [data set], https://doi.org/10.25423/CMCC/MEDSEA_MULTIYEAR_PHY_006_004_E3R1, 2022b.

EU Copernicus Marine Service Product: Global Ocean Physics Reanalysis, Mercator Ocean International [data set], https://doi.org/10.48670/moi-00021, 2023a.

EU Copernicus Marine Service Product: Multi Observation Global Ocean 3D Temperature Salinity Height Geostrophic Current and MLD, Mercator Ocean International [data set], https://doi.org/10.48670/moi-00052, 2023b.

Fasullo, J. T. and Trenberth, K. E.: The annual cycle of the energy budget. Part II: Meridional structures and poleward transports, J. Climate, 21, 2313–2325, https://doi.org/10.1175/2007JCLI1936.1, 2008.

Fofonoff, N. P. and Millard Jr., R. C.: Algorithms for the computation of fundamental properties of seawater. Paris, France, UNESCO, UNESCO Technical Papers in Marine Sciences; 44, 53 pp., https://doi.org/10.25607/OBP-1450, 1983.

Font, J., Millot, C., Salas, J., Juliá, A., and Chic, O.: The drift of Modified Atlantic Water from the Alboran Sea to the eastern Mediterranean, Sci. Mar., 62, 211–216, https://doi.org/10.3989/scimar.1998.62n3211, 1998.

Friocourt, Y., Levier, B., Speich, S., Blanke, B., and Drijfhout, S. S.: A regional numerical ocean model of the circulation in the Bay of Biscay, J. Geophys. Res., 112, C09008, https://doi.org/10.1029/2006JC003935, 2007.

Greiner, E., Verbrugge, N., Mulet, S., and Guinehut, S.: EU Copernicus Marine Service Product Quality Information Document for the Multi Observation Global Ocean 3D Temperature Salinity Heights Geostrophic Currents and MLD, MULTIOBS_GLO_PHY_TSUV_3D_MYNRT_015_012, Issue 1.2, Mercator Ocean International, https://catalogue.marine.copernicus.eu/documents/QUID/CMEMS-MOB-QUID-015-012.pdf (last access: 29 April 2024), 2023.

Holliday, N. P.: Air-sea interactionand circulation changes in the north-east Atlantic, J. Geophys. Res., 108, 3259, https://doi.org/10.1029/2002JC001344, 2003.

Holliday, N. P., Hughes, S. L., Bacon, S., Beszczynska-Möller, A., Hansen, B., Lavín, A., Loeng, H., Mork, K. A., Østerhus, S., Sherwin, T., and Walczowski, W.: Reversal of the 1960s to 1990s freshening trend in the northeast North Atlantic and Nordic Seas, Geophys. Res. Lett., 35, L03614, https://doi.org/10.1029/2007GL032675, 2008.

Jia, Y.: Formation of an Azores Current Due to Mediterranean Overflow in a Modeling Study of the North Atlantic, J. Phys. Oceanogr., 30, 9, 2342–2358, https://doi.org/10.1175/1520-0485(2000)030<2342:FOAACD>2.0.CO;2, 2000.

Knoll, M., Hernández-Guerra, A., Lenz, B., López Laatzen, F., Machín, F., Müller, T. J., and Siedler, G.: The Eastern Boundary Current system between the Canary Islands and the African Coast, Deep-Sea Res. Pt. I, 49–17, 3427–3440, https://doi.org/10.1016/S0967-0645(02)00105-4, 2002.

Lecci, R., Drudi, M., Grandi, A., Cretì, S., and Clementi, E.: Copernicus Marine Service Product User Manual for Mediterranenan Sea Physics Reanalysis, MEDSEA_MULTIYEAR_PHY_006_004, Issue 2.3, https://catalogue.marine.copernicus.eu/documents/PUM/CMEMS-MED-PUM-006-004.pdf (last access: 29 April 2024), 2022.

Levier, B., Reffray, G., Sotillo, M.G.: EU Copernicus Marine Service Product Quality Information Document for the Atlantic-Iberian Biscay Irish- Ocean Physics Reanalysis, IBI_MULTIYEAR_PHY_005_002, Issue 5.1, Mercator Ocean International, https://catalogue.marine.copernicus.eu/documents/QUID/CMEMS-IBI-QUID-005-002.pdf (last access: 29 April 2024), 2022.

Lozier, M. S. and Stewart, N. M.: On the temporally varying penetration ofMediterranean overflowwaters and eastward penetration ofLabrador Sea Water, J. Phys. Oceanogr., 38, 2097–2103, https://doi.org/10.1175/2008JPO3908.1, 2008.

Machín, F., Pelegrí, J. L., Fraile-Nuez, E., Vélez-Belchí, P., López-Laatzen, F., and Hernández-Guerra, A.: Seasonal Flow Reversals of Intermediate Waters in the Canary Current System East of the Canary Islands, J. Phys. Oceanogr., 40, 1902–1909, https://doi.org/10.1175/2010JPO4320.1, 2010.

Mason, E., Colas, F., Molemaker, J., Shchepetkin, A. F., Troupin, C., McWilliams, J. C., and Sangra, P.: Seasonal variability of the Canary Current: A numerical study, J. Geophys. Res.-Oceans, 116, C06001, https://doi.org/10.1029/2010JC006665, 2011.

Mazé, J. P., Arhan, M., Mercier, H., Volume budget of the eastern boundary layer off the Iberian Peninsula, Deep-Sea Res. Pt. I, 44, 1543–1574, https://doi.org/10.1016/S0967-0637(97)00038-1, 1997.

New, A. L. and Smythe-Wright, D.: Aspects of the circulation in the Rockall Trough, Cont. Shelf Res., 21, 777–810, https://doi.org/10.1016/S0278-4343(00)00113-8, 2001.

Pascual, A., Levier ,B., Sotillo, M., Verbrugge, N., Aznar, R., and Le Cann, B.: Characterization of Mediterranean Outflow Water in the Iberia-Gulf of Biscay-Ireland region, in: von Schuckmann et al. (2018) The Copernicus Marine Environment Monitoring Service Ocean State Report, J. Oper. Oceanogr., 11, S1–S142, https://doi.org/10.1080/1755876X.2018.1489208, 2018.

Peliz, A., Dubert, J., Marchesiello, P., and Teles-Machado, A.: Surface circulation in the Gulf of Cadiz: Model and mean flow structure, J. Geophys. Res.-Oceans, C11015, 112, https://doi.org/10.1029/2007JC004159, 2007.

Pérez, F. F., Castro, C. G., Álvarez-Salgado, X. A., and Ríos, A. F.: Coupling between the Iberian basin-scale circulation and the Portugal boundary current system: a chemical study, Deep-Sea Res. Pt. I, 48, 1519–1533, https://doi.org/10.1016/S0967-0637(00)00101-1, 2001.

Rayner, R., Jolly, C., and Gouldman, C.: Ocean observing and the blue economy, Frontiers in Marine Science, 6, 330, https://doi.org/10.3389/fmars.2019.00330, 2019.

Renshaw, R., Wakelin, S., Golbeck, I., and O'Dea, E.: Quality Information Document for the Atlantic–European North West Shelf- Ocean Physics Reanalysis, NWSHELF_MULTIYEAR_PHY_004_009, Issue 5.2, Mercator Ocean International, https://catalogue.marine.copernicus.eu/documents/QUID/CMEMS-NWS-QUID-004-009.pdf (last access: 5 July 2023), 2021.

Sotillo, M. G., Cailleau, S., Lorente, P., Levier, B., Aznar, R., Reffray, G., Amo-Baladrón, A., Chanut, J., Benkiran, M., and Alvarez-Fanjul, E.: The MyOcean IBI Ocean forecast and reanalysis systems: operational products and roadmap to the future Copernicus Service, J. Oper. Oceanogr., 8, 63–79, https://doi.org/10.1080/1755876X.2015.1014663, 2015.

Sotillo, M. G., Amo-Baladrón, A., Padorno, E., Garcia-Ladona, E., Orfila, A., Rodríguez-Rubio, P., Conti, D., Jiménez Madrid, J. A., de los Santos, F. J., and Alvarez Fanjul E.: How is the surface Atlantic water inflow through the Gibraltar Strait forecasted? A lagrangian validation of operational oceanographic services in the Alboran Sea and the Western Mediterranean, Deep-Sea Res. Pt. II, 133, 100–117, https://doi.org/10.1016/j.dsr2.2016.05.020, 2016.

Tintoré, J., La Violette, P. E., Blade, I., and Cruzado, A.: A study of an intense density front in the eastern Alboran Sea: the Almeria–Oran front, J. Phys. Oceanogr., 18, 1384–1397, https://doi.org/10.1175/1520-0485(1988)018<1384:ASOAID>2.0.CO;2, 1988.

Tonani, M., Ascione, I., and Saulter, A.: Product User Manual for the Atlantic- European North West Shelf- Ocean Physics Reanalysis, NWSHELF_MULTIYEAR_PHY_004_009, Issue 1.3, Mercator Ocean International, https://catalogue.marine.copernicus.eu/documents/PUM/CMEMS-NWS-PUM-004-009-011.pdf (last access: 5 July 2023), 2022.

van Aken, H. M.: The hydrography of the mid-latitude Northeast Atlantic Ocean II: The intermediate water masses, Deep-Sea Res. Pt. I, 47, 789–824, https://doi.org/10.1016/S0967-0637(99)00112-0, 2000.

Verbrugge, N.: Copernicus Marine Service Product User Manual for the Multi Observation Global Ocean 3D Temperature Salinity Heights Geostrophic Currents and MLD, MULTIOBS_GLO_PHY_TSUV_3D_MYNRT_015_012, Issue: 1.2, Mercator Ocean International, https://catalogue.marine.copernicus.eu/documents/PUM/CMEMS-MOB-PUM-015-012.pdf (last access: 29 April 2024), 2023.

White, M. and Bowyer, P.: The shelf-edge current northwest of Ireland, Ann. Geophys., 15, 1076–1083, https://doi.org/10.1007/s00585-997-1076-0, 1997.

State Planet, 4-osr8, 6, 2024
https://doi.org/10.5194/sp-4-osr8-6-2024

Statistical analysis of global ocean significant wave heights from satellite altimetry over the past 2 decades

Alice Laloue[1], **Malek Ghantous**[1], **Yannice Faugère**[1], **Alice Dalphinet**[2], **and Lotfi Aouf**[2]

[1]Collecte Localisation Satellites, Ramonville-Saint-Agne, 31520, France
[2]Météo-France, Toulouse, 31000, France

Correspondence: Alice Laloue (alaloue@groupcls.com)

Received: 28 July 2023 – Discussion started: 21 August 2023
Revised: 24 April 2024 – Accepted: 2 July 2024 – Published: 30 September 2024

Abstract. The analysis of global ocean surface waves and of long-term changes requires accurate time series of waves over several decades. Such time series have previously only been available from model reanalyses or from in situ observations. Now, altimetry provides a long series of observations of significant wave heights (SWHs) in the global ocean. The aim of this study is to analyse the climatology of significant wave heights and extreme significant wave heights derived from remote sensing in the global ocean and their long-term trends from 2002 to 2020 using different statistical approaches as the mean, the 95th percentile, and the 100-year return level of SWH. The mean SWH and the 95th percentile of SWH are calculated for two seasons: January, February, and March as well as July, August, and September and for each year. A trend is then estimated using linear regression for each cell in the overall grid. The 100-year return levels are determined by fitting a generalized Pareto distribution to all exceedances over a high threshold. The trend in 100-year return level is estimated using the transformed stationary approach, which, to our knowledge, is used for the first time to draw a global map based on altimetry. Predominantly large positive trends over 2002–2020 for both SWH and extreme SWH are mostly found in the Southern Hemisphere, including the South Atlantic, the Southern Ocean, and the southern Indian Ocean, which is consistent with previous studies. In the North Atlantic, SWH has increased poleward of 45° N, corroborating what was concluded in the Fifth IPCC Assessment Report; however, SWH has also largely decreased equatorward of 45° N in wintertime. The 100-year return levels of SWH have significantly increased in the North Atlantic and in the eastern tropical Pacific, where the cyclone tracks are located. Finally, in this study we find trends of SWH and 95th percentile of SWH over 2002–2020 to be much higher than those indicated in the literature for the period 1985–2018.

1 Introduction

Increasing our understanding of global ocean surface waves, their variability, and their long-term interannual changes is important to climate research and to ocean and coastal applications. As mentioned in the Sixth IPCC Assessment Report, waves contribute to extreme sea level events (Mentaschi et al., 2017), flooding (Storlazzi et al., 2018), and coastal erosion (Barnard et al., 2017). They modify the ocean circulation and mediate air–sea (Donelan et al., 1997) and sea–ice interactions (Thomas et al., 2019).

The analysis of long-term and interannual changes in ocean surface waves requires accurate time series of waves spanning several decades. Thus far these records have only been available in global model reanalyses or from in situ observations. Unfortunately, observations from buoys can only provide local analyses and in situ wave observations are especially lacking in the Southern Hemisphere. Altimeters offer global and high-quality measurements of significant wave heights (SWHs) (Gommenginger et al., 2002). The growing satellite record of SWH now makes global and long-term analyses more accessible than ever before.

Published by Copernicus Publications.

Table 1. Product table.

Product ref. no.	Product ID and type	Data access	Documentation
1	WAVE_GLO_PHY_SWH_L4_MY_014_007; Satellite observations	EU Copernicus Marine Service Product (2021)	Quality Information Document (QUID): Charles (2021) Product User Manual (PUM): Husson and Charles (2021)
2	WAVE_GLO_PHY_SWH_L4_NRT_014_003; Satellite observations	EU Copernicus Marine Service Product (2023)	Quality Information Document (QUID): Charles et al. (2023) Product User Manual (PUM): Mertz et al. (2022)

We use SWH observations from a multi-mission altimetric product over the period 2002–2020 to calculate global SWH and extreme SWH climatologies. Furthermore, trends in SWH and in extreme SWH are assessed. An identical analysis was performed with ERA5 (Hersbach et al., 2020) and WAVERYS (Law-Chune et al., 2021) reanalyses to compare with the literature. The multi-mission nature of our altimetric data, and their potential for bias, is then discussed in the context of long-term statistics.

2 Sea state datasets and methods

The level 4 (L4) altimetric time series of waves in the Copernicus Marine catalogue (Table 1, product reference 1) covers 19 years (2002–2020). It is based on Copernicus Marine Service multi-year L3 datasets and merges along-track measurements from seven different altimetric missions – Jason-1, Envisat, Jason-2, Cryosat-2, Saral/AltiKa, and CFOSat – and from up to four missions at the same time. Calibrated and filtered along-track measurements are then projected onto a 2° grid. Daily statistics (mean, maximum) are finally estimated for each grid cell.

We use this time series to calculate mean and extreme SWH climatologies and to assess long-term trends over the period 2002–2020. Meanwhile, the annual anomaly for 2022 is calculated as the difference between the climatology and the near-real-time time series (Table 1, product reference 2). The first part of our analysis is based on daily mean SWHs and 95th percentile (P_{95}) daily maximum SWHs over the globe. The 95th percentile is the value where only 5 % of the values in the time series are over it. Data are resampled in monthly mean and percentiles of SWH for each grid cell. The climatological mean SWH and P_{95} are calculated for both January–February–March (JFM) and July–August–September (JAS) separately to take seasonal variability of waves into account.

Trends in daily mean SWH and in P_{95} daily maximum SWH were determined for each grid cell. We then focused on certain regions with significant trends. Trends were assessed using linear regressions, applied separately to the two seasonal datasets (JFM and JAS) as in Timmermans et al. (2020), and the significance of the resulting slopes was then tested at the 5 % level using a Wald test with a t distribution of the test statistic.

The second part of the analysis is focused on determining 100-year return levels that are likely to be exceeded, on average, once every hundred years (Goda, 2000) using the non-seasonal transformed stationary approach (Mentaschi et al., 2016) and on assessing their trends. Extreme value analysis (EVA) consists of modelling the SWH with a statistical distribution and estimating return levels associated with long return periods and small probabilities of occurrence. The EVA allowed us to study 100-year SWH with only a 19-year-long altimetric time series. All the values of SWH exceeding the 95th percentile and separated by at least 72 h were selected according to the peaks-over-threshold method. A generalized Pareto distribution (GPD) could then be fitted to the exceedances (see equation below). The return levels associated with the 100-year return period were estimated from this GPD.

$$F(x) = 1 - \left[1 + \frac{\xi(x-\mu)}{\sigma}\right]^{-\frac{1}{\xi}},$$

with μ, ξ, and σ, which are the location, shape, and scale parameters.

The EVA has a major disadvantage in that it usually requires the time series to be stationary. The transformed stationary approach overcomes this issue by transforming the nonstationary altimetric time series $y(t)$ into a stationary one $x(t)$ through standardization (Eq. 1). The EVA is then applied to $x(t)$, and the location μ_x and scale σ_x parameters of the GPD are estimated by maximizing the likelihood function. The reverse transformation (Eqs. 2, 3) is finally used to recover the time-varying parameters $\mu_y(t)$ and $\sigma_y(t)$ associated with $y(t)$, enabling us to obtain the nonstationary extreme SWH distribution and to assess its trend. The transformation from $y(t)$ to $x(t)$ and the reverse transformation of the shape, location, and scale parameters associated with the nonstationary series are given by

$$x(t) = \frac{y(t) - T_y(t)}{S_y(t)}, \tag{1}$$

$$\mu_y(t) = S_y(t)\mu_x + T_y(t), \tag{2}$$

$$\sigma_y(t) = S_y(t)\sigma_x, \tag{3}$$

$$\xi_y = \xi_x, \tag{4}$$

where $T_y(t)$ and $S_y(t)$ are the trend and the standard deviation of $y(t)$, and μ_x, ξ_x, and σ_x are the parameters associated with the stationary series which are not dependent on time. To our knowledge, while this method has already been applied to ERA5 reanalysis (Takbash and Young, 2020), it has not been applied to altimetry at a global scale before. Thus, only results obtained using ERA5 can be compared with the literature. Finally, the same study was conducted for SWH from the ERA5 (Hersbach et al., 2020) and WAVERYS reanalyses (Law-Chune et al., 2021), as they allow for comparison with the literature (Timmermans et al., 2020) and the L4 altimetric time series.

3 Results

Climatologies of SWH and of high SWH are shown in Figs. 1a and 2a, respectively. Energetic conditions in the Northern Hemisphere, driven by extratropical storms, occur predominantly in the midlatitudes, reaching up to 4.5–5.0 m on average in the North Atlantic and 4.0–4.5 m in the North Pacific during the JFM seasonal average. This contrasts with the seasonal average during JAS that reveals corresponding energetic conditions in the Indian Ocean and in the Southern Ocean up to 5.0–5.5 m, along with seasonal events such as the Asian monsoon, demonstrating higher wave height in the Arabian Sea and in the Bay of Bengal. The spatial structure of the P_{95} of SWH is consistent and shares similar patterns to those seen in Fig. 1, with greater magnitude. Indeed, the highest SWHs can locally reach up to 9.0–10.0 m in the North Atlantic, up to 8.0–9.0 m in the North Pacific (both in JFM), and up to 8.0–10.0 m in the Indian Ocean in JAS. Other energetic conditions associated with typhoons are also revealed in the Philippine Sea, leading to high SWH of up to 6.0 m in JAS. Smaller regional processes are also observed despite the poor spatial resolution of altimeters, such as waves of 4.0–5.0 m in the eastern Pacific driven by Tehuantepecer events in JFM.

Trends of SWH and of P_{95} of SWH are displayed Figs. 1c and 2c, respectively. Some of these trend patterns have already been described in previous studies (Young and Ribal 2019; Shimura et al., 2016). Overall, large and significant trends mostly appear in the Southern Hemisphere: in the Southern Ocean, in the sector south of Africa, and in the Indian Ocean south of Australia. Young and Ribal (2019) already highlighted the existence of a broad region of positive and significant trend in the 90th percentile of SWH across the Southern Ocean with altimetric data spanning 1985–2018. Patterns associated with positive trends in SWH and in the P_{95} of SWH south of Africa, south of Australia, and in the South Pacific seem to mostly coincide with this broad region, as well as the decreasing SWH in the Indian Ocean around 45° S. However, in contrast to Young and Ribal (2019), our trend in P_{95} of SWH in the North Atlantic is not as significant and positive. Moreover, significant trends are found in wintertime in forms of complex spatial patterns of increasing and decreasing wave heights in the North Atlantic and North Pacific. In agreement with Young and Ribal (2019), SWH in the North Pacific shows a distinct negative trend that is especially true in our case during wintertime. The negative trend of SWH in JFM in the western North Pacific also agrees with the decreasing winter wave heights in global climate models (Shimura et al., 2016). As in Timmermans et al. (2020), significant positive trends are also found in the North Atlantic and in the Gulf Stream region. Finally, the results depicted in Figs. 1 and 2 suggest that significant upper percentile trends are changing orders of magnitude faster than trends of mean SWH.

Anomalies of SWH and of P_{95} of SWH for 2022 are shown Figs. 1b and 2b, respectively. The average interannual variability of wintertime SWH is of the order of 0.13 m at tropical and subtropical latitudes and 0.30–0.40 m at midlatitudes, with regional excursions exceeding 0.40 m, while the interannual variability of extreme wave heights averages 0.33 m at tropical and subtropical latitudes and 0.70–0.80 m at midlatitudes, with regional excursions exceeding 0.85 m in summer in the typhoon region and 0.90 m in the Southern Ocean. Despite this high interannual variability, some SWH anomalies for 2022 are found to exceed it and seem consistent with long-term changes in SWH (Figs. 1c and 2c). Strong positive anomalies found in the North Atlantic and North Pacific around 60° N in winter and for both SWH and P_{95} of SWH mostly coincide with increasing SWH and P_{95} of SWH. While the negative anomalies in the North Atlantic and in the North Pacific may not exceed the interannual variability, they still partly coincide with corresponding trends.

The most energetic conditions on the map of 100-year return levels (see Fig. 3) can be found on a large scale in the North Atlantic and western North Pacific, driven by extratropical storms and typhoons, and on a smaller scale in the tropical eastern Pacific and Indian Ocean driven by hurricanes and tropical cyclones. As expected, the strongly positive trend patterns found in the Southern Hemisphere are consistent with those highlighted by the SWH and the P_{95} of SWH. However, while both SWH and P_{95} of SWH show decreasing trends in the North Atlantic in winter, the 100-year return level trends are largely positive. Certain regions also stand out with a very significant trend, in contrast to that observed in the P_{95} of SWH, such as the western North Pacific, the Gulf of Mexico, and the Caribbean Sea, which demonstrate strong negative trends contrary to what Takbash and Young (2020) found. On the other hand, as shown by Tak-

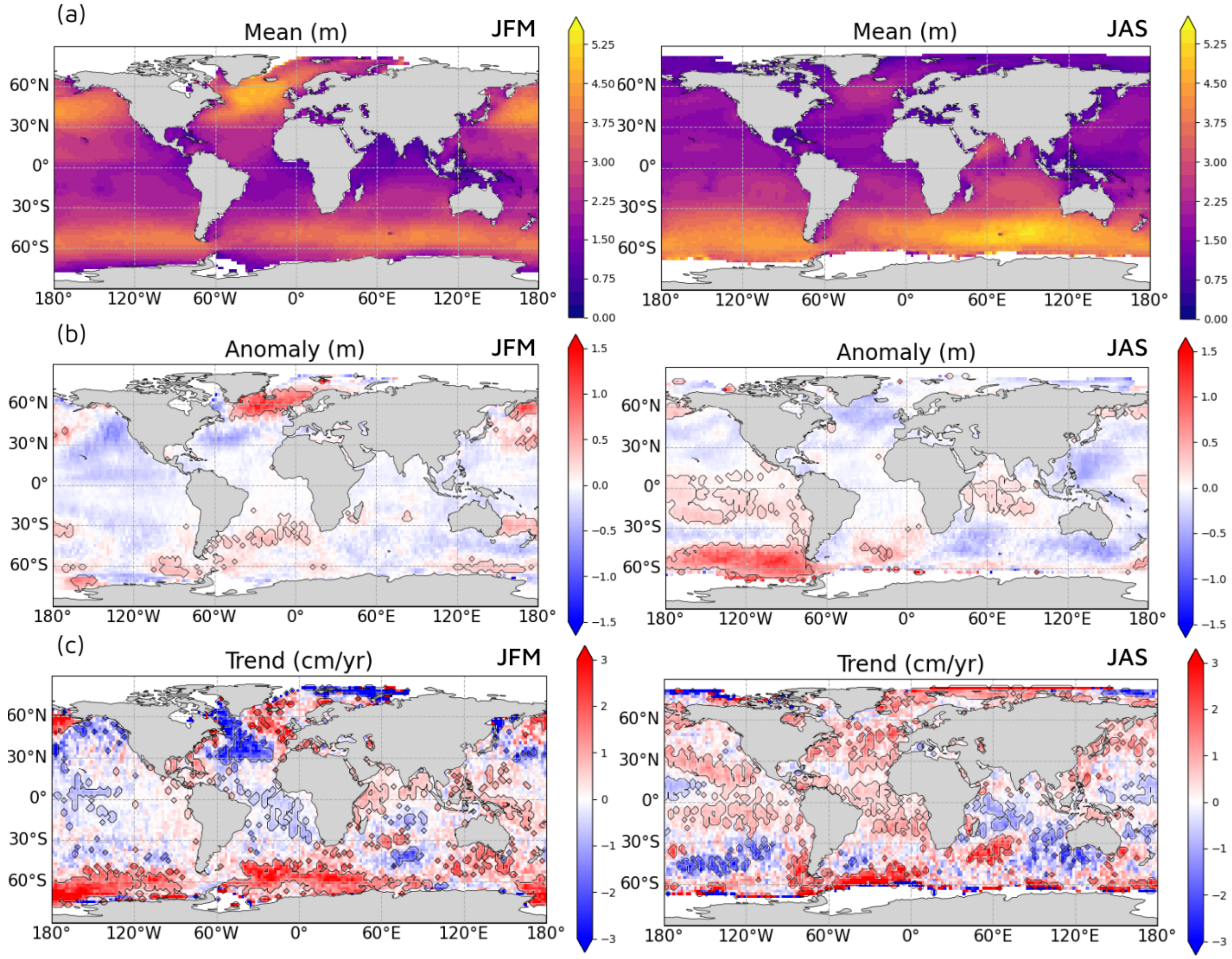

Figure 1. SWH **(a)** climatology (2002–2020), **(b)** annual anomaly for 2022, and **(c)** annual trend (2002–2020) for both JFM (left column) and JAS (right column) from the L4 altimetric time series of daily mean SWH (product reference 1). Areas with an anomaly above 1.5 times the interannual variability are outlined in black. Areas with a trend statistically significant at the 95 % level are outlined in black.

bash and Young (2020), localized positive trends can also be found in the hurricane regions in the eastern tropical Pacific and in the typhoon regions; these increases were not visible in the trends in SWH and P_{95} of SWH.

For comparison, the same figures were produced using ERA5 and WAVERYS data. Spatial patterns are mostly consistent among all three datasets. However, ERA5 and WAVERYS slightly underestimate the mean SWHs and their trends. ERA5 and WAVERYS overestimate the highest extreme waves and trends of P_{95} of SWH, especially in the Southern Hemisphere, but they underestimate 100-year return levels compared with altimetry as noted by Takbash and Young (2020).

4 Discussion

In this study, we found large positive trends over 2002–2020 for both SWH and extreme SWH, mostly in the Southern Hemisphere, which are consistent with findings by Young and Ribal (2019). In the North Atlantic, SWH has increased north of 45° N, corroborating what was concluded in the Fifth IPCC Assessment Report (AR5), and in 2022, a large positive anomaly of SWH and extreme SWH was found in the same region. However, SWH has also largely decreased south of 45° N in JFM, contrary to Young and Ribal's (2019) findings. The 100-year return levels have significantly increased in the North Atlantic and in the eastern North Pacific, where the cyclone tracks are located. Finally, we found trends of SWH and P_{95} of SWH for JFM and JAS over 2002–2020 to be much higher than those indicated by Young and Ribal (2019) for the period 1985–2018.

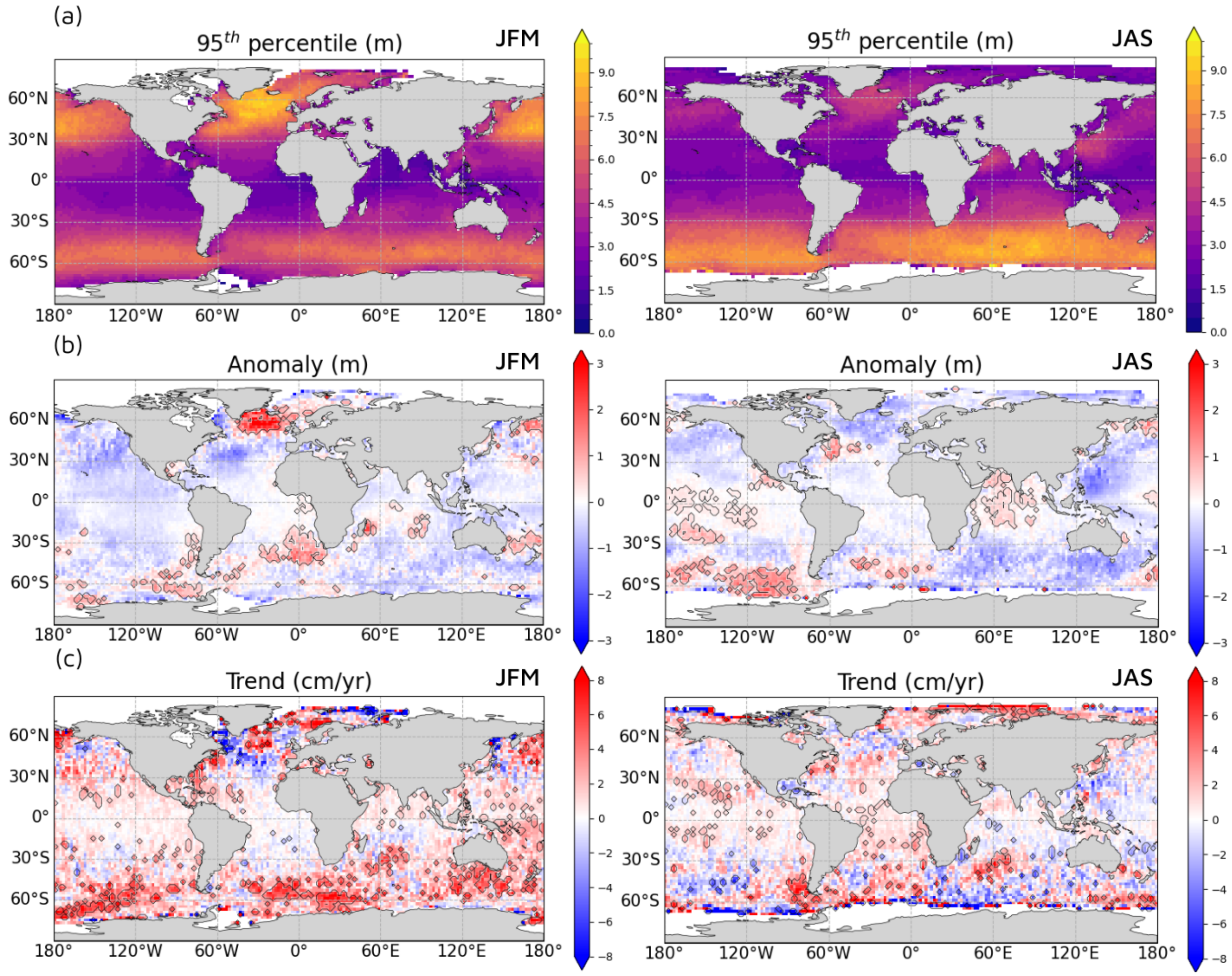

Figure 2. 95th SWH percentile **(a)** climatology (2002–2020), **(b)** annual anomaly for 2022, and **(c)** annual trend (2002–2020) for both JFM (left column) and JAS (right column) from the L4 altimetric time series (product reference 1). Areas with an anomaly above 1.5 times the interannual variability are outlined in black. Areas with a trend statistically significant at the 95 % level are outlined in black.

The mean trends of SWH and P_{95} of SWH were estimated for regions where the trend in the grid cells was predominantly statistically significant in the multi-mission product (Fig. 4), such as in the North Atlantic (box 1), in the South Atlantic Ocean and Southern Ocean (box 2), and in the southern Indian Ocean (box 3). In JFM, the SWH increases by 1.8 ± 1.1 cm each year poleward of 45° N and decreases by 2.1 ± 0.76 cm each year equatorward of 45° N in the North Atlantic. In box 2, the SWH increases by 1.8 ± 0.41 cm each year in JFM and 1.2 ± 0.61 cm each year in JAS, and the P_{95} of SWH increases by 3.5 ± 1.9 cm each year in JFM. Finally, the P_{95} of SWH increases by 3.1 ± 1.7 cm per year in JFM in box 3.

Unfortunately, no uncertainty is provided for the SWH data from the multi-mission product, so only an uncertainty in the trend adjustment and annual statistics could be calculated. The major concern regarding the estimates of the trends of daily mean SWH and P_{95} daily maximum SWH is the fact that the number of satellites combined in the multi-mission product has increased over time (Charles, 2021). This concern was previously addressed by Young and Ribal (2019) in relation to their own multi-mission altimetric product. With more satellites, the number of along-track measurements available from which daily statistics are estimated and the number of days available increase. Consequently, daily statistics are more frequent and precise at the end of the period than at the beginning. For example, it is likely that more storms or extreme waves were sampled by the altimeters in the latter years of the period than in the former. The distribution of SWH is not Gaussian and is largely affected by extreme events, hence producing a spurious pos-

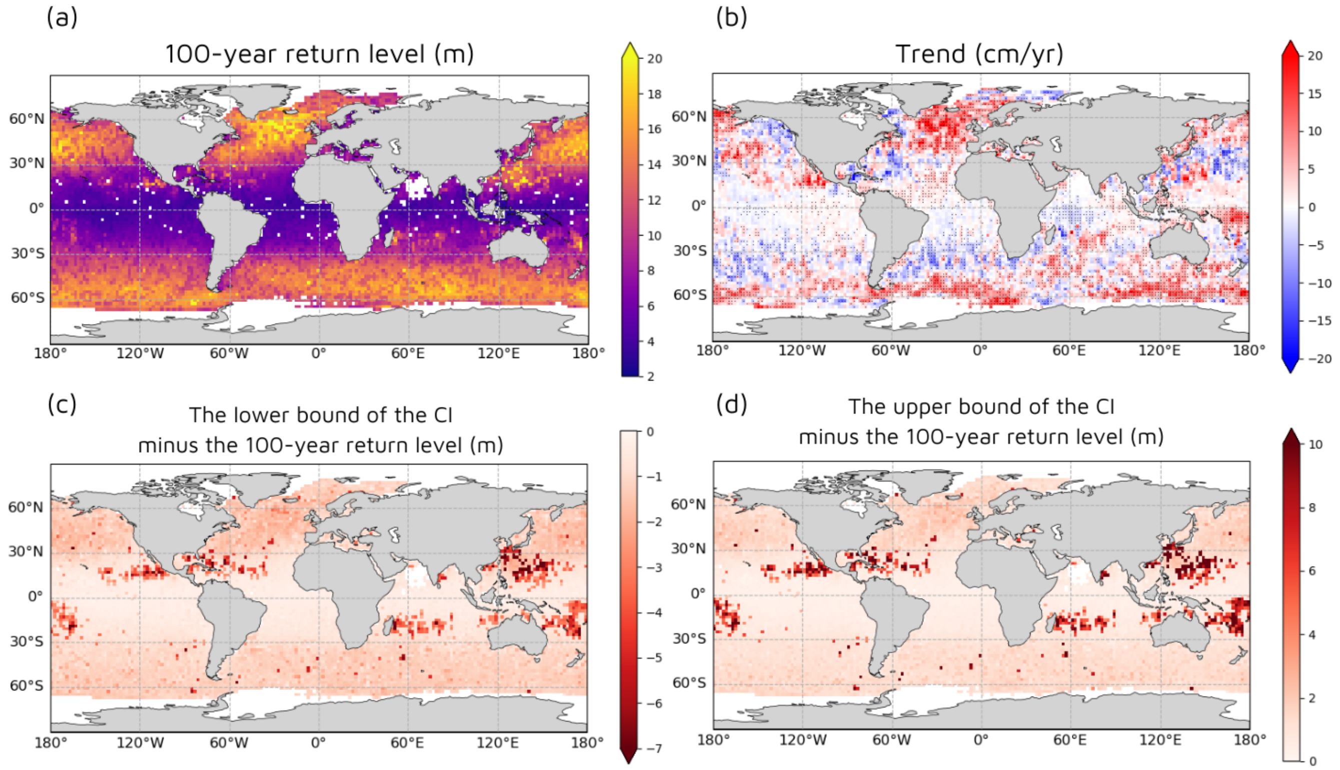

Figure 3. **(a)** Average 100-year return levels and **(b)** their trends over 2005–2018 from the L4 altimetric time series (product reference 1) using the non-seasonal transformed stationary approach. Areas with a trend statistically significant at the 95 % level are indicated by grey dots. White pixels correspond to grid cells that do not meet the requirements for calculating return levels, such as the minimum number of points selected with the peaks-over-threshold method. **(c, d)** Difference between the 100-year return level and the lower and upper bounds of the 95 % confidence interval.

itive trend in SWH. In addition, due to the polar altimeter orbits, the number of observations also varies with latitude.

A series of tests were performed to evaluate the effect of the increasing number of satellites on the trends. A new L4 altimetric time series was created by combining only two satellites at a time to serve as a means of comparison for the L4 multi-mission product. This new product only extends to 2019, so the two products were compared over the period 2002–2019. The SWH trends that are statistically significant for both products are plotted in Fig. 4. The time series differ from each other starting from 2008 with the introduction of more satellites in the multi-mission product, whereupon the number of observations doubles (Fig. 3b, c, d). The mean SWH is not greatly affected by the number of satellites and the trends of mean SWH are almost identical. On the other hand, the P_{95} daily maximum SWH is sensitive to the increase in the number of observations and the multi-mission product overestimates its trends compared with the two-satellite product. More importantly, the sign of the trend does not change, the spatial patterns of the trend are mostly consistent between the products, and trends in the two-satellite product are contained within the uncertainty of trends in the multi-mission product. However, as the two-satellite product is more consistent over time, the long-term trends measured with it may be more accurate than those measured with the multi-mission product.

There is a strong positive trend in the Southern Hemisphere which has also been observed in other studies and in reanalyses. However, the altimeter observations have been calibrated and validated using in situ observations almost entirely located in the Northern Hemisphere and near coastlines (Charles and Ollivier, 2021), potentially biasing the altimetry record. Although the trends should themselves be robust, caution should nevertheless be exercised in interpreting this result until more Southern Hemisphere and open-ocean in situ observations can be included in the calibration.

Finally, the EVA gave us a good initial estimate of SWH extremes based on altimetry measurements, in line with the literature. However, these results must be treated with caution, as the altimeter series is very short (less than 20 years), so few measurements could be selected to estimate the GPD parameters. Similarly, the measurement period is not necessarily representative of a longer time series. This ultimately leads to large confidence intervals for the extreme values estimated. In addition, the transformed stationary approach used

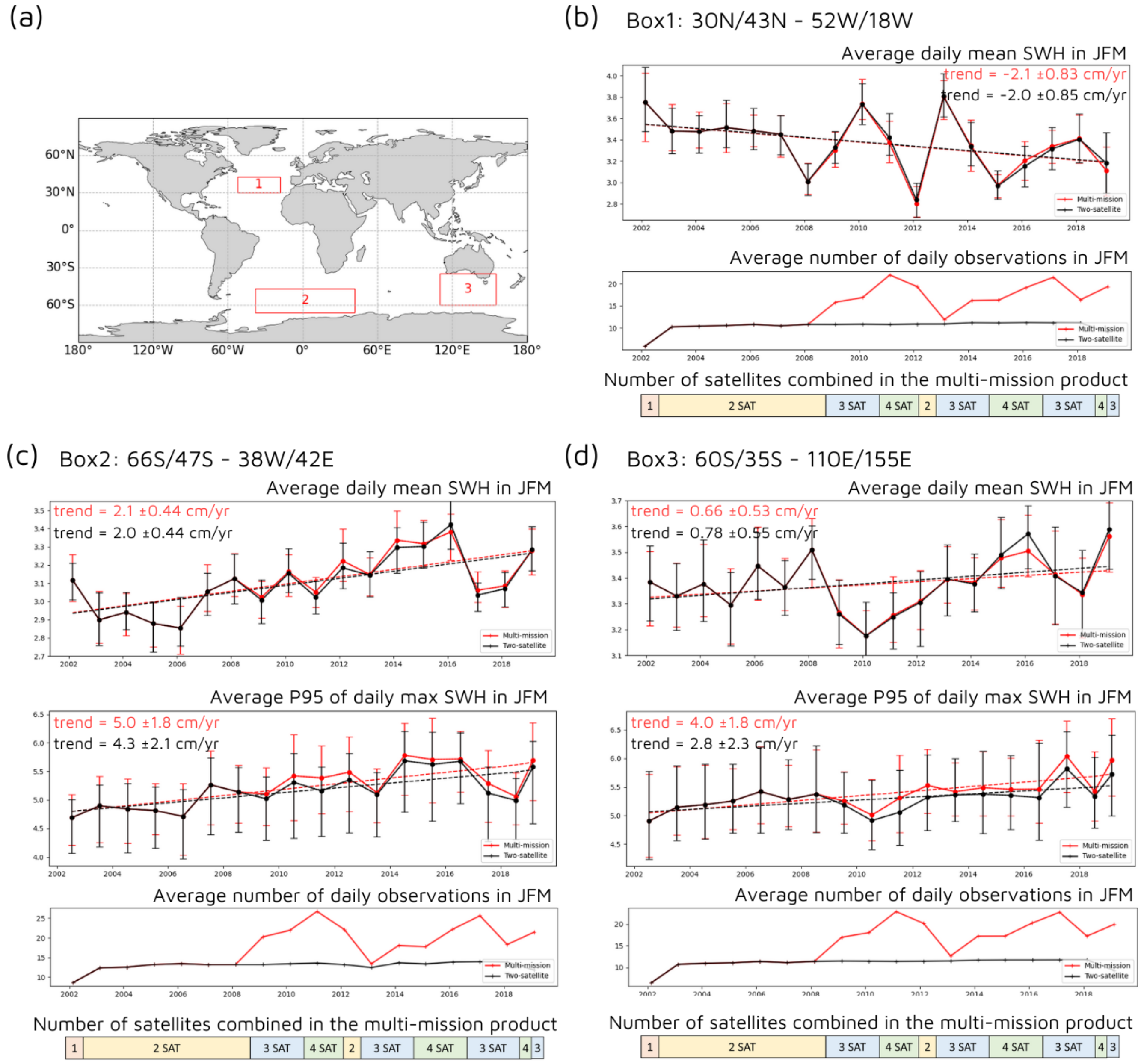

Figure 4. Effects of the number of satellites on the long-term trends in L4 altimetric time series. **(a)** Boxes in which regional trends were computed. Box 1: 30–43° N, 52–18° W; box 2: 66–47° S, 38° W–42° E; box 3: 60–35° S, 110–155° E. **(b–d)** Time series of daily mean SWH, of P_{95} daily maximum SWH, and of the daily number of observations in JFM averaged on a yearly basis, associated with each box. The bootstrap 95 % confidence interval is represented with error bars. In red: the L4 multi-mission product (product reference 1); in black: L4 two-satellite product. Trends are represented by dashed lines when statistically significant for both products. Finally, the number of satellites combined in the multi-mission product is represented by coloured blocks as a function of time as in Charles (2021).

assumes that the GPD shape parameter is constant, which is valid in most cases but may prove false in some.

5 Conclusion

We have derived global ocean wave and extreme wave height climatologies and their trends for the period 2002–2020 based on the mean, the 95th percentile, and the 100-year return level of SWH from an L4 altimetric time series. To our knowledge, this is the first time that a global 100-year return level trend map has been drawn from an altimeter series using the transformed stationary method. The climatologies and trends computed from satellite altimetry were very similar to ERA5 and WAVERYS.

Over the last 2 decades, predominantly large positive 2022 anomalies of SWH and significant 2002–2020 trends are mostly found in the Southern Hemisphere. Large significant positive trends in mean SWH and P_{95} of SWH are found in the South Atlantic, the Southern Ocean, and the southern Indian Ocean (up to $1.2 \pm 0.61\,\mathrm{cm\,yr^{-1}}$ for the SWH, up to $3.5 \pm 1.9\,\mathrm{cm\,yr^{-1}}$ for the P_{95} of SWH). According to the AR5, as winds are likely to strengthen in the Southern Hemisphere, this trend could be confirmed in the future. SWH has increased above 45° N in the North Atlantic ($1.76 \pm 1.14\,\mathrm{cm\,yr^{-1}}$), corroborating what was concluded in the AR5 from ship observations and reanalysis-forced wave model hindcasts. In particular, a strong positive anomaly of SWH and P_{95} of SWH was found in this region in JFM 2022. However, contrary to Young and Ribal (2019), a strong decrease in SWH of nearly $-2.1 \pm 0.76\,\mathrm{cm\,yr^{-1}}$ has also been observed in the altimetric record over the last 19 years in JFM in the North Atlantic below 45° N. Moreover, all the trends of SWH and P_{95} of SWH calculated in this study for JFM and JAS over 2002–2020 are much greater than those indicated by Young and Ribal (2019) over the period 1985–2018. The global maps of SWH extremes highlight the regions heavily affected by storms, such as the western North Pacific, the North Atlantic, and the eastern tropical Pacific. Trends in 100-year return levels seem to indicate an increase in wave levels linked to this energetic activity.

The L4 altimetric time series merges between one and four missions at a time. While the number of satellites does not impact the sign of the trends, it can affect their magnitudes, indicating that there is a need for a long, global, and more homogeneous altimetric time series. Additionally, this study reveals the need for knowledge of uncertainties. A new product was generated as part of this study to assess the effect of the number of satellites on the results. The conclusions given above nevertheless remain unchanged.

Code availability. The code can be retrieved by contacting the corresponding author by e-mail.

Data availability. The data used in this study can be downloaded directly from the Copernicus Marine Service website. The exact product names are given in Table 1, and the associated DOIs are indicated in the references.

Author contributions. AL conceptualized the statistical analysis and carried it out. MG provided the two-satellite altimetric time series used in the discussion. MG, YF, AD, and LA supervised the study and provided guidance. AL prepared the manuscript with contributions from MG.

Competing interests. The contact author has declared that none of the authors has any competing interests.

Disclaimer. The Copernicus Marine Service catalog is periodically updated to ensure that it remains at the cutting edge of quality and user needs. In the process, some of these products may then be removed, replaced or renamed.

Should you require assistance with any of these products, please do not hesitate to contact the user support team, who will be able to answer your questions and find suitable solutions.

Financial support. This research has been supported by the Copernicus Marine Service.

Review statement. This paper was edited by Joanna Staneva and reviewed by two anonymous referees.

References

Barnard, P. L., Hoover, D., Hubbard, D. M., Snyder, A., Ludka, B. C., Allan, J., Kaminsky, G. M., Ruggiero, P., Gallien, T. W., Gabel, L., McCandless, D., Weiner, H. M., Cohn, N., Anderson, D. L., and Serafin, K. A.: Extreme oceanographic forcing and coastal response due to the 2015–2016 El Niño, Nat. Commun., 8, 14365, https://doi.org/10.1038/ncomms14365, 2017.

Charles, E.: EU Copernicus Marine Service Quality Information Document for the Global Ocean L 4 Significant Wave Height From Reprocessed Satellite Measurements Product, WAVE_GLO_PHY_SWH_L4_MY_014_007, Issue 1.0, Mercator Ocean International, https://catalogue.marine.copernicus.eu/documents/QUID/CMEMS-WAV-QUID-014-007.pdf (last access: 21 July 2023), 2021.

Charles, E. and Ollivier, A.: EU Copernicus Marine Service Quality Information Document for the Global Ocean L3 Significant Wave Height From Reprocessed Satellite Measurements Product, WAVE_GLO_PHY_SWH_L3_MY_014_005, Issue 1.0, Mercator Ocean International, https://catalogue.marine.copernicus.eu/documents/QUID/CMEMS-WAV-QUID-014-005.pdf (last access: 27 July 2023), 2021.

Charles, E., Taburet, N., Husson, R., Philip, A., and Ghantous, M.: EU Copernicus Marine Service Quality Information Document for the Global Ocean L 4 Significant Wave Height From Nrt Satellite Measurements Product, WAVE_GLO_PHY_SWH_L4_NRT_014_003, Issue 1.5, Mercator Ocean International, https://catalogue.marine.copernicus.eu/documents/QUID/CMEMS-WAV-QUID-014-003.pdf, last access: 21 July 2023

Donelan, M. A., Drennan, W. M., and Katsaros, K. B.: The air–sea momentum flux in conditions of wind sea and swell, J. Phys. Oceanogr., 27, 2087–2099, https://doi.org/10.1175/1520-0485(1997)027<2087:tasmfi>2.0.co;2, 1997.

EU Copernicus Marine Service Product: Global Ocean L 4 Significant Wave Height From Reprocessed Satellite Measurements, Mercator Ocean International [data set], https://doi.org/10.48670/moi-00177, 2021.

EU Copernicus Marine Service Product: Global Ocean L 4 Significant Wave Height From Nrt Satellite Measurements, Mercator Ocean International [data set], https://doi.org/10.48670/moi-00180, 2023.

Goda, Y.: Random seas and design of maritime structures, World Scientific Publishing Co., Statistical Analysis of Extreme Waves, 377–425, https://doi.org/10.1142/9789812385444_0011, 2000.

Gommenginger, C. P., Srokosz, M. A., Challenor, P. G., and Cotton, P. D.: Development and validation of altimeter wind speed algorithms using an extended collocated Buoy/Topex dataset, IEEE T. Geosci. Remote, 40, 251–260, https://doi.org/10.1109/36.992782, 2002.

Hersbach, H., Bell, B., Berrisford, P., Hirahara, S., Horányi, A., Muñoz-Sabater, J., Nicolas, J., Peubey, C., Radu, R., Schepers, D., Simmons, A., Soci, C., Abdalla, S., Abellan, X., Balsamo, G., Bechtold, P., Biavati, G., Bidlot, J., Bonavita, M., Chiara, G., Dahlgren, P., Dee, D., Diamantakis, M., Dragani, R., Flemming, J., Forbes, R., Fuentes, M., Geer, A., Haimberger, L., Healy, S., Hogan, R. J., Hólm, E., Janisková, M., Keeley, S., Laloyaux, P., Lopez, P., Lupu, C., Radnoti, G., Rosnay, P., Rozum, I., Vamborg, F., Villaume, S., and Thépaut, J. N.: The ERA5 global reanalysis, Q. J. Roy. Meteor. Soc., 146, 1999–2049, https://doi.org/10.1002/qj.3803, 2020.

Husson, R. and Charles, E.: EU Copernicus Marine Service Product User Manual for the Global Ocean L 4 Significant Wave Height From Reprocessed Satellite Measurements Product, WAVE_GLO_PHY_SWH_L4_MY_014_007, Issue 2.0, Mercator Ocean International, https://catalogue.marine.copernicus.eu/documents/PUM/CMEMS-WAV-PUM-014-005-006-007.pdf (last access: 21 July 2023), 2021.

Law-Chune, S., Aouf, L., Dalphinet, A., Levier, B., Drillet, Y., and Drevillon, M.: WAVERYS: A CMEMS global wave reanalysis during the altimetry period, Ocean Dynam., 71, 357–378, https://doi.org/10.1007/s10236-020-01433-w, 2021.

Mentaschi, L., Vousdoukas, M., Voukouvalas, E., Sartini, L., Feyen, L., Besio, G., and Alfieri, L.: The transformed-stationary approach: a generic and simplified methodology for non-stationary extreme value analysis, Hydrol. Earth Syst. Sci., 20, 3527–3547, https://doi.org/10.5194/hess-20-3527-2016, 2016.

Mentaschi, L., Vousdoukas, M. I., Voukouvalas, E., Dosio, A., and Feyen, L.: Global changes of extreme coastal wave energy fluxes triggered by intensified teleconnection patterns, Geophys. Res. Lett., 44, 2416–2426, https://doi.org/10.1002/2016gl072488, 2017.

Mertz, F., Husson, R., Taburet, N., Charles, E., Estimbre, J.-J.: EU Copernicus Marine Service Product User Manual for the Global Ocean L 4 Significant Wave Height From Nrt Satellite Measurements Product, WAVE_GLO_PHY_SWH_L4_NRT_014_003, Issue 2.2, Mercator Ocean International, https://catalogue.marine.copernicus.eu/documents/PUM/CMEMS-WAV-PUM-014-001-002-003-004.pdf (last access: 21 July 2023), 2022.

Shimura, T., Mori, N., and Hemer, M. A.: Variability and future decreases in winter wave heights in the Western North Pacific, Geophys. Res. Lett., 43, 2716–2722, https://doi.org/10.1002/2016gl067924, 2016.

Storlazzi, C. D., Gingerich, S. B., van Dongeren, A., Cheriton, O. M., Swarzenski, P. W., Quataert, E., Voss, C. I., Field, D. W., Annamalai, H., Piniak, G. A., and McCall, R.: Most atolls will be uninhabitable by the mid-21st century because of sea-level rise exacerbating wave-driven flooding, Science Advances, 4, eaap9741, https://doi.org/10.1126/sciadv.aap9741, 2018.

Takbash, A. and Young, I.: Long-Term and seasonal trends in global wave height extremes derived from ERA-5 reanalysis data, Journal of Marine Science and Engineering, 8, 1015, https://doi.org/10.3390/jmse8121015, 2020.

Thomas, S., Babanin, A. V., Walsh, K. J. E., Stoney, L., and Heil, P.: Effect of wave-induced mixing on Antarctic sea ice in a high-resolution ocean model, Ocean Dynam., 69, 737–746, https://doi.org/10.1007/s10236-019-01268-0, 2019.

Timmermans, B. W., Gommenginger, C. P., Dodet, G., and Bidlot, J.-R.: Global wave height trends and variability from new multimission satellite altimeter products, reanalyses, and wave buoys, Geophys. Res. Lett., 47, e2019GL086880, https://doi.org/10.1029/2019gl086880, 2020.

Young, I. R. and Ribal, A.: Multiplatform evaluation of global trends in wind speed and wave height, Science, 364, 548–552, https://doi.org/10.1126/science.aav9527, 2019.

State Planet, 4-osr8, 7, 2024
https://doi.org/10.5194/sp-4-osr8-7-2024

STATE OF THE
PLANET

Characteristics and trends of marine heatwaves in the northwest European Shelf and the impacts on density stratification

Wei Chen and Joanna Staneva

Institute of Coastal Systems – Analysis and Modeling, Helmholtz-Zentrum Hereon,
Max-Planck-Straße 1, 21502 Geesthacht, Germany

Correspondence: Wei Chen (wei.chen@hereon.de)

Received: 16 August 2023 – Discussion started: 18 August 2023
Revised: 8 January 2024 – Accepted: 30 January 2024 – Published: 30 September 2024

Abstract. Marine heatwaves (MHWs) are characterized by anomalous and prolonged increases in sea surface temperatures driven by atmospheric and oceanic factors. The intensification of MHWs is an evident consequence of ongoing global climate change. The question of whether the northwest European Shelf (NWES) is experiencing increased stratification in recent decades is of significant interest with respect to understanding the impacts of these extreme events. In this study, we leverage ocean physics reanalysis data obtained from the Copernicus Marine Environment Monitoring Service (CMEMS) covering the temporal span from 1993 to 2023 to conduct a rigorous examination of the NWES domain. The focus centers on the assessment of potential energy anomaly (PEA) and its role in shaping stratification dynamics.

Our findings reveal an increase in both the frequency and duration of MHWs in the NWES area, especially in coastal areas, where the duration of MHWs is increasing the fastest, generally by more than $2\,\mathrm{d\,yr^{-1}}$ over the study period. However, despite the intensified MHWs, thermal stratification in the NWES is weakening, particularly in the middle and northern North Sea. This suggests that the warming effect due to MHWs is insufficient to counteract the overall decline in thermal stratification caused by global warming. Additionally, our study highlights the significance of seawater salinity in driving the trend of density stratification. Specifically, the discharge from the Baltic Sea plays a crucial role in influencing the stratification patterns in the North Sea region.

1 Introduction

Marine heatwaves (MHWs) are extreme oceanic events characterized by unusually warm sea surface temperatures (SSTs) that exceed the local 90th percentile for at least 5 consecutive days (Hobday et al., 2016). These events are characterized by their intensity, duration, and spatial extent, often leading to ecological disturbances and significant shifts in species distribution patterns (Frölicher et al., 2018). MHWs can occur in various oceanic regions, including coastal areas, and the occurrence of MHW events has shown an increasing trend globally over the past century (Oliver et al., 2018; IPCC, 2021).

Climate models project a continued upward trend in the occurrence of MHWs in the coming decades that is driven by anthropogenic climate change (Frölicher et al., 2018; Oliver et al., 2019, 2020; IPCC, 2021). The northwest European Shelf (NWES), which is a large area of shallow temperate sea located between 47–61° N latitude and 12° W–10° E (Fig. 1), is expected to experience a similar trend of increasing MHW events (IPCC, 2021). Understanding the dynamics of MHWs and their consequences is crucial for effective ecosystem management and conservation efforts (Smale et al., 2019).

Elevated SSTs can lead to widespread and severe ecological disturbances, including shifts in species distributions, alterations in community structure, and increased vulnerability to invasive species (Oliver et al., 2018; Smale et al., 2019). These events can disrupt important ecological processes, such as nutrient cycling, primary production, and trophic in-

Published by Copernicus Publications.

Table 1. CMEMS products used in this study.

Product ref. no.	Product ID and type	Data access	Documentation
1	NWSHELF_MULTIYEAR_PHY_004_009, numerical models	EU Copernicus Marine Service Product (2021)	Quality information document (QUID): Renshaw et al. (2021) Product user manual (PUM): Tonani et al. (2022)

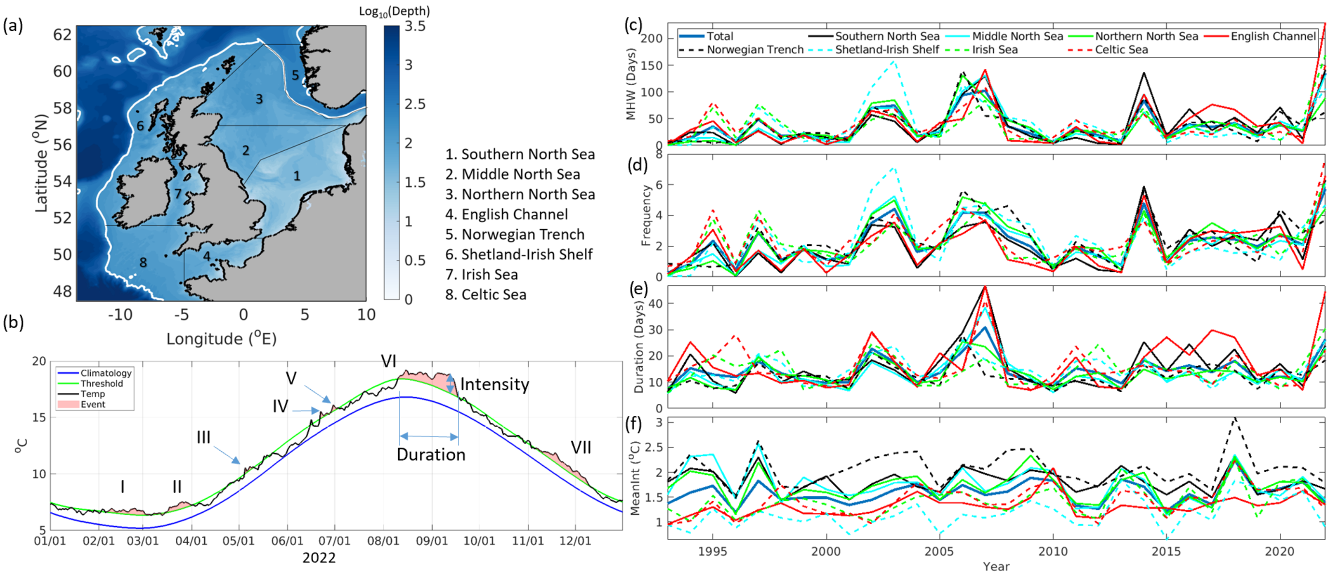

Figure 1. **(a)** Map of the northwest European Shelf Sea with sub-regional division (data from Table 1, ref. 1). Dashed curve indicates 200 m isobath. **(b)** Detection of MHW events and their characteristics in 2022 (data from Table 1, ref. 1) near the Dogger Bank region in the southern North Sea (region 1 in panel **(a)**). **(c–f)** Variations in the MHW characteristics between 1993 and 2022, with the bold solid curve indicating the mean of total subdomains of the NWES (daily SST data from Table 1, ref. 1).

teractions, with cascading effects on the entire marine food web (Wernberg et al., 2013, 2016; Oliver et al., 2020). In the NWES region, the increasing frequency of MHW occurrence is anticipated to have significant consequences for both the socioeconomic system and natural processes. For instance, Borges et al. (2019) observed a 3-fold increase in dissolved methane concentration in surface waters along the Belgian coast during the summer of 2018 compared to a typical year. Additionally, MHWs have been implicated in the occurrence and persistence of thermal stratification, leading to changes in vertical mixing and nutrient availability in the water column (Chen et al., 2022). Such alterations in thermal stratification can have profound implications for the functioning of marine ecosystems and their resilience to climate change (Herring et al., 2015). The recently published Copernicus Marine Service Ocean State Report, Issue 5 (Wakelin et al., 2021), documented the identification of extreme temperature events and their potential impacts on important fish and shellfish stocks. However, a lack of systematic studies to elucidate the long-term relationship between the vertical stratification and MHWs hampers our understanding of the impacts of extreme temperature events on ecosystem stability.

Given the potential consequences of increased MHW frequency on the NWES region, it is essential to address the following research question: is the NWES becoming more stratified due to the increased frequency of marine heatwave occurrence? Addressing this question requires a comprehensive assessment of long-term observational data, climate model simulations, and advanced analytical techniques to examine the relationships between MHW events, thermal stratification, and their ecological implications. This research will provide valuable insights into the potential impacts of MHWs on the NWES ecosystem and contribute to our understanding of the broader effects of climate change on marine environments.

2 Material and methods

The three-dimensional water temperature and salinity data from the Copernicus Marine Environment Monitoring Service (CMEMS) ocean physics reanalysis data (Table 1, product ref. 1) is applied in this study. These data cover the NWES with the assimilation model at 7 km horizontal resolution for the period 1993 to 2022. The modeled temperature and salinity are validated through comparisons with in situ observations from the World Ocean Database, mooring data, and the multimodel ensemble of multiyear products, which is an internal CMEMS product. More details of the CMEMS products are given in Table 1.

Moreover, the CMEMS SST reanalysis is extended by the European Space Agency Sea Surface Temperature Climate Change Initiative (ESA SST CCI; Table 1, product ref. 1) Level 3 product for the period 1982–1992 (Merchant et al., 2019). This product has a spatial resolution of 0.05° by 0.05° for the northwest Atlantic Shelf region. The ESA dataset is also employed as observational data for assimilating CMEMS data (see the quality information document (QUID) and product user manual (PUM) of the product; Table 1). All SST data are interpolated on the same spatial grid as the CMEMS product ref. 1 (Table 1), such that the 40-year period provides the baseline climatology reference period for computing the seasonally varying 90th percentile threshold, as defined in Hobday et al. (2016). The MATLAB toolbox by Zhao and Marin (2019) is applied for detecting MHW events and to properly computing means and trends of MHW properties.

The potential energy anomaly is used as a measure of the degree of density stratification as follows (Simpson, 1981):

$$\varnothing = \frac{1}{D}\int_{-H}^{\mu} gz(\overline{\rho}-\rho)\,\mathrm{d}z, \tag{1}$$

in which

$$\overline{\rho} = \frac{1}{D}\int_{-H}^{\mu} \rho\,\mathrm{d}z \tag{2}$$

is the vertical mean water density, and $g = 9.8\,\mathrm{m\,s^{-2}}$ is the gravitational acceleration. The instantaneous total water depth is given by $D = \eta + H$, with η and H being the sea surface elevation and the time mean water depth, respectively. The potential energy anomaly measures the amount of mechanical energy (per m^3) required to instantaneously homogenize the water column with given density stratification. The water density ρ was calculated (at 1 atm), following Millero and Poisso (1981):

$$\rho(S,T) = \rho_\mathrm{r} + AS + BS^{1.5} + CS^2. \tag{3}$$

In Eq. (3), S is the salinity of seawater in pptv (parts per thousand by volume). The reference density ρ_r and the coefficients A, B, and C are also functions of temperature T in degrees Celsius, with expressions given by Millero and Poisso (1981):

$$\begin{aligned}
\rho_\mathrm{r} ={}& 999.842594 + 6.793952\times10^{-2}T \\
&- 9.095290\times10^{-3}T^2 + 1.001685\times10^{-4}T^3 \\
&- 1.120083\times10^{-6}T^4 + 6.536332\times10^{-9}T^5; \\
A ={}& 8.24493\times10^{-1} - 4.0899\times10^{-3}T \\
&+ 7.6438\times10^{-5}T^2 - 8.2467\times10^{-7}T^3 \\
&+ 5.3875\times10^{-9}T^4; \\
B ={}& -5.72466\times10^{-3} + 1.0227\times10^{-4}T \\
&- 1.6546\times10^{-6}T^2; \\
C ={}& 4.8314\times10^{-4}.
\end{aligned}$$

Here, S and T, as well as the sea surface elevation η and water depth H (see Eqs. 1 and 2), are obtained from the CMEMS products.

Furthermore, the sensitivity of density stratification to the occurrence of MHWs is quantified with the ratio between the varying heatwave days and varying water-stratified days (Chen et al., 2022):

$$r = \frac{\sum_{i}^{n}\left|N_i - \overline{N_n}\right|}{\sum_{i}^{n}\left|M_i - \overline{M_n}\right|}. \tag{4}$$

Here, the number of MHW days (M) and the number of days that the water column was stratified (N) are counted in each year (i). The parameter $n = 30$ (i.e., 1993–2022) indicates the length of the computing period. The overline denotes the multiyear mean.

3 Results

A MHW in each year is characterized by the number of events and the duration and intensity of each event. As an example, Fig. 1b illustrates the detection of MHW events near the Dogger Bank region (region 1 in Fig. 1a), in the middle of the North Sea in 2022. The MHW occurs multiple times throughout the whole year, even during winter. The duration of each event varies from 5 d (e.g., events 4 and 5) to 40 d (events 6 and 7). The intensity, which measures the deviation of SST from the threshold, reaches its maximum of 2 °C in late September.

MHWs are exceptionally active in the year 2022. The total number of days of MHWs reaches 140 d on average (Fig. 1c), with the maximum exceeding 200 d in the English Channel. The lowest number of MHW days, 60 d, is found in the Norwegian Trench. Throughout this year, the Celtic Sea experienced more than seven MHW events. Apart from the events in 2022, MHWs were also active in the years 1995, 1997, 2003, 2007, and 2014, during which three or more MHW events were observed (Fig. 1d).

The occurrence of MHWs undergoes large temporal variations between the years 1993 and 2022, when MHW days appear much longer than during other years. During 1993–2022, the general duration of a MHW event is around 10 to 20 d (Fig. 1e). Longer durations are also observed. For example, in 2007, a duration with more than 40 d duration was observed in the English Channel and the Celtic Sea (region 8; Fig. 1a). The annual mean intensity of MHWs ranges on average between 1 and 2 °C and shows insignificant differences with the occurrences of MHW, the number of days, or the length of the duration (Fig. 1f). However, regional dependence can be observed. For example, in the Shetland–Irish Shelf (region 6; Fig. 1a), the mean intensity varies between 1 and 1.5 °C over the period 1993 to 2022. It also becomes stronger in the Irish Sea (region 7; Fig. 1a) and the North Sea (regions 1–3; Fig. 1a) over these periods. In general, the annual mean intensity of MHWs occurring in the Norwegian Trench (region 4; Fig. 1a) can reach values of up to 2 to 3 °C (Fig. 1f), which is more intense than in the other regions.

The mean and trend values of MHWs over the past 30 years are shown in Fig. 2. The lowest frequency of the occurrence of MHWs is found at the southern North Sea and the English Channel, where on average only one to two MHW events occurred every year (Fig. 2a). The Shetland–Irish Shelf and the Celtic Sea experienced two to three MHW events. Concurrently, all these regions had longer MHW periods (approximately 40–50 d) than the middle and northern North Sea (Fig. 2b). Furthermore, it is found that MHW events last longer further to the south. The longest duration, 30–40 d, occurred near the coast of the North Sea and the English Channel (Fig. 2c). This indicates that the MHWs that appear in the southern part of the NWES are mostly continuous and long term, while the MHWs that appear in the northern part of the NWES and the shelf edge are mostly intermittent and short term.

The occurrence of MHWs can be primarily attributed to the following two drivers: local air–sea heat exchange resulting from abnormally high air temperatures and nonlocal heat transport via ocean advection (Gupta et al., 2020; Schlegel et al., 2021). The atmospheric factor emerges as the predominant driver of MHWs in the southern to middle North Sea (Chen et al., 2022; Mohamed et al., 2023). Nonlocal heat fluxes, such as the influx of warm Atlantic water into NWES, may be responsible for the development of MHWs.

Compared to the long-term average, higher seawater temperatures will result in more heat fluxes into the NWES by the North Atlantic shelf current, particularly in the English Channel and the Shetland–Irish Shelf (zones 4 and 6 in Fig. 1a). The heightened seawater levels make these areas more prone to experiencing MHWs compared to regions less affected by the North Atlantic current, such as the Norwegian Trench (zone 5; Fig. 1a). This may explain why these regions have more days with MHWs. Furthermore, the mean intensity of MHWs in these two regions is notably lower than in the Norwegian Trench (Fig. 2d), which supports the assertion. The lowest mean intensity is observed in the Irish Sea and the English Channel. The MHW intensifies towards the east coast of the NWES. Along the coast of Denmark and Norway, the mean intensity reaches approximately 2.5–3 °C. However, compared to the southern NWES, the shorter durations and higher frequencies of MHWs in its northern region may be attributed to the distinct characteristics of climate drivers in their respective areas. This is because atmospheric influences, in contrast to oceanic influences, exhibit larger variability in affecting SST (Tinker and Howes, 2020). Other drivers, such as local wind (Mohamed et al., 2023), may introduce further uncertainties to the occurrence and persistence of MHWs. Identifying the dominant drivers of MHW features in NWES requires a systematic investigation of the relationship between air and sea temperature in various regions. However, this detailed analysis is not elaborated on in this paper due to space constraints.

Over the past 3 decades, the frequency of MHWs increased at a rate of 0.1–0.15 yr^{-1} (Fig. 2e). Correspondingly, the number of days experiencing MHWs increased by 1 to 4 $\mathrm{d\,yr}^{-1}$ (Fig. 2f). Coastal areas are where the number of days increases the fastest, with generally more than 2 $\mathrm{d\,yr}^{-1}$ over the study period. The fastest-increasing region is the English Channel, reaching or even exceeding 4 $\mathrm{d\,yr}^{-1}$. The duration of the MHW events shows no significant trend in the NWES, except for the English Channel, where each MHW event was 1 to 2 d longer, corresponding to increasing MHW days (Fig. 2g). The mean intensity (Fig. 2h) shows a completely different trend in the North Sea and the rest of the regions. In the North Sea, MHWs tend to be less intense, whereas in the Shetland–Irish Shelf and the Celtic Sea, MHWs intensified at a rate of 0.02–0.04 $^{\circ}\mathrm{C\,yr}^{-1}$. In the English Channel and the western part of the southern North Sea, the annual mean intensity remained the same from 1993 to 2023.

The degree of density stratification, quantified by the potential energy anomaly (PEA) $\varnothing$, is shown in Fig. 3. In this study, only the annual mean and summer period (June to September) mean stratification are considered. Following Chen et al. (2022), the water column is considered stratified when $\varnothing \geq 50\,\mathrm{J\,m}^{-3}$. The NWES is weakly stratified with $\varnothing \approx 70\,\mathrm{J\,m}^{-3}$. During summer, higher SST enhances the density stratification, leading to $\varnothing$ in summer being approximately twice as high as the annual mean. The PEA is low in the southern part of the North Sea, the Irish Sea, where the depth is shallower. Due to strong tides, the water column is generally well mixed in the English Channel (Pohlmann, 1996). In the middle North Sea and the Shetland–Irish Shelf, $\varnothing \geq 50\,\mathrm{J\,m}^{-3}$ during the summertime and $\varnothing < 50\,\mathrm{J\,m}^{-3}$ for the annual mean presents an obvious seasonal summer stratification. The Celtic Sea also exhibits seasonal cycles in PEA, with $\varnothing$ being 110–120 $\mathrm{J\,m}^{-3}$ during the summer and around 50 $\mathrm{J\,m}^{-3}$ over the entire year. The large annual mean PEA is mainly attributed to the extended warming period and stratification during autumn. The northern North Sea shows a seasonal cycle similar to that of the middle North Sea but with a

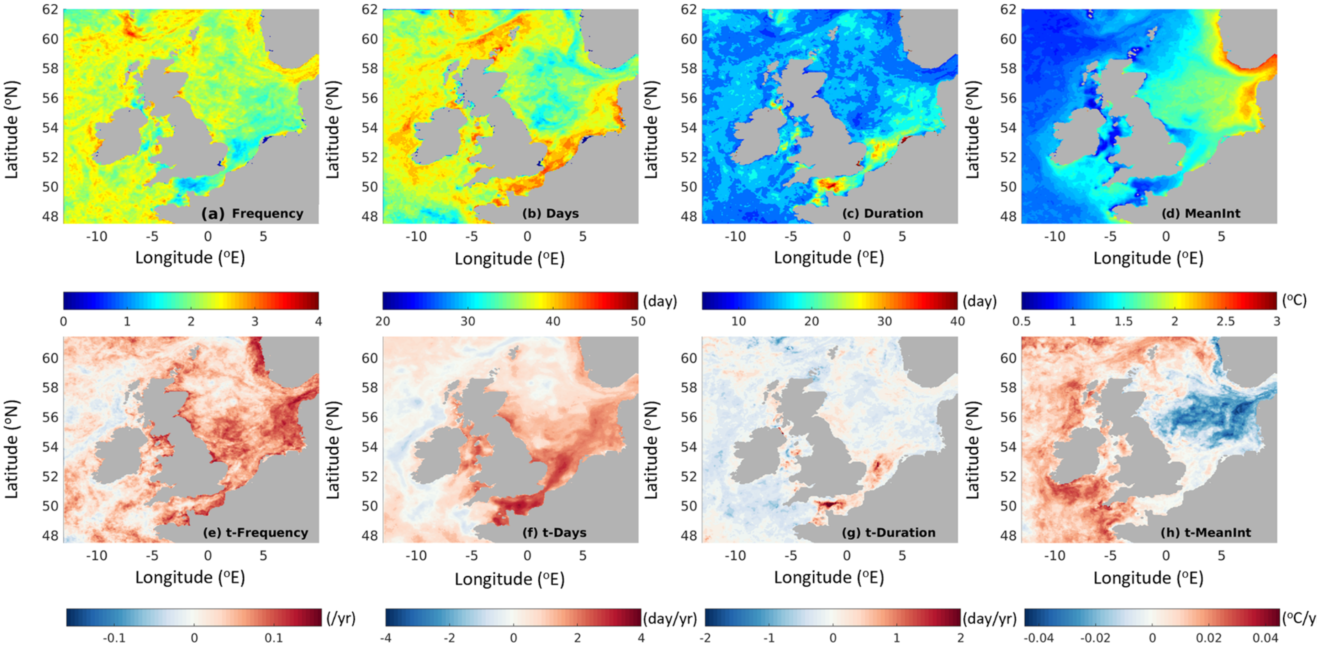

Figure 2. Mean and trend values of MHW over the past 30 years (1993–2022). Dashed lines indicate 200 m isobath (daily SST data from Table 1, ref. 1).

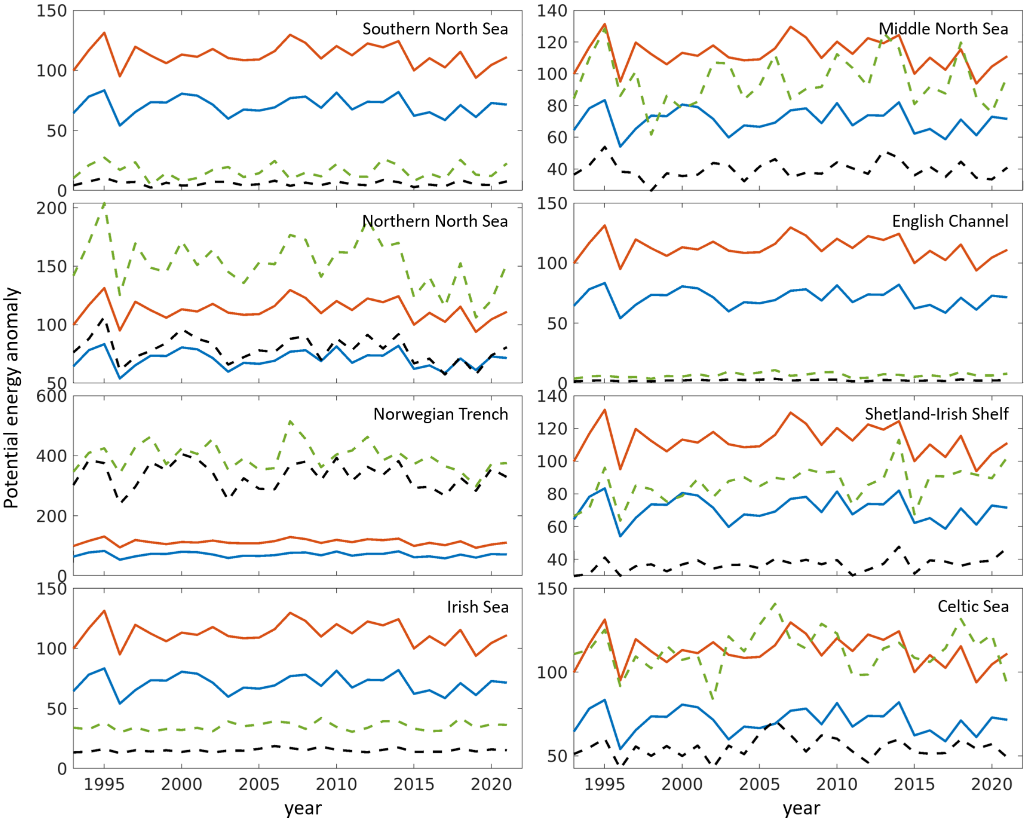

Figure 3. Potential energy anomaly ($\varnothing$; J m^{-3}) between 1993 and 2022. The solid curves denote the spatial mean PEA of the entire NWES domain. The red curves represent the summer period (June–September) mean in red, and the blue curves show the annual mean. The spatial mean PEA of different subdomains of the NWES (see Fig. 1a) is indicated by dashed curves, with green and black for the annual mean and summer mean, respectively.

larger $\varnothing$, both in the summer period and in the annual mean, due to larger depth. The potential energy anomaly in the Norwegian Trench is $\sim 400\,\mathrm{J\,m^{-3}}$. This is much larger than what is observed for the NWES region as a whole.

The density stratification has exhibited a trend opposite to that of MHWs over the past 30 years. Figure 4 illustrates the 10-year-averaged PEA across 3 decades, spanning from 1993 to 2022. Evident shifts in stratification are discernible. An obvious transformation of stratification is observed. Between 1993 and 2022, there was a decrease at a rate of -1 to $-2\,\mathrm{J\,m^{-3}\,yr^{-1}}$ only in the eastern part of the southern and middle North Sea, as well as in the Celtic Sea. Conversely, in the eastern part of the middle North Sea, the northern North Sea, and the Shetland–Irish Shelf, $\varnothing$ increased by approximately 1–1.5 $\mathrm{J\,m^{-3}\,yr^{-1}}$. During the second decade, the region where stratification grows was greatly reduced. Only parts of the northern North Sea near the Norwegian Trench and some areas of the Shetland–Irish Shelf still maintained a growth rate of 1 to $2\,\mathrm{J\,m^{-3}\,yr^{-1}}$. In the third decade, the entire North Sea tended to be less stratified, especially in the middle and northern parts of the North Sea, where the potential energy anomaly decreased by -2 to $-3\,\mathrm{J\,m^{-3}\,yr^{-1}}$. The transformation in the Norwegian Trench is consistent with that in the NWES (i.e., from an increased stratification from 1993 to 2012 to a decreased stratification in the most recent decade), although at a relatively higher rate (6–8 $\mathrm{J\,m^{-3}\,yr^{-1}}$).

The PEA trend is further decomposed to that due to the seawater temperature (T only; Fig. 4 second row) and salinity (S only; Fig. 4 third row). The former is related to the meteorological conditions, while the latter is related to the regional salt and freshwater changes. A positive PEA trend due to T or S implies a reduced vertical gradient in temperature or salinity, respectively. The decomposition reveals that in the North Sea region, both the water temperature and the salinity cause the weakening of the stratification. The changes in the trend in the Norwegian Trench results from the changing salinity trend (via freshwater inflow variability in the Baltic) (Tinker et al., 2016).

The sensitivity of stratification to the occurrence of marine heatwaves (MHWs), as quantified using Eq. (4), is demonstrated in Fig. 5. The illustration unequivocally indicates a profound linkage between summer stratification and MHWs, i.e., the seawater temperature T, particularly from June to September, within the southern North Sea expanse, notably in the eastern sector extending up to a longitude of 4.5° E (German Bight). This observation is consistent with the conclusions drawn by Chen et al. (2022). Another geographic area exhibiting a significant correlation between the presence of summer stratification and MHW events is the Shetland–Irish Shelf, which corresponds to region 6 in Fig. 1a. However, upon extending the temporal analysis window to encompass the entire year (i.e., all 12 months), it becomes evident that the northern North Sea (region 3; Fig. 1a), the Celtic Sea (region 8; Fig. 1a), and the Norwegian Trench (region 5; Fig. 1a) also reveal correlations with MHWs. This suggests that the manifestation of MHWs, especially those occurring during the winter season (see, e.g., Fig. 1b), instigate temperature disparities between the sea surface and its deeper layers, consequently giving rise to thermal stratification. Consequently, the escalating trend in MHW occurrences exerts an influence not only on the density stratification within the southern North Sea but also across other locales within the NWES, primarily due to the mounting incidence of MHWs during winter periods. However, in the English Channel (region 4; Fig. 1a) and the western portion of the southern North Sea (region 31; Fig. 1a) lying westward to the 4.5° E longitude, the water experiences annual thorough mixing attributed to tidal forces, thereby mitigating the impact of MHWs on density stratification.

4 Discussion

MHW events have become more frequent and prolonged over the period 1993–2022. The total number of days experiencing MHWs showed an upward trend, particularly in the English Channel with the rate of 2–4 $\mathrm{d\,yr^{-1}}$. These findings align with previous studies, which reported increasing MHW occurrences globally (e.g., Oliver et al., 2018; Smale et al., 2019) and in coastal regions (Marin et al., 2021). During the past 30 years, the most prolonged MHW found in the nearshore areas is mainly attributed to the long-term changes in mean SST, which increased fastest at the coastal oceans (Marin et al., 2021). Moreover, we observed an increase in MHW duration, indicating the potential for prolonged impacts on marine ecosystems (Frölicher and Laufkötter, 2018; Suryan et al., 2021). However, the results also show that the increase in MHW frequency and length may unnecessarily coincide with the heightening of SST. In the middle North Sea and near the Danish coast, the trend of mean MHW intensity is -2 to $-6\,\mathrm{J\,m^{-3}\,yr^{-1}}$, which appears contradictory to the increase in the MHW frequency and duration.

One possible explanation for the decrease in mean MHW intensity in the North Sea is the influence of large-scale climate patterns, such as atmospheric circulation changes. Woollings et al. (2018) demonstrated a weakening of the North Atlantic Jet Stream and an increase in atmospheric blocking events over the North Atlantic region. These changes can lead to stagnant atmospheric conditions and the trapping of warm air masses over the NWES, resulting in prolonged periods of high SST and MHW events. The increase in MHW frequency and duration may be a consequence of these altered atmospheric circulation patterns rather than a direct result of SST heightening. Furthermore, internal variability in the regional ocean, especially local processes that affect SST, play an important role (Marin et al., 2021). This includes variations in the fresh water–salt exchange and stratification (Mathis et al., 2015). Changes in these processes, particularly the Baltic Sea inflow, can affect the stability of the water column and result in a local-

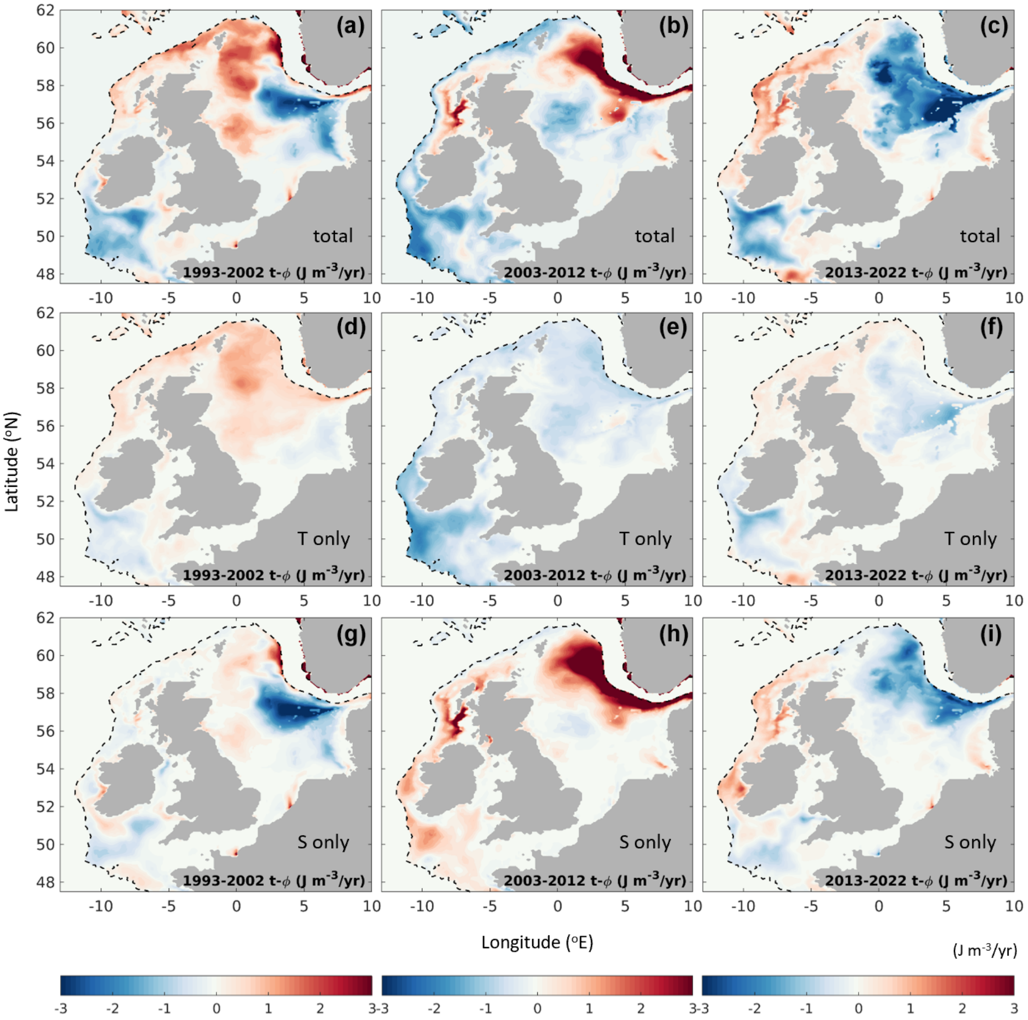

Figure 4. Trend of potential energy anomaly ($\varnothing$; $\mathrm{J\,m^{-3}\,yr^{-1}}$) over the last 30 years. The first row (total) shows $\varnothing$ computed with Eq. (1), where density depends on both temperature (T) and salinity (S) in the water column. The second and third rows are similar to the first row, but the density depends only on either T or S, respectively.

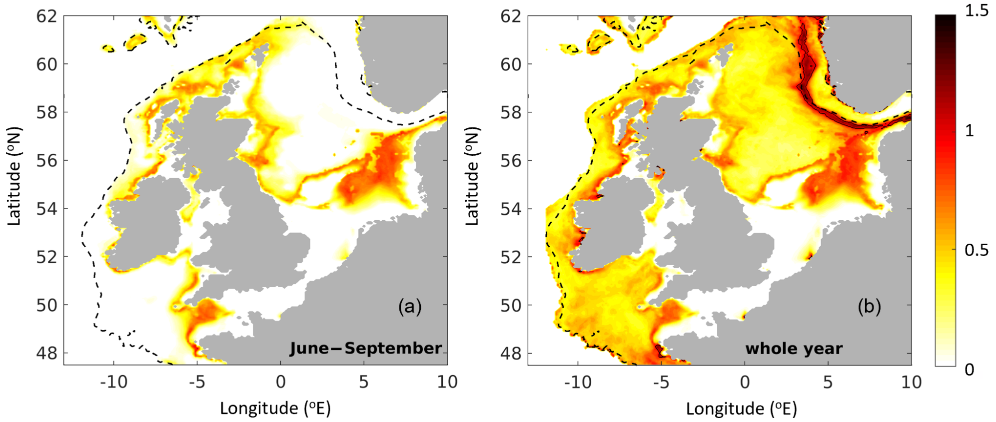

Figure 5. Ratio of the number of water stratification days to the number of MHW days for **(a)** June to September (summer period) and the whole year. The ratio is computed with Eq. (4), using the multiyear water temperature and salinity at different depths for 1992 to 2022 (details in Table 1, ref. 1). The thin dashed line indicates the 200 m isobaths.

ized decrease in mean MHW intensity, while outside the North Sea region, the intensity of MHWs increases due to different oceanic processes and heat transport mechanisms in the North Atlantic Ocean (Plecha et al., 2021). In addition, it is important to note that the observed decrease in mean MHW intensity in certain areas does not negate the overall increase in MHW frequency and duration. Climate change, with its warming trends and interactions with atmospheric and oceanic conditions, is a key driver of the intensification and increased occurrence of extreme events like MHWs. While localized decreases in mean intensity may be present, the number and duration of MHW events are surpassing these reductions. These findings highlight the complex interactions between climate change, atmospheric circulation patterns, and regional oceanic processes in shaping MHW characteristics.

Despite the more frequent and prolonged MHW leading to a more stable water column, the potential energy anomaly ($\varnothing$), a measure of stratification, showed a decreasing trend in the North Sea. This suggests that the MHW events and density stratification in the NWES region are not directly related. One notable piece of evidence is that the region where mean MHW intensity shows a downward trend overlaps with the area of reducing density stratification.

In general, MHW events lead to a significant increase in SST, resulting in intensified thermal stratification during these events (Chen et al., 2022). The analysis of annual mean SST trends in the NWES over the past 3 decades reveals a positive trend with a rate of change of 0.03–0.05 °C yr^{-1} (EU Copernicus Marine Service Product, 2023). Interestingly, the PEA due to seawater temperatures shows an opposite trend, particularly from 2003 to 2022 (Fig. 4). As this parameter quantifies the temperature heterogeneity of the water column, the decrease in PEA suggests a reduction in the temperature difference between the surface and the subsurface. With the observed increasing trend of NWES SST in response to a warming climate, the decline in PEA due to temperature can be solely attributed to the warming of the subsurface water. This warming is primarily driven by strong winter warming, leading to a weakening of the thermal stratification (Mathis and Pohlmann, 2014). This phenomenon is evident in the northern North Sea and the Celtic Sea, where the emergence of thermal stratification exhibits strong correlations with the occurrence of MHWs during winter seasons (Fig. 5). Additionally, the lower water column retains the memory of winter warming for a longer duration compared to the surface (Chen et al., 2022). Therefore, the rise in SST caused by increased MHW events is insufficient to counterbalance the overall weakening of thermal stratification due to seawater warming. Additionally, other factors and processes, such as oceanic circulation patterns and mixing mechanisms, may contribute to the observed changes in stratification (Guihou et al., 2017). Increased river runoff can lead to stronger salinity decreases at the sea surface compared to deeper layers, intensifying the stratification in terms of an increasing vertical salinity gradient (Lehmann et al., 2022). This can be seen at the estuarine zones, exemplified by the German Bight in the southern North Sea (Chegini et al., 2020). The analysis of PEA trends due to salinity also highlights the significant impact of variation in the Baltic discharge on stratification in the Norwegian Trench of the North Sea (Tinker et al., 2016).

It is notable that, within the NWES, the variability in salinity exerts a more pronounced influence on stratification compared to temperature variability. However, it is essential to recognize that climatic factors also potentially impact salinity fluctuations in the NWES. Schrum et al. (2016) reported a freshening trend in the North Sea attributed to increased river runoff and Baltic discharge, both intricately linked to an intensified water cycle and amplified net precipitation in mid- to high-latitude regions (Collins et al., 2013; Levang and Schmitt, 2015). Moreover, atmospheric heatwave events, known as significant contributors to MHW occurrences (Hobday et al., 2016), can notably affect precipitation and evaporation dynamics (Miralles et al., 2019), thereby further influencing river runoff and Baltic discharge (Lehmann et al., 2022). As a prospective avenue of research, delving into the NWES and Baltic as an integrated system would yield intriguing insights. Exploring the interplay between European continent-wide precipitation, evaporation patterns, and the evolving stratification trend in the NWES presents an intriguing prospect. Gaining comprehension of these intricate interactions would offer valuable revelations about the multifaceted mechanisms steering shifts in stratification and their intricate connections to regional climate dynamics.

5 Conclusion

Leveraging the wealth of high-resolution data furnished by the Copernicus Marine Environment Monitoring Service, we have analyzed the occurrence of MHW events and their underlying characteristics spanning the last 3 decades within the NWES region.

Our analysis revealed multiple MHW events throughout the year, including during the winter season. We find that despite showing spatial variations, MHWs have tended to become more frequent and prolonged over the past 3 decades in the NWES. The temporal dynamics of MHWs reveal a noteworthy trajectory, augmenting at a rate of 0.1 to 0.15 events yr^{-1} on average, contributing to a rise in annual occurrence by a range of 1 to 4 d. It is evident that coastal areas are the epicenters of this phenomenon, experiencing the swiftest augmentation in MHW duration when juxtaposed against other regions within the NWES. However, the NWES did not show a trend toward stronger stratification due to MHW occurring more frequently and lasting longer. On the contrary, it becomes less stratified, especially in the middle and northern North Sea region.

A closer examination of seawater temperature trends reveals that the rise in SST caused by increased MHW events is insufficient to offset the overall weakening of thermal stratification due to seawater warming. This is evident in the northern North Sea, where the emergence of thermal stratification exhibits a strong correlation with the occurrence of MHWs during winter seasons. However, the intricate dynamics extend beyond temperature alone. The variation in the salinity has a significant impact on the trend of change in density stratification. In particular, the influence of Baltic discharge, a veritable fulcrum of internal variability, emerges as a paramount process dictating the trajectory of changes in density stratification within the North Sea. The intricate interplay of freshwater influx from the Baltic Sea, influenced by climatic factors such as intensified water cycles and augmented net precipitation, intricately shapes the spatial distribution of salinity patterns within the North Sea realm. It is imperative to treat the NWES and Baltic as integral components of a larger, interconnected system. The interdependency between these domains necessitates a comprehensive approach that transcends arbitrary boundaries and delves into the subtle threads linking various climatic, oceanographic, and hydrological factors.

In summary, the interplay between temperature, salinity, and their intricate interactions with MHWs, Baltic discharge, and broader climatic phenomena collectively weave an intricate tapestry of density stratification trends within the North Sea region. This multifaceted narrative underscores the necessity of adopting a unified perspective that considers the complex interdependencies and feedback loops that characterize the intricate dance of nature's forces in this vital marine expanse. The outcomes of this research transcend theoretical confines, bearing practical significance for diverse sectors.

By unraveling the intricate interplay between MHWs, thermal stratification, and salinity dynamics, our study contributes to a more comprehensive understanding of climate change impacts on regional oceanic systems. The implications extend to domains such as ecosystem dynamics, fisheries, and related sectors, which are poised to be influenced by the enduring alterations in the thermal stratification patterns. These changes have far-reaching implications for the ecological and socioeconomic fabric of the NWES region.

Data availability. The datasets presented in this study can be found in the CMEMS online repository. Details are listed in Table 1 of this paper.

Author contributions. WC conceptualized the study, analyzed data, and wrote this article. JS contributed to the writing of the article and quality control.

Competing interests. The contact author has declared that neither of the authors has any competing interests.

Disclaimer. Views and opinions expressed are however those of the author(s) only and do not necessarily reflect those of the European Union or the European Health and Digital Executive Agency (HaDEA). Neither the European Union nor HaDEA can be held responsible for them.

Acknowledgements. Wei Chen acknowledges the Copernicus Marine Service Evolution Strategy 2022 project Coastal-risks: Predicting risks of the German Bight coast under extreme storm events (21036-COP-INNO SCI) and the EU Green Deal project REST-COAST: Large scale restoration of coastal ecosystems through rivers to sea connectivity (grant no. 101037097). Joanna Staneva acknowledges OLAMUR project: Offshore Low-trophic Aquaculture in Multi-Use Scenario Realisation (grant agreement 101094065). We also thank Lorena Moreira Mendez and Karina von Schuckmann for their comments and great help in improving the quality of this paper.

Financial support. This research has been funded by the Copernicus Marine Service Evolution (21036-COP-INNO SCI) and the European Union (grant agreement nos. 101037097 and 101094065).

Review statement. This paper was edited by Marilaure Grégoire and reviewed by two anonymous referees.

References

Borges, A., Royer, C., Martin, J. L., Champenois, W., and Gypens, N.: Response of marine methane dissolved concentrations and emissions in the Southern North Sea to the European 2018 heatwave, Cont. Shelf Res., 190, 104004, https://doi.org/10.1016/j.csr.2019.104004, 2019.

Chegini, F., Holtermann, P., Kerimoglu, O., Becker, M., Kreus, M., Klingbeil, K., Gräwe, U., Winter, C. and Burchard, H.: Processes of stratification and destratification during an extreme river discharge event in the German Bight ROFI, J. Geophys. Res.-Oceans, 125, e2019JC015987, https://doi.org/10.1029/2019JC015987, 2020.

Chen, W., Staneva, J., Grayek, S., Schulz-Stellenfleth, J., and Greinert, J.: The role of heat wave events in the occurrence and persistence of thermal stratification in the southern North Sea, Nat. Hazards Earth Syst. Sci., 22, 1683–1698, https://doi.org/10.5194/nhess-22-1683-2022, 2022.

Collins, M., Knutti, R., Arblaster, J., Dufresne, J.-L., Fichefet, T., Friedlingstein, P., Gao, X., Gutowski, W. J., Johns, T., Krinner, G., Shongwe, M., Tebaldi, C., Weaver, A. J., and Wehner, M.: Long-term climate change: projections, commitments and irreversibility, in: Climate change 2013: the physical science basis, Contribution of Working Group I to the Fifth Assessment Report of the Intergovernmental Panel on Climate Change, edited by: Stocker, T. F., Qin, D., Plattner, G.-K., Tignor, M., Allen, S. K., Boschung, J., Nauels, A., Xia, Y., Bex, V., and Midgley, P. M., Cambridge University Press, https://www.ipcc.ch/site/assets/uploads/2018/02/WG1AR5_Chapter12_FINAL.pdf (last access: 21 March 2024), 2013.

EU Copernicus Marine Service Product: Atlantic-European North West Shelf-Ocean Physics Reanalysis, Mercator Ocean International [data set], https://doi.org/10.48670/moi-00059, 2021.

EU Copernicus Marine Service Product: European North West Shelf Sea Surface Temperature trend map from Observations Reprocessing, Mercator Ocean International [data set], https://doi.org/10.48670/moi-00276, 2023.

Frölicher, T. L. and Laufkötter, C.: Emerging risks from marine heat waves, Nat. Commun., 9, 650, https://doi.org/10.1038/s41467-018-03163-6, 2018.

Frölicher, T. L., Fischer, E. M., and Gruber, N.: Marine heatwaves under global warming, Nature, 560, 360–364, https://doi.org/10.1038/s41586-018-0383-9, 2018.

Guihou, K., Polton, J., Harle, J., Wakelin, S., O'Dea, E., and Holt, J.: Kilometric scale modeling of the NorthWest European Shelf Seas: Exploringthe spatial and temporal variability ofinternal tides, J. Geophys. Res.-Oceans, 123, 688–707, https://doi.org/10.1002/2017JC012960, 2017.

Gupta, A. S., Thomsen, M., Benthuysen, J. A., Hobday, A. J., Oliver, E., Alexander, L. V., Burrows, M. T., Donat, M. G., Feng, M., Holbrook, N. J., Perkins-Kirkpatrick, S., Moore, P. J., Rodrigues, R. R., Scannell, H. A., Taschetto, A. S., Ummenhofer, C. C., Wernberg, T., and Smale, D. A.: Drivers and impacts of the most extreme marine heatwaves events, Sci. Rep., 10, 19359, https://doi.org/10.1038/s41598-020-75445-3, 2020.

Herring, S. C., Hoerling, M. P., Kossin, J. P., Peterson, T. C., and Stott, T. C.: Introduction to explaining extreme events of 2014 from a climate perspective, B. Am. Meteorol. Soc., 96, S1–S4, 2015.

Hobday, A. J., Alexander, L. V., Perkins, S. E., Smale, D. A., Straub, S. C., Oliver, E. C., Benthuysen, J. A., Burrows, M. T., Donat, M. G., Feng, M., Holbrook, N. J., Moore, P. J., Scannell, H. A., Sen Gupta, A., and Wernberg, T.: A hierarchical approach to defining marine heatwaves, Prog. Oceanogr., 141, 227–238, https://doi.org/10.1016/j.pocean.2015.12.014, 2016.

IPCC: Climate Change 2021: The Physical Science Basis. Contribution of Working Group I to the Sixth Assessment Report of the Intergovernmental Panel on Climate Change, edited by: Masson-Delmotte, V., Zhai, P., Pirani, A., Connors, S. L., Péan, C., Berger, S. , Caud, N., Chen, Y., Goldfarb, L., Gomis, M. I., Huang, M., Leitzell, K., Lonnoy, E., Matthews, J. B. R., Maycock, T. K., Waterfield, T., Yelekçi, O., Yu, R., and Zhou, B., Cambridge University Press, https://www.ipcc.ch/report/ar6/wg1/downloads/report/IPCC_AR6_WGI_SummaryVolume.pdf (last access: 21 March 2024), 2021.

Lehmann, A., Myrberg, K., Post, P., Chubarenko, I., Dailidiene, I., Hinrichsen, H.-H., Hüssy, K., Liblik, T., Meier, H. E. M., Lips, U., and Bukanova, T.: Salinity dynamics of the Baltic Sea, Earth Syst. Dynam., 13, 373–392, https://doi.org/10.5194/esd-13-373-2022, 2022.

Levang, S. J. and Schmitt, R. W.: Centennial changes of the global water cycle in CMIP5 models, J. Climate, 28, 6489–6502, https://doi.org/10.1175/jcli-d-15-0143.1, 2015.

Marin, M., Feng, M., Phillips, H. E., and Bindoff, N. L.: A global, multiproduct analysis of coastal marine heatwaves: Distribution, characteristics and long-term trends, J. Geophys. Res.-Oceans, 126, e2020JC016708, https://doi.org/10.1029/2020JC016708, 2021.

Mathis, M. and Pohlmann, T.: Projection of physical conditions in the North Sea for the 21st century, Clim. Res., 61, 1–17, https://doi.org/10.3354/cr01232, 2014.

Mathis, M., Elizalde, A., Mikolajewicz, U., and Pohlmann, T.: Variability patterns of the general circulation and sea water temperature in the North Sea, Prog. Oceanogr., 135, 91–112, 2015.

Merchant, C. J., Embury, O., Bulgin, C. E., Block, T., Corlett, G. K., Fiedler, E., Good, S. A., Mittaz, J., Rayner, N. A., Berry, D., Eastwood, S., Taylor, M., Tsushima, Y., Waterfall, A., Wilson R., and Donlon C.: Satellite-based time-series of sea-surface temperature since 1981 for climate applications, Sci. Data, 6, 1–18, 2019.

Millero, F. J. and Poisso, A.: International one-atmosphere equation of state of seawater, Deep-Sea Res. Pt. A, 28, 625–629, https://doi.org/10.1016/0198-0149(81)90122-9, 1981.

Miralles, D. G., Gentine, P., Seneviratne, S. I., and Teuling, A. J.: Land–atmospheric feedbacks during droughts and heatwaves: state of the science and current challenges, Ann. N. Y. Acad. Sci., 1436, 19–35, 2019.

Mohamed, B., Barth, A., and Alvera-Azcarate, A.: Extreme marine heatwaves and cold spells events in the Southern North Sea: classification, patterns, and trends, Front. Mar. Sci., 19, 1258117, https://doi.org/10.3389/fmars.2023.1258117, 2023.

Oliver, E. C., Donat, M. G., Burrows, M. T., Moore, P. J., Smale, D. A., Alexander, L. V., Benthuysen, J. A., Feng, M., Gupta, A. S., Hobday, A. J., Holbrook, N. J., Perkins-Kirkpatrick, S. E., Scannell, H. A., Straub, S. C., and Wernberg, T.: Longer and more frequent marine heatwaves over the past century, Nat. Commun., 9, 1–12, https://doi.org/10.1038/s41467-018-03732-9, 2018.

Oliver, E. C., Burrows, M. T., Donat, M. G., Sen Gupta, Alexander., Alexander, Lisa V., Perkins-Kirkpatrick, S. E., Benthuysen, Jessica A., Hobday, Alistair J., Holbrook, N. J., Moore, P. J., Thomsen, M. S., Wernberg, T., and Smale, D. A.: Projected marine heatwaves in the 21st century and the potential for ecological impact, Front. Mar. Sci., 6, 1–12, https://doi.org/10.3389/fmars.2019.00734, 2019.

Oliver, E. C., Benthuysen, J. A., Darmaraki, S., Donat, M. G., Hobday, A. J., Holbrook, N. J., Schlegel, R. W., and Gupta, A. S.: Marine heatwaves, Annu. Rev. Mar. Sci., 13, 313–342, https://doi.org/10.1146/annurev-marine-032720-095144, 2020.

Plecha, S. M., Soares, P. M. M., Silva-Fernandes, S. M., and Cabos, W.: On the uncertainty of future projections of Marine Heatwave events in the North Atlantic Ocean, Clim. Dynam., 56, 2027–2056, https://doi.org/10.1007/s00382-020-05529-3, 2021.

Pohlmann, T.: Calculating the development of the thermal vertical stratification in the North Sea with a three-dimensional baroclinic circulation, Cont. Shelf Res., 16, 163–194, 1996.

Renshaw, R., Wakelin, S., Golbeck, I., and O'Dea, E.: EU Copernicus Marine Service Quality Information Document for the Atlantic-European North West Shelf-Ocean Physics Reanalysis, NWSHELF_MULTIYEAR_PHY_004_009, Issue 5.2, Mercator Ocean International, https://catalogue.marine.copernicus.eu/documents/QUID/CMEMS-NWS-QUID-004-009.pdf (last access: 19 July 2023), 2021.

Schlegel R. W., Oliver E. C. J., and Chen K.: Drivers of marine heatwaves in the northwest atlantic: the role of air–sea interaction during onset and decline, Front. Mar. Sci., 8, 627970, https://doi.org/10.3389/FMARS.2021.627970, 2021.

Schrum, C., Lowe, J., Meier, H. M., Grabemann, I., Holt, J., Mathis, M., Pohlmann, T., Skogen, M. D., Sterl, A., and Wakelin, S.: Projected change – North Sea, North Sea Region Climate Change Assessment, Springer International Publishing, 175–217, ISBN 978-3-319-39745-0, 2016.

Simpson, J. H.: The shelf-sea fronts: implications of their existence and behaviour, Philos. T. Roy. Soc. A, 302, 531–546, https://doi.org/10.1098/rsta.1981.0181, 1981.

Smale, D. A., Wernberg, T., Oliver, E. C., Thomsen, M., Harvey, B. P., Straub, S. C., Burrows, M. T., Alexander, L. V., Benthuysen, J. A., Donat, M. G., Feng, M., Hobday, A. J., Holbrook, N. J., Moore, Perkins-Kirkpatrick, S. E., Scannell, H. A., Gupta, A. S., Payne, B. L., and Moore, P. J.: Marine heatwaves threaten global biodiversity and the provision of ecosystem services, Nat. Clim. Change, 9, 306–312, https://doi.org/10.1038/s41558-019-0412-1, 2019.

Suryan, R. M., Arimitsu, M. L., Coletti, H. A., Hopcroft, R. R., Lindeberg, M. R., Barbeaux, S. J., Batten, S. D., Burt, W. J., Bishop, M. A., Bodkin, J. L., Brenner, R., Campbell, R. W., Cushing, D. A., Danielson, S. L., Dorn, M. W., Drummond, B., Esler, D., Gelatt, T., Hanselman, D. H., Hatch, S. A., Haught, S., Holderied, K., Iken, K., Irons, D. B., Kettle, A. B., Kimmel, D. G., Konar, B., Kuletz, K. J., Laurel, B. J., Maniscalco, J. M., Matkin, C., McKinstry, C. A. E., Monson, D. H., Moran, J. R., Olsen, D., Palsson, W. A., Pegau, W. S., Piatt, J. F., Rogers, L. A., Rojek, N. A., Schaefer, A., Spies, I. B., Straley, J. M., Strom, S. L., Sweeney, K. L., Szymkowiak, M., Weitzman, B. P., Yasumiishi, E. M., and Zador, S. G.: Ecosystem response persists after a prolonged marine heatwave, Sci. Rep., 11, 6235, https://doi.org/10.1038/s41598-021-83818-5, 2021.

Tinker, J. and Howes, E. L.: The impacts of climate change on temperature (air and sea), relevant to the coastal and marine environment around the UK, MCCIP Science Review, https://doi.org/10.14465/2020.arc01.tem, 2020.

Tinker, J., Lowe, J., Pardaens, A., Holt, J., and Barciela, R.: Uncertainty in climate projections for the 21st century northwest European shelf seas, Prog. Oceanogr., 148, 56–73, 2016.

Tonani, M., Ascione, I., and Saulter, A.: EU Copernicus Marine Service Product User Manual for the Atlantic-European North West Shelf-Ocean Physics Reanalysis, NWSHELF_MULTIYEAR_PHY_004_009, Issue 1.3, Mercator Ocean International, https://catalogue.marine.copernicus.eu/documents/PUM/CMEMS-NWS-PUM-004-009-011.pdf (last access: 19 July 2023), 2022.

Wakelin, S., Townhill, B., Engelhard, G., Holt, J., and Renshaw, R.: Marine heatwaves and cold-spells, and their impact on fisheries in the southern North Sea, EGU General Assembly 2021, online, 19–30 April 2021, EGU21-7329, https://doi.org/10.5194/egusphere-egu21-7329, 2021.

Wernberg, T., Smale, D. A., Tuya, F., Thomsen, M. S., Langlois, T. J., De Bettignies, T., Bennett, S., and Rousseaux, C. S.: An extreme climatic event alters marine ecosystem structure in a global biodiversity hotspot, Nat. Clim. Change, 3, 78–82, https://doi.org/10.1038/NCLIMATE1627, 2013.

Wernberg, T., Bennett, S., Babcock, R. C., de Bettignies, T., Cure, K., Depczynski, M., Dufois, F., Fromont, J., Fulton, C. J., Hovey, R. K., Harvey, E. S., Holmes, T. H., Kendrick, G. A., Radford, B., Santana-Garcon, J., Saunders, B. J., Smale, D. A., Thomsen, M. S., Tuckett, C. A., Tuya, F., Vanderklift, M. A., and Wilson, S.: Climate-driven regime shift of a temperate marine ecosystem, Science, 353, 169–172, https://doi.org/10.1126/science.aad8745, 2016.

Woollings, T., Barriopedro, D., Methven, J., Son, S.-W., Martius, O., Harvey, B., Sillmann, J., Lupo, A. R., and Seneviratne, S.: Blocking and its Response to Climate Change, Curr. Clim. Change Rep., 4, 287–300, https://doi.org/10.1007/s40641-018-0108-z, 2018.

Zhao, Z. and Marin, M.: A MATLAB toolbox to detect and analyze marine heatwaves, Journal of Open Source Software, 4, 1124, https://doi.org/10.21105/joss.01124, 2019.

State Planet, 4-osr8, 8, 2024
https://doi.org/10.5194/sp-4-osr8-8-2024

Surface and bottom marine heatwave characteristics in the Barents Sea: a model study

Vidar S. Lien[1,2], **Roshin P. Raj**[2,3], **and Sourav Chatterjee**[4]

[1]Department of Oceanography & Climate, Institute of Marine Research, Bergen, Norway
[2]Polar Climate Group, Bjerknes Center for Climate Research, Bergen, Norway
[3]Ocean and Sea Ice Remote Sensing Group, Nansen Environmental and Remote Sensing Center, Bergen, Norway
[4]National Centre for Polar and Ocean Research, Ministry of Earth Sciences, Vasco-da-Gama, India

Correspondence: Vidar S. Lien (vidar.lien@hi.no)

Received: 7 July 2023 – Discussion started: 28 August 2023
Revised: 14 February 2024 – Accepted: 20 March 2024 – Published: 30 September 2024

Abstract. Anomalously warm oceanic events, often termed marine heatwaves (MHWs), can potentially impact the ecosystem in the affected region and have therefore become a hot topic for research in recent years. Determining the intensity and spatial extent of marine heatwaves, however, depends on the definition and climatological average used. Moreover, the stress applied by the heatwave to the marine ecosystem will depend on which component of the ecosystem is considered. Here, we utilize a model reanalysis (1991–2022) to explore the frequency, intensity, and duration of marine heatwaves in the Barents Sea, as well as regional heterogeneities. We find that major marine heatwaves are rather coherent throughout the region, but surface marine heatwaves occur more frequently while heatwaves on the ocean floor have a longer duration. Moreover, we investigate the sensitivity to the choice of climatological average length when calculating marine heatwave statistics. Our results indicate that severe marine heatwaves may become more frequent in a future Barents Sea due to ongoing climate change.

1 Introduction

A marine heatwave (MHW) is a period of a warm spell in an ocean region and is usually defined as a period when the temperature exceeds a given threshold relative to a climatological average (e.g., Marbá et al., 2015; Hobday et al., 2016; Scannell et al., 2016; Hu et al., 2020; Huang et al., 2021). Due to the potentially profound impact on marine life (e.g., Smale et al., 2019; Husson et al., 2022) and, hence, also socioeconomic impacts (Smith et al., 2021), MHWs have received increasing attention in recent years (see Oliver et al. (2021) for a comprehensive review of recent literature). While the criteria to define MHWs seem to converge to those proposed by Hobday et al. (2016), i.e., the temperature exceeding the 90th percentile of the moving climatological average, little attention has been given to the impact of the choice of climatological average on the MHW characteristics and statistics such as frequency, intensity, and duration (Chiswell, 2022). The underlying trends of global ocean warming (e.g., Cheng et al., 2022) and regional climate variability (e.g., Smedsrud et al., 2022) both impact the MHW statistics, and some regions may eventually enter a state of permanent MHW, depending on the climatological average chosen. As an example, while Fröhlicher et al. (2018) found a doubling of MHW days between 1982 and 2016 globally, Chiswell (2022) showed that accounting for climate change by removing the linear trend resulted in weaker MHWs in the tropics and stronger MHWs in the northern Pacific and Atlantic oceans.

When MHWs are calculated as a time series for a whole region, possible regional heterogeneities may be masked, thereby reducing the applicability of using the time series as an MHW index. The Barents Sea is a complex shelf sea that mainly consists of a relatively warm and ice-free Atlantic-Water-dominated part in the south and a cold, seasonally ice-

Published by Copernicus Publications.

Table 1. Products used and their documentation.

Product ref. no.	Product ID & type	Data access	Documentation
1	ARCTIC_MULTIYEAR_PHY_002_003; numerical models	EU Copernicus Marine Service Product (2023)	Quality Information Document (QUID): Xie and Bertino (2023) Product User Manual (PUM): Hackett et al. (2023)
2	Conductivity–Temperature–Depth data obtained in the Barents Sea	IMR database TINDOR (data accessible upon request)	
3	ERA5 gridded reanalysis (0.25° × 0.25°); monthly average on single level	Hersbach et al. (2023)	Hersbach et al. (2023)

covered Arctic-Water-dominated part in the north. The southern part is kept ice-free by relatively warm and saline Atlantic Water entering to the southwest. The Atlantic Water gives up most of its heat (relative to the average temperature of the Polar Basin) to the atmosphere while en route (e.g., Gammelsrød et al., 2009; Smedsrud et al., 2013). Moreover, the inflow of Atlantic Water has been shown to be a precursor for interannual variability in the Barents Sea sea-ice cover (Onarheim et al., 2015; Schlichtholz, 2019) and in the ocean heat content further downstream in the Barents Sea (Lien et al., 2017). Both the southern and northern Barents Sea have varying seasonal stratification, mainly from the melting of sea ice in the north and solar insolation causing thermal stratification in the south (e.g., Smedsrud et al., 2013; Lind et al., 2018). The marine ecosystem differs between the two main regions, with further diversification within each region. However, the extension of the two regimes is changing due to ongoing climate change, with the boreal southern part expanding at the expense of the northern Arctic part (e.g., Fossheim et al., 2015; Oziel et al., 2020). The Barents Sea is home to several important commercial fish stocks, both pelagic (e.g., capelin (*Mallotus villosus*) and Norwegian spring spawning herring (*Clupea harengus*)) and demersal (e.g., Northeast Arctic cod (*Gadus morhua*) and haddock (*Melanogrammus aeglefinus*)), in addition to a diverse marine ecosystem including large groups of marine mammals and sea birds, as well as unique benthos communities (see Jakobsen and Ozhigin, 2011, for a more comprehensive overview). Hence, MHWs may have profound impacts on marine living resources but with different species exhibiting differences in resilience to MHW events (e.g., Husson et al., 2022). Recent studies on MHWs in the Barents Sea, however, have focused on the surface or the upper parts of the water column (Mohamed et al., 2022; Husson et al., 2022). Here, we investigate the occurrences of both surface and bottom MHWs in four contrasting environments in the Barents Sea. Moreover, we explore the differences in frequency, intensity, and duration using varying climatological average lengths for estimating MHWs. We also focus on the highest-intensity MHW event in terms of cumulative degree days and investigate its oceanic and atmospheric preconditioning and decline.

2 Data & methods

2.1 Model data

We based our analysis on modelled daily averages from the EU Copernicus Marine Service ocean reanalysis for the Arctic region based on the TOPAZ model system for the period 1991–2022 (Sakov et al., 2012; Xie et al., 2016; Lien et al., 2016; product ref. 1, Table 1), hereinafter termed “TOPAZ reanalysis”.

2.2 Ocean observation data

We have used available Conductivity–Temperature–Depth (CTD) casts (product ref. 2, Table 1), covering the period 1986 to 2020, for assessing the quality of the model dataset with regard to bottom temperatures in four regions of the Barents Sea (Fig. 1) before we use the models results to calculate MHW statistics. The CTD data were obtained from the Institute of Marine Research database, The Integrated Database for Ocean Research (TINDOR).

2.3 Atmospheric data

Monthly averages of turbulent heat fluxes and outgoing longwave radiation for the period 1993 to 2021 were downloaded from the EU Copernicus Climate Service website (product ref. 3, Table 1; Hersbach et al., 2023).

2.4 Marine heatwave estimation method

We have adopted the definition of MHWs proposed by Hobday et al. (2016), where an MHW is defined as a period of more than 5 d where the temperature is above the 90th percentile of the daily varying climatology averaged over a period of at least 30 years. Moreover, two consecutive events divided by a gap of 2 d or less are considered a single event.

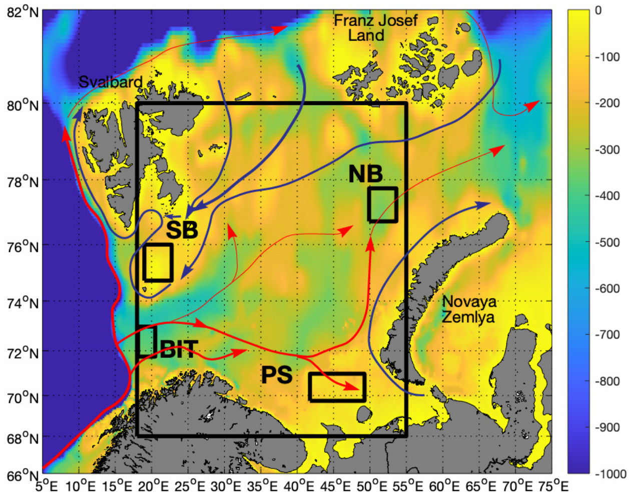

Figure 1. Map of the Barents Sea. Colours show the bathymetry (in metres). Arrows show the main current patterns for Atlantic Water (red) and Arctic Water (blue). Boxes show regions for estimating marine heatwave statistics from the TOPAZ reanalysis. BIT: Bear Island Trough. NB: Northeast Basin. SB: Spitsbergen Bank. PS: Pechora Sea.

The TOPAZ reanalysis covers the time period 1991–2022. In compliance with common standards set by the World Meteorological Organization (WMO, 2007, 2015), we have chosen the period 1991–2020 as the climatological average period. To study the effect of changing the climatological average period, we have also calculated the MHW statistics using the 25-year period 1996–2020 and the 20-year period 2001–2020 as the climatological average periods.

We have chosen four sub-regions where we compute the daily spatially averaged surface and bottom temperatures representing contrasting marine environments: the Bear Island Trough in the southwestern Atlantic Water inflow area to the Barents Sea; the adjacent Spitsbergen Bank which represents a productive, shallow bank with an Arctic marine environment; the Northeast Basin in the northeastern Barents Sea which represents the outflow region where strongly modified Atlantic-derived water masses leave the Barents Sea; and the Pechora Sea to the southeast which represents a shallow area influenced by coastal water (see map; Fig. 1). Our Bear Island Trough region is pushed towards the southern slope of the trough to cover the area around 72°30′ N which is where the core of the main inflow branch carrying Atlantic Water to the Barents Sea is located (e.g., Skagseth et al., 2008).

For estimating MHW statistics we have used the Python package provided by Eric C. J. Oliver (https://github.com/ecjoliver/marineHeatWaves/releases/tag/v0.16; last access: 24 March 2023; Oliver, 2016), using the default settings.

Table 2. Statistics summarizing the comparison between the model and observations at N CTD locations. Correlations are shown in boldface when $p < 0.05$ and underlined boldface when $p < 0.01$. BIT: Bear Island Trough. SB: Spitsbergen Bank. PS: Pechora Sea. NB: Northeast Basin.

Model	Statistic	BIT	SB	PS	NB
TOPAZ	N	202	49	34	11
	Bias [°C]	1.9	−2.1	−0.8	−0.6
	RMSd [°C]	2.0	2.4	1.0	0.7
	Correlation [r]	$\underline{\mathbf{0.55}}$	$\underline{\mathbf{0.39}}$	$\underline{\mathbf{0.78}}$	**0.66**

2.5 Model evaluation

The model product used in this study has previously been evaluated against a suite of ocean observations (e.g., Lien et al., 2016; Xie et al., 2019, 2023). However, because we also used the model for the analysis of MHWs near the ocean floor, we provide an assessment of the quality of the model by direct comparison with observations of near-bottom temperature from CTD casts where available in the four sub-regions. The motivation for comparing only bottom temperatures is that satellite sea surface temperature observations are assimilated into the TOPAZ reanalysis. Moreover, the sea surface temperature is also constrained by ocean–atmosphere bulk fluxes.

In this model quality assessment, we compared modelled and observed near-bottom temperatures averaged in time (monthly) and space (see sub-regions; Fig. 1). The modelled seasonal signal was removed from both model and observation time series before the correlation was calculated. The comparison is summarized in Table 2 and Fig. S1.

3 Results

We first calculated the MHW statistics based on the TOPAZ reanalysis for the full Barents Sea region for the period 1991–2022 (see Fig. 1 for area definition), which are summarized in Fig. 2 and Tables 3–5. A total of 29 MHWs were identified at the surface compared to 5 MHWs near the bottom, equating to a frequency of 0.90 yr^{-1} at the surface and 0.16 yr^{-1} near the bottom. The average maximum intensity was 1.41 and 1.07 °C at the surface and near the bottom, respectively. The duration was, on average, longer near the bottom (214 d) than at the surface (33 d). Moreover, we found a positive decadal trend in the MHW frequency at the surface of 0.82 yr^{-1} ($p < 0.05$), while for all the other metrics mentioned above the decadal trends were non-significant.

Two periods are distinguished in terms of MHW cumulative intensity (°C days), both at the surface and near the bottom. The strongest MHW in the Barents Sea as a whole, in terms of cumulative intensity, occurred in 2016 both at the surface and near the bottom (Fig. 3a, f). At the surface, the 2016 MHW had an average intensity of 1.29 °C (maximum of 3.41 °C) and a total duration of 480 d (from 19 December 2015 to 11 April 2017). Near the bottom, the 2016 MHW had an average intensity of 1.10 °C (maximum of 1.28 °C) and a total duration of 479 d (28 February 2016 to 20 June 2017). The second-strongest MHW in terms of cumulative intensity in the Barents Sea as a whole occurred in 2013 at the surface and in 2012 near the bottom (see Fig. S2). While an investigation on possible mechanisms for the decoupling between the surface and the bottom is beyond the scope of this work, we note that the 2012–13 MHW event was preceded by an extraordinarily large temperature anomaly but close-to-average volume transport in the Atlantic Water entering the Barents Sea to the southwest (e.g., ICES, 2022), as opposed to extraordinarily large volume transports preceding the 2016 MHW event (see below for more details). Moreover, previous studies have suggested that temperature anomalies that are advected into the Barents Sea at depth during the stratified summer season can re-emerge at the surface further downstream through vertical mixing during the following winter (e.g., Schlichtholz, 2019).

To investigate possible regional heterogeneity in MHWs within the Barents Sea, we calculated MHW statistics in the four sub-regions depicted in Fig. 1. The results are summarized in Tables 3, 4, and 5. In all regions, we found a higher frequency of MHW events than for the Barents Sea as a whole (except for near the bottom of the Northeast Basin). Moreover, all regions showed a larger positive decadal trend in the frequency compared with the Barents Sea as a whole, although this trend was only found to be statistically significant near the bottom of the Pechora Sea ($p < 0.05$; Table 3). For the average maximum intensity at the surface, we found that the Bear Island Trough, which is the upstream inflow region, had similar statistics to the Barents Sea as a whole, while for the other three regions the intensity was generally larger (Table 4). Near the bottom, the intensity in the Bear Island Trough was less than that of the Barents Sea as a whole, while in the downstream Northeast Basin the intensity was larger on average. In the two other regions the differences were smaller. In terms of duration, all regions experienced shorter MWHs on average compared to the Barents Sea as a whole, especially near the bottom. The exception was the Northeast Basin, where the average duration of near-bottom MHWs was found to be comparable to that of the Barents Sea as a whole (Table 5).

To investigate further regional heterogeneity, we considered the MHW event in 2016 in each of the regions. At the surface, the 2016 MHW event was the most severe MHW event in terms of cumulative intensity in three out of the four sub-regions investigated. The exception was the Bear Island Trough, where the 2012 MHW event was more severe (not shown). Near the bottom, the 2016 MHW event was the most severe MHW event in all four regions (Fig. 3). The progression of the 2016 MHW event was comparable in all regions, except for the Spitsbergen Bank where the onset of the MHW occurred later, near mid-summer, compared to the other regions where the onset occurred during late winter. However, on the Spitsbergen Bank the 2016 MHW was preceded by several but less intense and intermittent MHWs. It is also worth noting that the onset in the other three regions, as well as the Barents Sea as a whole, occurred in late February/early March, except for in the upstream Bear Island Trough where the onset occurred at the beginning of April. Moreover, both the average and maximum MHW intensity were less in the Bear Island Trough compared to the other regions.

3.1 Preconditioning and atmospheric forcing of the 2016 MHW event

Leading up to the onset of the 2016 MHW, the inflow of warm Atlantic Water to the Barents Sea was above average during the whole of 2015 (ICES, 2022). However, during the following winter of 2015–16, the turbulent (latent and sensible) heat loss was between 20 and 70 $\mathrm{W\,m^{-2}}$ below the 1993–2021 average in the southern Barents Sea (71–75° N, 25–45° E; i.e., along the Atlantic Water pathway through the Barents Sea; Fig. 4a), which was the lowest for the period 1993–2021. The reduced heat loss to the atmosphere occurred despite the preceding increase in advected oceanic heat (Fig. 4a, e). Note that, during the winter months, the solar radiation can be neglected due to the polar night conditions in the Barents Sea region. Moreover, wind-driven mixing during winter breaks down the upper water column stratification, connecting the surface with the deeper layers. Thus, the 2016 MHW event was preceded by an increased Atlantic Water heat transport and reduced heat loss to the atmosphere. While we did not perform a closed heat budget calculation, we note that the oceanic heat carried by the downstream outflow from the Barents Sea has previously been reported to be smaller than the inflow by 1 order of magnitude (e.g., Gammelsrød et al., 2009; Smedsrud et al., 2013) and that a previous study found that increased oceanic heat advection to the Barents Sea led to increased ocean heat content in the interior Barents Sea (Lien et al., 2017).

In the following winter of 2016–17, i.e., during the decline of the 2016 MHW event, the turbulent heat loss and outgoing longwave radiation in the northern Barents Sea (76–80° N, 25–45° E; Fig. 4b, e, f) reached the largest values in the 1993–2021 period. This was likely enhanced by a record low winter sea-ice extent (ICES, 2022) and negative cloud cover anomaly in the northern Barents Sea (not shown). In the southern Barents Sea, however, no heat loss anomaly at the ocean surface was observed during the winter of 2016–17 (Fig. 4b), but the Atlantic Water transport through the Barents Sea Opening decreased during 2016 (ICES, 2022). Thus, the 2016 MHW event in the Barents Sea can be linked to the combined effect of increased Atlantic Water transport into the Barents Sea and to reduced oceanic heat loss in the southern Barents Sea during the onset and increased oceanic heat loss in the northern Barents Sea during the decline.

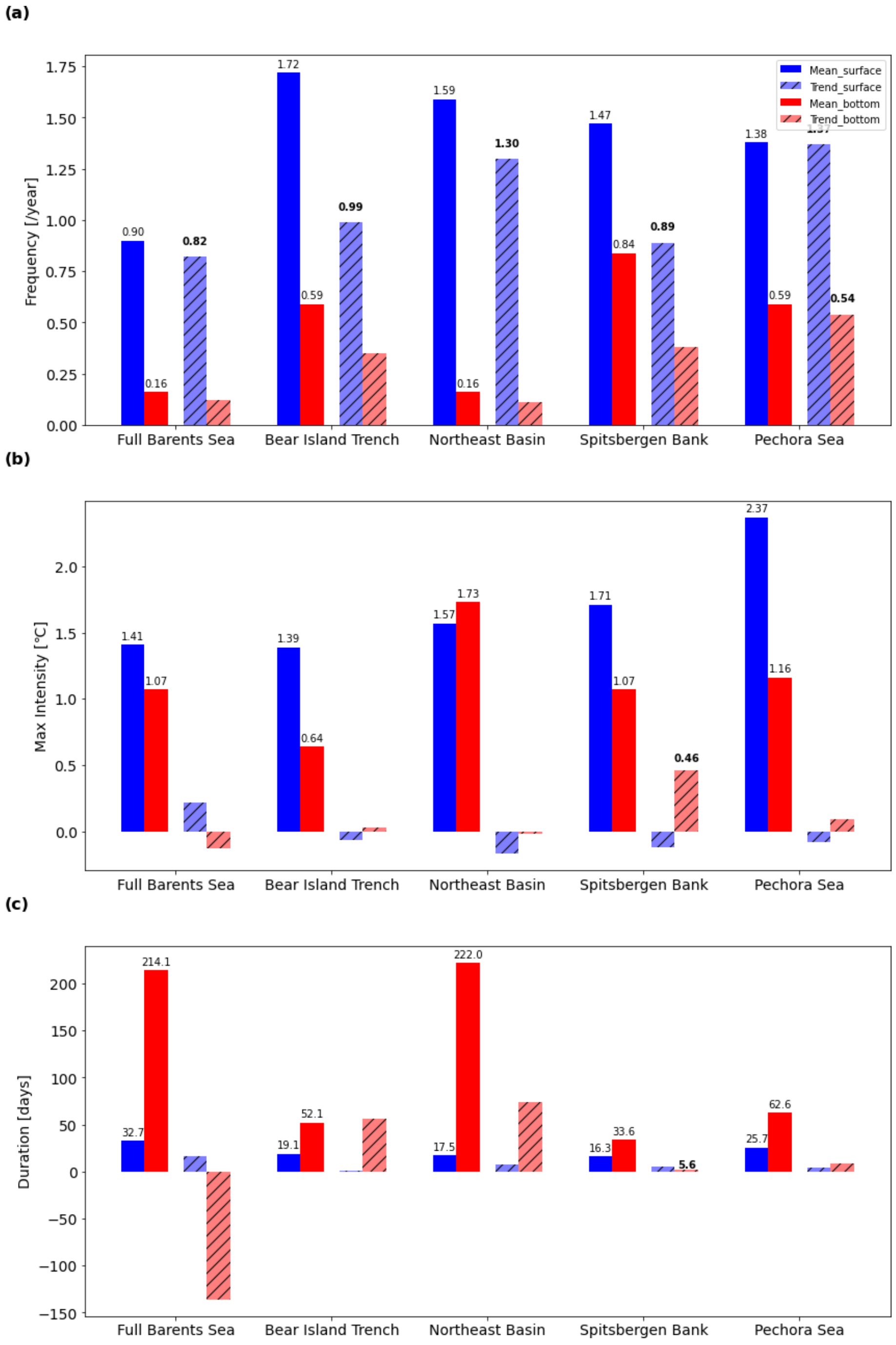

Figure 2. Marine heatwave statistics for the full Barents Sea for the period 1991–2022, using 1991–2020 as the climate average period. **(a)** Number of marine heatwave events per year. **(b)** Maximum intensity of the heatwave events. **(c)** Average marine heatwave duration. The associated decadal trends are shown in hatched colours. The trend is provided in boldface if significant to 95 % ($p < 0.05$). Surface values are shown by blue bars, and bottom values are shown by red bars. This figure is based on data from the TOPAZ reanalysis.

3.2 Effect of changing baselines

Next, we investigated the effect of changing the climatological average period from 30 years (1991–2020) to 25 years (1996–2020) and 20 years (2001–2020) when calculating the MHW statistics for both the surface and the bottom (Tables 3–5).

For all regions, including the Barents Sea as a whole, we found that the frequency of surface MHWs decreased with decreasing length of the climatological average period. For

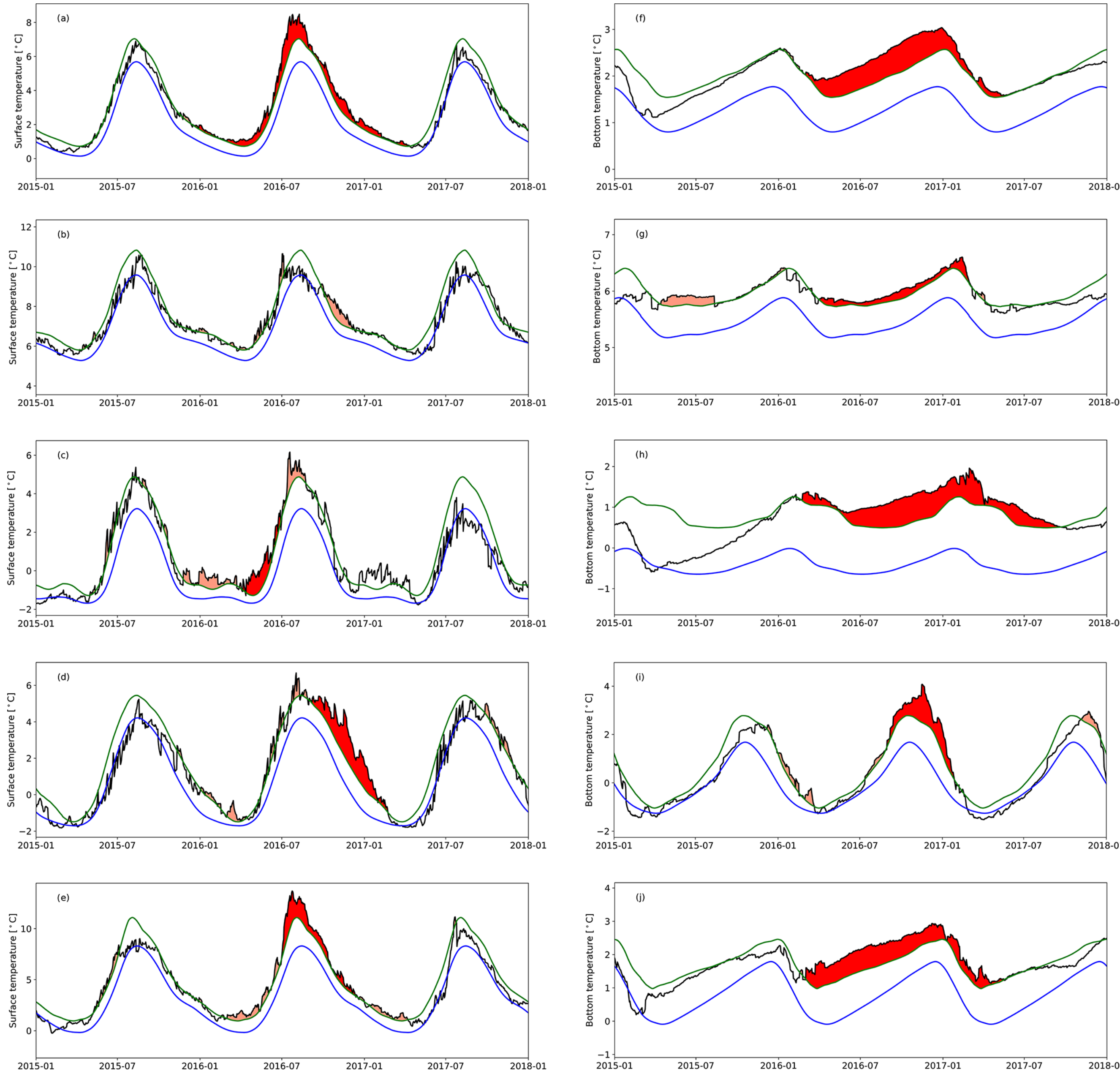

Figure 3. Time series (2015–2017; black lines) showing the temperature at the surface (left column) and near the bottom (right column) spatially averaged over the Barents Sea. Blue lines show daily climatology. Green lines show the 90th percentile. The highest-intensity marine heatwave in terms of cumulative degree days for the full 1991–2022 period is shown in dark-red shading. Other marine heatwaves are shown in pink shading. **(a)** The full Barents Sea (surface). **(b)** The Bear Island Trough (surface). **(c)** The Northeast Basin (surface). **(d)** The Spitsbergen Bank (surface). **(e)** The Pechora Sea (surface). **(f)** The full Barents Sea (bottom). **(g)** The Bear Island Trough (bottom). **(h)** The Northeast Basin (bottom). **(i)** The Spitsbergen Bank (bottom). **(j)** The Pechora Sea (bottom). All panels show the period 1 January 2015 to 1 January 2018. Note the different scales on the *y* axes.

near-bottom MHWs, the results were less clear except for a decrease in frequency in the two shallow-bank regions (the Spitsbergen Bank and the Pechora Sea). Similarly, for the intensity at the surface, there was a general trend of decreasing average intensity with decreasing length of the climatological average period. There was also a trend of decreasing intensities near the bottom, except for in the two shallow-bank regions. As opposed to the average frequency and intensity, the average duration seemed less dependent on the length of the climatological average period. Near the bottom, however, the duration was sensitive to the climatological average pe-

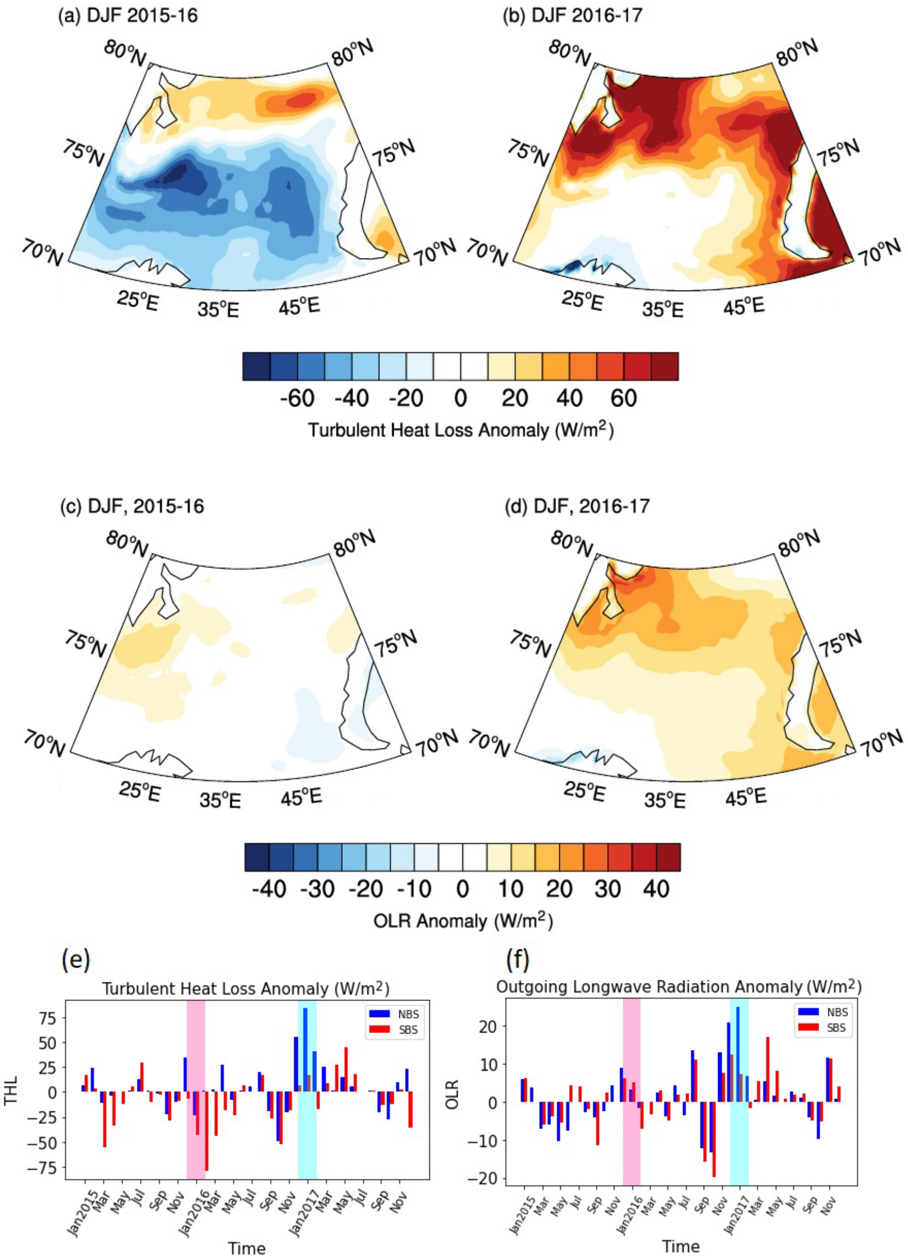

Figure 4. Atmospheric preconditioning leading up to the MHW depicted in Fig. 3. **(a, b)** DJF (December (−1), January, February (0)) turbulent (latent + sensible) heat loss anomaly (W m^{-2}) for 2016 **(a)** and 2017 **(b)**. Same as **(a)** and **(b)** but for outgoing longwave radiation (OLR). Positive values indicate upward fluxes. Monthly mean turbulent heat loss **(e)** and OLR **(f)** over the northern (blue; 76–80° N, 25–45° E) and southern (red; 71–75° N, 25–45° E) Barents Sea. The onset (DJF, 2015/2016) and decay (DJF, 2016/2017) phase of the 2016 MHW event are shaded in pink and cyan. Data: ERA5.

riod length due to the low number of MHWs and the dominance of the 2012 and 2016 MHW events.

4 Discussion

We have estimated average MHW frequency, duration, and intensity at the surface and near the bottom of the Barents Sea, based on an ocean reanalysis for the period 1991–2022. Moreover, we have investigated the impact of changing climatological average period length when estimating MHW statistics in the Barents Sea. We found two dominating and pervasive MHW events in the Barents Sea in the last 30 years that affected the whole region.

Previous studies of MHWs, including in the Barents Sea, have mainly focused on the ocean surface due to the availability of satellite remote sensing sea surface temperature

Table 3. Average frequency of marine heatwaves and the associated decadal trend for three different baseline periods, 1991–2020, 1996–2020, and 2001–2020. The trend is provided in boldface if significant to 95 % ($p < 0.05$) or in italics if not significant ($p > 0.05$). Values for the surface are shown on top, and values for bottom are shown below. BIT: Bear Island Trough. SB: Spitsbergen Bank. PS: Pechora Sea. NB: Northeast Basin.

Baseline \ Area	FULL	BIT	SB	PS	NB
1991–2020	**0.90** + **0.82** **0.16** + *0.12*	**1.72** + **0.99** **0.59** + *0.35*	**1.47** + **0.89** **0.84** + *0.38*	**1.38** + **1.37** **0.59** + **0.54**	**1.59** + **1.30** **0.16** + *0.11*
1996–2020	**0.84** + **0.85** **0.44** + *0.18*	**1.53** + **0.90** **0.59** + *0.39*	**1.16** + *0.78* **0.81** + *0.44*	**1.09** + **1.10** **0.53** + **0.47**	**1.44** + **1.36** **0.31** + *0.21*
2001–2020	**0.59** + **0.66** **0.19** + *0.14*	**1.19** + **0.64** **0.53** + *0.37*	**1.09** + **0.82** **0.59** + *0.35*	**0.84** + **0.89** **0.25** + **0.23**	**1.28** + **1.22** **0.25** + *0.24*

Table 4. Same as Table 3 but showing average maximum intensity (in °C).

Reference period \ Area	FULL	BIT	SB	PS	NB
1991–2020	**1.41** + *0.22* **1.07** − *0.13*	**1.39** − *0.07* **0.64** + *0.03*	**1.71** − *0.12* **1.07** + **0.46**	**2.37** + *0.08* **1.16** + *0.09*	**1.57** − *0.17* **1.73** − *0.02*
1996–2020	**1.35** + *0.23* **0.96** + *0.17*	**1.35** − *0.05* **0.61** − *0.01*	**1.57** − *0.07* **1.17** + **0.58**	**2.22** + *0.49* **1.16** + *0.03*	**1.58** − *0.25* **1.48** + *0.06*
2001–2020	**1.26** + *0.32* **0.85** + *0.06*	**1.31** − *0.08* **0.51** + *0.00*	**1.49** − *0.13* **1.17** + **0.51**	**2.01** + *0.35* **1.15** − *0.10*	**1.49** − *0.29* **1.43** − *0.01*

data (e.g., Mohamed et al., 2022). Our results also identified significant MHW events near the bottom of the ocean in the Barents Sea and showed that bottom MHWs tend to have lower frequency and intensity but longer duration compared to surface MHWs. Note, however, that these statistics need to be interpreted with care, especially the statistics on near-bottom MHWs, due to the low number of events (five near-bottom MHWs were detected in the Barents Sea during 1991–2022). Among other things, this severely affected the statistical significance of the trend estimates. Nevertheless, the longer duration near the bottom was more pronounced in the eastern parts of the Barents Sea, as represented by the Pechora Sea and the Northeast Basin. One likely explanation is the strong reduction in sea-ice formation in the shallow Pechora Sea in the southeastern Barents Sea and on the Novaya Zemlya Bank adjacent to the Northeast Basin and thus a reduction in the formation of cold, brine-enriched water. The eastern Barents Sea is one of the regions that has experienced the largest changes in sea-ice cover in recent decades (e.g., Yang et al., 2016; Onarheim and Årthun, 2017) and has thus experienced a strong reduction in the formation of cold, brine-enriched bottom water. Midttun (1985) observed very cold and saline water in the deeper parts of the Northeast Basin following cold winters in the 1970s, while Lien and Trofimov (2013) reported no such bottom water following the warmer winter of 2007–08. The occasional presence of such cold bottom water further west in the Barents Sea, adjacent to the Bear Island Trough, has been hypothesized to cause differences in the position of the polar front at the bottom, as detected by bottom-living organisms, compared to higher in the water column based on hydrographic properties in the pelagic zone (Jørgensen et al., 2015). Thus, the transition indicated by bottom MHWs in the eastern Barents Sea may have a profound impact on bottom fauna by allowing boreal species with less resilience to below-zero temperatures to settle.

Previous findings by Mohamed et al. (2022), based on satellite remote sensing sea-surface temperature data, contrasted the Spitsbergen Bank area showing no trend in MHW frequency and duration with the Pechora Sea area showing significant trends in both frequency and duration. Neither of the two regions showed significant trends in MHW intensity. Our findings agree with those of Mohamed et al. (2022) that the Pechora Sea has experienced a positive trend in MHW frequency and not in intensity, but our results showed no significant trend in duration at the surface. Our results indicated that there is also a significant, positive trend in MHW frequency near the bottom of the Pechora Sea (but not in intensity and duration). Moreover, our results showed positive trends in both the MHW frequency and duration on the Spitsbergen Bank (at the surface), although we did not find a statistically significant trend in MHW intensity, but our results indicated a positive trend in the MHW intensity near the bottom on the Spitsbergen Bank. Note, however, that the Spitsbergen Bank is also the area where the TOPAZ reanalysis showed the largest bias and RMS deviation, as well as

Table 5. Same as Table 3 but showing average duration (in days).

Baseline \ Area	FULL	BIT	SB	PS	NB
1991–2020	**32.7** + *16.2* **214.1** – *135.8*	**19.1** + *1.3* **52.1** + *56.2*	**16.3** + 5.6 **33.6** + *1.5*	**25.7** + *4.5* **62.6** + *8.7*	**17.5** + *7.8* **222.0** + *74.4*
1996–2020	**39.5** + *16.2* **139.2** + *32.0*	**20.0** – *0.6* **37.8** + *29.8*	**16.5** + *4.5* **28.7** – *3.5*	**70.8** + *24.0* **55.1** + *3.1*	**17.0** + *3.7* **109.9** – *36.3*
2001–2020	**38.0** – *13.9* **136.4** – *2.1*	**19.8** – *1.0* **37.8** + *24.0*	**15.6** – *0.07* **36.6** – *8.4*	**20.8** + *1.7* **101.6** + *0.7*	**15.3** + **6.8** **122.4** – *41.1*

the lowest correlation, when compared with in situ temperature observations. Thus, we cannot draw firm conclusions whether our results for the Spitsbergen Bank area contradict the findings of Mohamed et al. (2022).

Our findings that the strong 2016 MHW event was preceded by stronger-than-average Atlantic Water inflow and anomalously weaker ocean-to-atmosphere heat loss further suggest that MHWs may become more frequent and severe in terms of intensity and duration in a future Barents Sea with continued increase in oceanic heat advection from the North Atlantic (e.g., Årthun et al., 2019) in combination with reduced ocean-to-atmosphere heat loss within the Barents Sea (e.g., Skagseth et al., 2020).

Code and data availability. A list of the data products utilized in this paper, along with their availability and links to their documentation, is provided in Table 1. The MHW analysis toolbox developed by Oliver (2016) was used without adjustments or changes to the settings as provided in the GitHub repository https://github.com/ecjoliver/marineHeatWaves/releases/tag/v0.16 (Oliver, 2016).

Supplement. The supplement related to this article is available online at: https://doi.org/10.5194/sp-4-osr8-8-2024-supplement.

Author contributions. All authors contributed to the study design. RPR prepared the model data. VSL performed the MHW analysis. SC performed the atmospheric data analysis. All authors contributed to the interpretation and discussion of the results and the writing of the paper.

Competing interests. The contact author has declared that none of the authors has any competing interests.

Financial support. This research has been supported by the European Commission, Directorate-General for Maritime Affairs and Fisheries (grant no. 21002L1-COP-MFC ARC-5100).

Review statement. This paper was edited by Pierre Brasseur and reviewed by two anonymous referees.

References

Årthun, M., Eldevik, T., and Smedsrud, L. H.: The role of Atlantic heat transport in future Arctic winter sea ice loss, J. Climate, 32, 3327–3341, 2019.

Cheng, L., von Schuckmann, K., Abraham, J. P., Trenberth, K. E., Mann, M. E., Zanna, L., England, M. H., Zika, J. D., Fasullo, J. T., Yu, Y., Pan, Y., Zhu, J., Newsom, E. R., Bronselaer, B., and Lin X.: Past and future ocean warming, Nat. Rev. Earth Environ., 3, 776–794, 2022.

Chiswell, S. M.: Global Trends in Marine Heatwaves and Cold Spells: The Impacts of Fixed Versus Changing Baselines, J. Geophys. Res.-Oceans, 127, e2022JC018757, https://doi.org/10.1029/2022JC018757, 2022.

EU Copernicus Marine Service Product: Arctic Ocean Physics Reanalysis, Mercator Ocean International [data set], https://doi.org/10.48670/moi-00007, 2023.

Fossheim, M., Primicerio, R., Johannesen, E., Ingvaldsen, R. B., Aschan, M. M., and Dolgov, A. V.: Recent warming leads to a rapid borealization of fish communities in the Arctic, Nat. Clim. Change, 5, 673–677, https://doi.org/10.1038/nclimate2647, 2015.

Frölicher, T. L., Fischer, E. M., and Gruber, N.: Marine heatwaves under global warming, Nature, 560, 360–364, https://doi.org/10.1038/s41586-018-0383-9, 2018.

Gammelsrød, T., Leikvin, Ø., Lien, V., Budgell, W. P., Loeng, H., and Maslowski. W.: Mass and Heat transports in the NE Barents Sea: Observations and Models, J. Marine Syst., 75, 56–69, https://doi.org/10.1016/j.jmarsys.2008.07.010, 2009.

Hackett, B., Bertino, L., Alfatih, A., Burud, A., Williams, T., Xie, J., Yumruktepe, C., Wakamatsu, T., and Melsom, A.: EU Copernicus Marine Service Product User Manual for the Arctic Ocean Physics Reanalysis, ARCTIC_MULTIYEAR_PHY_002_003, Issue 5.17, Mercator Ocean International, https://catalogue.marine.copernicus.eu/documents/PUM/CMEMS-ARC-PUM-002-ALL.pdf, (last access: 22 March 2024), 2023.

Hersbach, H., Bell, B., Berrisford, P., Biavati, G., Horányi, A., Muñoz Sabater, J., Nicolas, J., Peubey, C., Radu, R., Rozum, I., Schepers, D., Simmons, A., Soci, C., Dee, D., and Thépaut, J.-N.: ERA5 monthly averaged data on single levels from 1940 to present, Copernicus Climate Change Service (C3S) Climate Data Store (CDS) [data set], https://doi.org/10.24381/cds.f17050d7, 2023.

Hobday, A. J., Alexander, L. V., Perkins, S. E., Smale, D. A., Straub, S. C., Oliver, E. C. J., Benthuysen, J. A., Burrows, M. T., Donat, M. G., Feng, M., Holbrook, N. J., Moore, P. J., Scannell, H. A., Gupta, A. S., and Wernberg, T.: A hierarchical approach to defining marine heatwaves, Progr. Oceanogr., 141, 227–238, 2016.

Hu, S., Zhang, L., and Qian, S.: Marine heatwaves in the Arctic region: Variation in different ice covers, Geophys. Res. Lett., 47, e2020GL089329, https://doi.org/10.1029/2020GL089329, 2020.

Huang, B., Wang, Z., Yin, X., Arguez, A., Graham, G., Liu, C., Smith, T., and Zhang H.-M.: Prolonged Marine Heatwaves in the Arctic: 1982–2020, Geophys. Res. Lett., 48, e2021GL095590, https://doi.org/10.1029/2021GL095590, 2021.

Husson, B., Lind, S., Fossheim, M., Kato-Solvag, H., Skern-Mauritzen, M., Pécuchet, L., Ingvaldsen, R. B., Dolgov, A. V., and Primicerio, R.: Successive extreme climatic events lead to immediate, large-scale, and diverse responses from fish in the Arctic, Glob. Change Biol., 28, 3728–3744, 2022.

ICES: Working Group on the Integrated Assessments of the Barents Sea (WGIBAR), ICES Scientific Reports, 4:50, 235 pp., https://doi.org/10.17895/ices.pub.20051438, 2022.

Jakobsen, T., and Ozhigin, V. K. (Eds.): The Barents Sea – Ecosystem, Resources, Management: Half a century of Russian-Norwegian cooperation, Tapir Academic Press, Trondheim, Norway, 825 pp., ISBN 978-82-519-2545-7, 2011.

Jørgensen, L. L., Ljubin, P., Skjoldal, H. R., Ingvaldsen, R. B., Anisimova, N. and Manushin, I.: Distribution of benthic megafauna in the Barents Sea: baseline for an ecosystem approach to management, ICES J. Mar. Sci., 72, 595–613, https://doi.org/10.1093/icesjms/fsu106, 2015.

Lien, V. S. and Trofimov, A. G.: Formation of Barents Sea Branch Water in the north-eastern Barents Sea, Polar Res., 32, 18905, https://doi.org/10.3402/polar.v32i0.18905, 2013.

Lien, V. S., Hjøllo, S. S., Skogen, M. D., Svendsen, E., Wehde, H., Bertino, L., Counillon, F., Chevallier, M., and Garric, G.: An assessment of the added value from data assimilation on modelled Nordic Seas hydrography and ocean transports, Ocean Modell., 99, 43–59, https://doi.org/10.1016/j.ocemod.2015.12.010, 2016.

Lien, V. S., Schlichtholz, P., Skagseth, Ø., and Vikebø, F. B.: Wind-driven Atlantic water flow as a direct mode for reduced Barents Sea ice cover, J. Climate, 30, 803–812, 2017.

Lind, S., Ingvaldsen, R. B., and Furevik, T.: Arctic warming hotspot in the northern Barents Sea linked to declining sea-ice import, Nat. Clim. Change, 8, 634–639, 2018.

Marbà, N., Jordà, G., Agustí, S., Girard, C., and Duarte, C. M.: Footprints of climate change on Mediterranean Sea biota, Front. Mar. Sci., 2, 56, https://doi.org/10.3389/fmars.2015.00056, 2015.

Midttun, L.: Formation of dense bottom water in the Barents Sea, Deep-Sea Res.-Pt. I, 32, 1233–1241, 1985.

Mohamed, B., Nilsen, F., and Skogseth, R.: Marine Heatwaves Characteristics in the Barents Sea Based on High Resolution Satellite Data (1982–2020), Front. Mar. Sci., 9, 821646, https://doi.org/10.3389/fmars.2022.821646, 2022.

Oliver, E. C. J.: marineHeatWaves v0.16, GitHub [code], https://github.com/ecjoliver/marineHeatWaves/releases/tag/v0.16 (last access: 24 March 2023), 2016.

Oliver, E. C. J., Benthuysen, J. A., Darmaraki, S., Donat, M. G., Hobday, A. J., Holbrook, N. J., Schlegel, R. W., and Gupta, A. S.: Marine heatwaves, Annu. Rev. Mar. Sci., 13, 313–342, https://doi.org/10.1146/annurev-marine-032720-095144, 2021.

Onarheim, I. H., Eldevik, T., Årthun, M., Ingvaldsen, R. B., and Smedsrud, L. H.: Skillful prediction of Barents Sea ice cover, Geophys. Res. Lett., 42, 5364–5371, 2015.

Onarheim, I. H. and Årthun, M.: Toward an ice-free Barents Sea, Geophys. Res. Lett., 44, 8387–8395, https://doi.org/10.1002/2017GL074304, 2017.

Oziel, L., Baudena, A., Ardyna, M., Massicotte, P., Randelhoff, A., Sallee, J.-B., Ingvaldsen, R. B., Devred, E., and Babin, M.: Faster Atlantic currents drive poleward expansion of temperate phytoplankton in the Arctic Ocean, Nat. Commun., 11, 1705, https://doi.org/10.1038/s41467-020-15485-5, 2020.

Sakov, P., Counillon, F., Bertino, L., Lisæter, K. A., Oke, P. R., and Korablev, A.: TOPAZ4: an ocean-sea ice data assimilation system for the North Atlantic and Arctic, Ocean Sci., 8, 633–656, https://doi.org/10.5194/os-8-633-2012, 2012.

Scannell, H. A., Pershing, A. J., Alexander, M. A., Thomas, A. C., and Mills, K. E.: Frequency of marine heatwaves in the north Atlantic and north Pacific since 1950, Geophys. Res. Lett., 43, 2069–2076, https://doi.org/10.1002/2015GL067308, 2016.

Schlichtholz, P.: Subsurface ocean flywheel of coupled climate variability in the Barents Sea hotspot of global warming, Sci. Reports, 9, 13692, https://doi.org/10.1038/s41598-019-49965-6, 2019.

Skagseth, Ø., Furevik, T., Ingvaldsen, R., Loeng, H., Mork, K. A., Orvik, K. A., and Ozhigin, V.: Volume and Heat Transports to the Arctic Ocean via the Norwegian and Barents Seas, in: Arctic Subarctic ocean fluxes: Defining the Role of the Northern Seas in Climate, edited by: Dickson, R., Meincke, J., and Rhines, P., Springer, New York, 45–64, ISBN 978-1-4020-6773-0, 2008.

Skagseth, Ø., Eldevik, T., Årthun, M., Asbjørnsen, H., Lien, V. S., and Smedsrud, L. H.: Reduced efficiency of the Barents Sea cooling machine, Nat. Clim. Change, 10, 661–666, https://doi.org/10.1038/s41558-020-0772-6, 2020.

Smale, D. A., Wernberg, T., Oliver, E. C. J., Thomsen, M., Harvey, B. P., Straub, S. C., Burrows, M. T., Alexander, L. V., Benthuysen, J. A., Donat, M. G., Feng, M., Hobday, A. J., Holbrook, N. J., Perkins-Kirkpatrick, S. E., Scannell, H. A., Gupta, A. S., Payne, B. L., and Moore, P. J.: Marine heatwaves threaten global biodiversity and the provision of ecosystem services, Nat. Clim. Change, 9, 306–312, https://doi.org/10.1038/s41558-019-0412-1, 2019.

Smedsrud, L. H., Esau, I., Ingvaldsen, R. B., Eldevik, T., Haugan, P. M., Li, C., Lien, V. S., Olsen, A., Omar, A. M., Otterå, O. H., Risebrobakken, B., Sandø, A. B., Semenov, V. A., and Sorokina, S. A.: The role of the Barents Sea in the climate system, Rev. Geophys., 51, 415–449, 2013.

Smedsrud, L. H., Muilwijk, M., Brakstad, A., Madonna, E., Lauvset, S. K., Spensberger, C., Born, A., Eldevik, T., Drange, H., Jeansson, E., Li, C., Olsen, A., Skagseth, Ø., Slater, D. A., Straneo, F., Våge, K., and Årthun, M.: Nordic

Seas heat loss, Atlantic inflow, and Arctic sea ice cover over the last century, Rev. Geophys., 60, e2020RG000725, https://doi.org/10.1029/2020RG000725, 2022.

Smith, K. E., Burrows, M. T., Hobday, A. J., Sen Gupta, A., Moore, P. J., Thomsen, M., Wernberg, R., and Smale, D. A.: Socioeconomic impacts of marine heatwaves: Global issues and opportunities, Science, 374, eabj3593, https://doi.org/10.1126/science.abj3593, 2021.

WMO: The Role of Climatological Normals in a Changing Climate (WMO/TD-No. 1377), Geneva, https://library.wmo.int/idurl/4/52499 (last access: June 2023), 2007.

WMO: Seventeenth World Meteorological Congress (WMO-No. 1157), Geneva, ISBN 978-92-63-11157-9, https://library.wmo.int/idurl/4/54771 (last access: June 2023), 2015.

Xie, J. and Bertino, L.: EU Copernicus Marine Service Quality Information Document for the Arctic Ocean Physics Reanalysis, ARCTIC_MULTIYEAR_PHY_002_003, Issue 1.3, Mercator Ocean International, https://catalogue.marine.copernicus.eu/documents/QUID/CMEMS-ARC-QUID-002-003.pdf, (last access: 22 March 2024), 2023.

Xie, J., Counillon, F., Bertino, L., Tian-Kunze, X., and Kaleschke, L.: Benefits of assimilating thin sea ice thickness from SMOS into the TOPAZ system, The Cryosphere, 10, 2745–2761, https://doi.org/10.5194/tc-10-2745-2016, 2016.

Xie, J., Raj, R. P., Bertino, L., Samuelsen, A., and Wakamatsu, T.: Evaluation of Arctic Ocean surface salinities from the Soil Moisture and Ocean Salinity (SMOS) mission against a regional reanalysis and in situ data, Ocean Sci., 15, 1191–1206, https://doi.org/10.5194/os-15-1191-2019, 2019.

Xie, J., Raj, R. P., Bertino, L., Martínez, J., Gabarró, C., and Catany, R.: Assimilation of sea surface salinities from SMOS in an Arctic coupled ocean and sea ice reanalysis, Ocean Sci., 19, 269–287, https://doi.org/10.5194/os-19-269-2023, 2023.

Yang, X.-Y., Yuan, X., and Ting, M.: Dynamical link between the Barents-Kara sea ice and the Arctic Oscillation, J. Climate, 29, 5103–5122, https://doi.org/10.1175/JCLI-D-15-0669.1, 2016.

State Planet, 4-osr8, 9, 2024
https://doi.org/10.5194/sp-4-osr8-9-2024

Oceanographic preconditions for planning seawater heat pumps in the Baltic Sea – an example from the Tallinn Bay, Gulf of Finland

Jüri Elken, Ilja Maljutenko, Priidik Lagemaa, Rivo Uiboupin, and Urmas Raudsepp

Department of Marine Systems, Tallinn University of Technology, Tallinn, 12618, Estonia

Correspondence: Jüri Elken (juri.elken@taltech.ee)

Received: 21 July 2023 – Discussion started: 24 August 2023
Revised: 4 April 2024 – Accepted: 19 June 2024 – Published: 30 September 2024

Abstract. The use of low-temperature seawater heat for renewable energy installations is demonstrated with an example from the Tallinn Bay, Baltic Sea, based on Copernicus Marine Service reanalysis data. Tallinn and its surrounding seaside counties are home to about half a million people and produce about half of Estonia's gross domestic product (GDP). The Tallinn Bay with an area of 223 km^2 extends to the north and has an open connection to the Gulf of Finland. Depths more than 50 m that cover the halocline already appear at a distance of 3–4 km from the coast. Surface layers get too cold during winter to be used in heat pumps for district heating; therefore, a feasible option is to pump slightly warmer seawater from the deeper halocline layers. The lowest monthly mean halocline temperature – down to 2.6 °C at 50 m depth and 3.3 °C at 70 m – is found in March and April based on reanalysis data from 1993–2019. The seawater seasonally cools below 3 °C on average on 1 January at 20 m depth and on 12 February at 50 m depth. At the 70 m depth, the average start of $T < 3$ °C was calculated on 28 February, although only 14 winters out of 26 had such water present; in 12 winters the condition $T > 3$ °C was always fulfilled. The median number of cold days is 11, with a maximum of 128 d in the winter 1993/1994 when stratification became rather weak due to the prolonged absence of Major Baltic Inflows of saltier and warmer North Sea waters. During the recent warmer period of 2009–2019, the start of the cold seawater period was delayed on average by 5–10 d. Tallinn has, among other Baltic Sea cities and industrial sites, a favorable location for seawater heat extraction because of the short distance to the unfreezing sub-halocline layers. Still, episodically there are colder-water events with $T < 3$ °C, when seawater heat extraction has to be complemented by other sources of heating energy.

1 Introduction

New developments in district heating (e.g., Lund et al., 2018) focus on the gradual exclusion of fossil fuels and transfer to 100 % renewable energy sources. Among the latter, large-scale heat pumps are considered to be an important component of the new energy systems. One energy source for the heat pumps is seawater (Bach et al., 2016) that has a stable temperature during the winter compared to the air temperature. Seawater heat pumps take seawater from the locations of appropriate temperature into the shore unit that transforms its low temperature to higher temperature suitable for district heating. Regarding feasibility studies, Su et al. (2020) performed a spatial evaluation of seawater-source heat pump performance along the coast of China depending on technical options and the thermal regime of seawater or other heat sources (wastewater, groundwater etc.). Pieper et al. (2019) evaluated combinations of heat pumps based on data from Copenhagen and noted that in shallow-water conditions seawater heat may contribute 14 % of the total heating energy. An important issue in coastal waters of ice-prone seas is to avoid lowering of temperature in the heat pump system below the freezing temperature, which depends on the salinity. Water temperature during winter usually increases at depth, and hence, even depths of a few tens of meters may be sufficient to avoid freezing temperature. One

Published by Copernicus Publications.

Table 1. Copernicus Marine Service and non-Copernicus products used in this study, including information on data documentation.

Product ref. no.	Product ID & type	Data access	Documentation
1	BALTICSEA_REANALYSIS_PHY_003_011; numerical models*	EU Copernicus Marine Service Product (2021);	Quality Information Document (QUID): Liu et al. (2019); Product User Manual (PUM): Axell et al. (2021)
2	INSITU_BAL_PHYBGCWAV_DISCRETE_MYNRT_013_032; in situ observations*	EU Copernicus Marine Service Product (2022)	Quality Information Document (QUID): Wehde et al. (2022); Product User Manual (PUM): In Situ TAC partners (2022)
3	EMODNET; bathymetry	EMODnet (2021)	EMODnet Bathymetry Consortium (2018); Jakobsson et al. (2019)
4	OpenStreetMap; coastline	HELCOM MADS (2023)	OpenStreetMap Contributors (2023)

* Data set updated during publication (see the "Disclaimer" section).

of the world's largest seawater heat pumps, built in Ropsten in Stockholm and operational since 1986, was designed to work with the lower limit of input water temperature of +2.5 °C (Friotherm, 2017). The system pumps large-volume flows of water from the 15 m depth; by cooling the water down to +0.5 °C, the system yields in total 180 MW from six units. In the Danish town of Esbjerg, a 60 MW seawater heat pump is in the construction phase to replace the town's existing coal power plant for heating purposes (CleanTechnica, 2023). The study by Volkova et al. (2022b), summarizing geographical and economic factors, concluded that among the Baltic countries, seawater is the best natural heat source in Estonia, but river water has higher potential for the other two countries. Contemporary housing also needs district cooling during the summer that can be performed based on the seawater (Volkova et al., 2022a).

Tallinn is a seaside city with about half a million inhabitants on the coast of the Gulf of Finland, Baltic Sea, where the use of seawater heat for district heating is currently under consideration. Unfortunately, during the winter period, i.e., when the highest demand for heating housing exists, coastal seawater at shallow depths may cool down close to the freezing temperature, which may hamper the efficiency of using the heat pumps. It is known from the larger Gulf of Finland area that during summer the mean halocline depth is located at about 67 m, keeping the temperatures in the range of 2.2–5.0 °C depending on the transport of deep, more saline waters from the open Baltic Sea (Liblik and Lips, 2011). The waters in the halocline and below are rather isolated from direct vertical heating and cooling; therefore, their temperature is more stable than in the surface layers. As a systematic analysis of the near-bottom water temperature in the Tallinn Bay is missing, the present study focused on the exploration of the new public data sets made available by the EU Copernicus program. The Copernicus Marine Service (https://marine.copernicus.eu/, last access: 13 February 2021) provided regular Baltic Sea reanalysis data during 1993–2019 with about a 3.7 km grid step, combining both modeling and observations (Table 1, product ref. no. 1).

The aim of the present study is to determine the basic features of seawater temperature variability, necessary for the evaluation of the feasibility and efficiency of using seawater thermal energy for heating and/or cooling of a city's built environment. The presentation of data and methods is followed by providing results and discussion with a focus on subsurface temperature variations with respect to the cold-water periods. The paper ends with recommendations for further studies and conclusions.

2 Data and methods

2.1 State of knowledge on oceanographic conditions in the Baltic Sea

The Baltic Sea is a multi-basin semi-enclosed sea (Fig. 1a) filled with brackish waters. Its temperature regime (Leppäranta and Myrberg, 2009) is to a great extent forced by the seasonal cycle of atmospheric heat fluxes that extend down to the thermocline during summer and to the halocline during winter (Fig. 1b). In halocline and deeper layers, temperature is determined mainly by the deep-water transport of the waters originating from the North Sea (Leppäranta and Myrberg, 2009). However, these waters are significantly transformed on their pathway from the Danish straits through the Baltic Proper to the Gulf of Finland.

While temperature and sea ice respond rapidly to changes in atmospheric heat fluxes, variations in salinity are governed mainly by lateral transport processes, resulting together with diapycnal mixing (i.e., mixing across the surfaces of constant water density) in response times of many decades (e.g., Omstedt and Hansson, 2006; Elken et al., 2015). The Gulf of Finland is an elongated sub-basin of the Baltic Sea, which has many specific features (Alenius et al., 1998). Stratification is generally composed of the following layers.

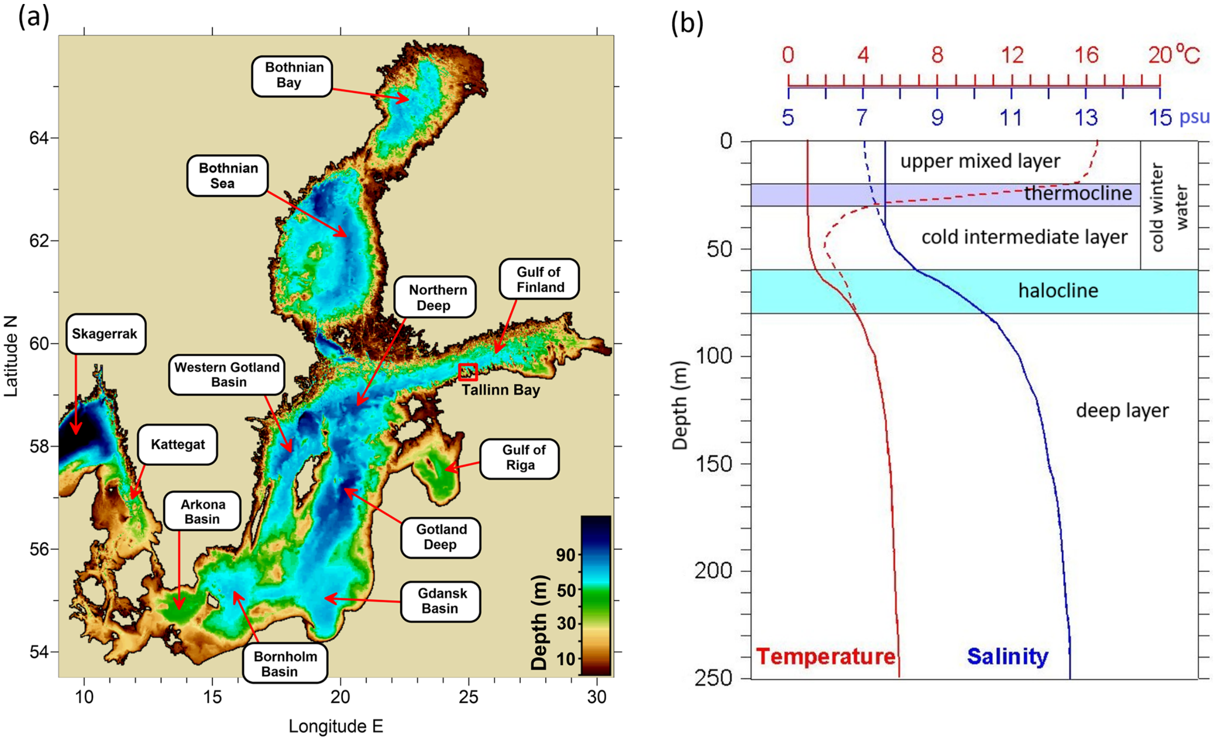

Figure 1. Topography and basins of the Baltic Sea **(a)**. The Baltic Proper includes Arkona Basin, Bornholm Basin, Gdansk Basin, Gotland Deep, and the western Gotland Basin. Typical vertical stratification in the Gotland Deep (**b**, adopted from Elken and Matthäus, 2008) in summer (dashed lines) and winter (solid). The location of Tallinn Bay is shown in **(a)** with a red box.

Upper mixed layer. Generally, the upper mixed layer is vertically rather uniform due to high mixing rates generated by winds, waves, and convection during cooling (Lepparanta and Myrberg, 2009). During summer, it typically has a thickness of 20 m in the Gulf of Finland (Liblik and Lips, 2011). On calm and sunny days, a thin warm "skin" layer may occur just at the surface. However, with increasing wind speed the whole upper layer undergoes overall mixing again. The yearly temperature maximum occurs in July or August depending on the region and yearly atmospheric conditions (Haapala and Alenius, 1994). During the autumn cooling period, the upper layers become hydrostatically unstable. If cooled water with higher density appears on top of warmer and less dense water, then instability generates convective mixing (Maljutenko and Raudsepp, 2019). As a result, mixed layer temperature decreases but its thickness increases until its lower boundary has eroded down to the halocline or to the bottom, whichever is shallower. Shallow sea areas warm and cool faster during spring and autumn (also called differential heating), respectively, because of the smaller water mass of the water column compared to deeper ocean areas.

Cooling of the upper layer is limited during winter by the salinity-dependent freezing point of seawater. For salinity values of 5, 6, and 7 psu, the freezing point is −0.27, −0.33, and −0.38 °C, respectively. The salinity-dependent temperature of maximum density T_{max} influences upper-layer dynamics during the cold period as well. For fresh water, $T_{\mathrm{max}} = 4\,^{\circ}\mathrm{C}$, and for typical Baltic surface salinity of 7 psu T_{max} is about 2.5 °C.

Thermocline. During summer, a sharp temperature drop at depth develops below the upper mixed layer. Individual instant profiles may exhibit the sharpest thermoclines with temperature drops from 5 to 10 °C per 5 m (Fig. 1b), and the mean summer thermocline thickness in the Gulf of Finland is 14 m (Liblik and Lips, 2011). With respect to the mean seasonal cycle, the thermocline may perform up- and downward motions with periods from a couple of hours to several days. Vertical movement of the thermocline of 10 m or even more creates significant near-bottom temperature variations. A special dynamical feature of the thermocline is upwelling, when cold waters (sometimes below 5 °C) may be found at the surface of coastal areas during summer (Aavaste et al., 2021). In the Gulf of Finland, upwelling occurs near the Estonian coast during easterly winds and near the Finnish coast during westerly winds (Uiboupin and Laanemets, 2009).

Cold intermediate layer. Cold waters from the last winter remain below the thermocline, trapped through the whole summer, until autumn cooling pushes the thermocline significantly downwards. In the Gulf of Finland, lowest summer temperature (from 1.3 to 3.6 °C) has been found on average at 42 m depth (Liblik and Lips, 2011).

Halocline and deep layers. This layer is formed by lateral (horizontal) transport of saline waters originating from the North Sea. Regular saline water inflow is complemented by the events of Major Baltic Inflows (MBIs) of large volume and high salinity; they occur sporadically with intervals from years to decades (Raudsepp et al., 2018). Depending on the seasonal timing of the MBI, there may be pulses of warmer or colder water reaching the deep areas of the Baltic Proper (Elken et al., 2015). For example, in the Gotland Deep at the 175 m depth, temperature varied during 1997–2013 between 4.5 and 7.0 °C depending on the type of the MBI. When large volumes of new water arrive to the Gotland Deep, the old water is pushed to the deep layers of the Gulf of Finland. After the 2014 December MBI, the first effects occurred in the Gulf of Finland in 9 months, whereas the arrival of the former northern Baltic Proper deep-layer water was observed (Liblik et al., 2018). Deep-layer temperature dynamics in the Gulf of Finland are also affected by the wind-dependent estuarine circulation reversals that may drastically reduce the stratification for several weeks (Elken et al., 2003).

Tallinn Bay is deep enough to have all of the above-described water column layers present. Its short-term hydrographic variability is characteristic of the southern coast of the Gulf of Finland: upwelling occurs during the persistent westerly and southwesterly winds, and pulses of more saline and less saline water observed in the southern Gulf of Finland also appear in the bay.

From May to July, the seasonal cycle of temperature in the central part of the Gulf of Finland shows delayed temperature increase of the layers 20–40 m during the warming season (Haapala and Alenius, 1994). The seasonal upper-layer temperature maximum usually develops in August. In the course of the cooling period, the thermocline deepens to 30 m (i.e., temperature of that level becomes equal to surface temperature) in September and 40 m in October. The 50 m depth level lies in the cold intermediate layer at temperatures below 8 °C through the year. Average temperature in the halocline (60–90 m) is stable, ranging from about 3 °C in February and March to 5 °C in November and December.

Sea surface temperature can be acquired in detail using regular satellite images, but subsurface data can be observed only using sparse in situ techniques. Elken et al. (2015) summarized that during 1990–2008, sea surface temperature increased in the Gulf of Finland at a mean rate of 0.8 °C per decade. Liblik and Lips (2019) explored large numbers of observations conducted in the water column. They have shown that from 1982 to 2016 the temperature of the Gulf of Finland was increasing on average at a rate of about 0.5 °C per decade, whereas faster warming has been detected in the thermocline (20 m) and at deeper (70 and 80 m) depth levels. Re-inspection of temperature observations in the Gulf of Finland from the HELCOM/ICES database at the 70 m depth level reveals that average deep-water temperature increased from 3.5 °C in 1988 to 5.2 °C in 2020. Oceanographic regional climate projections until 2100 have projected an annual increase in temperature in the Gulf of Finland of 0.2–0.4 °C per decade (Meier et al., 2022).

2.2 Data

2.2.1 Copernicus Marine Service reanalysis data for the Baltic Sea

We use the Baltic Sea physical reanalysis product (Axell, 2021) prepared within the Copernicus Marine Service (product ref. no. 1). This reanalysis covers the whole Baltic Sea with adjacent North Sea areas, presenting data on sea level, ice, water temperature, salinity, and currents. It has about a 3.7 km grid step and is the most advanced combination of numerical modeling made using the NEMO model and observations. The data set consists of daily mean reanalysis data from 1 January 1993 to 31 December 2019. The gridded data have a maximum of 56 vertical levels down to 361 m. Layer thickness is about 3 m in the upper levels but increases to about 6.3 m in the deepest point of the Tallinn Bay area, which has altogether 21 depth levels.

The quality of the reanalysis product was vigorously checked against observational data by Liu et al. (2019). The report concluded that the mean bias of water temperature was less than 0.1 °C and the remaining root mean square deviation (RMSD) was less than about 0.7 °C. Comparing with individual independent observations that were not included into the reanalysis procedure, the RMSD is generally between 0.4 and 1 °C. The largest RMSD values above 1.4 °C were found in the Kattegat and the Gulf of Finland. In the Tallinn Bay, the reanalysis results are compared to the independent sea surface temperature observations in Sect. 2.3.

The grid cells of the NEMO model are shown in Fig. 2, overlaid on the coastline and topography map of the Tallinn Bay. Although depths 40–70 m are evident in the inner bay, the reanalysis grid cells of the Baltic-wide product are too coarse to resolve the details of the coastline and topography. Setting up a more detailed topography for oceanographic reanalysis, dedicated to Estonian marine areas, is in the implementation phase.

For the present analysis, data from six grid cells were selected. The data on the original grid were converted to 10 m depth intervals.

2.2.2 Observations

Regular temperature observations are available from the automatic coastal station (59.449351° N, 24.775448° E) located in Tallinn Harbor (Fig. 2) from 1 January 2008 to 14 April 2018 (product ref. no. 2). The sea level part of the observing station has been described by Lagemaa et al. (2011). The raw data have been recorded mostly with a 5 min interval. After elimination of sensor and communication errors, a set of daily mean temperatures was generated to compare with reanalysis data. The same data, processed

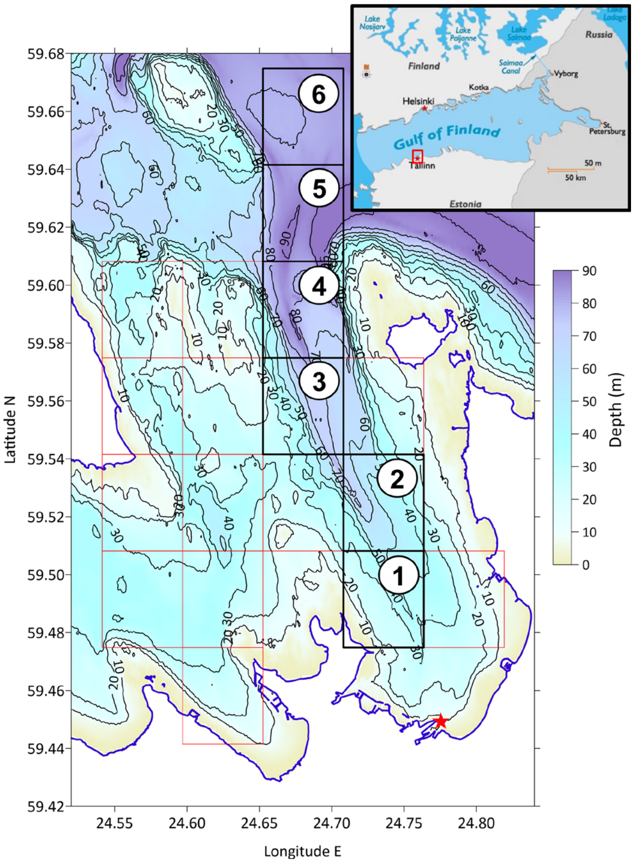

Figure 2. Map of the Tallinn Bay area with grid cells of the Copernicus Marine reanalysis data (product ref. no. 1) shown as boxes. The location of the Tallinn Bay is shown on the map of the Gulf of Finland, inset in the upper-right corner. The analysis uses data from bold cells noted by numbers. The red star denotes the location of the coastal automatic observing station. Depth data on the 1/16 arcmin (ca. 58 and 116 m along longitude and latitude) grid were adopted from EMODNET bathymetry (product ref. no. 3). The coastline has been adopted from the compilation by HELCOM (product ref. no. 4).

to the 1 h interval, are available from the Copernicus Marine Service.

2.3 Comparison of reanalysis data with observations

While observational data record the “point” values of sea surface temperature with a 5 min interval and are usually averaged to hourly values, the reanalysis data set presents the average temperature over ca. 3.7 km size grid cells as daily mean values. It means that reanalysis data do not present small-scale and short-term local temperature variations near the observation point. Still, it is interesting to compare how well point observations match averaged reanalysis data. Point observations reveal a number of short-term anomalies from the regular seasonal course (Fig. 3). Their origins are in (1) calm weather local anomalies, when a warm skin layer develops, mostly during spring; (2) faster heating and cooling in shallow coastal sites; and (3) cold waters due to wind-induced upwelling. In all the cases, the spatial and temporal scales could be too small to be captured by the coarser reanalysis data. This study did not focus on a detailed analysis of “negative temperature anomaly” events, but we can conclude that in many cases the observed events are also evident in the reanalysis data. Since the upwelling areas cover up to tens of kilometers and may exist for several days or a week (Uiboupin and Laanemets, 2009), these events are captured well by the reanalysis data.

Statistical comparison of surface reanalysis data with daily mean observations over existing data pairs reveals their good match. Bias is −0.12 °C and RMSD (root mean square difference) is 1.3 °C. Both time series contain a strong seasonal signal, with its variance exceeding 90 % of the total variance. While the original time series are highly correlated with the Pearson coefficient of determination at $R^2 = 0.96$, removing the mean seasonal cycle from both of the time series reduces the correlation to $R^2 = 0.44$. A histogram of the difference between observations and reanalysis (not shown) shows that on average observations reveal slightly higher temperature (the maximum is shifted by 0.2 °C), but occasionally much smaller observed temperatures occur. Such outliers can neither be explained by the local coastal effects in observations nor resolved by reanalysis.

3 Results

3.1 Seasonal temperature course and its variations

The temperature of the Tallinn Bay undergoes a similar seasonal cycle as described in Sect. 1. In the offshore area (point 6, Fig. 2) the upper layer is gradually warmed up from April to July (Fig. 4a). During summer, the upper mixed layer has 10–20 m thickness, whereas the annual temperature maximum, determined from the original non-averaged data, varies between 16 and 23 °C. In August, the maximum vertical gradient in the thermocline is found at about 25 m depth. During autumn, the upper layer and the thermocline are eroded down to 40 m where inherent salinity stratification (Fig. 4b) blocks further erosion. During winter, the upper layer may be cooled to the freezing point, which is from −0.27 to −0.33 °C for salinities from 5 to 6 psu. Below the thermocline, monthly mean temperature ranges from 2.4 to 7.4 °C at 40 m depth and from 3.4 to 5.2 °C at 70 m depth (Fig. 4a). Deeper temperature variations below 40 m are influenced by the seasonal dynamics of the halocline: intensified transport of more saline (and warmer) waters from the open Baltic occurs below 50 m in late spring and summer (Fig. 4b). The highest temperature occurs in deeper layers in November and December as a delayed response to the summer heating at the surface; the lowest temperature values are found on average in March and April when the weakest vertical gradients in the halocline occur.

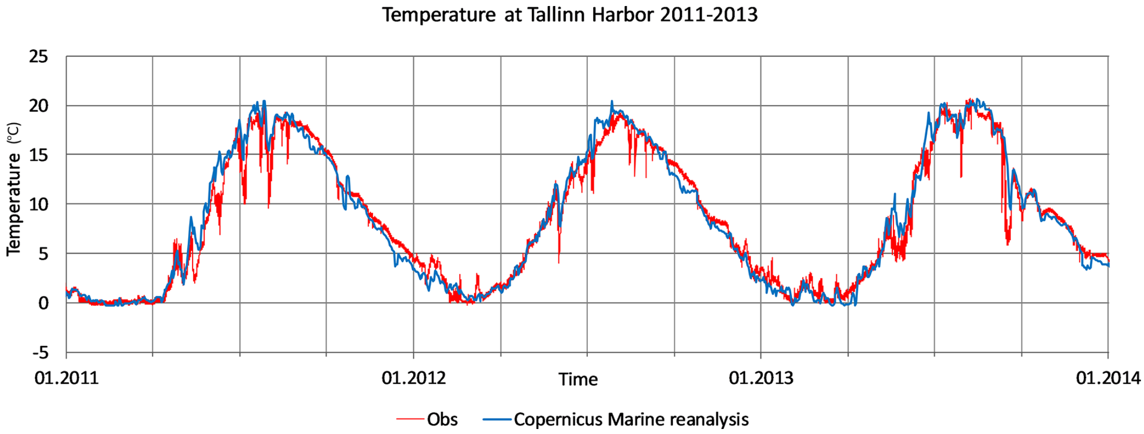

Figure 3. Example of near-surface temperature time series in 2011–2013. Shown are the automatic observations at Tallinn Harbor with a 5 min interval averaged to hourly values (red) (product ref. no. 2) and daily Copernicus Marine reanalysis data at point 1 (blue) (product ref. no. 1). For locations, see Fig. 2.

Although in the six selected reanalysis points (their locations are in Fig. 2) the mean seasonal temperature curves are rather similar (Fig. 5), the spread of the actual data is rather high. Histograms of weekly mean temperature reveal during the summer months a range from 4.5 to 22.5 °C at the depth of 10 m, with a maximum in overall seasonal mean of 16 °C. The cold anomalies are rather rare – summer temperatures below 10 °C cover only 7 % of occurrence frequency. During winter months, temperature variability is confined between −0.2 and 3.5 °C at 10 m depth, while at 50 m the limits are 0.5 and 5.4 °C. Mean seasonal data from individual reanalysis points reveal minor horizontal variations between the points compared to their temporal variations. For example, during the winter when deep seawater is needed for the heat pump, the pointwise monthly mean temperature varies at 50 m depth between 2.6 and 2.8 °C in March, but it has a mean seasonal maximum of about 5.9 °C in November and December. Detailed analysis reveals that the temperature of deep layers below 40 m depth can be considered practically uniform over the bay area on scales of a few kilometers and a few days, which is sufficient for the baseline evaluations of oceanographic conditions for seawater heat pumps.

3.2 Statistics of extractable seawater heat

The data were segmented into 26 yearly heating-centered periods from 1 July to 30 June. For the data visualization of each year, a date–year column diagram was drawn, where the color stripes in the column correspond to the actual temperature in a specific year based on the defined color scale (Fig. 6). Results show that at both the 50 and 70 m level of the offshore point 6, the highest temperatures above 4.0 °C occurred every year, but the duration and timing are variable. During the winters 2000–2001, 2007–2008, and 2008–2009, deep layers were warmer than usual through the whole year. In several years, the warmer deep waters were dominant until February or March. There were also years when colder waters were present in summer and extended to autumn, a time when deep-water temperature started to increase.

We define seawater heat as extractable when water temperature exceeds some predefined value, while cold water occurs when the temperature is below that limit. Cold period durations and start dates were determined by evaluating running 9 d slices of temperature criteria fulfillment in the time series. Shorter-duration spikes with fewer than four fulfillments were considered not fulfilled. For the heat pump problem, the time series were limited to periods from 1 October to 30 April, which is usually the heating period of city districts. The results reveal that at a depth level of 20 m (not shown), the water was cold in every winter. Even in the mildest winter of 2007/2008, water with $T < 2$ °C was present for several days. Going further to the deeper layers of 50, 60, and 70 m, the limit $T < 2$ °C is normally not found (except for very cold winters in 1993/1994, 1994/1995, 1999/2000, and 2010/2011), and even cases with $T < 3$ °C were rather rare.

Profiles of the mean number of non-cold days (when heat extraction is considered possible) reveal that favorable periods corresponding to different temperature limits are minimal in the surface layer down to 20 m (Fig. 7). Further, with increasing depths, extractable seawater heat becomes more frequent. A significant increase in the duration of seawater-based heating occurs from 30 to 50 m depth, from 107 to 166 d for 3 °C, and from 149 to 200 d for 2 °C. Considering the recent period 2009–2019, selected to cover the positive temperature trend, the mean duration of non-cold days was generally 5–10 d longer than for the whole period of 1993–2019, whereas the largest increase of up to 20 d was found in the deepest layers at 60 and 70 m.

Profiles of mean start dates of cold periods, when additional heating must be switched on, were calculated from 1 November of each year (Fig. 8). In both offshore and coastal waters the start dates are nearly the same. The tem-

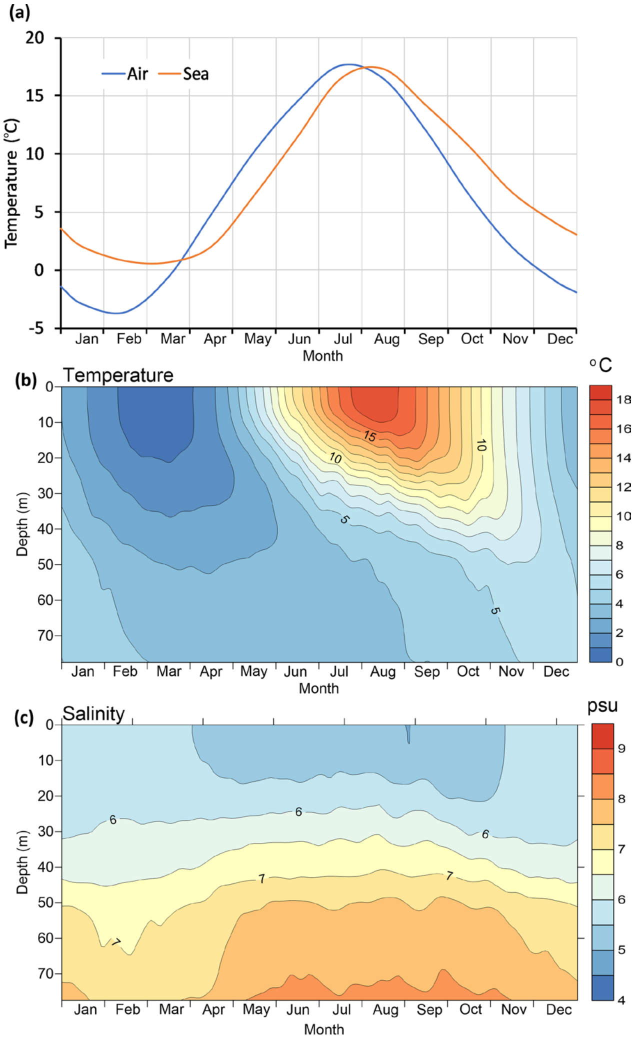

Figure 4. Monthly mean air temperature and surface water temperature in the Tallinn Bay **(a)** and mean seasonal depth distribution of temperature **(b)** and salinity **(c)** in the Tallinn Bay at reanalysis point 6 (Fig. 2) as a function of time of the year (month) and depth. Data are from Copernicus Marine reanalysis for 1993–2019 (product ref. no. 1).

perature goes below a certain limit first at the surface layer and later in the deeper layers. Seawater temperature becomes less than 3 °C on average on 1 January at 20 m depth and on 12 February at 50 m depth. At the 70 m depth, the average start of $T < 3\,°\mathrm{C}$ was calculated on 28 February, although only 14 winters out of 26 had such water present; in 12 winters the condition $T > 3\,°\mathrm{C}$ was always fulfilled. We note that calculations made with the mean seasonal cycle (Fig. 4) always revealed $T > 3\,°\mathrm{C}$. During the recent warmer period of 2009–2019, the start was delayed on average by 5–10 d. However, this estimation is rather uncertain, since there have been several winters where the criteria $T < 1\,°\mathrm{C}$, $T < 2\,°\mathrm{C}$, and $T < 3\,°\mathrm{C}$ have not been met due to dominating warmer waters. Among the winters in 1993–2019, temperature at 50 m depth was

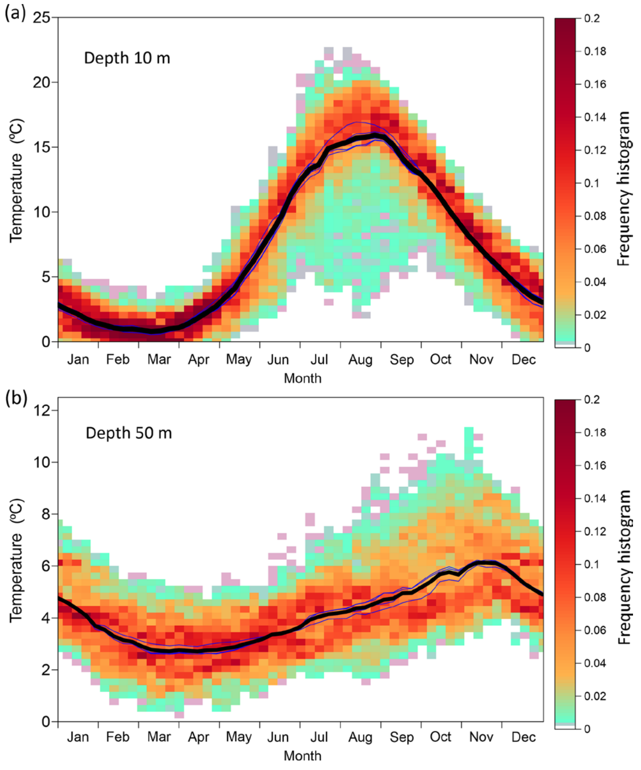

Figure 5. Mean seasonal curve (black solid line) and seasonal temperature histogram (color image) in Tallinn Bay at depths 10 m **(a)** and 50 m **(b)**. Shown are also mean temperature curves for individual horizontal points (thin lines). Copernicus Marine reanalysis data from 1993–2019 (product ref. no. 1) taken from six locations (Fig. 2) are processed with 7 d (weekly) intervals. The temperature histogram bins are 0.5 °C for 10 m depth **(a)** and 0.25 °C for 50 m depth **(b)**. For each week, the sum of histogram frequency shown by the color scale is 1.

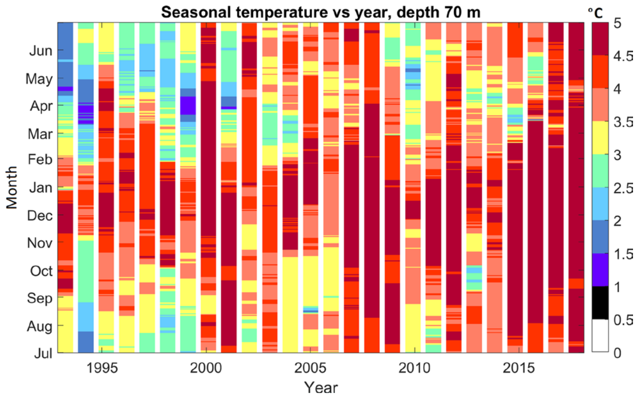

Figure 6. Temperature diagrams in Tallinn Bay at 70 m depth as a function of year (horizontal axis) and calendar day (vertical axis), calculated from Copernicus Marine reanalysis data (product ref. no. 1).

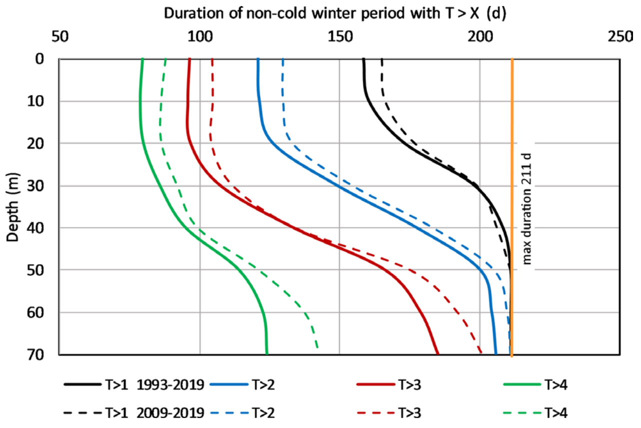

Figure 7. Profiles of the mean number of non-cold days for the reanalysis point 6 (Fig. 2). $X = 1$, 2, 3, and 4 °C as shown in the legend. Copernicus Marine reanalysis data are from 1993–2019 for the full period (solid line) and for the recent 11 years (2009–2019; dashed line). Data are taken from 1 October to 30 April (211 d) of each year (product ref. no. 1).

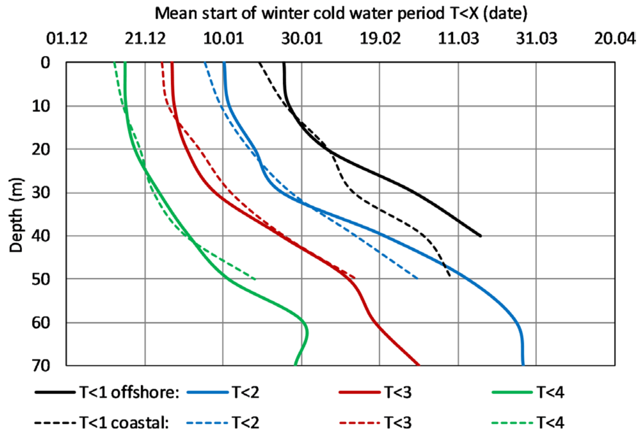

Figure 8. Profiles of the mean start date of the cold seawater period. $X = 1$, 2, 3, and 4 °C as shown in the legend. Copernicus Marine reanalysis data (product ref. no. 1) are shown for 1993–2019 from 1 October to 30 April at offshore point 6 (solid line) and internal bay point 3 (dashed line). The locations of points are given in Fig. 2.

above 3 °C for more than 5 d during 9 winters (35 %) and above 2 °C during 18 winters (70 %). The coldest winters, as shown in Fig. 6, with low deep-water temperature were 1993/1994, 1994/1995, 1999/2000, and 2010/2011.

The results in Fig. 8 show that statistical properties of cold or warm water occurrence are in the first approach horizontally uniform; i.e., average data from one location can be extended over the entire bay area. Since seawater intake for the heat pump systems is usually located on the bottom, in the small bay its baseline temperature regime can be characterized from the temperature time series of nearby deeper locations.

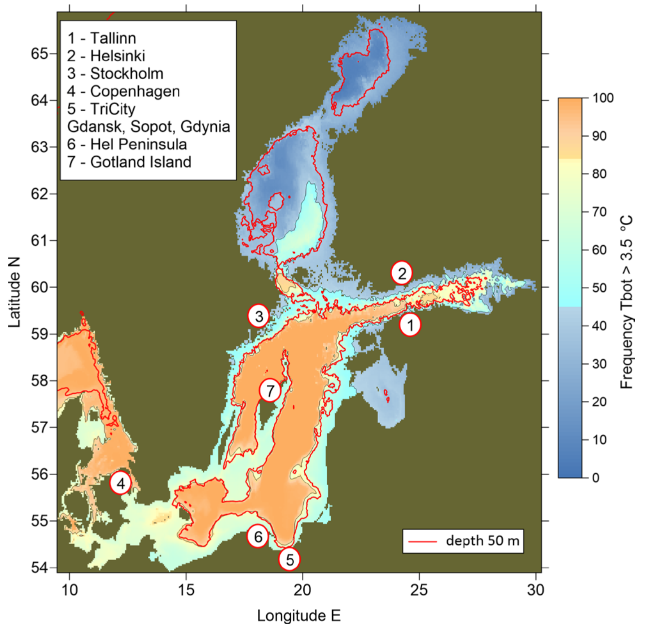

Figure 9. Frequency of occurrence of non-cold waters at $T_{\mathrm{bot}} > 3.5$ °C, calculated from the Copernicus Marine reanalysis data for 1993–2021 (product ref. no. 1).

3.3 Frequency of extractable seawater heat occurrence over the Baltic Sea bottom

Seawater heat pumps can use water with temperature above a certain limit: here $T > 3.5$ °C for non-cold water. Since intake tubes are located on the bottom, "good" locations for seawater heat pump installations are those where non-cold bottom waters of $T_{\mathrm{bot}} > 3.5$ °C occur most frequently, leaving a minimum number of days when an additional (usually less effective) energy source is needed.

Copernicus Marine reanalysis data were used to calculate Baltic-wide non-cold water occurrence frequency on the bottom using the data from the heating period (from October to April) during 1993–2021 (Fig. 9). At each grid cell of the reanalysis data, the near-bottom temperature value for each day was compared to the non-cold criteria, and the counted number of non-cold days was divided by the full number of days during the period, resulting in $F = 100\,\%$ for the regions where T_{bot} is always > 3.5 °C. We may infer that seawater heat is extractable in the regions with $F > 85\,\%$, as shown by the color scale in Fig. 9. Note that extractable seawater heat is found in the deeper basins of the Baltic Proper, where a permanent halocline exists (Fig. 1).

From the socioeconomic viewpoint, favorable locations for seawater heat extraction are a short distance from regions of extractable seawater heat and significant urban and/or industrial areas. Among larger cities, Tallinn has one of the most favorable locations for using seawater heat since the boundary for $F > 85\,\%$ lies just a few kilometers from the coast. In terms of extractable marine heat distance only, the best locations in the Baltic Proper are the western coast of Gotland island in Sweden and the tip of Hel Peninsula near Tri-City in Poland (Gdansk, Sopot, Gdynia), but these regions have only moderate coastal populations. Good locations for seawater heat extractions are found near Copenhagen and other Danish cities, as well as Tri-City in Poland.

4 Discussion and outlook

The design of seawater heat pumps is a complicated interdisciplinary optimization task (Schibuola et al., 2022). There should be heating or cooling energy users at a reasonable distance from the coast, since a fraction of gained energy is lost to the pumping. In ice-prone (boreal) seas, there should be locations near large-scale users where seawater temperature by depth does not frequently fall below +3 °C. In most cases, it is useful to combine seawater heat energy with other renewable sources, such as groundwater, wastewater, lakes, rivers, and air (Pieper et al., 2022; Volkova et al., 2022b).

Favorable oceanographic conditions are of crucial importance for the planning and operation of seawater heat pumps. Important factors include local bathymetry, water temperature, peak heating load, and screening requirements, i.e., to prevent the entrainment of biological organisms and other particulate matter in the system (Mitchell and Spitler, 2013). The present pilot study used long-term and regular, but coarse reanalysis, data to determine the near-bottom seawater temperature characteristics in the context of the potential use of seawater thermal energy for district heating. Heat pumps are operated continuously in an automated regime (although there is a response time depending on the system characteristics). Seawater intake systems have a limited horizontal extent (much smaller than 3.7 km, the grid step of present reanalysis); therefore, unresolved fine-scale coastal and topographic features (especially slope effects; e.g., Delpeche-Ellmann et al., 2018) may become important in the generation of mesoscale and submesoscale dynamics as well as related temperature variations.

In heat engineering, statistics of various meteorological factors (air temperature, wind, solar radiation, etc.) are synthesized in the concept of the "energy reference year" containing hourly forcing (Kalamees et al., 2012). It allows the design of different heat system components based on patterns of heat production and consumption. The reference year is composed of the monthly segments from different years of meteorological data and indicates that "clueing" should present the statistical distributions in the best way over the longer climatic period. For the design of seawater components of the overall district heating system it could be useful to also compose oceanographic reference years. This is not a trivial task since many aspects have to be kept in mind. The oceanographic reference year should match seawater conditions; therefore, the best segment years do not need to correspond to the years for the best meteorology statistical match. Since very-high-resolution data at the pumping sites are usually not available, modeling of such data requires the local forcing data and those from the adjacent sea area to agree, which contradicts the piecewise combination of meteorological reference data. Harmonizing the meteorological and oceanographic reference data for heat and energy engineering is a topic of joint ongoing studies by natural and engineering scientists.

We have calculated basic coarse-scale seawater temperature statistics from Copernicus Marine reanalysis and available observations. If evaluations by energy companies indicate that using seawater heat seems technically and economically feasible, further studies of the oceanographic component of a large-scale initiative should include the following steps.

1. Refine the statistics (including currents) using results from the sub-regional forecast and reanalysis model with higher resolution. There is an operational forecast model with 1 km resolution (Lagemaa et al., 2011) running since 2009. Corresponding reanalysis is in the implementation phase.

2. Together with engineers, identify potential locations of seawater intake and discharge or a heat exchanger. Conduct dedicated observations and VHR modeling at selected locations.

3. Synthesize data from (1)–(2) and Copernicus Marine reanalysis into the custom-tailored data products necessary for engineering designs. These data products could contain refined "reference year" time series in present and future climate and event-based statistics adjusted to the operation decisions for the heat pumps.

4. Also conduct other studies (seabed habitats, sediments, bathymetric, and geological data) in both the intake and pipeline locations, which are needed for an environmental impact assessment.

5 Conclusions

Due to growing interest in seawater heat extraction, variability of temperature in the Tallinn Bay was studied using the Baltic Sea reanalysis data for 1993–2019 from the Copernicus Marine Service. The reanalysis data match the coastal temperature observations with a bias of −0.12 °C and RMSD (root mean square difference) of 1.3 °C.

During summer, the upper mixed layer, located above a sharp thermocline, typically has 20 m thickness; its yearly temperature maximum varies between 16 and 23 °C. In autumn, the upper layer is eroded down to 40 m where inherent salinity stratification blocks further erosion or down to the bottom, whichever is shallower. During winter, the top of the upper layer can reach the freezing point, which is approximately −0.3 °C. At a depth of 40 m, the monthly mean temperature ranges from 2.4 to 7.4 °C, while at 70 m depth, it ranges from 3.4 to 5.2 °C. The highest temperatures at greater depths are typically observed in November and December, while the lowest values are commonly found on average in March and April.

Oceanographic conditions for seawater heat extraction are the least favorable in surface waters down to 20 m. Further, with increasing depths, extractable seawater heat becomes more frequent. A significant increase in the duration of seawater-based heating occurs from 30 to 50 m depth: from 107 to 166 d for 3 °C and 149 to 200 d for 2 °C. Seawater temperature becomes less than 3 °C on average on 1 January at 20 m depth and on 12 February at 50 m depth.

Among larger cities, Tallinn has one of the most favorable locations for using seawater heat. Good locations for seawater heat extractions are found near Copenhagen and other Danish cities, as well as Tri-City in Poland.

Data availability. Data are available from open sources as given in Table 1.

Author contributions. JE acted as a coordinating author. All the authors analyzed the data and wrote and edited the paper.

Competing interests. The contact author has declared that none of the authors has any competing interests.

Acknowledgements. The study was driven by the practical implementation interests of district heating and cooling, expressed by the company OÜ Utilitas, the Geological Survey of Estonia, and managers of a new climate-neutral Hundipea district in Tallinn. Cooperation within the Baltic Monitoring and Forecasting Centre of Copernicus Marine Service is highly appreciated.

Financial support. This study was co-funded by the European Union and the Estonian Research Council via project TEM-TA38 (Digital Twin of Marine Renewable Energy).

Review statement. This paper was edited by Johannes Karstensen and reviewed by two anonymous referees.

References

Aavaste, A., Sipelgas, L., Uiboupin, R., and Uudeberg, K.: Impact of thermohaline conditions on vertical variability of optical properties in the Gulf of Finland (Baltic Sea): Implications for water quality remote sensing, Frontiers in Marine Science, 8, 674065, https://doi.org/10.3389/fmars.2021.674065, 2021.

Alenius, P., Myrberg, K., and Nekrasov, A.: The physical oceanography of the Gulf of Finland: a review, Boreal Environ. Res. 3, 97–125, 1998.

Axell, L.: EU Copernicus Marine Service, Product User Manual for Baltic Sea Physical Reanalysis Product, BALTICSEA_REANALYSIS_PHY_003_011, Issue 2.1, Mercator Ocean International, https://doi.org/10.5281/zenodo.7935113, 2021.

Bach, B., Werling, J., Ommen, T., Münster, M., Morales, J. M., and Elmegaard, B.: Integration of large-scale heat pumps in the district heating systems of Greater Copenhagen, Energy, 107, 321–334, 2016.

CleanTechnica: Giant Heat Pump Takes Over Entire Danish Town, https://cleantechnica.com/2023/06/12/giant-heat-pump-takes-over-entire-danish-town/ (last access: 29 March 2024), 2023.

Delpeche-Ellmann, N., Soomere, T., and Kudryavtseva, N.: The role of nearshore slope on cross-shore surface transport during a coastal upwelling event in Gulf of Finland, Baltic Sea, Estuar. Coast. Shelf S., 209, 123–135, 2018.

Elken, J. and Matthäus, W.: Baltic Sea Oceanography, in: Assessment of Climate Change for the Baltic Sea Basin, edited by: The BACC Author Team, Springer-Verlag, Berlin, 379–386, ISBN 978-3-540-72786-6, 2008.

Elken, J., Raudsepp, U., and Lips, U.: On the estuarine transport reversal in deep layers of the Gulf of Finland, J. Sea Res., 49, 267–274, 2003.

Elken, J., Lehmann, A., and Myrberg. K.: Recent change – marine circulation and stratification. In Second assessment of climate change for the Baltic Sea Basin, Springer, 131–144, https://doi.org/10.1007/978-3-319-16006-1_7, 2015.

EMODnet: European Marine Observation and Data Network, EMODnet [data set], https://www.emodnet.eu/, 13 February 2021.

EMODnet Bathymetry Consortium: EMODnet Digital Bathymetry, European Marine Observation and Data Network, https://doi.org/10.12770/18ff0d48-b203-4a65-94a9-5fd8b0ec35f6, 2018.

EU Copernicus Marine Service Product: Baltic Sea Physical Reanalysis, Mercator Ocean International dataset-reanalysis-nemo-dailymeans [data set], https://doi.org/10.48670/moi-00013, 2021.

EU Copernicus Marine Service Product: Baltic Sea – In Situ Near Real Time Observations, Mercator Ocean International cmems_obs-ins_bal_phybgcwav_mynrt_na_irr [data set], https://doi.org/10.48670/moi-00032, 2022.

Friotherm: Värtan Ropsten – The largest sea water heat pump facility worldwide, with 6 Unitop® 50FY and 180 MW total capacity, https://www.friotherm.com/wp-content/uploads/2017/11/vaertan_e008_uk.pdf (last access: 18 July 2023), 2017.

Haapala, J. and Alenius, P.: Temperature and salinity statistics for the northern Baltic Sea 1961–1990, Finnish Marine Research, 262, 51–121, 1994.

HELCOM MADS: HELCOM Map and data service, HELCOM [data set], https://maps.helcom.fi/website/mapservice/, last access: 18 July 2023.

In Situ TAC partners: EU Copernicus Marine Service Product User Manual for In situ products, In Situ TAC partners: EU Copernicus Marine Service Product User Manual for In situ products, INSITU_BAL_PHYBGCWAV_DISCRETE_MYNRT_013_032, Issue 1.14, Mercator Ocean International, https://catalogue.marine.copernicus.eu/documents/PUM/CMEMS-INS-PUM-013-030-036.pdf (last access: 18 July 2023), 2022.

Jakobsson, M., Stranne, C., O'Regan, M., Greenwood, S. L., Gustafsson, B., Humborg, C., and Weidner, E.: Bathymetric properties of the Baltic Sea, Ocean Science, 15, 905–924, 2019.

Kalamees, T., Jylhä, K., Tietäväinen, H., Jokisalo, J., Ilomets, S., Hyvönen, R., and Saku, S.: Development of weighting factors for climate variables for selecting the energy reference year according to the EN ISO 15927-4 standard, Energ. Buildings, 47, 53–60, 2012.

Lagemaa, P., Elken, J., and Kõuts, T.: Operational sea level forecasting in Estonia, Estonian Journal of Engineering, 17, 301–331, 2011.

Leppäranta, M. and Myrberg, K.: Physical oceanography of the Baltic Sea, Springer Science & Business Media, https://doi.org/10.1007/978-3-540-79703-6, 2009.

Liblik, T. and Lips, U.: Characteristics and variability of the vertical thermohaline structure in the Gulf of Finland in summer, Boreal Environ. Res., 16, 73–83, 2011.

Liblik, T. and Lips, U.: Stratification has strengthened in the Baltic Sea–an analysis of 35 years of observational data, Front. Earth Sci., 7, 174, https://doi.org/10.3389/feart.2019.00174, 2019.

Liblik, T., Naumann, M., Alenius, P., Hansson, M., Lips, U., Nausch, G., Tuomi, L., Wesslander, K., Laanemets, J., and Viktorsson, L.: Propagation of impact of the recent Major Baltic Inflows from the Eastern Gotland Basin to the Gulf of Finland, Frontiers in Marine Science, 5, 222, https://doi.org/10.3389/fmars.2018.00222, 2018.

Liu, Y., Axell, L., Jandt-Scheelke S., Lorkowski, I., Lindenthal, A., Verjovkina S., and Schwichtenberg, F.: EU Copernicus Marine Service, Quality Information Document for Baltic Sea Physical Reanalysis Product, BALTICSEA_REANALYSIS_PHY_003_011, Issue 2.5, Mercator Ocean International, https://doi.org/10.5281/zenodo.7935113, 2019.

Lund, H., Østergaard, P. A., Chang, M., Werner, S., Svendsen, S., Sorknæs, P., Thorsen, J. E., Hvelplund, F., Mortensen, B. O. G., Mathiesen, B. V., and Bojesen, C.: The status of 4th generation district heating: Research and results, Energy, 164, 147–159, 2018.

Maljutenko, I. and Raudsepp, U.: Long-term mean, interannual and seasonal circulation in the Gulf of Finland – the wide salt wedge estuary or gulf type ROFI, J. Marine Syst., 195, 1–19, https://doi.org/10.1016/j.jmarsys.2019.03.004, 2019.

Meier, H. E. M., Dieterich, C., Gröger, M., Dutheil, C., Börgel, F., Safonova, K., Christensen, O. B., and Kjellström, E.: Oceanographic regional climate projections for the Baltic Sea until 2100, Earth Syst. Dynam., 13, 159–199, https://doi.org/10.5194/esd-13-159-2022, 2022.

Mitchell, M. and Spitler, J.: Open-loop direct surface water cooling and surface water heat pump systems – A review, HVAC&R Res., 19, 125–140, 2013.

Omstedt, A. and Hansson, D.: The Baltic Sea ocean climate system memory and response to changes in the water and heat balance components, Cont. Shelf Res., 26, 236–251, 2006.

OpenStreetMap Contributors: Coastline data, OpenStreetMap, https://www.openstreetmap.org/ (Acquired from the HELCOM Data Portal), last access 18 July 2023.

Pieper, H., Ommen, T., Elmegaard, B., and Markussen, W. B.: Assessment of a combination of three heat sources for heat pumps to supply district heating, Energy, 176, 156–170, 2019.

Pieper, H., Lepiksaar, K., and Volkova, A.: GIS-based approach to identifying potential heat sources for heat pumps and chillers providing district heating and cooling, International Journal of Sustainable Energy Planning and Management, 34, 29–44, https://doi.org/10.54337/ijsepm.7021, 2022.

Raudsepp, U., Legeais, J.-F., She, J., Maljutenko, I., and Jandt, S.: Baltic Inflows, J. Oper. Oceanogr., 11, s106–s110, https://doi.org/10.1080/1755876X.2018.1489208, 2018.

Schibuola, L., Tambani, C., and Buggin, A.: Seawater Opportunities to Increase Heating, Ventilation, and Air Conditioning System Efficiency in Buildings and Urban Resilience, Frontiers in Energy Research, 10, https://doi.org/10.3389/fenrg.2022.913411, 2022.

Su, C., Madani, H., Liu, H., Wang, R., and Palm, B.: Seawater heat pumps in China, a spatial analysis, Energ. Convers. Manage., 203, 112240, https://doi.org/10.1016/j.enconman.2019.112240, 2020.

Uiboupin, R. and Laanemets, J.: Upwelling characteristics derived from satellite sea surface temperature data in the Gulf of Finland, Baltic Sea, Boreal Environ. Res., 14, 297–304, 2009.

Volkova, A., Hlebnikov, A., Ledvanov, A., Kirs, T., Raudsepp, U., and Latõšov, E.: District cooling network planning. a case study of Tallinn, International Journal of Sustainable Energy Planning and Management, 34, 63–78, 2022a.

Volkova, A., Koduvere, H., and Pieper, H.: Large-scale heat pumps for district heating systems in the Baltics: Potential and impact, Renewable and Sustainable Energy Reviews, 167, 112749, https://doi.org/10.1016/j.rser.2022.112749, 2022b.

Wehde, H., Schuckmann, K. V., Pouliquen, S., Grouazel, A., Bartolome, T., Tintore, J., De Alfonso Alonso-Munoyerro, M., Carval, T., Racapé, V., and the INSTAC team: EU Copernicus Marine Service Quality Information Document for In Situ Products, INSITU_BAL_PHYBGCWAV_DISCRETE_MYNRT_013_032, Issue 2.2, Mercator Ocean International, https://catalogue.marine.copernicus.eu/documents/QUID/CMEMS-INS-QUID-013-030-036.pdf, last access: 18 July 2023, 2022.

State Planet, 4-osr8, 10, 2024
https://doi.org/10.5194/sp-4-osr8-10-2024

Event-based wave statistics for the Baltic Sea

Jan-Victor Björkqvist[1,2], **Hedi Kanarik**[1], **Laura Tuomi**[1], **Lauri Niskanen**[3], **and Markus Kankainen**[3]
[1]Finnish Meteorological Institute, Helsinki, 00560, Finland
[2]Norwegian Meteorological Institute, Bergen, 5007, Norway
[3]Natural Resources Institute Finland, Helsinki, 00790, Finland

Correspondence: Jan-Victor Björkqvist (jan-victor.bjorkqvist@fmi.fi)

Received: 12 July 2023 – Discussion started: 21 August 2023
Revised: 29 December 2023 – Accepted: 20 March 2024 – Published: 30 September 2024

Abstract. Typical statistics, such as mean or percentiles, provide an excellent baseline for studying variations and changes in physical variables that have socioeconomic relevance. Nonetheless, they lack information on how often, and for how long, a certain wave height is exceeded, which might be needed for practical applications, such as planning marine operations. Using a 29-year wave hindcast, we determined the individual events where the significant wave height exceeded warning thresholds for Baltic Sea marine traffic (2.5, 4, and 7 m). During the summer months (JJA), the significant wave height exceeded 2.5 m less than twice a month. During the winter months (DJF), a significant wave height of 2.5 m was exceeded on average once a week in the larger Baltic Proper and Bothnian Sea sub-basins. Events with wave heights of over 7 m occurred roughly once every other year in the larger sub-basins. Our case study for fish-farm-related operations compared two sites that are located 10 and 30 km from the coast in the Bothnian Sea, where we determined wave events that could affect operations at the cage – meaning a significant wave height over 1 m. During the growth period of rainbow trout (May–October) there were roughly twice as many possibly disruptive events at the location further offshore than at the location closer to the coast. Even at the less-exposed location half of the wave events lasted more than 12 h, with a few events in September and October lasting around a week.

1 Introduction

Wind-generated sea surface waves impact safety at seas and the planning of offshore structures and activities. These safety and financial considerations, along with scientific interest, have motivated studies mapping the global wave climate with in situ and remote sensing measurements and with numerical models (Semedo et al., 2011; Young et al., 2011; Semedo et al., 2015; Vanem et al., 2017). Wave statistics, trends, and extremes are therefore relatively well understood on a global and regional scale, but these general statistics might be too abstract for specific socioeconomic applications.

The Baltic Sea wave climate is relatively mild compared to the oceans (e.g. Cieślikiewicz et al., 2008; Tuomi et al., 2011; Björkqvist et al., 2018), but a significant wave height of 8 m has been measured during storms (Soomere et al., 2008; Björkqvist et al., 2017, 2020). Traditional mean, maximum, and percentile statistics have been used to determine the wave impact on sediment transport (Soomere and Viška, 2014) and the mean water level (Soomere et al., 2020), as well as the joint effects of waves and water-level variations (Hanson and Larson, 2008; Leijala et al., 2018; Kudryavtseva et al., 2020). Waves also affect structures in the sea, such as fish farms (Faltinsen and Shen, 2018; Karathanasi et al., 2022). Recommendations and best practices for the design of coastal and offshore structures typically rely on extreme values, such as 50-, 100-, or 250-year significant wave heights (e.g. NSF, 2003; Björkqvist et al., 2019).

The construction and maintenance of offshore structures require marine operations. While large cargo and passenger vessels can operate in the harshest wave conditions of the Baltic Sea, smaller vessels that are used for maintenance might be sensitive to lower sea states. Therefore, the planning of maintenance operations benefits from information on individual wave events that can affect these smaller vessels.

Published by Copernicus Publications.

Table 1. CMEMS and non-CMEMS products used in this study, including information on data documentation.

Product ref. no.	Product ID & type	Data access	Documentation
1	BALTICSEA_REANALYSIS_WAV_003_015; numerical models	EU Copernicus Marine Service Product (2023a)	Quality Information Document (QUID): Lindgren et al. (2023a) Product User Manual (PUM): Lindgren et al. (2023b)
2	WAVE_GLO_PHY_SWH_L3_NRT_014_001; satellite observations	EU Copernicus Marine Service Product (2023b)	QUID: Taburet et al. (2023) PUM: Mertz et al. (2023)
3	WAVE_GLO_PHY_SWH_L3_MY_014_005; satellite observations	EU Copernicus Marine Service Product (2021)	QUID: Charles and Ollivier (2021) PUM: Husson and Charles (2021)
4	FMI wave buoy measurements by the coast of the Bothnian Sea. Data originate from a Datawell Directional Waverider.	Upon request from FMI	Not available

A typical question might be as follows: how many times will a (possibly disruptive) wave event occur in May, and how long do such events typically last? This information cannot be deduced from traditional statistics.

This study aims to provide Baltic Sea-wide, practically applicable event-based wave statistics. The focus is on seasonal wave events occurring multiple times per year, thus impacting day-to-day operations at sea. The study also includes a nearshore case study applied to fish farming. This case study compares the wave conditions at two locations, of which one is further out to sea where the different pressures (i.e. societal and environmental) from the mainland are weaker and there is less eutrophication.

This paper is structured as follows: Sect. 2 introduces the model hindcast and the observational data. Section 3 presents the survey with fish farmers, and Sect. 4 defines the statistics. Section 5 gives wave event statistics for the entire Baltic Sea, while Sect. 6 presents the case study with a focus on the needs for fish farms. We end by discussing and concluding our findings.

2 Data and model accuracy

This study is based on the Copernicus Marine Service's Baltic Sea wave hindcast (product ref. no. 1, Table 1). The hourly hindcast data cover the entire Baltic Sea with a resolution of 1 nautical mile (ca. 1.85 km) for the years 1993–2021. Of the available wave parameters we use the significant wave height, defined as $H_\mathrm{s} = 4\sqrt{m_0}$, where m_0 is the variance of the wave field. The simulated H_s had a bias and root-mean-square error (RMSE) of −0.04 and 0.24 m when validated against in situ wave measurements from the Baltic Sea (Lindgren et al., 2023a). Nonetheless, these results do not quantify the model accuracy in coastal areas. Also, buoys located in the north typically need to be recovered before the ice season, causing measurement gaps in late autumn, winter, and early spring.

As an additional validation we compared the hindcast against the satellite L 3 Significant Wave Height product (product ref. nos. 2 and 3, Table 1). This validation, covering 2002–2021, was performed by collocating each along-track satellite measurement to the closest model grid point, allowing a time difference of at most 30 min. The number of data points used for comparison was 1 246 075, and the mean and median distances between the compared points were 0.66 and 0.68 km. The −0.06 m bias and a 0.25 m RMSE over the whole domain were similar to those reported by Lindgren et al. (2023a).

Finally, we compared the hindcast against coastal wave buoy measurements collected by the Finnish Meteorological Institute (FMI) near the coast in the eastern Bothnian Sea (61.325° N, 21.369° E) from July 2017 to 5 January 2018 (product ref. no. 4, Table 1). The buoy was located less than 10 km from the coast, and data were available every 30 min, of which we used the values coinciding with the hourly model output. The −0.04 m bias and 0.18 m RMSE suggest that the hindcast is accurate enough in our nearshore study region (see Sect. 6).

3 Survey with fish farmers

In a small survey – conducted as part of the fish farming national spatial plan – we asked three fish farmers in which wave conditions they can operate. We interviewed three companies with farms in harsh conditions in the Baltic Sea: Lännenpuolen Lohi Oy (LL), Offshore Fish Finland Oy (OF), and Brändö Lax Ab (BL). We asked the companies to estimate the wave heights in which they can feed their fish and do other maintenance operations on their cages and also to describe the vessels with which they operate.

LL mostly uses a small 7 m feeding boat, and they reported that 0.5 m sharp waves can already complicate the feeding of the fish and that other operations also become difficult in the submerged cage they use. OF reported that they stop feeding at a 1.2 m wave height, while BL reported that they have fed the fish in up to 2 m waves but that other operations become difficult and unsafe in 1 m waves. Both OF and BL have 15–20 m vessels that are designed to be used at fish farms in harsh conditions. All fish farmers noted that the sea should be relatively calm during harvesting when using a crane to troll fish from cages.

Based on the above results, we decided to use 1 m as an approximate threshold for when it is possible to perform normal operations safely at the cages (see Sect. 6).

4 Definition of wave events

We define the first hour of a wave event as the time when a specific threshold is exceeded. The last hour of an event is when the H_s again drops below this threshold. The duration of an event (in hours) is determined as the number of (hourly) data points between (and including) the start and the end points of the event. Nonetheless, two events are regarded as one if they are less than 12 h apart and if the H_s does not drop below 90 % of the threshold in between. For monthly statistics each event is assigned to the month when the maximum is reached, even if the majority of the event took place during another month.

We used the thresholds of 1, 2.5, 4, and 7 m. The three highest values have been chosen by the FMI to trigger national wave warnings, since they are regarded as potentially dangerous for ship traffic. The lowest threshold is relevant for lighter operations at sea and is based on the survey described in Sect. 3.

5 Baltic Sea-wide statistics

A 2.5 m H_s was exceeded over 10 times per year in all the sub-basins of the Baltic Sea (Fig. 1a), with median durations typically between 10 and 16 h (Fig. 1d). A 4 m H_s was still exceeded several times per year in most of the Baltic Sea, but median durations over 10 h were rare. Previous studies have shown that a 7 m H_s is reached only during strong winds in the larger basins (e.g. Tuomi et al., 2011; Björkqvist et al., 2018). In our data the median duration of the 7 m events exceeded 10 h in some parts of the larger basins (Fig. 1f). The 7 m threshold was not exceeded in the Gulf of Riga, the Gulf of Finland, or the Bothnian Bay (Fig. 1c).

The wave conditions in the Baltic Sea are seasonal, with the highest waves occurring in late autumn or early winter (Tuomi et al., 2011). While large vessels operate in the Baltic Sea year round, many activities are limited to the calmer months between late spring and early autumn. We studied the seasonality at five points: four of them coincide with the location of FMI operational wave buoys, and the fifth is taken in the southern Baltic Sea where the wave climate is the harshest (Fig. 2).

The H_s in the Baltic Proper and Bothnian Sea exceeded 2.5 m (at least) about once per week between October and February but only once every 2 to 4 weeks in April to August. Even in the smaller basins (Gulf of Finland and Bothnian Bay) the H_s exceeded 2.5 m around once every 1 to 2 weeks in the harsher period between October and January.

An H_s of 4 m occurred on average less than once every other calendar month throughout the year in the smallest basins (Gulf of Finland and Bay of Bothnia); for the larger basins this was true only between April and August. In the winter months (DJF) H_s exceeded 4 m on average 1–2 times per calendar month in the Baltic Proper main basin. The 4 m wave events can last 12 to 24 h even in the smaller basins (Fig. 2a).

A 7 m wave event was rare enough that a monthly breakdown was not meaningful. Most such events (16 events) occurred in the southern part of the Baltic Sea, with only 5 events taking place in the northern Baltic Proper (Fig. 2d). The assessment of high waves as being most probable in the southeastern Baltic Proper is in line with Björkqvist et al. (2018), while e.g. Tuomi et al. (2011) and Räämet and Soomere (2010) place the highest waves in the northern part of the Baltic Proper. These differences might be explained by the shorter time period used by Tuomi et al. (2011) or the use of geostrophic winds by Räämet and Soomere (2010). No 7 m wave events occurred in the Gulf of Finland and the Bothnian Bay, which is in line with existing statistics (e.g. Tuomi et al., 2011; Björkqvist et al., 2018). The 7 m wave events typically lasted under 8 h, but one 14 h event was identified in the southeastern Baltic.

6 Coastal case study

Wave conditions determine what operations, if any, fish farmers can perform near the facilities. Based on a survey with fish farmers, it is not feasible to feed the fish and do other operations in open-cage facilities when H_s is over 1 m. The EU Water Framework Directive requires aquaculture facilities to meet the environmental objectives for the ecological status. This asserts a pressure to establish new fish farms in open-sea areas, where their effect on the ecological status is mitigated by the more efficient transport and mixing of nutrients, instead of in coastal areas, where the ecological state of the water bodies is already weaker. Open-sea farms are exposed to harsher wave conditions, but the activities take place during the growth season for the fish (i.e. May–October for rainbow trout) when the waves are lower.

We determined events when H_s exceeded 1 m for a nearshore area where fish farms are planned. We investigated the difference between two locations: one located ca. 10 km from the shoreline and the second ca. 20 km further out

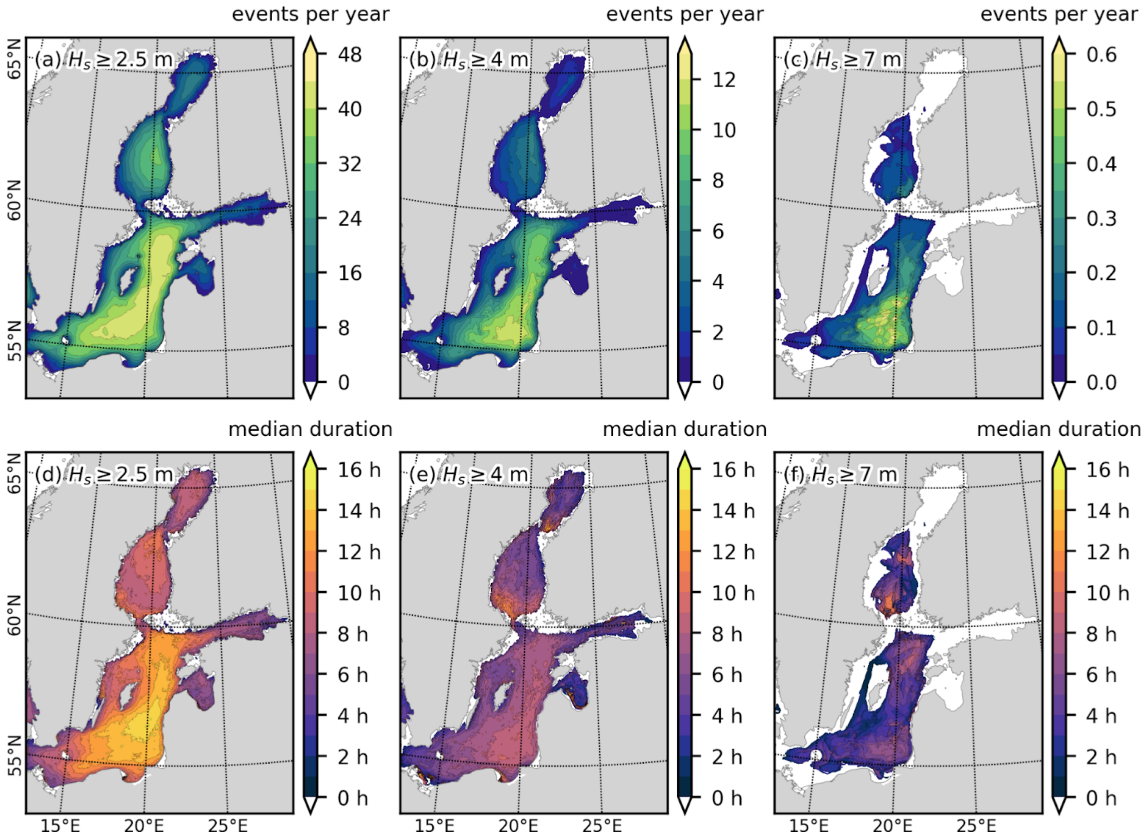

Figure 1. Number of events per year **(a–c)** and median duration in hours **(d–f)** of cases where H_s exceeds different thresholds: 2.5 m **(a, d)**, 4 m **(b, e)**, and 7 m **(c, f)**. Values are calculated from 29 years of hourly data from the Baltic Sea wave hindcast (product ref. no. 1, Table 1).

(Fig. 3). For the inner location, H_s exceeded 1 m around four times per calendar month during May–August. In September and October the numbers were six and eight times respectively – comparable to winter conditions. In the outer location, H_s exceeded 1 m roughly six to nine times per calendar month during May–September. Again, the conditions in October (10 times) were comparable to November–January outside the growth season.

For the more exposed location, H_s exceeded 1 m a larger percent of the times during the winter than during the summer, but this was not reflected in a significant increase in the number of 1 m wave events; the harsher winter wave climate simply caused longer events (Fig. 3). Half of the events lasted less than 12 h at the inner station and less than 15 h at the outer station. Nevertheless, even during the calmer growth season, 25 %–35 % of the events lasted over 24 h (Fig. 3c). An event lasting over 3 d is expected, on average, once every other growth season at the inner station and twice per growth season at the outer station. Still, considerably longer events are still possible: 5 events at the inner station and 18 at the outer station lasted over 100 h, all during September or October. The longest event in September 1997 lasted 13 d at the outer station.

7 Discussion

For certain applications, such as fatigue calculations, time-averaged values contain relevant information. Nonetheless, for many operations at sea – heavy commercial traffic, light recreational boating, or operations at installations like fish farms – information on how often and for how long a certain wave height is exceeded might be more important than simply knowing how many hours per year the threshold is exceeded.

A number of hours per year can mean a few long events or frequent shorter events. The type of operation and the amount of flexibility allowed in the planning and execution determine the impact of the event frequency and length. For example, fish farm operations with a small boat might need to be put on hold by a relatively low sea state. Nonetheless, the flexibility in the timing will allow for adaptive execution if adequate wave forecasts exist. Larger vessels, again, can withstand higher wave heights but typically run on a tight schedule, although with a possible slight leeway to accommodate passenger comfort, in the case of passenger ferries, and fuel consumption (Jalkanen et al., 2012).

The wave conditions in the Baltic Sea depend on the season and the ice cover (e.g. Tuomi et al., 2011). Our re-

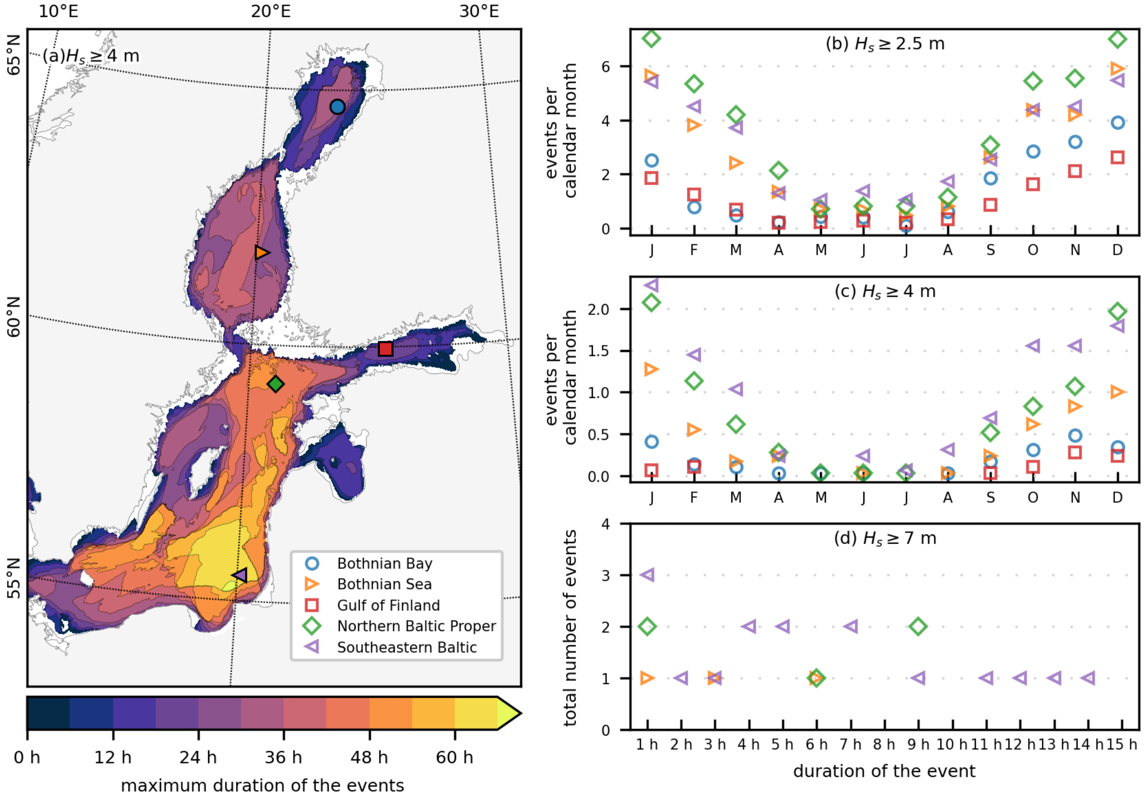

Figure 2. The maximum duration of events during 1993–2021 where the significant wave height exceeded 4 m **(a)**. The event incidence for thresholds of 2.5 and 4 m as a function of the calendar month (**b** and **c**). The number of events exceeding 7 m during the entire 29-year period as a function of the exceedance duration in hours **(d)**. The symbols in panels **(b)**–**(d)** refer to the areas given in panel **(a)**.

sults suggest that wave conditions also vary significantly within one season, highlighting the value of monthly statistics. Monthly statistics are especially useful when activities span only part of the year, with operations carried out at the beginning and end of the season.

The example used in this study is fish farming, where high waves make it difficult to feed the fish or conduct other operations. Floating fish farms also need to be installed and removed at specific time windows at the beginning and the end of the growth season for the fish. Moreover, all operations also depend on what kind of equipment, e.g. boat, is used. Fish farmers install fish cages around May and remove them in September or October. The towing of the fish cages should be done during calm sea conditions, but the process can take a considerable time since it is done at a speed of only 2–4 knots. Finding a window of possibility for towing is therefore highly relevant for the fish farmers.

The EU Water Framework Directive and, especially, the ECJ Weser ruling 2015 impact where it is feasible to grow fish. The ruling directly obligates member states, unless given an exemption, to reject projects that could potentially degrade the condition of a water body or endanger the achievement of its objectives. This ruling is central in balancing between the ecological status of the water and the desire to increase sustainable growth in the marine and maritime sectors as laid out in e.g. the EU Blue Growth Strategy. Therefore, even if aquaculture accounts for only 1 %–2 % of the total nutrient load to the Baltic Sea, this ruling has had a great impact on the allocation of new fish farms. The directive favours broad and open-sea areas where the impact of open-caged fish farms on the environment is mitigated, even though harsher environmental conditions mean less favourable conditions for practical operations, such as towing.

Also, other offshore operations might benefit from event-based statistics. For example, similar statistics can be used to plan the construction and maintenance of offshore wind farms. The method presented here can be applied to any threshold and variable relevant for the given operation. Furthermore, simultaneous information about, for example, the wave direction or wave period can also be extracted. This can be used to analyse wave events from a certain direction or with a certain steepness.

8 Conclusions

Based on a numerical hindcast we determined all individual wave events where the significant wave height (H_s) exceeded

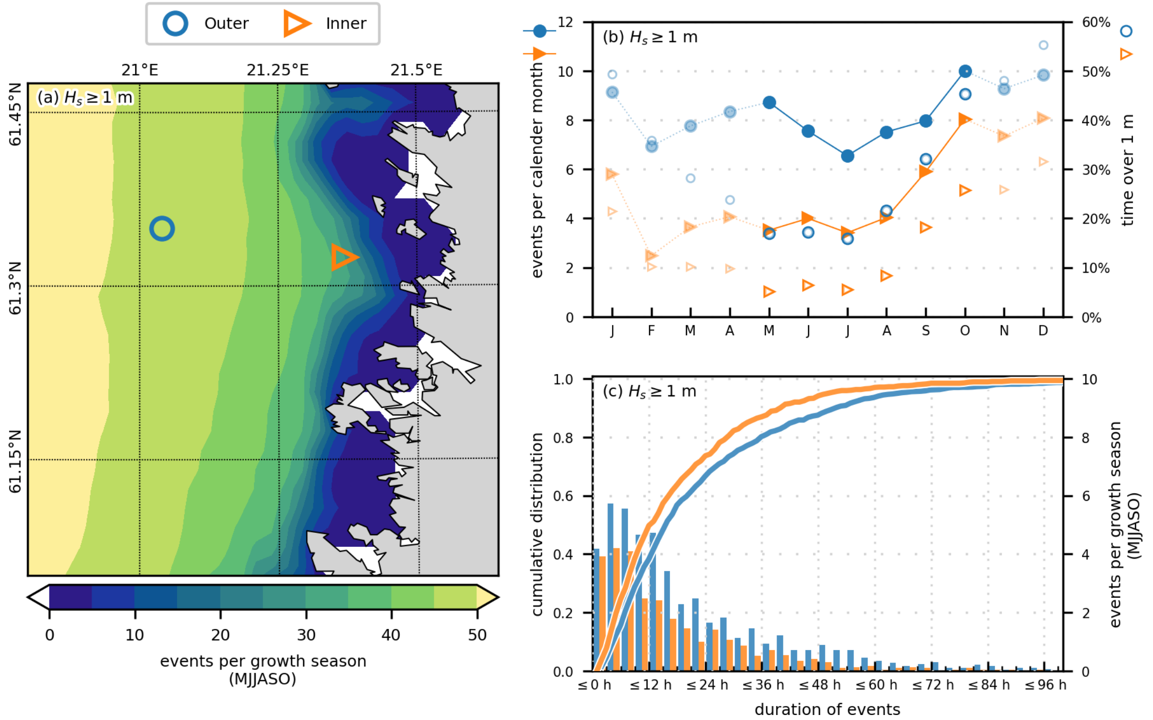

Figure 3. Events when the significant wave height (H_S) exceeded 1 m during the growth season of rainbow trout in Finland (May to October). Number of exceedances per growth season **(a)**, event occurrence from two locations as a function of calendar month (**b**, left axis, filled symbols), and percentage of time H_S stayed over 1 m (**b**, right axis, empty symbols). The duration of events during the growth season is presented as solid lines, and the number of each event length is indicated in a histogram **(c)**. The bin size of the histogram is 3 h so that the first blue and orange bars correspond to event durations of 1, 2, and 3 h. Symbols and colours in panels **(b)** and **(c)** correspond to locations in panel **(a)**.

2.5, 4, and 7 m in the Baltic Sea for the years 1993–2021. For a limited nearshore area in the Bothnian Sea we also determined events where the significant wave height exceeded 1 m.

The number of 2.5 and 4 m wave events was seasonal. A 7 m wave event occurred at most around 0.6 times per year on average and only in the Baltic Proper and Bothnian Sea. The median duration of 4 m wave events was less than 10 h in almost the entire Baltic Sea, but even 7 m wave events that last up to 15 h seem to be possible. Such long events are difficult to circumvent, and, while heavy marine traffic can mostly operate in any conditions in the Baltic Sea, the sea state will affect the fuel consumption and might cause delays.

The Bothnian Sea case study targeted conditions relevant specifically for fish farming and therefore focused on the growth season for rainbow trout (May–October). Based on a questionnaire, a 1 m H_S was found to be potentially disruptive for operations at fish farms that are typically carried out with small boats. We determined that the number of 1 m wave events in the growth season can potentially double if the fish farms are moved from 10 to 30 km from the shore. Since open-sea locations might otherwise be favoured because of e.g. nutrient loads, the challenges from harsher weather conditions need to be balanced with regulatory requirements and environmental concerns.

Code and data availability. The data containing the individual wave events for the thresholds used in this paper and the Python code to determine wave events for other thresholds from the original data, along with code to reproduce the figures of the papers, are available from the FMI data storage (https://doi.org/10.57707/fmi-b2share.fad6a08688ab493b9f8e5d0fdf5db432, Kanarik et al., 2024). Please see Table 1 for additional data sets that have been used in this study.

Author contributions. The study was initiated by LT, JVB, and HK. The methodology for computing the statistics was designed by HK, JVB, and LT and implemented by HK. HK calculated the wave statistics and performed the additional model validation. The case study was designed by LN and MK in collaboration with the other authors. The original version of the paper was prepared by JVB and HK and revised by all authors.

Competing interests. The contact author has declared that none of the authors has any competing interests.

Acknowledgements. We want to thank Tarmo Soomere and the two ananymous reveiwers. Their constructive comments helped us improve the final version of our manuscript.

Financial support. This research has been supported by the European Maritime and Fisheries Fund (grant no. 33436) and the EU Copernicus Marine Service Programme.

Review statement. This paper was edited by Joanna Staneva and reviewed by Tarmo Soomere and two anonymous referees.

References

Björkqvist, J.-V., Tuomi, L., Tollman, N., Kangas, A., Pettersson, H., Marjamaa, R., Jokinen, H., and Fortelius, C.: Brief communication: Characteristic properties of extreme wave events observed in the northern Baltic Proper, Baltic Sea, Nat. Hazards Earth Syst. Sci., 17, 1653–1658, https://doi.org/10.5194/nhess-17-1653-2017, 2017.

Björkqvist, J.-V., Lukas, I., Alari, V., van Vledder, G. Ph., Hulst, S., Pettersson, H., Behrens, A., and Männik, A.: Comparing a 41-year model hindcast with decades of wave measurements from the Baltic Sea, Ocean Eng., 152, 57–71, https://doi.org/10.1016/J.OCEANENG.2018.01.048, 2018.

Björkqvist, J.-V., Kahma, K. K., Johansson, M., Jokinen, H., Leijala, U., Särkkä, J., Tikka K., and Tuomi, L.: Turvalliset rakentamiskorkeudet Helsingin rannoilla, Kaupunkiympäristön julkaisuja 2019:20, https://www.hel.fi/static/liitteet/kaupunkiymparisto/julkaisut/julkaisut/julkaisu-20-19.pdf (last access: 12 June 2023), 2019.

Björkqvist, J.-V., Rikka, S., Alari, V., Männik, A., Tuomi, L., and Pettersson, H.: Wave height return periods from combined measurement–model data: a Baltic Sea case study, Nat. Hazards Earth Syst. Sci., 20, 3593–3609, https://doi.org/10.5194/nhess-20-3593-2020, 2020.

Charles, E. and Ollivier, A.: EU Copernicus Marine Service Quality Information Document for Global Ocean L 3 Significant Wave Height From Reprocessed Satellite Measurements, WAVE_GLO_PHY_SWH_L3_MY_014_005, Issue 1.0, Mercator Ocean International, https://catalogue.marine.copernicus.eu/documents/QUID/CMEMS-WAV-QUID-014-005.pdf (last access: 13 June 2023), 2021.

Cieślikiewicz, W. and Paplińska-Swerpel, B.: A 44-year hindcast of wind wave fields over the Baltic Sea, Coast. Eng., 55, 894–905, https://doi.org/10.1016/j.coastaleng.2008.02.017, 2008.

EU Copernicus Marine Service Product: Global Ocean L 3 Significant Wave Height From Reprocessed Satellite Measurements, Mercator Ocean International [data set], https://doi.org/10.48670/moi-00176, 2021.

EU Copernicus Marine Service Product: Baltic Sea Wave Hindcast, Mercator Ocean International [data set], https://doi.org/10.48670/moi-00014, 2023a.

EU Copernicus Marine Service Product: Global Ocean L 3 Significant Wave Height From Nrt Satellite Measurements, Mercator Ocean International [data set], https://doi.org/10.48670/moi-00179, 2023b.

Faltinsen, O. M. and Shen, Y.: Wave and Current Effects on Floating Fish Farms, J. Marine. Sci. Appl., 17, 284–296, https://doi.org/10.1007/s11804-018-0033-5, 2018.

Hanson, H. and Larson, M.: Implications of extreme waves and water levels in the southern Baltic Sea, J. Hydraul. Res., 46, 292–302, https://doi.org/10.1080/00221686.2008.9521962, 2008.

Husson, R., and Charles, E.: EU Copernicus Marine Service Product User for Global Ocean L 3 Significant Wave Height From Reprocessed Satellite Measurements, WAVE_GLO_PHY_SWH_L3_MY_014_005, Issue 2.0, Mercator Ocean International, https://catalogue.marine.copernicus.eu/documents/PUM/CMEMS-WAV-PUM-014-005-006-007.pdf (last access: 13 June 2023), 2021.

Jalkanen, J.-P., Johansson, L., Kukkonen, J., Brink, A., Kalli, J., and Stipa, T.: Extension of an assessment model of ship traffic exhaust emissions for particulate matter and carbon monoxide, Atmos. Chem. Phys., 12, 2641–2659, https://doi.org/10.5194/acp-12-2641-2012, 2012.

Kanarik, H., Björkqvist, J.-V., and Tuomi, L.: Data and code for the article "Event-based wave statistics for the Baltic Sea" by Björkqvist et al. (2024), Finnish Meteorological Institute [code and data set], https://doi.org/10.57707/fmi-b2share.fad6a08688ab493b9f8e5d0fdf5db432, 2024.

Karathanasi F. E., Soukissian T. H., and Hayes D. R.: Wave Analysis for Offshore Aquaculture Projects: A Case Study for the Eastern Mediterranean Sea, Climate, 10, 2, https://doi.org/10.3390/cli10010002, 2022.

Kudryavtseva, N., Räämet, A., and Soomere, T.: Coastal Flooding: Joint Probability of Extreme Water Levels and Waves along the Baltic Sea Coast, J. Coastal Res., 95, 1146–1151, https://doi.org/10.2112/SI95-222.1, 2020.

Leijala, U., Björkqvist, J.-V., Johansson, M. M., Pellikka, H., Laakso, L., and Kahma, K. K.: Combining probability distributions of sea level variations and wave run-up to evaluate coastal flooding risks, Nat. Hazards Earth Syst. Sci., 18, 2785–2799, https://doi.org/10.5194/nhess-18-2785-2018, 2018.

Lindgren, E., Tuomi, L., and Huess, V.: EU Copernicus Marine Service Quality Information Document for the Baltic Sea Wave Hindcast, BALTICSEA_REANALYSIS_WAV_003_015, Issue 1.1, Mercator Ocean International, https://catalogue.marine.copernicus.eu/documents/QUID/CMEMS-BAL-QUID-003-015.pdf (last access: 8 April 2024), 2023a.

Lindgren, E., Tuomi, L., Huess, V. and Kanarik, H.: EU Copernicus Marine Service Product User for the Baltic Sea Wave Hindcast, BALTICSEA_REANALYSIS_WAV_003_015, Issue 1.2, Mercator Ocean International, https://catalogue.marine.copernicus.eu/documents/PUM/CMEMS-BAL-PUM-003-015.pdf (last access: 8 April 2024), 2023b.

Mertz, F., Husson, R., Taburet, N., Charles E., Estimbre, J.-J. and Ghantous, M.: EU Copernicus Marine Service Product User Manual for Global Ocean L 3 Significant Wave Height From Nrt Satellite Measurements, WAVE_GLO_PHY_SWH_L3_NRT_014_001, Issue 2.3, Mercator Ocean International, https://catalogue.marine.copernicus.eu/documents/PUM/CMEMS-WAV-PUM-014-001-002-003-004.pdf (last access: 8 April 2024), 2023.

NSF: Flytende oppdrettsanlegg, Krav til utforming, dimensjonering, utførelse, installasjon og drift (Marine fish farms, Requirements for design, dimensioning, production, installation and operation), Norsk Standard NS 9415, 75 pp., https://online.standard.no/nb/ns-9415-2003 (last access: 27 May 2024), 2003.

Räämet, A. and Soomere, T.: The wave climate and its seasonal variability in the northeastern Baltic Sea, Est. J. Earth Sci., 59, 100–113, https://doi.org/10.3176/earth.2010.1.08, 2010.

Semedo, A., Sušelj, K., Rutgersson, A., and Sterl, A.: A global view on the wind sea and swell climate and variability from ERA-40, J. Climate, 24, 1461–1479, https://doi.org/10.1175/2010JCLI3718.1, 2011.

Semedo, A., Vettor, R., Breivik, Ø., Sterl, A., Reistad, M., Soares, C. G., and Lima, D.: The wind sea and swell waves climate in the Nordic seas, Ocean Dynam., 65, 223–240, https://doi.org/10.1007/s10236-014-0788-4, 2015.

Soomere, T. and Viška, M.: Simulated wave-driven sediment transport along the eastern coast of the Baltic Sea, J. Marine Syst., 129, 96–105, https://doi.org/10.1016/j.jmarsys.2013.02.001, 2014.

Soomere, T., Behrens, A., Tuomi, L., and Nielsen, J. W.: Wave conditions in the Baltic Proper and in the Gulf of Finland during windstorm Gudrun, Nat. Hazards Earth Syst. Sci., 8, 37–46, https://doi.org/10.5194/nhess-8-37-2008, 2008.

Soomere, T., Pindsoo, K., Kudryavtseva, N., and Eelsalu, M.: Variability of distributions of wave set-up heights along a shoreline with complicated geometry, Ocean Sci., 16, 1047–1065, https://doi.org/10.5194/os-16-1047-2020, 2020.

Taburet, N., Husson, R., Charles, E., Jettou, G., Philip, A., Philipps, S., Ghantous, M., and Kocha, C.: EU Copernicus Marine Service Quality Information Document for Global Ocean L 3 Significant Wave Height From Nrt Satellite Measurements, WAVE_GLO_PHY_SWH_L3_NRT_014_001, Issue 3.4, Mercator Ocean International, https://catalogue.marine.copernicus.eu/documents/QUID/CMEMS-WAV-QUID-014-001.pdf (last access: 8 April 2024), 2023.

Tuomi, L., Kahma, K. K., and Pettersson, H.: Wave hindcast statistics in the seasonally ice-covered Baltic Sea, Boreal Environ. Res., 16, 451–472, 2011.

Vanem, E.: A regional extreme value analysis of ocean waves in a changing climate, Ocean Eng., 144, 277–295, https://doi.org/10.1016/j.oceaneng.2017.08.027, 2017.

Young, I. R., Zieger, S., and Babanin, A. V.: Global Trends in Wind Speed and Wave Height, Science, 332, 451–455, https://doi.org/10.1126/science.1197219, 2011.

State Planet, 4-osr8, 11, 2024
https://doi.org/10.5194/sp-4-osr8-11-2024

The role of air–sea heat flux for marine heatwaves in the Mediterranean Sea

Dimitra Denaxa[1,2], **Gerasimos Korres**[1], **Giulia Bonino**[3], **Simona Masina**[3], **and Maria Hatzaki**[2]

[1]Hellenic Centre for Marine Research (HCMR), Anavyssos, 19013, Greece
[2]Department of Geology and Geoenvironment, National and Kapodistrian University of Athens,
Athens, 15771, Greece
[3]Centro Euro-Mediterraneo sui Cambiamenti Climatici (CMCC), Bologna, 40127, Italy

Correspondence: Dimitra Denaxa (ddenaxa@hcmr.gr)

Received: 28 July 2023 – Discussion started: 18 August 2023
Revised: 23 May 2024 – Accepted: 19 June 2024 – Published: 30 September 2024

Abstract. Recent studies have significantly contributed to understanding physical mechanisms associated with the occurrence of marine heatwaves (MHWs). Building upon prior research, this study investigates the relative role of air–sea heat exchange and oceanic processes during the onset and decline phases of surface MHWs in the Mediterranean Sea based on a joint analysis of remote sensing data and reanalysis outputs over the period 1993–2022. Results show that air–sea heat flux is the major driver in 44 % of the onset and only 17 % of the declining MHW phases. Thus, these findings suggest that oceanic processes play a key role in driving sea surface temperature (SST) anomalies during MHWs, particularly during declines. The role of surface flux becomes more important during warmer months and onset periods. Spatially, the heat flux contribution is greater in the Adriatic and Aegean sub-basins, where it becomes the major driver of most onset phases. Latent heat emerges as the most significant heat flux component in forming the SST evolution across all seasons. Onset and decline phases lasting less than 5 d experience a weaker contribution of heat flux compared to longer phases (lasting 5–10 or more than 10 d). Moreover, an inverse relationship between MHW severity and the contribution of heat flux is observed. At the subsurface, mixed layer shoaling is found over the entire duration of most MHWs, particularly for those of shorter duration. Therefore, the surface cooling right after the peak day is likely not associated with vertical mixing in such cases. These findings suggest that other oceanic processes, potentially horizontal advection, have a key role in modulating SST at the beginning of most MHW declines. In turn, further dissipation of heat is commonly driven by vertical mixing, as indicated by a significant mixed layer deepening after the MHW end day in most cases. This study emphasizes the need to consider subsurface information for future studies of MHWs and highlights the importance of accounting for limitations associated with the definitions employed for MHW phases.

1 Introduction

Marine heatwaves (MHWs) are extreme events, characterized by prolonged periods of anomalously high water temperature, lasting for at least 5 consecutive days (Hobday et al., 2016). These events have gathered increased attention due to their detrimental effects on marine life, especially given the increase observed in their frequency, intensity, and duration over the recent decades, at a global and Mediterranean scale (Oliver et al., 2018; Holbrook et al., 2019; Darmaraki et al., 2019a; Juza et al., 2022; Dayan et al., 2023; Pastor and Khodayar, 2023). Mass mortality events and local extinctions, coral bleaching, and massive shifts of marine species have been extensively reported (Wernberg et al., 2016; Frölicher and Laufkötter, 2018; Smale et al., 2019; Garrabou et al., 2022; Smith et al., 2023), along with socioeconomic impacts on fishery and aquaculture industries (Mills et al., 2013; Cavole, 2016). The intensification of MHW conditions has been attributed mostly to ocean warming (Oliver

Table 1. Overview of products.

Product ref. no	Product ID and type	Data access	Documentation
1	SST_MED_SST_L4_REP_OBSERVATIONS_010_021; satellite observations	EU Copernicus Marine Service Product (2023a)	Product User Manual (PUM): Pisano et al. (2023a) QUality Information Document (QUID): Pisano et al. (2023b)
2	SST_MED_SST_L4_NRT_OBSERVATIONS_010_004; satellite observations	EU Copernicus Marine Service Product (2023b)	PUM: Pisano et al. (2023c) QUID: Pisano et al. (2023d)
3	ERA5 hourly data on single levels; numerical models	Copernicus Climate Data Store	Hersbach et al. (2023) https://doi.org/10.24381/cds.adbb2d47
4	MEDSEA_MULTIYEAR_PHYS_006_004; numerical models	EU Copernicus Marine Service Product (2022)	PUM: Lecci et al. (2022) QUID: Escudier et al. (2022)
5	MEDSEA_ANALYSISFORECAST_PHY_006_013; numerical models	EU Copernicus Marine Service Product (2024)	PUM: Lecci et al. (2023) QUID: Goglio et al. (2024)

et al., 2018; Ciappa, 2022), while further intensification is expected in the future (Oliver et al., 2019; Darmaraki et al., 2019b; Plecha and Soares, 2019; Hayashida et al., 2020), driven by anthropogenic forcing and particularly pronounced under high-emission future scenarios (Oliver et al., 2019).

Given these concerns, it is crucial to enhance our understanding of the driving factors behind MHWs at a regional scale, particularly within the framework of exploring predictability options and facilitating marine decision-making (Holbrook et al., 2020; Spillman et al., 2021). Recent research has significantly contributed to identifying physical drivers and MHW-favoring conditions (e.g., Holbrook et al., 2019; Sen Gupta et al., 2020; Oliver et al., 2021; Vogt et al., 2022; Marin et al., 2022). Individual events in the Mediterranean Sea have also been explored, such as the widely known MHW in 2003 in the western Mediterranean Sea (e.g., Sparnocchia et al., 2006; Olita et al., 2007; Bonino et al., 2023), the short-lasting record-breaking MHW in May 2020 in the southeastern Mediterranean Sea (Ibrahim et al., 2021; Denaxa et al., 2022), and the most recent long-lasting MHW in summer 2022 (Marullo et al., 2023; McAdam et al., 2024; Pirro et al., 2024).

However, a limited number of studies have assessed physical drivers separately for the buildup and decay of MHW events, employing different methodologies and datasets. Schlegel et al. (2021) demonstrated that nearly 50 % of surface MHWs in the northwest Atlantic are heat-flux-driven but less than 20 % decay due to heat flux, suggesting that oceanic processes are mainly responsible for the MHW decline. Marin et al. (2022) investigated upper-ocean MHWs based on global ocean circulation model output and found that heat advection, followed by anomalous air–sea heat flux, explains most of the upper-ocean temperature anomalies during both MHW onset and decline phases. Within this context, the present study utilizes high-resolution observational sea surface temperature (SST) and modeled heat flux data to assess the driving role of air–sea heat exchange during onset and decline phases of surface MHWs in the Mediterranean Sea. Furthermore, it provides insights into the concurrent subsurface conditions by examining the mixed layer dynamics during MHWs.

2 Data and methods

MHWs in this study were identified based on high-resolution gridded satellite SST data in the Mediterranean Sea. Daily SST values from the reprocessed and near-real-time datasets from the Copernicus Marine (product ref. nos. 01 and 02 – Table 1; $0.05^\circ \times 0.05^\circ$ and $0.01^\circ \times 0.01^\circ$ horizontal resolution, respectively) were used to cover the period January 1993–December 2022. To study the net surface heat budget (Q_{net}), turbulent and radiative surface fluxes were obtained from the ECMWF ERA5 Reanalysis dataset at hourly frequency and $0.25^\circ \times 0.25^\circ$ horizontal resolution (product ref. no. 03; Table 1). Finally, daily values of mixed layer depth (MLD) for the period January 1993–December 2022 were obtained from the Mediterranean Sea Physics Reanalysis and the Mediterranean Sea Physics Analysis and Forecast (product ref. no. 04 and no. 05 – Table 1; $0.042^\circ \times 0.042^\circ$ horizontal resolution). Collocation of SST and MLD with the coarser ERA5 data was performed by using the nearest neighboring value to each ERA5 grid point. The paired values at daily frequency were used in the heat budget analysis.

MHW detection was performed based on the definition and detection methodology of Hobday et al. (2016) using the MATLAB toolbox provided by Zhao and Marin (2019). The reference period used in this study to create the daily climatology required for the event detection is the same as the 30-year study period (1993–2022). To compute the climatology, a time window of 11 d was employed, centered on the day when each daily climatological value was computed. For the computation of the daily threshold time series, the 90th percentile was selected, being widely used in MHW studies, thus allowing for a more direct intercomparison with the literature. Additionally, a 30 d window was applied for smoothing the threshold time series.

Basic properties were computed for each identified event (e.g., start and end day, mean and max intensity, duration). Next, events were split into their onset and decline phase. The onset phase was considered to last from the first day until the day of maximum intensity ($I_{\max}$) and the decline phase from $I_{\max}$ day until the last day of the event. As in Schlegel et al. (2021), for each phase, an ocean mixed layer heat budget analysis was applied to derive the change in SST attributed to Q_{net} based on the following equation:

$$\mathrm{SST}'_{t_2} - \mathrm{SST}'_{t_1} = \int_{t_1}^{t_2} \frac{Q'}{\rho_0 c_p h} \mathrm{d}t + R. \tag{1}$$

The left-hand side of Eq. (1) represents the observed change in SST anomaly ($\mathrm{DSST}'_{\mathrm{obs}}$) relative to climatology during a specific phase. Each phase starts at day t_1 and ends at day t_2, which are the start day and $I_{\max}$ day for onset phases or $I_{\max}$ day and end day for decline phases, respectively. On the right-hand side of Eq. (1), Q' is the daily anomaly of Q_{net}. The latter consists of the latent and sensible heat flux as well as net shortwave and net longwave radiation (LH, SH, SWR, and LWR, respectively), as follows:

$$Q_{\mathrm{net}} = \mathrm{LH} + \mathrm{SH} + \mathrm{SWR} + \mathrm{LWR}. \tag{2}$$

It should be noted that a simplified approach was used that does not account for the penetration of solar radiation below the mixed layer. Considering the Jerlov water type IA for relatively clear seawater, 77 % of the solar radiation is expected to be absorbed within the upper 10 m of the ocean based on the solar radiation attenuation equation in Paulson and Simpson (1977). Taking into account the MLD values obtained from the utilized reanalysis dataset, we have considered that the followed approach does not significantly affect our conclusions.

To compute heat flux anomalies, first a daily climatology was computed following the same methodology as with SST for the period 1993–2022. Daily heat flux anomalies were then constructed relative to the mean climatological value over the phase duration (e.g., as in Fewings and Brown, 2019). The time integral of Q' divided by the product of the constant values ρ (seawater density), c_p (specific heat capacity), and h (mixed layer thickness) represents the part of the $\mathrm{DSST}'_{\mathrm{obs}}$ explained by Q' during this phase (DSST_Q). The second term of the right-hand side in Eq. (1) stands for any contribution to $\mathrm{DSST}'_{\mathrm{obs}}$ from other mechanisms affecting SST: horizontal advection, vertical mixing processes, horizontal diffusion of heat flux, and radiative heat loss below the mixed layer. Therefore, the role of air–sea heat flux in this study is assessed in relation to a single residual term (i.e., the non-heat-flux terms merged into a single one), representing the cumulative effect of all other (oceanic) factors influencing the SST tendency during an MHW phase.

The contribution of Q' in driving an MHW onset or decline phase N is then quantified through the following proportion of change:

$$P(N) = \frac{\mathrm{DSST}_Q(N)}{\mathrm{DSST}'_{\mathrm{obs}}(N)}. \tag{3}$$

Therefore, a positive heat flux contribution value during an MHW phase indicates a favoring role of heat flux in the corresponding SST evolution, i.e., a warming (cooling) effect of heat flux during onset (decline). Analogously, a negative contribution value during either an onset or a decline phase indicates that heat flux opposes the corresponding SST tendency. Finally, to examine the evolution of MLD during MHWs, time series of cumulative MLD anomalies (MLDA) were constructed for onset and decline phases. These time series were computed by adding, at each MHW day, the daily anomaly of MLD of the previous day in order to account for longer timescales associated with the mixed layer evolution (as in Schlegel et al., 2021). To explore the correlation between MLDA and SST anomalies (SSTA), Pearson correlation coefficients were computed for onset and decline phases separately.

3 Results

3.1 MHW detection

Properties of MHWs exhibit high variability throughout the Mediterranean Sea (Fig. 1a–c). The northwestern part of the basin, along with the northern Adriatic and northern Aegean seas, experienced on average the highest event intensity over the period 1993–2022, exceeding 2.5 and 2 °C, respectively (Fig. 1b). Events tend to last longer in the eastern part of the basin (Aegean and Levantine seas) and in the central-western Mediterranean Sea, while the shortest durations are mostly found in the Ionian and Alboran seas (Fig. 1c). The mean event frequency over the study period shows some similarities to the mean intensity spatial distribution, suggesting that the most (least) intense and most (least) frequent MHWs are encountered in the northernmost (southernmost) flanks of the Mediterranean Sea (Fig. 1a, b). Results generally agree with the literature on MHWs in the Mediterranean Sea during the recent decades (Darmaraki et al., 2019a; Ibrahim et al., 2021; Juza et al., 2022; Dayan et al., 2023), despite some differences in event detection methods (e.g., choice for percentile-based threshold, accounting for MHW spatial extent) or study periods (choice of climatological period, period for event detection).

MHW frequency has been increasing over the past 30 years, with a trend of 1 ± 0.6 events per decade for the entire basin (Fig. 1d). Also, MHW duration has increased, particularly in the eastern basin, with trend values locally exceeding 10 d per decade (1.7 ± 1.5 d per decade for the entire basin) (Fig. 1f). Notably, intensity has not increased over the entire basin during the study period (0.08 ± 0.2 °C per

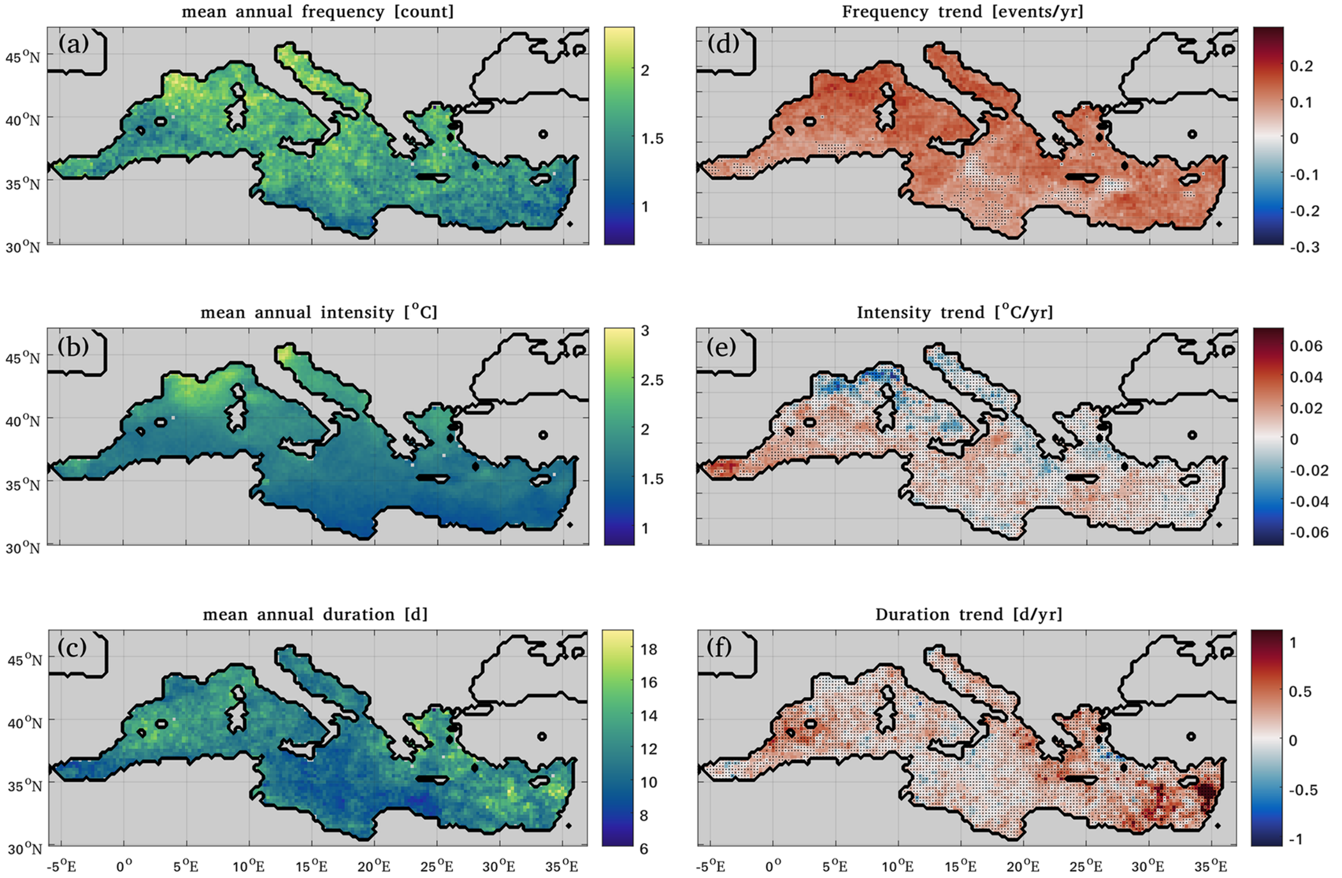

Figure 1. **(a–c)** Mean annual frequency, intensity, and duration of MHWs for the period 1993–2022 (**a**, **b**, **c**, respectively). **(d–f)** Linear trends of annual values of frequency, intensity, and duration (**d**, **e**, **f**, respectively). Black dots superimposed on trend fields correspond to statistically nonsignificant trends (Mann–Kendall test, 95 % confidence level).

decade for the basin, not significant at the 95 % confidence level) (Fig. 1e). The northernmost regions, which are characterized by higher MHW intensity, present small decreasing MHW intensity trends (though not statistically significant in most cases), which is in agreement with Dayan et al. (2023) and Ibrahim et al. (2021) for the eastern basin.

3.2 The role of heat flux during MHW onset and decline

Surface heat flux contributes to the observed surface warming during the onset phase of the majority of the events (92 %) detected in the Mediterranean Sea within 1993–2022 (Fig. 2a). In particular, in 44 % of the events, heat flux plays a major role during the development of MHWs in terms of explaining more than half of the observed change in SST anomaly (Fig. 2b). During the rest of the events (8 %), heat flux opposes the surface warming over the onset phases; therefore, other mechanisms compensate for their cooling effect and are responsible for the observed warming in such cases.

Air–sea heat exchange contributes to surface cooling during decline phases in a much smaller percentage of MHWs (58 %), while it is the primary driver in only 17 % of the decline phases (Fig. 2a, b). In other words, almost half (42 %) of the observed MHWs in the basin decay under non-favorable heat flux conditions (i.e., heat flux opposing the SST decrease), while oceanic processes are the dominant driver of most (83 %) MHW declines.

Heat flux exchange explains the MHW onset in all examined subregions to a great extent (Fig. 2d). The Adriatic and Aegean seas stand out with most of the observed heating during onset attributed to heat flux in more than half of the identified events (Fig. 2b). In six out of the seven subregions, the percentage of events primarily driven by heat flux during their onset ranges 39 %–53 %. The Alboran Sea presents a much lower percentage of events attributed to heat flux (22 %), potentially suggesting an enhanced role of advective processes in regulating SST in the area, likely associated with its proximity to the Strait of Gibraltar. In contrast, the corresponding percentages for the decline phases show less spatial variability across all subregions, with only 15 %–20 % of the examined declines found to be mainly driven by heat flux exchange (Fig. 2b).

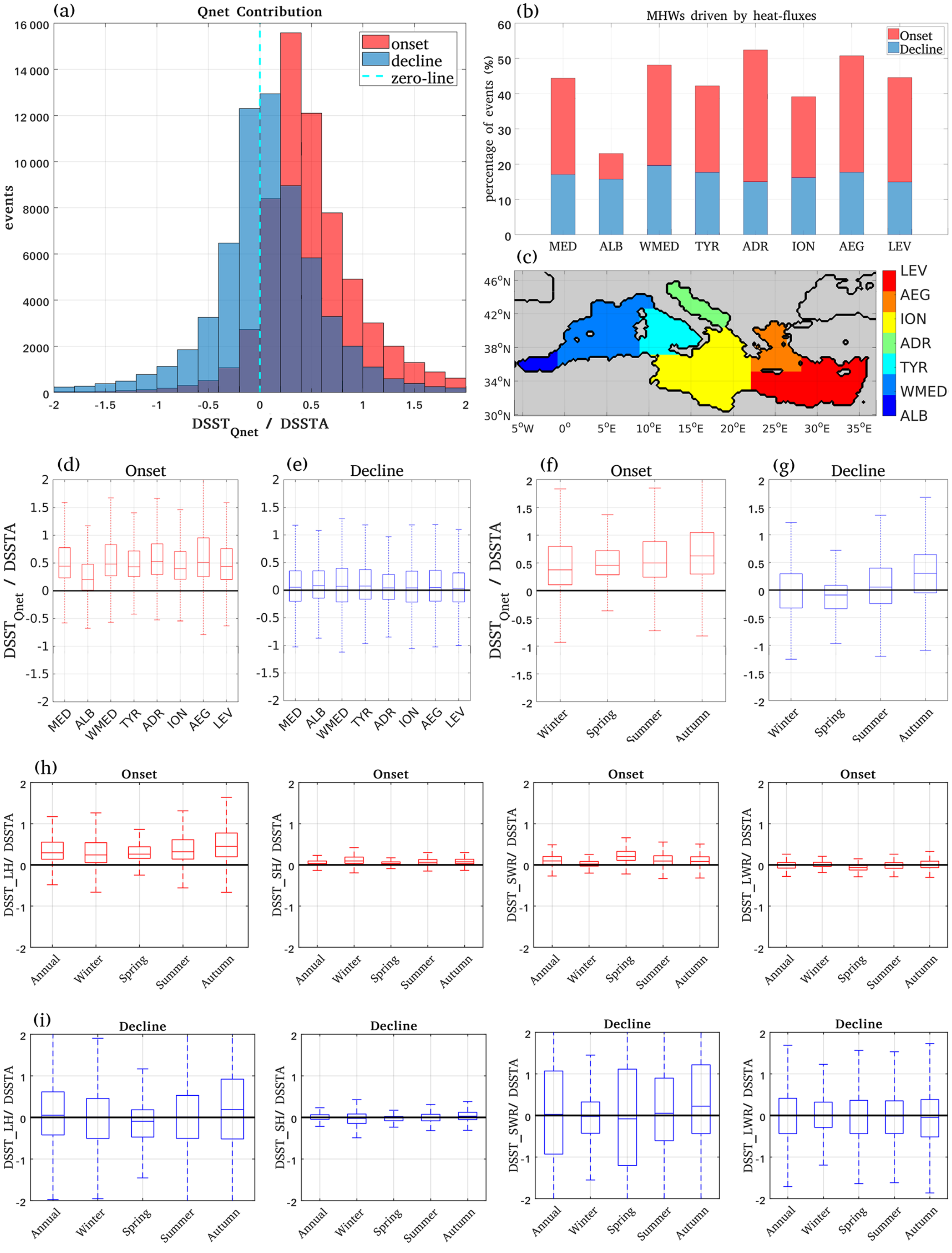

Figure 2. (a) Contribution of heat flux to the observed change in SSTA during MHW onset and decline phases for the period 1993–2022. **(b)** Percentage of events primarily driven by heat flux (i.e., with more than half of the observed warming or cooling attributed to heat flux during onset or decline) for the entire Mediterranean Sea and subregions mapped in **(c)**. **(d–e)** Box plots for the contribution of heat flux during onset (red) and decline (blue) for the entire Mediterranean Sea and the subregions. **(f–g)** Box plots for heat flux contribution per season for onset (red) and decline (blue). **(h–i)** Box plots per season for the contribution of heat flux components during onset (red) and decline (blue). From left to right: latent heat flux, sensible heat flux, net shortwave radiation, net longwave radiation. Note: a positive heat flux contribution during onset (decline) means that heat flux will warm (cool) the sea surface; boxes in box plots define the interquartile range from the 25th up to the 75th percentile, and whisker bars correspond to values falling within 1.5 times the interquartile range.

Seasonal analysis was performed considering winter to be the period from December to February, while events spanning different seasons were assigned to the season when their intensity maximizes. Most of the events were found to occur during summer, followed by spring, autumn, and then winter. As expected, the magnitude of SST anomalies during MHWs varies among the seasons (e.g., Thoral et al., 2022), but the contribution of heat flux to their formation is consistently weaker during decline compared to onset phases throughout the year (Fig. 2f, g).

Results suggest a greater contribution of heat flux exchange to the MHW evolution within warmer seasons (from an ocean perspective, i.e., summer and autumn) (Fig. 2f, g). Autumn shows the highest percentage of events driven by Q_{net} in both onset and decline. LH flux mainly regulates the contribution of Q_{net} during both phases and throughout the year, followed by SWR and then SH, while LWR exhibits less clear behavior in all seasons (Fig. 2h, i). With the exception of SH, the relative contribution of each heat flux component presents higher variability during decline compared to onset phases across all seasons. Specifically, approximately an equal number of decline cases are associated with positive and negative contributions of the heat flux components to the observed cooling, indicating a less predictable role of Q_{net} during decline compared to onset periods throughout the year (Fig. 2i). The lowest percentage of heat-flux-driven events is observed during the winter onset and spring decline phases. Particularly for spring, heat flux during most declines acts against the observed surface cooling (mainly through suppressed LH losses), suggesting that MHW dissipation in spring is commonly driven by oceanic factors.

Results show that the air–sea interaction, with a dominant role of LH flux, plays a major role in the development of nearly half (44 %) of the MHWs in the Mediterranean Sea. This finding suggests that oceanic processes play a key role during 56 % of the onset cases. A further weakened role of heat flux is found during decline periods (being the major contributor in only 17 % of declines), indicating that MHW decay is also primarily driven by oceanic processes.

3.3 Links with mixed layer depth and MHW characteristics

To gain insight into subsurface conditions during MHWs, we examined how MLD evolves in relation to SST. Negative (positive) correlation between MLDA and SSTA that was found for a large number of events during onset (decline) implies mixed layer shoaling over the entire MHW duration in these cases (Fig. 3a – top). While an MHW event develops, a reduction in MLD is commonly expected, as surface warming may strengthen the stratification of the water column (D’Ortenzio and Prieur, 2012). Given that heat flux is found to contribute to the warming phases in most cases, the concurrent mixed layer shoaling found during most onsets may be interpreted as an effect of the warming driven by the atmosphere. Nevertheless, a thinner-than-usual mixed layer may also exist before the event occurrence and act as a pre-conditioning factor (e.g., Lee et al., 2023). The greatest MLDA–SSTA correlation is found during spring and summer events, while no significant correlation is observed in winter (not shown), as the deeper mixed layer during colder months is expected to be less responsive to surface SST variations (D’Ortenzio and Prieur, 2012). High positive MLDA–SSTA correlation observed during declines implies that the mixed layer in such cases continues to shoal while SST decreases (Fig. 3a), similar to the mixed layer analysis by Schlegel et al. (2021) for the northwest Atlantic. This finding further supports the fact that oceanic processes play a significant role during MHW decline periods, as also indicated by the weaker contribution of heat flux during declines. It also suggests that the surface cooling occurring right after the peak intensity day is likely not due to mixing in the vertical (further discussed below).

To gain a better understanding of the relationship between subsurface conditions and the contribution of heat flux exchange at the air–sea interface during the evolution of MHWs, this information is integrated into Fig. 3a. Whereas during onset, MHWs are largely driven by heat flux exchange and most of them are accompanied by mixed layer shoaling, there are onset cases where MLDA is strongly positively correlated with SSTA, indicating that surface warming evolves while the mixed layer deepens (Fig. 3a – top). Regarding decline periods, almost equal numbers of cases show positive and negative heat flux contributions (Fig. 3a – bottom). While a decrease in MLD is evident in most decline phases (as indicated by correlation coefficient close to 1), a significant MLDA–SSTA correlation is absent in a considerable number of decline phases. Additionally, there are cases during declines where a high negative correlation between MLDA and SSTA is observed, indicating mixed layer deepening while SST decreases. Such cases are encountered when heat flux contributes to surface cooling (Fig. 3a – bottom), suggesting that vertical mixing (most probably wind-induced) works in the same direction.

MHW onset and decline phases were also examined in relation to their duration. They were grouped into short, medium, and long duration, considering phases lasting less than 5 d, from 5 to 10 d, and more than 10 d, respectively (Fig. 4a). Shorter onset or decline periods, being the most prevalent category, slightly overshadow the contribution of heat flux during longer-lasting MHW phases (Fig. 4a–c vs. Fig. 2a). In particular, compared to medium followed by long durations, short durations (both for onset and decline) tend to exhibit a smaller contribution of heat flux exchanges triggering the SST evolution (Fig. 4a–c). For long-duration onset phases, the contribution of heat flux surpasses the contribution of oceanic factors, as the former explains more than half of the surface warming in more than half of the events (Fig. 4c). Similarly, it is mostly during shorter declines that heat flux does not present a systematically pos-

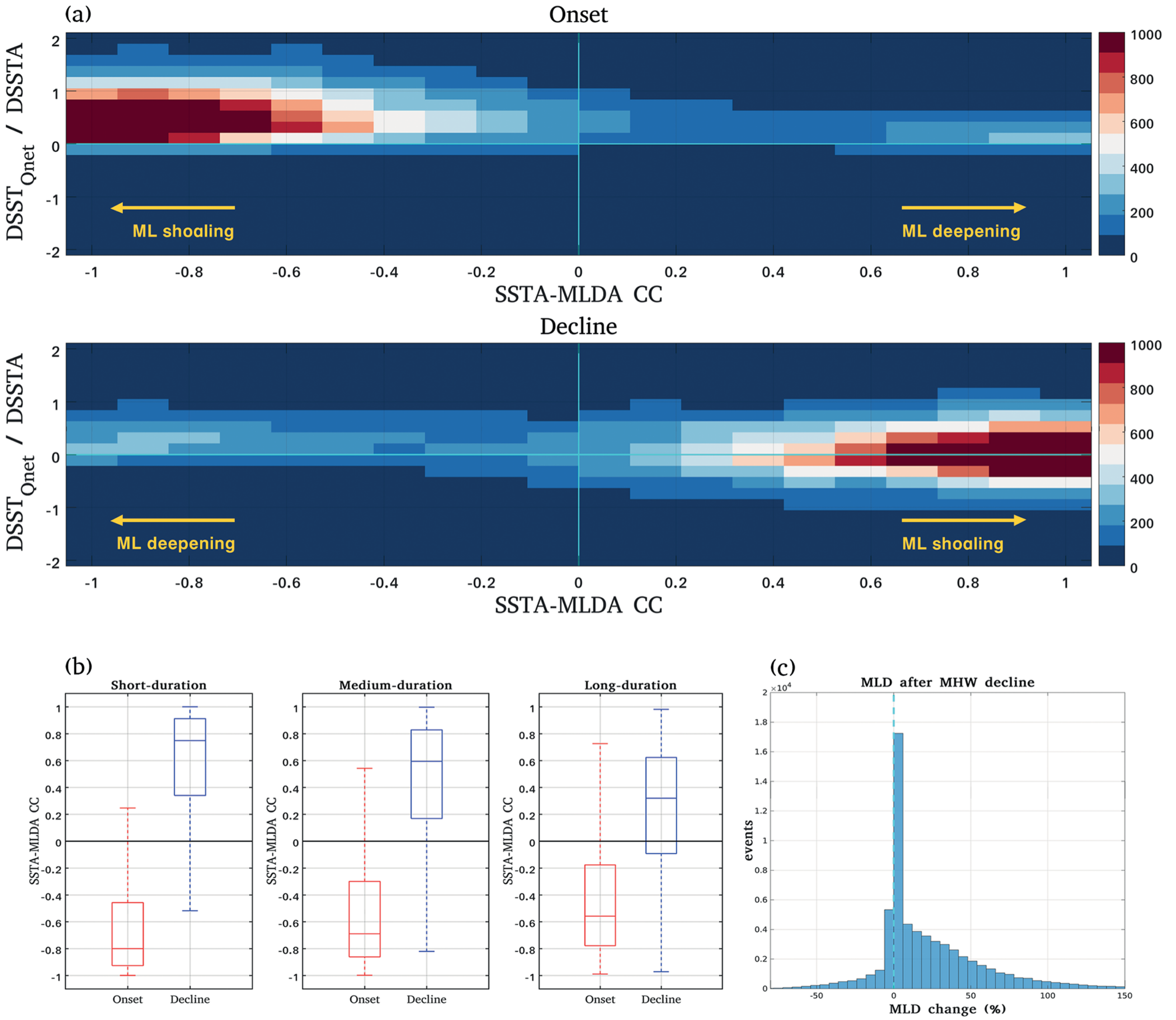

Figure 3. **(a)** Heatmap relating the net heat flux contribution to the Pearson correlation coefficient (CC) between time series of SST anomalies and time series of mixed layer depth cumulative anomalies computed for each MHW onset and decline phase (upper and lower heatmap, respectively) for the period 1993–2022. Colors correspond to the number of events falling in each bin. **(b)** Box plots for the distribution of CC values for onset and decline phases lasting less than 5 d, between 5–10 d, and more than 10 d (short, medium, and long duration phases, respectively). **(c)** Percentage change (%) in MLD over a fixed 7 d period after the MHW end day compared to MLD during the onset period. Note: a positive heat flux contribution during onset (decline) means that heat flux will warm (cool) the sea surface. Negative (positive) CC values close to -1 ($+1$) during onset (decline) correspond to a reduction of the mixed layer depth while SST increases (decreases). Boxes in box plots define the interquartile range from the 25th up to the 75th percentile, and whisker bars correspond to values falling within 1.5 times the interquartile range.

itive or negative contribution to the SST decrease, while a shift towards higher contributions of heat flux is found for longer phases (Fig. 4a–c). Importantly, the relationship between MLDA and SSTA becomes less clear during onset and decline phases of medium and, in turn, long duration, as indicated by weaker correlation (Fig. 3b). In the case of decline periods, mixed layer shoaling is more frequently observed during short-lasting declines, suggesting a continuation of mixed layer shoaling already present during the onset in such cases.

These findings suggest that the definition followed for an MHW evolution phase needs to be cautiously taken into account when interpreting results, especially when surface and subsurface conditions are examined for the same phases. This

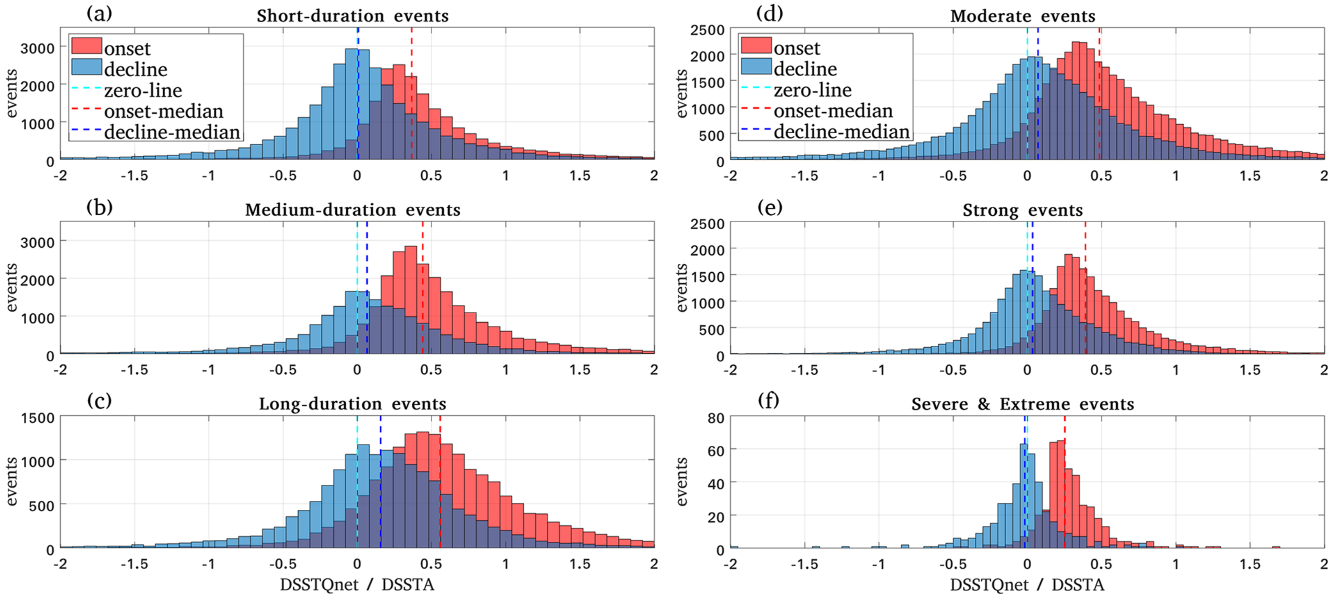

Figure 4. **(a–c)** Contribution of heat flux to the observed change in SSTA during MHW onset and decline phases for the period 1993–2022 for phases lasting less than 5 d **(a)**, between 5–10 d **(b)**, and more than 10 d **(c)** (short, medium, and long duration phases, respectively). **(d–f)** Same as left but for different MHW severity categories: moderate **(d)**, strong **(e)**, and severe/extreme **(f)** based on the categorization scheme by Hobday et al. (2018).

is due to the time needed for a surface warming signal to penetrate below as well as due to the longer timescales associated with processes at deeper layers. Notably, on the end day of a surface MHW, which is the end day of the decline phase (as defined in this study), SST is still above the event detection threshold and will fall below this value by the following day. Therefore, events further dissipate after the decline phase ends. Given such considerations and depending on the specific purpose of a study, different approaches for defining a decline period may be followed. For instance, Darmaraki (2019) considered the entire MHW duration to be the event development phase and treated the following period as decline, and Schlegel et al. (2021) used the same definitions as the present study, while Marin et al. (2022) considered a dynamic criterion for defining the decay period, including a larger portion of the temperature change during the event dissipation after the MHW end day.

On these grounds, we additionally examine how MLD evolves after the MHW end day to shed light on what follows the progressively increasing stratification we observed during MHWs. To this aim, we compute for each event the percentage change in the mean MLD between the onset period and a fixed 7 d period following the MHW end day (Fig. 3c). Results reveal the existence of a deeper mixed layer after the decline of most events (83.5 %) compared to the onset period. In these cases, the magnitude of change in MLD is also significantly greater, occasionally exceeding 100 %, compared to instances when the mixed layer is thinner during this period than during the onset (changing the predetermined length of the examined post-decline period does not significantly alter these conclusions). This analysis shows that a significant mixed layer deepening most likely occurs after the end of MHW decline phases in the Mediterranean Sea, suggesting that vertical mixing eventually contributes to the heat dissipation.

Considering the continuation of mixed layer shoaling found mostly during shorter declines, results suggest that the oceanic factor regulating the SST decrease after the peak intensity day of most events is probably heat advection, while vertical mixing in these cases becomes important over the following days. In line with our findings, Marin et al. (2022) found that the principal driver of the upper-ocean temperature changes during MHW onset and decline phases in midlatitudes is horizontal heat advection. However, their results cannot be directly intercompared to ours, as they use modeled depth-integrated upper-ocean temperatures (thus not detecting surface events), they focus only on extreme cases, and they employ a different definition of the onset and decay period.

Finally, results were examined in relation to MHW intensity and severity to account for the perspective of MHW extremity in terms of absolute and normalized SST anomalies, respectively. Events were split based on their severity category following the categorization scheme proposed by Hobday et al. (2018) (definitions included therein). Results suggest a smaller contribution of heat flux in the evolution of more severe events (Fig. 4d–f). Half of the moderate events were found to be mainly driven by heat flux, while this percentage decreases for strong, severe, and extreme events, as illustrated in Fig. 4d–f. This may be associated with the enhanced role of heat flux during longer events, as was previously discussed, and the fact that events of higher severity categories tend to present a shorter duration. Similar results were found when examining the contribution of air–sea heat flux in relation to the mean intensity of MHWs (not included). Nevertheless, further investigations are needed to unravel how our methodological choices affect these findings.

4 Conclusions

This study investigates the role of air–sea heat exchange during MHWs in the Mediterranean Sea using satellite and reanalysis data within 1993–2022. An ocean mixed layer heat budget analysis is performed to derive the change in SST attributed to the net surface heat budget during onset and decline phases.

Air–sea heat flux is the primary driver in 44 % of the onset and only in 17 % of the decline phases in the basin. Heat flux acts in favor of the development of most MHWs across all seasons and especially during warmer months and onset phases. Moreover, its contribution is greater in the Adriatic and Aegean sub-basins, where it becomes the major driver of most onset phases. Among the heat flux components, LH emerges as the most significant contributor to SST anomalies, in line with prior studies (Sen Gupta et al., 2020; Oliver et al., 2021; Schlegel et al., 2021; Marin et al., 2022). Short-lasting onset or decline phases (shorter than 5 d) tend to experience a smaller contribution of heat flux in forming the SST evolution compared to longer phases (lasting 5–10 or more than 10 d). Furthermore, there is an inverse relationship between MHW severity and the contribution of heat flux. As fewer than half of the events are primarily driven by air–sea heat flux, our results imply a key role of oceanic processes in regulating SST during most events and particularly during decline periods.

Examining the mixed layer during MHWs revealed a progressively decreasing MLD over the entire event duration, particularly for shorter-lasting events. In turn, a significant mixed layer deepening was found to occur after the end of the decline period of most events in the basin. In cases of smaller contribution of heat flux (e.g., during shorter compared to longer events or during declines compared to onsets), a stronger correlation between SSTA and MLDA is also found, further supporting the key role of oceanic processes in such cases. These findings suggest that the surface cooling occurring right after the peak intensity day is likely not associated with vertical mixing. Moreover, this potentially suggests that horizontal advection is the oceanic factor playing the most significant role by the time the decline period begins, especially for shorter declines. This hypothesis finds support in the results of Marin et al. (2022), who highlighted the role of horizontal heat advection during the MHW evolution, and Schlegel et al. (2021), who suggested that advection and mixing should drive the MHW decline based on similar indications.

Nevertheless, the authors suggest taking into account potential limitations associated with the definition of MHW phases followed within a study, especially while examining concurrent subsurface conditions. These considerations concern the longer timescales below the sea surface, as well as the complexity associated with long-lasting events which are not expected to be adequately described by two single phases. Specifically, subsequent warming and cooling periods may occur within a long onset or decline phase, complicating their representation by the definition employed in this study for onset and decline. These concerns are part of the broader discussion on challenges related to the lack of a standardized framework for analyzing MHW drivers, as many other methodological approaches (e.g., the choice of integration depths in heat budget analyses) may potentially influence findings on MHW drivers. For this reason, alongside recommending the use of definitions and methods aligned with the specific contexts of individual studies, we highlight the fact that clearly articulating the employed methods within a study is vital for both the precise interpretation of results and meaningful comparisons across different studies on MHW drivers. Despite the aforementioned caveats, this study provides useful insights into the role of surface heat flux and mixed layer dynamics during MHWs in the Mediterranean Sea. Importantly, following the methodology applied by Schlegel et al. (2021) allowed for a fair intercomparison of results among two substantially different regions (Mediterranean Sea vs. northwest Atlantic). The results are surprisingly similar, which is largely attributed to the same methodology employed to assess drivers of SST-defined events and especially the same definition followed for onset and decline periods. The striking similarities in the results for the two regions may also imply inherent characteristics of the interplay of air–sea interaction and oceanic processes during anomalous SST fluctuations over similar latitudinal zones, which is also observed to a certain extent in Marin et al. (2022).

This study highlights the need to consider subsurface information in MHW studies to gain insight into ocean internal dynamics throughout their evolution. In this context, combining observations and ocean reanalysis systems, such as in Dayan et al. (2023), and considering MHW evolution periods aligned with the objectives and specific characteristics of a study appear to constitute a promising direction towards understanding physical drivers as well as improving monitoring and therefore enabling early warning of MHWs.

Data availability. Information on the products used in this paper is included in Table 1.

Author contributions. DD defined the research problem. DD conducted the analysis and wrote the manuscript, with contributions from GK and MH. All authors contributed to the interpretation of results.

Competing interests. The contact author has declared that none of the authors has any competing interests.

Financial support. This work has been partly funded by the Copernicus Med-MFC (LOT reference: 21002L5-COP-MFC MED-5500) within the framework of the Copernicus Marine Service.

Review statement. This paper was edited by Piero Lionello and reviewed by Robert Schlegel and one anonymous referee.

References

Bonino, G., Masina, S., Galimberti, G., and Moretti, M.: Southern Europe and western Asian marine heatwaves (SEWA-MHWs): a dataset based on macroevents, Earth Syst. Sci. Data, 15, 1269–1285, https://doi.org/10.5194/essd-15-1269-2023, 2023.

Cavole, L. M., Demko, A. M., Diner, R. E., Giddings, A., Koester, I., Pagniello, C. M. L. S., Paulsen, M. L., Ramirez-Valdez, A., Schwenck, S. M., Yen, N. K., Zill, M. E., and Franks, P. J. S.: Biological impacts of the 2013–2015 warm-water anomaly in the northeast Pacific: Winners, Losers, and the Future, Oceanography, 29, 273–285, https://doi.org/10.5670/oceanog.2016.32, 2016.

Ciappa, A. C.: Effects of Marine Heatwaves (MHW) and Cold Spells (MCS) on the surface warming of the Mediterranean Sea from 1989 to 2018, Prog. Oceanogr., 205, 102828, https://doi.org/10.1016/j.pocean.2022.102828, 2022.

Darmaraki S.: Mediterranean marine heatwaves: detection, past variability and future evolution, PhD thesis, Université Paul Sabatier – Toulouse III, https://theses.hal.science/tel-02893812 (last access: 2 August 2024), 2019.

Darmaraki, S., Somot, S., Sevault, F., and Nabat, P.: Past Variability of Mediterranean Sea Marine Heatwaves, Geophys. Res. Lett., 46, 9813–9823, https://doi.org/10.1029/2019GL082933, 2019a.

Darmaraki, S., Somot, S., Sevault, F., Nabat, P., Cabos Narvaez, W. D., Cavicchia, L., Djurdjevic, V., Li, L., Sannino, G., and Sein, D. V.: Future evolution of Marine Heatwaves in the Mediterranean Sea, Clim. Dynam., 53, 1371–1392, https://doi.org/10.1007/s00382-019-04661-z, 2019b.

Dayan, H., McAdam, R., Juza, M., Masina, S., and Speich, S.: Marine heat waves in the Mediterranean Sea: An assessment from the surface to the subsurface to meet national needs, Front. Mar. Sci., 10, 1–21, https://doi.org/10.3389/fmars.2023.1045138, 2023.

Denaxa, D., Korres, G., Sotiropoulou, M., and Perivoliotis L.: Extreme Marine Heatwave in the eastern Mediterranean in May 2020, in: Copernicus Ocean State Report, J. Oper. Oceanogr., 15, s119–s126, https://doi.org/10.1080/1755876X.2022.2095169, 2022.

D'Ortenzio, F. and Prieur, L.: The upper mixed layer, in: Life in the Mediterranean Sea: A Look at Habitat Changes, Noga Stambler, Nova Science Publisher, Hauppage, NY, USA, 127–156, https://www.researchgate.net/publication/267555983_The_upper_mixed_layer (last access: 10 August 2024), 2012.

Escudier, R., Clementi, E., Nigam, T., Aydogdu, A., Fini, E., Pistoia, J., Grandi, A., and Miraglio, P.: EU Copernicus Marine Service Quality Information Document for the Mediterranean Sea Physics Reanalysis Product, MEDSEA_MULTIYEAR_PHY_006_004, Issue 2.3, Mercator Ocean International, https://catalogue.marine.copernicus.eu/documents/QUID/CMEMS-MED-QUID-006-004.pdf (last access: 13 July 2023), 2022.

EU Copernicus Marine Service Product: Mediterranean Sea Physics Reanalysis, Mercator Ocean International [data set], https://doi.org/10.25423/CMCC/MEDSEA_MULTIYEAR_PHY_006_004_E3R1, 2022.

EU Copernicus Marine Service Product: Mediterranean Sea – High Resolution L4 Sea Surface Temperature Reprocessed, Mercator Ocean International [data set], https://doi.org/10.48670/moi-00173, 2023a.

EU Copernicus Marine Service Product: Mediterranean Sea High Resolution and Ultra High Resolution Sea Surface Temperature Analysis, Mercator Ocean International [data set], https://doi.org/10.48670/moi-00172, 2023b.

EU Copernicus Marine Service Product: Mediterranean Sea Physics Analysis and Forecast, Mercator Ocean International [data set], https://doi.org/10.25423/CMCC/MEDSEA_ANALYSISFORECAST_PHY_006_013_EAS7, 2024.

Fewings, M. R. and Brown, K. S.: Regional Structure in the Marine Heat Wave of Summer 2015 Off the Western United States, Front. Mar. Sci., 6, 1–14, https://doi.org/10.3389/fmars.2019.00564, 2019.

Frölicher, T. L. and Laufkötter, C.: Emerging risks from marine heat waves, Nat. Commun., 9, 650, https://doi.org/10.1038/s41467-018-03163-6, 2018.

Garrabou, J., Gómez-Gras, D., Medrano, A., Cerrano, C., Ponti, M., Schlegel, R., Bensoussan, N., Turicchia, E., Sini, M., Gerovasileiou, V., Teixido, N., Mirasole, A., Tamburello, L., Cebrian, E., Rilov, G., Ledoux, J. B., Souissi, J. Ben, Khamassi, F., Ghanem, R., Benabdi, M., Grimes, S., Ocaña, O., Bazairi, H., Hereu, B., Linares, C., Kersting, D. K., la Rovira, G., Ortega, J., Casals, D., Pagès-Escolà, M., Margarit, N., Capdevila, P., Verdura, J., Ramos, A., Izquierdo, A., Barbera, C., Rubio-Portillo, E., Anton, I., López-Sendino, P., Díaz, D., Vázquez-Luis, M., Duarte, C., Marbà, N., Aspillaga, E., Espinosa, F., Grech, D., Guala, I., Azzurro, E., Farina, S., Cristina Gambi, M., Chimienti, G., Montefalcone, M., Azzola, A., Mantas, T. P., Fraschetti, S., Ceccherelli, G., Kipson, S., Bakran-Petricioli, T., Petricioli, D., Jimenez, C., Katsanevakis, S., Kizilkaya, I. T., Kizilkaya, Z., Sartoretto, S., Elodie, R., Ruitton, S., Comeau, S., Gattuso, J. P., and Harmelin, J. G.: Marine heatwaves drive recurrent mass mortalities in the Mediterranean Sea, Glob. Change Biol., 28, 5708–5725, https://doi.org/10.1111/gcb.16301, 2022.

Goglio, A. C., Clementi, E., Grandi, A., Mariani, A., Giurato, M., and Aydogdu, A.: EU Copernicus Marine Service Quality Information Document for the Mediterranean Sea Physics Analysis and Forecast Product, MEDSEA_ANALYSISFORECAST_PHY_006_013, Issue 2.4, Mercator Ocean International, https://catalogue.marine.copernicus.eu/documents/QUID/CMEMS-MED-QUID-006-013.pdf, last access: 26 June 2024.

Hayashida, H., Matear, R. J., Strutton, P. G., and Zhang, X.: Insights into projected changes in marine heatwaves from a high-resolution ocean circulation model, Nat. Commun., 11, 4352, https://doi.org/10.1038/s41467-020-18241-x, 2020.

Hersbach, H., Bell, B., Berrisford, P., Biavati, G., Horányi, A., Muñoz Sabater, J., Nicolas, J., Peubey, C., Radu, R., Rozum, I., Schepers, D., Simmons, A., Soci, C., Dee, D., and Thépaut, J.-N.: ERA5 hourly data on single levels from 1940 to present, Copernicus Climate Change Service (C3S) Climate Data Store (CDS) [data set], https://doi.org/10.24381/cds.adbb2d47, 2023.

Hobday, A. J., Alexander, L. V., Perkins, S. E., Smale, D. A., Straub, S. C., Oliver, E. C. J., Benthuysen, J. A., Burrows, M. T., Donat, M. G.., Feng, M., and Holbrook, N. J.: A hierarchical approach to defining marine heatwaves, Prog. Oceanogr., 141, 227–238, 2016.

Hobday, A. J., Oliver, E. C. J., Sen Gupta, A, Benthuysen, J. A., Burrows, M. T., Donat, M. G., Holbrook, N. J., Moore, P. J., Thomsen, M. S., Wernberg, T., and Smale, D. A.: Categorizing and naming marine heatwaves, Oceanography, 31, 162–173, 2018.

Holbrook, N. J., Scannell, H. A., Sen Gupta, A., Benthuysen, J. A., Feng, M., Oliver, E. C. J., Alexander, L. V., Burrows, M. T., Donat, M. G., Hobday, A. J., Moore, P. J., Perkins-Kirkpatrick, S. E., Smale, D. A., Straub, S. C., and Wernberg, T.: A global assessment of marine heatwaves and their drivers, Nat. Commun., 10, 2624, https://doi.org/10.1038/s41467-019-10206-z, 2019.

Holbrook, N. J., Sen Gupta, A., Oliver, E. C. J., Hobday, A. J., Benthuysen, J. A., Scannell, H. A., Smale, D. A., and Wernberg, T.: Keeping pace with marine heatwaves, Nat. Rev. Earth Environ., 1, 482–493, https://doi.org/10.1038/s43017-020-0068-4, 2020.

Ibrahim, O., Mohamed, B., and Nagy, H.: Spatial Variability and Trends of Marine Heat Waves in the Eastern Mediterranean Sea over 39 Years, J. Mar. Sci. Eng., 9, 643, https://doi.org/10.3390/jmse9060643, 2021.

Juza, M., Fernández-Mora, A., and Tintoré, J.: Sub-Regional Marine Heat Waves in the Mediterranean Sea From Observations: Long-Term Surface Changes, Sub-Surface and Coastal Responses, Front. Mar. Sci., 9, 785771, https://doi.org/10.3389/fmars.2022.785771, 2022.

Lecci, R., Drudi, M., Grandi, A., Cretì, S., and Clementi, E.: EU Copernicus Marine Service Product User Manual for the Mediterranean Sea Physics Reanalysis Product, MEDSEA_MULTIYEAR_PHY_006_004, Issue 2.3, Mercator Ocean International, https://catalogue.marine.copernicus.eu/documents/PUM/CMEMS-MED-PUM-006-004.pdf (last access: 26 June 2024), 2022.

Lecci, R., Drudi, M., Grandi, A., Cretì, S., and Clementi, E.: EU Copernicus Marine Service Product User Manual for the Mediterranean Sea Physics Analysis and Forecast Product, MEDSEA_ANALYSISFORECAST_PHY_006_013, Issue 2.3, Mercator Ocean International, https://catalogue.marine.copernicus.eu/documents/PUM/CMEMS-MED-PUM-006-013.pdf (last access: 26 June 2024), 2023.

Lee, E. Y., Lee, D. E., Park, Y. G., Kang, H., and Baek, H.: The local stratification preconditions the marine heatwaves in the Yellow Sea, Front. Mar. Sci., 10, 1–9, https://doi.org/10.3389/fmars.2023.1118969, 2023.

Marin, M., Feng, M., Bindoff, N. L., and Phillips, H. E.: Local Drivers of Extreme Upper Ocean Marine Heatwaves Assessed Using a Global Ocean Circulation Model, Front. Clim., 4, 1–16, https://doi.org/10.3389/fclim.2022.788390, 2022.

Marullo, S., Serva, F., Iacono, R., Napolitano, E., di Sarra, A., Meloni, D., Monteleone, F., Sferlazzo, D., De Silvestri, L., de Toma, V., Pisano, A., Bellacicco, M., Landolfi, A., Organelli, E., Yang, C., and Santoleri, R.: Record-breaking persistence of the 2022/23 marine heatwave in the Mediterranean Sea, Environ. Res. Lett., 18, 114041, https://doi.org/10.1088/1748-9326/ad02ae, 2023.

McAdam, R., Bonino, G., Clementi, E., and Masina, S.: Forecasting the Mediterranean Sea marine heatwave of summer 2022, in: 8th edition of the Copernicus Ocean State Report (OSR8), edited by: von Schuckmann, K., Moreira, L., Grégoire, M., Marcos, M., Staneva, J., Brasseur, P., Garric, G., Lionello, P., Karstensen, J., and Neukermans, G., Copernicus Publications, State Planet, 4-osr8, 13, https://doi.org/10.5194/sp-4-osr8-13-2024, 2024.

Mills, K. E., Pershing, A. J., Brown, C. J., Chen, Y., Chiang, F. S., Holland, D. S., Lehuta, S., Nye, J. A., Sun, J. C., Thomas, A. C., and Wahle, R. A.: Fisheries management in a changing climate: Lessons from the 2012 ocean heat wave in the Northwest Atlantic, Oceanography, 26, 191–195, https://doi.org/10.5670/oceanog.2013.27, 2013.

Olita, A., Sorgente, R., Natale, S., Gaberšek, S., Ribotti, A., Bonanno, A., and Patti, B.: Effects of the 2003 European heatwave on the Central Mediterranean Sea: surface fluxes and the dynamical response, Ocean Sci., 3, 273–289, https://doi.org/10.5194/os-3-273-2007, 2007.

Oliver, E. C. J., Donat, M. G., Burrows, M. T., Moore, P. J., Smale, D. A., Alexander, L. V., Benthuysen, J. A., Feng, M., Sen Gupta, A., Hobday, A. J., Holbrook, N. J., Perkins-Kirkpatrick, S. E., Scannell, H. A., Straub, S. C., and Wernberg, T.: Longer and more frequent marine heatwaves over the past century, Nat. Commun., 9, 1324, https://doi.org/10.1038/s41467-018-03732-9, 2018.

Oliver, E. C. J., Burrows, M. T., Donat, M. G., Sen Gupta, A., Alexander, L. V., Perkins-Kirkpatrick, S. E., Benthuysen, J. A., Hobday, A. J., Holbrook, N. J., Moore, P. J., Thomsen, M. S., Wernberg, T., and Smale, D. A.: Projected Marine Heatwaves in the 21st Century and the Potential for Ecological Impact, Front. Mar. Sci., 6, 1–12, https://doi.org/10.3389/fmars.2019.00734, 2019.

Oliver, E. C. J., Benthuysen, J. A., Darmaraki, S., Donat, M. G., Hobday, A. J., Holbrook, N. J., Schlegel, R. W., and Sen Gupta, A.: Marine Heatwaves, Ann. Rev. Mar. Sci., 13, 313–342, https://doi.org/10.1146/annurev-marine-032720-095144, 2021.

Pastor, F. and Khodayar, S.: Marine heat waves: Characterizing a major climate impact in the Mediterranean, Sci. Total Environ., 861, 160621, https://doi.org/10.1016/j.scitotenv.2022.160621, 2023.

Paulson, C. A. and Simpson, J. J.: Irradiance Measurements in the Upper Ocean, J. Phys. Oceanogr., 7, 952–956, https://doi.org/10.1175/1520-0485(1977)007<0952:IMITUO>2.0.CO;2, 1977

Pirro, A., Martellucci, R., Gallo, A., Kubin, E., Mauri, E., Juza, M., Notarstefano, G., Pacciaroni, M., Bussani, A., and Menna, M.: Subsurface warming derived from Argo floats during the 2022 Mediterranean marine heat wave, in: 8th edition of the Copernicus Ocean State Report (OSR8), edited by: von Schuckmann, K., Moreira, L., Grégoire, M., Marcos, M., Staneva, J., Brasseur, P., Garric, G., Lionello, P., Karstensen, J., and Neukermans, G., Copernicus Publications, State Planet, 4-osr8, 18, https://doi.org/10.5194/sp-4-osr8-18-2024, 2024.

Pisano, A., Fanelli, C., Cesarini, C., Tronconi, C., La Padula, F., and Buongiorno Nardelli, B.: EU Copernicus Marine Service Product User Manual for the Mediterranean Sea – High Resolution L4 Sea Surface Temperature Reprocessed Product, SST_MED_SST_L4_REP_OBSERVATIONS_010_021, Issue 3.0, Mercator Ocean International, https://catalogue.marine.copernicus.eu/documents/PUM/CMEMS-SST-PUM-010-021-022-041-042.pdf (last access: 26 June 2024), 2023a.

Pisano, A., Fanelli, C., Cesarini, C., Tronconi, C., La Padula, F., and Buongiorno Nardelli, B.: EU Copernicus Marine Service Quality Information Document for the Mediterranean Sea – High Resolution L4 Sea Surface Temperature Reprocessed Product, SST_MED_SST_L4_REP_OBSERVATIONS_010_021, Issue 3.0, Mercator Ocean International, https://catalogue.marine.copernicus.eu/documents/QUID/CMEMS-SST-QUID-010-021-022-041-042.pdf (last access: 26 June 2024), 2023b.

Pisano, A., Fanelli, C., Buongiorno Nardelli, B., Tronconi, C., Cesarini, C., and La Padula, F.: EU Copernicus Marine Service Product User Manual for the Mediterranean Sea High Resolution and Ultra High Resolution Sea Surface Temperature Analysis Product, SST_MED_SST_L4_NRT_OBSERVATIONS_010_004, Issue 4.0, Mercator Ocean International, https://catalogue.marine.copernicus.eu/documents/PUM/CMEMS-SST-PUM-010-004-006-012-013.pdf (last access: 26 June 2024), 2023c.

Pisano, A., Fanelli, C., Buongiorno Nardelli, B., Tronconi, C., La Padula, F., and Cesarini, C.: EU Copernicus Marine Service Quality Information Document for the Mediterranean Sea High Resolution and Ultra High Resolution Sea Surface Temperature Analysis Product, SST_MED_SST_L4_NRT_OBSERVATIONS_010_004, Issue 4.0, Mercator Ocean International, https://catalogue.marine.copernicus.eu/documents/QUID/CMEMS-SST-QUID-010-004-006-012-013.pdf (last access: 26 June 2024), 2023d.

Plecha, S. M. and Soares, P. M. M.: Global marine heatwave events using the new CMIP6 multi-model ensemble: From shortcomings in present climate to future projections, Environ. Res. Lett., 15, 124058, https://doi.org/10.1088/1748-9326/abc847, 2019.

Schlegel, R. W., Oliver, E. C. J., and Chen, K.: Drivers of Marine Heatwaves in the Northwest Atlantic: The Role of Air–Sea Interaction During Onset and Decline, Front. Mar. Sci., 8, 1–18, https://doi.org/10.3389/fmars.2021.627970, 2021.

Sen Gupta, A., Thomsen, M., Benthuysen, J. A., Hobday, A. J., Oliver, E., Alexander, L. V, Burrows, M. T., Donat, M. G., Feng, M., Holbrook, N. J., Perkins-Kirkpatrick, S., Moore, P. J., Rodrigues, R. R., Scannell, H. A., Taschetto, A. S., Ummenhofer, C. C., Wernberg, T., and Smale, D. A.: Drivers and impacts of the most extreme marine heatwave events, Sci. Rep., 10, 19359, https://doi.org/10.1038/s41598-020-75445-3, 2020.

Smale, D. A., Wernberg, T., Oliver, E. C. J., Thomsen, M., Harvey, B. P., Straub, S. C., Burrows, M. T., Alexander, L. V., Benthuysen, J. A., Donat, M. G., Feng, M., Hobday, A. J., Holbrook, N. J., Perkins-Kirkpatrick, S. E., Scannell, H. A., Sen Gupta, A., Payne, B. L., and Moore, P. J.: Marine heatwaves threaten global biodiversity and the provision of ecosystem services, Nat. Clim. Change, 9, 306–312, https://doi.org/10.1038/s41558-019-0412-1, 2019.

Smith, K. E., Burrows, M. T., Hobday, A. J., King, N. G., Moore, P. J., Sen Gupta, A., Thomsen, M. S., Wernberg, T., and Smale, D. A.: Biological Impacts of Marine Heatwaves, Ann. Rev. Mar. Sci., 15, 119–145, https://doi.org/10.1146/annurev-marine-032122-121437, 2023.

Sparnocchia, S., Schiano, M. E., Picco, P., Bozzano, R., and Cappelletti, A.: The anomalous warming of summer 2003 in the surface layer of the Central Ligurian Sea (Western Mediterranean), Ann. Geophys., 24, 443–452, https://doi.org/10.5194/angeo-24-443-2006, 2006.

Spillman, C. M., Smith, G. A., Hobday, A. J., and Hartog, J. R.: Onset and Decline Rates of Marine Heatwaves: Global Trends, Seasonal Forecasts and Marine Management, Front. Clim., 3, 1–13, https://doi.org/10.3389/fclim.2021.801217, 2021.

Thoral, F., Montie, S., Thomsen, M. S., Tait, L. W., Pinkerton, M. H., and Schiel, D. R.: Unravelling seasonal trends in coastal marine heatwave metrics across global biogeographical realms, Sci. Rep., 12, 7740, https://doi.org/10.1038/s41598-022-11908-z, 2022.

Vogt, L., Burger, F. A., Griffies, S. M., and Frölicher, T. L.: Local Drivers of Marine Heatwaves: A Global Analysis With an Earth System Model, Front. Clim., 4, 1–18, https://doi.org/10.3389/fclim.2022.847995, 2022.

Wernberg, T., Bennett, S., Babcock, R. C., De Bettignies, T., Cure, K., Depczynski, M., Dufois, F., Fromont, J., Fulton, C. J., Hovey, R. K., Harvey, E. S., Holmes, T. H., Kendrick, G. A., Radford, B., Santana-Garcon, J., Saunders, B. J., Smale, D. A., Thomsen, M. S., Tuckett, C. A., Tuya, F., Vanderklift, M. A., and Wilson, S.: Climate-driven regime shift of a temperate marine ecosystem, Science, 353, 169–172, https://doi.org/10.1126/science.aad8745, 2016.

Zhao, Z. and Marin, M.: A MATLAB toolbox to detect and analyze marine heatwaves, J. Open Source Softw., 4, 1124, https://doi.org/10.21105/joss.01124, 2019.

State Planet, 4-osr8, 12, 2024
https://doi.org/10.5194/sp-4-osr8-12-2024

Variability in manometric sea level from reanalyses and observation-based products over the Arctic and North Atlantic oceans and the Mediterranean Sea

Andrea Storto[1], Giulia Chierici[1], Julia Pfeffer[2], Anne Barnoud[2], Romain Bourdalle-Badie[3], Alejandro Blazquez[4], Davide Cavaliere[1], Noémie Lalau[2], Benjamin Coupry[2], Marie Drevillon[3], Sebastien Fourest[4], Gilles Larnicol[2], and Chunxue Yang[1]

[1]Institute of Marine Sciences (ISMAR), National Research Council (CNR), 00133 Rome, Italy
[2]Magellium, 31520 Ramonville-Saint-Agne, France
[3]Mercator Ocean International (MOI), 31400 Toulouse, France
[4]Laboratory of Space Geophysical and Oceanographic Studies (LEGOS), 31401 Toulouse, France

Correspondence: Andrea Storto (andrea.storto@cnr.it)

Received: 2 August 2023 – Discussion started: 29 August 2023
Revised: 25 July 2024 – Accepted: 16 August 2024 – Published: 30 September 2024

Abstract. Regional variations in the mass component of sea level (manometric sea level) are intimately linked with the changes in the water cycle, volume transports, and inter-basin exchanges. Here, we investigate the consistency at the regional level of the manometric sea level from the Copernicus Marine Service Global Reanalysis Ensemble Product (GREP) and compare with observation-based products deduced from either gravimetry (GRACE missions) or altimetry and in situ ocean observations (sea level budget, SLB, approach) for some climate-relevant diagnostics such as interannual variability, trends, and seasonal amplitude. The analysis is performed for three basins (the Mediterranean Sea and Arctic and North Atlantic oceans) and indicates very different characteristics across the three. The Mediterranean Sea exhibits the largest interannual variability, the Arctic Ocean the largest trends, and the North Atlantic a nearly linear increase that is highly correlated to global barystatic sea level variations. The three datasets show significant consistency at both the seasonal and the interannual timescales, although the differences in the linear trends are sometimes significant (e.g. GRACE overestimates the trend in the Arctic and underestimates it in the Mediterranean Sea when compared to the other products). Furthermore, the Gravity Recovery and Climate Experiment (GRACE) and GREP data prove to be mutually more consistent than SLB in most cases. Finally, we analyse the main modes of climate variability affecting the manometric sea level variations over the selected ocean basins through regularised regression; the North Pacific Gyre Oscillation, the Arctic Oscillation, and the Atlantic Multidecadal Oscillation are proven to be the most influential modes for the North Atlantic Ocean, Mediterranean Sea, and Arctic Ocean manometric sea levels, respectively.

1 Introduction

Contemporary changes in global sea level are driven mostly by two contributions. The first is density-driven variations in the sea level, the so-called steric sea level that responds to the expansion and contraction of seawater due, mostly, to increasing heat in the oceans (Storto et al., 2019a). The other contributor to global sea level change is the ocean mass change, called the barystatic sea level (Gregory et al., 2019). The barystatic sea level has been recently found to be responsible for the majority (about 60 %) of the global sea level changes (Frederikse et al., 2020; Fox-Kemper et al., 2021). Recent estimates indicate $2.25 \pm 0.16\,\mathrm{mm\,yr^{-1}}$ of sea level rise due to barystatic changes for the recent period (2005–2016; Amin et al., 2020). Changes in the barystatic sea level are due to the loss of mass from glaciers and ice sheets

Published by Copernicus Publications.

Table 1. Product table.

Product ref. no	Product ID and type	Data access	Documentation
1	GLOBAL_MULTIYEAR_PHY_ENS_001_031 (GREP), numerical models	EU Copernicus Marine Service Product (2022a)	QUID (quality information document): Desportes et al. (2022) PUM (product user manual): Gounou et al. (2022)
2	Barystatic and manometric from satellite gravimetry (LEGOS – MAGELLIUM)	Magellium/LEGOS (2023a): https://doi.org/10.24400/527896/A01-2023.011	PUM (product user manual): https://www.aviso.altimetry.fr/fileadmin/documents/data/products/indic/WAMBOR-DT-009-MAG_CopernicusMarine_ServiceEvolution_PUM_v2.0.pdf*
3	Barystatic and manometric from sea level budget (LEGOS and MAGELLIUM)	Magellium/LEGOS (2023b): https://doi.org/10.24400/527896/A01-2023.012	PUM (product user manual): https://www.aviso.altimetry.fr/fileadmin/documents/data/products/indic/WAMBOR-DT-009-MAG_CopernicusMarine_ServiceEvolution_PUM_v2.0.pdf*
4	SEALEVEL_GLO_PHY_L4_MY_008_047, L4 reprocessed altimetry observations	EU Copernicus Marine Service Product (2022b)	QUID (quality information document): Pujol et al. (2022) PUM (product user manual): Pujol (2022)

* Last access: 10 September 2024.

(Greenland and Antarctica) and changes in the global water cycle and land water storage. As such, barystatic sea level changes are a fundamental proxy for climate change and are expected to increase even more dramatically in the future due to increased ice melting, according to future projections (Oppenheimer et al., 2019).

At the regional scale, local dynamics and regional hydrology, together with cross-basin exchanges, modulate regional ocean mass exchanges, called the manometric sea level (Gregory et al., 2019). For instance, Camargo et al. (2022) show that regional trends in the manometric sea level may vary from -0.4 to $3.3\,\mathrm{mm\,yr^{-1}}$ across the global ocean for the 2003–2016 period. Typically, regions characterised by high dynamic variability are characterised by large manometric variations. Strong climate modes of variability (e.g. the North Atlantic Oscillation) are also responsible for large deviations in manometric sea level (e.g. Criado-Aldeanueva et al., 2014; Volkov et al., 2019); fingerprinting techniques can be used to estimate the influence of a specific climate index on the resulting sea level variability (e.g. Pfeffer et al., 2022). In the Mediterranean Sea, for instance, variations are intimately linked to the exchanges with the Atlantic Ocean through the Gibraltar Strait and variations in the atmospheric freshwater input, which are both strongly linked to the North Atlantic variability (e.g. Tsimplis and Josey, 2001).

Since 2002, methods to observe and analyse manometric and barystatic sea level variations have generally relied on GRACE (Gravity Recovery And Climate Experiment; e.g. Tapley et al., 2004) and GRACE-FO (GRACE Follow-On; Landerer et al., 2020) satellite mission measurements of the temporal and spatial variations in the Earth's gravity field. Barystatic and manometric sea level signals can also be inferred from the difference between the total sea level, measured by altimetry missions, and steric sea level, estimated through in situ observations (e.g. Horwath et al., 2022). This approach will be referred to as the sea level budget (SLB) method in the remainder of this article.

Alternatively, ocean general circulation model (OGCM) simulations embed the variability in the sea level and its components, although they significantly lack realism (e.g. Kohl et al., 2007). Ocean reanalyses, which combine an ocean model with observations through data assimilation (Storto et al., 2019b) are in turn able to provide a good estimation of the ocean's long-term changes (e.g. Storto and Yang, 2024) and associated sea level variability at global and basin scales (e.g. Storto et al., 2017); they are thus complementary to gravimetry- and sea-level-budget-based observational counterparts and can be used for several investigations (e.g. Peralta-Ferriz et al., 2014; Marcos, 2015; Hughes et al., 2018). A few limitations in the use of reanalyses exist, though. First, the usual Boussinesq approximation in the OGCMs leads to a zero global steric sea level by construction, as the models cannot represent the global expansion and contraction in the constant volume framework. However, the global steric sea level can be computed and added to the model sea surface height retrospectively, since it does not have any dynamical signature (e.g. Greatbatch, 1994).

There is a more critical and long-standing issue in reanalyses with regard to the barystatic and manometric sea level components. Indeed, both the use of climatological freshwater input from land and ice and the imbalance of the atmospheric freshwater forcing combined with the evaporation and sublimation calculated by the ocean model often make barystatic and manometric terms unrealistic. Some reanalyses correct the barystatic sea level with globally uniform offsets which can be either time-varying or constant. In any case, the barystatic signal is generally unrealistic, and the manometric one may be affected by inaccuracies in the freshwater input into the oceans. In general, ocean-bottom pressure data derived from gravimetry could also be directly assimilated into ocean models (see, e.g., Köhl et al., 2012). However, this approach was found to be suboptimal, mostly due to the low signal-to-noise ratio of the gravimetry data compared to altimetry data assimilation (e.g. Storto et al., 2011) and their issues related to the pre-processing (persistent stripes and land water leakage). More recently, however, ingesting gravimetry data (e.g. in ECCOv4r4; Fukumori et al., 2020) has proven promising to better capture high-frequency sea level variability (Schindelegger et al., 2021). Finally, the limited spatial resolution of the models may limit the representativeness of sea level variations in mesoscale-active areas (e.g. Androsov et al., 2020).

The goal of this paper is manifold. First, we aim to estimate the consistency of the manometric sea level from notably different approaches which use numerical ocean models, gravimetry or altimetry, and in situ observations. These approaches are known to contain different sources of uncertainty, and none of them is fully trustable, as discussed in detail in this section and the next sections. Particular attention is devoted to assessing whether the latest generation of the Copernicus Marine Service global reanalyses can capture the interannual variations in the manometric sea level. Second, we aim at quantifying regional trends and amplitudes to identify the emerging levels and scales of manometric sea level variability, depending on the specific basin. Finally, we aim to fingerprint the manometric sea level with several climate mode indices to connect such variations with large-scale climate variability.

The structure of the paper is as follows: we compare regional (Sect. 3) manometric sea levels from reanalyses with those coming from satellite gravimetry or the sea level budget approach (described in Sect. 2). The exercise will therefore indicate the consistency of the reanalyses and observation-based products for selected metrics. Finally, we summarise the findings and conclude the paper (Sect. 4).

2 Data and methods

In this section, we shortly introduce the datasets used in the assessment. We refer to Gregory et al. (2019) for the terminology and definitions used to characterise the sea level components.

2.1 Gravimetry-based dataset

Barystatic and manometric sea level anomalies have been estimated from April 2002 to August 2022 at a monthly timescale and with a spatial resolution of 1°, using an ensemble of GRACE and GRACE-FO solutions (product ref. no. 2 in Table 1). The GRACE and GRACE-FO ensemble is constituted of 120 solutions, allowing us to estimate the uncertainties associated with different processing strategies and geophysical corrections needed for ocean applications. The ensemble is based on coefficients of the Earth’s gravitational potential anomalies estimated by five different processing centres (CNES: Centre National d’Etudes Spatiales; CSR: Center for Space Research; JPL: Jet Propulsion Laboratory; GFZ: GeoForschung Zentrum; ITSG: Institute of Geodesy at Graz University of Technology). A large variety of post-processing corrections are applied to the ensemble, including two geocentric motions (Lemoine and Reinquin, 2017; Sun et al., 2016), three oblateness values (C20) of the Earth (Cheng et al., 2013; Lemoine and Reinquin, 2017; Loomis et al., 2019), and two glacial isostatic adjustment (GIA) corrections (Peltier et al., 2015; Caron et al., 2018). To reduce the anisotropic noise characterised by typical stripes elongated in the north–south direction, decorrelation filters, called decorrelation and denoising kernel (DDK) filters (Kusche et al., 2009), are applied to GRACE solutions (e.g. Horvath et al., 2018) using two different orders (DDK3 and DDK6) corresponding to different levels of filtering. The ensemble of 120 solutions results from the combination of these five processing centres, two geocentric models, three oblateness models, two GIA corrections, and two filters. The ensemble standard deviation provides a measure of uncertainty for both the barystatic and manometric sea level time series.

2.2 Sea level budget-based dataset

The estimation of barystatic and manometric sea level changes is extended to the altimetry era (January 1993–December 2020) using the sea level budget approach (product ref. no. 3 in Table 1). The manometric sea level changes are calculated as the difference between the geocentric sea level changes based on satellite altimetry and steric sea level changes based on in situ measurements of the seawater temperature and salinity. The reliability of this dataset is intrinsically linked to the altimetry and in situ observational sampling. Only within the global mean values, i.e. the barystatic sea level, are changes computed as the difference between the global mean geocentric sea level changes and thermosteric sea level changes to avoid drifts due to Argo salinity measurement errors (Barnoud et al., 2021; Wong et al., 2020); however, regional (manometric) sea level estimates include the halosteric contribution in the steric evaluation.

Geocentric sea level changes are estimated using the vDT2021 sea level product provided by the Copernicus Climate Change Service (C3S; Legeais et al., 2021). Geocentric sea level changes are corrected for the drifts in the TOPEX-A altimeter (Ablain et al., 2017) and the Jason-3 microwave radiometer wet tropospheric correction (Barnoud et al., 2023a, b) for the GIA effect, using the ensemble mean of 27 GIA models (Prandi et al., 2021) centred on ICE5G-VM2 (Peltier, 2004), and for the elastic deformation of the solid Earth due to present-day ice melting (Frederikse et al., 2017). The uncertainty in the geocentric sea level changes is calculated with the uncertainty budget and method detailed in Guérou et al. (2023) for the global mean sea level changes and in Prandi et al. (2021) for the local sea level changes. Altimetry data are masked over sea-ice-covered areas using the Copernicus Climate Change Service sea ice product (Lavergne et al., 2019).

Steric sea level changes are estimated as the sum of the thermosteric and halosteric sea level changes calculated from gridded temperature and salinity estimates from three different centres, including EN4 (Good et al., 2013), IAP (Cheng et al., 2020), and Ishii et al. (2006). EN4 provides four datasets with different combinations of corrections for expendable bathythermograph (XBT) and mechanical bathythermograph (MBT) measurements applied, leading to an ensemble of six temperature and salinity datasets. From these datasets, we compute the thermosteric and halosteric sea level changes due to temperature and salinity variations between 0 and 2000 m depth. The deep-ocean contribution (i.e. below 2000 m) is considered only in the global barystatic signal and taken as a linear trend of $0.12 \pm 0.03\,\mathrm{mm\,yr^{-1}}$ (Chang et al., 2019) added to the time-varying steric sea level; for the regional estimates of the manometric sea level, the deep-ocean and abyssal-ocean contribution is neglected, as there are not enough data for constraining it at the regional level.

Steric sea level changes are estimated as the ensemble mean of the six solutions, and their uncertainties are estimated with the covariance matrix of the ensemble. The resulting barystatic and manometric uncertainties are described by the covariance matrix obtained by summing the sea level and steric covariance matrices; the sea-ice mask from the altimetry product is propagated onto the resulting manometric product.

2.3 The reanalysis dataset

In this work, we use the Global Reanalysis Ensemble Product (GREP) from the Copernicus Marine Service (product ref. no. 1 in Table 1), which is a small-ensemble global reanalysis product, including in turn the four reanalyses of (i) C-GLORS (v7) from CMCC, (ii) GloSea5 from UKMO, (iii) GLORYS2 (V4) from Mercator Ocean, and (iv) ORAS5 from ECMWF. All reanalyses are performed using the NEMO ocean model (Madec and The NEMO System Team, 2017) configured at about 1/4° of the horizontal resolution and 75 levels. However, the four reanalyses differ for several issues, which can be summarised in the (i) NEMO model version and a few selected parameterisations, including the specific choice in the use of the ECMWF reanalysis (ERA-Interim and ERA5) atmospheric forcing; (ii) initial conditions in 1993 at the beginning of the reanalysed period (1993–2019); (iii) the data assimilation scheme; and (iv) the set of observations assimilated, including their source and pre-processing procedures. Thus, GREP can span, to a good extent, the uncertainty linked with model physics and input datasets. We have used monthly mean data at 1/4° of the horizontal resolution for the comparisons shown in Sect. 3. More details about the four reanalyses, together with some in-situ-based validation and assessment of the ensemble standard deviation, are provided by Storto et al. (2019c).

The estimation approach for GREP follows that of the sea level budget approach (see Sect. 2.2), where the manometric sea level is calculated as the difference in the total sea surface height anomaly from the reanalysis, and the steric sea level anomaly, calculated from the reanalysis output temperature and salinity fields. Thus, we can cross-compare GREP data with GRACE and SLB datasets in terms of the interannual variability, trend, and seasonal amplitude.

2.4 Analysis methods

Basin-averaged time series are analysed in the next section as monthly means to assess the main variability signal over three oceanic basins (the Arctic Ocean, defined as the region covering from 67° N in the Atlantic to the Bering Strait; the North Atlantic Ocean, defined from 0 to 67° N; the Mediterranean Sea). Time series are also analysed in terms of their interannual and seasonal signal, where the interannual signal is the time series to which the monthly climatology has been subtracted and the seasonal is the residual part, assuming that the majority of the subannual signal can be attributed to seasonal variation, due to the monthly temporal frequency of the data. The uncertainty in the time series corresponds to that provided by the dataset (which in turn uses an ensemble approach to estimate the uncertainty as ensemble standard deviation); by construction, GREP, with only four members, is known to underestimate the uncertainty in the sea level (Storto et al., 2019c). Uncertainty in the trends is estimated through bootstrapping (Efron, 1979) and closely resembles the estimates calculated following Storto et al. (2022). The bootstrapping technique randomly removes part of the time series and thus quantifies the sensitivity of the trend to individual years and periods. Explained variance is used to quantify how much of the regional signal is explained by the global barystatic signal due to fast barotropic motion. For this analysis, we use only global GRACE and SLB time series and show only SLB for the sake of clarity (see, e.g., Barnoud et al., 2023b, for a discussion on their comparison) because the GREP barystatic sea level is either unreliable due to drifts in the freshwater forcing, or it is adjusted to GRACE-derived data and, thus, is not independent. Seasonal amplitude is defined by fitting the monthly data to a curve with sinusoidal (seasonal signal) and linear (trend signal) terms; the interannual variability is the standard deviation of the detrended and deseasonalised time series. Percent values of manometric sea level trends over the total sea level ones are calculated from the Copernicus Marine Service dataset (product ref. no. 4 in Table 1) over each region.

LASSO regression (Tibshirani, 1997), performed between the normalised manometric sea level and normalised climate indices, is a regularisation technique for multivariate regression, which is used in this study to rank the influence of the climate indices on the basin-averaged manometric sea level in a way similar to what Pfeffer et al. (2022) proposed. Like the previous studies, raw monthly means were used without low-pass filtering the data, which could induce arbitrary preferences in the regression within our multi-variate analysis. After performing a k-fold cross-validation (with 10 folds) to identify the best hyperparameters, the LASSO regression avoids overfitting the regression, such that absolute values of the regression coefficients quantify the impact of a predictor on the manometric sea level. By construction, LASSO minimises the collinearities across the predictors; however, when predictors are strongly correlated, the preference provided by LASSO might be less obvious than expected (Tibshirani, 1996). We also verified that other methods (e.g. the R^2 hierarchical decomposition from Chevan and Sutherland, 1991) provide the same results. For these analyses, the glmnet (Friedman et al., 2010) and relaimpo (Groemping, 2006) R packages are used. Finally, for the statistical significance of the correlations and their differences, we used the *psych* R package (Revelle, 2023) that implements Steiger's test for comparing dependent correlations (Steiger, 1980; Olkin and Finn, 1995). All statistical significance results are provided at the 99 % confidence level. The time series and spatial patterns of the climate modes are as in Pfeffer et al. (2022) (see Figs. 1, 3, and 4 therein).

3 Results

We present the results of the assessment by first analysing the time series and several diagnostics of the basin-averaged manometric sea level. Then, the consistency between the manometric sea level products is addressed; finally, the influence of the climate modes of variability on the manometric sea level variability is analysed. All results presented refer to the 2003–2019 period that is common to the three datasets.

3.1 Manometric sea level time series

The monthly means of the manometric sea level for the three basins considered in this study is shown in Fig. 1, while several diagnostics (trend, seasonal amplitude, interannual variability, and mean uncertainty, i.e. the time-averaged uncertainty, estimated in turn as the ensemble standard deviation for each product according to Sect. 2) are provided in Table 2 for the three datasets considered.

The three basins (Arctic Ocean, North Atlantic Ocean, and the Mediterranean Sea) exhibit different behaviour; GRACE, SLB, and GREP show, however, that there is qualitatively good consistency in all three seas. The Arctic Ocean has a regular periodicity and a large seasonal amplitude with a generally increasing yearly mean signal, except during the first years of the time series (2003–2005). For both GRACE and GREP, the latest years are the ones with the largest manometric sea level, which is reflected in large trends found (3.45 ± 0.57 and $2.45 \pm 0.44\,\mathrm{mm\,yr^{-1}}$, respectively) when compared to the other seas, while the SLB shows a weaker trend.

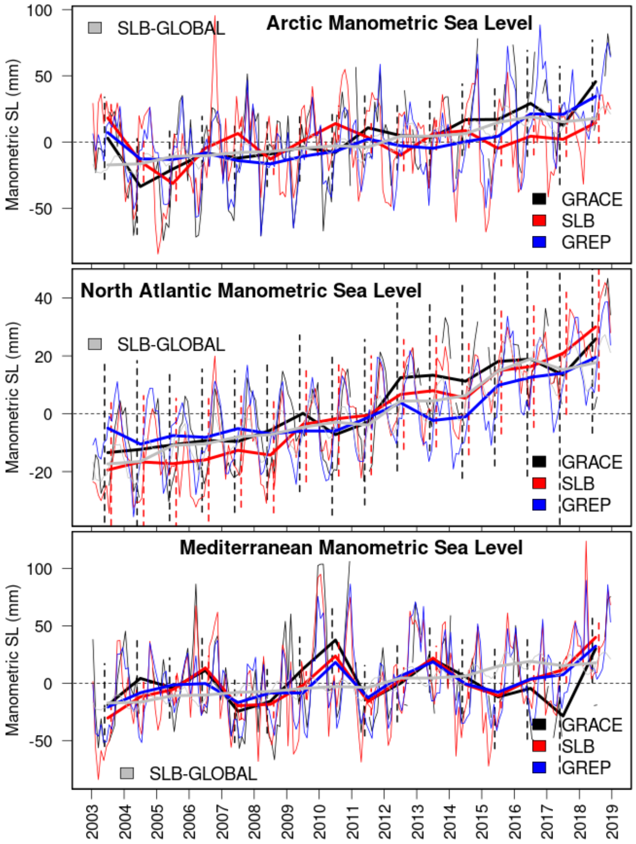

Figure 1. Manometric sea level time series for the Arctic, the Mediterranean, and the North Atlantic basins. Both monthly (thin lines) and yearly (thick lines) means are shown for GRACE, SLB, and GREP. The global barystatic sea level (SLB method) is also added in gray. The North Atlantic Ocean is defined from 0 to 67° N, and the Arctic Ocean from 67° N in the Atlantic Ocean to the Bering Strait. Dashed vertical lines correspond to the yearly uncertainty (for GRACE and SLB only; values for GREP are not shown for sake of clarity, given their underestimated value due to the small ensemble size).

Manometric sea level changes at interannual timescales are very different over the Arctic Ocean than the global ocean (Table 3), meaning that internal dynamics, strait connections, and the sea ice seasonal cycle significantly modulate the regional manometric sea level. Seasonal time series are more largely explained by the global signal for both datasets (38 %–48 %).

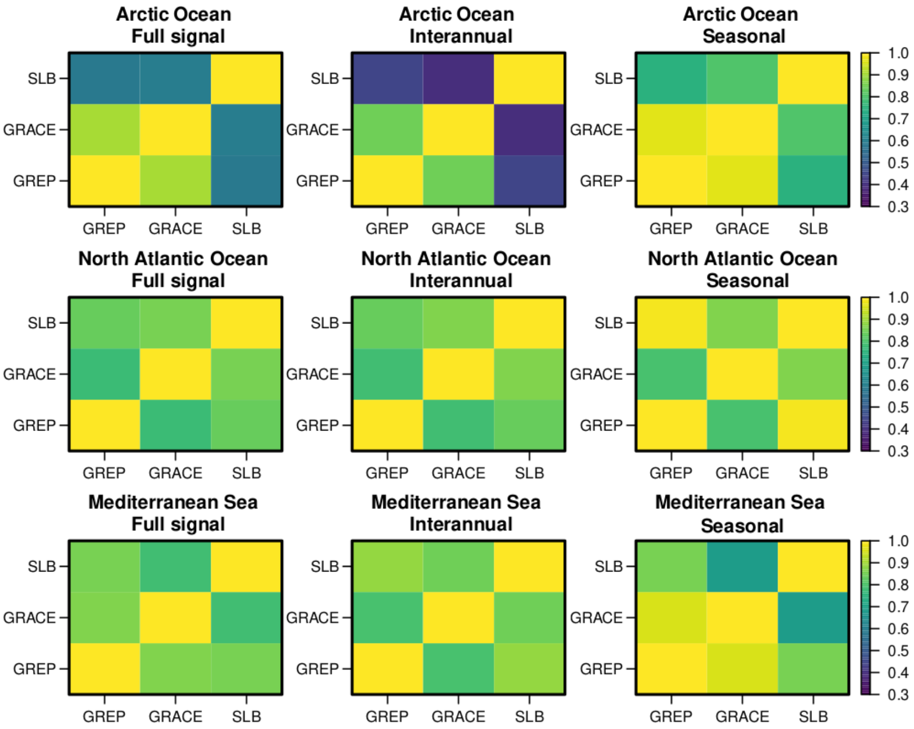

Figure 2. Correlation matrix for the three datasets in the three ocean basins investigated in this study, for the full, the interannual, and the seasonal signals. All values of correlation are statistically significant at the 99 % confidence level. Note that the correlation matrix is symmetric, but all terms are shown for the sake of clarity; note also that the minimum correlation in the palette is 0.3, whereas the minimum correlation across all data shown is 0.39.

Table 2. Manometric sea level diagnostics for the three basins considered in this study, calculated from the three datasets GREP (ensemble mean), GRACE, and SLB. The trend is calculated as a linear fit, with the uncertainty found through bootstrapping. Seasonal amplitude and interannual variability are defined according to Sect. 2.4. Average uncertainty is calculated from the grid point values. For GREP, it is given by the ensemble standard deviation. Units are given in millimetres per year (mm yr^{-1}) for the trend and millimetres (mm) for the other metrics.

Region	Trend			Seasonal amplitude			Interannual variability			Average uncertainty		
	GRACE	SLB	GREP	GRACE	SLB	GREP	GRACE	SLB	GREP	GRACE	SLB	GREP
Arctic Ocean	3.45 ± 0.57	1.09 ± 0.44	2.45 ± 0.44	29.0	26.0	28.7	20.9	22.2	17.6	29.0	12.9	8.5
North Atlantic Ocean	2.67 ± 0.23	3.24 ± 0.16	1.81 ± 0.18	14.2	10.7	14.4	6.0	6.6	6.1	29.9	20.8	8.0
Mediterranean Sea	0.87 ± 0.65	2.44 ± 0.50	1.93 ± 0.46	31.5	25.5	30.0	27.8	29.2	20.0	31.8	11.8	13.1

The North Atlantic manometric sea level signal has a seasonality (10 to 14 mm, depending on the dataset) that is smaller than the other basins, the smallest interannual variability (6.0 to 6.6 mm), and a nearly linearly increasing mean signal that dominates the variability. The percent variance explained by the global barystatic sea level is large (71 % and 79 % for GRACE and SLB, respectively, for the interannual signal), meaning that the North Atlantic largely resembles the global signal. Here, the manometric trend accounts for about 60 %–80 % of the total sea level trend (provided by altimetry), depending on the specific product used.

In the Mediterranean Sea, the interannual variability is the largest (more than 20 mm for all datasets) and does not follow the global barystatic signal (see the low percent variance explained in Table 3), especially for the interannual signal, no matter which dataset is considered. This suggests that the regional water cycle and sea level budget are mostly independent of the global one, and this is ascribed to the role of Gibraltar Strait (see, e.g., Landerer and Volkov, 2013). Trends in the Mediterranean Sea are generally lower than in the other basins and explain about 40 %, on average, of the total sea level trend from altimetry. All the datasets exhibit the largest trends in the western part of the Mediterranean Sea (not shown), although with slightly different patterns. Remarkable peaks of the manometric sea level are visible in 2006, 2010, 2011, and 2018; for these events, GREP tends to underestimate the maxima compared to the other two datasets, likely due to the use of climatological discharge

Table 3. Percent of the regional manometric sea level variance explained by the global barystatic signal (also for the interannual and seasonal signals). The global barystatic signal is shown in Fig. 1 with gray lines.

Region	Monthly time series		Interannual timescale		Seasonal timescale	
	GRACE	SLB	GRACE	SLB	GRACE	SLB
Arctic Ocean	35 %	11 %	25 %	11 %	48 %	38 %
North Atlantic Ocean	56 %	80 %	71 %	79 %	34 %	85 %
Mediterranean Sea	4 %	19 %	1 %	11 %	8 %	37 %

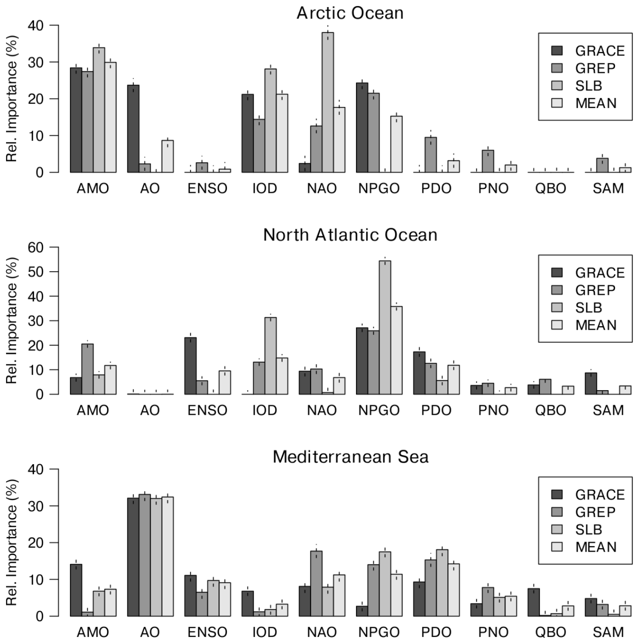

Figure 3. Relative importance (defined in Sect. 2.4) of the selected climate indices for the manometric sea level in the three basins investigated in this study, using the three datasets for GRACE, GREP, and SLB. Also shown is the mean of the relative importance over the three datasets (indicated as MEAN). The acronyms for the climate indices are as follows: AMO is for the Atlantic Multidecadal Oscillation; AO is for the Arctic Oscillation; ENSO is for the multivariate El Niño–Southern Oscillation; IOD is for the Indian Ocean Dipole; NAO is for the North Atlantic Oscillation; NPGO is for the North Pacific Gyre Oscillation; PDO is for the Pacific Decadal Oscillation; PNO is for the Pacific North American Oscillation; QBO is for the quasi-biennial oscillation; SAM is for the Southern Annular Mode. Vertical bars indicate the standard errors of the regression coefficients.

from rivers in the reanalyses and the low resolution at Gibraltar Strait affecting the representation of the Mediterranean inflow.

In terms of the uncertainty (see Table 2 and Fig. 1), the GRACE dataset exhibits the largest mean uncertainty (about 30 mm in all basins), while the uncertainty in SLB ranges from about 12 mm in the Arctic Ocean and the Mediterranean Sea to about 21 mm in the North Atlantic Ocean. GREP uncertainty is the lowest, except in the Mediterranean Sea, where it is comparable to SLB. However, the uncertainty estimates are strongly affected by the ensemble size, which is substantially different across the three datasets (see Sect. 2). Besides, common errors associated, for example, with spatial undersampling, which may be large for the SLB method, will be neglected with the ensemble approach.

3.2 Consistency between time series

The consistency between the three time series is investigated by decomposing the full signal into the interannual and seasonal time series. The correlation matrix for the three temporal scales and the three basins is shown in Fig. 2.

In the North Atlantic Ocean and the Mediterranean Sea, the largest correlations are generally between SLB and GREP. SLB and GREP are not independent due to the use of altimetry and in situ observations in both, so this result likely reflects their dependency. At the interannual timescale, the correlation between GRACE and SLB is slightly larger (but the difference is not statistically significant) than that between GRACE and GREP, suggesting that for these regions SLB might capture the year-to-year variations better than the reanalyses. At the seasonal scale in the Mediterranean Sea, however, the consistency between GRACE and GREP is larger than that between GRACE and SLB (with a statistically significant difference), suggesting that the reanalyses capture the seasonal cycle better than SLB with respect to gravimetry data. For both regions, the high consistency of manometric sea level from reanalyses compared to the two observation-based datasets suggests the good reliability of the GREP ensemble mean in capturing the sea level variations.

In the Arctic Ocean, a large consistency is found between GRACE and GREP; the correlations involving SLB are statistically significantly lower than the others at all timescales (full, interannual, and seasonal) at the 99 % confidence level; this is also visible in Fig. 1, as fluctuations in the SLB time series are not reproduced by the other two datasets. On the one hand, the meridional transports, sea ice modelling, and atmospheric forcing that are implicit in the reanalysis systems are known to be able to shape the Arctic Ocean interannual variability realistically (see, e.g., Mayer et al., 2016, 2019); on the other hand, altimetry and in situ data are poorly sampled in the Arctic Ocean, making it more challenging to apply the SLB approach therein. By separating the total sea level and the steric sea level contributions for the SLB and GREP methods (not shown), we have found good consistency for the total sea level interannual signal (correlation coefficient equal to 0.69) compared to the steric component (0.35); this suggests that the SLB method has problems over the Arctic basin with respect to representing steric sea level variations, possibly due to the poor in situ observational sampling.

3.3 Influence of climate indices on manometric sea level variations

Several climate indices are considered predictors for the manometric sea level in the three basins (Arctic Ocean, North Atlantic Ocean, and the Mediterranean Sea). Their acronyms and meanings are listed in the caption of Fig. 3. The detailed justification for inclusion in the analysis is provided by Han et al. (2017), Cazenave and Moreira (2022), and Pfeffer et al. (2022), among many others. Through representing well-determined atmospheric circulation regimes and internal climate variability, the indices synthesise the water cycle and the atmospheric forcing variability regimes, leading in turn to variations in the regional manometric sea level due to changes in oceanic divergence and freshwater forcing. For instance, the El Niño–Southern Oscillation (ENSO) has a prominent role in modifying precipitation patterns, with obvious implications for the manometric sea level (e.g. Muis et al., 2018); changes in the North Atlantic Oscillation (NAO) modify atmospheric and oceanic transport in North America and Europe, also implying changes in the Mediterranean Sea through modifications and exchanges at Gibraltar and precipitation patterns (Landerer et al., 2013; Storto et al., 2019a). It is beyond the scope of this study to explain all of the possible modes of co-variability, and the interested readers are referred to the specific literature for a broad overview (e.g. Andrew et al., 2006; Peralta-Ferriz et al., 2014; Merrifield and Thompson, 2018; Volkov et al., 2019; Pfeffer et al., 2022). Raw monthly means of the manometric sea level are used in this study to avoid arbitrary filtering affecting the regression results; the climate indices, however, are used with filtering (as in their standard definition).

In the Arctic Ocean, the largest influence is found to be due to the Atlantic Multidecadal Oscillation (AMO), with values ranging from 25 % to 35 %, depending on the dataset. AMO is known to modulate the sea ice interannual variations and the Arctic amplification (Li et al., 2018; Fang et al., 2022), which are both important contributors to the sea level manometric fluctuations, due to the increased melting of land ice and disturbances in atmospheric and ocean circulation that jointly influence the variability in manometric sea levels (see, e.g., Previdi et al., 2021). The IOD (Indian Ocean Dipole), NAO, and NPGO (North Pacific Gyre Oscillation) also significantly affect the Arctic manometric sea level, although the consensus between the datasets varies, and the influence of the IOD is questionable. The Arctic Oscillation is found to be influential when using the GRACE dataset consistently with previous studies (Peralta-Ferriz et al., 2014), although the other datasets show, in general, other preferences.s

The North Atlantic manometric sea level is characterised by the largest impact of NPGO, and this is consistent across all of the datasets. While NPGO explains the variations in the eastern North Pacific Ocean well (Di Lorenzo et al., 2008), its impact on the North Atlantic manometric sea level likely depends on its global- and large-scale influence (Iglesias et al., 2017; Litzow et al., 2020; Pfeffer et al., 2022), which in turn drives, to a large extent, the North Atlantic manometric sea level variability (see Table 3). NPGO accounts for more than 25 % of the North Atlantic manometric sea level variability, peaking at more than 40 % for the SLB dataset. A significant impact in the North Atlantic manometric sea level is also given by variations described by the PDO (Pacific Decadal Oscillation), AMO, and IOD, although for the latter there is a small consistency found across the datasets.

Finally, in the Mediterranean Sea, the largest influence is provided by the Arctic Oscillation (AO), which explains more than 30 % of the manometric sea level covariations for all datasets. AO is an expression of the North Atlantic variability, strictly linked to the NAO and closely linked to the northern European wind circulation (e.g. Ambaum et al., 2001); while these are strictly connected, the regularisation technique used here clearly indicates that AO is a better predictor than NAO for the regional manometric sea level; however, this might be an artefact of the LASSO minimisation that chooses only one among strongly correlated predictors. Other influential climate modes of variability in the Mediterranean Sea are linked to the North Pacific variability, namely the PDO and NPGO, likely due to their effect on the North Atlantic variability.

4 Summary and discussion

In this study, we have focused on the basin-averaged manometric sea level for a few regional basins (Arctic Ocean, North Atlantic Ocean, and the Mediterranean Sea) and from different datasets to investigate the consistency, the emerging climate signals, the differences between the basin characteristics, and the link with the main large-scale modes of variability. These three basins were chosen as part of the focus of the EU Copernicus Marine Service and are large enough to be resolved at the basin scale by the observational and modelling systems used herein, unlike other smaller basins.

To the authors' knowledge, this is the first time that different datasets of manometric sea level from reanalyses, gravimetry, and altimetry (minus in situ data) are compared at the regional level to infer their strengths and weaknesses. The three basins (Arctic Ocean, North Atlantic Ocean, and the Mediterranean Sea) exhibit inherently different features, with the Mediterranean Sea showing, on average over the three products, the largest interannual variability and the smallest trends; the Arctic Ocean shows a large seasonal amplitude and the largest trend, and the North Atlantic Ocean shows a quasi-linear trend, which is very well explained by the global barystatic signal. The three products are found to be in reasonable agreement, with all pairs significantly correlated at both interannual and seasonal timescales. There are, however, non-negligible differences in the quantitative assessment; for instance, GRACE leads to a large trend in the Arctic basin ($3.45 \pm 0.57\,\mathrm{mm\,yr^{-1}}$) which is not reproduced by either GREP or SLB and needs to be investigated in more detail. There is also a trend in the Mediterranean Sea that is smaller than the others.

In the Arctic Ocean, the altimetry minus in situ (SLB) information is generally in less agreement with the other datasets based on correlation scores; this seems to be due to the poor in situ observation sampling on which the SLB approach is based (see the product user manual, PUM; Table 1), which could be alleviated in reanalyses, to some extent, by the atmospheric forcing information and the meridional exchanges. In the Mediterranean Sea, seasonal-scale agreement is also the largest between GRACE and GREP, suggesting in turn that the Copernicus Marine Service global reanalyses can capture the manometric sea level variability in the studied regions.

Finally, a fingerprinting technique based on a regularisation in the regression is used to quantify the influence of several large-scale climate modes of variability in the basin-averaged manometric sea level. In most cases, we found consistency in the results using the three different datasets. The analysis indicates the NPGO (North Pacific Gyre Oscillation), AO (Arctic Oscillation), and AMO (Atlantic Multidecadal Oscillation) to be the most influential modes for the North Atlantic Ocean, the Mediterranean Sea, and the Arctic Ocean, respectively. This is the combined result of the barystatic sea level signature, cross-basin exchanges, and teleconnection patterns, as explained in detail in previous studies (Landerer and Volkov, 2013; Iglesias et al., 2017; Fang et al., 2022). These results are useful as a reference for further fingerprinting technique applications and as a possible tool for statistical prediction of manometric variations.

The results provide a summary of the manometric sea level variability within the three basins investigated here and guide users with respect to the choice of the specific product, depending on the region of interest. The overarching conclusions are that reanalyses, when an ensemble mean of different systems is adopted, provide good performances in all basins; SLB performance is the most affected by observational sampling and thus should be avoided in regions with poorly developed networks; and gravimetry data provide realistic sub-seasonal and interannual variability, although long-term trends are less consistent than other datasets, and the monthly uncertainty is the largest.

Further studies are needed to understand the different behaviour of the datasets for certain aspects (e.g. the overestimation of the Arctic Ocean manometric sea level trend by GRACE or its underestimation in the Mediterranean Sea), namely whether this is due to some intrinsic limitation of the data processing or the different processes implied by the measurement techniques.

Data availability. See Table 1 to access the data through the associated DOIs.

Author contributions. AS designed the analysis and wrote most of the text. GC and AS performed the analysis. JP coordinated the processing of the manometric sea level data from GRACE, revised the paper, and provided many comments on the use of the observation-based datasets and the fingerprinting technique. AB corrected the detail in Sect. 2. All authors contributed with data production and suggestions for improving the study.

Competing interests. The contact author has declared that none of the authors has any competing interests.

Disclaimer. The Copernicus Marine Service offering is regularly updated to ensure it remains at the forefront of user requirements. In this process, some products may undergo replacement or renaming, leading to the removal of certain product IDs from our catalogue. If you have any questions or require assistance regarding these modifications, please feel free to reach out to our user support team for further guidance. They will be able to provide you with the necessary information to address your concerns and find suitable alternatives, maintaining our commitment to delivering top-quality services.

Acknowledgements. The authors thank the OSR8 team (Karina von Schuckmann and Lorena Moreira Mendez) for their coordination efforts and suggestions to improve the quality of the original version of the paper.

Financial support. This work has been supported by the GLORAN-Lot8 and the WAMBOR contracts of the Copernicus Marine Service.

Review statement. This paper was edited by Marta Marcos and reviewed by Don Chambers and two anonymous referees.

References

Ablain, M., Legeais, J. F., Prandi, P., Marcos, M., Fenoglio-Marc, L., Dieng, H. B., Benveniste, J., and Cazenave, A.: Satellite altimetry-based sea level at global and regional scales, Surv. Geophys., 38, 7–31, 2017.

Ambaum, M. H. P., Hoskins, B. J., and Stephenson, D. B.: Arctic Oscillation or North Atlantic Oscillation?, J. Climate, 14, 3495–3507, https://doi.org/10.1175/1520-0442(2001)014<3495:AOONAO>2.0.CO;2, 2001.

Amin, H., Bagherbandi, M., and Sjöberg, L. E.: Quantifying barystatic sea-level change from satellite altimetry, GRACE and Argo observations over 2005–2016, Adv. Space Res., 65, 1922–1940, 2020.

Andrew, J. A. M., Leach, H., and Woodworth, P. L.: The relationships between tropical Atlantic sea level variability and major climate indices, Ocean Dynam., 56, 452–463, https://doi.org/10.1007/s10236-006-0068-z, 2006.

Androsov, A., Boebel, O., Schröter, J., Danilov, S., Macrander, A., and Ivanciu, I.: Ocean bottom pressure variability: Can it be reliably modeled? J. Geophys. Res.-Oceans, 125, e2019JC015469, https://doi.org/10.1029/2019JC015469, 2020.

Barnoud, A., Pfeffer, J., Guérou, A., Frery, M.-L., Siméon, M., Cazenave, A., Chen, J., Llovel, W., Thierry, V., Legeais, J.-F., and Ablain, M.: Contributions of altimetry and Argo to non-closure of the global mean sea level budget since 2016, Geophys. Res. Lett., 48, e2021GL092824, https://doi.org/10.1029/2021gl092824, 2021.

Barnoud, A., Picard, B., Meyssignac, B., Marti, F., Ablain, M., and Roca, R.: Reducing the uncertainty in the satellite altimetry estimates of global mean sea level trends using highly stable water vapor climate data records, J. Geophys. Res.-Oceans, 128, e2022JC019378, https://doi.org/10.1029/2022JC019378, 2023a.

Barnoud, A., Pfeffer, J., Cazenave, A., Fraudeau, R., Rousseau, V., and Ablain, M.: Revisiting the global mean ocean mass budget over 2005–2020, Ocean Sci., 19, 321–334, https://doi.org/10.5194/os-19-321-2023, 2023b.

Camargo, C. M. L., Riva, R. E. M., Hermans, T. H. J., and Slangen, A. B. A.: Trends and uncertainties of mass-driven sea-level change in the satellite altimetry era, Earth Syst. Dynam., 13, 1351–1375, https://doi.org/10.5194/esd-13-1351-2022, 2022.

Caron, L., Ivins, E., Larour, E., Adhikari, S., Nilsson, J., and Blewitt, G.: GIA model statistics for GRACE hydrology, cryosphere, and ocean science, Geophys. Res. Lett., 45, 2203–2212, 2018.

Cazenave, A., and Moreira, L.: Contemporary sea-level changes from global to local scales: a review, P. Math. Phys. Eng. Sci., 25, 478, 20220049, https://doi.org/10.1098/rspa.2022.0049, 2022.

Chang, L., Tang, H., Wang, Q., and Sun, W.: Global thermosteric sea level change contributed by the deep ocean below 2000 m estimated by Argo and CTD data, Earth Planet. Sc. Lett., 524, 115727, https://doi.org/10.1016/j.epsl.2019.115727, 2019.

Cheng, M., Tapley, B. D., and Ries, J. C.: Deceleration in the Earth's oblateness, J. Geophys. Res., 118, 740–747, https://doi.org/10.1002/jgrb.50058, 2013.

Criado-Aldeanueva, F., Soto-Navarro, F. J., and García-Lafuente, J.: Large-scale atmospheric forcing influencing the long-term variability of Mediterranean heat and freshwater budgets: Climatic indices, J. Hydrometeorol., 15, 650–663, 2014.

Cheng, L., Trenberth, K. E., Gruber, N., Abraham, J. P., Fasullo, J. T., Li, G., Mann, M. E., Zhao, X., and Zhu, J.: Improved Estimates of Changes in Upper Ocean Salinity and the Hydrological Cycle, J. Climate, 33, 10357–10381, https://doi.org/10.1175/JCLI-D-20-0366.1, 2020.

Chevan, A. and Sutherland, M.: Hierarchical Partitioning, Am. Stat. 45, 90–96, 1991.

Desportes, C., Garric, G., Régnier, C., Drévillon, M., Parent, L., Drillet, Y., Masina, S., Storto, A., Mirouze, I., Cipollone, A., Zuo, H., Balmaseda, M., Peterson, D., Wood, R., Jackson, L., Mulet, S., Grenier, E., and Gounou, A.: EU Copernicus Marine Service Quality Information Document for the Global Ocean Ensemble Physics Reanalysis, GLOBAL_REANALYSIS_PHY_001_031, Issue 1.1, Mercator Ocean International, https://catalogue.marine.copernicus.eu/documents/QUID/CMEMS-GLO-QUID-001-031.pdf (last access: 24 July 2023), 2022.

Di Lorenzo, E., Schneider, N., Cobb, K. M., Franks, P. J. S., Chhak, K., Miller, A. J., McWilliams, J. C., Bograd, S. J., Arango, H., Curchitser, E., Powell, T. M., and Rivière, P.: North Pacific Gyre Oscillation links ocean climate and ecosystem change, Geophys. Res. Lett., 35, L08607, https://doi.org/10.1029/2007GL032838, 2008.

Efron, B.: Bootstrap methods: Another look at the jackknife, Ann. Stat., 7, 1–26, https://doi.org/10.1214/aos/1176344552, 1979.

EU Copernicus Marine Service Product: Global Ocean Ensemble Physics Reanalysis, Mercator Ocean International [data set], https://doi.org/10.48670/moi-00024, 2022a.

EU Copernicus Marine Service Product: Global Ocean Gridded L 4 Sea Surface Heights And Derived Variables Reprocessed 1993 Ongoing, Mercator Ocean International [data set], https://doi.org/10.48670/moi-00148, 2022b.

Fang, M., Li, X., Chen, H. W., and Chen, D.: Arctic amplification modulated by Atlantic Multidecadal Oscillation and greenhouse forcing on multidecadal to century scales, Nat. Commun., 13, 1865, https://doi.org/10.1038/s41467-022-29523-x, 2022.

Fox-Kemper, B., Hewitt, H. T., Xiao, C., Aðalgeirsdóttir, G., Drijfhout, S. S., Edwards, T. L., N. R. Golledge, M. H., Kopp, R. E., Krinner, G., Mix, A., Notz, D., Nowicki, S., Nurhati, I. S., Ruiz, L., Sallée, J.-B., Slangen, A. B. A., and Yu, Y.: Ocean, Cryosphere and Sea Level Change, in: Climate Change 2021: The Physical Science Basis. Contribution of Working Group I to the Sixth Assessment Report of the Intergovernmental Panel on Climate Change, edited by: Masson-Delmotte, V., Zhai, P., Pirani, A., Connors, S. L., Péan, C., Berger, S., Caud, N., Chen, Y., Goldfarb, L., Gomis, M. I., Huang, M., Leitzell, K., Lonnoy, E., Matthews, J. B. R., Maycock, T. K., Waterfield, T., Yelekçi, O., Yu, R., and Zhou B., Cambridge University Press, Cambridge, United Kingdom and New York, NY, USA, 1211–1362, https://doi.org/10.1017/9781009157896.011, 2021.

Frederikse, T., Riva, R. E. M., and King, M. A.: Ocean bottom deformation due to present-day mass redistribution and its impact on sea level observations, Geophys. Res. Lett., 44, 12306–12314, https://doi.org/10.1002/2017GL075419, 2017.

Frederikse, T., Landerer, F., Caron, L., Adhikari, S., Parkes, D., Humphrey, V. W., Dangendorf, S., Hogarth, P., Zanna, L., Cheng, L., and Wu, Y. H.: The causes of sea-level rise since 1900, Nature, 584, 393–397, https://doi.org/10.1038/s41586-020-2591-3, 2020.

Friedman, J. H., Hastie, T., and Tibshirani, R.: Regularization Paths for Generalized Linear Models via Coordinate Descent, J. Stat. Softw., 33, 1–22, https://doi.org/10.18637/jss.v033.i01, 2010.

Fukumori, I., Wang, O., Fenty, I., Forget, G., Heimbach, P., Ponte, R. M.: ECCO Version 4 Release 4, https://ecco-group.org/docs/v4r4_synopsis.pdf, last access: 7 August 2020.

Good, S. A., Martin, M. J., and Rayner, N. A.: EN4: quality controlled ocean temperature and salinity profiles and monthly objective analyses with uncertainty estimates, J. Geophys. Res.-Oceans, 118, 6704–6716, https://doi.org/10.1002/2013JC009067, 2013.

Gounou, A., Drevillon, M., and Clavier, M.: EU Copernicus Marine Service Product User Manual for the Global Ocean Ensemble Physics Reanalysis, GLOBAL_REANALYSIS_PHY_001_031, Issue 1.1, Mercator Ocean International, https://catalogue.marine.copernicus.eu/documents/PUM/CMEMS-GLO-PUM-001-031.pdf (last access: 24 July 2023), 2022.

Greatbatch, R. J.: A note on the representation of steric sea level in models that conserve volume rather than mass, J. Geophys. Res., 99, 12767–12771, https://doi.org/10.1029/94JC00847, 1994.

Gregory, J. M., Griffies, S. M., Hughes, C. W., Lowe, J. A., Church, J. A., Fukimori, I., Gomez, N., Kopp, R. E., Landerer, F., Cozannet, G. L., Ponte, R. M., Stammer, D., Tamisiea, M. E., and van de Wal, R. S.: Concepts and Terminology for Sea Level: Mean, Variability and Change, Both Local and Global, Surv. Geophys., 40, 1251–1289, https://doi.org/10.1007/s10712-019-09525-z, 2019.

Groemping, U.: Relative Importance for Linear Regression in R: The Package relaimpo, J. Stat. Softw., 17, 1–27, https://doi.org/10.18637/jss.v017.i01, 2006.

Guérou, A., Meyssignac, B., Prandi, P., Ablain, M., Ribes, A., and Bignalet-Cazalet, F.: Current observed global mean sea level rise and acceleration estimated from satellite altimetry and the associated measurement uncertainty, Ocean Sci., 19, 431–451, https://doi.org/10.5194/os-19-431-2023, 2023.

Han, W., Meehl, G. A., Stammer, D., Hu, A., Hamlington, B., Kenigson, J., Palanisamy, H., and Thompson, P.: Spatial Patterns of Sea Level Variability Associated with Natural Internal Climate Modes, Surv. Geophys., 38, 217–250, https://doi.org/10.1007/s10712-016-9386-y, 2017.

Horvath, A., Murböck, M., Pail, R., and Horwath, M.: Decorrelation of GRACE time variable gravity field solutions using full covariance information, Geosciences, 8, 323, https://doi.org/10.3390/geosciences8090323, 2018.

Horwath, M., Gutknecht, B. D., Cazenave, A., Palanisamy, H. K., Marti, F., Marzeion, B., Paul, F., Le Bris, R., Hogg, A. E., Otosaka, I., Shepherd, A., Döll, P., Cáceres, D., Müller Schmied, H., Johannessen, J. A., Nilsen, J. E. Ø., Raj, R. P., Forsberg, R., Sandberg Sørensen, L., Barletta, V. R., Simonsen, S. B., Knudsen, P., Andersen, O. B., Ranndal, H., Rose, S. K., Merchant, C. J., Macintosh, C. R., von Schuckmann, K., Novotny, K., Groh, A., Restano, M., and Benveniste, J.: Global sea-level budget and ocean-mass budget, with a focus on advanced data products and uncertainty characterisation, Earth Syst. Sci. Data, 14, 411–447, https://doi.org/10.5194/essd-14-411-2022, 2022.

Hughes, C. W., Williams, J., Blaker, A., Coward, A., and Stepanov, V.: A window on the deep ocean: The special value of ocean bottom pressure for monitoring the large-scale, deep-ocean circulation, Prog. Oceanogr., 161, 19–46, https://doi.org/10.1016/j.pocean.2018.01.011, 2018.

Iglesias, I., Lorenzo, M. N., Lázaro, C., Fernandes, M. J., and Bastos, L.: Sea level anomaly in the North Atlantic and seas around Europe: Long-term variability and response to North Atlantic teleconnection patterns, Sci. Total Environ., 609, 861–874, 2017.

Ishii, M., Kimoto, M., Sakamoto, K., and Iwasaki, S. I.: Steric sea level changes estimated from historical ocean subsurface temperature and salinity analyses, J. Oceanogr., 62, 155–170, 2006.

Köhl, A., Stammer, D., and Cornuelle, B.: Interannual to Decadal Changes in the ECCO Global Synthesis, J. Phys. Oceanogr., 37, 313–337, 2007.

Köhl, A., Siegismund, F., and Stammer, D.: Impact of assimilating bottom pressure anomalies from GRACE on ocean circulation estimates, J. Geophys. Res., 117, C04032, https://doi.org/10.1029/2011JC007623, 2012.

Kusche, J., Schmidt, R., Petrovic, S., and Rietbroek, R.: Decorrelated GRACE time-variable gravity solutions by GFZ, and their validation using a hydrological model, J. Geodesy, 83, 903–913, https://doi.org/10.1007/s00190-009-0308-3, 2009.

Landerer, F. W. and Volkov, D. L.: The anatomy of recent large sea level fluctuations in the Mediterranean Sea, Geophys. Res. Lett., 40, 553–557, https://doi.org/10.1002/grl.50140, 2013.

Landerer, F. W., Flechtner, F. M., Save, H., Webb, F. H., Bandikova, T., Bertiger, W. I., Bettadpur, S. V., Byun, S. H., Dahle, C., Dobslaw, H., and Fahnestock, E.: Extending the global mass change data record: GRACE Follow-On instrument and science data performance, Geophys. Res. Lett., 47, e2020GL088306, https://doi.org/10.1029/2020GL088306, 2020.

Lavergne, T., Sørensen, A. M., Kern, S., Tonboe, R., Notz, D., Aaboe, S., Bell, L., Dybkjær, G., Eastwood, S., Gabarro, C., Heygster, G., Killie, M. A., Brandt Kreiner, M., Lavelle, J., Saldo, R., Sandven, S., and Pedersen, L. T.: Version 2 of the EUMETSAT OSI SAF and ESA CCI sea-ice concentration climate data records, The Cryosphere, 13, 49–78, https://doi.org/10.5194/tc-13-49-2019, 2019.

Legeais, J.-F., Meyssignac, B., Faugère, Y., Guerou, A., Ablain, M., Pujol, M.-I., Dufau, C., and Dibarboure G: Copernicus Sea Level Space Observations: A Basis for Assessing Mitigation and Developing Adaptation Strategies to Sea Level Rise, Front. Mar. Sci., 8, 704721, https://doi.org/10.3389/fmars.2021.704721, 2021.

Lemoine, J.-M. and Reinquin, F.: Processing of SLR Observations at CNES, Newsletter EGSIEM, 3 pp., http://www.egsiem.eu/images/Newsletters/EGSIEM_newsletter_no10.pdf (last access: 10 September 2024), 2017.

Li, F., Orsolini, Y. J., Wang, H., Gao, Y., and He, S.: Atlantic multidecadal oscillation modulates the impacts of Arctic sea ice decline, Geophys. Res. Lett., 45, 2497–2506, https://doi.org/10.1002/2017GL076210, 2018.

Litzow, M. A., Malick, M. J., Bond, N. A., Cunningham, C. J., Gosselin, J. L., and Ward, E. J.: Quantifying a novel climate through changes in PDO-climate and PDO-salmon relationships, Geophys. Res. Lett., 47, e2020GL087972, https://doi.org/10.1029/2020GL087972, 2020.

Loomis, B. D., Rachlin, K. E., and Luthcke, S. B.: Improved Earth oblateness rate reveals increased ice sheet losses and mass-driven sea level rise, Geophys. Res. Lett., 46, 6910–6917, https://doi.org/10.1029/2019GL082929, 2019.

Madec G. and The NEMO System Team: NEMO ocean engine, note Du pole de modélisation (Paris, France: Institut Pierre-Simon Laplace), Zenodo [code], https://doi.org/10.5281/zenodo.3248739, 2017.

Magellium/LEGOS: Barystatic and manometric sea level changes from GRACE and GRACE-FO (Version 4) [NetCDF], CNES [data set], https://doi.org/10.24400/527896/A01-2023.011, 2023a.

Magellium/LEGOS: Barystatic and manometric sea level changes from a sea level budget approach (Version 2) [NetCDF], CNES [data set], https://doi.org/10.24400/527896/A01-2023.012, 2023b.

Marcos, M.: Ocean bottom pressure variability in the Mediterranean Sea and its relationship with sea level from a numerical mode, Global Planet. Change, 124, 10–21, 2015.

Mayer, M., Haimberger, L., Pietschnig, M., and Storto, A.: Facets of Arctic energy accumulation based on observations and reanalyses 2000–2015, Geophys. Res. Lett., 43, 10420–10429, https://doi.org/10.1002/2016GL070557, 2016.

Mayer, M., Tietsche, S., Haimberger, L., Tsubouchi, T., Mayer, J., and Zuo, H.: An Improved Estimate of the Coupled Arctic Energy Budget, J. Climate, 32, 7915–7934, https://doi.org/10.1175/JCLI-D-19-0233.1, 2019.

Merrifield, M. A. and Thompson, P. R.: Interdecadal sea level variations in the Pacific: Distinctions between the tropics and extratropics, Geophys. Res. Lett., 45, 6604–6610, 2018.

Muis, S., Haigh, I. D., Guimarães Nobre, G., Aerts, J. C. J. H., and Ward, P. J.: Influence of El Niño-Southern Oscillation on global coastal flooding, Earth's Future, 6, 1311–1322, https://doi.org/10.1029/2018EF000909, 2018.

Olkin, I. and Finn, J. D.: Correlations redux, Psychol. Bull., 118, 155–164, https://doi.org/10.1037/0033-2909.118.1.155, 1995.

Oppenheimer, M., Abdelgawad, A., Hay, J., Glavovic, B., Cai, R., Marzeion, B., Hinkel, J., Cifuentes-Jara, M., Meyssignac, B., Van De Wal, R., DeConto, R., Sebesvari, Z., Magnan, A., and Ghosh, Hay, T. J., Isla, F., Marzeion, B., Meyssignac, B., and Sebesvari, Z.: Sea Level Rise and Implications for Low-Lying Islands, Coasts and Communities, in: IPCC Special Report on the Ocean and Cryosphere in a Changing Climate, edited by: Pörtner, H.-O., Roberts, D. C., Masson-Delmotte, V., Zhai, P., Tignor, M., Poloczanska, E., Mintenbeck, K., Alegría, A., Nicolai, M., Okem, A., Petzold, J., Rama, B., Weyer, N. M., Cambridge University Press, Cambridge, UK and New York, NY, USA, 321–445, https://doi.org/10.1017/9781009157964.006, 2019.

Peltier, W. R.: Global Glacial Isostasy and the Surface of the Ice-Age Earth: The ICE-5G (VM2) Model and GRACE, Annu. Rev. Earth Pl. Sc., 32, 111–149, 2004.

Peltier, W. R., Argus, D. F., and Drummond, R.: Space geodesy constrains ice age terminal deglaciation: the global ICE-6GC (VM5a) model, J. Geophys. Res., 120, 450–487, 2015.

Peralta-Ferriz, C., Morison, J. H., Wallace, J. M., Bonin, J. A., and Zhang, J.: Arctic Ocean Circulation Patterns Revealed by GRACE, J. Climate, 27, 1445–1468, https://doi.org/10.1175/JCLI-D-13-00013.1, 2014.

Pfeffer, J., Cazenave, A., and Barnoud, A.: Analysis of the interannual variability in satellite gravity solutions: detection of climate modes fingerprints in water mass displacements across continents and oceans, Clim. Dynam., 58, 1065–1084, https://doi.org/10.1007/s00382-021-05953-z, 2022.

Prandi, P., Meyssignac, B., Ablain, M., Spada, G., Ribes, A., and Benveniste, J.: Local sea level trends, accelerations and uncertainties over 1993–2019, Sci. Data, 8, 1, https://doi.org/10.1038/s41597-020-00786-7, 2021.

Previdi, M., Smith, K. L., and Polvani, L. M.: Arctic amplification of climate change: a review of underlying mechanisms, Environ. Res. Lett., 16, 093003, https://doi.org/10.1088/1748-9326/ac1c29, 2021.

Pujol, M.-I.: EU Copernicus Marine Service Product User Manual for the For Sea Level Altimeter products, Issue 7.0, Mercator Ocean International, https://catalogue.marine.copernicus.eu/documents/PUM/CMEMS-SL-PUM-008-032-068.pdf (last access: 24 July 2023), 2022.

Pujol, M.-I., Taburet, G., and SL-TAC team: EU Copernicus Marine Service Quality Information Document for the Sea Level TAC – DUACS products, Issue 8.2, Mercator Ocean International, https://catalogue.marine.copernicus.eu/documents/QUID/CMEMS-SL-QUID-008-032-068.pdf (last access: 24 July 2023), 2022.

Revelle, W.: Psych: Procedures for Psychological, Psychometric, and Personality Research, R package version 2.3.6, Northwestern University, Evanston, Illinois [code], https://CRAN.R-project.org/package=psych (last access: 27 June 2024), 2023.

Schindelegger, M., Harker, A. A., Ponte, R. M., Dobslaw, H., and Salstein, D. A.: Convergence of daily GRACE solutions and models of submonthly ocean bottom pressure variability, J. Geophys. Res.-Oceans, 126, e2020JC017031, https://doi.org/10.1029/2020JC017031, 2021.

Steiger, J. H.: Tests for comparing elements of a correlation matrix, Psychol. Bull., 87, 245–251, 1980.

Storto, A. and Yang, C.: Acceleration of the ocean warming from 1961 to 2022 unveiled by large-ensemble reanalyses, Nat. Commun., 15, 545, https://doi.org/10.1038/s41467-024-44749-7, 2024.

Storto, A., Dobricic, S., Masina, S., and Di Pietro, P.: Assimilating Along-Track Altimetric Observations through Local Hydrostatic Adjustment in a Global Ocean Variational Assimilation System, Mon. Weather Rev., 139, 738–754, https://doi.org/10.1175/2010MWR3350.1, 2011.

Storto A, Masina, S., Balmaseda, M., Guinehut, S., Xue, Y., Szekely, T., Fukumori, I., Forget, G., Chang, Y.-S., Good, S. A., Köhl, A., Vernieres, G., Ferry, N., Peterson, K. A., Behringer, D., Ishii, M., Masuda, S., Fujii, Y., Toyoda, T., Yin, Y., Valdivieso, M., Barnier, B., Boyer, T., Lee, T., Gourrion, J., Wang, O., Heimbach, P., Rosati, A., Kovach, R., Hernandez, F., Martin, M. J., Kamachi, M., Kuragano, T., Mogensen, K., Alves, O., Haines, K., and Wang, X.: Steric sea level variability (1993–2010) in an ensemble of ocean reanalyses and objective analyses, Clim. Dynam., 49, 709–729, https://doi.org/10.1007/s00382-015-2554-9, 2017.

Storto, A., Bonaduce, A., Feng, X., and Yang, C.: Steric Sea Level Changes from Ocean Reanalyses at Global and Regional Scales, Water, 11, 1987, https://doi.org/10.3390/w11101987, 2019a.

Storto, A., Alvera-Azcárate, A., Balmaseda, M. A., Barth, A., Chevallier, M., Counillon, F., Domingues, C. M., Drevillon, M., Drillet, Y., Forget, G., Garric, G., Haines, K., Hernandez, F., Iovino, D., Jackson, L. C., Lellouche, J.-M., Masina, S., Mayer, M., Oke, P. R., Penny, S. G., Peterson, K. A., Yang, C., and Zuo, H.: Ocean Reanalyses: Recent Advances and Unsolved Challenges, Front. Mar. Sci., 6, 418, https://doi.org/10.3389/fmars.2019.00418, 2019b.

Storto, A., Masina, S., Simoncelli, S., Iovino, D., Cipollone, A., Drevillon, M., Drillet, Y., von Schuckman, K., Parent, L., Garric, G., Greiner, E., Desportes, C., Zuo, H., Balmaseda, M., and Peterson, K. A.: The added value of the multi-system spread information for ocean heat content and steric sea level investigations in the CMEMS GREP ensemble reanalysis product, Clim. Dynam., 53, 287–312, https://doi.org/10.1007/s00382-018-4585-5, 2019c.

Storto, A., Cheng, L., and Yang, C.: Revisiting the 2003–18 Deep Ocean Warming through Multiplatform Analysis of the Global Energy Budget, J. Climate, 35, 4701–4717, https://doi.org/10.1175/JCLI-D-21-0726.1, 2022.

Sun, Y., Ditmar, P., and Riva, R.: Observed changes in the Earth's dynamic oblateness from GRACE data and geophysical models, J. Geod., 90, 81–89, https://doi.org/10.1007/s00190-015-0852-y, 2016.

Tapley, B. D., Bettadpur, S., Ries, J. C., Thompson, P. F., and Watkins, M. M.: GRACE measurements of mass variability in the Earth system, Science, 305, 503–505, https://doi.org/10.1126/science.1099192, 2004.

Tibshirani, R.: Regression shrinkage and selection via the lasso, J. Roy. Stat. Soc. B, 58, 267–288, 1996.

Tibshirani, R.: The LASSO method for variable selection in the Cox model, Statist. Med., 16, 385-395, https://doi.org/10.1002/(SICI)1097-0258(19970228)16:4<385::AID-SIM380>3.0.CO;2-3, 1997.

Tsimplis, M. N. and Josey, S. A.: Forcing of the Mediterranean Sea by atmospheric oscillations over the North Atlantic, Geophys. Res. Lett., 28, 803–806, https://doi.org/10.1029/2000GL012098, 2001.

Volkov, D. L., Baringer, M., Smeed, D., Johns, W., and Landerer, F. W.: Teleconnection between the Atlantic Meridional Overturning Circulation and Sea Level in the Mediterranean Sea, J. Climate, 32, 935–955, https://doi.org/10.1175/JCLI-D-18-0474.1, 2019.

Wong, A. P. S., Wijffels, S. E., Riser, S. C., Pouliquen, S., Hosoda, S., Roemmich, D., Gilson, J., Johnson, G. C., Martini, K., Murphy, D. J., Scanderbeg, M., Bhaskar, T. V. S. U., Buck, J. J. H., Merceur, F., Carval, T., Maze, G., Cabanes, C., André, X., Poffa, N., Yashayaev, I., Barker, P. M., Guinehut, S., Belbéoch, M., Ignaszewski, M., Baringer, M. O., Schmid, C., Lyman, J. M., McTaggart, K. E., Purkey, S. G., Zilberman, N., Alkire, M. B., Swift, D., Owens, W. B., Jayne, S. R., Hersh, C., Robbins, P., West-Mack, D., Bahr, F., Yoshida, S., Sutton, P. J. H., Cancouët, R., Coatanoan, C., Dobbler, D., Juan, A. G., Gourrion, J., Kolodziejczyk, N., Bernard, V., Bourlès, B., Claustre, H., D'Ortenzio, F., Le Reste, S., Le Traon, P.-Y., Rannou, J.-P., Saout-Grit, C., Speich, S., Thierry, V., Verbrugge, N., Angel-Benavides, I. M., Klein, B., Notarstefano, G., Poulain, P.-M., Vélez-Belchí, P., Suga, T., Ando, K., Iwasaska, N., Kobayashi, T., Masuda, S., Oka, E., Sato, K., Nakamura, T., Sato, K., Takatsuki, Y., Yoshida, T., Cowley, R., Lovell, J. L., Oke, P. R., van Wijk, E. M., Carse, F., Donnelly, M., Gould, W. J., Gowers, K., King, B. A., Loch, S. G., Mowat, M., Turton, J., Rama Rao, E. P., Ravichandran, M., Freeland, H. J., Gaboury, I., Gilbert, D., Greenan, B. J. W., Ouellet, M., Ross, T., Tran, A., Dong, M., Liu, Z., Xu, J., Kang, K., Jo, H., Kim, S.-D., and Park, H.-M.: Argo Data 1999–2019: Two Million Temperature-Salinity Profiles and Subsurface Velocity Observations From a Global Array of Profiling Floats, Front. Mar. Sci., 7, 700, https://doi.org/10.3389/fmars.2020.00700, 2020.

State Planet, 4-osr8, 13, 2024
https://doi.org/10.5194/sp-4-osr8-13-2024

Forecasting the Mediterranean Sea marine heatwave of summer 2022

Ronan McAdam, Giulia Bonino, Emanuela Clementi, and Simona Masina

CMCC Foundation – Euro-Mediterranean Center on Climate Change, Bologna, Italy

Correspondence: Ronan McAdam (ronan.mcadam@cmcc.it)

Received: 24 July 2023 – Discussion started: 28 August 2023
Revised: 11 January 2024 – Accepted: 6 February 2024 – Published: 30 September 2024

Abstract. Early warning of marine heatwaves requires short-term forecasts to provide precise information on timings, local-scale coverage, and intensities of coming events. Here, we describe our successful efforts to track the onset, peak, and decay of the Mediterranean Sea marine heatwave of summer 2022 with the Copernicus MedFS short-term (10 d) forecast system. First, we show that the 2022 event eclipses the economically and ecologically damaging event of 2003 in terms of marine heatwave (MHW) activity (a measure of intensity and duration). Forecasts of MHW area and activity provide a means of basin-wide validation, highlighting the capability of MedFS to capture regional behaviour. On local scales, we found that the MHW occurrence in the Ligurian Sea and Gulf of Taranto, two regions of economic and ecological importance, was also reliably forecast. Encouragingly, we note that the forecast has demonstrated skill in capturing not just the season-long MHW cycle but also breaks in MHW persistence and abrupt changes in local activity. Subseasonal forecasts do not yet demonstrate the capacity to predict MHW response to short-lived weather patterns, but this study confirms that short-term forecasts, at least in the Mediterranean Sea, can fill this gap.

1 Introduction

Disease outbreaks, mass mortality events, and the redistribution of species induced by marine heatwaves (MHWs) lead to economic losses to fisheries and aquaculture farms, as well as hampering conservation efforts (Barbeaux et al., 2020; Smith et al., 2021; Garrabou et al., 2022; Smith et al., 2023). The need to prepare for and mitigate these MHW-induced impacts has driven developments in understanding the drivers and predictability of MHWs (Holbrook et al., 2019; Rodrigues et al., 2019; Amaya et al., 2020; Sen Gupta et al., 2020; Li et al., 2020; Schlegel et al., 2021) and in quantifying the skill of forecasts of MHWs (Benthuysen et al., 2021; Jacox et al., 2022; McAdam et al., 2023). The Mediterranean Sea is a particular "hot spot" for MHWs, with much literature documenting the increases in intensity, duration, frequency, and impacts (Darmaraki et al., 2019; Ibrahim et al., 2021; Juza et al., 2022; Dayan et al., 2023). Despite this, there is currently less information on forecasting capability and event predictability in the Mediterranean region than in others (e.g. the North Pacific: Jacox et al., 2019; de Boisesson et al., 2022). With marine services projected to play an ever-increasing role in global sustainability and economic security (Rayner et al., 2019), early-warning systems of heat extremes can aid their planning and day-to-day management (Hartog et al., 2023).

While interannual variability of MHW occurrence and characteristics is derived from ocean warming and preconditioning (de Boisesson et al., 2022), ENSO (Jacox et al., 2022), and atmospheric teleconnections (e.g. Rossby wave trains; Rodrigues et al., 2019), short-lived atmospheric processes and weather systems can disrupt MHW persistence or halt their continuation completely (Benthuysen et al., 2021). The definition of MHWs assumes persistent conditions are harmful to marine life if the duration is 5 d or longer (Hobday et al., 2016), although this number is quite arbitrary and in principle should be species-dependent. The average duration of MHWs across most of the global ocean, as well as in the Mediterranean Sea, falls within the definition of short-term forecasting (< 2 weeks) (Oliver et al., 2021; Dayan et

Published by Copernicus Publications.

Table 1. Product table.

Product ref. no	Product ID and type	Data access	Documentation
1	SST_MED_SST_L4_REP_OBSERVATIONS_010_021; Satellite observations	EU Copernicus Marine Service Product (2023a)	PUM: Pisano et al. (2023a) QUID: Pisano et al. (2023b)
2	MEDSEA_ANALYSISFORECAST_PHY_006_013; Numerical models	EU Copernicus Marine Service Product (2023b)	PUM: Lecci et al. (2023) QUID: Goglio et al. (2023)
3	MED_MULTIYEAR_PHYS_006_004; Numerical models	EU Copernicus Marine Service Product (2022)	PUM: Lecci et al. (2022) QUID: Escudier et al. (2022)
4	ECMWF Integrated Forecast System (IFS) Forecast & Analysis	Copernicus Climate Changes Service	https://www.ecmwf.int/en/forecasts/datasets/set-i#I-i-a_fc (last access: 13 February 2022)
5	ERA5	Copernicus Climate Changes Service	Hersbach et al. (2023)

al., 2023). A short-term view of MHWs is therefore crucial to understanding their predictability and their impacts.

Short-term forecasting of MHWs has a range of potential roles in marine activities. While some contingency plans for extreme heat events in the aquaculture and fishing industries require several months notice (e.g. relocating or switching species), others should be performed at the latest possible moment in order to avoid or minimize losses (e.g. early harvesting or cooling of farm water) (Holsman et al., 2019; Galappaththi et al., 2020). In these cases, accurate information on daily timescales is crucial. Short-term forecasts are also useful for marine protected areas (MPAs), allowing them to prepare to monitor ecosystem damage (e.g. coral bleaching) and recovery, which in turn helps assess the effectiveness of their conservation efforts (McLeod et al., 2009). Forecasts of SST can also, in theory, be coupled to distribution models to forecast changes in species habitat for highly mobile species (Abrahms et al., 2019). “Early warnings” are a key means of climate resilience for marine services (Galappaththi et al., 2020); an assessment of their ability to track MHWs will contribute to further uptake by these services and unlock potential socio-economic benefits.

During the summer of 2022, the Copernicus Marine Service Mediterranean Physical Forecasting system (MedFS) was employed to monitor and forecast sea surface temperature (SST) increases which eventually evolved into a record-breaking MHW for the region. MedFS has already demonstrated skill in detecting past extreme events in the Mediterranean Sea: the “aqua alta” flooding in Venice in 2019 (Giesen et al., 2021), Medicane Ianos (Clementi et al., 2022), and Storm Gloria (Álvarez-Fanjul et al., 2022) in 2020 provides evidence that the forecast system has the ability to capture a wide range of concurrent conditions (e.g. high surface air temperatures, moisture, atmospheric instability for medicanes; Cavicchia et al., 2014). Here, we provide a basin-wide description of the event and demonstrate the ability of MedFS to accurately predict many facets of the event (e.g. the onset, spread, persistence, and decay). First, we introduce the high-resolution regional forecast system and the satellite-derived SST data used to identify MHWs. Then, the record-breaking characteristics (intensity, geographic extent) of the 2022 event are described. We demonstrate the system’s ability to predict the MHW spread across the basin and daily temperature variability in regions of key economic and ecological importance. Finally, we explore the potential role of short-term forecasting in the early warning of MHWs compared to other forecasting timescales.

2 Dataset and methods

Here, MHWs are detected with a 0.05° resolution reprocessing of a blend of satellite-derived products provided by the ESA Climate Change Initiative (CCI) and the Copernicus Climate Change Service (C3S) initiatives, including AVHRR Pathfinder dataset version 5.3 to increase the input observation coverage (Table 1, product ref. no. 1). The dataset provides daily SST of the Mediterranean Sea from 1 January 1982 to the present (currently up to 6 months before real time).

The Mediterranean Near Real Time Analysis and Forecast is a 3D coupled hydrodynamic–wave modelling system implemented at $1/24°$ (~ 4 km) horizontal spatial resolution, which produces analysis and 10 d forecasts of the main ocean essential variables (Table 1, product ref. no. 2). The analysis system assimilates satellite sea level anomalies as well as in situ temperature and salinity observations and nudges SST towards an ultrahigh-resolution satellite product. The same model framework is used to provide a multi-decadal reanalysis of the ocean, extending from 1987 to the present (Table 1, product ref. no. 3). Forecasts are made daily; once a week (on Tuesdays) an analysis is used to initialize forecasts, while on other days a hindcast is used. A schematic of the provision of forecast and analysis data is found in the Quality Information Document (QUID) and Product User Manual (PUM) of the product.

Forecasts of 2 m temperature (T2M) and wind speed are obtained from the European Centre for Medium-Range Weather Forecasts (ECMWF) operational forecast and analysis (Table 1, product ref. no. 4) distributed by the Italian National Meteorological Service (USAM/CNMA). Variables are available at 1-hourly resolution for the first 3 d of forecast, 3-hourly for the following 3 d, and 6-hourly for the following 4 d. The horizontal resolution is 0.1°. The T2M anomaly is calculated using the same variables in the ERA5 reanalysis over the period 1987–2021.

MHWs are defined as SSTs which persist above the 90th percentile for 5 d or longer (Hobday et al., 2016). Here, the 90th percentile threshold corresponds to the 33-year baseline period of 1987–2021 calculated individually for satellite-derived and model-derived data and smoothed with an 11 d moving window. MHWs in MedFS are defined relative to the climatology of the physical reanalysis. Although there are benefits of detrending SST prior to detecting MHWs (Amaya et al., 2023), we chose not to detrend in order to present the true values of temperature because they are of more relevance to species impacts (e.g. Galli et al., 2017).

We use the MHW activity as a means to describe the event on a basin scale and to validate the forecast ability to capture the spatial scale of the event. Previously, activity has been defined as the product of event intensity, duration, and area over a target period (Simon et al., 2022). Here, in order to study basin-wide spread at daily resolution, we define activity as the sum of the intensity over the area undergoing an MHW in the Mediterranean Basin. We assume that all MHW activity in the basin corresponds to the same event, unlike more novel methods of MHW tracking which employ spatial clustering (Bonino et al., 2023). Nonetheless, the activity metric used here identifies very similar phases of MHW activity during the 2003 event as the more advanced clustering method (Fig. 1a; Bonino et al., 2023).

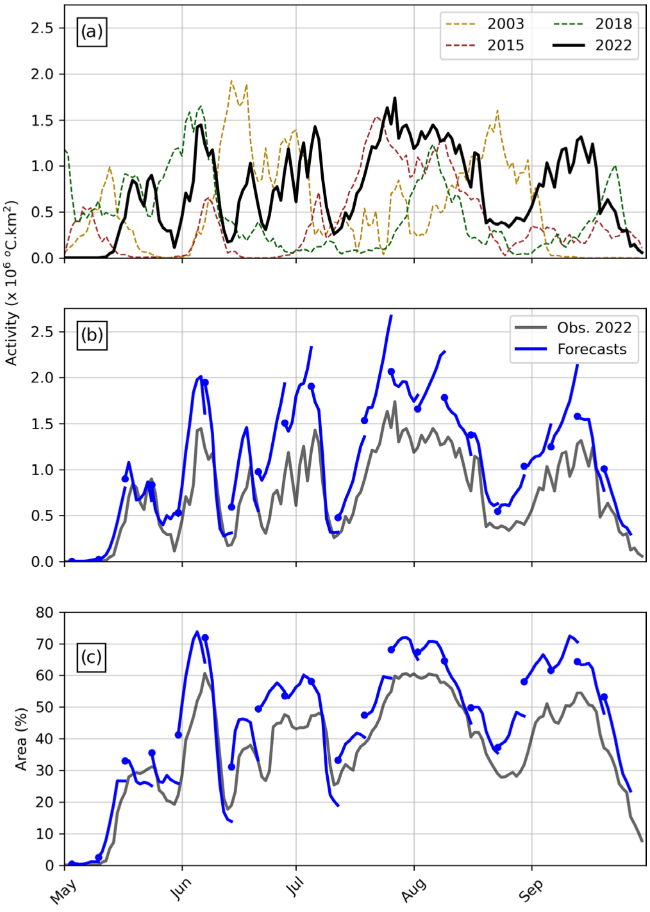

Figure 1. MHW activity across the Mediterranean Sea. **(a)** MHW activity defined by reprocessed satellite observations for 2022 and the 3 previous record years according to Simon et al. (2022). **(b)** Comparison between satellite observations and forecasts of 2022 MHW activity. **(c)** Area of the Mediterranean Sea experiencing an MHW (as a percentage of total basin area). Activity is defined as the sum of the intensity over the area undergoing an MHW. Shown here are the first 8 d of forecasts initiated on Tuesdays. Forecast start dates are shown by the blue dots.

3 Results

First, we describe the event on a basin scale using satellite observations. We remind the reader that references to specific dates are for indication only, as the precise timings of peaks and onsets may differ when using different datasets and climatologies. In 2022, the onset of summer MHW conditions began in mid-May; by 23 May, 35 % of the area of the Mediterranean Sea was already experiencing MHW conditions (Fig. 1c). Maps of temperature anomaly confirm that the onset occurred mostly in the western regions and the Adriatic Sea (Fig. 2a). The geographic extent of MHW extended into the central and eastern parts of the basin (e.g. Fig. 2b), and MHW area remained above a third of the total basin area until the decay at the end of September. Peak area (70 %) was reached on 6 June, while notable peaks of activity occurred later on 29 June, 6 July, and 27 July (Fig. 1a). The peak temperature anomaly of 6.45 °C (above the 1987–2019 average) was reached in the Gulf of Lion on 18 July.

Prior to 2022, the MHWs of the summers of 2003, 2015, and 2018 had been found to have the highest activities on record (using a slightly different definition of activity, but which is still based on intensity and duration; Simon et al., 2022). Here, we find that the activity in 2022 clearly eclipses that of 2015 and 2018 in terms of both maxima and persistence of activity (Fig. 1a). Though the summer of 2003 reached similarly high peaks of activity (twice, in mid-June and at the end of August), the total activity during the summer (defined as the area under the curve) is lower (82×10^6 °C km^2) than for 2022 (139×10^6 °C km^2). While

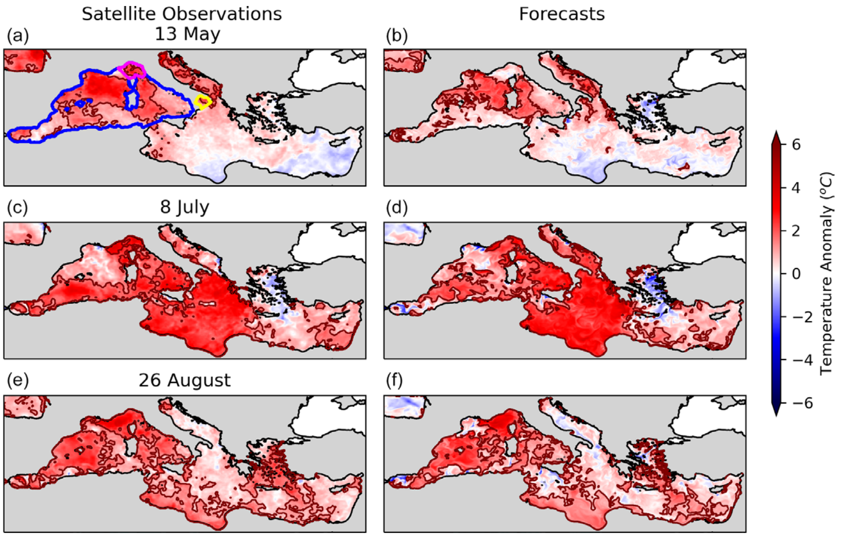

Figure 2. Snapshots of SST anomalies and MHW occurrence during the different stages of the 2022 MHW. **(a, c, e)** Reprocessed satellite observations. **(b, d, f)** Forecasts with a lead time of 4 d. Areas in which SST is above the 90th percentile threshold are indicated by the dark red contour. The day of 13 May highlights the MHW onset, 9 July highlights the peak activity, and 26 August highlights the (first) decay. Regions used in Figs. 3 and 4 are highlighted: Ligurian Sea (magenta), Gulf of Taranto (yellow), and the western Mediterranean (blue).

in 2003 the MHW activity returned to zero in late May and mid-July, in 2022 it persisted throughout the summer above at least 0.5 °C km^2 each day. Using the total activity as a measure, the summer of 2022 now holds the record for MHW activity.

Using the MHW activity provides an efficient, if not complete, means of validating MedFS on the basin scale. It is important to remember that activity time series cannot identify where and when MHWs are occurring (we study forecast ability in specific regions later). Here, we show both the activity (Fig. 1b) and the area (Fig. 1c) predicted to infer whether forecast inaccuracies are caused by an inability to capture the geographic extent or the temperature intensity. Overall, we find that MedFS was able to forecast the evolution of basin-wide MHW activity (Fig. 1b). In particular, we highlight the accurate predictions of the timings of the May onset, the various peaks throughout the summer, the two stages of the decay, and the September rebound. On several occasions, MHW activity rapidly increases, often doubling or tripling over the period of less than a week; such increases in activity are predicted by the forecasts in mid-May, early June, mid-June (twice), and mid-July. Timings of declines in activity are also correctly forecast on all occasions, in some cases even with lead times of 5 d or more (e.g. early June). Similar capabilities are found for the forecasts of the area of MHW conditions. Ability to capture both the activity and the area implies accuracy in capturing the intensity as well, although this analysis does not yet determine the geographic distribution of MHW intensity.

There are indeed forecast inaccuracies to highlight. Firstly, there are instances of peaks of activity being overestimated (e.g. by up to a third in early June) and of false alarms about growth being raised (e.g. early August; Fig. 1b). Overestimations of both activity and area occur throughout the summer, except for the onset in May. Then, there are instances in which MHW area tendencies follow the activity but are overestimated (late July to early August); given that activity continues to increase while area decreases (e.g. early September), there is an implied overestimation of the sea surface temperatures. Elsewhere, we see fluctuations in activity on daily timescales which dominate the longer-term growth tendencies (e.g. during the growth period beginning at the end of June). Throughout the summer of 2022, we see various examples of the activity forecasts being unable to detect this higher-frequency variability. Variability in area, on the other hand, is lower and the forecasts generally follow the observed tendencies. In summary, the forecasts sometimes persist or increase temperature anomalies for too long, suggesting that they fail to capture sporadic cooling. Candidate drivers for short-term cooling mechanisms not captured by the forecasts include cloud cover changes or winds.

It is important to also consider the ability to capture the spread of MHW occurrence. The geographical distribution of intensity in key phases of the MHW life cycle in forecasts agrees well with observations (Fig. 2). During the onset, forecasts capture the basin-wide patterns, with MHW occurrence at this stage correctly forecast in the Tyrrhenian Sea, Gulf of Lion, and parts of the Adriatic Sea. The spread of the MHW conditions during the peak was correctly predicted to cover the southern part of the Alboran Sea, the Ionian, and southern regions of the Levantine Basin. Meanwhile, the Aegean Sea was predicted to be shielded from MHWs and instead experience cold anomalies, most likely caused by cooling related to the Etesian winds (Poupkou et al., 2011). Lastly, the first decay phase at the end of August produced very inhomogeneous MHW conditions across the basin. This “patchiness”, indicative of local-scale processes acting to cool the ocean such as increased cloud cover or weak winds, was indeed predicted, but how well the forecast matches observations depends greatly on the local regions of interest and the exact day and lead time considered. Although it is not possible to draw rigorous conclusions from snapshots, the accuracy of basin-wide occurrence (Fig. 1b) suggests that forecast ability to capture MHW patterns and spread was generally high across the entire summer.

While basin-scale analysis allows an overview of forecasting skill, local-scale testing is imperative as forecasting tools are expected to be used for local-scale analysis (Dayan et al., 2023). Here, we also provide MHW forecasts for two key areas of maritime activity in the Mediterranean Sea: the Ligurian Sea and the Gulf of Taranto (Fig. 3). Each region experienced MHW conditions at different times during the summer, and in each case the forecasts accurately predicted the onset, persistence, intensity, and decays. The Ligurian Sea, bordered by Italy and France, is a crucial location for marine conservation; it doubles as a marine protected area (the Pelagos Sanctuary for Mediterranean Marine Mammals) which is home to unique species of fin whales and striped dolphins, amongst other species (Notarbartolo-de-Sciara et al., 2008). The Ligurian Sea experienced 115 d of MHWs throughout the summer, and temperature anomalies reached a maximum of 4.46 °C above the 1987–2019 average at the end of July, coinciding with the peak temperature of the summer (28.74 °C). The forecasts of SST were highly accurate; the root mean squared difference (RMSD) of the forecasts shown in Fig. 3a (across lead times) was 0.12 °C, lower than the reported RMSDs averaged over the entire Mediterranean Sea between the analysis and independent observations (Goglio et al., 2023). For an indication of forecast reliability, we highlight the false alarms (MHW days forecast but not observed) and misses (MHW days observed but not forecast). First we note that in the 89 % of days the correct conditions are forecast, with a few sporadic exceptions. For example, the forecast made on 10 May captured the sharp rise in SST but not the MHW conditions at the end of the week. However, reducing the lead time (i.e. checking forecasts made on 12 or 13 May) correctly forecast the MHW state.

The Gulf of Taranto, situated in the northern Ionian Sea, is one of the most productive areas of shellfish (mussels) farming in Italy (Prioli, 2004), but there are no data yet on MHW-induced mass mortality or economic loss in this region (Garrabou et al., 2022). Unlike the Ligurian Sea, the Gulf of Taranto experienced three short but intense periods of MHW occurrence in June and July, adding up to 61 d of MHWs in total. The peak temperature anomaly was 4.76 °C on 6 June, though peak temperatures occurred later in the season. As in the Ligurian Sea, the forecasts were highly accurate (demonstrating an RMSD of 0.08 °C). Regarding the reliability of MHW forecasts, the continuation of the start of the heatwave in early May was missed by the forecast of 17 May, while the forecast of 2 August missed several days of MHW occurrence. However, in both cases, SST increases were predicted. None of the forecasts shown in Fig. 3 raised false alarms.

Table 2. Root mean square differences of forecasts of summer 2022 MHW activity and atmospheric conditions (Fig. 4). Values in parenthesis are RMSD values normalized by standard deviation over the summer. Differences in MHW activity and area are relative to reprocessed satellite observations, while differences in T2M anomaly and wind speed are relative to ECMWF analysis. Each column corresponds to a different lead time.

RMSD (normalized)	Lead: 1 d	Lead: 4 d	Lead: 7 d
MHW activity	0.16 (0.48)	0.20 (0.59)	0.28 (0.82)
MHW area	8.88 (0.33)	11.65 (0.43)	16.50 (0.61)
T2M anomaly	0.18 (0.21)	0.31 (0.38)	0.52 (0.62)
Wind speed	0.22 (0.18)	0.52 (0.42)	0.94 (0.76)

So far we have studied the accuracy of the entire forecast period, but, in some applications, it might be necessary or of more interest to have a specific warning time (e.g. 4 d). As MedFS produces forecasts every day, we now study forecast accuracy for the summer of 2022 at different lead times; we focus on the western Mediterranean Sea, as opposed to the entire basin, in order to investigate local forcings as reasons for poor skill (Fig. 4). Table 2 quantifies the error of forecasts over the western Mediterranean Sea. The overestimation of MHW activity in July and August occurred in forecasts with lead time of 1 d. In many instances, lead time 1 and lead time 4 are similarly far from the observed values, while lead time 7 further overestimates the peaks in activity (Table 2). MHW area, on the other hand, while predicted more accurately than activity on all lead times, is typically underestimated by the forecasts. This implies an overestimation of SST (i.e. MHW intensity) during the activity peaks. The RMSD normalized by the standard deviation indicates where errors fall within the range of natural variability (normalized RMSD < 1); in all lead times, this is true for both area and activity, suggesting their skill is similar to atmospheric variables (Table 2).

The decreases in skill with lead time can partly be explained by the decrease in skill of the ECMWF atmospheric forecasts used to force MedFS. T2M and wind speed correlate strongly and significantly with the MHW activity (correlation values of 0.89 and 0.50 with the ECMWF analysis respectively), evidencing their role in MHW formation. Errors of forecasts of T2M and wind speed grow with time but do not exceed natural variability at lead time 7 (Table 2). In the first half of the summer, forecasts at lead time 7 of both T2M and wind speed are frequently out of phase with the observed changes. In fact, the underestimations of MHW area

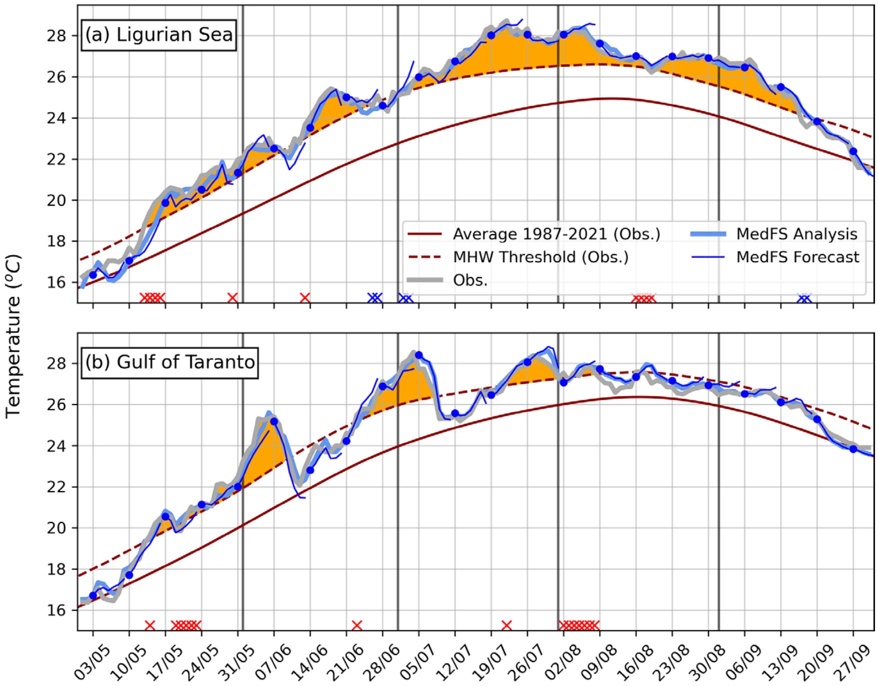

Figure 3. Time series of SST and MHW occurrence in summer 2022. Orange shading highlights MHW occurrence in reprocessed satellite observations. Forecast start dates are shown by the blue dots. Definitions of the Ligurian Sea **(a)** and Gulf of Taranto **(b)**. Note that the climatology lines (red) correspond to the satellite data, not to the model output (analysis and forecasts). Crosses correspond to misses (red) and false alarms (blue) in the forecast output.

in this period occur simultaneously with underestimations of T2M. For example, the underestimation of MHW area at the end of May, by an area of roughly 30 % of the western Mediterranean, corresponds to overestimations of wind speed by up to 1 $\mathrm{m\,s^{-1}}$ and temperature anomalies roughly 1 °C weaker than observed. However, the overestimation of activity in July and August, found to be linked to overestimations of SST, does not correspond to overestimations of T2M, implying that other phenomena are not well represented. It should be noted that the use of area-averaged atmospheric variables may hide sub-regional-scale processes which impact the MHW location and intensity.

4 Discussion and summary

The MHW of summer 2022 in the Mediterranean Sea was record-breaking, eclipsing 2003 in terms of basin-wide activity (defined as the integral of intensity, duration, and area). Other contributions to the Ocean State Report 8 also define the MHW of 2022 as a record-breaking event using other definitions (e.g. local SST records). Here, we provide a basin-wide view of the MHW conditions. The Copernicus Mediterranean Physical forecasting system was used to track this event, serving as the first validation of MHW prediction for this system. Forecasts captured the full life cycle of the MHWs several days in advance: onset (mid-May) in the western part of the basin, spread into the Adriatic and Ionian Sea, sporadic local-scale occurrences in the Levantine Basin, persistence of peak conditions throughout July and August, breaks in MHW persistence and abrupt changes in local occurrence, and the gradual decay (September). The forecasts also identified regions shielded from MHWs, e.g. during cooling in the Aegean Seas. Subseasonal forecasts do not yet demonstrate the capacity to predict MHW response to weather patterns (Benthuysen et al., 2021), but this study confirms that short-term forecasts, at least in the Mediterranean Sea, can fill this gap.

A full analysis of potential drivers and attribution of forecast skill to certain processes was outside the scope of this study, but the dependence on accurate atmospheric forcings (here provided by ECMWF forecasts) has been shown to be crucial for accurate forecasts of the 2022 event. Unlike the other extreme events, the common drivers of MHWs in the Mediterranean are yet to be identified. The MHW of 2022, as well as the concurrent and record-breaking atmospheric heatwave which occurred over western Europe, appears to be linked to the northward extension of the subtropical ridge (Barriopedro et al., 2023), while model studies have suggested that mid-latitude MHWs in summer typically arise from reduced ocean heat loss to the atmosphere and reduced vertical diffusion (Vogt et al., 2022). Here, the decay in skill of MHW forecasts matches the decay in skill of key atmospheric conditions (T2M and wind speed). Erroneous forecasts of early summer in the western Mediterranean Sea are

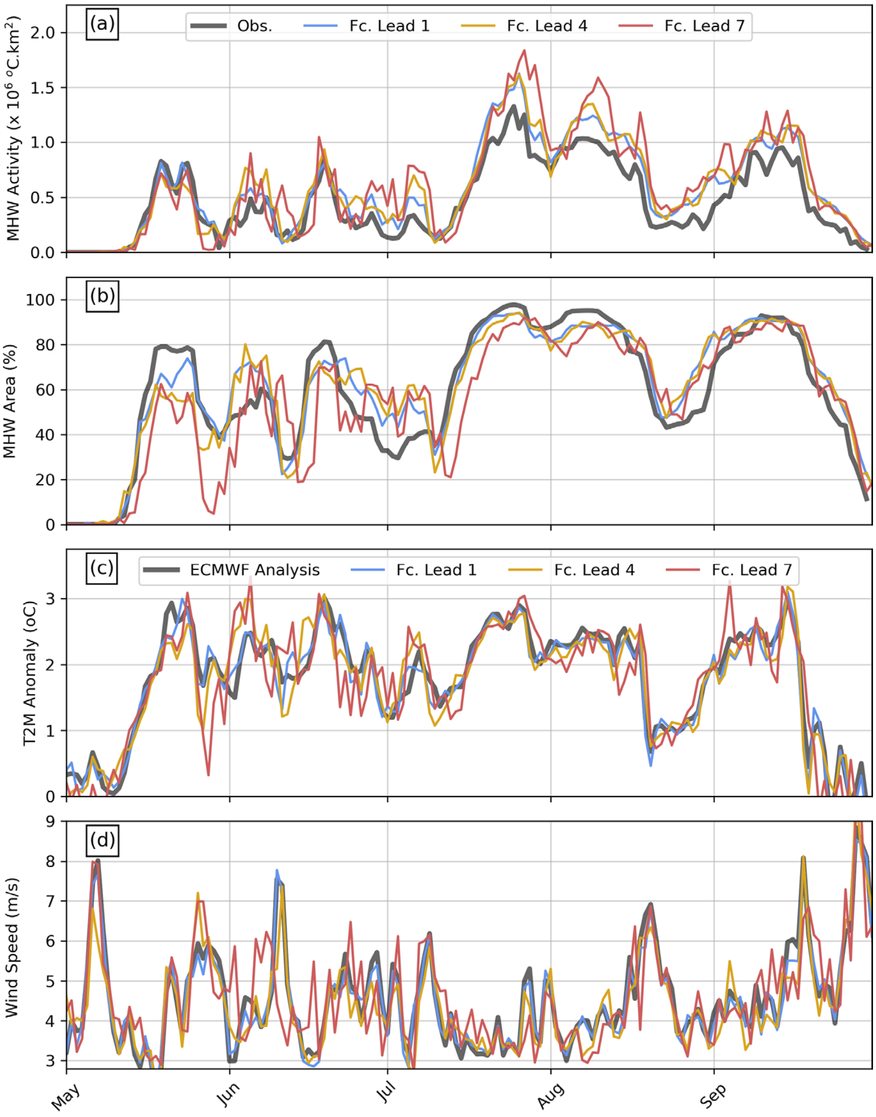

Figure 4. Effect of lead time and atmospheric forcings on forecasts of MHW activity and area. Comparison between reprocessed satellite observations and forecasts of 2022 MHW activity **(a)** and area **(b)**. Each forecast time series corresponds to a different lead time (i.e. how many days in advance the forecast was made). Forecasts of MHW activity were calculated for forecasts initiated every day; the lead time from each forecast was extracted to construct the time series. Area-averaged 2 m temperature anomaly **(c)** and wind speed **(d)** from the ECMWF analysis and forecasts used to force the MedFS system. All time series correspond to the western Mediterranean Sea (Fig. 2).

explained by inaccurate forecasts of these atmospheric conditions. Peak summer conditions, such as the overestimation of MHW activity, are not yet understood, meaning further studies of short-term forecasting of MHWs are necessary.

The timescale of forecasting determines the information that can be provided and the type of response to that information. Here, we make the case for using short-term forecasting in MHW tracking tools and studies. Seasonal forecasting informs management decisions and contingency plans, while subseasonal forecasting can update these plans (White et al., 2017). Short-term forecasting, on the other hand, can then be used to determine the precise timings of events and instruct users on when to implement urgent response actions. Longer-term forecasts are typically global in scale and have a relatively low model resolution, while short-term forecasting centres, benefitting from the reduced timescale, can put more computational power towards regional-scale forecasting at a finer scale more relevant to stakeholders. In principle, for MHWs, this means the following: seasonal forecasts provide forewarning of extreme summer temperatures (e.g. seasonal averages above the 90th percentile, identification of ocean basins affected). Sub-seasonal forecasts then update this to provide forewarning of MHW occurrence (e.g. daily temperatures persisting above 90th percentile, greater detail on geographic spread). Finally, short-term forecasts can provide key details such as the start date, onset rate, and breaks in occurrence on a local to regional scale. Currently, more effort is being devoted to seasonal forecasting of MHWs (de Burgh-Day et al., 2022; Liu et al., 2018; Jacox et al., 2022). With the level of accuracy for local-scale MHW indicators shown here, such tools should be complemented with daily short-term updates.

In particular, we found that the MHW occurrence in the Ligurian Sea and Gulf of Taranto, two regions of economic and ecological importance, was also reliably forecast. There is, though, a need to include subsurface temperatures or heat content to report MHWs occurring at depth (Dayan et al., 2023; McAdam et al., 2023). For example, caged fish have been observed to avoid the top of cages when surface temperatures increase (Gamperl et al., 2021), meaning truly stakeholder-relevant tracking tools need a 3D view. The near-real-time analysis, as well as the forecast system, provides 3D temperatures and can track subsurface propagation of MHWs (unlike satellite observations). The MHW record in the analysis aligns exceptionally well with satellite observations for the two target regions shown (Fig. 3), suggesting a high level of accuracy (the same is found for the basin-wide MHW activity; not shown). However, a subsurface validation with in situ data should be performed in the near future, before using the analysis and forecast to track subsurface MHWs.

Code availability. Codes used to analyse data and produce figures in this study are available at https://github.com/RJMcAdam (last access: 8 April 2024; https://doi.org/10.5281/zenodo.10944086, McAdam et al., 2024).

Data availability. The underlying data can be found in the product table (Table 1).

Author contributions. RM, GB, SM, and EC conceived the study. RM and GB performed the analysis and prepared the figures. RM wrote the paper. GB, SM, and EC contributed to the interpretation of the results and to the paper writing. RM, GB, SM, and EC reviewed the paper.

Competing interests. The contact author has declared that none of the authors has any competing interests.

Acknowledgements. We acknowledge the CMCC Foundation for providing computational resources.

Review statement. This paper was edited by Pierre Brasseur and reviewed by Francisco Pastor and one anonymous referee.

References

Abrahms, B., Welch, H., Brodie, S., Jacox, M. G., Becker, E. A., Bograd, S. J., Irvine, L. M., Palacios, D. M., Mate, B. R., and Hazen, E. L.: Dynamic ensemble models to predict distributions and anthropogenic risk exposure for highly mobile species, Divers Distrib., 25, 1182–1193, https://doi.org/10.1111/ddi.12940, 2019.

Álvarez Fanjul, E., Pérez Gómez, B., Alfonso Alonso-Muñoyerro, M. D., Lorente Jiménez, P., García Sotillo, M., Lin-Ye, J., Aznar Lecocq, R., Ruiz Gil de la Serna, M., Pérez-Rubio, S., Clementi, E., and Coppini, G.: Western Mediterranean record-breaking storm Gloria: An integrated assessment based on models and observations, in: Copernicus Ocean State Report, Issue 6, J. Oper. Oceanogr., 15, s151–s159, https://doi.org/10.1080/1755876X.2022.2095169, 2022.

Amaya, D. J., Miller, A. J., Xie, S. P., and Kosaka, Y.: Physical drivers of the summer 2019 North Pacific marine heatwave, Nat. Commun., 11, 1903, https://doi.org/10.1038/s41467-020-15820-w, 2020.

Amaya, D. J., Jacox, M. G., Fewings, M. R., Saba, V. S., Stuecker, M. F., Rykaczewski, R. R., Ross, A. C., Stock, C. A., Capotondi, A., Petrik, C. M., and Bograd, S. J.: Marine heatwaves need clear definitions so coastal communities can adapt, Nature, 616, 29–32, 2023.

Barbeaux, S. J., Holsman, K., and Zador, S.: Marine heatwave stress test of ecosystem-based fisheries management in the Gulf of Alaska Pacific cod fishery, Front. Mar. Sci., 7, 703, https://doi.org/10.3389/fmars.2020.00703, 2020.

Barriopedro, D., García-Herrera, R., Ordóñez, C., Miralles, D. G., and Salcedo-Sanz, S.: Heat waves: Physical understanding and scientific challenges, Rev. Geophys., 61, e2022RG000780, https://doi.org/10.1029/2022RG000780, 2023.

Benthuysen, J. A., Smith, G. A., Spillman, C. M., and Steinberg, C. R.: Subseasonal prediction of the 2020 Great Barrier Reef and Coral Sea marine heatwave, Environ. Res. Lett., 16, 124050, https://doi.org/10.1088/1748-9326/ac3aa1, 2021.

Bonino, G., Masina, S., Galimberti, G., and Moretti, M.: Southern Europe and western Asian marine heatwaves (SEWA-MHWs): a dataset based on macroevents, Earth Syst. Sci. Data, 15, 1269–1285, https://doi.org/10.5194/essd-15-1269-2023, 2023.

Cavicchia, L., von Storch, H., and Gualdi, S.: A long-term climatology of medicanes, Clim. Dynam., 43, 1183–1195, 2014.

Clementi, E., Korres, G., Cossarini, G., Ravdas M., Federico, I., Goglio., A. C., Salon, S., Zacharioudaki, A., Pattanaro, M., and Coppini, G.: The September 2020 Medicane Ianos predicted by the Mediterranean Forecasting systems, in: Copernicus Ocean State Report, Issue 6, J. Oper. Oceanogr., 15, s168–s175, https://doi.org/10.1080/1755876X.2022.2095169, 2022.

Darmaraki, S., Somot, S., Sevault, F., and Nabat, P.: Past variability of Mediterranean Sea marine heatwaves, Geophys. Res. Lett., 46, 9813–9823, 2019.

Dayan, H., McAdam, R., Juza, M., Masina, S., and Speich, S.: Marine heat waves in the Mediterranean Sea: An assessment from the surface to the subsurface to meet national needs, Front. Mar. Sci., 10, 142, https://doi.org/10.3389/fmars.2023.1045138, 2023.

de Boisseson, E., Balmaseda, M., Mayer, M., and Zuo, H.: Monitoring and predictions of the series of marine heatwave events impacting the Northeast Pacific in 2020, in: Copernicus Ocean State Report, Issue 6, J. Oper. Oceanogr., 15, s168–s175, https://doi.org/10.1080/1755876X.2022.2095169, 2022.

de Burgh-Day, C. O., Spillman, C. M., Smith, G., and Stevens, C. L.: Forecasting extreme marine heat events in key aquaculture regions around New Zealand, Journal of Southern Hemisphere Earth Systems Science, 72, 58–72, https://doi.org/10.1071/ES21012, 2022.

Escudier, R., Clementi, E., Nigam, T., Aydogdu, A., Fini, E., Pistoia, J., Grandi, A., and Miraglio, P.: EU Copernicus Marine Service Quality Information Document for the Mediterranean Sea Physics Reanalysis, MEDSEA_MULTIYEAR_PHY_006_004, Issue 2.3, Mercator Ocean International, https://catalogue.marine.copernicus.eu/documents/QUID/CMEMS-MED-QUID-006-004.pdf (last access: 23 June 2023), 2022.

EU Copernicus Marine Service Product: Mediterranean Sea Physics Reanalysis, Mercator Ocean International [data set], https://doi.org/10.25423/CMCC/MEDSEA_MULTIYEAR_PHY_006_004_E3R1, 2022.

EU Copernicus Marine Service Product: Mediterranean Sea – High Resolution L4 Sea Surface Temperature Reprocessed, Mercator Ocean International [data set], https://doi.org/10.48670/moi-00173, 2023a.

EU Copernicus Marine Service Product: Mediterranean Sea Physics Analysis and Forecast, Mercator Ocean International [data set], https://doi.org/10.25423/CMCC/MEDSEA_ANALYSISFORECAST_PHY_006_013_EAS7, 2023b.

Galappaththi, E. K., Ichien, S. T., Hyman, A. A., Aubrac, C. J., and Ford, J. D.: Climate change adaptation in aquaculture, Rev. Aquacult., 12, 2160–2176, https://doi.org/10.1111/raq.12427, 2020.

Galli, G., Solidoro, C., and Lovato, T.: Marine heat waves hazard 3D maps and the risk for low motility organisms in a warming Mediterranean Sea, Front. Mar. Sci., 4, 136, https://doi.org/10.3389/fmars.2017.00136, 2017.

Gamperl, A. K., Zrini, Z. A., and Sandrelli, R. M.: Atlantic salmon (Salmo salar) cage-site distribution, behavior, and physiology during a Newfoundland heat wave, Front. Physiol., 12, 719594, https://doi.org/10.3389/fphys.2021.719594, 2021.

Garrabou, J., Gómez-Gras, D., Medrano, A., Cerrano, C., Ponti, M., Schlegel, R., Bensoussan, N., Turicchia, E., Sini, M., Gerovasileiou, V., Teixido, N., Mirasole, A., Tamburello, L., Cebrian, E., Rilov, G., Ledoux, J.-B., Souissi, J. B., Khamassi, F., Ghanem, R., Benabdi, M., Grimes, S., Ocaña, O., Bazairi, H., Hereu, B., Linares, C., Kersting, D. K., la Rovira, G., Ortega, J., Casals, D., Pagès-Escolà, M., Margarit, N., Capdevila, P., Verdura, J., Ramos, A., Izquierdo, A., Barbera, C., Rubio-Portillo, E., Anton, I., López-Sendino, P., Díaz, D., Vázquez-Luis, M., Duarte, C., Marbà, N., Aspillaga, E., Espinosa, F., Grech, D., Guala, I., Azzurro, E., Farina, S., Gambi, M. C., Chimienti, G., Montefalcone, M., Azzola, A., Pulido Mantas, T., Fraschetti, S., Ceccherelli, G., Kipson, S., Bakran-Petricioli, T., Petricioli, D., Jimenez, C., Katsanevakis, S., Kizilkaya, I. T., Kizilkaya, Z., Sartoretto, S., Elodie, R., Ruitton, S., Comeau, S., Gattuso, J. P., and Harmelin, J.-G.: Marine heatwaves drive recurrent mass mortalities in the Mediterranean Sea, Glob. Change Biol., 28, 5708–5725, https://doi.org/10.1111/gcb.16301, 2022.

Giesen, R., Clementi, E., Bajo, M., Federico, I., Stoffelen, A., and Santoleri, R.: The November 2019 record high water levels in Venice, Italy, in: Copernicus Ocean State Report, Issue 5, J. Oper. Oceanogr., 14, s156–s162, https://doi.org/10.1080/1755876X.2021.1946240, 2021.

Goglio, A. C., Clementi, E., Grandi, A., Moulin, A., Giurato, M., Aydogdu, A., Pistoia, J., Miraglio, P., Mariani, A., and Drudi, M.: EU Copernicus Marine Service Quality Information Document for the Mediterranean Sea Physics Analysis and Forecast, MEDSEA_ANALYSISFORECAST_PHY_006_013, Issue 2.4, Mercator Ocean International, https://catalogue.marine.copernicus.eu/documents/QUID/CMEMS-MED-QUID-006-013.pdf (last access: 14 January 2024), 2023.

Hartog, J. R., Spillman, C. M., Smith, G., and Hobday, A. J.: Forecasts of marine heatwaves for marine industries: Reducing risk, building resilience and enhancing management responses, Deep-Sea Res. Pt. II, 209, 105276, https://doi.org/10.1016/j.dsr2.2023.105276, 2023.

Hersbach, H., Bell, B., Berrisford, P., Biavati, G., Horányi, A., Muñoz Sabater, J., Nicolas, J., Peubey, C., Radu, R., Rozum, I., Schepers, D., Simmons, A., Soci, C., Dee, D., and Thépaut, J.-N.: ERA5 hourly data on single levels from 1940 to present, Copernicus Climate Change Service (C3S) Climate Data Store (CDS) [data set], https://doi.org/10.24381/cds.adbb2d47, 2023.

Hobday, A. J., Alexander, L. V., Perkins, S. E., Smale, D. A., Straub, S. C., Oliver, E. C., Benthuysen, J. A., Burrows, M. T., Donat, M. G., Feng, M., and Holbrook, N. J.: A hierarchical approach to defining marine heatwaves, Prog. Oceanogr., 141, 227–238, 2016.

Holbrook, N. J., Scannell, H. A., Sen Gupta, A., Benthuysen, J. A., Feng, M., Oliver, E. C., Alexander, L. V., Burrows, M. T., Donat, M. G., Hobday, A. J., and Moore, P. J.: A global assessment of marine heatwaves and their drivers, Nat. Commun., 10, 2624, https://doi.org/10.1038/s41467-019-10206-z, 2019.

Holsman, K. K., Hazen, E. L., Haynie, A., Gourguet, S., Hollowed, A., Bograd, S. J., Samhouri, J. F., and Aydin, K.: Towards climate resiliency in fisheries management, ICES J. Mar. Sci., 76, 1368–1378, https://doi.org/10.1093/icesjms/fsz031, 2019.

Ibrahim, O., Mohamed, B., and Nagy, H.: Spatial variability and trends of marine heat waves in the eastern mediterranean sea over 39 years, Journal of Marine Science and Engineering, 9, 643, https://doi.org/10.3390/jmse9060643, 2021.

Jacox, M. G., Tommasi, D., Alexander, M. A., Hervieux, G., and Stock, C. A.: Predicting the evolution of the 2014–2016 California Current System marine heatwave from an ensemble of coupled global climate forecasts, Front. Mar. Sci., 6, 497, https://doi.org/10.3389/fmars.2019.00497, 2019.

Jacox, M. G., Alexander, M. A., Amaya, D., Becker, E., Bograd, S. J., Brodie, S., Hazen, E. L., Pozo Buil, M., and Tommasi, D.: Global seasonal forecasts of marine heatwaves, Nature, 604, 486–490, https://doi.org/10.1038/s41586-022-04573-9, 2022.

Juza, M., Fernández-Mora, À., and Tintoré, J.: Sub-Regional marine heat waves in the Mediterranean Sea from observations: Long-term surface changes, Sub-surface and coastal responses, Front. Mar. Sci., 9, 785771, https://doi.org/10.3389/fmars.2022.785771, 2022.

Lecci, R., Drudi, M., Grandi, A., Cretì, S., and Clementi, E.: EU Copernicus Marine Service Product User Manual for the Mediterranean Sea Physics Reanalysis, MEDSEA_MULTIYEAR_PHY_006_004, Issue 2.3, Mercator Ocean International, https://catalogue.marine.copernicus.eu/documents/PUM/CMEMS-MED-PUM-006-004.pdf (last access: 23 June 2023), 2022.

Lecci, R., Drudi, M., Grandi, A., Cretì, S., and Clementi, E.: EU Copernicus Marine Service Product User Manual for the Mediterranean Sea Physics Analysis and Forecast, MEDSEA_ANALYSISFORECAST_ PHY_ 006_013, Issue 2.3, Mercator Ocean International, https://catalogue.marine.copernicus.eu/documents/PUM/CMEMS-MED-PUM-006-013.pdf (last access: 14 February 2024), 2023.

Li, Z., Holbrook, N. J., Zhang, X., Oliver, E. C., and Cougnon, E. A.: Remote forcing of Tasman Sea marine heatwaves, J. Climate, 33, 5337–5354, https://doi.org/10.1175/JCLI-D-19-0641.1, 2020.

Liu, G., Eakin, C. M., Chen, M., Kumar, A., De La Cour, J. L., Heron, S. F., Geiger, E. F., Skirving, W. J., Tirak, K. V., and Strong, A. E.: Predicting heat stress to inform reef management: NOAA Coral Reef Watch's 4-month coral bleaching outlook, Front. Mar. Sci., 5, 57, https://doi.org/10.3389/fmars.2018.00057, 2018.

McAdam, R., Masina, S., and Gualdi, S.: Seasonal forecasting of subsurface marine heatwaves, Commun. Earth Environ., 4, 225, https://doi.org/10.1038/s43247-023-00892-5, 2023.

McAdam, R., Bonino, G., Clementi, E., and Masina, S.: Forecasting the Mediterranean Sea marine heatwave of summer 2022, Zenodo [data set], https://doi.org/10.5281/zenodo.10944086, 2024.

McLeod, E., Salm, R., Green, A., and Almany, J.: Designing marine protected area networks to address the impacts of climate change, Front. Ecol. Environ., 7, 362–370, https://doi.org/10.1890/070211, 2009.

Notarbartolo-di-Sciara, G., Agardy, T., Hyrenbach, D., Scovazzi, T., and Van Klaveren, P.: The Pelagos sanctuary for Mediterranean marine mammals, Aquat. Conserv., 18, 367–391, https://doi.org/10.1002/aqc.855, 2008.

Oliver, E. C., Benthuysen, J. A., Darmaraki, S., Donat, M. G., Hobday, A. J., Holbrook, N. J., Schlegel, R. W., and Sen Gupta, A.: Marine heatwaves, Annu. Rev. Mar. Sci., 13, 313–342, https://doi.org/10.1146/annurev-marine-032720-095144, 2021.

Pisano, A., Fanelli, C., Tronconi, C., Cesarini, C., La Padula, F., and Buongiorno Nardelli, B.: EU Copernicus Marine Service Product User Manual for the Mediterranean Sea – High Resolution L4 Sea Surface Temperature Reprocessed Product, SST_MED_SST_L4_REP_OBSERVATIONS_010_021, Issue 3.0, Mercator Ocean International, https://catalogue.marine.copernicus.eu/documents/PUM/CMEMS-SST-PUM-010-021-022-041-042.pdf (last access: 14 February 2024), 2023a.

Pisano, A., Fanelli, C., Tronconi, C., Cesarini, C., La Padula, F., and Buongiorno Nardelli, B.: EU Copernicus Marine Service Quality Information Document for the Mediterranean Sea – High Resolution L4 Sea Surface Temperature Reprocessed Product, SST_MED_SST_L4_REP_OBSERVATIONS_010_021, Issue 3.0, Mercator Ocean International, https://catalogue.marine.copernicus.eu/documents/QUID/CMEMS-SST-QUID-010-021-022-041-042.pdf (last access: 14 February 2024), 2023b.

Poupkou, A., Zanis, P., Nastos, P., Papanastasiou, D., Melas, D., Tourpali, K., and Zerefos, C.: Present climate trend analysis of the Etesian winds in the Aegean Sea, Theor. Appl. Climatol., 106, 459–472, 2011.

Prioli, G.: Shellfish farming: technologies and production, Vet. Res. Commun., 28, 51–56, https://doi.org/10.1023/b:verc.0000045378.40910.7e, 2004.

Rayner, R., Jolly, C., and Gouldman, C.: Ocean observing and the blue economy, Front. Mar. Sci., 6, 330, https://doi.org/10.3389/fmars.2019.00330, 2019.

Rodrigues, R. R., Taschetto, A. S., Sen Gupta, A., and Foltz, G. R.: Common cause for severe droughts in South America and marine heatwaves in the South Atlantic, Nat. Geosci., 12, 620–626, https://doi.org/10.1038/s41561-019-0393-8, 2019.

Schlegel, R. W., Oliver, E. C., and Chen, K.: Drivers of marine heatwaves in the Northwest Atlantic: The role of air–sea interaction during onset and decline, Front. Mar. Sci., 8, 627970, https://doi.org/10.3389/fmars.2021.627970, 2021.

Sen Gupta, A., Thomsen, M., Benthuysen, J. A., Hobday, A. J., Oliver, E., Alexander, L. V., Burrows, M. T., Donat, M. G., Feng, M., Holbrook, N. J., and Perkins-Kirkpatrick, S.: Drivers and impacts of the most extreme marine heatwave events, Sci. Rep., 10, 19359, https://doi.org/10.1038/s41598-020-75445-3, 2020.

Simon, A., Plecha, S. M., Russo, A., Teles-Machado, A., Donat, M. G., Auger, P. A., and Trigo, R. M.: Hot and cold marine extreme events in the Mediterranean over the period 1982–2021, Front. Mar. Sci., 9, 892201, https://doi.org/10.3389/fmars.2022.892201, 2022.

Smith, K. E., Burrows, M. T., Hobday, A. J., Sen Gupta, A., Moore, P. J., Thomsen, M., Wernberg, T., and Smale, D. A.: Socioeconomic impacts of marine heatwaves: Global issues and opportunities, Science, 374, eabj3593, https://doi.org/10.1126/science.abj3593, 2021.

Smith, K. E., Burrows, M. T., Hobday, A. J., King, N. G., Moore, P. J., Sen Gupta, A., Thomsen, M. S., Wernberg, T., and Smale, D. A.: Biological impacts of marine heatwaves, Annu. Rev. Mar. Sci., 15, 119–145, https://doi.org/10.1146/annurev-marine-032122-121437, 2023.

Vogt, L., Burger, F. A., Griffies, S. M., and Frölicher, T. L.: Local drivers of marine heatwaves: a global analysis with an earth system model, Front. Clim., 4, 847995, https://doi.org/10.3389/fclim.2022.847995, 2022.

White, C. J., Carlsen, H., Robertson, A. W., Klein, R. J. T., Lazo, J. K., Kumar, A., Vitart, F., Coughlan de Perez, E., Ray, A. J., Murray, V., Bharwani, S., MacLeod, D., James, R., Fleming, L., Morse, A. P., Eggen, B., Graham, R., Kjellström, E., Becker, E., Pegion, K. V., Holbrook, N. J., McEvoy, D., Depledge, M., Perkins-Kirkpatrick, S., Brown, T. J., Street, R., Jones, L., Remenyi, T. A., Hodgson-Johnston, I., Buontempo, C., Lamb, R., Meinke, H., Arheimer, B., and Zebiak, S. E.: Potential applications of subseasonal-to-seasonal (S2S) predictions, Met. Apps, 24, 315–325, https://doi.org/10.1002/met.1654, 2017.

State Planet, 4-osr8, 14, 2024
https://doi.org/10.5194/sp-4-osr8-14-2024

Coastal ocean response during the unprecedented marine heatwaves in the western Mediterranean in 2022

Mélanie Juza[1], **Marta de Alfonso**[2], **and Ángels Fernández-Mora**[1]

[1]Balearic Islands Coastal Observing and Forecasting System (SOCIB), Palma, Spain
[2]Puertos del Estado, Madrid, Spain

Correspondence: Mélanie Juza (mjuza@socib.es)

Received: 16 July 2023 – Discussion started: 23 August 2023
Revised: 13 December 2023 – Accepted: 8 January 2024 – Published: 30 September 2024

Abstract. The western Mediterranean Sea suffered unprecedented marine heatwaves (MHWs) in 2022. This study focuses on the response of coastal ocean, which is highly vulnerable to global warming and extreme events that threaten the biodiversity, as well as goods and services that humans rely on. Using remote sensing and in situ observations, strong spatiotemporal variations in the MHW characteristics are observed in the coastal ocean over the last decade (2013–2022). In 2022, shallow-water moorings in the western Mediterranean Sea detected between 23 and 131 d of MHWs. While the highest MHW mean and maximum intensities were detected at the surface in French waters, the highest duration was observed nearshore at 17 m depth in the Balearic Islands. As thermal stress indicators for marine ecosystems, the highest cumulative intensity and total days were found at the surface at Tarragona, and MHW temperatures warmer than 28 °C were observed to last up to 58 d at Palma. Differences between datasets are also highlighted. In 2022, depending on the sub-regions, satellites underestimated or overestimated MHW duration and intensity compared with in situ measurements at the surface. In addition, daily data underestimate maxima reached during the extreme warm events up to 1.52 °C difference compared with hourly measurements. These results invite us to continue the efforts in deploying and maintaining multi-platform observing systems in both open-ocean and coastal ocean waters to better address the coastal adaptation and mitigation in the context of climate change.

1 Introduction

The Mediterranean Sea is one of the most vulnerable regions to climate change and responds rapidly to global warming with strong spatial variations (Giorgi, 2006; Lionello and Scarascia, 2018; Pisano et al., 2020; Juza and Tintoré, 2021a; Juza et al., 2022). In 2022, the western Mediterranean Sea (WMed) suffered extreme ocean temperatures and several marine heatwaves (MHWs) in a row from May to December 2022, as displayed in operational applications (Juza and Tintoré, 2020, 2021b) and recently reported (Marullo et al., 2023). These MHWs were exceptional for their early occurrence, intensity, duration, and spatial extent. In the Balearic Islands region, the warmest spatially averaged satellite sea surface temperature (SST) ever registered since 1982 has been observed on 13 August 2022, with a value of 29.2 °C, corresponding to an anomaly of 3.3 °C with respect to the period 1982–2015, exceeding the previous regional record from summer 2003 (Juza and Tintoré, 2020, 2021b). Warmer temperatures and anomalies can be found more locally than regionally, due to their strong spatial variations (Juza and Tintoré, 2021a). In summer 2022, ocean temperatures reaching more than 32 °C were observed in the Mallorca Channel (SOCIB news in August 2022, https://www.socib.es, last access: 19 June 2023), while SST anomalies exceeded 5 °C in French waters, reaching the highest historical record ever registered since 1982 (Guinaldo et al., 2023).

The Mediterranean Sea is the largest semi-enclosed sea, with 46 000 km of coastline and many islands, and is also considered a hot spot of biodiversity, with many endemic species (Coll et al., 2010). Its coastal zone provides goods and services that humans rely on (Smith et al., 2021; UNEP/MAP and Plan Bleu, 2020), but it concentrates and ac-

Published by Copernicus Publications.

Table 1. Product table describing data products used in this study.

Product ref. no.	Product ID and type	Data access	Documentation
1	SST_MED_SST_L4_NRT_OBSERVATIONS_010_004 (1982–2021) (https://doi.org/10.48670/moi-00172); satellite observations	EU Copernicus Marine Service Product (2023a)	Quality Information Document (QUID); Pisano al. (2023a) Product User Manual (PUM); Pisano et al. (2023b)
2	SST_MED_SST_L4_REP_OBSERVATIONS_010_021 (2022) (https://doi.org/10.48670/moi-00173); satellite observations	EU Copernicus Marine Service Product (2023b)	Quality Information Document (QUID); Pisano al. (2023c) Product User Manual (PUM); Pisano et al. (2023d)
3	INSITU_MED_PHYBGCWAV_DISCRETE_MYNRT_013_035 (2013–2022) (https://doi.org/10.48670/moi-00044); in situ observations	EU Copernicus Marine Service Product (2023c)	Quality Information Document (QUID); Wehde et al. (2023) Product User Manual (PUM); In Situ TAC partners (2023)
4	Buoy Bahia de Palma physicochemical parameters of seawater data (2013–2022) (https://doi.org/10.25704/S6JB-CK61); in situ observations	Balearic Islands Coastal Observing and Forecasting System (SOCIB) product, 2022	Tintoré and Casas Pérez (2022)
5	Two Nortek Acoustic Wave and Current Profilers (AWACs) in nearshore Balearic Islands; in situ observations (extended until 2022) (https://doi.org/10.25704/ra9h-5127)	Balearic Islands Coastal Observing and Forecasting System (SOCIB) data, 2022	Fernández-Mora et al. (2021)

cumulates human pressures (e.g. contamination, population in cities, overfishing, coastline artificialisation, marine traffic, offshore industry, and tourism) (UNEP/MAP and Plan Bleu, 2020). In addition, the coastal areas and ecosystems are highly vulnerable to global warming and extreme temperature events that threaten the biodiversity in the Mediterranean Sea (Cerrano et al., 2000; Garrabou et al., 2009, 2019, 2022; Bensoussan et al., 2019; Verdura et al., 2019). Recently, Garrabou et al. (2022) have shown that MHWs drive recurrent mass mortalities of marine organisms in the Mediterranean Sea. These mass mortality events affected thousands of kilometres of coastline from the surface to 45 m depth, across a range of marine habitats and taxa. Also, *Posidonia oceanica*, which is the dominant seagrass in the Mediterranean Sea living between surface and 40 m depth, is very sensitive to high temperatures above 27 °C, particularly in its early stage of development (Guerrero-Meseguer et al., 2017). Verdura et al. (2021) also highlighted, during the 2015 event, high mortalities of habitat-forming seaweeds at temperatures of 28 °C, with most severe implications for the early life stage and fertility. In 2017, concomitant with the thermal context, the large-scale and long-lasting mucilaginous benthic algal bloom was observed along the coasts of the northern Catalan Sea, affecting benthic coastal habitats (Bensoussan et al., 2019).

The climate signal manifests differently from coastal areas to the open ocean and in the different sub-regions due to the variety and complexity of coastal ocean processes (Juza et al., 2022). Satellite products and in situ measurements are complementary ocean data sources. There is a benefit of using in situ data as a complement of satellite products, since they provide a more accurate representation of the thermal characteristics in the nearshore environment (Schlegel et al., 2017a). Satellite data are not always accurate close to the land and have a lower temporal resolution. In this study, the coastal ocean response to the unprecedented MHWs that occurred in the WMed in 2022 is analysed using daily data from satellite observations and coastal mooring measurements. Then, the events detected by moorings in 2022 are compared to those observed over the last decade since 2013. In addition, since MHW events are addressed in coastal areas where ecosystems are highly present and sensitive, the range of temperatures reached during these events is also studied, in particular MHW temperatures exceeding 28 °C, when strongly altering marine habitat and accelerating species mortality. Finally, these extreme temperature ranges are investigated through the analyses of daily and hourly data, highlighting differences in thermal stress estimations.

2 Datasets and methodology

2.1 Datasets

Daily reprocessed (REP) and near-real-time (NRT) satellite products in the Mediterranean Sea distributed by the Copernicus Marine Service (https://marine.copernicus.eu/, last access: 19 June 2023) are used (product ref. nos. 1 and 2; Table 1). These products provide optimally interpolated estimates of SST into regular horizontal grids of $1/20°$ and $1/16°$ spatial resolutions, respectively, covering the period

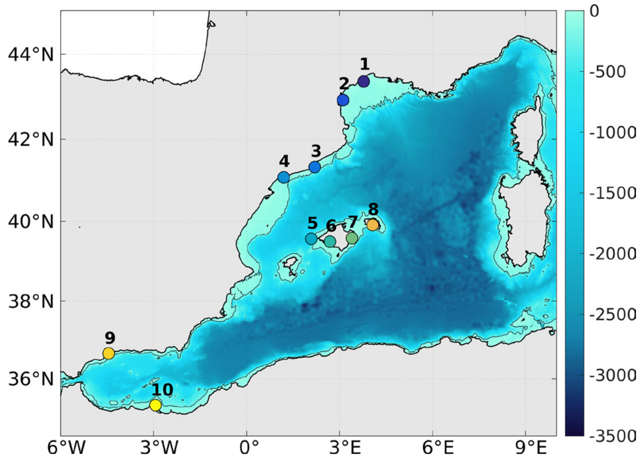

Figure 1. Bathymetry (in m) in the western Mediterranean Sea, with the contour at 200 m (grey line) and locations of selected mooring for the study (coloured points), as listed in Table 2.

1982–2022 (Pisano et al., 2016; Buongiorno Nardelli et al., 2013).

Hourly temperature time series from moorings in the WMed were uploaded from the Copernicus Marine In Situ data portal (product ref. no. 3; Table 1; http://www.marineinsitu.eu/, last access: 19 June 2023) and the Balearic Islands Coastal Observing and Forecasting System (SOCIB) data catalogue (product ref. nos. 4 and 5; Table 1; https://thredds.socib.es/thredds/catalog.html, last access: 19 June 2023). Fixed stations with data covering the period 2013–2022 with limited temporal gaps have been selected. In addition, focusing the study on the coastal response to extreme temperature events means that deep water stations (off the continental shelf) have been excluded. A total of 10 coastal moorings located at depths shallower than 200 m are used in this study (Table 2; Fig. 1). Finally, all moorings data were post-processed to remove spikes and erroneous data.

2.2 Methodology

The commonly used methodology for MHW identification and characterisation from Hobday et al. (2016) is applied. MHWs correspond to daily SSTs exceeding the daily 90th percentile of the local SST distribution over a long-term reference period during at least 5 consecutive days. In addition, two successive MHW events with 2 consecutive days or shorter time break are considered to be a continuous event. This also allows discarding the unrealistic jumps in the SST time series due to sparse erroneous daily interpolated data in the NRT satellite product or in temperature time series from in situ measurements. Finally, the daily climatological mean and threshold time series are smoothed using a 30 d moving window to extract useful climatology from inherently variable data.

First, daily SST from satellites are used to compute climatology over the period 1982–2015 and to detect MHWs from 1982 to 2022, providing valuable information about the 2022 thermal situation over the whole Mediterranean. The chosen reference period starts as early as possible, covers at least a 30-year period as recommended (Hobday et al., 2016), and is aligned with the methodology applied in recent publications in the Mediterranean Sea (Juza and Tintoré, 2021a; Juza et al., 2022). Then, the computation and detection are applied to the daily mean temperature time series from mooring and the nearest satellite point when in situ data are available over the commonly available period 2013–2022 for their direct comparison. Although the in situ time series are shorter than the recommended 30-year minimum for the calculation of climatology and characterisation of MHWs, the calculation of MHWs using their own climatology allows quantifying the amount they differ from their localities (Schlegel et al., 2017b; Juza et al., 2022).

MHW indices are then calculated to characterise the 2022 MHW event and to estimate changes over the last decade. For each year, the MHW mean and maximum intensities above the mean climatology, mean duration, and number of discrete events are computed. MHW cumulative intensity and total days are also provided as interesting indicators for ecosystem stressor, although they are an aggregation of MHW intensity and duration and of duration and frequency, respectively. Finally, ocean temperatures exceeding 28 °C are also identified during the detected MHW events. The combination of abnormal conditions (MHW) and stressful threshold (temperature ranges) allows identifying high thermal stress situations that strongly impact marine ecosystems. In this respect, these extreme temperatures are also investigated through the use and analysis of hourly data, as observed by the moorings.

3 MHWs in the Mediterranean Sea

MHWs are firstly detected using satellite SST with respect to the reference period 1982–2015. MHW characteristics are quantitatively sensitive to the baseline period but remain qualitatively consistent (Dayan et al., 2023). All MHW characteristics have been substantially increasing in the Mediterranean Sea over the last few decades, as studied over 1982–2020 (Juza et al., 2022), 1987–2019 (Dayan et al., 2023), and 1982–2021 (Pastor and Khodayar, 2023). Over the recent period 1982–2022, the local trend estimates with 95 % confidence for the MHW characteristics have reached maximum values of MHW mean and maximum intensities, mean duration, frequency, and total days of 0.18 and 0.65 °C per decade, 12.4 d per decade, 2.4 events per decade, and 42.2 d per decade, respectively (Juza and Tintoré, 2021b; Vargas-Yáñez et al., 2023). In 2022, annual mean and maximum intensities, mean duration, frequency, and total days in the whole Mediterranean oscillate locally over 0.95–3.10 and 1.24–6.47 °C, 5–235 d, 1–15 events, and 5–291 d, respec-

Table 2. Characteristics of the study moorings in the western Mediterranean Sea (name, coordinates of the station and the nearest satellite point, their distance, sensor depth, and bathymetry), as displayed in Fig. 1. The distance is the one to the nearest satellite point and its orientation from the mooring.

Mooring	No.	Location mooring	Location satellite	Distance (km)	Sensor depth (m)	Bathymetry (m)
Sète	1	43.37° N–3.78° E	43.35° N–3.77° E	1.8 (SSW)	0.0, 0.4 (Since 16 April 2019)	32.4
Leucate	2	42.92° N–3.12° E	42.94° N–3.10° E	2.4 (NW)		38.2
Barcelona	3	41.32° N–2.21° E	41.31° N–2.23° E	2.1 (SEE)	0.5	76.8
Tarragona	4	41.07° N–1.19° E	41.06° N–1.19° E	0.8 (SW)	0.5	18.2
Dragonera	5	39.56° N–2.10° E	39.56° N–2.10° E	0.5 (NE)	3	183.4
Palma Bay	6	39.49° N–2.70° E	39.48° N–2.69° E	1.9 (SW)	1	31.8
Cala Millor	7	39.59° N–3.40° E	39.60° N–3.40° E	1.5 (NW)	17	17
Son Bou	8	39.90° N–4.06° E	39.90° N–4.06° E	0.5 (SW)	17	17
Málaga	9	36.66° N–4.44° W	36.65° N–4.44° W	1.4 (SSE)	0.5	21.3
Melilla	10	35.32° N–2.94° W	35.35° N–2.94° W	3.4 (NNE)	0.5	16.2

tively (Fig. 2a for MHW total days). In 2022, there are strong differences in MHW characteristics between the western and eastern sub-basins. In the WMed, unprecedented MHWs occurred in 2022, which was the year with the highest annual total days of MHWs over the period 1982–2022, reaching up to 291 d locally along the Spanish coast in the Balearic Sea (Fig. 2a). Spatially integrated in the WMed, annual MHW characteristics reached the highest records ever registered since 1982 during the year 2022 (Fig. 2b for MHW total days). In particular, mean and maximum intensities, mean duration, and total days reached 2.25 and 4.36 °C, 36.6, and 180 d, respectively.

4 Coastal MHWs in 2022

MHWs are then detected from daily temperature from mooring and satellite with respect to the reference period 2013–2022, which is the longest common period available in the moorings of study. The use of shorter time series for climatology induces errors in MHW detection and characterisation, in particular due to ocean warming trend (Juza et al., 2022; Izquierdo et al., 2022). More precisely, MHW characteristics detected by satellites at the nearest point from moorings differ according to the reference period used (not shown). Since the SST climatologies have higher values over 2013–2022 than 1982–2015, fewer MHW events are detected using the 2013–2022 reference period. More specifically, annual MHW total days and maximum and cumulative intensities are underestimated by at least 21 %, 5 %, and 29 %, respectively, according to the year and mooring location over 2013–2022, and up to 100 % in some years when MHWs are not detected with the recent and short reference period for climatology (Table 3).

4.1 Results from moorings

In 2022, all moorings of the coastal WMed detected MHWs (Fig. 3), although MHWs were computed using the reference period 2013–2022. As mentioned above, the use of recent baseline periods underestimates these extreme events (Table 3) due to ocean warming. Different responses are highlighted between the moorings (Fig. 3; Table 4) not only because of the different depths of the sensor installation but also because of their geographical location. Indeed, results from satellite data at the nearest point also indicate the strong spatial variability. In 2022, the highest mean and maximum intensities of MHWs detected by moorings are found along the French coast (Sète and Leucate) and the southern Spanish coast (Málaga) up to 3.67 and 5.17 °C, respectively. The highest mean duration is detected in the nearshore moorings at Cala Millor (40 d) and Son Bou (31 d) installed at 17 m depth, as well as in the coastal Balearic Sea (Tarragona, Dragonera, and Palma), where the highest total days is observed with values up to 131 d at Tarragona in 2022. Such responses have led to highest cumulative intensity and possibly associated thermal stress on ecosystems in the moorings at Palma, Dragonera, Tarragona, Sète, and Leucate. Finally, MHW days with temperature exceeding 28 °C are found in the Balearic Sea, from Barcelona to Cala Millor and Son Bou, with the highest numbers at Tarragona (47), Dragonera (53), and Palma (58). In addition, these highly stressful thermal situations with temperatures higher than 28 °C occurred several times during the summer in 2022, with long periods of consecutive warm days (up to 33 d at Palma). Moorings located along the French coast (Leucate and Sète) and in the Alboran Sea (Málaga and Melilla) did not face daily temperatures warmer than 28 °C.

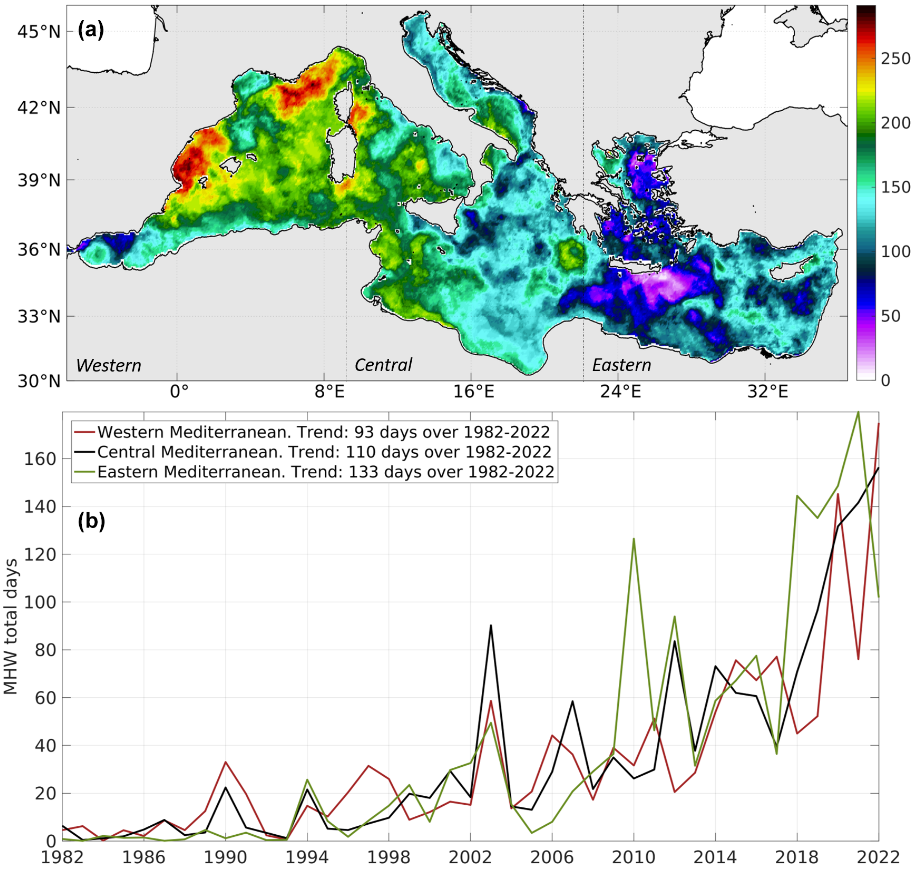

Figure 2. **(a)** MHW total days in 2022 from satellite (product ref. no. 1; Table 1) with respect to the historical data (product ref. no. 2; Table 1) over the period 1982–2015. **(b)** Time series of annual MHW total days averaged in the western, central, and eastern Mediterranean sub-basins from 1982 to 2022.

Table 3. Underestimation error (in %) of annual MHW characteristics (maximum and cumulative intensities and total days), as detected by the nearest satellite points (product ref. nos. 1 and 2; Table 1) from moorings (product ref. nos. 3, 4, and 5; Table 1) over 2013–2022 with respect to the reference periods 2013–2022 and 1982–2015 (reference for error estimation).

	Maximum intensity	Cumulative intensity	Total days
Sète	5–69	54–95	53–93
Leucate	15–100	52–100	50–100
Barcelona	17–100	64–100	65–100
Tarragona	16–100	58–100	56–100
Dragonera	19–100	51–100	42–100
Palma	26–100	51–100	37–100
Cala Millor	20–100	55–100	43–100
Son Bou	16–100	48–100	34–100
Málaga	8–100	29–100	21–100
Melilla	14–100	49–100	35–100

4.2 Difference between moorings and satellites

Differences between moorings and satellites are found in all locations, although the satellite points are very close to corresponding moorings (Table 4). In 2022, along the French coast, moorings observed higher MHW mean intensity at Sète and Leucate (by 0.39 and 0.23 °C, respectively) and higher MHW maximum intensity at Leucate (by 1.47 °C) than satellites. On the contrary, satellites detected higher MHW mean and maximum intensity at Barcelona than moorings, with differences around 0.5 and 1.07 °C, respectively. Strong differences in MHW maximum intensities are also

Table 4. Annual MHW characteristics (mean, maximum, and cumulative intensities, mean duration, frequency, and total days) and number of MHW days with temperatures warmer than 28 °C, as detected by moorings (product ref. nos. 3, 4, and 5; Table 1; top number) and the satellite nearest point (product ref. no. 1; Table 1; bottom number in italics) in 2022.

	Mean intensity	Maximum intensity	Cumulative intensity	Duration	Frequency	Total days	Total days with $T > 28$ °C (consecutive days)
Sète	3.67 *(3.28)*	5.11 *(5.35)*	146.68 *(118.16)*	10 *(9)*	4 *(4)*	40 *(36)*	– *(–)*
Leucate	2.72 *(2.49)*	5.17 *(3.70)*	212.07 *(221.64)*	9.8 *(14.8)*	8 *(6)*	78 *(89)*	– *(–)*
Barcelona	1.80 *(2.30)*	2.64 *(3.71)*	108.07 *(188.23)*	15 *(16.4)*	4 *(5)*	60 *(82)*	8 [6–2] *(17 [1–16])*
Tarragona	2.10 *(2.18)*	4.21 *(4.22)*	274.48 *(242.01)*	21.8 *(13.9)*	6 *(8)*	131 *(111)*	47 [11–19–11–1–4–1] *(22 [2–4–15–1])*
Dragonera	1.87 *(1.87)*	3.34 *(3.19*	209.58 *(253.11)*	18.7 *(27)*	6 *(5)*	112 *(135)*	53 [1–9–17–26] *(56 [7–24–9–10–6])*
Palma	1.80 *(1.91)*	2.45 *(2.98)*	221.27 *(237.14)*	17.6 *(31)*	7 *(4)*	123 *(124)*	58 [33–25] *(59 [43 10 6])*
Cala Millor	1.85 *(1.90)*	3.09 *(3.24)*	147.76 *(237.71)*	40 *(25)*	2 *(5)*	80 *(125)*	20 [3–4–5–1–6–1] *(55 [40–6–3–6])*
Son Bou	1.90 *(1.90)*	2.65 *(3.17)*	117.91 *(235.27)*	31 *(20.7)*	2 *(6)*	62 *(124)*	8 [5–1–2] *(45 [4–29–4–3–3–2])*
Málaga	3.51 *(3.34)*	4.38 *(4.51)*	80.69 *(76.82)*	7.7 *(7.7)*	3 *(3)*	23 *(23)*	– *(–)*
Melilla	1.66 *(1.71)*	2.75 *(3.82)*	77.90 *(168.37)*	9.4 *(12.5)*	5 *(8)*	47 *(98)*	1 *(1)*

found at Melilla, Palma, and Son Bou (by 1.13, 0.53, and 0.52 °C, respectively). The MHW mean duration is found to be longer in moorings than satellites, particularly at Cala Millor, Son Bou, and Tarragona (by 15, 10.3, and 7.9 d, respectively), while it is far longer in satellites than in moorings at Dragonera and Palma (by 8.3 and 13.4 d, respectively). The MHW total days and cumulative intensity in 2022 are higher in moorings at Sète and Tarragona than in satellites at the nearest point, while they are found higher in satellites at Leucate, Barcelona, the Balearic Islands stations (particularly at Cala Millor and Son Bou), and Melilla. Finally, where MHW days with temperatures warmer than 28 °C are found (from Barcelona to Son Bou), the number of days is higher in satellites than in moorings, except at Tarragona.

Differences between MHWs detected by satellites and moorings may be explained by several factors, such as the sensor or platform type, spatial and temporal coverage, specific bias at a particular platform, instrumental corrections, validation and calibration, and interpolation methods, as well as the effective depth of measurements (Alvera-Azcárate et al., 2011). While satellites provide SST, the selected moorings collected temperatures at surface or subsurface (from 0.4 to 17 m depths; Table 2). However, even for moorings with sensors installed near the surface (up to 0.5 m), strong differences with satellites are pointed out, as found at Sète, Leucate, and Barcelona for MHW mean and maximum intensities (up to 0.5 and 1.47 °C, respectively) and at Tarragona for MHW mean duration (13.4 d). Also, importantly, results at Cala Millor and Son Bou strongly differ between satellites at the surface and moorings in subsurface (particularly in MHW total days and days with temperatures warmer than 28 °C), as well as between satellite locations and between moorings, highlighting how the coastal ocean response differs from surface to subsurface and from one location to another at both surface and subsurface even in the same subregion (on each side of the Menorca Channel in the Balearic Islands).

5 Coastal MHWs from 2013 to 2022

MHWs observed by the moorings are now analysed from 2013 to 2022, and the events in 2022 are compared with those over the last decade (Fig. 4). All years from 2013–2022 suffered from MHWs in several locations of the coastal WMed.

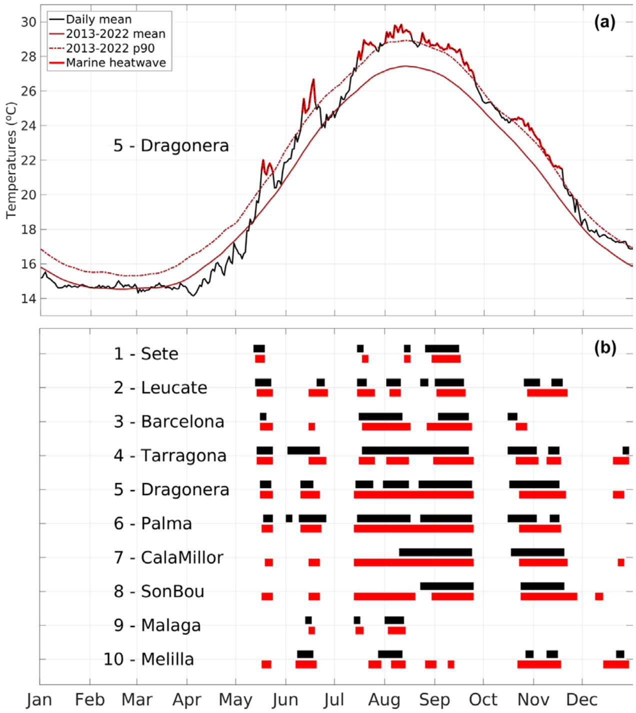

Figure 3. **(a)** Daily SST and MHWs from mooring at Dragonera in 2022 with respect to the reference period 2013–2022 (product ref. no. 3; Table 1). **(b)** MHW days from study moorings (black) and satellites at the nearest point (red) during the year 2022 (product ref. nos. 3, 4, and 5; Table 1).

In 2020 and 2022, all moorings detected MHWs. While 2020 events mostly happened in winter, 2022 MHWs mainly occurred in summer, reaching high ocean temperatures.

Time series of annual MHW characteristics from moorings show strong spatiotemporal variability. Variations in MHW mean and maximum intensities are highlighted between years, while the increase in MHW frequency and duration in recent years leads to a clear increase in MHW total days and cumulative intensity. In recent years, MHWs did not only occur during their usual season over a longer period but also extended over more seasons. While one season was concerned in 2013 (summer or autumn depending on the mooring), MHW occurrences covered three seasons in 2022 (mainly spring, summer, and autumn) (not shown).

The analysis over the period 2013–2022 highlights that many thermal records were reached in 2022. MHW total days reached the highest number in 2022 for the stations at Leucate, Barcelona, Tarragona, Dragonera, Palma, and Cala Millor; the second highest for Sète, Son Bou, and Melilla; and the fourth highest for Málaga. The MHW cumulative intensity in 2022 is the warmest observed since 2013 for the stations at Leucate, Barcelona, Tarragona, Dragonera, Palma, Cala Millor, and Melilla; the second warmest at Sète and Son Bou; and the third warmest at Málaga. In addition, in 2022, the number of MHW days with temperatures exceeding 28 °C is the highest and can be considered to be a unique year until now for the moorings at Barcelona, Tarragona, Dragonera, Palma, Cala Millor, and Son Bou, although Palma and Tarragona also experienced 7 and 5 d, respectively, with similar warm temperatures in 2015.

6 Discussion

Hourly measurements from moorings were averaged on a daily basis to be compared with the daily satellite products. The associated standard deviations over 2013–2022 oscillate between 0.23 and 0.39 °C, depending on the stations. In this section, the temporal resolution impact on the estimation of thermal stress during MHW events is analysed, in particular when high temperatures of 28 °C or more are reached. As highlighted above, the MHW events concerned are those in 2022 at the moorings from Barcelona to Son Bou.

Due to the diurnal cycle, maxima of MHW temperatures are found in the hourly datasets (Fig. 5). While the maxima from the daily datasets vary between 28.37 (Barcelona) and 29.95 °C (Palma), in the hourly datasets they oscillated between 28.96 (Cala Millor) and 31.36 °C (Dragonera), with this latter temperature range being the highest record ever registered by the Spanish mooring network Puertos del Estado. The difference between the daily and hourly data maxima is the highest at Dragonera (1.52 °C) and the smallest at Palma (0.05 °C). The distribution of the temperatures higher than 28 °C is schematically represented by the median, as well as the 5th and 95th percentiles, whose difference allows estimating the width (Fig. 5). This latter value is larger in the hourly than daily datasets due to the diurnal cycle. Comparing the moorings between themselves, the width is larger in both daily and hourly datasets at Dragonera (1.34 and 1.56 °C, respectively), Palma (1.33 and 1.42 °C, respectively), and Tarragona (1.07 and 1.30 °C, respectively), where warmer temperatures were reached.

At Palma, the daily and hourly data provide similar results on the maxima reached and distribution characteristics of extreme ocean temperatures in summer. At the moorings located further off the coast of the peninsula (Barcelona, Tarragona, and Dragonera), the temporal resolution of in situ data clearly impacts the extreme temperature observations. Such findings are also highlighted in the two nearshore stations, although their sensors are located at 17 m depth.

7 Conclusions

Society is facing unprecedented challenges arising from climate change impacts. Among them, marine heatwaves (MHWs) are becoming more frequent, longer, and more intense worldwide (Frölicher et al., 2018; Oliver et al., 2018), particularly in the Mediterranean Sea (Juza et al., 2022; Dayan et al., 2023; Pastor and Khodayar, 2023). Such physical changes have major ecological impacts, with socioeco-

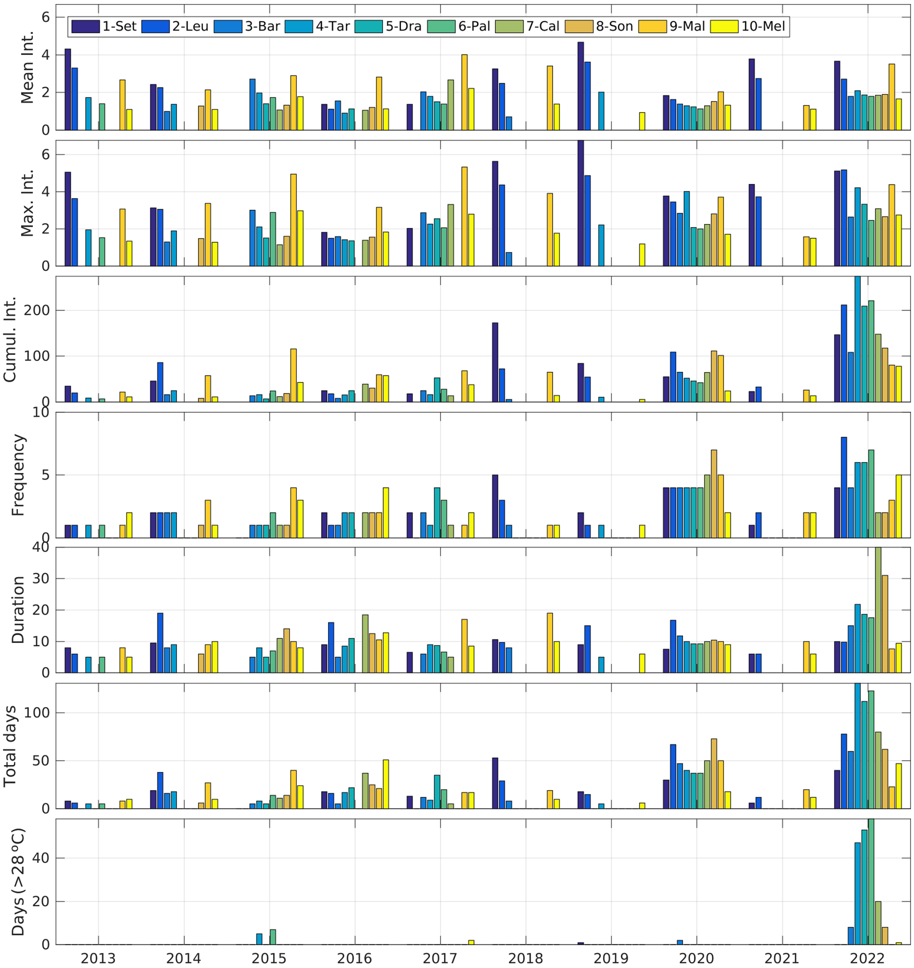

Figure 4. Annual MHW characteristics (mean, maximum, and cumulative intensities, mean duration, frequency, and total days) and number of MHW days with temperatures exceeding 28 °C, as detected by moorings (product ref. nos. 3, 4, and 5; Table 1) from 2013 to 2022.

nomic implications and compromising carbon storage, particularly in coastal ocean waters (Smith et al., 2021, 2023). Although MHWs are mainly induced by large-scale anomalous atmospheric conditions in the Mediterranean Sea (Holbrook et al., 2019; Guinaldo et al., 2023; Hamdeno and Alvera-Azcaráte, 2023), the ocean response strongly differs from the open-ocean to nearshore areas and from one coastal location to another (Juza et al., 2022).

In this study, MHWs in the coastal and shallow waters of the western Mediterranean Sea (WMed) have been investigated during the year 2022 and the period 2013–2022. Satellite and moorings observed MHWs along the coast of the WMed, whose characteristics strongly vary in time and space. Coastal MHWs were observed almost every year over the last decade, and they were exceptional in 2022 in intensity, duration, and geographical extension. In 2022, although the coastal MHW events have a strong spatial variation, all moorings – from the northern to the southern WMed and from the surface to the subsurface – observed MHWs registering new records in intensity (in French waters), duration (in subsurface in the Balearic Islands), total days, cumulative intensity (at Tarragona), and number of days with temperatures warmer than 28 °C (at Dragonera and Palma).

Although the satellite products have the great benefit of monitoring all of the ocean surface, differences with the moorings have been detected in the characterisation of MHWs in coastal areas and shallow waters. Compared with mooring measurements at the surface (between 0 and 3 m depth) in 2022, satellites underestimate MHW intensities in French waters and MHW duration at Tarragona, while they overestimate MHW intensities at Barcelona, Palma, and Melilla, as well as MHW duration at Dragonera and Palma. The thermal stress estimation from high-temperature peaks on the physical and biological oceans is also minimised with the use of daily data, which detect underestimated maxima with an up to 1.52 °C difference during the warm events compared to hourly measurements. Finally, the coastal ocean response to extreme warm events strongly differs from the northern to the southern WMed. No coincidence is found between north and south, nor is there a per-

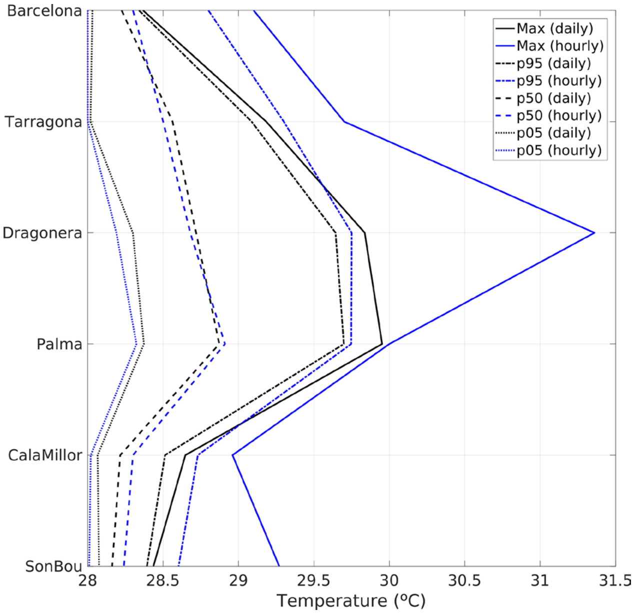

Figure 5. The 5th, 50th, and 95th percentiles and maxima of the distribution of MHW temperatures warmer than 28 °C, as detected with the daily (black) and hourly (blue) data from moorings (product ref. nos. 3, 4, and 5; Table 1).

sistent feature in regional differences. Coastal MHWs also vary within the same sub-region (Sète–Leucate, Barcelona–Tarragona, Dragonera–Palma, Cala Millor–Son Bou, and Málaga–Melilla), where extreme events coincide with differences in intensity and duration both at the surface and in subsurface. Such findings assert the importance of multi-platform, multi-sensor, and sustainable ocean observing systems from open-ocean to coastal and nearshore waters and from the surface to the subsurface to continue the investigation concerning MHWs and conduct an impact assessment.

Data availability. The datasets used in this study can be found in online repositories. The name of the repositories can be found in the article in Table 1.

Author contributions. MJ conducted the study and contributed to the data processing, interpretation of the data, scientific discussion, and writing of the paper. MdA and AFM contributed to the in situ data collection, data processing (quality control), and the revision of the paper.

Competing interests. The contact author has declared that none of the authors has any competing interests.

Disclaimer. Publisher's note: Copernicus Publications remains neutral with regard to jurisdictional claims made in the text, published maps, institutional affiliations, or any other geographical representation in this paper. While Copernicus Publications makes every effort to include appropriate place names, the final responsibility lies with the authors.

Acknowledgements. We gratefully acknowledge the reviewers and the handling editor for their revision of the article and their comments. The study has been conducted using EU Copernicus Marine Service Information and in situ data which have been collected, processed, and distributed by the Balearic Islands Coastal Observing and Forecasting System (SOCIB).

Review statement. This paper was edited by Piero Lionello and reviewed by Francisco Pastor, Salvatore Marullo, and one anonymous referee.

References

Alvera-Azcárate, A., Troupin, C., Barth, A., and Beckers, J. M.: Comparison between satellite and in situ sea surface temperature data in the Western Mediterranean Sea, Ocean Dynam., 61, 767–778, https://doi.org/10.1007/s10236-011-0403-x, 2011.

Bensoussan, N., Chiggiato, J., Buongiorno Nardelli, B., Pisano, A., and Garrabou, J.: Insights on 2017 marine heat waves in the Mediterranean Sea, Copernicus marine service ocean state report: issue 3, J. Oper. Oceanogr., 12, 101–108, https://doi.org/10.1080/1755876X.2019.1633075, 2019.

Buongiorno Nardelli, B., Tronconi, C., Pisano, A., and Santoleri, R.: High and Ultra-High resolution processing of satellite Sea Surface Temperature data over Southern European Seas in the framework of MyOcean project, Remote Sens. Environ., 129, 1–16, https://doi.org/10.1016/j.rse.2012.10.012, 2013.

Cerrano, C., Bavestrello, G., Bianchi, C. N., Cattaneo-Vietti, R., Bava, S., Morganti, C., Morri, C., Picco, P., Sara, G., Schiaparelli, S., Siccardi, A., and Sponga, F.: A catastrophic mass-mortality episode of gorgonians and other organisms in the Ligurian Sea (North-western Mediterranean), summer 1999, Ecol. Lett., 3, 284–293, https://doi.org/10.1046/j.1461-0248.2000.00152.x, 2000.

Coll, M., Piroddi, C., Steenbeek, J., Kaschner, K., Lasram, F. B. R., Aguzzi, J., Ballesteros, E., Bianchi, C. N., Corbera, J., Dailianis, T., Danovaro, R., Estrada, M., Froglia, C., Galil, B. S., Gasol, J. M., Gertwagen, R., Gil, J., Guilhaumon, F., Kesner-Reyes, K., Kitsos, M.-S., Koukouras, A., Lampadariou, N., Laxamana, E., López-Fé de la Cuadra, C. M., Lotze, H. K. Martin, D., Mouillot, D., Oro, D., Raicevich, S., Rius-Barile, J., Saiz-Salinas, J. I., San Vicente, C., Somot, S., Templado, J., Turon, X., Vafidis, D., Villanueva, R., and Voultsiadou, E.: The biodiversity of the Mediterranean Sea: estimates, patterns, and threats, PLoS One, 5, e11842, https://doi.org/10.1371/journal.pone.0011842, 2010.

Dayan, H., McAdam, R., Juza, M., Masina, S., and Speich, S.: Marine heat waves in the Mediterranean Sea: An assessment from the surface to the subsurface to meet national needs, Front. Mar. Sci., 10, 142, https://doi.org/10.3389/fmars.2023.1045138, 2023.

EU Copernicus Marine Service Product: Mediterranean Sea High Resolution and Ultra High-Resolution Sea Surface Temperature Analysis, Mercator Ocean International [data set], https://doi.org/10.48670/moi-00172, 2023a.

EU Copernicus Marine Service Product: Mediterranean Sea – High Resolution L4 Sea Surface Temperature Reprocessed, Mercator Ocean International [data set], https://doi.org/10.48670/moi-00173, 2023b.

EU Copernicus Marine Service Product: Mediterranean Sea – In-Situ Near Real Time Observations, Mercator Ocean International [data set], https://doi.org/10.48670/moi-00044, 2023c.

Fernández-Mora, À., Juza, M., and Tintoré, J.: Hourly in situ data of ocean temperature in the near-shore Balearic Islands over 2012–2020 (Version 1.0.0), Balearic Islands Coastal Observing and Forecasting System (SOCIB) [data set], https://doi.org/10.25704/ra9h-5127, 2021.

Frölicher, T. L., Fischer, E. M., and Gruber, N.: Marine heatwaves under global warming, Nature, 560, 360–364, https://doi.org/10.1038/s41586-018-0383-9, 2018.

Garrabou, J., Coma, R., Bensoussan, N., Bally, M., Chevaldonné, P., Cigliano, M., Diaz, D., Harmelin, J. G., Gambi, M. C., Kersting, D. K., Ledoux, J. B., Lejeusne, C., Linares, C., Marschal, C., Pérez, T., Ribes, M., Romano, J. C., Serrano, E., Teixido, N., Torrents, O., Zabala, M., Zuberer, F., and Cerrano, C.: Mass mortality in North-western Mediterranean rocky benthic communities: effects of the 2003 heat wave, Glob. Change Biol., 15, 1090–1103, https://doi.org/10.1111/j.1365-2486.2008.01823.x, 2009.

Garrabou, J., Gómez-Gras, D., Ledoux, J. B., et al.: Collaborative database to track mass mortality events in the Mediterranean Sea, Front. Mar. Sci., 6, 707, https://doi.org/10.3389/fmars.2019.00707, 2019.

Garrabou, J., Gómez-Gras, D., Medrano, A., et al.: Marine heatwaves drive recurrent mass mortalities in the Mediterranean Sea, Glob. Change Biol., 28, 5708–5725, https://doi.org/10.1111/gcb.16301, 2022.

Giorgi, F.: Climate change hot-spots, Geophys. Res. Lett., 33, L08707, https://doi.org/10.1029/2006GL025734, 2006.

Guerrero-Meseguer, L., Marín, A., and Sanz-Lázaro, C.: Future heat waves due to climate change threaten the survival of *Posidonia oceanica* seedlings, Environ. Pollut., 230, 40–45, https://doi.org/10.1016/j.envpol.2017.06.039, 2017.

Guinaldo, T., Voldoire, A., Waldman, R., Saux Picart, S., and Roquet, H.: Response of the sea surface temperature to heatwaves during the France 2022 meteorological summer, Ocean Sci., 19, 629–647, https://doi.org/10.5194/os-19-629-2023, 2023.

Hamdeno, M. and Alvera-Azcaráte, A.: Marine heatwaves characteristics in the Mediterranean Sea: Case study the 2019 heatwave events, Front. Mar. Sci., 10, 1093760, https://doi.org/10.3389/fmars.2023.1093760, 2023.

Hobday, A. J., Alexander, L. V. , Perkins, S. E., Smale, D. A., Straub, S. C., Oliver, E. C. J., Benthuysen, J. A., Burrows, M. T., Donat, M. G., Feng, M., Holbrook, N. J., Moore, P. J., Scannell H. A., Sen Gupta, A., and Wernberg, T.: A hierarchical approach to defining marine heatwaves, Prog. Oceanogr., 141, 227–238, https://doi.org/10.1016/j.pocean.2015.12.014, 2016.

Holbrook, N. J., Scannell, H. A., Sen Gupta, A, Benthuysen, J. A., Feng, M., Oliver, E. C. J. Alexander, L. V. Burrows, M. T., Donat, M. G., Hobday, A. J., Moore, P. J., Perkins-Kirkpatrick, S. E., Smale, D. A., Straub, S. C., and Wernberg, T.: A global assessment of marine heatwaves and their drivers, Nat. Commun. 10, 2624, https://doi.org/10.1038/s41467-019-10206-z, 2019.

In Situ TAC partners: EU Copernicus Marine Service Product User Manual for Mediterranean Sea- In-Situ Near Real Time Observations, Issue 2.0, Mercator Ocean International, https://catalogue.marine.copernicus.eu/documents/PUM/CMEMS-INS-PUM-013-030-036.pdf (last access: 22 January 2024), 2023.

Izquierdo P., Taboada F. G., González-Gil R., Arrontes J., and Rico J. M.: Alongshore upwelling modulates the intensity of marine heatwaves in a temperate coastal sea, Sci. Total Environ., 835, 155478, https://doi.org/10.1016/j.scitotenv.2022.155478, 2022.

Juza, M. and Tintoré, J.: Sub-regional Mediterranean Sea Indicators, Balearic Islands Coastal Observing and Forecasting System (SOCIB) [web app], https://apps.socib.es/subregmed-indicators (last access: 1 June 2023), 2020.

Juza, M. and Tintoré, J.: Multivariate Sub-regional ocean indicators in the Mediterranean Sea: From event detection to climate change estimations, Front. Mar. Sci., 8, 610589, https://doi.org/10.3389/fmars.2021.610589, 2021a.

Juza, M. and Tintoré, J.: Sub-regional Mediterranean Marine Heat Waves, Balearic Islands Coastal Observing and Forecasting System (SOCIB) [web app], https://apps.socib.es/subregmed-marine-heatwaves (last access: 1 June 2023), 2021b.

Juza, M., Fernández-Mora, A., and Tintoré, J.: Sub-regional marine heat waves in the Mediterranean Sea from observations: long-term surface changes, sub-surface and coastal responses, Front. Mar. Sci., 9, 785771, https://doi.org/10.3389/fmars.2022.785771, 2022.

Lionello, P. and Scarascia, L.: The relation between climate change in the Mediterranean region and global warming, Reg. Environ. Change, 18, 1481–1493, https://doi.org/10.1007/s10113-018-1290-1, 2018.

Marullo, S., Serva, F., Iacono, R., Napolitano, E., di Sarra, A., Meloni, D., Monteleone, F., Sferlazzo, D., De Silvestri, L., de Toma, V., Pisano, A,, Bellacicco, M., Landolfi, A., Organelli, E., Yang, C., and Santoleri, R.: Record-breaking persistence of the 2022/23 marine heatwave in the Mediterranean Sea, Environ. Res. Lett., 18 114041, https://doi.org/10.1088/1748-9326/ad02ae, 2023.

Oliver, E. C., Donat, M. G., Burrows, M. T., Moore, P. J., Smale, D. A., Alexander, L. V., Benthuysen, J. A., Feng, M., Sen Gupta, A., Hobday, A. J., Holbrook, N. J., Perkins-Kirkpatrick, S. E., Scannell, H. A., Straub, S. C., and Wernberg, T.: Longer and more frequent marine heatwaves over the past century, Nat. Commun., 9, 1324, https://doi.org/10.1038/s41467-018-03732-9, 2018.

Pastor, F. and Khodayar, S.: Marine heat waves: Characterizing a major climate impact in the Mediterranean, Sci. Total Environ., 861, 160621, https://doi.org/10.1016/j.scitotenv.2022.160621, 2023.

Pisano, A., Buongiorno Nardelli B., Tronconi, C., and Santoleri, R.: The new Mediterranean optimally interpolated pathfinder AVHRR SST Dataset (1982–2012), Remote Sens. Environ., 176, 107–116, https://doi.org/10.1016/j.rse.2016.01.019, 2016.

Pisano, A., Marullo, S., Artale, V., Falcini, F., Yang, C., Leonelli, F. E., Santoleri, R., and Nardelli, B. B.: New evidence of Mediterranean climate change and variability from sea surface temperature observations, Remote Sens., 12, 132, https://doi.org/10.3390/rs12010132, 2020.

Pisano, A., Fanelli, C., Tronconi, C., La Padula, F., Cesarini, C., Buongiorno Nardelli, B.: EU Copernicus Marine Service Quality Information Document for Mediterranean Sea High Resolution and Ultra High Resolution Sea Surface Temperature Analysis, Issue 4.0, Mercator Ocean International, https://catalogue.marine.copernicus.eu/documents/QUID/CMEMS-SST-QUID-010-004-006-012-013.pdf (last access: 22 January 2024), 2023a.

Pisano, A., Fanelli, C., Buongiorno Nardelli, B., Tronconi, C., Cesarini, C., and La Padula, F.: EU Copernicus Marine Service Product User Manual for Mediterranean Sea High Resolution and Ultra High Resolution Sea Surface Temperature Analysis, Issue 4.0, Mercator Ocean International, https://catalogue.marine.copernicus.eu/documents/PUM/CMEMS-SST-PUM-010-004-006-012-013.pdf (last access: 22 January 2024), 2023b.

Pisano, A., Fanelli, C., Tronconi, C., Cesarini, C., La Padula, F., and Buongiorno Nardelli, B.: EU Copernicus Marine Service Quality Information Document for Mediterranean Sea – High Resolution L4 Sea Surface Temperature Reprocessed, Issue 3.0, Mercator Ocean International, https://catalogue.marine.copernicus.eu/documents/QUID/CMEMS-SST-QUID-010-021-022-041-042.pdf (last access: 22 January 2024), 2023c.

Pisano, A., Fanelli, C., Tronconi, C., Cesarini, C., La Padula, F., and Buongiorno Nardelli, B.: EU Copernicus Marine Service Product User Manual for Mediterranean Sea – High Resolution L4 Sea Surface Temperature Reprocessed, Issue 3.0, Mercator Ocean International, https://catalogue.marine.copernicus.eu/documents/PUM/CMEMS-SST-PUM-010-021-022-041-042.pdf (last access: 22 January 2024), 2023d.

Schlegel, R. W., Oliver, E. C., Perkins-Kirkpatrick, S., Kruger, A., and Smit, A. J.: Predominant atmospheric and oceanic patterns during coastal marine heatwaves, Front. Mar. Sci., 4, 323, https://doi.org/10.3389/fmars.2017.00323, 2017a.

Schlegel, R. W., Oliver, E., Wernberg, T., and Smit, A. J.: Nearshore and offshore co-occurrence of marine heatwaves and cold-spells, Prog. Oceanogr. 151, 189–205, https://doi.org/10.1016/j.pocean.2017.01.004, 2017b.

Smith, K. E., Burrows, M. T., Hobday, A. J., Sen Gupta, A., Moore, P. J., Thomsen, M., Wernberg, T., and Smale, D. A.: Socioeconomic impacts of marine heatwaves: Global issues and opportunities, Science, 374, 6566, https://doi.org/10.1126/science.abj3593, 2021.

Smith, K. E., Burrows, M. T., Hobday, A. J., King, N. G., Moore, P. J., Sen Gupta, A., Thomsen, M. S., Wernberg, T., and Smale, D. A.: Biological impacts of marine heatwaves, Annu. Rev. Mar. Sci., 15, 119–145, https://doi.org/10.1146/annurev-marine-032122-121437, 2023.

Tintoré, J. and Casa Pérez, B.: Buoy BahiaDePalma data (Version 1.0.0), Balearic Islands Coastal Observing and Forecasting System (SOCIB) [data set], https://doi.org/10.25704/S6JB-CK61, 2022.

Vargas-Yáñez, M., Moya, F., Serra, M., Juza, M., Jordà, G., Ballesteros, E., Alonso, C., Pascual, J., Salat, J., Moltó, V., Tel, E., Balbín, R. Santiago, R., Piñeiro, S., and García-Martínez, M. C.: Observations in the Spanish Mediterranean waters: A review and update of results from 30-year monitoring, J. Mar. Sci. Eng., 11, 1284, https://doi.org/10.3390/jmse11071284, 2023.

Verdura, J., Santamaría, J., Ballesteros, E., Smale, D. A., Cefalì, M. E., Golo, R., and Cebrian, E.: Biodiversity loss in a Mediterranean ecosystem due to an extreme warming event unveils the role of an engineering gorgonian species, Sci. Rep., 9, 5911, https://doi.org/10.1038/s41598-019-41929-0, 2019.

Verdura, J., Santamaría, J., Ballesteros, E., Smale, D. A., Cefalì, M. E., Golo, R., de Caralt, S., Vergés, A., and Cebrian, E.: Local-scale climatic refugia offer sanctuary for a habitat-forming species during a marine heatwave, J. Ecol., 109, 1758–1773, https://doi.org/10.1111/1365-2745.13599, 2021.

United Nations Environment Programme/Mediterranean Action Plan and Plan Bleu: State of the Environment and Development in the Mediterranean, Nairobi, https://planbleu.org/wp-content/uploads/2021/04/SoED_full-report.pdf (last access: 1 June 2023), 2020.

Wehde, H., von Schuckmann, K., Pouliquen, S., Grouazel, A., Bartolome, T., Tintoré, J., De Alfonso Alonso-Munoyerro, M., Carval, T., Racapé V., and the INSTAC team: EU Copernicus Marine Service Quality Information Document for Mediterranean Sea- In-Situ Near Real Time Observations, INSITU_MED_PHYBGCWAV_DISCRETE_MYNRT_013_035, Issue 2.3, Mercator Ocean International, https://catalogue.marine.copernicus.eu/documents/QUID/CMEMS-INS-QUID-013-030-036.pdf (last access: 22 January 2024), 2023.

State Planet, 4-osr8, 15, 2024
https://doi.org/10.5194/sp-4-osr8-15-2024

Anomalous 2022 deep-water formation and intense phytoplankton bloom in the Cretan area

Anna Teruzzi[1], **Ali Aydogdu**[2], **Carolina Amadio**[1], **Emanuela Clementi**[2], **Simone Colella**[3], **Valeria Di Biagio**[1], **Massimiliano Drudi**[2], **Claudia Fanelli**[3], **Laura Feudale**[1], **Alessandro Grandi**[2], **Pietro Miraglio**[2], **Andrea Pisano**[3], **Jenny Pistoia**[2], **Marco Reale**[1], **Stefano Salon**[1], **Gianluca Volpe**[3], and **Gianpiero Cossarini**[1]

[1]National Institute of Oceanography and Applied Geophysics – OGS, 34010 Trieste, Italy
[2]CMCC Foundation – Euro-Mediterranean Center on Climate Change, Bologna, Italy
[3]Consiglio Nazionale delle Ricerche, Istituto di Scienze Marine (CNR-ISMAR), 00133 Rome, Italy

Correspondence: Anna Teruzzi (ateruzzi@ogs.it)

Received: 3 August 2023 – Discussion started: 10 October 2023
Revised: 28 March 2024 – Accepted: 5 June 2024 – Published: 30 September 2024

Abstract. The Mediterranean Sea is a quasi-permanently stratified and oligotrophic basin with intense late-winter and early-spring phytoplankton blooms typically limited to few regions (i.e. northwestern Mediterranean Sea, the southern Adriatic Sea, and the Rhodes Gyre). In these areas, blooms are sustained by nutrient injection to surface layers by winter vertical mixing and convective processes. A markedly intense bloom was predicted in spring 2022 in an unusual area of the southeastern Mediterranean Sea (i.e. southeast of Crete) by the Mediterranean Sea Copernicus Marine Forecasting Centre (MED MFC) system. Combining Copernicus modelling and observation products, the 2022 event and a number of driving and concurrent features have been investigated in a multidisciplinary way. A noticeable cold spell that occurred in Eastern Europe at the beginning of 2022 has been identified as the main driver of an intense deep-water formation event, with associated high nutrient concentrations in the surface layers. Consequently, an extreme phytoplankton bloom that was 50 % more intense than usual occurred in the area southeast of Crete, starting nearly 1 month later than usual and lasting for 3–4 weeks. Impacts on primary production were also relevant in the 2022 event area and were 35 % higher than the climatological annual primary production. Furthermore, the documented link between primary productivity and fishery catches suggests possible consequences along the whole food chain up to the marine ecosystem in the eastern Mediterranean Sea.

1 Introduction

The Mediterranean, the main regional sea of southern Europe, is a semi-enclosed basin located in a transitional zone between the midlatitude and subtropical climate regimes (Coppini et al., 2023; Cossarini et al., 2019; Lazzari et al., 2012; Siokou-Frangou et al., 2010). The Mediterranean Sea is an almost permanently stratified and oligotrophic basin with a few areas exhibiting recurrent late-winter and early-spring phytoplankton blooms in the northwestern Mediterranean, the southern Adriatic Sea, and the Rhodes Gyre (Siokou-Frangou et al., 2010). In these regions, the blooms are driven by winter deep convective processes, which bring nutrients into the surface layer, and by the subsequent stratification when the phytoplankton is no longer diluted across the water column. At this moment, conditions are suitable for the surface phytoplankton bloom onset since both light and nutrients are available in the surface layer (Habib et al., 2023; Mayot et al., 2017; D'Ortenzio and Ribera d'Alcalà, 2009).

The eastern Mediterranean experiences particularly sharp oligotrophic conditions, and productive areas are limited to the Rhodes Gyre, where deep-water mixing and related bloom events typically occur (Varkitzi et al., 2020), and to the coast of Türkiye (Kubin et al., 2019).

Current evidence suggests that the Mediterranean Sea is facing an increase in marine heat waves and a de-

Published by Copernicus Publications.

Table 1. Datasets used in the present work, together with references and DOIs.

Product ref. no.	Product ID and type	Data access	Documentation
1	MEDSEA_ANALYSISFORECAST_BGC_006_014, numerical models	EU Copernicus Marine Service Product (2022a)	Quality information document (QUID): Feudale et al. (2023); product user manual (PUM): Lecci et al. (2023a)
2	MEDSEA_MULTIYEAR_BGC_006_008, numerical models	EU Copernicus Marine Service Product (2022b)	Quality information document (QUID): Teruzzi et al. (2022); product user manual (PUM): Lecci et al. (2022a)
3	OCEANCOLOUR_MED_BGC_L3_MY_009_143, satellite observations	EU Copernicus Marine Service Product (2022c)	Quality information document (QUID): Colella et al. (2023a); product user manual (PUM): Colella et al. (2023b)
4	MEDSEA_ANALYSISFORECAST_PHY_006_013, numerical models	EU Copernicus Marine Service Product (2022d)	Quality information document (QUID): Goglio et al. (2024); product user manual (PUM): Lecci et al. (2023b)
5	MEDSEA_MULTIYEAR_PHY_006_004, numerical models	EU Copernicus Marine Service Product (2022e)	Quality information document (QUID): Escudier et al. (2022); product user manual (PUM): Lecci et al. (2022b)
6	SST_MED_SST_L4_REP_OBSERVATIONS_010_021, satellite observations	EU Copernicus Marine Service Product (2022f)	Quality information document (QUID): Pisano et al. (2023b); product user manual (PUM): Pisano et al. (2023b)
7	OMI_VAR_EXTREME_WMF_MEDSEA_area_averaged_mean, numerical models	EU Copernicus Marine Service Product (2023g)	Quality information document (QUID): Lyubartsev et al. (2023b); product user manual (PUM): Lyubartsev et al. (2023a)
8	ECMWF AST	https://www.ecmwf.int/en/forecasts/datasets/set-i, atmospheric model high-resolution 10 d forecast	ECMWF (2021)

crease in cold-spell events (Simon et al., 2022) as a potential consequence of changes in regional climate. However, in March 2022, a strong and unusual atmospheric cold spell affected the eastern Mediterranean region (Demirtaş, 2023), with strong surface air temperature negative anomalies recorded over southeastern Europe (up to −3 °C, according to Copernicus Climate Change Service bulletin; C3S monthly climate bulletin explorer, 2023; Copernicus, 2023).

In the present work, implications for marine physical and biogeochemical dynamics of the unusual 2022 cold event are investigated by exploiting the products of the Copernicus Marine Service (CMEMS, 2023). We use both models and observations to highlight the interplay between biogeochemical and physical processes, considering that intense cold spells usually drive deep-water column mixing and consequent nutrient injections in the surface layer and onset of phytoplankton blooms (Auger et al., 2014). In order to describe the exceptionality of the 2022 event and its possible implications for the Mediterranean ecosystem, its spatial and temporal extent are defined based on the phytoplankton bloom anomaly, and its characteristics in terms of sea surface temperature, mixed-layer depth, surface chlorophyll, nutrient concentrations, and primary production are investigated.

2 Methods

The occurrence and mechanism driving the anomalous deep-convection and phytoplankton bloom episode southeast of Crete (eastern Mediterranean Sea) in spring 2022 was investigated using both model- and satellite-based products. The Mediterranean Sea Copernicus Marine Forecasting Centre (MED MFC) provides 3D ocean biogeochemical and physical variables at $1/24^\circ$ resolution (product ref. 1, 2, 4, and 5; Table 1). The sea surface temperature (SST) and surface layer chlorophyll concentration are provided by the Copernicus Marine Sea Surface Temperature and Ocean Colour Thematic Assembly Centre (SST TAC and OC TAC, respectively) (product ref. 3 and 6; Table 1). Both near-real time and multi-year products are used to characterise the 2022 event.

A daily climatology based on the 1999–2019 MED MFC biogeochemistry reanalysis (Cossarini et al., 2021; Teruzzi et al., 2022; product ref. 2; Table 1) was calculated, following Hobday et al. (2016), for a subset of variables, namely surface chlorophyll concentration, phosphocline depth, average phosphate concentration above the phosphocline, and primary production integrated in the 0–200 m layer. The nutrient analysis was focused on phosphate since it is known to be the limiting nutrient for the Mediterranean Sea (Siokou-Frangou et al., 2010). For each variable, a set of percentiles is calculated to identify specific thresholds (i.e. 1st, 25th, 50th, 75th, and 99th percentile) using a 10 d window centred on each date of the climatological year. Comparing the 2022 MED MFC analysis and forecast (Salon et al., 2019; Feudale et al., 2023 version 2.1; product ref. 1; Table 1) with the corresponding climatology in the time window of the bloom (20 March–30 April), the chlorophyll concentrations in all the surface grid points of the investigated area (22–32° E, 32–35° N) resulted in values above the 99th percentile for at least 20 % of the time window, indicating that the whole area was affected by intense and anomalous bloom conditions. In order to define the region mostly affected by the anomalous 2022 bloom, following Hobday et al. (2016), the maximum difference with respect to climatology between 20 March and 30 April is calculated (Imax), and the event area is defined as indicated by all the surface grid points with Imax higher than its 90th percentile (0.23 mg chl m^{-3}) (Fig. 1). The characteristics of the anomalous convection and bloom event are investigated by considering marine physical and biogeochemical properties averaged over the event area contoured in Fig. 1. Moreover, a daily sea surface temperature (SST) climatology derived from the Mediterranean SST multi-year satellite product over the period 1982–2021 (Pisano et al., 2023a, b; product ref. 6; Table 1) is used to compare modelled surface temperatures (i.e. first layer of the MED MFC SST; product ref. 4) during the 2022 event time window. To compare the physical and biogeochemical dynamics in the event area and in the Rhodes Gyre area, vertical profiles of temperature, phosphate, and chlorophyll are investigated at two locations (Fig. 1).

Finally, the Copernicus Marine Ocean Monitoring Indicator (Lyubartsev et al., 2023b; product ref. 7; Table 1), computed from the Mediterranean Sea Physics Reanalysis (Escudier et al., 2022; product ref. 6; Table 1), which provides water mass formation rates in the Mediterranean Sea, is considered to analyse the exceptionality of the 2022 event. In particular, the Levantine Deep Water (LDW) formation index is calculated for 2022 and compared with values that occurred in the past (from 1987 onwards).

3 Results

The signal of the 2022 cold outbreak over Eastern Europe (Demirtaş, 2023) is clearly detectable in the atmospheric surface temperature (AST) extracted from the ECMWF analysis products (ECMWF, 2021; product ref. 8; Table 1). In the second half of January 2022, the AST daily time series reaches a relative minimum (nearly 15 °C), and it is followed by two minima in the March–April time window (Fig. 2a). Accordingly, with a less noticeable variability, sea surface temperature (SST) gradually decreases in the area of interest (Fig. 2a). The satellite SST (Pisano et al., 2023a; product ref. 6; Table 1) shows a constantly negative anomaly of winter 2022 with respect to its climatology (−0.46 °C on average) from the beginning of January to the end of March, indicating that sea surface cooling is the most likely driver of an anomalous deep-convection event. Even lower SST values are provided by the MED MFC analysis and forecast (Goglio et al., 2024 version 2.2; product ref. 4; Table 1), with a minimum in the second half of March, followed by a relatively sharp increase towards the SST satellite climatology. According to the relatively low SST and, similarly, to the typical winter mixing conditions in the Rhodes Gyre area (Kubin et al., 2019), in the 2022 event area (Fig. 1) the mean mixed layer (MLD; calculated as the depth at which the density increases by 0.01 kg m^{-3} compared to the density at 10 m depth; product ref. 4; Table 1) is deeper than 500 m (Fig. 2b) on several occasions from the end of January to the end of March, which is when the mean MLD gets shallower (up to 50 m). Consistent with the strong March 2022 sea surface cooling, the mean MLD reaches its maximum in March (equal to or deeper than 700 m). The daily maps of AST, SST, SST anomaly, MLD, and heat fluxes during March 2022 provided in Appendix A (Figs. A1–A5) further detail the spatial extent and temporal sequence of the atmospheric and oceanic processes summarised in Fig. 2. Two close and significant drops in AST are, in fact, observed in the area (11–14 March and 19–23 March), according to a cold-air intrusion from the northwest (Fig. A1). Together with the January cold spell (Fig. 2), the March cooling events resulted in significant negative SST anomalies, especially south of Crete, which persisted in the area until the end of March (Fig. A2) with more steady occurrences in the anomalous-event area. Moreover, relatively cold SSTs are also observed by the L3 satellite product (Fig. A3), although only on 7 March and from 14 March onwards (the region is cloudy between 9 and 13 March). Modelling products show that the strong mixing event that started on 9 March and ended on 25 March (Fig. A4) is possibly driven by the cooling and that the area with the highest mixed-layer depths (larger than 1000 m) overlaps well with the April 2022 anomalous bloom. The strong negative heat fluxes into the sea, which occur at the same dates of the cooling events (Fig. A5), further confirm that the driving mechanism of the event is represented by significant heat losses. Considering the Copernicus Marine Ocean Monitoring Indicator (Lyubartsev et al., 2023b; product ref. 7; Table 1), in the Levantine basin, a large dense-water formation rate of approximately 1.3 Sv is documented (not shown[1]) in the winter of 2022. Confirming the relevant effects of the 2022 cold outbreak on physical marine processes, the same LDW formation index was higher only during the noteworthy eastern Mediterranean transient (EMT; 1992–1993), which is when the formation rate reached up to 1.8 Sv. After that, the LDW formation index showed only two maxima with relatively low values in 2008 and 2012 (0.7 and 1.0 Sv, respectively).

---

[1] The Ocean Monitoring Indicator of the water mass formation will be extended to 2022 and published in the Copernicus Marine catalogue by 2024.

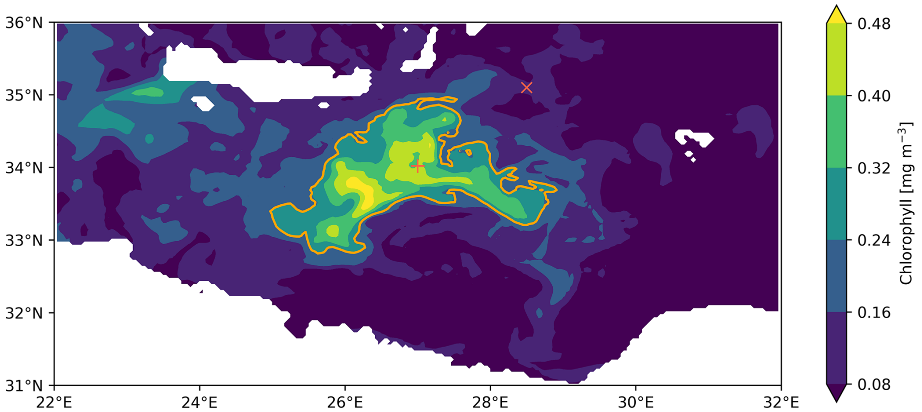

Figure 1. Mediterranean Sea analysis and forecast product (product ref. 1; Table 1). Filled contours of the maximum intensity of surface chlorophyll concentration between 20 March and 30 April 2022 and line contour of the 90th percentile of the maximum intensity (0.23 mg chl m^{-3}). The "+" and "×" markers indicate positions inside and outside of the 2022 event.

Slightly later, with respect to AST minima and during the strong mixing in March 2022, in the event area southeast of Crete (Fig. 1), the phosphocline depth (PCLD; depth of the maximum phosphate vertical gradient; Salon et al., 2019) is deeper than 400 m, and the PCLD climatology is at the 99th percentile, with two peaks that go down to nearly 600 m (Fig. 2b). The March 2022 anomalous deepening of the phosphocline is preceded in February by a more typical event with the deepening of the phosphocline that stays within its climatology at the 99th percentile and goes down to nearly 400 m. Due to its role as the limiting nutrient in the Mediterranean Sea (Siokou-Frangou et al., 2010), only phosphocline is included in Fig. 3, but we verified that nitrate is very similarly impacted by the 2022 anomalous event processes.

At the bloom peak (8 April), the mean surface chlorophyll concentration in the event area (Feudale et al., 2023, version Q4/2022; Fig. 1, product ref. 1; Table 1) is higher than 0.4 mg m^{-3}, i.e. more than twice the climatological 99th percentile (Fig. 2c). Chlorophyll concentrations are higher than the 99th climatological percentile from 2 to 10 April, indicating that the 2022 bloom event is anomalous, both in terms of intensity and timing. In fact, according to the chlorophyll climatology, typical late-winter chlorophyll peaks occur in the first half of March. With the similar timing of the anomalous surface chlorophyll concentration, the primary production integrated over the 0–200 m layer largely exceeds the 99th climatological percentile (Fig. 2d). Related to the strong mixing event that occurred in the late winter of 2022 and to the deepening of the phosphocline (Fig. 2b), the mean phosphate concentration above the phosphocline is higher than the 99th percentile in the month preceding the phytoplankton bloom, with a sharp decrease during the bloom-establishing phase (Fig. 2e). The delay between the large availability of nutrients in the surface layer and the bloom peak is consistent with the Sverdrup theory (Mayot et al., 2017), according to which the surface bloom starts when the MLD becomes shallower than the euphotic layer. Indeed, when the mixing is limited to the surface, phytoplankton is no longer diluted over the water column but remains in the surface layer where both light and nutrients (brought to the surface by the previous deep mixing) are available and favourable to the bloom onset.

The anomalous bloom event is clearly detectable in surface chlorophyll observations (multi-sensor ocean colour product; Colella et al., 2023a; product ref. 3; Table 1) that reach values comparable to those simulated by the analysis and forecast system (Fig. 3). In particular, Fig. 3 shows that high chlorophyll concentrations are observed on 27 and 29 March and on 1 and 6 April, indicating that the event started at around 27 March, maintained high-concentration values on 29 March and 1 and 6 April, and possibly ended between 8 and 9 April. On these dates, the observed chlorophyll concentration is higher than 0.5 mg m^{-3} (up to 3 mg m^{-3} on 29 March). Moreover, high chlorophyll concentrations are located in an area that differs (southwestern shifted) from the usual Rhodes Gyre bloom region which, in Fig. 3, is represented by the magenta contour identifying satellite climatology above 0.115 mg m^{-3} (i.e. half of the threshold used to define the event area; Fig. 1). Furthermore, we observed that the area with climatological concentration above the threshold is largest at the beginning of March (not shown). Model daily maps of model surface chlorophyll concentration provided in the Appendix (Fig. A6) show that in the simulation, the bloom started on 4 April, reached a peak between 8 and 9 April with a concentration larger than 0.5 mg m^{-3} (i.e. similar values to the ones observed in satellite maps), and gradually extinguished from 11 April onwards. An analysis of the deviation of satellite chlorophyll observations with respect to the 1999–2020 climatology (Fig. A7) demonstrates that on 27 and 29 March and on 1 and 8 April, chlorophyll is at least 3 standard deviations higher than the mean in the event area.

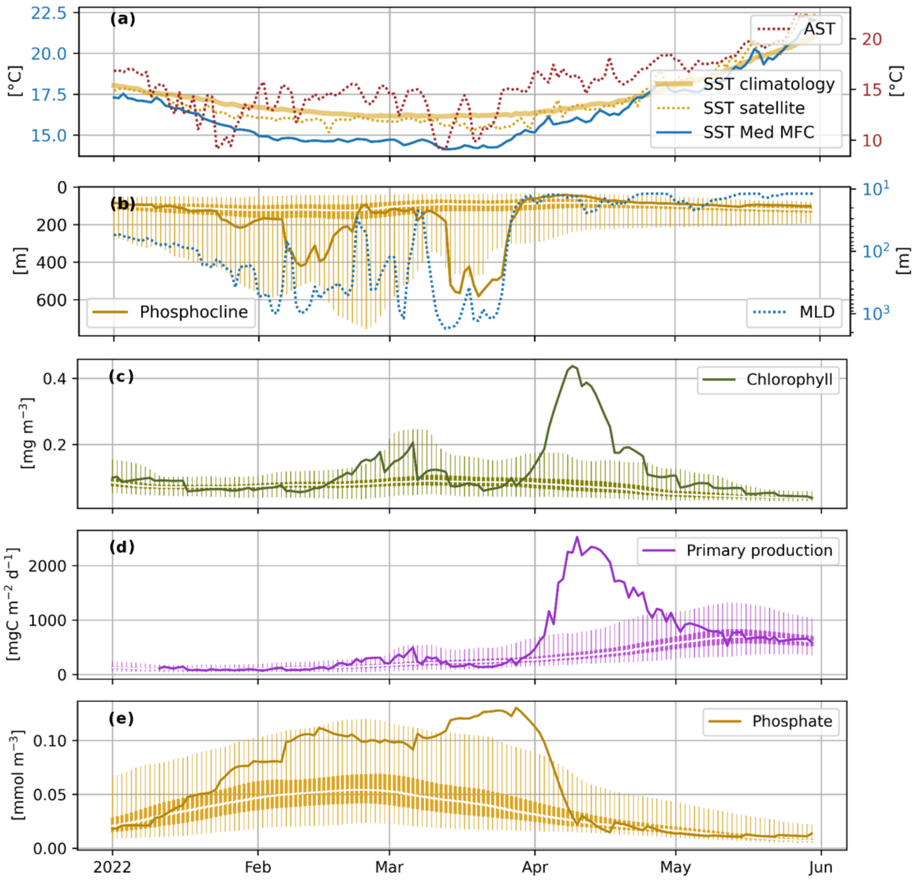

Figure 2. Daily time series – spatially averaged over the event area (Fig. 1) – from January to May 2022 for the **(a)** air surface temperature (AST), sea surface temperature for satellite (SST satellite, product ref. 6; Table 1) and model (SST MED MFC, product ref. 4; Table 1), and SST satellite climatology. **(b)** Mixed-layer depth (MLD; product ref. 4; Table 1) and phosphocline (product ref. 1; Table 1). **(c)** Surface chlorophyll concentration. **(d)** Mean concentration of phosphate above the phosphocline. **(e)** Primary production integrated in the 0–200 m layer. Climatological percentiles are shown in panels **(b)**, **(c)**, **(d)**, and **(e)** (thin vertical line: 1st and 99th percentiles; thick vertical line: 25th and 75th percentiles; white marker: median).

Since the 2022 anomalous surface bloom is the result of a sequence of processes (cold spell, sea surface cooling, vertical mixing, fertilisation, and subsequent stratification), uncertainties in the representation of each of these dynamics by the atmospheric ocean and biogeochemical models may combine and result in inaccuracies in the spatiotemporal representation of the bloom. However, even if the bloom simulation shows a delay of 5–8 d, the use of 3D modelled data allowed us to (i) define the temporal and spatial boundaries of the event and (ii) tackle the sequence of physical and biogeochemical processes that are involved in the bloom dynamics.

The anomalous localisation of the 2022 bloom can be further supported by comparing the vertical processes at two locations (Fig. 4): (i) inside the area of the event and (ii) in the Rhodes Gyre area where the late winter bloom typically occurs ("+" and "×" markers in Fig. 1, respectively). The Hovmöller diagram of temperature inside the event area reveals the gradual outcropping of deep-water masses that reached the surface from 2000 m on 25 March (Fig. 4a). At the same time, the phosphate concentration shows a nearly vertical uniform distribution with persistent high values in the surface layer ($>0.15\,\mathrm{mmol\,m^{-3}}$) until the beginning of the event (4 April), when the nutrient started to be consumed (Fig. 4c). Starting on 4 April, the large chlorophyll concentration in the surface and subsurface layer follows the nutrient injection (Fig. 4e). Finally, a transition to stratified conditions with the formation of a deep-chlorophyll maximum (DCM) occurs from 10 April. The location outside the 2022 event (right column of Fig. 4) shows much less intense and shorter water column mixing with the lower phosphate concentration in surface layers (Fig. 4b and d). In the chlorophyll Hovmöller diagram (Fig. 4f), a transition phase (non-negligible surface concentration with subsurface chlorophyll maximum; Lavigne et al., 2015) toward summer-stratified DCM conditions is already in place at the end of March.

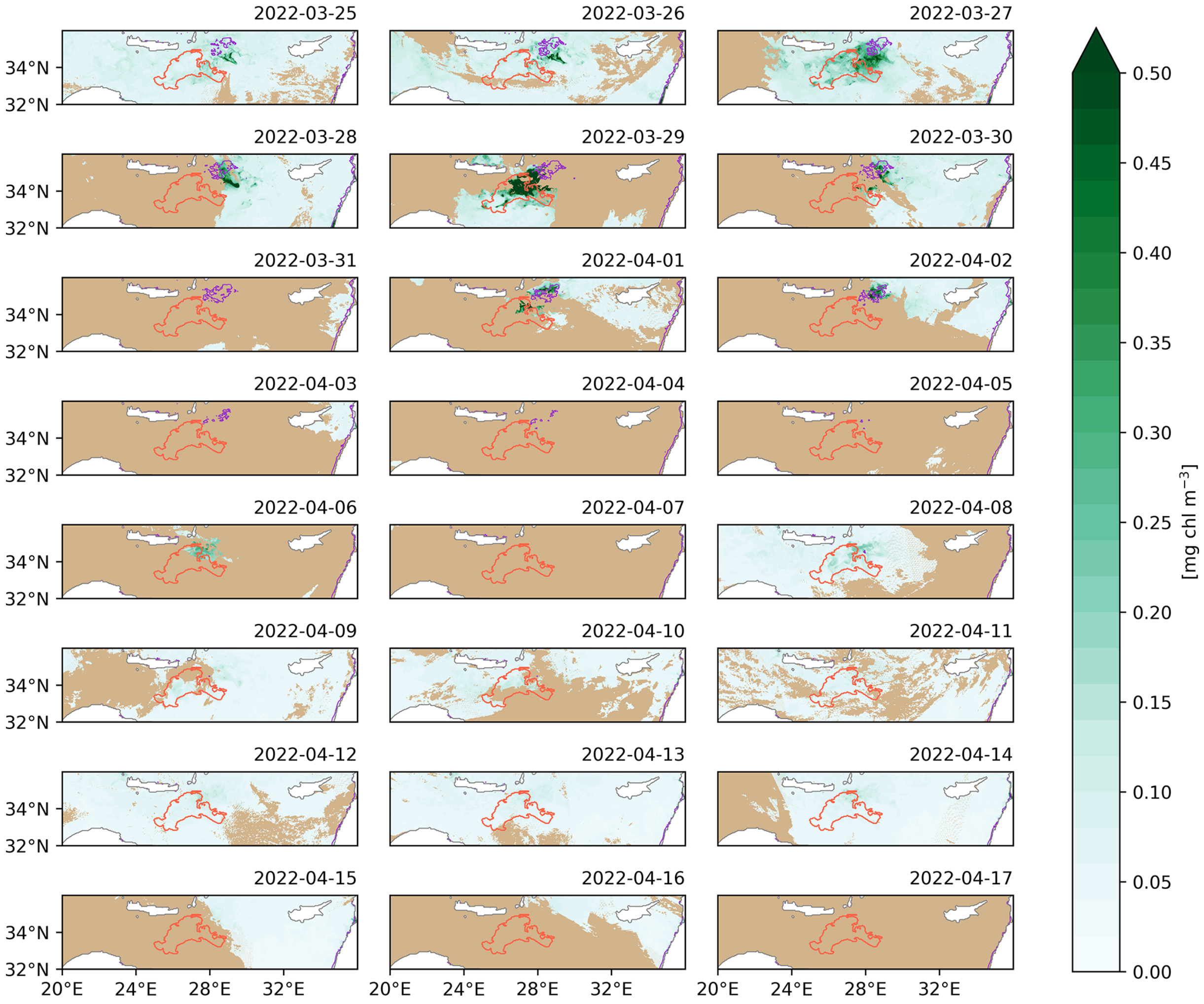

Figure 3. Daily maps of satellite surface chlorophyll concentration [mg chl m^{-3}] (product ref. 3; Table 1) from 25 March (upper-left panel) to 17 April 2022 (lower-right panel), with the orange line contour showing the event area (Fig. 1), and the purple line contour identifying satellite climatology above 0.115 mg m^{-3}. Areas without satellite observations are masked in light brown.

4 Discussion and conclusions

An anomalous deep-mixing and bloom event in the southeastern Mediterranean in the 2022 early-spring period was detected by means of the Copernicus Marine MED MFC products. In this region, intense phytoplankton blooms related to vertical mixing processes and consequent nutrient supply are usually located in the Rhodes Gyre area and have been previously investigated using in situ and satellite observations and modelling products (e.g. Habib et al., 2023; D'Ortenzio et al., 2021; Varkitzi et al., 2020; Siokou-Frangou et al., 2010), while the 2022 event was located southeast of Crete (Fig. 1). In this work, we analysed and described the 2022 event main features and its drivers.

The deep-convection and the phytoplankton bloom events in the Cretan area are consistent with the anomalous cooling that occurred in southeastern Europe at the beginning of 2022, showing a dynamic similar to the one of the Mediterranean marine cold-spell events described in Simon et al. (2022). For instance, the impact of the 2022 cold spells on the north–central Aegean Sea has been recently demonstrated by Potiris et al. (2024), who show that buoyancy losses during the winter 2021–2022 were comparable to those of 1993–1994, 2002–2003, and 2012, which were all years of dense-water formation (DWF) in the Aegean Sea, as discussed in Sect. 3. The findings of Potiris et al. (2024) further support the fact that the 2022 winter and related marine processes can be considered anomalous for the eastern Mediterranean. Furthermore, the connection between the 2022 atmospheric conditions and sea cooling is corroborated when considering the impacts of atmospheric modes of variability on the Mediterranean Sea surface heat exchange discussed by Josey et al. (2011) and Reale et al. (2020). Indeed, both pattern indexes that are associated with negative heat

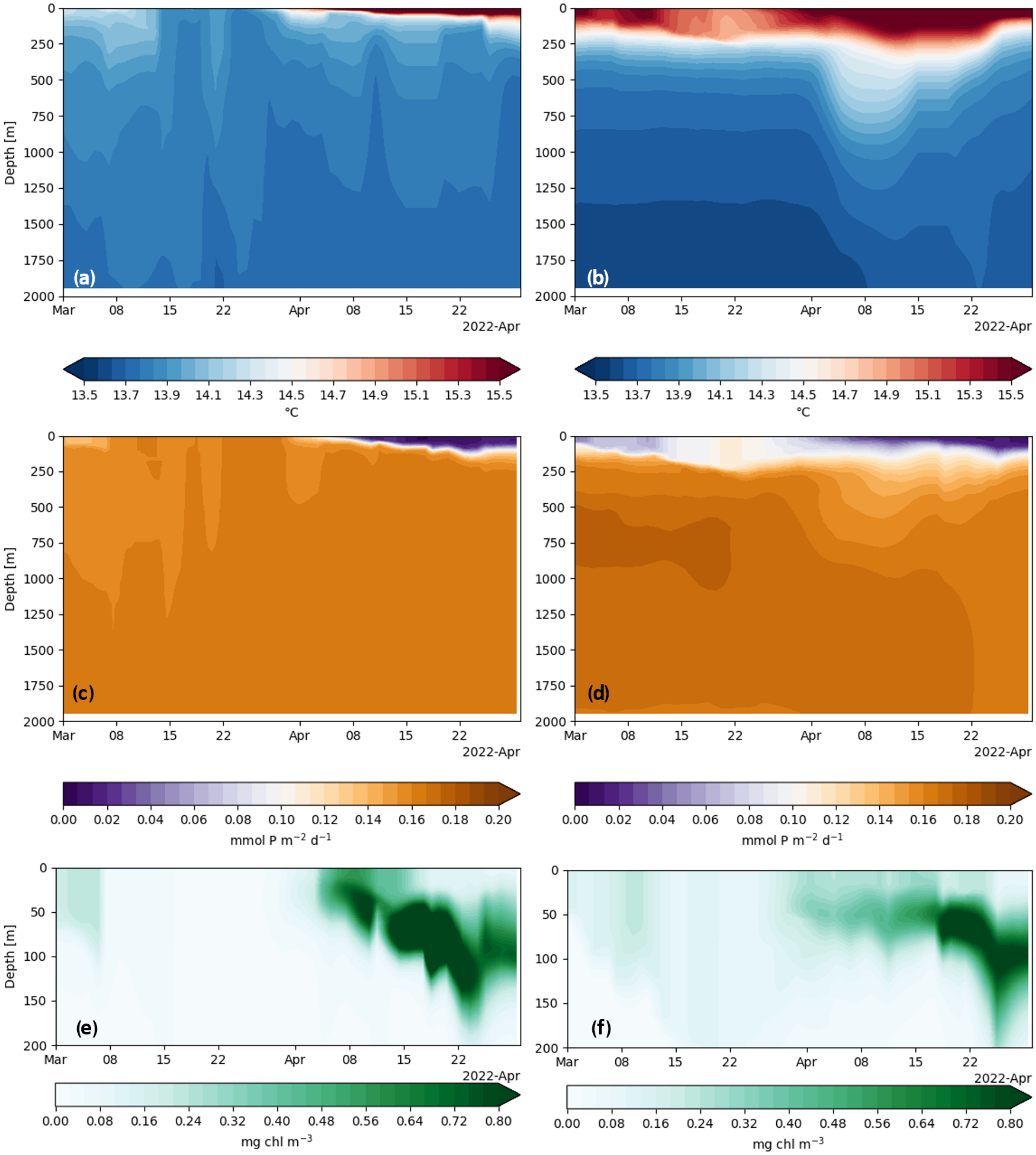

Figure 4. Hovmöller diagrams in March and April of temperature (**a, b**), phosphate and chlorophyll concentrations (**c, d** and **e, f**, respectively) inside the event area at 34.02° N–27° E (left panels; white "+" marker in Fig. 1) and outside the event area at 35.1° N–28.5° E (right panels; white "×" marker in Fig. 1).

fluxes in the eastern Mediterranean were relatively high in March 2022 (Index of /cwlinks, 2023).

The frequency and the impacts of marine extreme events in recent years have been investigated in the Mediterranean Sea (Dayan et al., 2023; Martínez et al., 2023; McAdam et al., 2023; Simon et al., 2022; Darmaraki et al., 2019), with the literature also proposing innovative techniques to analyse prolonged episodes in marine ecosystems (Di Biagio et al., 2020). Together with the relatively high number of variables exceeding their 99th percentile during the event (Figs. 2 and 3), the recent decrease in the occurrence of cold-marine extremes in the eastern Mediterranean (Simon et al., 2022) further highlights the exceptionality of the 2022 event.

Our study documents the importance of the value chain composed by atmospheric, ocean, and biogeochemical prediction models in detecting anomalies with respect to the typical state and variability. In particular, the strong anomaly in phytoplankton bloom intensity was revealed to be a suitable descriptor to define the 2022 event localisation, extent, and duration. Moreover, the evaluation of the spatial and temporal mismatch of the simulated event with respect to the Copernicus Marine Ocean Colour product provides an assessment of the capability of the prediction chain to simulate specific events.

Considering that previous anomalous cooling events (1992–1993) were among the drivers of the EMT that impacted the of the whole Mediterranean Sea dynamics (e.g. Pinardi et al., 2019; Roether et al., 2007; Theocharis et al., 2002), with consequences on other marine compartments (e.g. nutrients and productivity, biodiversity, and acidification; Tsiaras et al., 2012; Touratier and Goyet, 2011; Danovaro et al., 2004; Stratford and Haines, 2002; Civitarese and Gacic, 2001), the 2022 event and the related deep-water formation might be worth further investigation.

Our results show that the 2022 anomalous event increased the annual primary production by 35 % in an area of approximately 35 000 km^2 (i.e. 11 % and 1.4 % of the Levantine basin and Mediterranean Sea surface, respectively). As a consequence of the increased organic matter synthesis, a non-negligible impact along the whole food chain might have occurred, given the well-proven link between productivity and fish catch sizes (Canu et al., 2022; Colloca et al., 2017; Piroddi et al., 2017; Conti and Scardi, 2010). Due to the relative time proximity of the event and to the non-trivial work needed to collect fish catch data, it was not possible to gather quantitative information on this aspect, although the impact of the 2022 anomaly on the higher trophic level deserves a closer look.

Appendix A: Daily maps of observed and simulated marine properties in the Cretan area

The spatial and temporal extent of the 2022 bloom event and of its drivers can be further investigated using daily maps of a range of marine features in the Cretan area during March 2022. The atmospheric, model sea surface temperature anomaly, and satellite sea surface temperature are shown in Figs. A1–A3, providing evidence of the intense cooling event that occurred in March 2022 and are described in the Sect. 3. Looking at the MLD daily maps (Fig. A4), it is worth noting that on 3 and 4 March the bloom event is already interested by deep mixing (also visible in Fig. 2), possibly related to the relatively low SST values already present at the beginning of March (Fig. A2) and resulting from early-winter cooling events (starting in January 2022, as shown by the AST time series in Fig. 2). Remarkably, the strong MLD deepening in the anomalous event area are followed by positive total heat fluxes in the sea (e.g. 17 March, Fig. A5), due to the deep water reaching the surface layers, together with its temperature being lower than the AST.

Finally, the spatiotemporal evolution of the event as simulated by the Mediterranean Sea Copernicus Marine Forecasting Centre is detailed in the modelled daily maps of surface chlorophyll concentration on the same dates of the satellite observations provided in Fig. 4 (from 25 March to 17 April 2022; Fig. A6).

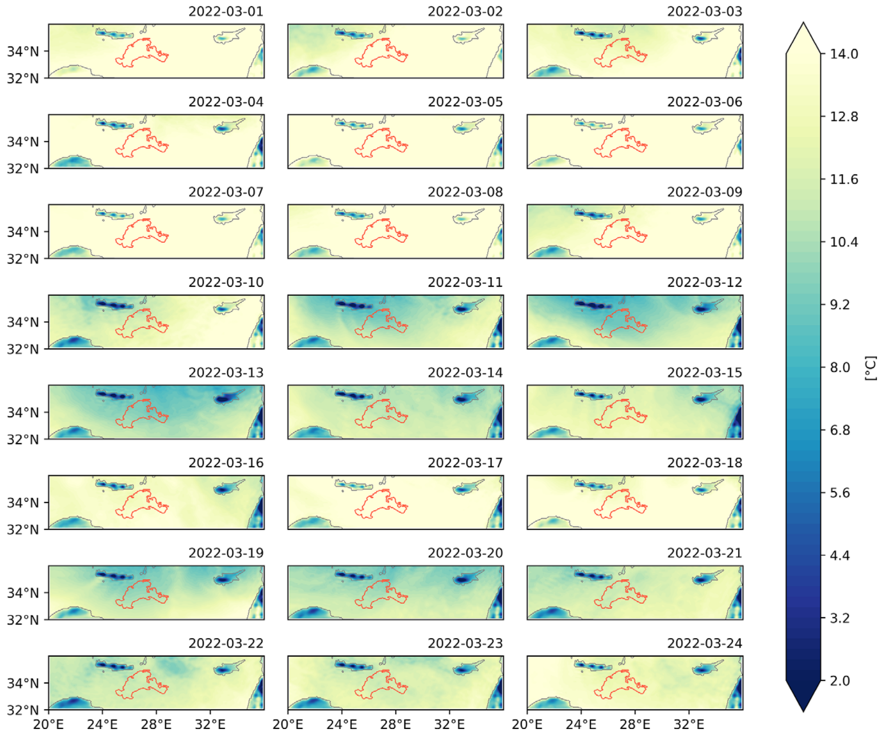

Figure A1. Daily maps of ECMWF atmospheric surface temperature [°C] (product ref. 8; Table 1) from 1 March (upper-left panel) to 24 March 2022 (lower-right panel), together with the orange line contour of the event area (Fig. 1).

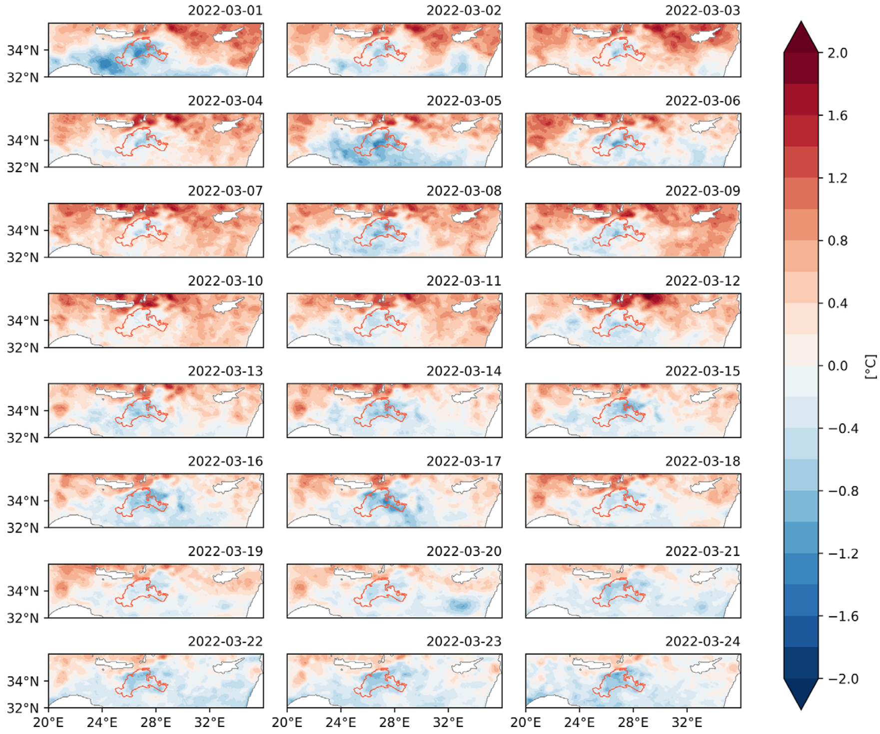

Figure A2. Daily maps of the modelled sea surface temperature anomaly [°C] (product ref. 4; Table 1) from 1 March (upper-left panel) to 24 March 2022 (lower-right panel), together with the orange line contour of the event area (Fig. 1).

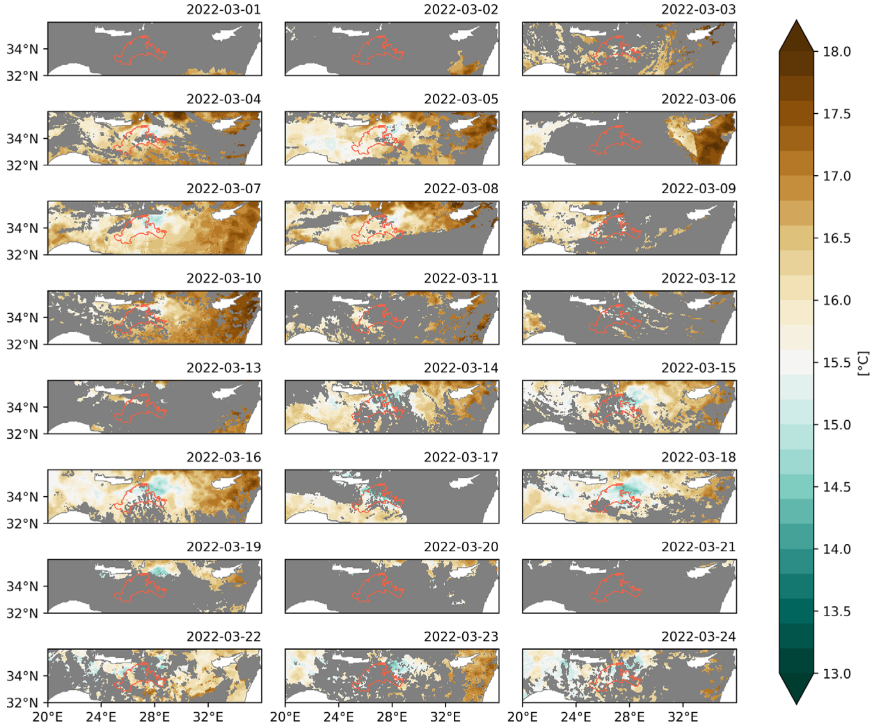

Figure A3. Daily maps of satellite sea surface temperature [°C] (product ref. 6; Table 1) from 1 March (upper-left panel) to 24 March 2022 (lower-right panel), together with the orange line contour of the event area (Fig. 1). Areas without satellite observations are masked with grey.

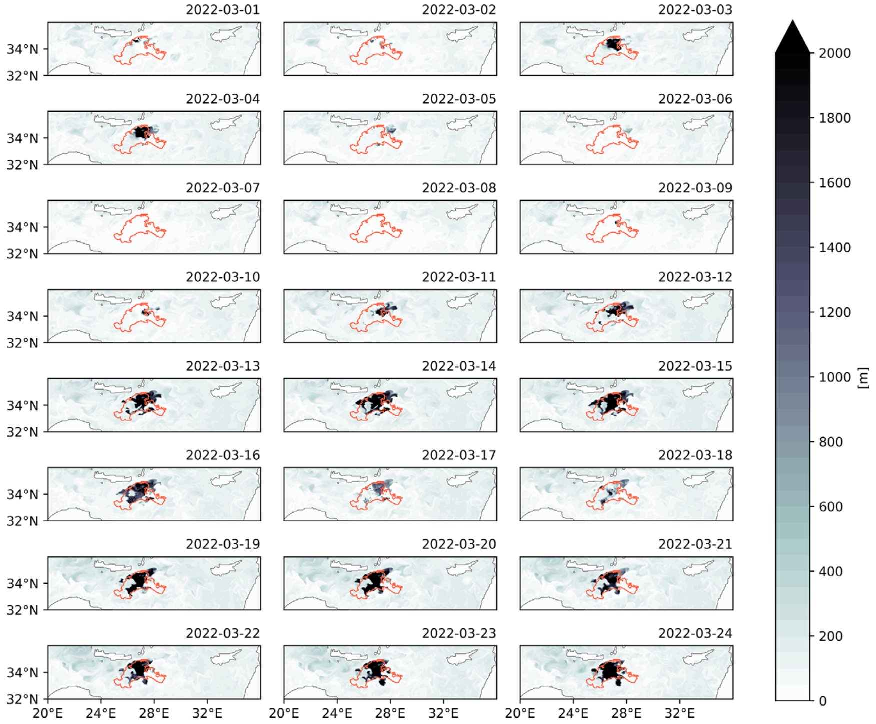

Figure A4. Daily maps of mixed-layer depth [m] (product ref. 4; Table 1) from 1 March (upper-left panel) to 24 March 2022 (lower-right panel), together with the orange line contour of the event area (Fig. 1).

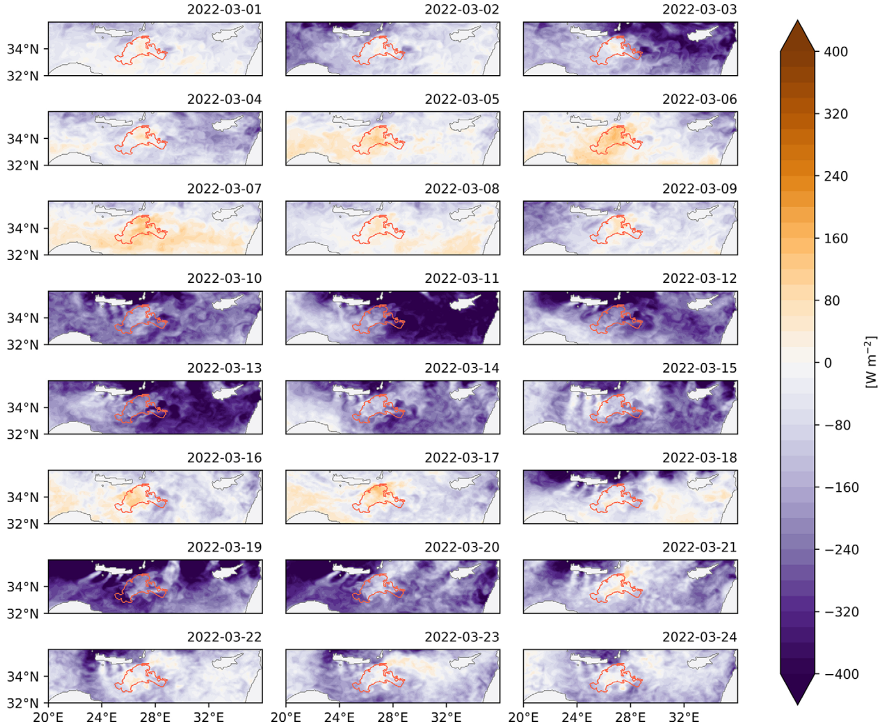

Figure A5. Daily maps of total heat fluxes in seawater [W m^{-2}] (product ref. 4; Table 1) from 1 March (upper-left panel) to 24 March 2022 (lower-right panel), together with the orange line contour of the event area (Fig. 1).

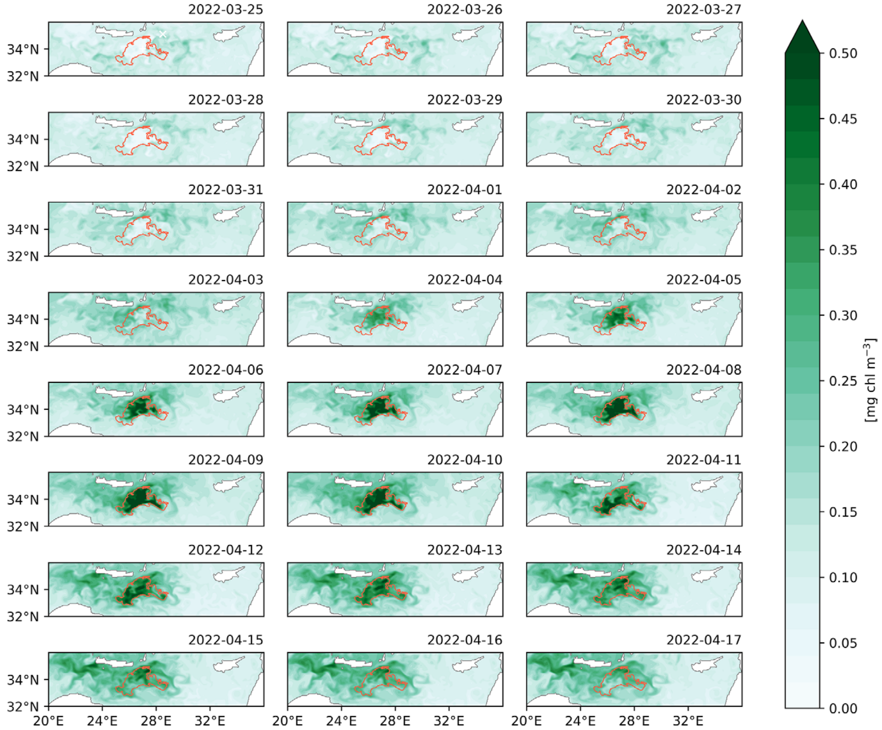

Figure A6. Daily maps of modelled surface chlorophyll concentration [mg chl m^{-3}] (product ref. 1; Table 1) from 25 March (upper-left panel) to 17 April 2022 (lower-right panel), together with the orange line contour of the event area (Fig. 1).

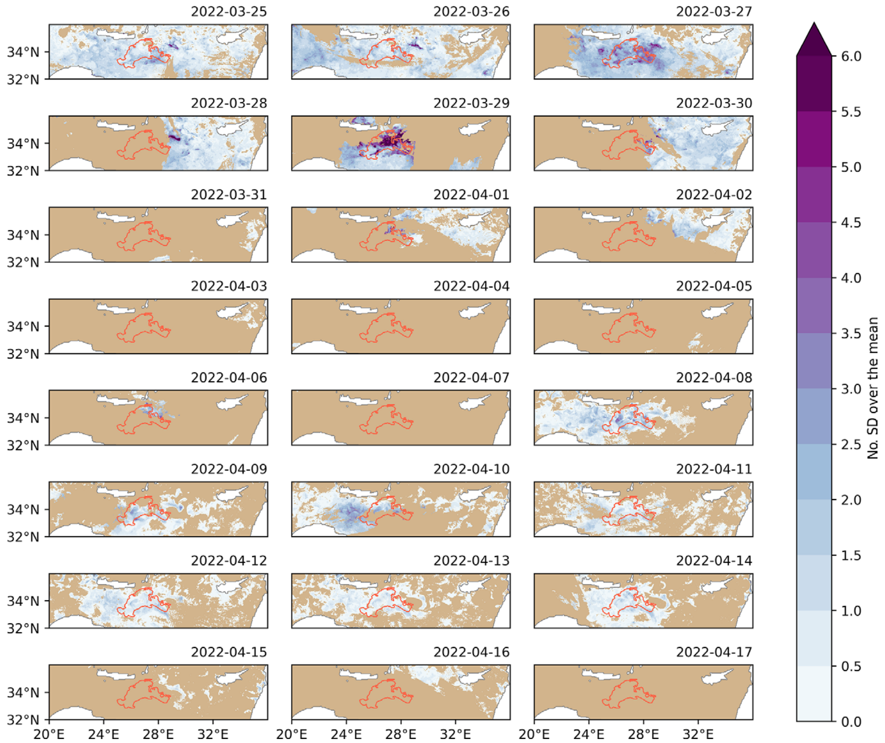

Figure A7. Daily maps of the number of standard deviations over the climatological mean (product ref. 3; Table 1) from 25 March (upper-left panel) to 17 April 2022 (lower-right panel), together with the orange line contour of the event area (Fig. 1). Areas without satellite observations are masked with light brown.

Data availability. Publicly available datasets were analysed in this study. Modelling and in situ data can be found at the Copernicus Marine Service, with references and DOIs indicated in the Table 1 of the paper.

Author contributions. AT, AA, and GC conceived the idea. AT, AA, CF, and SC conducted the analysis. AT, AA, and GC wrote the first draft with contributions from the other co-authors. All the authors discussed and reviewed the submitted article.

Competing interests. The contact author has declared that none of the authors has any competing interests.

Acknowledgements. This study has been conducted using EU Copernicus Marine Service Information.

Financial support. This study has been partly funded by the Copernicus Mediterranean – Monitoring Forecasting Centre (contract LOT reference: 21002L5-COP-MFC MED-5500, issued by Mercator Ocean) within the framework of the Marine Copernicus Service.

Review statement. This paper was edited by Griet Neukermans and reviewed by Maurizio Ribera d'Alcalà and Griet Neukermans.

References

Auger, P. A., Ulses, C., Estournel, C., Stemmann, L., Somot, S., and Diaz, F.: Interannual control of plankton communities by deep winter mixing and prey/predator interactions in the NW Mediterranean: Results from a 30-year 3D modeling study, Prog. Oceanogr., 124, 12–27, https://doi.org/10.1016/j.pocean.2014.04.004, 2014.

C3S monthly climate bulletin explorer: https://cds.climate.copernicus.eu/cdsapp#!/software/app-c3s-monthly-climate-bulletin-explorer?tab=app, last access: 28 July 2023.

Canu, D., Rosati, G., Cossarini, G., Laurent, C., Bolzon, G., and Solidoro, C.: Winter nutrient content as a basic proxy of ocean fertility, in: Copernicus Ocean State

Report, Issue 6, J. Oper. Oceanogr., 15, s133–s138, https://doi.org/10.1080/1755876X.2022.2095169, 2022.

Civitarese, G. and Gacic, M.: Had the Eastern Mediterranean Transient an impact on the new production in the southern Adriatic?, Geophys. Res. Lett., 28, 1627–1630, https://doi.org/10.1029/2000GL012079, 2001.

Colella, S., Brando, V. E., Di Cicco, A., D'Alimonte, D., Forneris, V., and Bracaglia, M.: EU Copernicus Marine Service Quality Information Document for the Mediterranean Sea Ocean Colour Plankton, Reflectance, Transparency and Optics L3 MY daily observations, OCEANCOLOUR_MED_BGC_L3_NRT_009_143, Issue 3.0, Mercator Ocean International, https://catalogue.marine.copernicus.eu/documents/QUID/CMEMS-OC-QUID-009-141to144-151to154.pdf (last access: 17 July 2024), 2023a.

Colella, S., Böhm, E., Cesarini, C., Garnesson, P., Netting, J., and Calton, B.: EU Copernicus Marine Service Product User Manual for the Mediterranean Sea Ocean Colour Plankton, Reflectance, Transparency and Optics L3 MY daily observations, OCEANCOLOUR_MED_BGC_L3_NRT_009_143, Issue 4.0, Mercator Ocean International, https://catalogue.marine.copernicus.eu/documents/PUM/CMEMS-OC-PUM.pdf (last access: 17 July 2024), 2023b.

Colloca, F., Scarcella, G., and Libralato, S.: Recent Trends and Impacts of Fisheries Exploitation on Mediterranean Stocks and Ecosystems, Frontiers in Marine Science, 4, 00244, https://doi.org/10.3389/fmars.2017.00244, 2017.

Conti, L. and Scardi, M.: Fisheries yield and primary productivity in large marine ecosystems, Mar. Ecol. Prog. Ser., 410, 233–244, https://doi.org/10.3354/meps08630, 2010.

Copernicus: Surface air temperature for March 2022, Copernicus, https://climate.copernicus.eu/surface-air-temperature-march-2022, last access: 28 July 2023.

Coppini, G., Clementi, E., Cossarini, G., Salon, S., Korres, G., Ravdas, M., Lecci, R., Pistoia, J., Goglio, A. C., Drudi, M., Grandi, A., Aydogdu, A., Escudier, R., Cipollone, A., Lyubartsev, V., Mariani, A., Cretì, S., Palermo, F., Scuro, M., Masina, S., Pinardi, N., Navarra, A., Delrosso, D., Teruzzi, A., Di Biagio, V., Bolzon, G., Feudale, L., Coidessa, G., Amadio, C., Brosich, A., Miró, A., Alvarez, E., Lazzari, P., Solidoro, C., Oikonomou, C., and Zacharioudaki, A.: The Mediterranean Forecasting System – Part 1: Evolution and performance, Ocean Sci., 19, 1483–1516, https://doi.org/10.5194/os-19-1483-2023, 2023.

Cossarini, G., Mariotti, L., Feudale, L., Mignot, A., Salon, S., Taillandier, V., Teruzzi, A., and D'Ortenzio, F.: Towards operational 3D-Var assimilation of chlorophyll Biogeochemical-Argo float data into a biogeochemical model of the Mediterranean Sea, Ocean Model., 133, 112–128, https://doi.org/10.1016/j.ocemod.2018.11.005, 2019.

Cossarini, G., Feudale, L., Teruzzi, A., Bolzon, G., Coidessa, G., Solidoro, C., Di Biagio, V., Amadio, C., Lazzari, P., Brosich, A., and Salon, S.: High-Resolution Reanalysis of the Mediterranean Sea Biogeochemistry (1999–2019), Frontiers in Marine Science, 8, 741486, https://doi.org/10.3389/fmars.2021.741486, 2021.

Danovaro, R., Dell'Anno, A., and Pusceddu, A.: Biodiversity response to climate change in a warm deep sea, Ecol. Lett., 7, 821–828, https://doi.org/10.1111/j.1461-0248.2004.00634.x, 2004.

Darmaraki, S., Somot, S., Sevault, F., Nabat, P., Cabos Narvaez, W. D., Cavicchia, L., Djurdjevic, V., Li, L., Sannino, G., and Sein, D. V.: Future evolution of Marine Heatwaves in the Mediterranean Sea, Clim. Dynam., 53, 1371–1392, https://doi.org/10.1007/s00382-019-04661-z, 2019.

Dayan, H., McAdam, R., Juza, M., Masina, S., and Speich, S.: Marine heat waves in the Mediterranean Sea: An assessment from the surface to the subsurface to meet national needs, Frontiers in Marine Science, 10, 1045138, https://doi.org/10.3389/fmars.2023.1045138, 2023.

Demirtaş, M.: The Cold Snaps of January 2022 in the Euro-Mediterranean Region in a Warming Climate: In Association with Atmospheric Blocking and the Positive North Atlantic Oscillation, Pure Appl. Geophys., 180, 2889–2900, https://doi.org/10.1007/s00024-023-03297-9, 2023.

Di Biagio, V., Cossarini, G., Salon, S., and Solidoro, C.: Extreme event waves in marine ecosystems: an application to Mediterranean Sea surface chlorophyll, Biogeosciences, 17, 5967–5988, https://doi.org/10.5194/bg-17-5967-2020, 2020.

D'Ortenzio, F. and Ribera d'Alcalà, M.: On the trophic regimes of the Mediterranean Sea: a satellite analysis, Biogeosciences, 6, 139–148, https://doi.org/10.5194/bg-6-139-2009, 2009.

D'Ortenzio, F., Taillandier, V., Claustre, H., Coppola, L., Conan, P., Dumas, F., Durrieu du Madron, X., Fourrier, M., Gogou, A., Karageorgis, A., Lefevre, D., Leymarie, E., Oviedo, A., Pavlidou, A., Poteau, A., Poulain, P. M., Prieur, L., Psarra, S., Puyo-Pay, M., Ribera d'Alcalà, M., Schmechtig, C., Terrats, L., Velaoras, D., Wagener, T., and Wimart-Rousseau, C.: BGC-Argo Floats Observe Nitrate Injection and Spring Phytoplankton Increase in the Surface Layer of Levantine Sea (Eastern Mediterranean), Geophys. Res. Lett., 48, e2020GL091649, https://doi.org/10.1029/2020GL091649, 2021.

ECMWF: IFS Documentation CY47R3, E.: IFS Documentation CY47R3 https://doi.org/10.21957/eyrpir4vj, 2021.

Escudier, R., Clementi, E., Nigam, T., Aydogdu, A., Fini, E., Pistoia, J., Grandi, A., and Miraglio, P.: EU Copernicus Marine Service Quality Information Document for the Mediterranean Sea Physics Reanalysis, MEDSEA_MULTIYEAR_PHY_006_004, Issue 2.3, Issue 2.3, Mercator Ocean International, https://catalogue.marine.copernicus.eu/documents/QUID/CMEMS-MED-QUID-006-004.pdf (last access: 18 July 2024), 2022.

EU Copernicus Marine Service Product: Mediterranean Sea Biogeochemistry Analysis and Forecast, Mercator Ocean international [data set], https://doi.org/10.25423/CMCC/MEDSEA_ANALYSISFORECAST_BGC_006_014_MEDBFM4, 2022a.

EU Copernicus Marine Service Product: Mediterranean Sea Biogeochemistry Reanalysis, Mercator Ocean international [data set], https://doi.org/10.25423/cmcc/medsea_multiyear_bgc_006_008_medbfm3, 2022b.

EU Copernicus Marine Service Product: Mediterranean Sea Ocean Colour Plankton, Reflectance, Transparency and Optics L3 NRT daily observations, Mercator Ocean international [data set], https://doi.org/10.48670/moi-00297, 2022c.

EU Copernicus Marine Service Product: Mediterranean Sea Physics Analysis and Forecast, Mercator Ocean international [data set], https://doi.org/10.25423/CMCC/MEDSEA_ANALYSISFORECAST_PHY_006_013_EAS7, 2022d.

EU Copernicus Marine Service Product: Mediterranean Sea Physics Reanalysis, Mercator Ocean international [data set], https://doi.org/10.25423/CMCC/MEDSEA_MULTIYEAR_PHY_006_004_E3R1, 2022e.

EU Copernicus Marine Service Product: Mediterranean Sea – High Resolution L4 Sea Surface Temperature Reprocessed, Mercator Ocean international [data set], https://doi.org/10.48670/moi-00173, 2022f.

EU Copernicus Marine Service Product: Mediterranean Water Mass Formation Rates from Reanalysis, Mercator Ocean international [data set], https://doi.org/10.48670/mds-00318, 2022g.

Feudale, L., Teruzzi, A., Salon, S., Bolzon, G., Lazzari, P., Coidessa, G., Di Biagio, V., Álvarez, E., Amadio, C., and Cossarini, G.: EU Copernicus Marine Service Quality Information Document for the Mediterranean Sea Biogeochemistry Analysis and Forecast, MEDSEA_ANALYSISFORECAST_BGC_006_014, Issue 3.1, Mercator Ocean International, https://catalogue.marine.copernicus.eu/documents/QUID/CMEMS-MED-QUID-006-014.pdf (last access: 17 July 2024), 2023.

Goglio, A. C., Clementi, E., Grandi, A., Moulin, A., Giurato, M., Aydogdu, A., Pistoia, J., Miraglio, P., Mariani, A., and Drudi, M.: EU Copernicus Marine Service Quality Information Document for the Mediterranean Sea Physics Analysis and Forecast, MEDSEA_ANALYSISFORECAST_PHY_006_013, Issue 2.4, Mercator Ocean International, https://catalogue.marine.copernicus.eu/documents/QUID/CMEMS-MED-QUID-006-013.pdf, last access: 17 July 2024.

Habib, J., Ulses, C., Estournel, C., Fakhri, M., Marsaleix, P., Pujo-Pay, M., Fourrier, M., Coppola, L., Mignot, A., Mortier, L., and Conan, P.: Seasonal and interannual variability of the pelagic ecosystem and of the organic carbon budget in the Rhodes Gyre (eastern Mediterranean): influence of winter mixing, Biogeosciences, 20, 3203–3228, https://doi.org/10.5194/bg-20-3203-2023, 2023.

Hobday, A. J., Alexander, L. V., Perkins, S. E., Smale, D. A., Straub, S. C., Oliver, E. C. J., Benthuysen, J. A., Burrows, M. T., Donat, M. G., Feng, M., Holbrook, N. J., Moore, P. J., Scannell, H. A., Sen Gupta, A., and Wernberg, T.: A hierarchical approach to defining marine heatwaves, Prog. Oceanogr., 141, 227–238, https://doi.org/10.1016/j.pocean.2015.12.014, 2016.

CMEMS: https://marine.copernicus.eu/, last access: 28 July 2023.

Index of /cwlinks: https://ftp.cpc.ncep.noaa.gov/cwlinks/, last access: 31 July 2023.

Josey, S. A., Somot, S., and Tsimplis, M.: Impacts of atmospheric modes of variability on Mediterranean Sea surface heat exchange, J. Geophys. Res.-Oceans, 116, C02032, https://doi.org/10.1029/2010JC006685, 2011.

Kubin, E., Poulain, P.-M., Mauri, E., Menna, M., and Notarstefano, G.: Levantine Intermediate and Levantine Deep Water Formation: An Argo Float Study from 2001 to 2017, Water, 11, 1781, https://doi.org/10.3390/w11091781, 2019.

Lavigne, H., D'Ortenzio, F., Ribera D'Alcalà, M., Claustre, H., Sauzède, R., and Gacic, M.: On the vertical distribution of the chlorophyll a concentration in the Mediterranean Sea: a basin-scale and seasonal approach, Biogeosciences, 12, 5021–5039, https://doi.org/10.5194/bg-12-5021-2015, 2015.

Lazzari, P., Solidoro, C., Ibello, V., Salon, S., Teruzzi, A., Béranger, K., Colella, S., and Crise, A.: Seasonal and inter-annual variability of plankton chlorophyll and primary production in the Mediterranean Sea: a modelling approach, Biogeosciences, 9, 217–233, https://doi.org/10.5194/bg-9-217-2012, 2012.

Lecci, R., Salon S., Bolzon, G., and Cossarini, G.: EU Copernicus Marine Service Product User Manual for the Mediterranean Sea Biogeochemistry Reanalysis, MEDSEA_MULTIYEAR_BGC_006_008, Issue 3.2, Mercator Ocean International, https://catalogue.marine.copernicus.eu/documents/PUM/CMEMS-MED-PUM-006-008.pdf (last access: 17 July 2024), 2022a.

Lecci, R., Drudi, M., Grandi, A., Cretì, S., and Clementi, E.: EU Copernicus Marine Service Product User Manual forMediterranean Sea Physics Reanalysis, MEDSEA_MULTIYEAR_PHY_006_004, Issue 2.3, Mercator Ocean International, https://catalogue.marine.copernicus.eu/documents/PUM/CMEMS-MED-PUM-006-004.pdf (last access: 17 July 2024), 2022b.

Lecci, R., Salon S., Bolzon, G., and Cossarini, G.: EU Copernicus Marine Service Product User Manual for the Mediterranean Sea Biogeochemistry Analysis and Forecast, MEDSEA_ANALYSISFORECAST_BGC_006_014, Issue 2.3, Mercator Ocean International, https://catalogue.marine.copernicus.eu/documents/PUM/CMEMS-MED-PUM-006-014.pdf (last access: 17 July 2024), 2023a.

Lecci, R., Drudi, M., Grandi, A., Cretì, S., and Clementi, E.: EU Copernicus Marine Service Product User Manual for the the Mediterranean Sea Physics Analysis and Forecast, MEDSEA_ANALYSISFORECAST_PHY_006_013, Issue 2.3, Mercator Ocean International, https://catalogue.marine.copernicus.eu/documents/PUM/CMEMS-MED-PUM-006-013.pdf (last access: 17 July 2024), 2023b.

Lyubartsev, V., Miraglio, P., and Clementi, E.: EU Copernicus Marine Service Product User Manual for the Mediterranean Water Mass Formation Rates from Reanalysis, OMI_VAR_EXTREME_WMF_MEDSEA_area_averaged_mean, Issue 1.1, Mercator Ocean International, https://catalogue.marine.copernicus.eu/documents/PUM/CMEMS-OMI-PUM-VAR-EXTREME-WMF-MEDSEA.pdf (last access: 17 July 2024), 2023a.

Lyubartsev, V., Clementi, E., Aydogdu, A., Miraglio, P., Masina, S., and Pinardi, N.: EU Copernicus Marine Service Quality Information Document for the Mediterranean Water Mass Formation Rates from Reanalysis, OMI_VAR_EXTREME_WMF_MEDSEA_area_averaged_mean, Issue 1.1, Mercator Ocean International, https://catalogue.marine.copernicus.eu/documents/QUID/CMEMS-OMI-QUID-VAR-EXTREME-WMF-MEDSEA.pdf (last access: 17 July 2024), 2023b.

Martínez, J., Leonelli, F. E., García-Ladona, E., Garrabou, J., Kersting, D. K., Bensoussan, N., and Pisano, A.: Evolution of marine heatwaves in warming seas: the Mediterranean Sea case study, Frontiers in Marine Science, 10, 1193164, https://doi.org/10.3389/fmars.2023.1193164, 2023.

Mayot, N., D'Ortenzio, F., Taillandier, V., Prieur, L., Fommervault, O. P. de, Claustre, H., Bosse, A., Testor, P., and Conan, P.: Physical and Biogeochemical Controls of the Phytoplankton Blooms in North Western Mediterranean Sea: A Multiplatform Approach Over a Complete Annual Cycle (2012–2013 DEWEX Experiment), J. Geophys. Res.-Oceans, 122, 9999–10019, https://doi.org/10.1002/2016JC012052, 2017.

McAdam, R., Masina, S., and Gualdi, S.: Seasonal forecasting of subsurface marine heatwaves, Commun. Earth Environ., 4, 225, https://doi.org/10.1038/s43247-023-00892-5, 2023.

Pinardi, N., Cessi, P., Borile, F., and Wolfe, C. L. P.: The Mediterranean Sea Overturning Circulation, J. Phys. Oceanogr., 49, 1699–1721, https://doi.org/10.1175/JPO-D-18-0254.1, 2019.

Piroddi, C., Coll, M., Liquete, C., Macias, D., Greer, K., Buszowski, J., Steenbeek, J., Danovaro, R., and Christensen, V.: Historical changes of the Mediterranean Sea ecosystem: modelling the role and impact of primary productivity and fisheries changes over time, Sci. Rep., 7, 44491, https://doi.org/10.1038/srep44491, 2017.

Pisano, A., Fanelli, C., Tronconi, C., Cesarini, C., La Padula, F., and Buongiorno Nardelli, B.: EU Copernicus Marine Service Quality Information Document for the Mediterranean Sea High Resolution L4 Sea Surface Temperature Reprocessed, SST_MED_SST_L4_REP_OBSERVATIONS_010_021, Issue 3.0, Mercator Ocean International, https://catalogue.marine.copernicus.eu/documents/QUID/CMEMS-SST-QUID-010-021-022-041-042.pdf (last access: 17 July 2024), 2023a.

Pisano, A., Fanelli, C., Tronconi, C., Cesarini, C., La Padula, F., and Buongiorno Nardelli, B.: EU Copernicus Marine Service Product User Manual for the Mediterranean Sea High Resolution L4 Sea Surface Temperature Reprocessed, SST_MED_SST_L4_REP_OBSERVATIONS_010_021, Issue 3.0, Mercator Ocean International, https://catalogue.marine.copernicus.eu/documents/PUM/CMEMS-SST-PUM-010-021-022-041-042.pdf (last access: 20 June 2023), 2023b.

Potiris, M., Mamoutos, I. G., Tragou, E., Zervakis, V., Kassis, D., and Ballas, D.: Dense Water Formation in the North–Central Aegean Sea during Winter 2021–2022, Journal of Marine Science and Engineering, 12, 221, https://doi.org/10.3390/jmse12020221, 2024.

Reale, M., Salon, S., Somot, S., Solidoro, C., Giorgi, F., Crise, A., Cossarini, G., Lazzari, P., and Sevault, F.: Influence of large-scale atmospheric circulation patterns on nutrient dynamics in the Mediterranean Sea in the extended winter season (October–March) 1961–1999, Clim. Res., 82, 117–136, https://doi.org/10.3354/cr01620, 2020.

Roether, W., Klein, B., Manca, B. B., Theocharis, A., and Kioroglou, S.: Transient Eastern Mediterranean deep waters in response to the massive dense-water output of the Aegean Sea in the 1990s, Prog. Oceanogr., 74, 540–571, https://doi.org/10.1016/j.pocean.2007.03.001, 2007.

Salon, S., Cossarini, G., Bolzon, G., Feudale, L., Lazzari, P., Teruzzi, A., Solidoro, C., and Crise, A.: Novel metrics based on Biogeochemical Argo data to improve the model uncertainty evaluation of the CMEMS Mediterranean marine ecosystem forecasts, Ocean Sci., 15, 997–1022, https://doi.org/10.5194/os-15-997-2019, 2019.

Simon, A., Plecha, S. M., Russo, A., Teles-Machado, A., Donat, M. G., Auger, P.-A., and Trigo, R. M.: Hot and cold marine extreme events in the Mediterranean over the period 1982–2021, Frontiers in Marine Science, 9, 892201, https://doi.org/10.3389/fmars.2022.892201, 2022.

Siokou-Frangou, I., Christaki, U., Mazzocchi, M. G., Montresor, M., Ribera d'Alcalá, M., Vaqué, D., and Zingone, A.: Plankton in the open Mediterranean Sea: a review, Biogeosciences, 7, 1543–1586, https://doi.org/10.5194/bg-7-1543-2010, 2010.

Stratford, K. and Haines, K.: Modelling nutrient cycling during the eastern Mediterranean transient event 1987–1995 and beyond, Geophys. Res. Lett., 29, 5-1–5-4, https://doi.org/10.1029/2001GL013559, 2002.

Teruzzi, A., Di Biagio, V., Feudale, L., Bolzon, G., Lazzari, P., Salon, S., Coidessa, G., and Cossarini, G.: EU Copernicus Marine Service Quality Information Document for the Mediterranean Sea Biogeochemistry Reanalysis, MEDSEA_MULTIYEAR_BGC_006_008, Issue 3.2, Mercator Ocean International, https://catalogue.marine.copernicus.eu/documents/QUID/CMEMS-MED-QUID-006-008.pdf (last access: 17 July 2024), 2022.

Theocharis, A., Klein, B., Nittis, K., and Roether, W.: Evolution and status of the Eastern Mediterranean Transient (1997–1999), J. Marine Syst., 33–34, 91–116, https://doi.org/10.1016/S0924-7963(02)00054-4, 2002.

Touratier, F. and Goyet, C.: Impact of the Eastern Mediterranean Transient on the distribution of anthropogenic CO2 and first estimate of acidification for the Mediterranean Sea, Deep-Sea Res. Pt. I, 58, 1–15, https://doi.org/10.1016/j.dsr.2010.10.002, 2011.

Tsiaras, K. P., Kourafalou, V. H., Raitsos, D. E., Triantafyllou, G., Petihakis, G., and Korres, G.: Inter-annual productivity variability in the North Aegean Sea: Influence of thermohaline circulation during the Eastern Mediterranean Transient, J. Marine Syst., 96–97, 72–81, https://doi.org/10.1016/j.jmarsys.2012.02.003, 2012.

Varkitzi, I., Psarra, S., Assimakopoulou, G., Pavlidou, A., Krasakopoulou, E., Velaoras, D., Papathanassiou, E., and Pagou, K.: Phytoplankton dynamics and bloom formation in the oligotrophic Eastern Mediterranean: Field studies in the Aegean, Levantine and Ionian seas, Deep-Sea Res. Pt. II, 171, 104662, https://doi.org/10.1016/j.dsr2.2019.104662, 2020.

State Planet, 4-osr8, 16, 2024
https://doi.org/10.5194/sp-4-osr8-16-2024

Baltic Sea surface temperature analysis 2022: a study of marine heatwaves and overall high seasonal temperatures

Anja Lindenthal[1], **Claudia Hinrichs**[1], **Simon Jandt-Scheelke**[1], **Tim Kruschke**[1], **Priidik Lagemaa**[3], **Eefke M. van der Lee**[2], **Ilja Maljutenko**[3], **Helen E. Morrison**[2], **Tabea R. Panteleit**[1], and **Urmas Raudsepp**[3]

[1]Marine Sciences Department, Federal Maritime and Hydrographic Agency, 20539 Hamburg, Germany
[2]Marine Sciences Department, Federal Maritime and Hydrographic Agency, 18057 Rostock, Germany
[3]Department of Marine Systems, Tallinn University of Technology, Tallinn, 12618, Estonia

Correspondence: Anja Lindenthal (anja.lindenthal@bsh.de) and Claudia Hinrichs (claudia.hinrichs@bsh.de)

Received: 22 July 2023 – Discussion started: 11 August 2023
Revised: 18 March 2024 – Accepted: 20 March 2024 – Published: 30 September 2024

Abstract. In 2022, large parts of the Baltic Sea surface experienced the third-warmest to the warmest temperatures over the summer and autumn months since 1997. Warm temperature anomalies can lead to marine heatwaves (MHWs), which are discrete periods of anomalous high temperatures relative to the usual local conditions. Here, we describe the overall sea surface temperature (SST) conditions observed in the Baltic Sea in 2022 and provide a spatiotemporal description of surface MHW events based on remote sensing, reanalysis, and in situ station data. The most MHWs, locally up to seven MHW events, were detected in the western Baltic Sea and the Inner Danish Straits, where maximum MHW intensities reached values of up to 4.6 °C above the climatological mean. The northern Baltic Proper and the Gulf of Bothnia were impacted mainly by two MHWs at maximum intensities of 7.3 and 9.6 °C, respectively. Our results also reveal that MHWs in the upper layer occur at a different period than at the bottom layers and are likely driven by different mechanisms. Reanalysis data from two exemplary stations, "Lighthouse Kiel (LT Kiel)" and "Northern Baltic", show a significant increase in MHW occurrences of +0.73 MHW events per decade at LT Kiel and of +0.64 MHW events per decade at Northern Baltic between 1993 and 2022. Moreover, we discuss the expected future increased occurrence of MHWs based on a statistical analysis at both locations.

1 Introduction

Global warming has led to an increase in ocean heat content (OHC) by about 350 ZJ in the upper 2000 m from 1958 to 2019, with the year 2022 being the warmest on record as of writing (Cheng et al., 2022; WMO, 2023). Simultaneously, marine heatwaves (MHWs), extreme events of high water temperature (Hobday et al., 2016), have increased in frequency, duration, spatial extent, and intensity during the past 4 decades (Sun et al., 2023). In 2022, MHWs were recorded on 58 % of the ocean surface (WMO, 2023).

The Baltic Sea is one of the marine ecosystems with the fastest recorded warming of surface temperatures of 1.35 °C between 1982 and 2006, i.e., 0.54 °C per decade (Belkin, 2009). Sea surface temperature (SST) data operationally produced by the German Federal Maritime and Hydrographic Agency (in the following BSH, product ref. no. 1 in Table 1) show a warming trend of 0.58 °C per decade for the period 1990–2022. High SSTs can affect phytoplankton production, while unprecedented high temperatures in the subsurface layers of the sea could have even more devastating effects on the marine ecosystem (Kauppi et al., 2023). Conditions that facilitate the fast warming of the Baltic Sea are the limited exchange between surface and deeper layers due to a permanent halocline at a depth of 60–80 m (Väli et al., 2013) and the limited water exchange between the Baltic Sea and the open ocean through the narrow Skagerrak. That is why local air–sea heat exchange is the main physical factor for the sur-

Table 1. Product table.

Product ref. no.	Product ID & type	Data access	Documentation
1	BSH Sea Surface Temperature (AVHRR/3); satellite data	Upon request; overview and contact data via https://www.bsh.de/EN/TOPICS/Monitoring_systems/Remote_sensing/remote_sensing_node.html (last access: 24 April 2024)	https://www.bsh.de/DE/THEMEN/Beobachtungssysteme/Fernerkundung/fernerkundung_node.html (last access: 24 April 2024)
2	INSITU_GLO_PHYBGCWAV_DISCRETE_MYNRT_013_030; in situ, near-real-time observations	EU Copernicus Marine Service Product (2023a)	Quality Information Document (QUID): Wehde et al. (2023) Product User Manual (PUM): In Situ TAC partners (2023)
3	BALTICSEA_MULTIYEAR_PHY_003_011 (BAL-MYP); numerical model	EU Copernicus Marine Service Product (2023c)	Quality Information Document (QUID): Panteleit et al. (2023) Product User Manual (PUM): Ringgaard et al. (2023)
4	EMODNET_CHEMISTRY_Baltic_Sea_aggregated_eutrophication_and_acidity_datasets_1902-2017_v2018; observations	SMHI (2018)	Buga et al. (2018), Giorgetti et al. (2020)

face layer water temperature and heat content in the Baltic Sea (Raudsepp et al., 2022).

Global mean air temperature in 2022 was among the six warmest in the 173-year instrumental record (WMO, 2023). For Europe especially, the Copernicus Climate Change Service/ECMWF (2022a) states that the air temperatures in August 2022 were higher than the 1991–2020 average across most of the continent, especially in a band in Eastern Europe stretching from the Barents and Kara seas to the Caucasus. In November 2022, air temperatures were higher than the 1991–2020 average, especially over the west, southeast, and far north of Europe, and were unusually mild over the northern European seas (Copernicus Climate Change Service/ECMWF, 2022b). These large-scale weather patterns likely lead to high sea surface temperatures (SST) in marginal seas like the Baltic Sea and are a likely driver of MHWs. This hypothesis is further supported by a study by Holbrook et al. (2019), which found that MHWs at middle- and high-latitude regions were driven by large-scale atmospheric pressure anomalies which cause anomalous ocean warming. Stalled atmospheric high-pressure systems coincide with clear skies, warm air, and reduced wind speeds. These conditions then lead to quick warming of the upper ocean and increased thermal stratification due to reduced vertical mixing.

So far, there generally have been only a few studies on MHWs in the Baltic Sea (Goebeler at al., 2022; She et al., 2020). In this study, we show that remote sensing data revealed several SST anomalies over the entire Baltic Sea in 2022. We thus use reanalysis and in situ station data to provide a spatiotemporal description of the corresponding MHWs. Both datasets contain data collected over a long enough period to also provide its own respective climatology, thereby enabling a consistent representation of MHWs. While the in situ data provide accurate point-wise measurements of the temperature at selected locations, the reanalysis data allow for a widespread analysis of MHWs over the entire Baltic Sea, including their extension into subsurface layers. Furthermore, we extend our study by providing a climatology of MHWs at two specific mooring locations, namely at the Lighthouse Kiel (LT Kiel) and Northern Baltic stations. The overall aim of this study is to highlight the areas of the Baltic Sea that were (most) affected by MHWs and determine whether surface MHWs can propagate into deeper layers and thus potentially threaten the subsurface ecosystem. Furthermore, analyzing the climatology of MHWs can provide insight into whether the global increase in MHWs can also be expected to occur on a local scale for the Baltic Sea.

2 Data and methods

2.1 Satellite data

The satellite data service at the BSH compiles daily maps of SST data (product ref. no. 1 in Table 1). These have contributed, for example, to the assessment of climate change in the Baltic Sea (The BACC Author Team, 2008) and to the model evaluation in the Baltic Sea Model Intercomparison Project (Gröger et al., 2022). The SST data are recorded as radiances by the Advanced Very High Resolution Radiometer (AVHRR/3) in two thermal infrared channels aboard the NOAA-19 and MetOp B satellites, providing a spatial resolution of 1.1 km, swath widths of 1447 km, and orbital periods of 100 min (EUMETSAT, 2015; Minnett et al., 2019). The raw data of eight or nine daytime passes over the Baltic and North Sea are received directly from EUMETSAT and processed using automated, standardized correction procedures (atmospheric correction, cloud masking, georeferencing, etc.). Additionally, each flyover is corrected manually in order to preserve as much data as possible whilst eliminating any faulty or cloudy pixels. All available single images from a calendar day are combined and averaged, on a single pixel basis, into one daily mean image. These daily images are then used to produce a weekly analysis on an operational basis. While the BSH has been carrying out the processing of the satellite data itself on the 1.1 km grid since 1990, operational SST analysis for the Baltic Sea did not start until the autumn of 1996. The analysis of the BSH SST dataset presented in this chapter is therefore limited to the period from 1997–2022.

2.2 Station data

In situ temperature time series from mooring stations located in the Baltic Sea are used for (1) model validation and (2) cross validation of the MHW computation from the reanalysis data. Except for SST data from Northern Baltic (Hedi Kanarik, FMI, personal communication, 2023), the station data are obtained from product ref. no. 2 in Table 1. Each available dataset has already been quality controlled by the regional production units (In Situ TAC partners, 2023). The temporal resolution varies from hourly at the German stations to half-hourly at the stations in the northern Baltic Proper and Gulf of Finland. Due to failures, maintenance, and other circumstances, no mooring station entirely covers the period from 1 January 1993 until now.

Of all available mooring stations, we selected those that contain data from 2022 and from at least 10 additional years from 1993 until 2021 for at least one depth. Out of the remaining seven mooring stations that contained surface temperature data, two mooring stations were chosen for the cross validation of MHWs: Lighthouse Kiel (LT Kiel) and Northern Baltic (Fig. 1). Regarding the observation data, LT Kiel has the greatest time coverage (1989 until the present, missing data: 9.1 % of days). This mooring station lies in the far western part of the southern Baltic, and the water depth there is about 12 m. The station Northern Baltic is located in the northern Baltic Proper, and the SST observations there cover the period from 1997 until now (missing data: 8.0 % of days). No mooring station provides a time series in deeper layers long or consistent enough to analyze subsurface MHWs, thus reducing the scope of measurement-based analysis of MHWs to the surface layers.

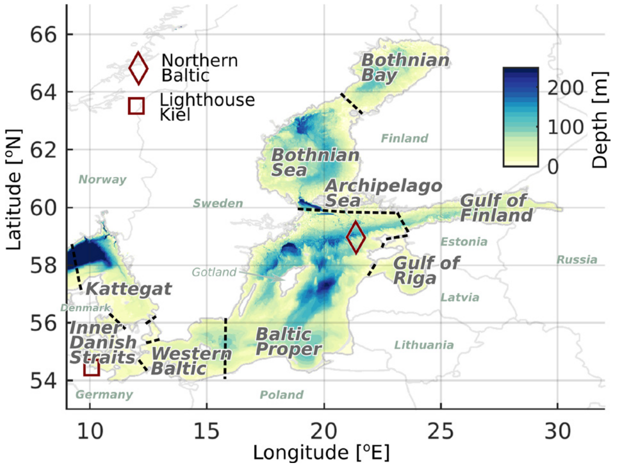

Figure 1. Map of the Baltic Sea with relevant locations mentioned in the study. Boundaries between subregions are marked with dashed lines.

2.3 Baltic Sea physics reanalysis data

The Baltic Sea physics reanalysis multi-year product (BAL-MYP; product ref. no. 3 in Table 1) is a dataset based on the ocean model NEMO v4.0 (Gurvan et al., 2019). The model system assimilates satellite observations of SST (EU Copernicus Marine Service Product, 2023b) and in situ temperature and salinity profile observations from the ICES database (ICES Bottle and low-resolution CTD dataset, 2022). The product provides gridded information on SST and subsurface temperature conditions. The spatial coverage is 1 nautical mile, i.e., approximately 1.8 km. The grid covers the entire Baltic Sea, including the transition zone to the North Sea, with a vertical resolution of 56 non-equidistant depth levels. This multi-year product (MYP) covers the reference period from 1993 up to 2022. The model setup is described in the product user manual (PUM; Ringgaard et al., 2023).

2.4 Heatwave detection

Marine heatwaves refer to a discrete period of unusually high seawater temperatures. While several definitions describe MHWs quantitatively, the most commonly used method defines them as periods when temperatures exceed the 90th percentile of the local climatology for 5 d or more (Hobday et al., 2016). We use open-source tools to detect MHWs (Oliver, 2016; Zhao and Marin, 2019a) in station and reanalysis data. The identified MHWs can be classified following Hobday et al. (2018), in which the MHW category is based on the maximum intensity in multiples of threshold exceedances, i.e., the local difference between the 90th percentile threshold and the climatology. If the threshold is exceeded less than two times, the MHW is classified as moderate (Category I), at two to three times it is classified as strong (Category II), at three to four times it is classified as severe (Category III), and at four or more times it is classified as extreme (Category IV).

Here, the occurrence of MHWs in the Baltic Sea in 2022 is analyzed based on the BAL-MYP (product ref. no. 3 in Table 1). MHWs are computed at every third surface grid point, resulting in a resolution of approximately 5.4 km for the following statistical metrics: cumulative intensity, mean intensity, duration of the longest heatwave, number of heatwaves (frequency), maximum intensity and total days of MHW conditions.

Then, in order to evaluate the development of those MHW metrics over time, block averages (using a block length of one year) for each MHW metric are computed for both the observations (product ref. no. 2 in Table 1) and the BAL-MYP (product ref. no. 3 in Table 1) at two stations: Lighthouse Kiel and Northern Baltic. The yearly MHW metrics from observations and the reanalysis are correlated for evaluation, and linear trends (95 % significance) are calculated for each of those metrics. Finally, the correlation of the annual MHW metrics to the annual mean temperature based on reanalysis data was assessed using a linear least-squares regression and a two-sided *t* test for significance.

All MHW assessments in the following sections use the period from 1993 to 2021 for the climatology, except for Sect. 3.2.1, in which the comparison of the multi-year evolution of MHWs at Northern Baltic uses the overlapping period from 1997 to 2021 due to the lack of observations at this station before 1997.

2.5 Validation of the Baltic Sea physics reanalysis

The BAL-MYP (product ref. no. 3 in Table 1) has already been extensively validated in the corresponding quality information document (QuID; Panteleit et al., 2023), where the reanalysis data are validated within the time period from 1 January 1993 to 31 December 2018. The validation in the QuID shows a negative bias at the surface with a shift towards more positive values at deeper levels. A variation in statistical values with depth is also clearly visible in the estimated accuracy number (EAN), which represents the root-mean-square difference (RMSD) of a specific depth layer. The RMSD varies between 0.29 °C at 200–400 m over 0.63 °C at the surface to 1.3 °C at 5–30 m depth.

For this study, we additionally evaluated the BAL-MYP data in more detail using a clustering approach, which offers insights into the overall accuracy of the reanalysis by grouping the errors. This clustering procedure employs the *k*-means algorithm (Raudsepp and Maljutenko, 2022). In this evaluation, all available data within the model's domain and simulation period are considered. A two-dimensional error space ($\mathrm{d}S$, $\mathrm{d}T$) is established using simultaneously measured temperature and salinity values as the foundation for clustering. Here, $\mathrm{d}S = (S_{\mathrm{mod}} - S_{\mathrm{obs}})$ and $\mathrm{d}T = (T_{\mathrm{mod}} - T_{\mathrm{obs}})$ represent the differences between the reanalysis (S_{mod} and T_{mod}) and observed (S_{obs} and T_{obs}) salinity and temperature, respectively. The dataset employed in this validation study was sourced from the EMODNET dataset compiled by SMHI (product ref. no. 4 in Table 1). It consists of a total of 3 094 089 observations aligning with the simulation period of the BAL-MYP and covering the years 1993 to 2022. A comprehensive explanation of the *k*-means method and detailed results describing the accuracy of the BAL-MYP can be found in Appendix A. The results can be summarized as in that approximately 82 % of all validation points exhibit relatively low temperature bias, standard deviation (SD), and RMSD (Table A1). The surface layer validation shows that less than 10 % of comparison points have significant temperature errors (Fig. A1c). Due to the low proportion of these validation points, we do not expect a significant impact on the determination of the surface MHWs and their statistics. Below the surface layer, i.e., at depths ranging from 0.5–40 m, up to 25 % of the points correspond to clusters with temperature errors greater than ±2.0 °C; in deeper layers, this percentage gets smaller again (Fig. A1c). Consequently, we anticipate that the reanalysis data provide sufficiently accurate information for calculating both surface and subsurface MHWs and their statistics for the Baltic Sea.

The BAL-MYP is also validated in terms of how accurately it reproduces the MHWs of 2022 and how well it represents their characteristics during the overlapping time periods of data availability at the two locations (1993–2022 for LT Kiel and 1997–2022 for Northern Baltic). For this, the reanalysis was compared to the available station data (product ref. no. 2 in Table 1 for LT Kiel; Hedi Kanarik, FMI, personal communication, 2023, for Northern Baltic) at these locations. Table 2 shows the Pearson correlation coefficients for the MHW metrics in Fig. 4 between observational and reanalysis data for the two stations, which show overall good agreement between the two datasets with respect to MHW detection.

We also compared the 2022 temperature curves from both the reanalysis and the station data at each location (Fig. A2). Overall, the curves show the same progression. The temperature from the BAL-MYP is generally slightly lower, and consequently this results in a slightly lower temperature climatology and threshold (here, the 90th percentile) on which MHW detection is based. In general, the MHWs and their respective intensities and lengths are detected equally in both the station and reanalysis data.

3 Results

3.1 Sea surface temperature anomalies in satellite data

In the summer of 2022, large parts of the Baltic Sea featured strong warm anomalies based on the BSH SST analysis (product ref. no. 1 in Table 1, Fig. 2). The highest values were up to 3 °C above the long-term mean (1997–2021) in the Bothnian Sea in June and in the Bothnian Bay in July. In August, however, these areas were neutral or exhibited cold

Table 2. Pearson correlation coefficients from linear regression between the MHW metrics computed from the station data and the reanalysis data at the stations Lighthouse Kiel and Northern Baltic.

Station	Common climatology period	MHW count	MHW max intensity	MHW cumulative intensity	Total MHW days
Lighthouse Kiel	1993–2021	0.82	0.88	0.66	0.93
Northern Baltic	1997–2021	0.74	0.89	0.82	0.94

anomalies, while the Baltic Proper, as well as the Gulf of Finland and the Gulf of Riga, showed the warmest anomalies of +1.5 to 2.5 °C. At the beginning of autumn, the Baltic Sea is marked by a substantial east-to-west gradient of SST anomalies due to a series of upwelling events along its eastern shores. In November, the whole Baltic Sea features strong warm anomalies, again with peak values above +2 °C around southern Sweden.

To provide some climatological context for the observed SST anomalies in a straightforward way, we also present maps ranking the SST anomalies for the summer and autumn months of 2022 against the same months in previous years (right two columns of Fig. 2). These anomaly rankings provide information on how extreme an anomaly of a given magnitude is. For every grid point and for each calendar month, the monthly anomalies are ranked by magnitude. The warm anomalies over large parts of the Baltic Sea during the summer and autumn of 2022 are among the warmest eight on record for the respective months. In September, coastal upwelling led to cold anomalies along the eastern shores, but the other 5 months of the summer and fall of 2022 (June, July and August as well as October and November) show large areas of the Baltic Sea with warm anomalies that are among the four most pronounced on record. In August and November, we see several large areas along the coastlines of the Baltic countries as well as off the Polish coast and around Gotland that according to the BSH SST analysis dataset featured the highest ever surface temperatures.

3.2 Marine heatwaves

MHWs describe exceptionally warm temperature anomalies. As the monthly overview in Fig. 2 already provides an indication of possible MHW conditions in 2022, the MHW metrics defined by Hobday et al. (2016) are assessed using the BAL-MYP (product ref. no. 3 in Table 1). Each region of the Baltic Sea experienced different MHW characteristics during 2022 (Fig. 3, Table 3).

The most MHWs during 2022 occurred in the Inner Danish Straits and the western Baltic Sea (Fig. 3d). In most areas, four to five MHWs were detected, with some assessed locations experiencing up to seven MHWs and a maximum of 94 total days of MHW conditions (Fig. 3f). The mean and maximum intensities of all MHWs in the Western Baltic reached up to 3.8 and 4.6 °C, respectively (Fig. 3b and e). The highest mean and maximum intensity values were reached in the northern Baltic Proper and in the Bothnian Sea and Bothnian Bay (Fig. 3b and e), though these regions were affected mainly by only two MHWs. The maximum intensity in the Bothnian Bay even reached 9.6 °C, the highest within the entire studied period from 1993 to 2022. The longest MHW is found in the Baltic Proper (32 d), followed by the Bothnian Sea (31 d) and the Inner Danish Straits (29 d) (Fig. 3c). The highest values of cumulative intensity (of a single MHW), with up to 119.3 °C d, are found in the Kvarken, a strait between the Bothnian Sea and the Bothnian Bay (Fig. 3a).

3.2.1 Multi-year evaluation of MHW metrics

Next, we assess the frequency and other characteristics of the MHWs that occurred in 2022 in a climatological context based on both observations and reanalysis data for the two stations, LT Kiel (based on the overlapping climatology period 1993–2021, Fig. 4a–h) and Northern Baltic (based on the overlapping climatology period 1997–2021, Fig. 4i–p). Overall, the results for the yearly MHW metric calculation are well correlated between the observations and the reanalysis data (Table 2).

In 2022, a total of five MHWs (four in the BAL-MYP) occurred throughout the year at LT Kiel (Fig. A2a). Though none of them was extraordinarily long or intense at LT Kiel, the time series of yearly MHW metrics shows that, based on observational data, the number of MHW occurrences in 2022 was the second highest there since 1989 (Fig. 4a). The time series of MHW frequencies per year suggests that the occurrence of MHW events has increased over the last 3 decades (Fig. 4a). The linear trend computed from reanalysis data is +0.73 MHWs per decade for the period 1993–2022. The number of MHW events per year is positively correlated ($R = 0.76$) with the increasing annual mean SST at this mooring station (Fig. 4b). The maximum (Fig. 4c) and cumulative intensities (Fig. 4e) of observed MHWs do not show a clear trend and are not correlated to the warming annual mean temperatures (Fig. 4d and f). There is no significant trend in total MHW days (Fig. 4g) at LT Kiel, but there is a positive correlation ($R = 0.71$) with rising average temperatures (Fig. 4h).

For Northern Baltic, neither the station data nor the reanalysis data exhibit a statistically significant trend in MHW events for the overlapping period (Fig. 4i). However, when

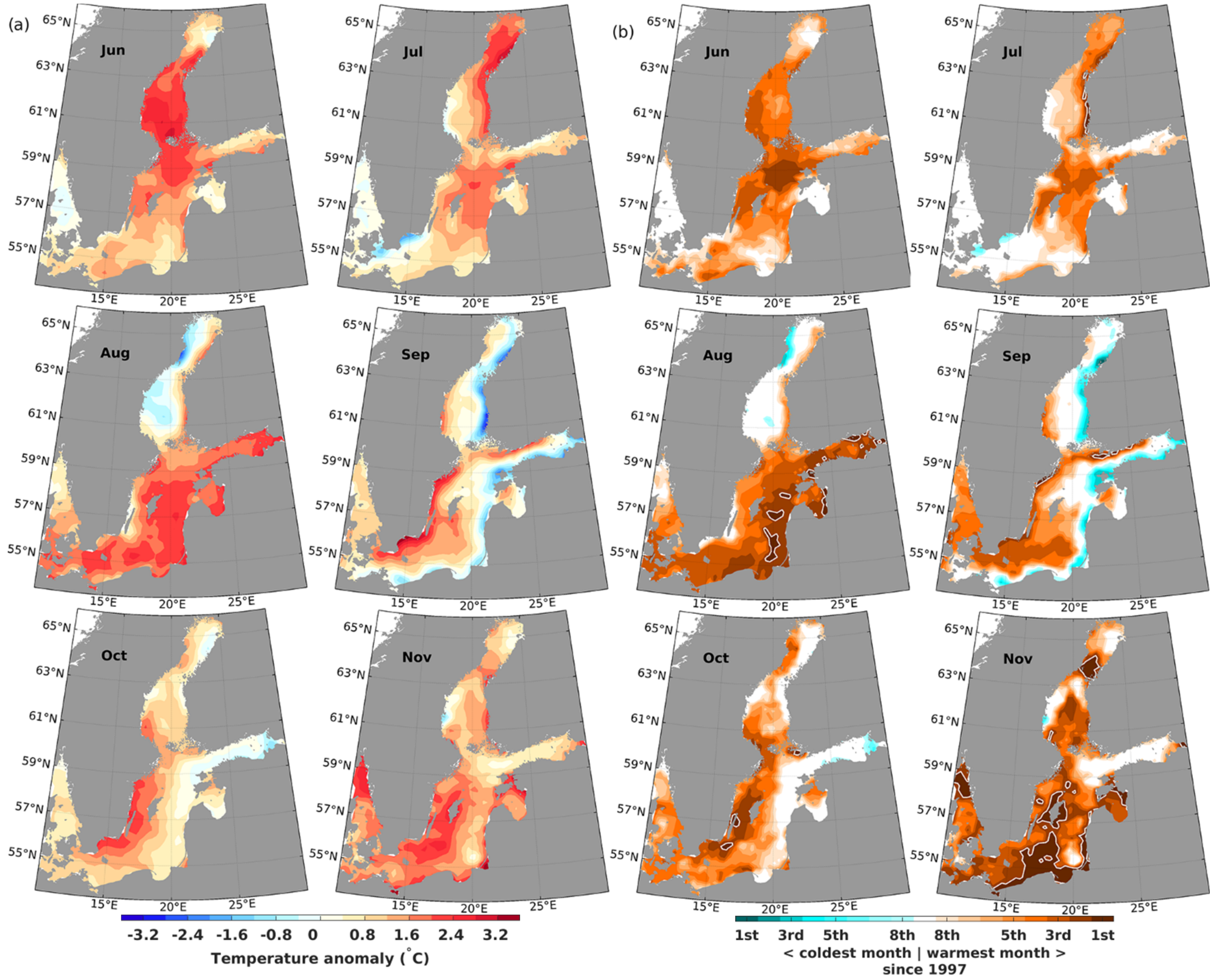

Figure 2. Anomalies (difference from climatology of 1997–2021) of SST for the Baltic Sea according to the BSH SST analysis (product ref. no. 1 in Table 1) during the summer and autumn months in 2022 **(a)** and ranks of these SST anomalies **(b)** when compared to the full dataset starting in 1997. In **(b)**, brownish (cyan) colors denote anomalies belonging to the warmest (coldest) eight anomalies found since 1997. Record warm anomalies (rank 1) are highlighted by white contours.

all of the available reanalysis data from 1993–2022 are taken into account, the trend in MHW occurrences becomes significant at the 95 % level, with +0.64 MHWs per decade. Again, the number of events is positively correlated with annual mean temperature ($R = 0.58$, Fig. 4j). The highest maximum MHW intensities were recorded in recent years (2016, 2018, 2021, 2022), with 2022 showing the highest intensity of any MHW, at 7.3 °C (reanalysis data) to 7.4 °C (station data) above the climatologically expected temperature (Fig. 4k, l, see also Fig. A2b). The cumulative MHW intensities show no clear trend or correlation with annual mean temperatures at this station (Fig. 4m, n). In terms of total MHW days, 2018 shows the highest numbers (Fig. 4o), but otherwise no trend is detectable for this metric, though there is a positive correlation with annual mean temperatures ($R = 0.56$, Fig. 4p).

3.2.2 Analysis of vertical MHW distribution at Northern Baltic

At Northern Baltic, which is about 103 m deep and located in the western Baltic Proper, the surface temperature has been measured continuously over several decades. However, no quality-controlled temperature measurements exist for the lower layers at this station. The validation of the BAL-MYP shows that at other locations the reanalysis represents temperatures generally well, both at the surface and in the lower stratum. In order to obtain further insights into heatwave

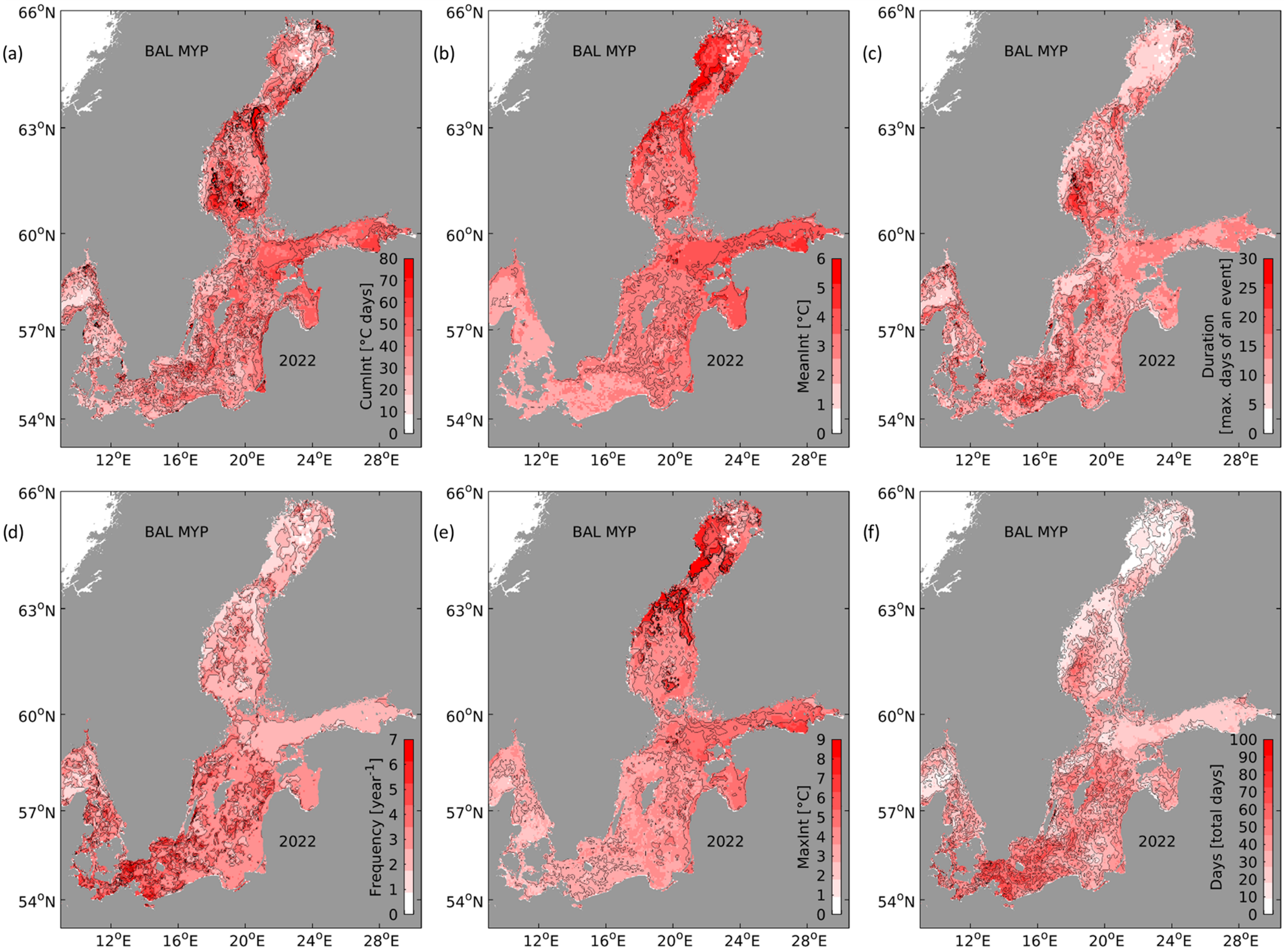

Figure 3. Statistical metrics of MHWs in 2022 in the Baltic Sea based on SST data of the BAL-MYP (product ref. no. 3 in Table 1) with the climatological period covering the years 1993 to 2021: **(a)** cumulative intensity of the longest heatwave, **(b)** mean intensity, **(c)** duration of the longest heatwave, **(d)** number of heatwaves during 2022, **(e)** maximum intensity during the longest heatwave, **(f)** summed up days of all heatwave during 2022. The definition of these metrics follows Hobday et al. (2016).

propagation towards the seafloor, we analyzed the reanalysis data along the water column.

A seasonal SST signal is clearly visible in Fig. 5a. In general, the temperature tends to decrease with depth while the bottom temperature is comparably cold and uniform. In early summer (June), a so-called cold intermediate layer (CIL), defined as a minimum temperature between the thermocline and the perennial halocline (Chubarenko et al., 2017; Dutheil et al., 2023), develops at a depth of 20–60 m and acts as a barrier between the surface and bottom waterbodies. At Northern Baltic, the upper boundary of the CIL coincides with the mixed layer depth (MLD), which is depicted in Fig. 5b–c. Starting from around June, a water stratum with a significantly lower temperature than the climatological mean (up to −7 °C deviation) is located immediately under the MLD (Fig. 5b), which suggests that the CIL was significantly colder at this time in 2022. This also coincides with the onset of significantly higher temperatures near the surface, at 0.5 m depth, compared to the climatological mean, though these were initially not high enough to result in a MHW (Fig. 5e). At this depth, there is a significant temperature surge of 5 °C above the climatological mean, followed by abrupt and substantial fluctuations in temperature within in a brief time frame. This eventually leads to a MHW which lasts for 15 d starting from the end of June and which contains a 1 d long extreme MHW (Category IV) event at a temperature of 7.4 °C above the climatological mean, followed by a severe MHW (Category III) for another 3 d. Significant temperature deviations can also be observed at a depth of 10.8 m, i.e., at the MLD, after 2 July, just after the Category IV MHW at 0.5 m depth. However, these temperature deviations did not result in a MHW at 10.8 m depth. A comparably weak MHW can be detected in mid-August at both 0.5 m (Fig. 5e) and 10.8 m (Fig. 5f). Thus, this weaker MHW

Table 3. Statistical MHW parameter values in various subregions of the Baltic Sea for 2022 based on the reanalysis data from the BAL-MYP (product ref. no. 3 in Table 1) using daily values of SST between 1 January 1993 and 31 December 2022. The climatological period covers the years 1993 to 2021.

	Kattegat	Inner Danish Straits	Western Baltic	Baltic Proper	Gulf of Riga	Gulf of Finland	Archipelago Sea	Bothnian Sea	Bothnian Bay
Cumulative intensity of longest MHW (°C days)	81.5	63.8	64	79.4	63	66.5	61.1	119.3	85.1
Mean intensity (°C)	3.6	3.5	3.8	5.3	4.9	5.8	4.5	6.4	6.5
Duration of longest MHW (days)	24	29	26	32	17	17	21	31	20
Number of MHWs (modal) per year	1–6 (3)	2–7 (4)	2–7 (5)	1–7 (3)	1–4 (3)	1–4 (2)	2–4 (3)	1–6 (2)	1–5 (2)
Maximum intensity (°C)	4.5	4.2	4.6	7.3	5.9	6.8	5.1	8.6	9.6
Total days of MHW conditions (days)	56	86	94	79	50	48	55	63	47

penetrates past the MLD into slightly deeper levels before reaching the comparably cold layer of water underneath.

As shown in Fig. 5c and d, the intensity of the MHW tends to decrease as the depth increases. Four MHWs in regions close to the seafloor (i.e., below 60 m) were detected during specific periods from February to April, September to October, and in December. These MHWs are mostly moderate, with temperatures reaching up to 1.59 °C above the climatological mean. At the end of September, only 3 d can be classified as a Category II MHW in one specific depth layer close to the seafloor. In the bottom-most depth layer, the corresponding subsurface MHW is interrupted by 5 d of temperatures below the 90th percentile. However, as the temperatures are only slightly below the threshold and the MHW criteria are still met in the depth layers above, one might still count this as one continuous MHW. Furthermore, Fig. 5c also shows isolated Category I MHWs at depths between 20 and 50 m.

4 Discussion and conclusions

During August and November 2022, record warm sea surface temperatures were observed in substantial areas of the Baltic Sea proper. Large parts of the Baltic Sea exhibited the third-warmest to the warmest temperatures in summer and autumn months since 1997. Both periods, in August and November, coincided with atmospheric temperature anomalies. Over the entire year of 2022, the distribution in quantity and intensity of MHWs within the Baltic Sea was twofold: up to seven individual MHW occurrences were recorded and simulated in the southwestern part of the Baltic Sea, and as a result this region experienced the maximum number of total MHW days of anywhere in the Baltic Sea in 2022. In the northern Baltic Sea, the number of MHWs was lower, with some locations registering only one MHW; remarkably, however, this one MHW led to the highest mean and maximum MHW intensities in the Baltic Sea since the reanalysis started in 1993. In some areas in the Bothnian Bay, the BAL-MYP revealed temperatures that exceeded 9 °C above the 90th percentile of the climatologically expected temperature values (Fig. 3d, e). This can be considered an extraordinarily high MHW intensity, since maximum SST anomalies above 5 °C have only been observed in about 5 % of the global ocean, while MHW intensities normally peak at 2.5 to 3.7 °C (Sen Gupta et al., 2020). In our case, the area in the Bothnian Bay experienced a short period with southerly winds and air temperatures up to 28 °C at the end of June 2022 (SMHI, 2023a, b), which led to a short but very intense MHW in the shallow areas of the bay.

A significant increase in MHW occurrences is detectable over time at our two exemplary stations: +0.73 MHW events per decade at LT Kiel and +0.64 MHW events per decade at Northern Baltic. Both MHW frequency and the total number of MHW days are statistically related to rising mean temperatures. This confirms that an increasing number of MHWs can also be expected in the future in the Baltic Sea due to global warming (Frölicher et al., 2018; Oliver, 2019). The adverse impact of MHWs on the ecosystem's various trophic levels has been widely documented (Smale et al., 2019; IPCC, 2022; Smith et al., 2023). The Baltic Sea, which has a relatively vulnerable ecosystem, could experience a significant negative impact from MHWs (Kauppi and Villnäs, 2022; Kauppi et al., 2023), and the analysis of subsurface MHWs opens up further potential ways to study their effects. At the Northern Baltic mooring station, MHWs were

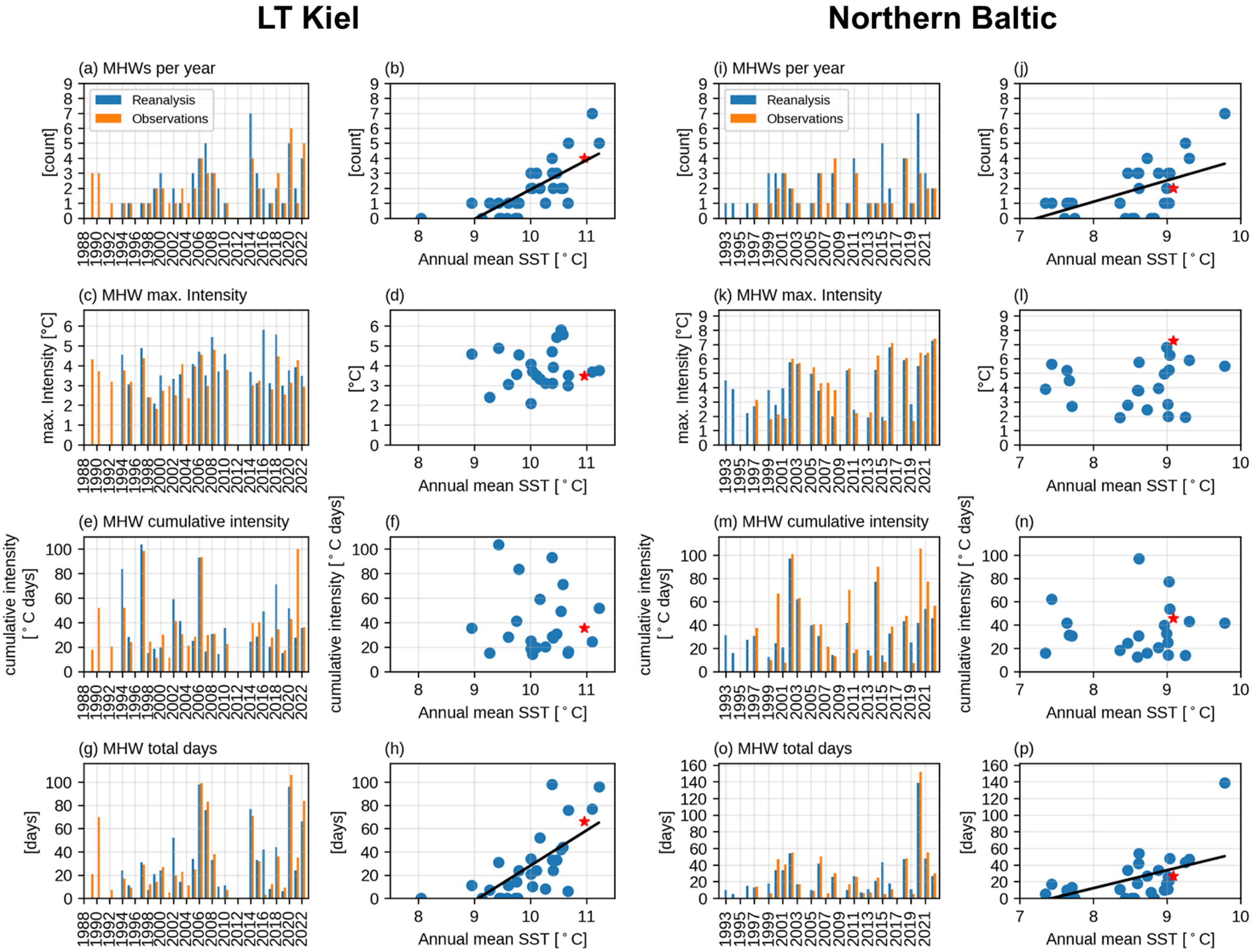

Figure 4. Comparison and time series of annual MHW metrics (**a, i**: MHW events; **c, k**: maximum intensity (°C); **e, m**: cumulative intensity (°C days); **g, o**: MHW days) for station data (orange bars) and BAL-MYP (blue bars) at the stations LT Kiel (left) and Northern Baltic (right). The MHW metrics from the reanalysis are plotted against the annual mean SST at that station with the year 2022 marked in red. Statistically significant (95 %) correlations are indicated with a black line.

found close to the surface, propagating into deeper layers until reaching the CIL, and some were also detected close to the seafloor. Isolated MHWs were also observed at depths between 20 and 50 m. However, these are subject to higher uncertainty compared to the ones in the surface and bottom layers due to a higher uncertainty in modeling variability in the pycnocline (QuID; Panteleit et al., 2023). Possible reasons for the development of the four MHWs close to the seafloor at Northern Baltic could, for example, be vertical heat transport from the surface or a lateral transport of warmer water due to bottom currents. However, a more detailed evaluation would be required to assess their precise cause.

Potential avenues for future studies include examining whether and how surface MHWs are able to propagate into the deeper water masses close to the halocline and examining the correlation between the strength (i.e., the classification category) of the MHW and its propagation into deeper water masses. At Northern Baltic, severe and extreme MHWs occurred close to the surface when the CIL was particularly cold compared to the climatology. This therefore raises questions of whether a strong CIL might be linked to the development of MHWs at the surface and whether the one might even favor the development of the other. Additional studies could also focus on the positive feedback on the bottom temperature, as was observed in 2022. It might be interesting to determine if this phenomenon can also be found in other years and whether it is triggered by the superposition of either lateral currents or MHWs or of both together. Understanding the effects that potentially lead to the vertical propagation of MHWs like those observed particularly in the late summer of 2022 will become increasingly crucial in order to evaluate how the already increasing occurrences of surface MHWs may affect the ecosystem in subsurface layers.

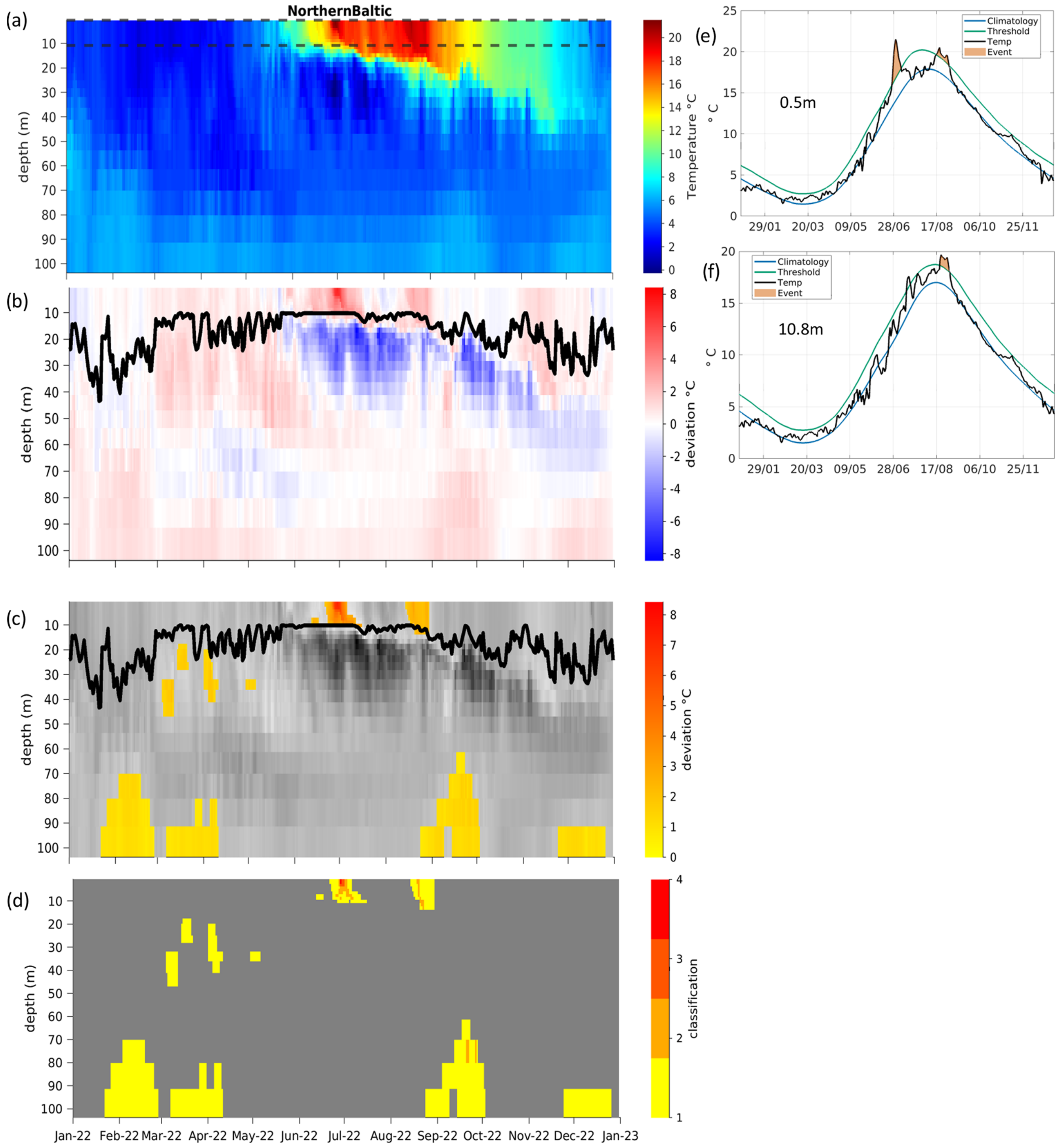

Figure 5. Hovmöller diagrams showing absolute water temperature **(a)** and temperature deviation between the climatology and the BAL-MYP data for 2022 **(b)** and MHWs **(c)** and their classifications (**d**, 1 – moderate; 2 – strong; 3 – severe; 4 – extreme) including the mixed-layer depth as the thick black line **(b, c)** at Northern Baltic based on the BAL-MYP (product ref. no. 3 in Table 1). The time series on the right **(e–f)** are located at the vertical positions marked as dashed lines in **(a)** and show temperature (black), climatology (blue), 90th percentile threshold for MHW analysis (green), and MHWs (red shading) based on reanalysis data at depths of 0.5 m **(e)** and 10.8 m **(f)**. The period used for the climatology is 1993–2021.

Appendix A

We apply a clustering approach to evaluate the precision of the Baltic Sea physics reanalysis multi-year product (BAL-MYP, product ref. no. 3 in Table 1) in order to highlight its ability to accurately capture both surface and subsurface MHWs over the entire domain. This clustering approach offers insights into the overall accuracy of the reanalysis with respect to temperature and salinity by grouping the respective errors. The procedure employs the k-means algorithm, a type of unsupervised machine learning (Jain, 2010). The original explanation of this technique can be found in a study by Raudsepp and Maljutenko (2022). In our evaluation, all available data within the model's domain and simulation period are considered, even if the observation data are unevenly distributed or occasionally sparse. This strategy enables us to assess the quality of the reanalysis at each specific location and time instance at which measurements have been acquired.

Initially, a two-dimensional error space ($\mathrm{d}S$, $\mathrm{d}T$) was established using simultaneously measured temperature and salinity values as the foundation for clustering. Here, $\mathrm{d}S = (S_{\mathrm{mod}} - S_{\mathrm{obs}})$ and $\mathrm{d}T = (T_{\mathrm{mod}} - T_{\mathrm{obs}})$ represent the differences between the model (S_{mod} and T_{mod}) and observed (S_{obs} and T_{obs}) salinity and temperature, respectively. The dataset employed in this validation study was sourced from the EMODNET dataset compiled by SMHI (product ref. no. 4 in Table 1). It consists of a total of 3 094 089 observations aligning with the simulation period of the BAL-MYP and covering the years 1993 to 2022. For each observation, we extracted the nearest model values from the reanalysis dataset.

The next stage involves choosing the number of clusters, and for simplicity we opted in advance for five clusters. Subsequently, the third step entails conducting k-means clustering on the two-dimensional errors. This clustering process is applied to the normalized errors achieved through separate normalization for temperature and salinity errors using the corresponding standard deviations. The k-means algorithm then identifies the centroids' positions within the error space for the predetermined number of clusters. These centroids' locations signify the bias of the error set for each cluster. In the fourth step, statistical metrics for non-normalized clustered errors are computed. Standard deviation (SD), root-mean-square deviation (RMSD) and the correlation coefficient are examples of common statistics that can be calculated for the parameters associated with each cluster.

The fifth step involves examining the spatiotemporal distributions of errors associated with different clusters. During the creation of the error space, we retained the coordinates of each error point $(\mathrm{d}S, \mathrm{d}T)(x, y)$, allowing us to map the errors of each cluster back onto the locations where the measurements were conducted. To achieve this, the model domain is partitioned into horizontal grid cells (i, j) of $27 \times 27\,\mathrm{km}^2$ in size. Subsequently, the number of error points attributed to various clusters at each grid cell (i, j) is tallied. The total number of error points linked to the grid cell (i, j) is the sum of points from each cluster. The proportion of error points in each grid cell affiliated with cluster k is determined by the ratio of the number of error points of cluster k to the total number of error points in each grid cell.

Figure A1 displays the results of the k-means clustering for non-normalized errors. Table A1 presents the corresponding metrics. Within cluster $k = 5$, the salinity and temperature values closely align with the observations, with a bias of $\mathrm{d}S = -0.40\,\mathrm{g\,kg^{-1}}$ and $\mathrm{d}T = -0.02\,^{\circ}\mathrm{C}$, respectively. This cluster encompasses 57 % of all data points. The points are distributed throughout the Baltic Sea and the great majority of them exceed 0.5 (Fig. A1b). Clusters $k = 3$ and $k = 4$ exhibit relatively even spatial distributions across the Baltic Sea, accounting for 11 % and 8 % of the points, respectively. These clusters are particularly noteworthy due to their relatively high temperature biases and variability, both of which are crucial for the calculation of marine heatwaves. The clusters $k = 1$ and $k = 2$ represent points with low temperature but a high salinity error (Table A1). Spatially, these points are predominantly located in the southwestern Baltic Sea (Fig. A1b), which points to the occasional underestimation or overestimation of the inflow and outflow salinity.

Collectively, approximately 82 % of all validation points exhibit relatively low temperature bias, SD, and RMSD (Table A1). The surface layer validation shows that less than 10 % of comparison points have significant temperature errors (Fig. A1c). Due to the low proportion of these validation points, we do not expect a significant impact on the determination of surface MHWs and their statistics. Below the surface layer, i.e., at depths ranging from 0.5–40 m, up to 25 % of the points correspond to clusters $k = 3$ and $k = 4$ (Fig. A1c). Consequently, we anticipate that the reanalysis data provides sufficiently accurate information for calculating subsurface MHWs and their statistics for the Baltic Sea.

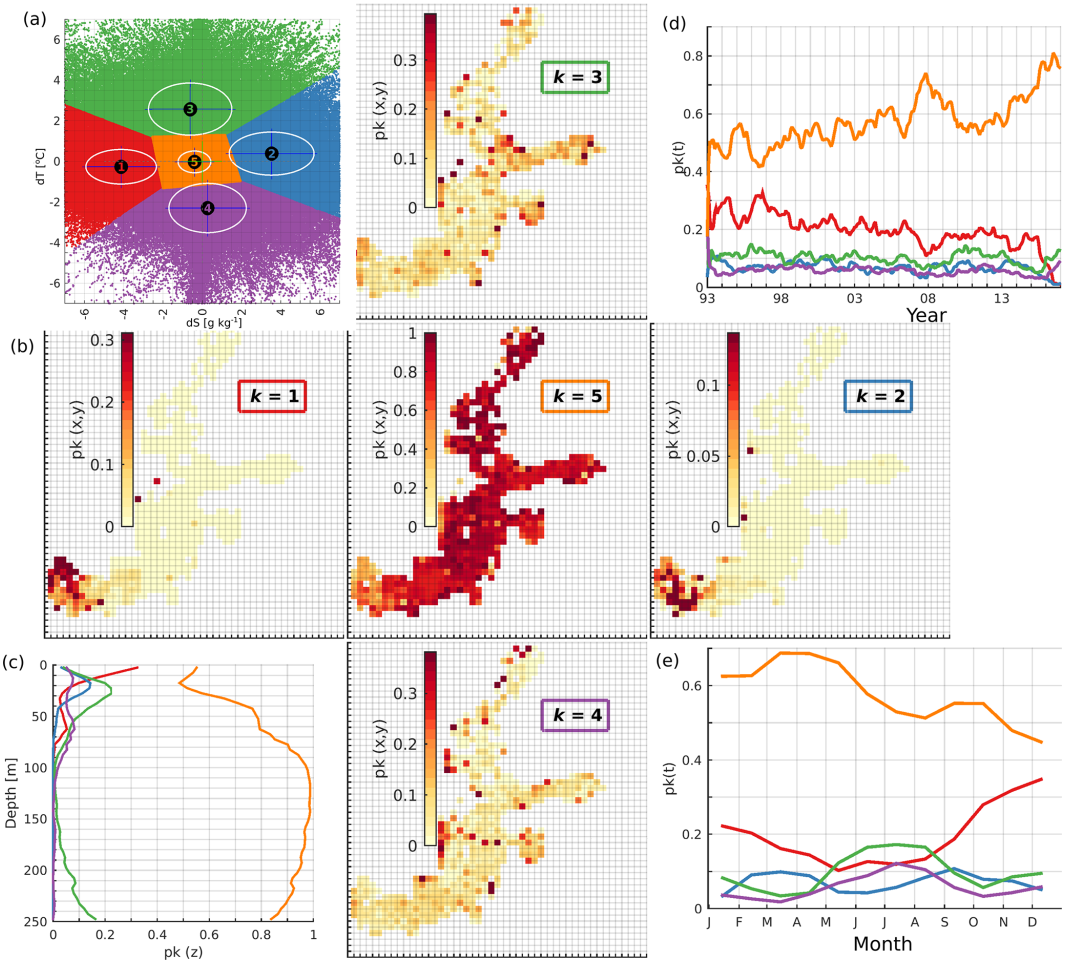

Figure A1. Distribution of normalized error clusters for the BAL-MYP for $k = 5$ **(a)** and the spatial distribution (**b**, shaded sub-plots), vertical distribution **(c)**, temporal distribution **(d)**, and seasonal distribution **(e)** of the share of error points belonging to the five different clusters.

Table A1. The share (%), bias, root-mean-square error (RMSE), standard deviation (SD), and correlation coefficient (Corr) for each of the five clusters.

	Shares	Bias		SD		RMSE		Corr		
k	%	dS (g kg^{-1})	dT (°C)	dS (g kg^{-1})	dT (°C)	S (g kg^{-1})	T (°C)	S	T	dSdT
1	18.6	−4.14	−0.26	1.80	0.85	4.51	0.89	0.90	0.78	−0.09
2	7.4	3.53	0.39	2.16	1.06	4.14	1.13	0.93	0.75	−0.11
3	10.5	−0.62	2.58	2.12	1.28	2.21	2.88	0.97	0.58	−0.06
4	6.3	0.27	−2.29	1.97	1.21	1.99	2.59	0.95	0.71	−0.14
5	57.2	−0.40	−0.02	0.83	0.54	0.92	0.54	0.99	0.89	0.07

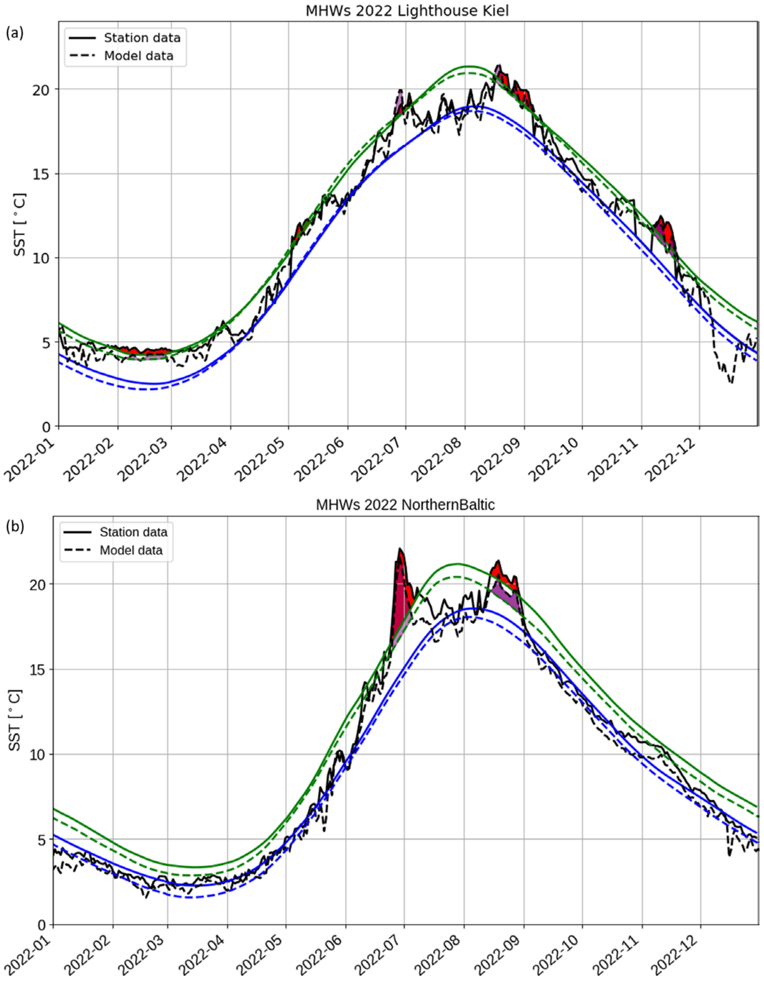

Figure A2. Comparison of station data with BAL-MYP data at **(a)** LT Kiel (product ref. no. 2 and 3 in Table 1) and **(b)** Northern Baltic (Hedi Kanarik, FMI, personal communication, 2023, and product ref. no. 3 in Table 1). The dashed lines correspond to the reanalysis, while the continuous lines correspond to the station data. The climatological mean is shown in blue. The green lines show the 90th percentile threshold for MHW detection, and the black lines are the respective 2022 temperature data. The purple (BAL-MYP) and red (station data) marked areas show the detected MHWs in 2022. The reference period is 1993–2021 for LT Kiel **(a)** and 1997–2021 for Northern Baltic **(b)**.

Code availability. The Python-based toolbox for marine heatwave detection is available at https://github.com/ecjoliver/marineHeatWaves (Oliver, 2016). The MATLAB toolbox for marine heat wave detection is available at https://github.com/ZijieZhaoMMHW/m_mhw1.0 (Zhao and Marin, 2019b, a).

Data availability. This study is based on public databases, and the references are listed in Table 1. Weather observations at Umeå airport (close to southwestern Bothnian Bay) are available from SMHI at https://www.smhi.se/data/meteorologi/ladda-ner-meteorologiska-observationer/#param=wind,stations=core,stationid=140480 (SMHI, 2023b) and https://www.smhi.se/data/meteorologi/ladda-ner-meteorologiska-observationer/#param=airtemperatureInstant,stations=core,stationid=140480 (SMHI, 2023a).

Author contributions. The idea for and concept behind this chapter were formed by AL, CH, PL, HEM, and UR. The data curation was done by EMvdL and TK for the data from product ref. no. 1 in Table 1, by CH and TRP for the data from product ref. no. 2 in Table 1, and by SJS and TRP for the data from product ref. no. 3 in Table 1. The formal analyses of the datasets and the resulting investigations were performed by AL, CH, SJS, TK, and TRP. The k-means model validation was performed by UR and IM. CH, SJS, IM, TK, and TRP were responsible for the visualization of the data. AL, CH, SJS, TK, EMvdL, TRP, and UR were involved in the original draft preparation. The final manuscript was reviewed and edited by CH, PL, HEM, and UR with contributions from all co-authors.

Competing interests. The contact author has declared that none of the authors has any competing interests.

Acknowledgements. This work is supported by the Copernicus Marine Service for the Baltic Sea Monitoring and Forecasting Center (21002L2-COP-MFC BAL-5200).

Review statement. This paper was edited by Marilaure Grégoire and reviewed by Álvaro de Pascual Collar and one anonymous referee.

References

Belkin, I. M.: Rapid warming of large marine ecosystems, Prog. Oceanogr., 81, 207–213, https://doi.org/10.1016/j.pocean.2009.04.011, 2009.

Buga, L., Sarbu, G., Fryberg, L., Magnus, W., Wesslander, K., Gatti, J., Leroy, D., Iona, S., Larsen, M., Koefoed Rømer, J., Østrem, A. K., Lipizer, M., and Giorgetti A.: EMODnet Chemistry Eutrophication and Acidity aggregated datasets v2018, EMODnet, Thematic Lot no. 4/SI2.749773, https://doi.org/10.6092/EC8207EF-ED81-4EE5-BF48-E26FF16BF02E, 2018.

Cheng, L., von Schuckmann, K., Abraham, J. P., Trenberth, K. E., Mann, M. E, Zanna, L., England, M. H., Zika, J. D., Fasullo, J. T., Yu, Y., Pan, Y., Zhu, J., Newsom, E. R., Bronselaer, B., and Lin, X.: Past and future ocean warming, Nature Reviews Earth and Environment, 3, 776–794, https://doi.org/10.1038/s43017-022-00345-1, 2022.

Chubarenko, I. P., Demchenko, N. Y., Esiukova, E. E., Lobchuk, O. I., Karmanov, K. V., Pilipchuk, V. A., Isachenko, I. A., Kuleshov, A. F., Chugaevich, V. Y., Stepanova, N. B., Krechik, V. A., and Bagaev, A. V.: Spring thermocline formation in the coastal zone of the southeastern Baltic Sea based on field data in 2010–2013, Oceanology, 57, 632–638, https://doi.org/10.1134/S000143701705006X, 2017.

Copernicus Climate Change Service/ECMWF: Surface air temperature for August 2022, Copernicus Climate Change Service/ECMWF, https://climate.copernicus.eu/surface-air-temperature-august-2022 (last access: 11 July 2023), 2022a.

Copernicus Climate Change Service/ECMWF: Surface air temperature for November 2022, Copernicus Climate Change Service/ECMWF, https://climate.copernicus.eu/surface-air-temperature-november-2022 (last access: 11 July 2023), 2022b.

Dutheil, C., Meier, H. E. M., Gröger, M., and Börgel, F.: Warming of Baltic Sea water masses since 1850, Clim. Dynam., 61, 1311–1331, https://doi.org/10.1007/s00382-022-06628-z, 2023.

EU Copernicus Marine Service Product: Global Ocean – In-Situ Near-Real-Time Observations, Mercator Ocean International [data set], https://doi.org/10.48670/moi-00036, 2023a.

EU Copernicus Marine Service Product: Baltic Sea – L3S Sea Surface Temperature Reprocessed, Mercator Ocean International [data set], https://doi.org/10.48670/moi-00312, 2023b.

EU Copernicus Marine Service Product: Baltic Sea Physics Reanalysis, Mercator Ocean International [data set], https://doi.org/10.48670/moi-00013, 2023c.

EUMETSAT: AVHRR Factsheet, Doc. No. EUM/OPS/-DOC/09/5183, https://www-cdn.eumetsat.int/files/2020-04/pdf_avhrr_factsheet.pdf (last access: 24 April 2024), 2015.

Frölicher, T. L., Fischer, E. M., and Gruber, N.: Marine heatwaves under global warming, Nature, 560, 360–364, https://doi.org/10.1038/s41586-018-0383-9, 2018.

Giorgetti, A., Lipizer, M., Molina Jack, M. E., Holdsworth, N., Jensen, H. M., Buga, L., Sarbu, G., Iona, A., Gatti, J., Larsen, M., and Fyrberg, L.: Aggregated and Validated Datasets for the European Seas: The Contribution of EMODnet Chemistry, Front. Mar. Sci., 7, 583657, https://doi.org/10.3389/fmars.2020.583657, 2020.

Goebeler, N., Norkko, A., and Norkko, J.: Ninety years of coastal monitoring reveals baseline and extreme ocean temperatures are increasing off the Finnish coast, Commun. Earth Environ., 3, 215, https://doi.org/10.1038/s43247-022-00545-z, 2022.

Gröger, M., Placke, M., Meier, H. E. M., Börgel, F., Brunnabend, S.-E., Dutheil, C., Gräwe, U., Hieronymus, M., Neumann, T., Radtke, H., Schimanke, S., Su, J., and Väli, G.: The Baltic Sea Model Intercomparison Project (BMIP) – a platform for model development, evaluation, and uncertainty assessment, Geosci. Model Dev., 15, 8613–8638, https://doi.org/10.5194/gmd-15-8613-2022, 2022.

Gurvan, M., Bourdallé-Badie, R., Chanut, J., Clementi, E., Coward, A., Ethé, C., Iovino, D., Lea, D., Lévy, C., Lovato, T., Martin, N., Masson, S., Mocavero, S., Rousset, C., Storkey, D., Vancoppenolle, M., Müeller, S., Nurser, G., Bell, M., and Samson, G.: NEMO ocean engine, in: Notes du Pôle de modélisation de l'Institut Pierre-Simon Laplace (IPSL) (v4.0, Number 27), Zenodo, https://doi.org/10.5281/zenodo.3878122, 2019.

Hobday, A. J., Alexander, L. V., Perkins, S. E., Smale, D. A., Straub, S. C., Oliver, E. C. J., Benthuysen, J. A., Burrows, M. T., Donat, M. G., Feng, M., Holbrook, N. J., Moore, P. J., Scannell, H. A., Sen Gupta, A., and Wernberg, T.: A hierarchical approach to defining marine heatwaves, Prog. Oceanogr., 141, 227–238, https://doi.org/10.1016/j.pocean.2015.12.014, 2016.

Hobday, A. J., Oliver, E. C. J., Sen Gupta, A., Benthuysen, J. A., Burrows, M. T., Donat, M. G., Holbrook, N. J., Moore, P. J., Thomsen, M. S., Wernberg, T., and Smale, D. A.: Categorizing and naming marine heatwaves, Oceanography, 31, 162–173, https://doi.org/10.5670/oceanog.2018.205, 2018.

Holbrook, N. J., Scannell, H. A., Sen Gupta, A., Benthuysen, J. A., Feng, M., Oliver, E. C., Alexander, L. V., Burrows, M. T., Donat, M. G., Hobday, A. J., and Moore, P. J.: A global assessment of marine heatwaves and their drivers, Nat. Commun., 10, 2624, https://doi.org/10.1038/s41467-019-10206-z, 2019.

ICES Bottle and low-resolution CTD dataset: Extractions 22 DEC 2013 (for years 1990–2012), 25 FEB 2015 (for year 2013), 13 OCT 2016 (for year 2015), 15 JAN 2019 (for years 2016–2017), 22 SEP 2020 (for year 2018), 10 MAR 2021 (for years 2019–2020), 28 FEB 2022 (for year 2021), ICES, Copenhagen [data set], https://data.ices.dk (last access: 30 April 2024), 2022.

In Situ TAC partners: EU Copernicus Marine Service Product User Manual for the Global Ocean- In-Situ Near-Real-Time Observations, INSITU_GLO_PHYBGCWAV_DISCRETE_MYNRT_013_030, Issue 2.0, Mercator Ocean International, https://catalogue.marine.copernicus.eu/documents/PUM/CMEMS-INS-PUM-013-030-036.pdf (last access: 22 March 2024), 2023.

IPCC: Climate Change 2022: Impacts, Adaptation, and Vulnerability. Contribution of Working Group II to the Sixth Assessment Report of the Intergovernmental Panel on Climate Change, edited by: Pörtner, H.-O., Roberts, D. C., Tignor, M., Poloczanska, E. S., Mintenbeck, K., Alegría, A., Craig, M., Langsdorf, S., Löschke, S., Möller, V., Okem, A., and Rama, B., Cambridge University Press, Cambridge, UK and New York, NY, USA, 3056 pp., https://doi.org/10.1017/9781009325844, 2022.

Jain, A. K.: Data clustering: 50 years beyond K-means, Pattern Recogn. Lett., 31, 651–666, https://doi.org/10.1016/j.patrec.2009.09.011, 2010.

Kauppi, L. and Villnäs, A.: Marine heatwaves of differing intensities lead to distinct patterns in seafloor functioning, P. Roy. Soc. B, 289, 20221159, https://doi.org/10.1098/rspb.2022.1159, 2022.

Kauppi, L., Göbeler, N., Norkko, J., Norkko, A., Romero-Ramirez, A., and Bernard, G.: Changes in macrofauna bioturbation during repeated heatwaves mediate changes in biogeochemical cycling of nutrients, Front. Mar. Sci., 9, 1070377, https://doi.org/10.3389/fmars.2022.1070377, 2023.

Minnett, P. J., Alvera-Azcárate, A., Chin, T. M., Corlett, G. K., Gentemann, C. L., Karagali, I., Li, X., Marsouin, A., Marullo, S., Maturi, E., Santoleri, R., Saux Picart, S., Steele, M., and Vazquez-Cuervo, J.: Half a century of satellite remote sensing of sea-surface temperature, Remote Sens. Environ., 233, 111366, https://doi.org/10.1016/j.rse.2019.111366, 2019.

Oliver, E. C. J.: marineHeatWaves v0.16, GitHub [code], https://github.com/ecjoliver/marineHeatWaves (last access: 17 March 2023), 2016.

Oliver, E. C. J.: Mean warming not variability drives marine heatwave trends, Clim. Dynam., 53, 1653–1659, https://doi.org/10.1007/s00382-019-04707-2, 2019.

Panteleit, T., Verjovkina, S., Jandt-Scheelke, S., Spruch, L., and Huess, V.: EU Copernicus Marine Service Quality Information Document for the Baltic Sea Physics Reanalysis, BALTICSEA_MULTIYEAR_PHY_003_011, Issue 4.0, Mercator Ocean International, https://catalogue.marine.copernicus.eu/documents/QUID/CMEMS-BAL-QUID-003-011.pdf (last access: 12 April 2023), 2023.

Raudsepp, U. and Maljutenko, I.: A method for assessment of the general circulation model quality using the K-means clustering algorithm: a case study with GETM v2.5, Geosci. Model Dev., 15, 535–551, https://doi.org/10.5194/gmd-15-535-2022, 2022.

Raudsepp, U., Maljutenko, I., Haapala, J., Männik, A., Verjovkina, S., Uiboupin, R., von Schuckmann, K., and Mayer, M.: Record high heat content and low ice extent in the Baltic Sea during winter 2019/20, in: Copernicus Ocean State Report, Issue 6, J. Oper. Oceanogr., 15, Supplement, s175–s185, https://doi.org/10.1080/1755876X.2022.2095169, 2022.

Ringgaard, I., Korabel, V., Spruch, L., Lindenthal, A., and Huess, V.: EU Copernicus Marine Service Product User Manual for the Baltic Sea Physics Reanalysis, BALTICSEA_MULTIYEAR_PHY_003_011, Issue 1.0, Mercator Ocean International, https://catalogue.marine.copernicus.eu/documents/PUM/CMEMS-BAL-PUM-003-011_012.pdf (last access: 12 April 2023), 2023.

Sen Gupta, A., Thomsen, M., Benthuysen, J. A., Hobday, A. J., Oliver, E., Alexander, L. V., Burrows, M. T., Donat, M. G., Feng, M., Holbrook, N. J., Perkins-Kirkpatrick, S., Moore, P. J., Rodrigues, R. R., Scannell, H. A., Taschetto, A. S., Ummenhofer, C. C., Wernberg, T., and Smale, D. A.: Drivers and impacts of the most extreme marine heatwave events, Sci. Rep., 10, 19359, https://doi.org/10.1038/s41598-020-75445-3, 2020.

She, J., Su, J., and Zinck, A.-S.: Anomalous surface warming in the Baltic Sea in summer 2018 and mechanism analysis, in: Copernicus Marine Service Ocean State Report, Issue 4, J. Oper. Oceanogr., 13, Supplement, s125–s132, https://doi.org/10.1080/1755876X.2020.1785097, 2020.

Smale, D. A., Wernberg, T., Oliver, E. C. J., Thomsen, M., Harvey, B. P., Straub, S. C., Burrows, M. T., Alexander, L. V., Benthuysen, J. A., Donat, M. G., Feng, M., Hobday, A. J., Holbrook, N. J., Perkins-Kirkpatrick, S. E., Scannell, H. A., Sen Gupta, A., Payne, B. L., and Moore, P. J.: Marine heatwaves threaten global biodiversity and the provision of ecosystem services, Nat. Clim. Change, 9, 306–312, https://doi.org/10.1038/s41558-019-0412-1, 2019.

SMHI: Baltic Sea – Eutrophication and Acidity aggregated datasets 1902/2017 v2018, Swedish Meteorological and Hydrological Institute, EMODnet Chemistry [data set], https://doi.org/10.6092/595D233C-3F8C-4497-8BD2-52725CEFF96B, 2018.

SMHI: Meteorological observations, air temperature, station number 140480 (Umeå Flygplats), Swedish Meteorological and Hydrological Institute [data set], https://www.smhi.se/data/meteorologi/ladda-ner-meteorologiska-observationer/#param=airtemperatureInstant,stations=core,stationid=140480 (last access: 19 December 2023), 2023a.

SMHI: Meteorological observations, wind, station number 140480 (Umeå Flygplats), Swedish Meteorological and Hydrological Institute [data set], https://www.smhi.se/data/meteorologi/ladda-ner-meteorologiska-observationer/#param=wind,stations=core,stationid=140480 (last access: 19 December 2023), 2023b.

Smith, K. E., Burrows, M. T., Hobday, A. J., King, N. G., Moore, P. J., Gupta, A. S., Thomsen, M. S., Wernberg, T., and Smale, D. A.: Biological Impacts of Marine Heatwaves, Annu. Rev. Mar. Sci., 15, 119–145, https://doi.org/10.1146/annurev-marine-032122-121437, 2023.

Sun, D., Jing, Z., Li, F., and Wu, L.: Characterizing global marine heatwaves under a spatio-temporal framework, Prog. Oceanogr., 211, 102947, https://doi.org/10.1016/j.pocean.2022.102947, 2023.

The BACC Author Team: Assessment of Climate Change for the Baltic Sea Basin, Springer Berlin, Heidelberg, p. 88, https://doi.org/10.1007/978-3-540-72786-6, 2008.

Väli, G., Meier, H. M., and Elken, J.: Simulated halocline variability in the Baltic Sea and its impact on hypoxia during 1961–2007, J. Geophys. Res.-Oceans, 118, 6982–7000, https://doi.org/10.1002/2013JC009192, 2013.

Wehde, H., Schuckmann, K. V., Pouliquen, S., Grouazel, A., Bartolome, T., Tintore, J., De Alfonso Alonso-Munoyerro, M., Carval, T., Racapé, V., and the INSTAC team: EU Copernicus Marine Service Quality Information Document for the Global Ocean- In-Situ Near-Real-Time Observations, INSITU_GLO_PHYBGCWAV_DISCRETE_MYNRT_013_030, Issue 2.3, Mercator Ocean International, https://catalogue.marine.copernicus.eu/documents/QUID/CMEMS-INS-QUID-013-030-036.pdf (last access: 22 March 2024), 2023.

WMO: State of the Global Climate 2022, WMO-No. 1316, World Meteorological Organization, 2023, 48 pp., ISBN 978-92-63-11347-4, https://library.wmo.int/idurl/4/66214 (last access: 2 May 2023), 2023.

Zhao, Z. and Marin, M.: A MATLAB toolbox to detect and analyze marine heatwaves, Journal of Open Source Software, 4, 1124, https://doi.org/10.21105/joss.01124, 2019a.

Zhao, Z. and Marin, M.: A MATLAB toolbox to detect and analyze marine heatwaves (MHWs), GitHub [code], https://github.com/ZijieZhaoMMHW/m_mhw1.0 (last access: 28 May 2024), 2019b.

State Planet, 4-osr8, 17, 2024
https://doi.org/10.5194/sp-4-osr8-17-2024

Characterization of marine heat waves in the Iberia–Biscay–Ireland (IBI) region in 2022

Lluís Castrillo-Acuña[1], **Axel Alonso-Valle**[1,2], **and Álvaro de Pascual-Collar**[1]

[1]Nologin Oceanic Weather Systems, Paseo de las Delicias 30, 3rd floor, offices 3–5, Madrid, 28045, Spain
[2]Earth Physics and Astrophysics Department, Complutense University of Madrid, Madrid, 28040, Spain

Correspondence: Lluís Castrillo-Acuña (lluis.castrillo@nowsystems.eu)

Received: 3 August 2023 – Discussion started: 4 September 2023
Revised: 19 January 2024 – Accepted: 20 March 2024 – Published: 30 September 2024

Abstract. Marine heat waves (MHWs) are defined as prolonged periods of anomalously high sea surface temperatures. These events have a profound impact on marine ecosystems, resulting in ecological and economic impacts such as coral bleaching, reduced surface chlorophyll due to increased surface layer stratification, mass mortality of marine invertebrates due to heat stress, rapid species migrations, and fishery closures or quota changes, among others.

This research focuses on the study of the MHWs that occurred in the IBI (Iberia–Biscay–Ireland) region during the year 2022, assessing their climatologic properties, analyzing the mean values for the year 2022, and discretizing the events in four subregions representative of the entire domain. Satellite-derived sea surface temperature data were used to detect and characterize the events, revealing that in some areas the year 2022 showed peak anomaly values of (i) 15 MHW events, (ii) 128 d of mean durations, and (iii) 261 total days of MHWs. Through observational and modeling data, the discrete events located in the Bay of Biscay were also examined in the subsurface layers, demonstrating a strong seasonal modulation and heat diffusion through deeper layers, where cold-season events reach higher MHW mean depth values and subsurface positive anomalies of temperature can remain for weeks once an MHW has ended.

1 Introduction

Marine heat waves (MHWs) are a physical process which results in extreme temperatures, at least, on the ocean surface. As they are known to be related to multiple drastic alterations in marine ecosystems and services (Holbrook et al., 2020; Smale et al., 2019), and due to the recently observed ocean surface warming of 0.88 °C in the last decade (Lee et al., 2023), which is also related to an increase in the MHW frequency and the intensity of the events, the scientific community has shown a growing interest in this topic (Hobday et al., 2018).

In this contribution, an analysis of the MHWs in the IBI (Iberia–Biscay–Ireland) domain during the year 2022 is performed. The IBI region is one of the areas handled by the Monitoring and Forecasting Centers of the Copernicus Marine Service, located in the northeastern Atlantic Ocean between the Canary Archipelago in the south and Great Britain and Ireland in the north (Fig. 1). This region clusters multiple dynamical systems, such as upwelling areas, open waters, straits, and bays, and it is hence a region characterized by a remarkable range of physical processes at various spatial and temporal scales (Sotillo et al., 2015).

To detect and analyze MHWs, the standard method of Hobday et al. (2016) is used, defining an MHW as a discrete event that lasts for at least 5 consecutive days exhibiting temperatures warmer than the 90th percentile of the climatological distribution. This method has been widely used, and hence an important number of comparable MHW studies around the world have been published. Unfortunately, there is an unsolved issue regarding the Hobday et al. (2016) method: how to deal with sea surface temperature (SST) trends and MHW detection. Different authors have assessed this issue, but a consensus has not been reached yet. It is demonstrated

Published by Copernicus Publications.

Table 1. List of Copernicus Marine products used for the computation of marine heat waves (MHWs) in Iberia–Biscay–Ireland (IBI) region.

Product ref. no.	Product ID Acronym Type	Data access	Documentation: QUID: Quality Information Document PUM: Product User Manual
1	SST_GLO_SST_L4_REP_OBSERVATIONS_010_024 (GLO-REP) Satellite observations	EU Copernicus Marine Service Product (2021)	QUID: Good (2021) PUM: Good (2022)
2	INSITU_IBI_PHYBGCWAV_DISCRETE_MYNRT_013_033 (ARGO) In situ observations	EU Copernicus Marine Service Product (2023a)	QUID: Wehde et al. (2023) PUM: In Situ TAC Partners (2023)
3	IBI_ANALYSISFORECAST_PHY_005_001 (IBI-NRT) Numerical models	EU Copernicus Marine Service Product (2023b)	QUID: Levier et al. (2023) PUM: Amo-Baladrón et al. (2023)
4	IBI_MULTIYEAR_PHY_005_002 (IBI-REA) Numerical models	EU Copernicus Marine Service Product (2022)	QUID: Levier et al. (2022) PUM: Amo-Baladrón et al. (2022)

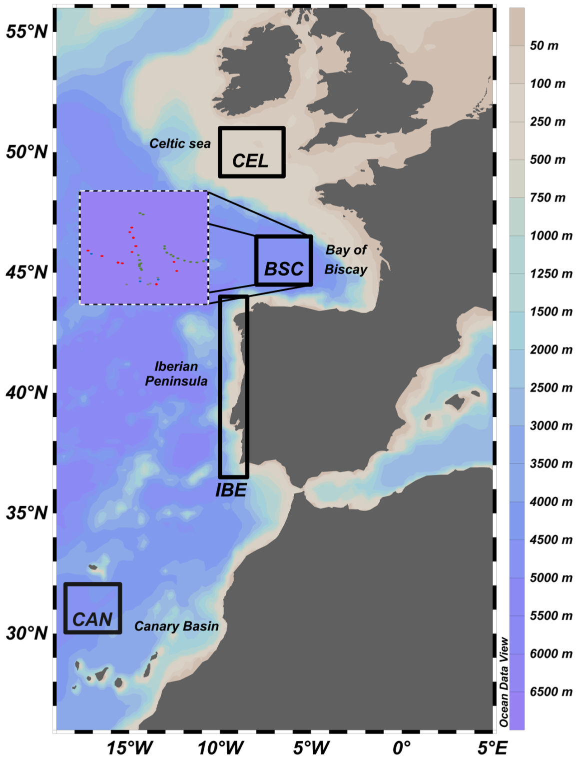

Figure 1. Study area with bathymetry from 19° W to 5° E of longitude and 25 to 59° N of latitude. Black boxes with acronyms represent the areas in which we discretize the MHW events of 2022 by spatial averaging of SST; areas are the Canary Basin (CAN) (18.5–15° W, 30–32° N), the Iberian Peninsula (IBE) (10–8.5° W, 36.5–44° N), the Bay of Biscay (BSC) (8–5° W, 44.5–46.5° N), and the Celtic Sea (CEL) (10–6.5° W, 49–51° N). For the BSC area, the position of the ARGO profiles is shown with points in different colors. This map has been obtained through Ocean Data View v.5.6.3. (Schlitzer, 2021).

that long-term trends influence the MHW results; for example, the global assessment of Oliver et al. (2018) shows that just the SST trend may explain the MHW trends in 80 %, 59 %, and 53 % of the ocean surface for the frequency, intensity, and duration, respectively. Also, through the use of synthetic SST time series and sensitivity experiments, Schlegel et al. (2019) demonstrated that SST long-term linear trends can have a much greater effect on the trend of MHW properties than the length of the series or even the presence of missing data. So, the underlying issue is about considering the long-term mean modulation to be part of the MHW process (not detrending) or consider the MHW just looking into the modulation of the extreme values independent of the evolution of mean ones (detrending).

Considering the results of the recent MHW global assessments, it is expected for such events to increase in frequency and duration during the next years in most parts of the world (Oliver et al., 2018; Yao et al., 2022; Collins et al., 2019; Fox-Kemper et al., 2021). These predictions also include the IBI domain, a region characterized by Yao et al. (2022) as presenting MHWs with an intensity mean close to 1 °C and approximately 15 to 30 MHW days per year from 1982 to 2020. A wide range of physical processes can be pointed out as drivers of the occurrence of MHWs depending on the subregions assessed. Specifically, our study area covers the Canary Basin, the Iberian Peninsula, the Bay of Biscay, and the Celtic Sea (Fig. 1).

Canary and Iberian MHWs are mostly linked to processes of atmospheric blocking, the negative phase of the North Atlantic Oscillation (NAO), the regional air–sea coupling, the regional changes in wave stress and the jet stream position, local advective processes, and air–sea heat fluxes (Holbrook et al., 2019; Varela et al., 2021). In a rare instance, the influence of ENSO has also been observed in a record-breaking event recorded in the area (Hu et al., 2011).

In the case of the Bay of Biscay and the Celtic Sea the main interannual drivers of MHWs are the NAO and the East Atlantic pattern (EA) (Izquierdo et al., 2022; Simon et al., 2023), while other processes such as the inflow from the English Channel and the strength of the tidal currents also play a key role in the regional changes in the SST (Cornes et al., 2023).

In this research we aim to characterize the year 2022 regarding the MHWs in the IBI domain, considering not only the annual mean values but also the 2022 discrete events in four different subregions representative of the domain. Also, we shed light on the first steps of learning how MHWs behave under the surface by using Copernicus products.

2 Data and methods

In the present work several Copernicus Marine products (described in Table 1) have been used to provide a description of the MHWs which occurred in the IBI region during the year 2022. The diversity of products used is due to our leverage of their different strengths in the detection and description of MHWs.

2.1 Data

To detect the MHW events, we used the ESA SST CCI and C3S global Sea Surface Temperature Reprocessed product (GLO-REP, Table 1, product ref. 1), which is a homogenous level 4 analysis. This dataset provides daily gridded gap-free SST data from 1 September 1981 at 0.05° × 0.05° of spatial resolution. The input data of the system derive from three different satellite sensors, the ATSRs, the SLSTR, and the AVHRR (Merchant et al., 2019), and are processed through the Operational Sea Surface Temperature and Sea Ice Analysis (OSTIA) system developed by the UK's Met Office (Good et al., 2020). The availability of gridded data for this product has enabled (i) the generation of a reference climatology and seasonal threshold to detect MHWs and (ii) the compilation of a catalogue of MHWs that impacted the study area during 2022.

Once a specific event was located in space and time, we observed how some of these events behaved under the surface. To achieve this goal, we used seawater temperature data from the ocean surface down to 350 m of depth from both in situ observations and numerical models. Thus, we examined specific events with in situ data and also estimated their development during all the MHW days through numerical modeling data, which have no spatial or temporal limitations.

ARGO is the collective name of a global array of 3000 automated free-drifting profiling floats that measure seawater temperature and salinity in the upper ocean as well as, in some cases, bio-geo parameters such as oxygen or chlorophyll concentration. All collected data are freely available from the international ARGO project and the national programs that contribute to it (ARGO, 2019). The specific Copernicus Marine Environment Monitoring Service (CMEMS) product that we used is the Atlantic–Iberian Biscay–Irish Ocean in situ near-real-time observations (hereafter the ARGO product, Table 1, product ref. 2), which compiles level 2 processed in situ near-real-time data from ARGO floats and other observational sources in the IBI region since 1 January 1990 to the current day. They are hourly-updated and distributed by the Copernicus Marine In Situ Thematic Assembly Centre (In Situ TAC) within 24–48 h of acquisition. The ARGO observations consist of instantaneous values, quality-controlled and irregularly distributed in time and space as a result of the diverse modes of operation, problems with the sensors, and drifting movement of the buoys.

With the aim of acquiring data that allow a more detailed study at a regular daily scale, two three-dimensional, gridded, and gap-free CMEMS datasets from numerical models have also been used, both run and provided by the IBI Monitoring and Forecasting Center. The first one is the Atlantic–Iberian–Biscay–Irish Ocean Physics Analysis and Forecast (IBI-NRT, Table 1, product ref. 3), a product with a spatial resolution of 0.028° × 0.028° and 50 depth levels down to 5728 m. It provides best estimates with level 4 processing of different physical variables for the last 2 years, as well as a forecast with a 5 d horizon, updated daily. Secondly, we used the Atlantic–Iberian–Biscay–Irish Ocean Physics Reanalysis (IBI-REA, Table 1, product ref. 4), which extends from 1 January 1993 to 28 December 2021. It has a spatial resolution of 0.083° × 0.083° with the same vertical levels as IBI-NRT and a time resolution that ranges from hourly to yearly. Observational data assimilated for the reanalysis include altimeter measurements, in situ temperature and salinity vertical profiles, and satellite sea surface temperature. For the purposes of this study, we extracted daily averaged values of potential temperature (θ) in the water column from 2005 to 2021 for IBI-REA and the year 2022 for IBI-NRT. Thereby, we obtained a dataset to use as a mean reference (IBI-REA) and another one to assess the year 2022 (IBI-NRT) deep inside the ocean.

2.2 Methods

2.2.1 Surface MHW assessment

The study and detection of the MHWs were accomplished through the standard definition of Hobday et al. (2016) applied to the GLO-REP product from January 1982 to December 2022. We chose the usual parameters in order to obtain results comparable to those of similar studies on this topic: a minimum duration of 5 d to consider an MHW, a maximum gap tolerance of 2 d between two events, a threshold calculated through the 90th percentile, and a climatology and threshold computed for the whole period smoothed out using a moving window of 31 d. The reference period for the climatology corresponds to the entire time series in order to use all the possible values to compute the mean without arbitrary selections.

Among the set of parameters available to characterize the MHW we selected the ones that we understand as fundamental to evaluate the state of MHWs in the IBI domain during 2022: the frequency of the events, the duration, the maximum intensity point relative to the climatology and the absolute value, and the cumulative intensity, which can be assessed as the total energy of an event.

Regarding the possible presence of linear trends in SST, in this research we did not apply any kind of trend assessment or detrending method due to the lack of any standard procedure.

For a deeper analysis of MHWs in the region, we defined four subregions to be representative of the different oceanographic systems in our study area and performed a spatial average to assess them. According to this criterion, the selected subregions were the continental shelf near the British Islands and English Channel (CEL), the offshore region of the Gulf of Biscay (BSC), the upwelling region next to the coast of the Iberian Peninsula (IBE), and the Azores and Canary Islands Basin (CAN) (Fig. 1). In this manner, we were able to analyze the discrete events in 2022 and the record-breaking ones for all the years as a reference for each sub-domain.

2.2.2 Subsurface MHW assessment

The ARGO float network is used to assess specific events from the ocean surface down to a maximum depth of 350 m. With the aim of computing a temperature anomaly or deviation profile which represents a single event, we first converted pressure into depth by using the UNESCO formula (Fofonoff and Millard, 1993) and interpolated them to a common depth scale, which in our case consisted of vertical steps of 0.5 m. The mean MHW profile is then calculated as the mean temperature value at each depth level of all the available data that concur in time and space with the event recorded by the GLO-REP dataset. The reference profile is the mean temperature value at each depth level of all the ARGO observations which agree in space and time for the year with each MHW singled out in 2022. Lastly, the deviation or anomaly profile is computed as the mean MHW profile minus the reference one for each event. The uncertainty for the deviation profile has been computed through a bootstrap procedure at 95 % confidence, iterating through the mean values of the MHW and reference profiles. Also, the Elzahaby and Schaeffer (2019) method allowed us to compute the mean depth of an MHW according to a threshold calculated through the accumulated positive anomaly along the vertical dimension. The threshold modulation depends on some parameterization, which in our case was chosen arbitrarily as the same that was used by the authors in order to acquire comparable results.

To obtain robust results according to the available data, we decided to focus on the BSC subregion (Fig. 1), given that this area contained a substantial number of ARGO profiles and MHWs during the year 2022. However, data limitations arose which implied that the long-term reference profiles were not consistent among the events, with the year of the first profile varying between 2004 and 2006 and the year of the last one between 2019 and 2021. We also had to deal with some data issues regarding fragmentation and low reliability. In this research, we discarded profiles that were too fragmented and the specific values that were not labeled as completely reliable by In Situ TAC.

To analyze the subsurface daily evolution of specific MHWs we used a Hovmöller diagram of daily mean θ anomalies. This methodology demands a dataset with regular data in time and space that is long enough to get a representative long-term reference. We achieved these requirements by using the IBI-REA from 2005 to 2021 and the IBI-NRT for 2022, calibrated as an elongation of the IBI-REA product. The calibration procedure consisted of (i) selecting the common period for both datasets (May to December 2021) for the first 100 m, (ii) averaging the IBI-NRT and IBI-REA θ values horizontally across the entire BSC region and interpolating both datasets to a common vertical grid of 0.5 m, (iii) computing the linear regression parameters of IBI-NRT to predict IBI-REA trough the ordinary least squares method (Chatterjee and Simonoff, 2020), concluding in $\beta = 0.9767$, $\alpha = 0.3298$, $R^2 = 0.990$, and significant F statistic, and (iv) correcting 2022 IBI-NRT with the regression parameters to compute the anomalies.

3 Results and discussion

3.1 MHW characterization

The analysis of the 40-year SST time series (Fig. 2) showed that the MHWs in the IBI domain during this period took place from 1 to 2.5 times per year, concurring with the results of Oliver et al. (2018). The annual total days take annual mean values close to 30 d, a few more days per year than the estimations of Yao et al. (2022). As shown in Fig. 2, the frequency and the annual total days do not show any clear climatological zonation over the IBI domain, while for the case of the maximum intensity, it shows a clear increment near the coastal areas reaching values of 4 °C relative to the climatology; in relation to the duration, the maximum values of 30 d are located near the English Channel. The presence of abnormal values is also remarkable in some waters of England and Ireland, for instance the Humber estuary (0° E, 57° N), which in small areas showed mean values of five MHW events per year. This is probably due to its semi-enclosed waters, which have multiple biologically, chemically, and physically distinctive features (Elliott and Whitfield, 2011).

The annual mean properties from January to December 2022 indicate that the MHWs during this period were un-

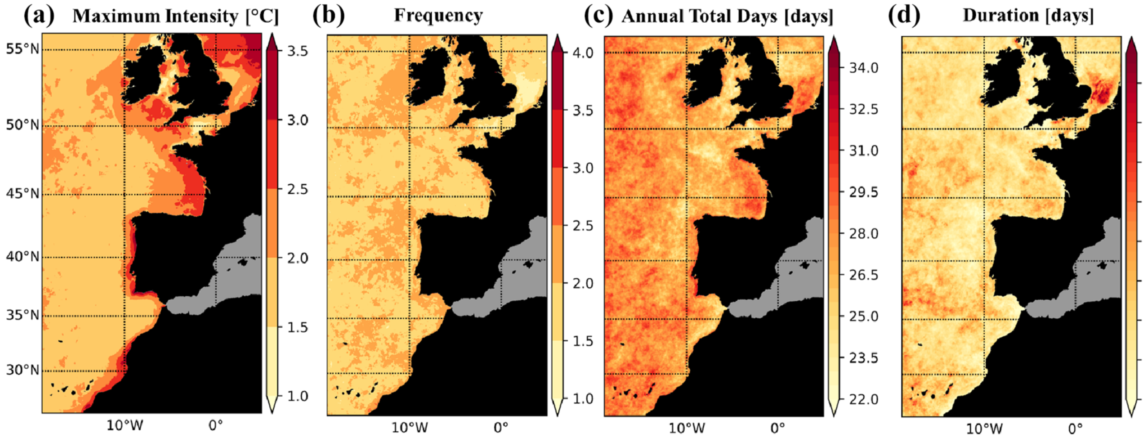

Figure 2. Climatologic values of **(a)** maximum intensity, **(b)** frequency, **(c)** annual total days, and **(d)** duration for all the recorded events through the GLO-REP dataset from January 1982 to December 2022.

usual (Fig. 3). Severe positive anomalies of frequency and total annual days are found in almost all the IBI region, especially in proximity to the Celtic Sea and the English Channel, reaching peak anomaly values of 15 events and 261 d of MHWs. Regarding the duration, it stands out for having locations with positive anomalies of 128 d and multiple areas with negative anomalies. As a generalization in the IBI domain, it seems that near the coast, there were more events but shorter than normal. The maximum intensity parameter is the only one with equivalent positive and negative anomaly values in a range from -3 to $3\,°\mathrm{C}$. The area around 18° W, 37° N shows peak negative anomaly values for the maximum intensity, but this "low-activity area" is also appreciable for the rest of the studied parameters (Figs. 2 and 3). It is an interesting feature, but we do not find an explanation in our results or in the literature.

Despite these results being, at least, quite alarming, we must point out that we understand that they may be strongly affected by the SST long-term trend. As mentioned above, different authors have addressed this issue but there is not a common agreement about how to deal with SST trends and MHWs. For the IBI domain, regional studies also corroborate the influence of the SST trends on the MHWs detected. For instance, in the Bay of Biscay, Izquierdo et al. (2022) demonstrated that SST trends may be responsible for a $\sim 20\,\%$ increase in the total MHW days during a decade. Also, in the English Channel, Simon et al. (2023) observed a positive correlation between the SST trend and the MHW duration, frequency, and extent. Furthermore, for the coastal areas subjected to an upwelling system such as the Canary Upwelling System, it is considered that global warming does not produce a direct effect on MHW trends (Varela et al., 2021). In summary, we consider Figs. 2 and 3 to manifest the need to establish a criterion about how to proceed with SST long-term trends because this method will be useless if all the days of the year are considered to be part of an MHW.

Another way to describe 2022 anomalies was by comparing the discrete events that occurred during 2022 and the record-breaking events over the past 40 years in four different subregions (Fig. 1), choosing for comparisons those events which reached the most extreme values of maximum intensity (int. max) and maximum duration (dur. max) (Table 3). From Table 2 we deduced that the number of events in 2022 increased with latitude and were more intense during the summer period as also shown for previous events by Sen Gupta et al. (2020). The event of 29 October in CAN almost reached the cumulative intensity value of the maximum intensity event of 2004 in the same area; almost all the 2022 MHWs in IBE showed bigger absolute maximum intensity values than the maximum duration event recorded in 1997, probably due to global warming. In the BSC area, the event starting on 29 April stands out for having 13 more days of duration and a greater cumulative intensity by $4.37\,°\mathrm{C}$ per day than the 2018 maximum intensity event. Lastly, from the CEL subregion we can highlight the event of 7 August for having $14.86\,°\mathrm{C}$ per day more cumulative intensity than the maximum duration event recorded in 2015–2016. Although it may not be strictly adequate to make direct comparisons between maximum duration and maximum intensity events given that intensity and duration are independent, an event can be very long and mild in intensity or vice versa, and these results demonstrate that the MHWs during the year 2022 were present in all the IBI domain with severe properties in various cases. Also, this comparison allowed us to embrace a general perspective and observe how, at least regarding the cumulative intensity, which represents the intensity–duration interaction fairly well, two 2022 events in two different subregions – the 29 April event in BSC and the 7 August event in CEL – surpassed two previous record-breaking events in their respective zones. The last remarkable result lies in the last events recorded for CAN, IBE, and BSC; in all cases the last event occurred until the last day of data, starting 29 Octo-

Table 2. Record of the 2022 MHWs in the IBI area grouped by the subregions shown in Fig. 1. The MHW detection was applied to each subregion using the GLO-REP product (January 1982–December 2022). The listed events are ordered by the start date.

		Start date	End date	Duration (days)	Intensity max (°C)	Cumulative intensity (°C d)	Intensity max absolute (°C)
CEL	1	20 January	24 January	5	0.59	2.75	11.02
	2	9 February	8 March	28	0.72	17.60	10.81
	3	13 March	2 April	21	0.98	15.47	10.86
	4	13 April	22 April	10	1.30	10.43	11.64
	5	30 April	20 May	21	1.95	34.46	13.21
	6	26 May	17 June	23	2.16	40.06	15.69
	7	14 July	20 July	7	1.93	11.92	18.58
	8	7 August	5 September	30	3.06	57.42	20.31
	9	16 September	27 September	12	1.47	16.00	17.34
	10	24 October	2 November	10	1.40	12.26	14.96
BSC	1	22 March	29 March	8	0.70	4.92	12.84
	2	15 April	19 April	5	1.17	5.33	13.76
	3	29 April	12 June	45	2.45	71.89	16.70
	4	11 August	15 August	5	1.91	8.10	21.55
	5	22 August	2 September	12	1.59	15.49	21.06
	6	25 December	31 December	7	0.73	4.69	13.78
IBE	1	3 June	9 June	7	1.36	8.83	18.19
	2	14 July	20 July	7	1.35	8.10	19.41
	3	8 September	23 September	16	2.13	26.05	20.70
	4	10 November	14 November	5	1.26	5.86	18.33
	5	12 December	31 December	20	1.50	22.54	16.60
CAN	1	17 May	24 May	8	1.67	11.26	21.37
	2	29 October	31 December	64	1.38	71.83	21.07

Table 3. List of the record-breaking MHWs grouped by the subregions shown in Fig. 1. The first row of each group represents the strongest event in terms of maximum intensity, which is the peak point reached by the MHW relative to the climatology. The second one is the biggest event in terms of duration.

		Start date	End date	Duration (days)	Intensity max (°C)	Cumulative intensity (°C d)	Intensity max absolute (°C)
CEL	Int. max	26 June 2018	28 July 2018	33	3.86	86.51	20.30
	Dur. max	19 December 2015	13 February 2016	57	0.98	42.56	11.28
BSC	Int. max	28 June 2018	29 July 2018	32	2.76	67.52	21.34
	Dur. max	8 September 2014	15 November 2014	69	2.26	114.17	18.41
IBE	Int. max	4 September 2014	12 November 2014	70	2.66	139.27	21.11
	Dur. max	26 February 1997	12 May 97	76	2.35	119.32	17.07
CAN	Int. max	27 July 2004	10 September 2004	46	2.66	83.10	25.63
	Dur. max	15 October 2009	18 February 2010	127	1.36	130.41	21.94

ber in CAN, 12 December in IBE, and 25 December in BSC. Despite this being something out of the scope of this study it could be related to abnormal atmospheric patterns not yet described in the literature. Coinciding in time and almost in space Marullo et al. (2023) described a record-breaking event in the Mediterranean Sea which started in May 2022 and lasted until 2023 spring. In this case, it seems to be related to persistent anticyclonic conditions and mid-tropospheric seasonal anomalies which could also influence the northeastern Atlantic.

The extreme events recorded in Table 3 allow us to link long-term physical processes with MHWs and, consequently, with some of their impacts. According to the literature, the influence of the NAO can be considered one of the main drivers, at least for the cases of 2010 in CAN and 2014 in IBE and BSC, years when Pereira et al. (2020) found the most

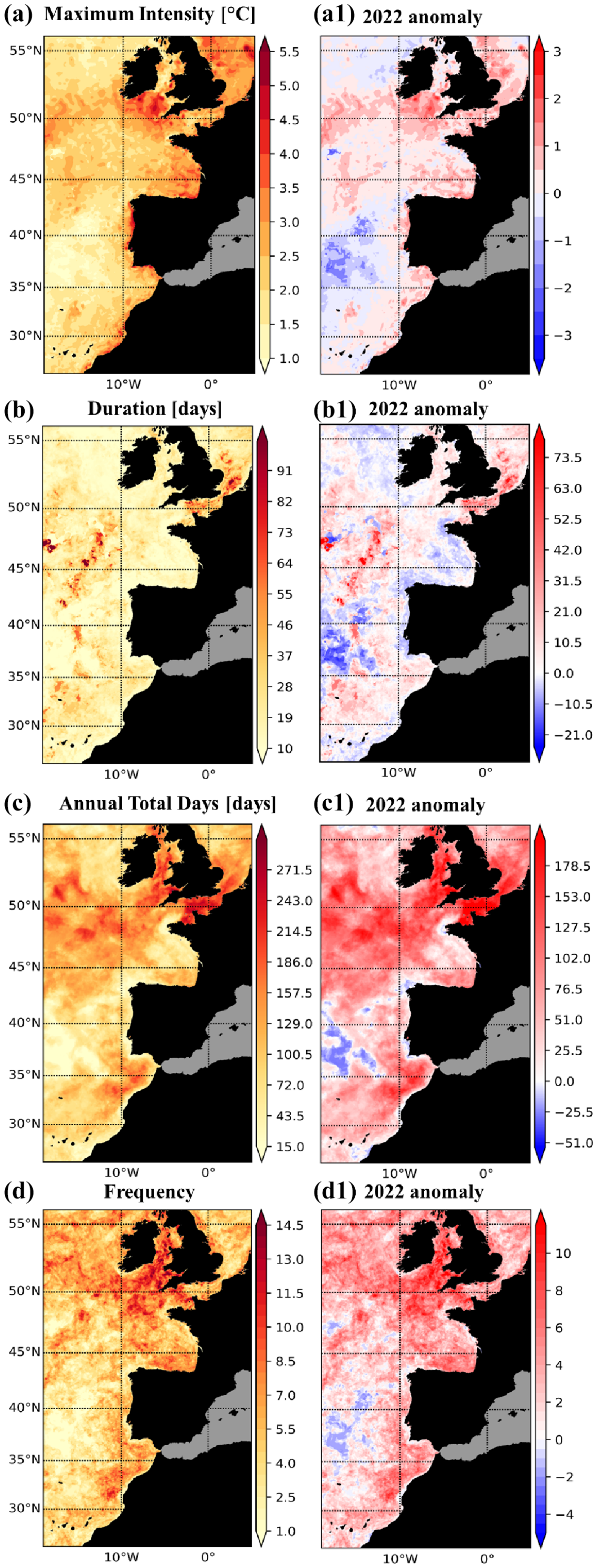

Figure 3. The 2022 mean values of **(a)** maximum intensity, **(b)** frequency, **(c)** annual total days, and **(d)** duration and its respective 2022 anomaly for each parameter **(a1–d1)**. The anomaly corresponds to the 2022 mean value minus the climatologic values of Fig. 2. The 2022 data correspond to the GLO-REP product.

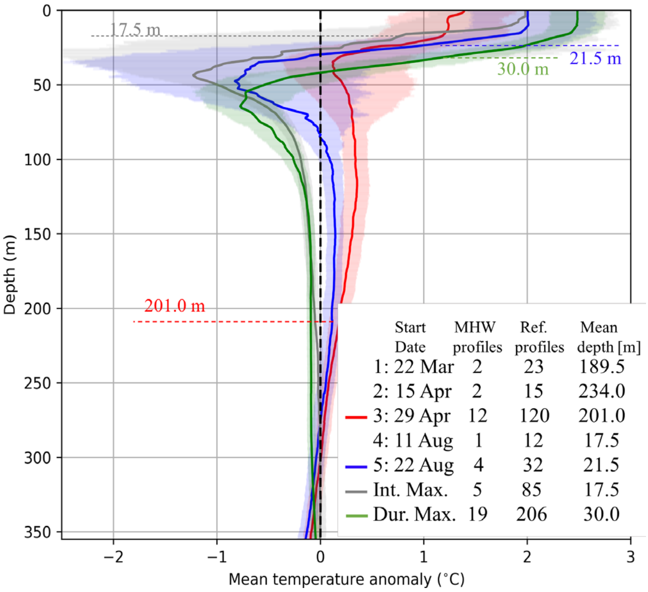

Figure 4. Mean temperature anomaly profiles down to 350 m of depth for the BSC events with more than three MHW profiles and uncertainty at 95 % confidence. The position of the MHW profiles is shown in Fig. 1, and the colors are set for each event. MHW mean depth estimation by the Elzahaby and Schaeffer (2019) method is indicated in the legend and through dotted lines. In order to facilitate the identification of each event the start date is indicated, as is the number of profiles used in the computation of the mean profile during the MHW and the long-term reference for each event. All these results are from the ARGO dataset.

negative (2010) and positive (2015) NAO index from 1870 to 2020. Also, as described by Hu et al. (2011), the event of 2010 in CAN is even more singular as it is the longest ever registered for the IBI domain, and it is considered to be influenced not only by the negative NAO but also by the ENSO. Finally, the event recorded during June 2018 is also remarkable as it reached the highest values of maximum intensity not only for CEL but also for BSC. This event can be linked to the NAO (Simon et al., 2023), and it is known to have had huge biological impacts in the area such as harmful phytoplankton blooms (Brown et al., 2022) and mass mortality events for mussels (Seuront et al., 2019).

3.2 Subsurface 2022 BSC events

The next paragraphs assess the discrete events recorded for the BSC subregion. In Fig. 4 we can observe the temperature anomaly profiles for the events detected in 2022, which featured more than three ARGO profiles during the MHW, and for the maximum intensity and maximum duration events in BSC from 1982 to 2022 (Table 3), as well as the number of available ARGO profiles during the MHW, the reference period for each event, and the mean depth estimations through the Elzahaby and Schaeffer (2019) method. The anomaly profiles during the record-breaking events (gray and green

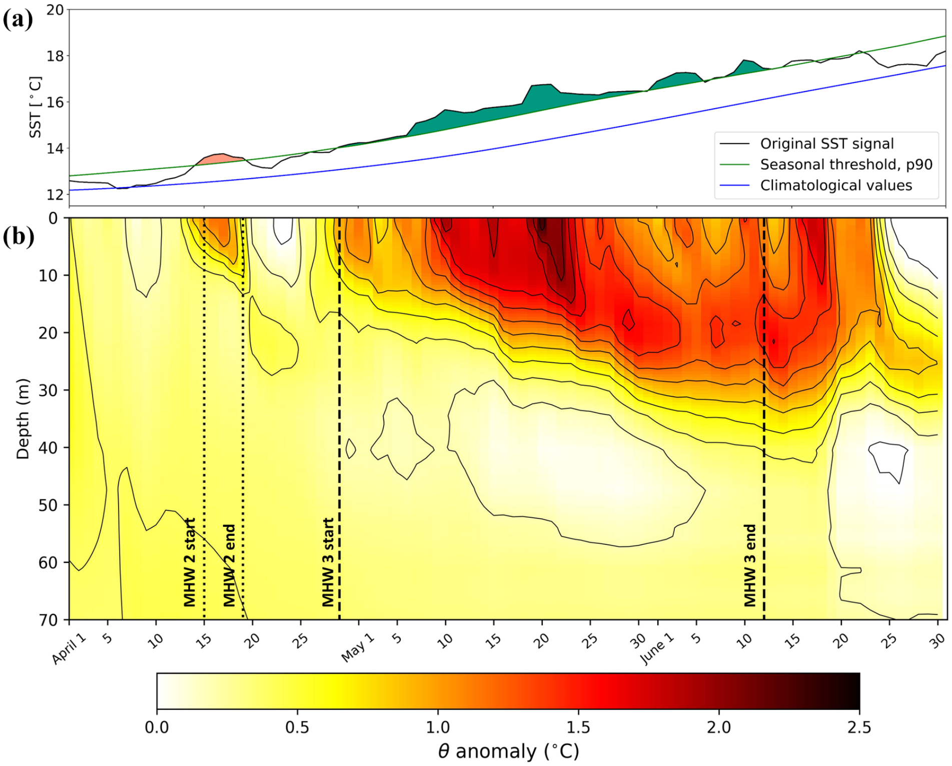

Figure 5. **(a)** Time series from 1 April to 30 June of 2022 (GLO-REP dataset) where the black line represents the original SST signal, the blue line the climatological series from 1982 to 2022, the green line the seasonal threshold obtained through the 90th percentile, and the shaded areas the detected MHWs for the BSC during this period described in Table 2. **(b)** Hovmöller diagram of the mean potential temperature (θ) anomalies from 0 to 70 m depth between 1 April and 30 June of 2022. IBI-REA is used as a long-term reference from 2005 to 2021 and calibrated 2022 IBI-NRT for the MHW days. This section corresponds to a spatial average of temperature in the BSC subregion, where the dotted lines represent the start and end date of events 2 and 3 for the BSC area recorded in Table 2. Notice that the isotherms are drawn at 0.2 °C.

profiles) show that the subsurface anomalies in BSC lie in an approximate range between −2.5 and 3 °C, where we ascribe the surface positive anomalies to the MHW processes and the negative ones, appearing at depths of 30 m and below, to the ascension of the thermocline in summer due to processes such as atmospheric blocking (Talley et al., 2011, p. 79). Other relevant results from Fig. 4 are the following: (i) the MHW mean depths calculated through the Elzahaby and Schaeffer (2019) method point to substantial differences between events during cold and warm seasons – MHWs during cold seasons are less intense but reach higher depths; (ii) the uncertainty inherent to the long-term reference and MHW profiles showed that subsurface interpretations had to be made carefully; (iii) for the maximum duration event (green profile), we detected a drastic reduction of the uncertainty, probably related to the higher number of ARGO observations available in this case; and (iv) the event of 22 August 2022 bore strong similarities in mean anomaly profile, mean depth, and also uncertainty ranges to the maximum intensity event for the region (gray profile).

From Fig. 5 we can observe the GLO-REP SST time series during MHW events 2 and 3 for the BSC (Table 2) and also a Hovmöller diagram during the same period, obtained using IBI-REA data as a long-term reference and IBI-NRT data for the 2022 days. The formation of a layer with an intense thermal gradient of approximately 0.2 to 0.7 °C is observed, expanding from 10 to 30 m in depth. If a suspected subsurface positive anomaly, which coincides in time with a detected MHW through the GLO-REP dataset in surface and that is limited downward by an intense thermal gradient, could be understood as a subsurface MHW, then MHW 2 and MHW 3 in Table 2 reach 10 and 30 m depth, respectively.

According to the positive anomalies in Fig. 5a and b, they coincide fairly well, even the peak points of the MHWs. On the other side, the MHW parameterization seems to fail at the end of the second event. The period from 12 to 21 June is not considered to be an MHW despite the fact that there are days above the threshold due to the default parameterization of the Hobday et al. (2016) method. Is this error relevant enough? We think it is, as we are assuming an error of 9 d when we consider an MHW from 5 d. Furthermore, if we want to assess and understand the regional drivers of MHWs we should probably consider a single event from 15 April to 21 June, as all this period remains in a single abnormal positive anomaly and follows an approximate common slope in the thermal gradient between the two events. In this way, future subsurface MHW characterization could help by being more precise in the parameterization and, in this way, expand our knowledge of this matter.

4 Conclusions

This study, through the usage of satellite-derived, observational, and modeling data, has assessed the mean 2022 properties of the MHWs in the IBI domain, the single events in four different subregions, and the subsurface structures of some of the events detected in the Bay of Biscay.

We showed that MHWs in the IBI domain from January 1982 to December 2022 happened on average from 1 to 2.5 times per year, with a maximum mean duration of 31 d and mean maximum intensities or deviations from the climatology of 4 °C (Fig. 2). For the year 2022, the MHW frequency ranged from 0 to 18 events, with maximum mean duration values of 145 d and mean maximum intensity values of 6 °C (Fig. 3). According to the observed SST long-term trends' effect on MHW detection by Schlegel et al. (2019) and Oliver et al. (2018), it is probably accurate to assume that these results are strongly modulated by those tendencies, meaning that we cannot be sure if extreme values are truly varying or if the MHW temperature threshold is surpassed more often due to global warming. From the catalogue of 2022 MHWs (Table 2) we singled out two of them for surpassing record-breaking events in each sub-domain. These are the 29 April event in BSC and the 7 August event in CEL, featuring 4.37 and 14.63 °C d more cumulative intensity, an approximation to the total energy of an event, than the maximum intensity event recorded on 26 June 2018 for the BSC subregion and the maximum duration event in CEL recorded on 19 December 2015, respectively (Table 2).

Subsurface MHW assessment in the BSC area through the ARGO dataset (Table 1) revealed a strong seasonal modulation. Cold-season events reached higher mean MHW depths of around 200 m, while the warm-season ones remained shallower at close to 20 m; despite the fact that it is out of the scope of this study, we understand that it may be directly related to the annual variability of the mixed layer thickness, which also could explain the observed negative thermal anomalies in summer events below 25–30 m (Fig. 4). Through model source data (Table 1) it is demonstrated how the increase in sea surface temperature, associated with the development of an MHW, is vertically moved downward in such a way that the positive anomalies persist at depth at least for weeks once the MHW has ended. In the case under investigation, the formation of a drastic thermal gradient is observed, descending from 10 to 30 m in depth within 1 month (Fig. 5).

Code availability. The tools to detect and analyze MHWs can be found at https://github.com/ecjoliver/marineHeatWaves (Oliver, 2016).

Data availability. The underlying data can be found in the product table (Table 1).

Author contributions. In this work all contributors participated in all the roles to a certain degree. But we can mention the role of ÁdPC as supervisor and project administrator, as well as conceptualization. The role of AAV was to provide data curation and formal analysis. And lastly, LCA took the role of developing software, investigation, and writing.

Competing interests. The contact author has declared that none of the authors has any competing interests.

Acknowledgements. This work has been conducted under contract number 21002L6-COP-MFC IBI-5600, part of the ongoing partnership between Nologin and Mercator Ocean International.

We would like to thank Eric Oliver (Dalhousie University, Canada) for providing the main tools to detect and analyze MHWs through https://github.com/ecjoliver open-source. We are also grateful to the Copernicus Service for making available all kinds of oceanographic data. Lastly, thanks to Miriam Selwyn (Autonomous University of Barcelona, Spain) for her wise and kind notes, which have improved the text of this contribution.

Review statement. This paper was edited by Piero Lionello and reviewed by two anonymous referees.

References

Amo-Baladrón, A., Levier, B., Aznar, R., and Sotillo, M. G.: EU Copernicus Marine Service Product User Manual for the Atlantic-Iberian Biscay Irish-Ocean Physics Reanalysis, IBI_MULTIYEAR_PHY_005_002, Issue 4.1, Mercator Ocean International, https://catalogue.marine.copernicus.eu/documents/PUM/CMEMS-IBI-PUM-005-002.pdf (last access: 2 April 2024), 2022.

Amo-Baladrón, A., Reffray, G., Levier, B., Escudier, R., Gutknecht, E., Aznar, R., and Sotillo, M. G.: EU Copernicus Marine Service Product User Manual for the Atlantic-Iberian Biscay Irish-Ocean Physics Analysis and Forecast, IBI_ANALYSISFORECAST_PHY_005_001, Issue 8.1, Mercator Ocean International, https://catalogue.marine.copernicus.eu/documents/PUM/CMEMS-IBI-PUM-005-001.pdf (last access: 2 April 2024), 2023.

Argo: Argo float data and metadata from Global Data Assembly Centre (Argo GDAC), SEANOE [data set], https://doi.org/10.17882/42182, 2019.

Brown, A. R., Lilley, M. K. S., Shutler, J., Widdicombe, C., Rooks, P., McEvoy, A., Torres, R., Artioli, Y., Rawle, G., Homyard, J., Tyler, C. R., and Lowe, C.: Harmful Algal Blooms and their impacts on shellfish mariculture follow regionally distinct patterns of water circulation in the western English Channel during the 2018 heatwave, Harmful Algae, 111, 102166, https://doi.org/10.1016/j.hal.2021.102166, 2022.

Chatterjee, S. and Simonoff, J. S.: Handbook of regression analysis with applications in R, 2nd edn., Wiley Series in Probability and Statistics, John Wiley & Sons, Hoboken (NJ), USA, ISBN 9781119392491, https://doi.org/10.1002/9781119392491, 2020.

Collins, M., Sutherland, M., Bouwer, L., Cheong, S.-M., Frölicher, T., Jacot Des Combes, H., Koll Roxy, M., Losada, I., McInnes, K., Ratter, B., Rivera-Arriaga, E., Susanto, R. D., Swingedouw, D., and Tibig, L.: Extremes, abrupt changes and managing risk, in: IPCC Special Report on the Ocean and Cryosphere in a Changing Climate, edited by: Pörtner, H.-O., Roberts, D.C., Masson-Delmotte, V., Zhai, P., Tignor, M., Poloczanska, E., Mintenbeck, K., Alegrìia, A., Nicolai, M., Okem, A., Petzold, J., Rama, B., and Weyer, N. M., Cambridge University Press, Cambridge, UK and New York, NY, USA, 589–655, https://doi.org/10.1017/9781009157964.008, 2019.

Cornes, R. C., Tinker, J., Hermanson, L., Oltmanns, M., Hunter, W. R., Lloyd-Hartley, H., Kent, E. C., Rabe, B., and Renshaw, R.: The impacts of climate change on sea temperature around the UK and Ireland, MCCIP Science Review 2023, 18 pp., https://doi.org/10.14465/2023.reu08.tem, 2023.

Elliott, M. and Whitfield, A. K.: Challenging paradigms in estuarine ecology and management, Estuar. Coast. Shelf S., 94, 306–314, https://doi.org/10.1016/j.ecss.2011.06.016, 2011.

Elzahaby, Y. and Schaeffer, A.: Observational insight into the subsurface anomalies of marine heatwaves, Front. Mar. Sci., 6, 745, https://doi.org/10.3389/fmars.2019.00745, 2019.

EU Copernicus Marine Service Product: ESA SST CCI and C3S Reprocessed Sea Surface Temperature Analyses, Mercator Ocean international [data set], https://doi.org/10.48670/moi-00169, 2021.

EU Copernicus Marine Service Product: Atlantic-Iberian Biscay Irish- Ocean Physics Reanalysis, Mercator Ocean International [data set], https://doi.org/10.48670/moi-00028, 2022.

EU Copernicus Marine Service Product: Atlantic Iberian Biscay Irish Ocean- In-Situ Near Real Time Observations, Mercator Ocean International [data set], https://doi.org/10.48670/moi-00043, 2023a.

EU Copernicus Marine Service Product: Atlantic-Iberian Biscay Irish- Ocean Physics Analysis and Forecast, Mercator Ocean International [data set], https://doi.org/10.48670/moi-00027, 2023b.

Fofonoff, N. P. and Millard Jr., R. C.: Algorithms for the computation of fundamental properties of seawater, UNESCO Technical Papers in Marine Sciences, 44, UNESCO, Paris, France, 53 pp., https://doi.org/10.25607/OBP-1450, 1993.

Fox-Kemper, B., Hewitt, H. T., Xiao, C., Aðalgeirsdóttir, G., Drijfhout, S. S., Edwards, T. L., Golledge, N. R., Hemer, M., Kopp, R. E., Krinner, G., Mix, A., Notz, D., Nowicki, S., Nurhati, I. S., Ruiz, L., Sallée, J.-B., Slangen, A. B. A., and Yu, Y.: Ocean, cryosphere and sea level change, in: Climate Change 2021: The Physical Science Basis. Contribution of Working Group I to the Sixth Assessment Report of the Intergovernmental Panel on Climate Change, edited by: Masson-Delmotte, V., Zhai, P., Pirani, A., Connors, S. L., Péan, C., Berger, S., Caud, N., Chen, Y., Goldfarb, L., Gomis, M. I., Huang, M., Leitzell, K., Lonnoy, E., Matthews, J. B. R., Maycock, T. K., Waterfield, T., Yelekçi, O., Yu, R., and Zhou, B., Cambridge University Press, Cambridge, United Kingdom and New York, NY, USA, 1211–1362, https://doi.org/10.1017/9781009157896.011, 2021.

Good, S.: EU Copernicus Marine Service Quality Information Document for the ESA SST CCI and C3S global Sea Surface Temperature Reprocessed product, SST-GLO-SST-L4-REP-OBSERVATIONS-010-024, Issue 2.3, Mercator Ocean International, https://catalogue.marine.copernicus.eu/documents/QUID/CMEMS-SST-QUID-010-024.pdf (last access: 6 June 2023), 2021.

Good, S.: EU Copernicus Marine Service Product User Manual for the ESA SST CCI and C3S global Sea Surface Temperature Reprocessed product, SST-GLO-SST-L4-REP-OBSERVATIONS-010-024, Issue 3.0, Mercator Ocean International, https://catalogue.marine.copernicus.eu/documents/PUM/CMEMS-SST-PUM-010-024.pdf (last access: 6 June 2023), 2022.

Good, S., Fiedler, E., Mao, C., Martin, M. J., Maycock, A., Reid, R., Roberts-Jones, J., Searle, T., Waters, J., While, J., and Worsfold, M.: The current configuration of the OSTIA system for operational production of foundation sea surface temperature and ice concentration analyses, Remote Sens., 12, 4, https://doi.org/10.3390/rs12040720, 2020.

Hobday, A. J., Alexander, L. V., Perkins, S. E., Smale, D. A., Straub, S. C., Oliver, E. C. J., Benthuysen, J. A., Burrows, M. T., Donat, M. G., Feng, M., Holbrook, N. J., Moore, P. J., Scannell, H. A., Sen Gupta, A., and Wernberg, T.: A hierarchical approach to defining marine heatwaves, Prog. Oceanogr., 141, 227–238, https://doi.org/10.1016/j.pocean.2015.12.014, 2016.

Hobday, A. J., Oliver, E. C. J., Sen Gupta, A., Benthuysen, J. A., Burrows, M. T., Donat, M. G., Holbrook, N. J., Moore, P. J., Thomsen, M. S., Wernberg, T., and Smale, D. A.: Categorizing and naming marine heatwaves, Oceanography, 31, 162–173, https://doi.org/10.5670/oceanog.2018.205, 2018.

Holbrook, N. J., Scannell, H. A., Sen Gupta, A., Benthuysen, J. A., Feng, M., Oliver, E. C. J., Alexander, L. V., Burrows, M., Donat, M. G., Hobday, A. J., Moore, P. J., Perkins-Kirkpatrick, S. E., Smale, D. A., Straub, S. C., and Wernberg, T.: A global assessment of marine heatwaves and their drivers, Nat. Commun., 10, 2624, https://doi.org/10.1038/s41467-019-10206-z, 2019.

Holbrook, N. J., Sen Gupta, A., Oliver, E. C. J., Hobday, A. J., Benthuysen, J. A., Scannell, H. A., Smale, D. A., and Wernberg, T.: Keeping pace with marine heatwaves, Nat. Rev. Earth Environ., 1, 482–493, https://doi.org/10.1038/s43017-020-0068-4, 2020.

Hu, Z.-Z., Kumar, A., Huang, B., Xue, Y., Wang, W., and Jha, B.: Persistent atmospheric and oceanic anomalies in the North Atlantic from Summer 2009 to Summer 2010, J. Climate, 24, 5812–5830, https://doi.org/10.1175/2011JCLI4213.1, 2011.

In Situ TAC partners: EU Copernicus Marine Service Product User Manual for the Atlantic Iberian Biscay Irish Ocean- In-Situ Near Real Time Observations, INSITU_IBI_PHYBGCWAV_DISCRETE_MYNRT_013_033, Issue 2.0, Mercator Ocean International, https://catalogue.marine.copernicus.eu/documents/PUM/CMEMS-INS-PUM-013-030-036.pdf (last access: 2 April 2024), 2023.

Izquierdo, P., Taboada, F. G., González-Gil, R., Arrontes, J., and Rico, J. M.: Alongshore upwelling modulates the Intensity of marine heatwaves in a temperate coastal sea, Sci. Total Environ., 835, 155478, https://doi.org/10.1016/j.scitotenv.2022.155478, 2022.

Lee, H., Calvin, K., Dasgupta, D., Krinner, G., Mukherji, A., Thorne, P., Trisos, C., Romero, J., Aldunce, P., Barrett, K., Blanco, G., Cheung, W. W. L., Connors, S. L., Denton, F., Diongue-Niang, A., Dodman, D., Garschagen, M., Geden, O., Hayward, B., Jones, C., Jotzo, F., Krug, T., Lasco, R., Lee, J.-Y., Masson-Delmotte, V., Meinshausen, M., Mintenbeck, K., Mokssit, A., Otto, F. E. L., Pathak, M., Pirani, A., Poloczanska, E., Pörtner, H.-O., Revi, A., Roberts, D. C., Roy, J., Ruane, A. C., Skea, J., Shukla, P. R., Slade, R., Slangen, A., Sokona, Y., Sörensson, A. A., Tignor, M., Van Vuuren, D. P., Wei, Y.-M., Winkler, H., Zhai, P., and Zommers, Z.: Synthesis Report of the IPCC Sixth Assessment Report (AR6): Longer Report, IPCC, Intergovernmental Panel on Climate Change, https://doi.org/10.59327/IPCC/AR6-9789291691647, 2023.

Levier, B., Reffray, G., and Sotillo, M. G.: EU Copernicus Marine Service Quality Information Document for the Atlantic-Iberian Biscay Irish- Ocean Physics Reanalysis, IBI_MULTIYEAR_PHY_005_002, Issue 5.1, Mercator Ocean International, https://catalogue.marine.copernicus.eu/documents/QUID/CMEMS-IBI-QUID-005-002.pdf (last access: 7 May 2024), 2022.

Levier, B., Reffray, G., Escudier, R., Gutknecht, E., Amo-Baladrón, A., Ciliberti, S., Aznar, R., and Sotillo, M. G.: EU Copernicus Marine Service Quality Information Document for the Atlantic-Iberian Biscay Irish- Ocean Physics Analysis and Forecast product, IBI_ANALYSISFORECAST_PHY_005_001, Issue 6.1, Mercator Ocean International, https://catalogue.marine.copernicus.eu/documents/QUID/CMEMS-IBI-QUID-005-001.pdf (last access: 7 May 2024), 2023.

Marullo, S., Serva, F., Iacono, R., Napolitano, E., di Sarra, A., Meloni, D., Monteleone, F., Sferlazzo, D., Silvestri, L. D., de Toma, V., Pisano, A., Bellacicco, M., Landolfi, A., Organelli, E., Yang, C., and Santoleri, R.: Record-breaking Persistence of the 2022/23 marine heatwave in the Mediterranean Sea, Environ. Res. Lett., 18, 114041, https://doi.org/10.1088/1748-9326/ad02ae, 2023.

Merchant, C. J., Embury, O., Bulgin, C. E., Block, T., Corlett, G. K., Fiedler, E., Good, S. A., Mittaz, J., Rayner, N. A., Berry, D., Eastwood, S., Taylor, M., Tsushima, Y., Waterfall, A., Wilson, R., and Donlon, C.: Satellite-based time-series of sea-surface temperature since 1981 for climate applications, Scientific Data, 6, 223, https://doi.org/10.1038/s41597-019-0236-x, 2019.

Oliver, E.: marineHeatWaves, GitHub [code], https://github.com/ecjoliver/marineHeatWaves (last access: 5 April 2024), 2016.

Oliver, E. C. J., Donat, M. G., Burrows, M. T., Moore, P. J., Smale, D. A., Alexander, L. V., Benthuysen, J. A., Feng, M., Sen Gupta, A., Hobday, A. J., Holbrook, N. J., Perkins-Kirkpatrick, S. E., Scannell, H. A., Straub, S. C., and Wernberg, T.: Longer and more frequent marine heatwaves over the past century, Nat. Commun., 9, 1324, https://doi.org/10.1038/s41467-018-03732-9, 2018.

Pereira, J., Paiva, V., Ceia, F., and Ramos, J.: Facing extremes: Cory's shearwaters adjust their foraging behaviour differently in response to contrasting phases of North Atlantic Oscillation, Reg. Environ. Change, 22, 77, https://doi.org/10.1007/s10113-020-01662-1, 2020.

Schlegel, R. W., Oliver, E. C. J., Hobday, A. J., and Smit, A. J.: Detecting marine heatwaves with sub-optimal data, Front. Mar. Sci., 6, 737, https://doi.org/10.3389/fmars.2019.00737, 2019.

Schlitzer, R.: Ocean Data View, https://odv.awi.de (last access: 30 July 2023), 2021.

Sen Gupta, A., Thomsen, M., Benthuysen, J. A., Hobday, A. J., Oliver, E., Alexander, L. V., Burrows, M. T., Donat, M. G., Feng, M., Holbrook, N. J., Perkins-Kirkpatrick, S., Moore, P. J., Rodrigues, R. R., Scannell, H. A., Taschetto, A. S., Ummenhofer, C. C., Wernberg, T., and Smale, D. A.: Drivers and impacts of the most extreme marine heatwave events, Sci. Rep., 10, 19359, https://doi.org/10.1038/s41598-020-75445-3, 2020.

Seuront, L., Nicastro, K. R., Zardi, G. I., and Goberville, E.: Decreased thermal tolerance under recurrent heat stress conditions explains summer mass mortality of the blue mussel Mytilus edulis, Sci. Rep., 9, 17498, https://doi.org/10.1038/s41598-019-53580-w, 2019.

Simon, A., Poppeschi, C., Plecha, S., Charria, G., and Russo, A.: Coastal and regional marine heatwaves and cold spells in the northeastern Atlantic, Ocean Sci., 19, 1339–1355, https://doi.org/10.5194/os-19-1339-2023, 2023.

Smale, D. A., Wernberg, T., Oliver, E. C., Thomsen, M., Harvey, B. P., Straub, S. C., Burrows, M. T., Alexander, L. V., Benthuysen, J. A., and Donat, M. G.:. Marine heatwaves threaten global biodiversity and the provision of ecosystem services, Nat. Clim. Change, 9, 306–312, https://doi.org/10.1038/s41558-019-0412-1, 2019.

Sotillo, M. G., Cailleau, S., Lorente, P., Levier, B., Aznar, R., Reffray, G., Amo-Baladrón, A., Chanut, J., Benkiran, M., and Alvarez Fanjul, E.: The MyOcean IBI Ocean Forecast and Reanalisys Systems: Operational products and roadmap to the future Copernicus Service, J. Oper. Oceanogr., 8, 63–79, https://doi.org/10.1080/1755876X.2015.1014663, 2015.

Talley, L. D., Pickard, G. L., Emery, W. J., and Swift, J. H.: Descriptive Physical Oceanography: An Introduction, 6th edn., Academic Press, Amsterdam, ISBN 978-0-08093-911-7, 2011.

Varela, R., Rodríguez-Díaz, L., De Castro, M., and Gómez-Gesteira, M.: Influence of eastern upwelling systems on marine heatwaves occurrence, Global Planet. Change, 196, 103379, https://doi.org/10.1016/j.gloplacha.2020.103379, 2021.

Wehde, H., Schuckmann, K. V., Pouliquen, S., Grouazel, A., Bartolome, T., Tintore, J., De Alfonso Alonso-Munoyerro, M., Carval, T., Racapé, V., and the INSTAC team: EU Copernicus Marine Service Quality Information Document for the Atlantic Iberian Biscay Irish Ocean- In-Situ Near Real Time Observations Product, INSITU_IBI_PHYBGCWAV_DISCRETE_MYNRT_013_033, Issue 2.3, Mercator Ocean International, https://catalogue.marine.copernicus.eu/documents/QUID/CMEMS-INS-QUID-013-030-036.pdf (last access: 7 May 2024), 2023.

Yao, Y., Wang, C., and Fu, Y.: Global marine heatwaves and cold-spells in present climate to future projections, Earths Future, 10, e2022EF002787, https://doi.org/10.1029/2022EF002787, 2022.

State Planet, 4-osr8, 18, 2024
https://doi.org/10.5194/sp-4-osr8-18-2024

Subsurface warming derived from Argo floats during the 2022 Mediterranean marine heat wave

Annunziata Pirro[1], **Riccardo Martellucci**[1], **Antonella Gallo**[1], **Elisabeth Kubin**[1], **Elena Mauri**[1], **Mélanie Juza**[2], **Giulio Notarstefano**[1], **Massimo Pacciaroni**[1], **Antonio Bussani**[1], **and Milena Menna**[1]

[1]National Institute of Oceanography and Applied Geophysics (OGS), Trieste, 34010, Italy
[2]Balearic Islands Coastal Observing and Forecasting System (SOCIB), Palma, 07122, Spain

Correspondence: Annunziata Pirro (apirro@ogs.it)

Received: 26 July 2023 – Discussion started: 19 September 2023
Revised: 1 August 2024 – Accepted: 9 September 2024 – Published: 30 September 2024

Abstract. The Mediterranean marine heat wave (MHW) during the warm season (May–September) and the fall period (October–December) of 2022 is analyzed using Argo float in situ observations in the upper 2000 m of depth. The five study regions (North Western Mediterranean, South Western Mediterranean, central Ionian Sea, Pelops Gyre, and South Adriatic Pit) most affected by warming in different layers were selected and investigated. The primary goal is to provide insights into how the water column responds to the onset and progression of the MHW during the warming period, characterized by peak stratification and reduced vertical mixing. Additionally, this study aims to examine how the heat accumulated in the upper layers is redistributed to deep layers within regions with different dynamic characteristics through advection and/or mixing during the subsequent fall period.

Temperature anomaly profiles, T_a (z), computed for each area and for both periods were divided into three categories based on vertical heat penetration: Category 1 (shallow, 0–150 m), Category 2 (intermediate, 150–700 m), and Category 3 (deep, $>$ 700 m). During the warm season, Category 1 profiles had a temperature anomaly near zero or slightly negative in a thin layer between 50 and 150 m depth, while warming was observed in the 0–50 m layer and below the middle layer. Profiles characterized by greater vertical heat penetration (categories 2 and 3) were mainly in mesoscale or subbasin structures and showed the largest positive temperature anomaly in the surface and intermediate layers. All profile categories showed a warming between 200 and 800 m depth. This increase is roughly split, with half attributed to the impact of the 2022 MHW and the other half linked to the ongoing long-term trend in ocean temperatures. During the fall period and in the layer below 200 m depth, the shapes of the T_a profiles are similar for all sectors with the exception of the South Adriatic Pit, which depicts a $+0.5$ °C warming at 800 m depth.

The present work highlights the warming characteristics throughout the entire water column across different regions of the Mediterranean Sea, and it seeks to connect the impacts of the warm season on the cold period with oceanic dynamic processes, such as dense water formation, upwelling, or water column stratification. These regions are characterized by dynamic activities (e.g., dense water formation, upwelling); therefore, any variation in these ocean processes can influence the thermohaline circulation and, consequently, the climate system.

Published by Copernicus Publications.

Table 1. Product data used to perform the analysis of the present work.

Product ref. no.	Product ID and type	Data access	Documentation
1	INSITU_MED_PHYBGCWAV_DISCRETE_ MYNRT_013_035; in situ observations*	EU Copernicus Marine Service Product (2022a)	Quality Information Document (QUID): Wehde et al. (2022); Product User Manual (PUM): In Situ TAC partners (2022)
2	MEDSEA_MULTIYEAR_PHY_006_004; numerical models*	EU Copernicus Marine Service Product (2022b)	Quality Information Document (QUID): Escudier al. (2022); Product User Manual (PUM): Lecci et al. (2022)
3	SEALEVEL_EUR_PHY_L4_NRT_008_060; satellite observations*	EU Copernicus Marine Service Product (2023)	Quality Information Document (QUID): Pujol al. (2023); Product User Manual (PUM): Pujol (2022)
4	SEADATANET_MedSea_climatology_V2; climatology	SeaDataNet Product; Simoncelli et al. (2020b)	Product Information Document (PIDoc): Simoncelli et al. (2020a)

* Dataset updated during publication (see the Disclaimer section).

1 Introduction

Marine heat waves (MHWs) are extreme ocean temperature events occurring over extended periods of time (Hobday et al., 2016). Over the past decade, the frequency of MHW events has increased by 50 % (IPCC, 2023), as well as their duration and magnitude (Oliver et al., 2018). They can affect small areas of coastline or span multiple ocean areas across latitudes with significant impacts on ecosystems, coastal communities, and economies (Wernberg et al., 2013; Garrabou et al., 2022; Dayan et al., 2023).

Since the beginning of the 21st century, the particularly rapid warming trend of the Mediterranean Sea surface layer has been associated with a strong increase in MHW events (Bensoussan et al., 2019; Ibrahim et al., 2021; Juza et al., 2022; Pastor and Khodayar, 2023; Dayan et al., 2023). Several studies, with measurements mainly confined at the surface, have addressed this topic covering different aspects of MHWs using satellite observations and model simulations. In particular, from basin to subregional scale, previous studies have analyzed MHW drivers and indicators; estimated the frequency, duration, and intensity of MHWs; evaluated their trends; and assessed the risks for and impacts on ecosystems (Darmaraki et al., 2019; Galli et al., 2017; Garrabou et al., 2022; Juza et al., 2022; Dayan et al., 2023; Martínez et al., 2023; Marullo et al., 2023; Pastor and Khodayar, 2023; Simon et al., 2023). However, MHWs are not exclusively limited to the surface layer, but they can also propagate throughout the deeper layers of the water column (Darmaraki et al., 2019; Hu et al., 2021; Scannell et al., 2020; Juza et al., 2022). This can cause negative ecological consequences, compromising the maintenance of biodiversity, the provision of food, and the regulation of air quality (Garrabou et al., 2022; Holbrook et al., 2020; Santora et al., 2020; Smale et al., 2019; Schaeffer and Roughan, 2017; Liquete et al., 2016; Martín-López et al., 2016; Mills et al., 2013). A recent study in the Mediterranean Sea shows that although MHW frequency is higher at the surface, the maximum intensity and duration of MHWs are registered in the subsurface layers (Dayan et al., 2023). Moreover, in situ data collected in the tropical western Pacific Ocean show that the maximum intensity of almost every MHW event is found in the subsurface layer, and many of the MHWs occurred even when no significant warming anomalies were detected at the surface (Hu et al., 2021). Using satellite data, Marullo et al. (2023) defined the occurrence of an event in the Mediterranean Sea from May 2022 to spring 2023, with higher intensity in summer 2022 and in the band from 0 to 25° E. Starting from this result, the present work analyzes the subsurface properties of the 2022 MHW in the upper 2000 m depth using in situ hydrographic Argo profiles (product ref. no. 1, Table 1; Wong et al., 2020), collected during the period of highest intensity (warm season, May–September) and in the period thereafter (cold season, October–December). Focusing on the results by Marullo et al. (2023) and on the availability of Argo float profiles, five study areas were selected for our analysis (Fig. 1b).

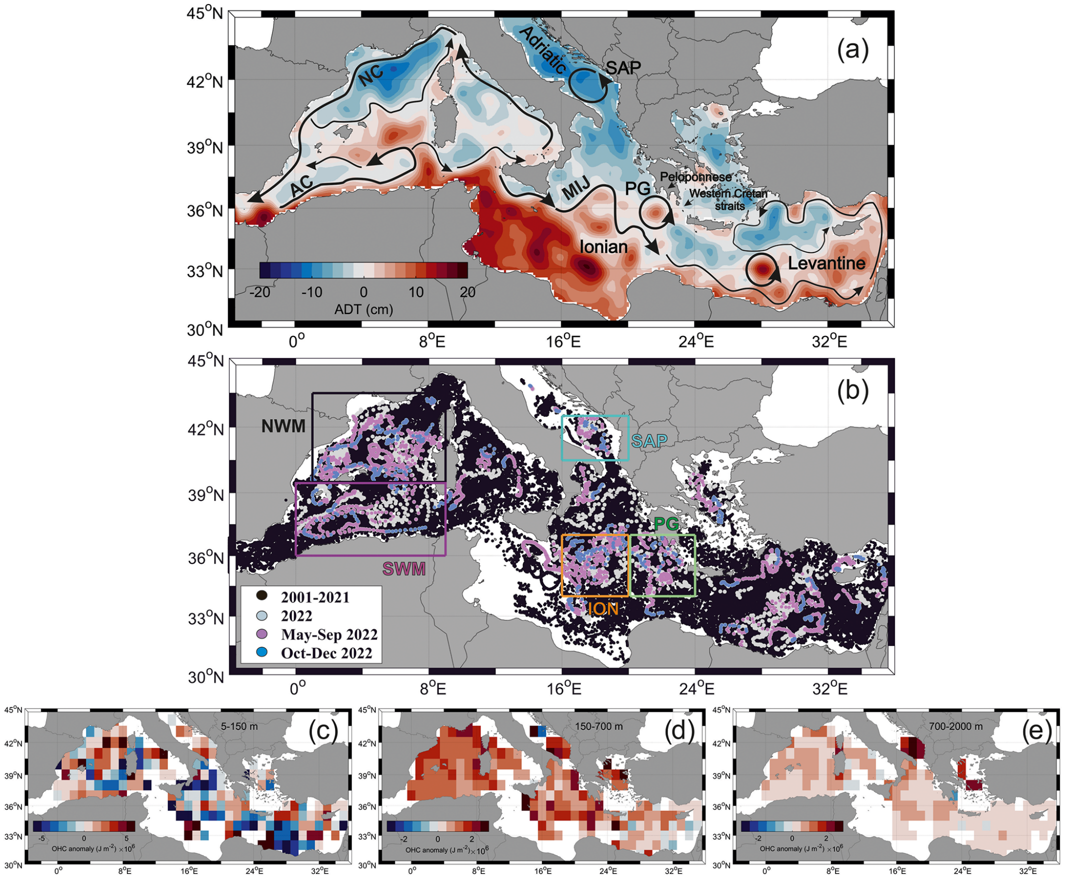

Figure 1. **(a)** Absolute dynamic topography (colors) averaged for the warm season (May–September 2022) along with schematic pathways (black arrows) of the Algerian Current (AC), Northern Current (NC), Mid-Ionian Jet (MIJ), South Adriatic Pit (SAP), and Pelops Gyre (PG); **(b)** Argo float positions for the whole Mediterranean Sea. Black, magenta, cyan, orange, and green boxes indicate the North West Mediterranean (NWM: 39.5–43.5° N and 1–9° E), South West Mediterranean (SWM: 36–39.5° N and 0–9° E), South Adriatic Pit (SAP: 40.5–42.5° N and 16–20° E), Ionian (ION: 34–37° N and 16–20° E), and Pelops Gyre (PG: 34–37° N and 20–24° E) areas, respectively. **(c–e)** The 2022 ocean heat content (OHC) anomaly estimated every meter with respect to the 2001–2018 FLOAT climatology period from Argo float profiles in different layers: **(c)** 5–150, **(d)** 150–700, and **(e)** 700–2000 m.

Based on the vertical heat penetration (MHW depth; see the Methods section), the temperature profiles collected in May–September 2022 from each study area were divided into three categories (shallow, intermediate, and deep penetration), and the median profile of temperature anomaly ($\tilde{T}_a$) was computed for each of them. Changes in the vertical temperature anomalies were described and analyzed in relation to the ocean stratification, circulation, and dynamics of each specific area. Lastly, this study examines the properties of the water column during the fall period and speculates on its relationship with the dynamics of the previous warm season's MHW. An estimation of the horizontal and vertical distributions of the ocean heat content (OHC) anomaly in 2022 was also made in the whole Mediterranean Sea (Fig. 1c–e).

2 Methods

The vertical propagation of the 2022 MHW in the Mediterranean Sea was investigated using temperature data collected by Argo floats in the period 2001–2022 (Fig. 1b). These data were collected and made freely available by the international Argo program (which is part of the Global Ocean Observing System; Argo, 2023) and by the national program Argo-Italy that contributes to it (https://argo.ucsd.edu, last access: 23 April 2023; https://www.ocean-ops.org, last access: 23 April 2023).

A comprehensive characterization of the event over the whole Mediterranean Sea was performed starting from the OHC analysis. The OHC, defined as the total amount of heat absorbed and stored by the ocean, can be considered a good indicator for assessing the Earth's energy imbalance (Von Schuckmann et al., 2016). A float-derived OHC climatology ($\mathrm{OHC}_{2001–2018}$) for the period 2001–2018 was estimated in 1° × 1° bins and in different layers (0–150, 150–700, 700–2000 m) using the method by Kubin et al. (2023). Subsequently, Argo temperature data collected in 2022 were averaged on the same grid as $\mathrm{OHC}_{2001\text{–}2018}$ to compute the 2022 OHC (OHC_{2022}). The OHCA_{2022} (ocean heat content anomaly) was then calculated as the difference between the OHC_{2022} and $\mathrm{OHC}_{2001\text{–}2018}$ fields.

The five Mediterranean Sea regions most affected by surface warming (Fig. 1b) were selected using the results of Marullo et al. (2023) and considering the availability of float data. In these regions, we analyzed the vertical penetration of the 2022 MHW signal in the water column during both the warm and cold seasons. The regions selected are the following: the North Western Mediterranean (NWM), the South Western Mediterranean (SWM), the Ionian (ION), the Southern Adriatic Pit (SAP), and the Pelops Gyre (PG) sectors.

The temperature anomaly T_a at each depth z and for each profile and sector was computed as

$$T_\mathrm{a}(z) = T(z) - \overline{T}(z), \tag{1}$$

where $T(z)$ is the 2022 temperature derived from Argo floats, while $\overline{T}(z)$ is the climatological (1985–2018) averaged temperature derived from the SeaDataCloud (SDC) dataset (product ref. no. 4, Table 1; denoted SDC climatology). Specifically, the gridded (0.125° × 0.125°) monthly climatological profiles were linearly interpolated in depth (every 10 m) and at the position of each float profile. Moreover, to compare the 2022 MHW event with the averaged conditions estimated by floats in the selected sectors, T_a profiles were also computed for the whole float dataset in the period 2001–2018 (denoted FLOAT climatology). It is important to highlight that while this study utilizes the SDC climatology, the FLOAT climatology was utilized to facilitate a straightforward comparison with the OHC findings from Kubin et al. (2023). The time window used for the present work (May–September 2022) was chosen based on the latest European Space Agency specification (https://www.esa.int/Applications/Observing_the_Earth/Mediterranean_Sea_hit_by_marine_heatwave, last access: 18 February 2023) and on the estimations by Marullo et al. (2023). These estimations indicate that the 2022 MHW developed in the second half of April in the northwest Mediterranean Sea and extended over the central Mediterranean into September. In this period, T_a profiles were quality-controlled to remove any inconsistency (e.g., profiles with negative surface anomalies) and used to estimate the vertical propagation of the MHW (or MHW depth), following the method by Elzahaby and Schaeffer (2019). For each profile, the positive threshold depth (hereafter Z_N) is defined as the depth at which the first negative or zero temperature anomaly occurred:

$$Z_N = \min\left(z\left(T_\mathrm{a}(z) \le 0\right)\right). \tag{2}$$

Knowing Z_N, the vertical cumulative temperature anomaly ($\mathrm{CT_a}$), defined as

$$\mathrm{CT_a}(Z_N) = \sum_{z=0}^{Z_N} T_\mathrm{a}(z)\,\Delta z, \tag{3}$$

with $\Delta z = 10$ m, was computed for each profile from the surface ($z = 0$) to the positive threshold depth ($z = Z_N$). To reduce the effect of the insignificant warming at depths per water profile, we define the MHW depth as the depth where a fraction ($\varepsilon = 0.95$) of the cumulative T_a is reached:

$$\text{MHW depth} = \max\left(z\left(\mathrm{CT_a}(z) \le \varepsilon \cdot \mathrm{CT_a}(Z_N)\right)\right). \tag{4}$$

Based on MHW depth values, T_a profiles were then divided into three categories: Category 1 (shallow, 0–150 m), Category 2 (intermediate, 150–700 m), and Category 3 (deep, > 700 m). It is noteworthy that, within the SAP area, float profiles categorized as Categories 2 and 3 consistently exhibit no negative temperature anomalies. However, they are classified into these categories based on their respective depths, shallower or deeper than 700 m. Additionally, despite the limited number of profiles available in this region, they all fall within the cyclonic gyre. Hence, we are confident in considering them as representative of the entire SAP region. The median profile ($\tilde{T}_\mathrm{a}$) for each category was obtained by spatially averaging all the available data in the different sectors in the warm period using 2022 and FLOAT climatology Argo data. Considering that the 2022 MHW extends until the spring of 2023 (Marullo et al., 2023), the median profiles $\tilde{T}_\mathrm{a}$ for the fall period were also examined to investigate the accumulation of the heat in the water column. The mean T_a values averaged in the surface, intermediate, and deep layers as well as other additional information (number of profiles, MHW depth, max T_a, and depth of max) are listed in Table 2.

Lastly, the Brunt–Väisälä frequency squared (N^2) for the year 2022 and in the upper 150 m depth was computed using monthly averaged temperature and salinity Argo float profiles for each sector in order to support the vertical heat penetration. The same procedure was adopted to calculate the N^2 anomaly with respect to the FLOAT climatology.

3 Results and discussion

In the surface layer, the OHCA_{2022} displayed inhomogeneous warming patterns, with positive anomaly areas adjacent to others with strong negative anomalies (Fig. 1c). Largest positive anomalies were observed in the western Mediterranean, southern Adriatic, eastern Ionian, and northern Levantine basins. In the intermediate and deep layers, the warming was more homogeneous and widespread (Fig. 1d, e), where the majority of bins showed positive values of OHCA_{2022}; specifically, the western and central Mediterranean areas along with the Aegean Sea showed a more pronounced warming compared to the Levantine basin, which

Table 2. Characteristics of the 2022 MHW in Category 1 (C1), Category 2 (C2), and Category 3 (C3): MHW depth, surface temperature anomaly (“Surface”), maximum temperature anomaly (“Max”), and the depth where it occurs (“Depth of max”). Also shown are mean temperature anomaly values for the surface (0–150 m), intermediate (150–700 m), and deep (700–2000 m) layers for each category and for the FLOAT climatology (“clim.”).

			No. of observations	MHW depth (m)	Temperature anomaly			Averaged values		
					Surface (10 m)	Max	Depth of max (m)	0–150 m	150–700 m	700–2000 m
NWM	spring summer	C1	335	24.8	2.3	5.82	22.5	0.28	0.32	0.097
		C2	16	571.9	2.2	5.48	50	0.32	0.4	NA
		C3	43	1457.9	2.92	5.58	19.5	0.8	0.36	0.1
		clim.	–	–	–	–	–	0.12	0.06	0.025
	fall	fall	306	–	–	–	–	0.66	0.33	0.11
		clim. fall	–	–	–	–	–	0.08	0.07	0.04
SWM	spring summer	C1	159	25.6	2.13	5.79	22.5	0.19	0.33	0.088
		C2	5	630	1.83	5.46	24	0.43	0.3	NA
		C3	27	1409.6	2.24	5.05	24.1	0.86	0.36	0.095
		clim.	–	–	–	–	–	0.028	0.059	0.028
	fall	fall	148	–	–	–	–	0.18	0.31	0.11
		clim. fall	–	–	–	–	–	0.1	0.05	0.02
ION	spring summer	C1	105	22.8	1.34	4.58	22.2	0.03	0.27	0.12
		C2	5	644	2.18	2.87	18	0.58	0.35	0.54
		C3	3	1383.4	1.39	1.97	20	0.47	0.54	0.15
		clim.	–	–	–	–	–	0.071	0.091	0.057
	fall	fall	119	–	–	–	–	−0.21	0.26	0.12
		clim. fall	–	–	–	–	–	−0.06	0.07	0.05
PG	spring summer	C1	50	37	1.34	3.82	41	0.15	0.32	0.03
		C2	15	553.4	0.95	6.15	47.3	0.97	0.34	0
		C3	20	1043.5	0.88	5.34	40	1.14	0.58	0.05
		clim.	–	–	–	–	–	0.3	0.15	0.02
	fall	fall	70	–	–	–	–	−0.2	0.19	−0.02
		clim. fall	–	–	–	–	–	0.27	0.13	0
SAP	spring summer	C1	9	32.2	1.18	3	24.5	0.57	0.39	0.66
		C2	10	411	1.95	7.25	27	1.04	0.46	NA
		C3	17	945.3	0.88	4.36	78.8	0.72	0.4	0.59
		clim.	–	–	–	–	–	0.3	0.21	0.21
	fall	fall	44	–	–	–	–	0.27	0.41	0.69
		clim. fall	–	–	–	–	–	0.29	0.2	0.16

NA – not available.

exhibits a slight cooling in some bins of the central and eastern sectors. It can be stated that half of this warming in the intermediate and deep layers is due to the 2022 MHW, while the other half is due to the long-term warming of the ocean. This consideration stems from comparing the current OHCA$_{2022}$ with OHC trends defined by Kubin et al. (2023). To perform this study, five regions (NWM, SWM, ION, SAP, and PG; colored boxes in Fig. 1b) were selected. This choice was motivated by the highest 2022 sea surface temperature (SST) anomaly registered in the band from 0 to 25° E (Marullo et al., 2023) and by the availability of float data in both May–September and October–December 2022 periods. Figure 2 shows $\tilde{T}_a$ profiles for the warm season of each sector for each MHW depth category and for the FLOAT climatology.

In the NWM and SWM sectors, the circulation is strongly influenced by the presence of two intense and permanent currents (Fig. 1a): the southwestward Northern Current (Poulain et al., 2012; Escudier et al., 2021) and the eastward along-slope Algerian Current (which transports waters of Atlantic origin in the upper water column; Poulain et al., 2021) in the NWM and in the SWM, respectively. Therefore, float pro-

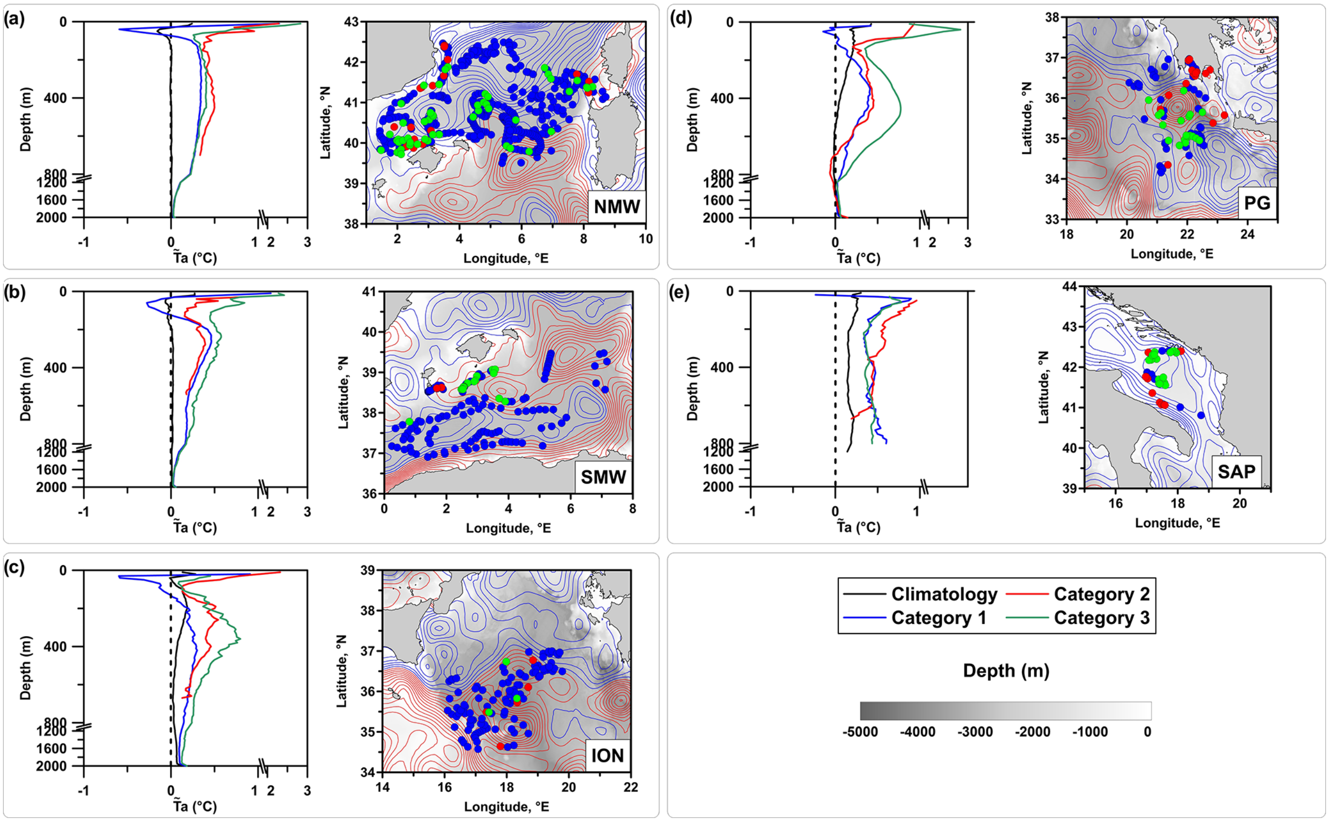

Figure 2. (**a–c**, left) Median profiles of temperature anomaly computed for each sector (NWM, SWM, ION, PG, SAP) and for the 2022 warm season (May–September) using Argo float data with respect to the 1985–2018 SDC climatology dataset. Black lines highlight the FLOAT climatology profiles, while blue, red, and green profiles indicate shallow (0–150 m), intermediate (150–700 m), and deep (> 700 m) categories, respectively. (**d, e**, right) Positive and negative contours of the absolute dynamic topography with 1 cm spacing are displayed by red and blue lines, while the colored dots are associated with the float positions of each category.

files were mainly located along the boundary of cyclonic circulations as highlighted by the absolute dynamic topography (product ref. no. 3, Table 1; Fig. 2a, b). In the ION sector, float profiles were mainly distributed in the anticyclonic meander of the Mid-Ionian Jet (Fig. 2c), a strong meandering current that, together with the Atlantic–Ionian Stream (AIS), transports Atlantic Water from the western to the eastern Mediterranean Sea (Poulain et al., 2012, 2013; Menna et al., 2019a; Fig. 1a). Although the NWM, SWM, and ION sectors have different oceanographic characteristics, they showed a similar response to the 2022 MHW (Fig. 2a–c). Most $\tilde{T}_\mathrm{a}$ profiles belong to Category 1, and the mean MHW depth falls into the 20–25 m layer (Table 2). Profiles, characterized by shallow MHW penetration (blue lines in Fig. 2a–c), showed a decreasing warming in the first 50 m with the maximum $\tilde{T}_\mathrm{a}$ close to the surface (22.2–22.5 m; Table 2). The layer between 50 and 100 m depth showed a negative $\tilde{T}_\mathrm{a}$ with maxima of −0.65, −0.2, and −0.53 °C at 50, 70, and 40 m depth, in the NWM, SWM, and ION sectors, respectively (Fig. 2a–c). The median profiles derived from the FLOAT climatology (black lines in Fig. 2a–c) do not exhibit this negative anomaly (or only to a very small extent), suggesting, therefore, a possible link between this behavior and the occurrence of the 2022 MHW. Below 100 m depth, $\tilde{T}_\mathrm{a}$ becomes positive again with mean values of ∼ 0.3 °C in the intermediate layer and values lower than 0.12 °C in the deep layer. Profiles characterized by intermediate MHW penetration (red lines in Fig. 2a–c; MHW depth between 570 and 650 m, Table 2) were located in coastal areas of the western Mediterranean and in frontal zones in the ION sector and showed positive $\tilde{T}_\mathrm{a}$ throughout the water column, with values in the range of 0.3–0.6 °C. Profiles, characterized by deep MHW penetration (green lines in Fig. 2a–c; MHW depth ∼ 1400 m, Table 2), showed the largest $\tilde{T}_\mathrm{a}$ in the surface layer in the two sectors of the western Mediterranean (> 0.8 °C), while the ION sector depicted the largest anomalies in the intermediate layer (> 0.5 °C). These results are consistent with the warming trend of the western Mediterranean Sea over the last 15 years of $0.09 \pm 0.02\,°\mathrm{C\,yr^{-1}}$ and $0.03 \pm 0.01\,°\mathrm{C\,yr^{-1}}$ for surface waters and intermediate waters, respectively (Kubin et al., 2023).

The PG is located on the eastern side of the northern Ionian Sea, southwest of the Peloponnese coast (Fig. 1a). It is a subbasin anticyclonic feature (diameter of ~ 120 km; Pinardi et al., 2015) that extends from the surface down to 800–1000 m depth (Malanotte-Rizzoli et al., 1997; Kovačević et al., 2015), and it is forced by the Etesian winds (Ayoub et al., 1998; Mkhinini et al., 2014; Menna et al., 2021). In the late summer to fall, the Etesian winds amplify their acceleration and wind shear in the region of the western Cretan straits (Mkhinini et al., 2014); therefore, larger anticyclonic vorticities are observed during these months in the PG region (Menna et al., 2019a). In the PG sector, $\tilde{T}_\mathrm{a}$ profiles for the three categories showed positive temperature anomalies in the first 800 m of the water column, which coincides with the vertical extension of the gyre itself (Fig. 2d). Profiles that fall into Category 1 showed a decreasing warming in the first 70 m, anomaly values close to zero in the 70–150 m layer, and increasing warming in the 150–400 m layer. The mean anomaly in the intermediate layer of Category 1 is 0.3 °C (Table 2). Category 2 profiles were retrieved mainly in the coastal area near the Peloponnese, while Category 3 profiles were found within the gyre area. Categories 2 and 3 showed a strong warming in the surface layer (0.97 and 1.14 °C, respectively), a mean warming in the range of 0.3–0.6 °C in the intermediate layer and no warming compared to the SDC climatology was observed in the deep layer (Table 2).

The SAP is one of the sites of open ocean convection in the Mediterranean Sea, characterized by a complex thermohaline circulation that influences the physical and biogeochemical properties of the dense waters formed in its interior and the strength of winter convection (Martellucci et al., 2024; Di Biagio et al., 2023; Menna et al., 2022, OSR6; Pirro et al., 2022). This sector showed positive temperature anomalies in all layers and in all categories (Fig. 2d). Most profiles belong to Category 3 with a mean MHW depth of ~ 950 m and maximum $\tilde{T}_\mathrm{a}$ at ~ 80 m depth. The largest mean warming was observed in the surface layer of each category (0.6–1.04 °C) followed by the deep layer that had an exceptional warming of ~ 0.6 °C and finally by the intermediate layer that had a mean warming of ~ 0.4 °C (Table 2).

All five sectors showed a larger warming than the FLOAT climatology with a mean temperature increase in the 2022 warm season between 0.2 and 0.8 °C in response to the MHW event (Table 2). Some differences in warming observed among the sectors are related to their peculiar hydrological and dynamical characteristics. During the warm season, the surface layer of the NWM and SWM sectors and partially of the ION sector was characterized by both larger stratifications and stratification anomalies compared to the FLOAT climatology (Fig. 3a, b). Strong stratification prevents vertical heat penetration, causing negative $\tilde{T}_\mathrm{a}$ in the 50–100 m layer (Fig. 2a–c). In the PG sector, the warm-season stratification anomaly was consistent with the climatology (Fig. 3b), and vertical heat penetration was closely related to the gyre dynamics. In the SAP sector, stratification during the warm period was lower than the climatology, suggesting an instability of the water column and, therefore, of the transport of the vertical heat to the deep layers. The median of all profiles available in the 2022 warm season, when not categorized, closely aligns with the median of profiles in Category 1 (Fig. 3c, d). This condition arises because Category 1 consistently boasts the highest number of profiles across various sectors.

Larger warming of the water column was observed in fall 2022 compared to the SDC climatology in all sectors, except for the surface layer of the ION and PG sectors (Fig. 3e). The stronger warm-season stratification observed in the NWM and SWM sectors (Fig. 3a, b) corresponds to enhanced vertical heat propagation in the surface and intermediate layers in fall 2022 (Fig. 3e, Table 2). Negative $\tilde{T}_\mathrm{a}$ values in the surface layer of the ION sector were attributed to an upwelling event along the southern coast of Sicily between November and December 2022 as shown by the sea surface temperature (product ref. no. 2, Table 1; Fig. 3g, h). The northern part of the Sicily Channel is an area of strong eddy kinetic energy (Poulain et al., 2012), influenced by Ekman transport and advection of waters from the western to the eastern Mediterranean (Molcard et al., 2002; Falcini and Salusti, 2015; Schroeder et al., 2017; Menna et al., 2019b). The cold waters upwelled off the southern coast of Sicily in November 2022 (Fig. 3g) were advected to the Ionian Sea through the Atlantic–Ionian Stream and the Mid-Ionian Jet pathways (Fig. 1a), gradually cooling the waters in the ION sector (Fig. 3h). The negative anomaly in the surface layer of the ION sector is not only limited to 2022 but is also a permanent characteristic of the area related to the upwelling phenomena, as confirmed by the $\tilde{T}_\mathrm{a}$ profile derived from the FLOAT climatology (orange line in Fig. 3f) and by trends in the OHC anomaly estimated by Dayan et al. (2023) over the period 1987–2019. Negative $\tilde{T}_\mathrm{a}$ values in the PG sector were attributable to the typical downwelling process of this region that is associated with the gyre dynamics. The downwelling contributed to the vertical propagation of the 2022 MHW, with a strong spring–summer warming in the first 800 m of the water column (Fig. 2d), keeping the stratification values similar to the FLOAT climatology (no significant increases in N^2 anomaly were registered due to the 2022 heat wave; Fig. 3b). In this way, fall cooling can penetrate deep into the water column, therefore causing negative $\tilde{T}_\mathrm{a}$ values in the surface layer (Fig. 3e; Table 2).

In recent years, the SAP has been experiencing a significant temperature increase in the deep layer (trend of ~ 0.06 °C yr^{-1} in the 2013–2020 period according to Kubin et al., 2023) and salinity increase in the surface and intermediate layers (Martellucci et al., 2024; Menna et al., 2022, OSR6; Mihanović et al., 2021), with possible future impacts on the entire thermohaline circulation of the Eastern Mediterranean. It is of general understanding that convection sites contribute to the propagation of the MHW signal from the surface to the subsurface interior of the water column (Dayan

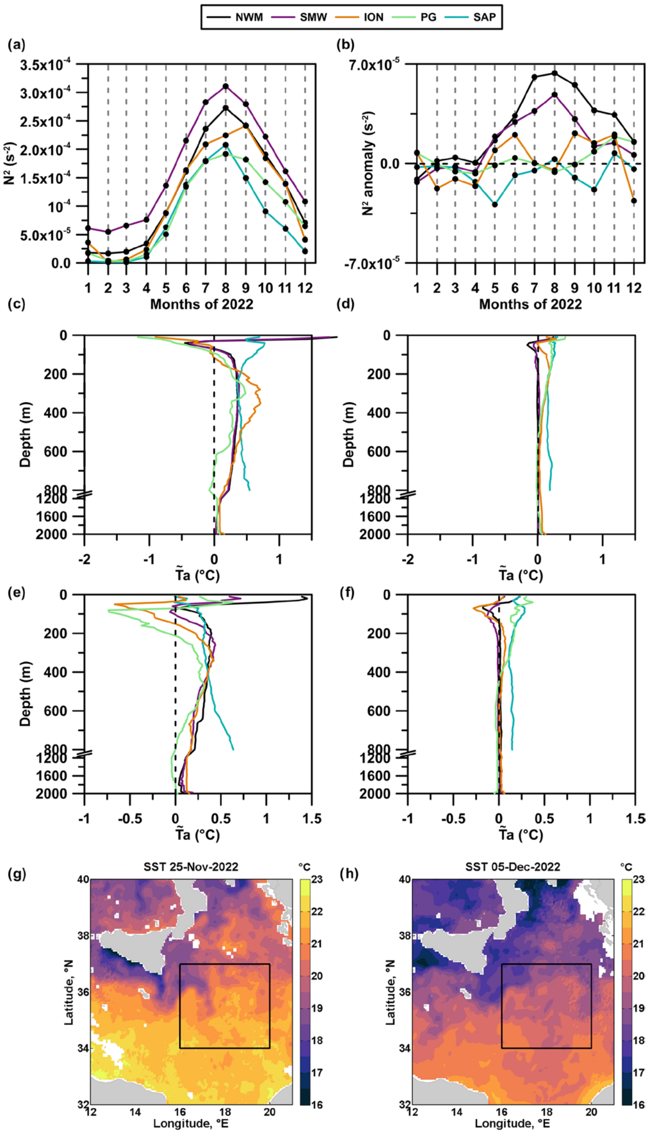

Figure 3. **(a)** Monthly averaged Brunt–Väisälä frequency squared (N^2) computed in the surface layer (0–150 m) using 2022 Argo float data. **(b)** Monthly averaged Brunt–Väisälä frequency squared anomaly (N^2 anomaly) computed in the surface layer with respect to the FLOAT climatology. **(c)** Median temperature anomaly (°C) computed in the warm season (May–September) from Argo float profiles in 2022 and **(d)** in 2001–2018 with respect to the SDC climatology. **(e)** Median temperature anomaly (°C) computed in the fall period (October–December) from Argo float profiles in 2022 and **(f)** in 2001–2018 with respect to the SDC climatology. Daily sea surface temperature (°C) in the ION sector (black box) for **(g)** late November 2022 and **(h)** early December 2022.

et al., 2023; Kubin et al., 2023), but specific analyses at the local scale are not yet available (Juza et al., 2022). Our results show a fairly significant warming of the SAP in both spring–summer (Figs. 2e and 3c) and fall 2022 (light blue line in Fig. 3f) and a significant positive anomaly of the FLOAT climatology compared to the SDC one (black line in Fig. 2e and light blue line in Fig. 3f). In fall, the largest $\tilde{T}_\mathrm{a}$ values in the SAP were observed in the deep layer (∼ 0.69 °C; Table 2, Fig. 3e). Mean profiles derived from the FLOAT climatology (black line in Fig. 2e and light blue line in Fig. 3f) showed positive values compared to the SDC one, confirming the warming trend throughout the water column over the past decade. Beyond the impact of global warming on the Mediterranean Sea, the 2022 MHW led to an additional heating in the SAP, which was transferred to the deeper layers and favored by dynamical features of this area.

This study aimed to characterize the 2022 MHW in the subsurface layers and attempted to explain the mechanisms that drive the heat penetration to deep layers. However, further and more detailed investigations are needed to better support this last point. We showed that the effects of the 2022 MHW were felt in all layers of the Mediterranean Sea with vertical heat propagation extending from the surface to ∼ 1500 m depth. In the surface layer, heat penetration and storage are related to the strength of the stratification and/or advection from adjacent regions. In contrast, the transport and the storage of heat in the intermediate and deep layers are closely linked to the dynamics of each area. These considerations are in line with the findings by Elzahaby et al. (2021) and Zhang et al. (2023), who noted that shallower MHWs are primarily influenced by surface air–sea fluxes, whereas deeper MHWs are predominantly driven by advection, manifesting distinct dynamics across various oceanic regions.

In the western Mediterranean and western Ionian Sea sectors, heat is mainly stored in the surface layer (shallow MHW depths and stronger stratification), so this layer is significantly warmer than the climatology even during the following fall. Although deep MHW penetration in these regions is limited to coastal and frontal/eddy zones, it reaches the higher MHW depth estimated during the event. Sectors characterized by specific dynamics (downwelling, convection) quickly distribute the heat in the water column, even during the event. Intermediate layers exhibit comparable heating both during and after the MHW event, implying that heat can be stored there for extended periods and can be regarded as a long-term signal.

The warming signal in the intermediate and deep layers could also be influenced by heat advection from adjacent basins; however, we are aware that this topic needs to be studied in more detail in the future. In this context, the use of two climatologies and the cumulative anomaly threshold in the present analysis should have eliminated most of the signal associated with the ocean warming trend and advection; therefore, the additional warming registered in spring–summer 2022 compared to the FLOAT climatology can be attributed to the effects of the 2022 MHW along the entire water column. Further studies are needed to investigate the effects that this warming may have on the physical and biological oceanic processes, with implications for the thermohaline circulation of the entire Mediterranean Sea.

Code and data availability. The codes and data are available upon request to Annunziata Pirro (apirro@ogs.it). Further information can also be found in Table 1.

Author contributions. AP, MM, and RM conceptualized the study. AP and MM prepared the original manuscript. AP, MM, RM, EM, AG, GN, EK, and MJ reviewed and edited the manuscript. AP, MM, and RM created the methodology. AP, MM, RM, and EK created the codes and performed the formal analysis. AP, MM, and RM conducted the investigation. AG, AB, and MP curated the data. EM was in charge of the Argo-Italy infrastructure management and funding acquisition. All authors have read and agreed to the published version of the paper.

Competing interests. The contact author has declared that none of the authors has any competing interests.

Disclaimer. The Copernicus Marine Service offering is regularly updated to ensure it remains at the forefront of user requirements. In this process, some products may undergo replacement or renaming, leading to the removal of certain product IDs from the catalogue.

If readers have any questions or require assistance regarding these modifications, please feel free to reach out to the Copernicus Marine Service user support team for further guidance. They will be able to provide the necessary information to address concerns and find suitable alternatives.

Review statement. This paper was edited by Gilles Garric and reviewed by two anonymous referees.

References

Argo: Argo float data and metadata from Global Data Assembly Centre (Argo GDAC), SEANOE, https://doi.org/10.17882/42182, 2023.

Ayoub, N., Le Traon, P.-Y., and De Mey, P.: A description of the Mediterranean surface variable circulation from combined ERS-1 and TOPEX/POSEIDON altimetric data, J. Marine Syst., 18, 3–40, https://doi.org/10.1016/S0924-7963(98)80004-3, 1998.

Bensoussan, N., Chiggiato, J., Buongiorno Nardelli, B., Pisano, A., and Garrabou, J.: Insights on 2017 marine heat waves in the Mediterranean sea, J. Oper. Oceanogr., 12, s26–s30, https://doi.org/10.1080/1755876X.2019.1633075, 2019.

Darmaraki, S., Somot, S., Sevault, F., and Nabat, P.: Past variability of Mediterranean Sea marine heatwaves, Geophys. Res. Lett., 46, 9813–9823, https://doi.org/10.1029/2019GL082933, 2019.

Dayan, H., McAdam, R., Juza, M., Masina, S., and Speich, S.: Marine heat waves in the Mediterranean Sea: An assessment from the surface to the subsurface to meet national needs, Front. Mar. Sci., 10, 1045138, https://doi.org/10.3389/fmars.2023.1045138, 2023.

Di Biagio, V., Martellucci, R., Menna, M., Teruzzi, A., Amadio, C., Mauri, E., and Cossarini, G.: Dissolved oxygen as an indicator of multiple drivers of the marine ecosystem: the southern Adriatic Sea case study, in: 7th edition of the Copernicus Ocean State Report (OSR7), edited by: von Schuckmann, K., Moreira, L., Le Traon, P.-Y., Grégoire, M., Marcos, M., Staneva, J., Brasseur, P., Garric, G., Lionello, P., Karstensen, J., and Neukermans, G., Copernicus Publications, State Planet, 1-osr7, 10, https://doi.org/10.5194/sp-1-osr7-10-2023, 2023.

Elzahaby, Y. and Schaffer, A.: Observational insight into the subsurface anomalies of marine heatwaves, Front. Mar. Sci., 6, 745, https://doi.org/10.3389/fmars.2019.00745, 2019.

Elzahaby, Y., Schaeffer, A., Roughan, M., and Delaux, S.: Oceanic circulation drives the deepest and longest marine heatwaves in the East Australian Current system, Geophys. Res. Lett., 48, e2021GL094785, https://doi.org/10.1029/2021GL094785, 2021.

Escudier, R., Clementi, E., Cipollone, A., Pistoia, J., Drudi, M., Grandi, A., Lyubartsev, V., Lecci, R., Aydogdu, A., Delrosso, D., Omar, M., Masina, S., Coppini, G., and Pinardi, N.: A High Resolution Reanalysis for the Mediterranean Sea, Front. Earth Sci., 9, 702285, https://doi.org/10.3389/feart.2021.702285, 2021.

Escudier, R., Clementi, E., Nigam, T., Aydogdu, A., Fini, E., Pistoia, J., Grandi, A., and Miraglio, P.: EU Copernicus Marine Service Quality Information Document for Mediterranean Sea Physics Reanalysis, MEDSEA_MULTIYEAR_PHY_006_004, Issue 2.3, Mercator Ocean International, https://catalogue.marine.copernicus.eu/documents/QUID/CMEMS-MED-QUID-006-004.pdf (last access: 19 May 2023), 2022.

EU Copernicus Marine Service Product: Mediterranean Sea – In-Situ Near Real Time Observations, Mercator Ocean International [data set], https://doi.org/10.48670/moi-00044, 2022a.

EU Copernicus Marine Service Product: Mediterranean Sea Physics Reanalysis, CMCC Foundation [data set], https://doi.org/10.25423/CMCC/MEDSEA_MULTIYEAR_PHY_006_004_E3R1I, 2022b.

EU Copernicus Marine Service Product: European Seas Gridded L 4 Sea Surface Heights And Derived Variables Nrt, Mercator Ocean International [data set], https://doi.org/10.48670/moi-00142, 2023.

Falcini, F. and Salusti, E.: Friction and mixing effects on potential vorticity for bottom current crossing a marine strait: an application to the Sicily Channel (central Mediterranean Sea), Ocean Sci., 11, 391–403, https://doi.org/10.5194/os-11-391-2015, 2015.

Galli, G., Solidoro, C., and Lovato, T.: Marine heat waves hazard 3D maps and the risk for low motility organisms in a warming Mediterranean Sea, Front. Mar. Sci., 4, 136, https://doi.org/10.3389/fmars.2017.00136, 2017.

Garrabou, J., Gómez-Gras, D., Medrano, A., et al.: Marine heatwaves drive recurrent mass mortalities in the Mediterranean Sea, Glob. Change Biol., 28, 5708–5725, https://doi.org/10.1111/gcb.16301, 2022.

Hobday, A. J., Alexander, L. V., Perkins, S. E., Smale, D. A., Straub, S. C., Oliver, E. C., Benthuysen, J. A., Burrows, M. T., Donat, G. M., Feng, M., Holbrook, N., J., Moore, P. J., Scannel, H. A., Gupta, A. S., and Wernberg, T.: A hierarchical approach to defining marine heatwaves, Prog. Oceanogr., 141, 227–238, https://doi.org/10.1016/j.pocean.2015.12.014, 2016.

Holbrook, N. J., Gupta, A. S., Oliver, E. C., Hobday, A. J., Benthuysen, J. A., Scannell, H. A., Smale, D. A., and Wernberg, T.: Keeping pace with marine heatwaves, Nat. Rev. Earth Env., 1, 482–493, https://doi.org/10.1038/s43017-020-0068-4, 2020.

Hu, S., Li, S., Zhang, Y., Guan, C., Du, Y., Feng, M., Ando, K., Wang, F., Schiller, A., and Hu, D.: Observed strong subsurface marine heatwaves in the tropical western Pacific Ocean, Environ. Res. Lett., 16, 104024, https://doi.org/10.1088/1748-9326/ac26f2, 2021.

Ibrahim, O., Mohamed, B., and Nagy, H.: Spatial variability and trends of marine heat waves in the Eastern Mediterranean Sea over 39 years, J. Mar. Sci. Eng., 9, 643, https://doi.org/10.3390/jmse9060643, 2021.

In Situ TAC partners: EU Copernicus Marine Service Product User Manual for Mediterranean Sea – In-Situ Near Real Time Observations, INSITU_MED_PHYBGCWAV_DISCRETE_MYNRT_013_035, Issue 1.14, Mercator Ocean International, https://catalogue.marine.copernicus.eu/documents/PUM/CMEMS-INS-PUM-013-030-036.pdf (last access: 19 May 2023), 2022.

IPCC (Intergovernmental Panel on Climate Change): Summary for Policymakers, in: Climate Change 2023: Synthesis Report. Contribution of Working Groups I, II and III to the Sixth Assessment Report of the Intergovernmental Panel on Climate Change, edited by: Core Writing Team, Lee, H., and Romero, J., IPCC, Geneva, Switzerland, 1–34, https://doi.org/10.59327/IPCC/AR6-9789291691647.001, 2023.

Juza, M., Fernández-Mora, A., and Tintoré, J.: Sub-Regional marine heat waves in the Mediterranean Sea from observations: long-term surface changes, subsurface and coastal responses, Front. Mar. Sci., 9, 785771, https://doi.org/10.3389/fmars.2022.785771, 2022.

Kovačević, V., Ursella, L., Gačić, M., Notarstefano, G., Menna, M., Bensi, M., and Poulain, P.-M.: On the Ionian thermohaline properties and circulation in 2010-2013 as measured by Argo floats, Acta Adriat., 56, 97–114, 2015.

Kubin, E., Menna, M., Mauri, E., Notarstefano, G., Mieruch, S., and Poulain, P.-M.: Heat content and temperature trends in the Mediterranean Sea as derived from Argo float data, Front. Mar. Sci., 10, 1271638, https://doi.org/10.3389/fmars.2023.1271638, 2023.

Lecci, R., Drudi, M., Grandi, A., Cretì, S., and Clementi, E.: EU Copernicus Marine Service Product User Manual for For Mediterranean Sea Physics Reanalysis, MEDSEA_MULTIYEAR_PHY_006_004, Issue 2.3, Mercator Ocean International, https://catalogue.marine.copernicus.eu/documents/PUM/CMEMS-MED-PUM-006-004.pdf (last access: 19 May 2023), 2022.

Liquete, C., Piroddi, C., Macías, D., Druon, J. N., and Zulian, G.: Ecosystem services sustainability in the Mediterranean Sea: assessment of status and trends using multiple modelling approaches, Sci. Rep., 6, 1–14, https://doi.org/10.1038/srep34162, 2016.

Malanotte-Rizzoli, P., Manca, B. B., Ribera D'Alcalà, M., Theocharis, A., Bergamasco, A., Bregant, D., Budillon, G., Civitarese, G., Georgoupoulos, D., Michelato A., Sansone, E., Scarazzato, P., Souvermezoglou, E.: A synthesis of the Ionian Sea hydrography, circulation and water masses pathways during POEM-Phase I, Prog. Oceanogr., 39, 153–204, https://doi.org/10.1016/S0079-6611(97)00013-X, 1997.

Martín-López, B., Oteros-Rozas, E., Cohen-Shacham, E., Santos-Martín, F., Nieto-Romero, M., Carvalho-Santos, C., González, J. A., García-Llorente, M., Klass, K., Geijzendorffer, I., Montes, C., and Cramer, W.: Ecosystem services supplied by Mediterranean Basin ecosystems, in: Routledge handbook of ecosystem services, 405–414, Routledge, ISBN 9781315775302, 2016.

Martellucci, R., Menna, M., Mauri, E., Pirro, A., Gerin, R., de Mendoza, F. P., Garić, R., Batistić, M., di Biagio, V., Giordano, P., Langone, L., Miserocchi, S., Gallo, A., Notarstefano, G., Savonitto, G., Bussani, A., Pacciaroni, M., Zuppelli, P., and Poulain, P. M.: Recent changes of the dissolved oxygen distribution in the deep convection cell of the southern Adriatic Sea, J. Marine Syst., 245, 103988, https://doi.org/10.1016/j.jmarsys.2024.103988, 2024.

Martínez, J., Leonelli, F. E., García-Ladona, E., Garrabou, J., Kersting, D., Bensoussan, N., and Pisano, A.: Evolution of marine heatwaves in warming seas: the Mediterranean Sea case study, Front. Mar. Sci., 10, 1193164, https://doi.org/10.3389/fmars.2023.1193164, 2023.

Marullo, S., Serva, F., Iacono, R., Napolitano, E., di Sarra, A., Meloni, D., Monteleone, F., Sferlazzo, D., De Silvestri L., de Toma, V., Pisano, A., Bellacicco, M., Landolfi, A., Organelli, E., Yang, C., and Santoleri, R.: Record-breaking persistence of the 2022/23 marine heatwave in the Mediterranean Sea, Environ. Res. Lett., 18, 114041, https://doi.org/10.1088/1748-9326/ad02ae, 2023.

Menna, M., Suarez, N. R., Civitarese, G., Gačić, M., Rubino, A., and Poulain, P. M.; Decadal variations of circulation in the Central Mediterranean and its interactions with mesoscale gyres, Deep-Sea Res. Pt. II, 164, 14–24, https://doi.org/10.1016/j.dsr2.2019.02.004, 2019a.

Menna, M., Poulain, P. M., Ciani, D., Doglioli, A., Notarstefano, G., Gerin, R., Rio, M. H., Santoleri, R., Gauci, A., and Drago, A.: New Insights of the Sicily Channel and Southern Tyrrhenian Sea Variability, Water, 11, 1355, https://doi.org/10.3390/w11071355, 2019b.

Menna, M., Gerin, R., Notarstefano, G., Mauri, E., Bussani, A., Pacciaroni, M., and Poulain, P. M.: On the circulation and thermohaline properties of the Eastern Mediterranean Sea, Front. Mar. Sci., 8, 671469, https://doi.org/10.3389/fmars.2021.671469, 2021.

Menna, M., Martellucci, R., Notarstefano, G., Mauri, E., Gerin, R., Pacciaroni, M., Bussani, A., Pirro, A., and Poulain, P. M.: Record-breaking high salinity in the South Adriatic Pit in 2020, J. Oper. Oceanogr., s199–s205, https://doi.org/10.1080/1755876X.2022.2095169, 2022.

Mihanović, H., Vilibić, I., Šepić, J., Matić, F., Ljubešić, Z., Mauri, E., and Gerin, R.: Observation, preconditioning and recurrence of exceptionally high salinities in the Adriatic Sea, Front. Mar. Sci., 8, 672210, https://doi.org/10.3389/fmars.2021.672210, 2021.

Mills, K. E., Pershing, A. J., Brown, C. J., Chen, Y., Chiang, F. S., Holland, D. S., Lehuta, S., Nye, J. A., Sun, J. C., Thomas, A. C., and Wahle, R. A.: Fisheries management in a changing climate: lessons from the 2012 ocean heat wave in the Northwest Atlantic, Oceanography, 26, 191–195, https://doi.org/10.5670/oceanog.2013.27, 2013.

Molcard, A., Gervasio, L., Gria, A., Gasparini, G. P., Mortier, L., Ozgokmen, T. M.: Numerical investigation of the Sicily Channel dynamics: density currents and water mass advection, J. Marine Syst., 36, 219–238, https://doi.org/10.1016/S0924-7963(02)00188-4, 2002.

Mkhinini, N., Coimbra, A. L. S., Stegner, A., Arsouze, T., Taupier-Letage, I., and Beranger, K.: Long-lived mesoscale eddies in the Eastern Mediterranean Sea: analysis of 20 years of AVISO geostrophic velocities, J. Geophys. Res.-Oceans, 119, 8603–8626, https://doi.org/10.1002/2014JC010176, 2014.

Oliver, E. C., Donat, M. G., Burrows, M. T., Moore, P. J., Smale, D. A., Alexander, L. V., Benthuysen, J. A., Feng, M., Gupta, A. S., Hobday, A. J., Holbrook, N. J., Perkins-Kirkpatrick, S. E., Scannell, H. E., Straub, S. C., and Wernberg, T.: Longer and more frequent marine heatwaves over the past century, Nat. Commun., 9, 1324, https://doi.org/10.1038/s41467-018-03732-9, 2018.

Pastor, F. and Khodayar, S.: Marine heat waves: Characterizing a major climate impact in the Mediterranean, Sci. Total Environ., 861, 160621, https://doi.org/10.1016/j.scitotenv.2022.160621, 2023.

Pinardi, N., Zavatarelli, M., Adani, M., Coppini, G., Fratianni, C., Oddo, P., Simoncelli, S., Tonani, M., and Lyubartsev, V.: Mediterranean Sea large-scale low-frequency ocean variability and water mass formation rates from 1987 to 2007: a retrospective analysis, Prog. Oceanogr., 132, 318–332, https://doi.org/10.1016/j.pocean.2013.11.003, 2015.

Pirro, A., Mauri, E., Gerin, R., Martellucci, R., Zuppelli, P., and Poulain, P. M.: New insights on the formation and breaking mechanism of convective cyclonic cones in the South Adriatic Pit during winter 2018, J. Phys. Oceanogr., 52, 2049–2068, https://doi.org/10.1175/JPO-D-21-0108.1, 2022.

Poulain, P. M., Menna, M., and Mauri, E.: Surface geostrophic circulation of the Mediterranean Sea derived from drifter and satellite altimeter data, J. Phys. Oceanogr., 42, 973–990, https://doi.org/10.1175/JPO-D-11-0159.1, 2012.

Poulain, P. M., Bussani, A., Gerin, R., Jungwirth, R., Mauri, E., Menna, M., and Notarstefano, G.: Mediterranean surface currents measured with drifters: From basin to subinertial scales, Oceanography, 26, 38–47, https://doi.org/10.5670/oceanog.2013.03, 2013.

Poulain, P. M., Centurioni, L., Özgökmen, T., Tarry, D., Pascual, A., Ruiz, S., Mauri, E., Menna, M., and Notarstefano, G.: On the structure and kinematics of an Algerian Eddy in the southwestern Mediterranean Sea, Remote Sens., 13, 3039, https://doi.org/10.3390/rs13153039, 2021.

Pujol, M.-I.: EU Copernicus Marine Service Product User Manual for European Seas Gridded L 4 Sea Surface Heights And Derived Variables Nrt, SEALEVEL_EUR_PHY_L4_NRT_OBSERVATIONS_008_060, Issue 7.0, Mercator Ocean International, https://catalogue.marine.copernicus.eu/documents/PUM/CMEMS-SL-PUM-008-032-068.pdf (last access: 19 May 2023), 2022.

Pujol, M.-I., Taburet, G., and SL-TAC team: EU Copernicus Marine Service Quality Information Document for European Seas Gridded L 4 Sea Surface Heights And Derived Variables Nrt, SEALEVEL_EUR_PHY_L4_NRT_OBSERVATIONS_008_060, Issue 8.2, Mercator Ocean International, https://catalogue.marine.copernicus.eu/documents/QUID/CMEMS-SL-QUID-008-032-068.pdf (last access: 19 May 2023), 2023.

Santora, J. A., Mantua, N. J., Schroeder, I. D., Field, J. C., Hazen, E. L., Bograd, S. J., Sydeman, W. J., Wells, B. K., Calambokidis, J., Saez, L., Lawson, D., and Forney, K. A.: Habitat compression and ecosystem shifts as potential links between marine heatwave and record whale entanglements, Nat. Commun., 11, 1–12, https://doi.org/10.1038/ s41467-019-14215-w, 2020.

Scannell, H. A., Johnson, G. C., Thompson, L., Lyman, J. M., and Riser, S. C.: Subsurface evolution and persistence of marine heatwaves in the Northeast Pacific, Geophys. Res. Lett., 47, e2020GL090548, https://doi.org/10.1029/2020GL090548, 2020.

Schaeffer, A. and Roughan, M.: Subsurface intensification of marine heatwaves off southeastern Australia: the role of stratification and local winds, Geophys. Res. Lett., 44, 5025–5033, https://doi.org/10.1002/2017gl073714, 2017.

Schroeder, K., Chiggiato, J., Josey, S. A., Borghini, M., Aracri, S., and Sparnocchia, S.: Rapid response to climate change in a marginal sea, Sci. Rep., 7, 4065, https://doi.org/10.1038/s41598-017-04455-5, 2017.

Simon, A., Pires, C., Frölicher, T. L., and Russo, A.: Long-term warming and interannual variability contributions' to marine heatwaves in the Mediterranean, Weather and Climate Extremes, 42, 100619, https://doi.org/10.1016/j.wace.2023.100619, 2023.

Simoncelli, S., Oliveri, P., Mattia, G., Myroshnychenko, V., Barth, A., and Troupin, C.: SeaDataCloud Temperature and Salinity Climatology for the Mediterranean Sea (Version 2), Product Information Document (PIDoc), SeaDataCloud, https://doi.org/10.13155/77514, 2020a.

Simoncelli, S., Oliveri, P., and Mattia, G.: SeaDataCloud Mediterranean Sea – V2 Temperature and Salinity Climatology, Sextant [data set], https://doi.org/10.12770/3f8eaace-9f9b-4b1b-a7a4-9c55270e205a (last access: 19 May 2023), 2020b.

Smale, D. A., Wernberg, T., Oliver, E., Thomsen, M., Harvey, B. P., Straub, S. C., Burrows, M., Alexander, L., Benthuysen, J., Donat, M., Feng, M., Hobday, A., Holbrook, N., Perkins-Kirkpatrick, S., Scannell, H. A., Sen Gupta, A., Payne, B. L., and Moore, P.: Marine heatwaves threaten global biodiversity and the provision of ecosystem services, Nat. Clim. Change, 9, 306–312, https://doi.org/10.1038/s41558-019-0412-1, 2019.

Von Schuckmann, K., Palmer, M. D., Trenberth, K. E., Cazenave, A., Chambers, D., Champollion, N., Hansen, J., Josey, S. A., Loeb, N., Mathieu, P. P., Meyssignac, B., and Wild, M.: An imperative to monitor earth's energy imbalance, Nat. Clim. Change, 6, 138–144, https://doi.org/10.1038/nclimate2876, 2016.

Wehde, H., Schuckmann, K. V., Pouliquen, S., Grouazel, A., Bartolome, T., Tintore, J., De Alfonso Alonso-Munoyerro, M., Carval, T., Racapé, V., and the INSTAC team: EU Copernicus Marine Service Quality Information Document for

Mediterranean Sea – In-Situ Near Real Time Observations, INSITU_MED_PHYBGCWAV_DISCRETE_MYNRT_013_035, Issue 2.2, Mercator Ocean International, https://catalogue.marine.copernicus.eu/documents/QUID/CMEMS-INS-QUID-013-030-036.pdf (last access: 19 May 2023), 2022.

Wernberg, T., Smale, D. A., Tuya, F., Thomsen, M. S., Langlois, T. J., De Bettignies, T., Bennet, S., and Rousseaux, C. S.: An extreme climatic event alters marine ecosystem structure in a global biodiversity hotspot, Nat. Clim. Change, 3, 78–82, https://doi.org/10.1038/nclimate1627, 2013.

Wong, A. P., Wijffels, S. E., Riser, S. C., et al.: Argo Data 1999–2019: Two Million Temperature-Salinity Profiles and Subsurface Velocity Observations From a Global Array of Profiling Floats, Front. Mar. Sci., 7, 700, https://doi.org/10.3389/fmars.2020.00700, 2020.

Zhang, Y., Du, Y., Feng, M., and Hobday, A. J.: Vertical structures of marine heatwaves, Nat. Commun., 14, 6483, https://doi.org/10.1038/s41467-023-42219-0, 2023.

State Planet, 4-osr8, 19, 2024
https://doi.org/10.5194/sp-4-osr8-19-2024

Monitoring the record-breaking wave event in Melilla harbour (SW Mediterranean Sea)

Pablo Lorente, Marta de Alfonso, Pilar Gil, Fernando Manzano, Anna Magdalena Matulka, Begoña Pérez-Gómez, Susana Pérez-Rubio, and M. Isabel Ruiz

Puertos del Estado, Madrid, 28042, Spain

Correspondence: Pablo Lorente (plorente@puertos.es)

Received: 3 August 2023 – Discussion started: 29 August 2023
Revised: 29 January 2024 – Accepted: 27 February 2024 – Published: 30 September 2024

Abstract. During 4–5 April 2022, a record-breaking wave storm hit Melilla harbour (SW Mediterranean Sea) with the violent overtopping of breakwaters. This unprecedented episode was compared against the six most extreme events previously registered by the Melilla coastal buoy during 2011–2022 to disentangle their common atmospheric driving mechanisms. A dipole-like sea level pressure (SLP) pattern, characterised by two adjacent (northwestern) high- and (southeastern) low-pressure systems, induced intense easterly winds and high waves over the entire SW Mediterranean Sea. The record-breaking 2022 event differed from the rest in the much stronger SLP gradient ($2\,\mathrm{Pa\,km^{-1}}$) and northeasterly winds (above $20\,\mathrm{m\,s^{-1}}$), which concurrently gave rise to a maximum significant wave height (SWH_o) and mean period (T_m) of 7.32 m and 9.42 s, respectively, beating previous historical records. The associated return period decreased from 53 to 25 years, which must be considered for updated security protocols and the sound design of future port facilities. Hourly observations from the Melilla tide gauge covering the 2011–2022 period were used to investigate the relationship between offshore energetic waves penetrating into the harbour and the sea state inside. The harbour agitation, which also reached a record-breaking value (1.41 m) during the storm, was proved to be modulated by both the offshore SWH_o (correlation coefficient of 0.87) and T_m. The highest values of agitation (above 1 m) were registered for incident high waves coming from the angular sector between 50 and 70° (clockwise from true north) with T_m and peak period (T_p) values above 7 and 10 s, respectively. By contrast, the astronomical tide and the storm surge had negligible effects on harbour agitation during the seven extreme wave events. Infragravity waves, with periods between 30 and 300 s and maximum values up to 0.58 m during the 2022 storm, were also detected within the harbour basins and exceeded previously reported peaks. The energy in the infragravity band (IGE) was significantly correlated (0.96) with an offshore forcing parameter proportional to $\mathrm{SWH}_o^2 \cdot T_\mathrm{p}$, evidencing that energetic swell was responsible for the highest IGE values (above $2000\,\mathrm{m^2\,s}$). Furthermore, a 30-year (1993–2022) regional wave reanalysis was used to characterise the intra-annual variability in the 99th percentile of SWH_m over the Alborán Sea on a monthly timescale and identify the existence of trends. Results revealed that the intensity of extreme wave events impacting Melilla harbour and surrounding areas increased for April, while observed trends indicate a significant decrease of the 99th percentile of SWH_m for June and October. Finally, outcomes from this work could be useful for implementing a multi-hazard early warning system and ad hoc mitigation plans within the harbour territory.

1 Introduction

Over recent decades, climate change and extreme weather events have attracted growing public concern and political attention due to their widespread detrimental impact on the marine environment and human well-being (Konisky et al., 2015). While the global ocean is already experiencing anthropogenically driven variations such as gradual warming, acidification, and sea level rise (IPCC, 2022), sustained pressure from climate change is even more significant in semi-enclosed basins like the Mediterranean Sea (Chiggiato et al., 2023; Juza and Tintoré, 2021) and also in exposed sectors like harbour systems (Verschuur et al., 2023; Izaguirre et al., 2021).

Published by Copernicus Publications.

Table 1. Products from the Copernicus Marine Service and other complementary datasets used in this study, including the Product User Manual (PUM) and Quality Information Document (QUID). For complementary datasets, the links to the product description, data access, and scientific references are provided. Last access for all web pages cited in this table: 11 January 2024.

Product ref. no.	Product ID & type	Data access	Documentation
1	INSITU_IBI_PHYBGCWAV_DISCRETE_MYNRT_013_033, in situ observations	EU Copernicus Marine Service Product (2023a)	PUM: in situ TAC partners (2023) QUID: Wehde et al. (2023)
2	2 Hz data, high-frequency sea level oscillations and agitation parameters from the Melilla tide gauge, in situ observations	Puertos del Estado websites: https://portus.puertos.es, https://portuscopia.puertos.es/, http://opendap.puertos.es/thredds/catalog/tidegauge_meli/catalog.html	Product description: García Valdecasas et al. (2021) https://bancodatos.puertos.es/BD/informes/INT_3.pdf
3	ERA5 global reanalysis, numerical models	Hersbach et al. (2023)	Product description: https://confluence.ecmwf.int/display/CKB/ERA5:+data+documentation
4	MEDSEA_MULTIYEAR_WAV_006_012, numerical models	EU Copernicus Marine Service Product (2023b)	PUM: Denaxa et al. (2023) QUID: Zacharioudaki et al. (2023)

The Mediterranean Sea has long been recognised as a vulnerable climate change hot spot (Tuel and Eltahir, 2020), seriously jeopardised by marine pollution episodes or litter accumulation (Soussi et al., 2020; Ramirez-Llodra et al., 2013). This region is often affected by marine heat waves, mass mortality events, and violent hazards, ranging from storm surges and flash floods to rogue waves and medicanes (Dayan et al., 2023; Clementi et al., 2022; Garrabou et al., 2022; Milglietta and Rotunno, 2019; Wolff et al., 2018; Cavaleri et al., 2012). To serve as examples, Medicane Zorbas (2018) and Storm Gloria (2020) caused several casualties and multi-million-euro damage in susceptible coastal areas (Lorente et al., 2021; de Alfonso et al., 2021; Pérez-Gómez et al., 2021; Sotillo et al., 2021; Scicchitano et al., 2021).

Consequently, there is an increasing awareness not only of the potential anthropogenic influence on the intensity of these extreme weather episodes (Eyring et al., 2021) but also of the unavoidable need to gain deeper insight into the underlying physical processes, already identified as one of the World Climate Research Programme's Grand Challenges (WCRP website, 2024). The accurate monitoring of extreme events is crucial for implementing adaptation policies and adopting prevention strategies that should eventually result in the enhancement of coastal communities' resilience (Linnenluecke et al., 2012). In response to this requisite, successive editions of the Copernicus Ocean State Report initiative have traditionally placed special emphasis on the multi-parameter analysis of severe sea states previously occurring in the Mediterranean Basin (Álvarez-Fanjul et al., 2022; Clementi et al., 2022; Giesen et al., 2021; de Alfonso et al., 2020; Berta et al., 2020; Bensoussan et al., 2019; Notarstefano et al., 2019; Kokkini and Notarstefano, 2018).

Recent initiatives like ECCLIPSE (assEssment of CLImate change in Ports of Southwest Europe) Interreg Sudoe project (ECCLIPSE website, 2024) have focused on analysing the impact of climate change on seaports. Although this topic has historically received less consideration than the corresponding impact for beach systems (Sánchez-Arcilla et al., 2016a), the central role of ports in countries' growth and a globalised economy have motivated a plethora of new studies (Portillo Juan et al., 2022; Izaguirre et al., 2021), some of them devoted to the Mediterranean Sea (Sierra et al., 2015 and 2017; Sánchez-Arcilla et al., 2016b). In this sense, one of the main objectives of ECCLIPSE was to establish the fundamentals of a climate change observatory for Spanish ports, aimed at monitoring essential ocean variables and gaining a holistic understanding of violent weather from its physical drivers to its impact on port operability and infrastructure. Climate-driven extreme coastal hazards have been acknowledged as imposing heavy socio-economic tolls, as port downtime leads to a reduction in safety levels and wide trade losses due to the interruption of both the maritime transport and global supply-chain networks (Verschuur et al., 2022).

Following in the footprints of ECCLIPSE, this work attempts to characterise the record-breaking storm that hit the Alborán Sea (SW Mediterranean Sea; Fig. 1a) with wave heights above 7 m during 4–5 April 2022 and evaluate the energetic response of Melilla harbour basins (Fig. 1b) under the penetrating wave action. Port operations were disrupted as a precaution due to the prevailing harsh weather conditions and the violent overtopping of breakwaters. While one ship was evacuated from its berth and later sheltered at the lee of the Ras Taksefi cape (Fig. 1b), structural damages were reported in the seawall tip and in several boats and marina pontoons.

A retrospective comparison of the present study case to extreme wave events previously registered at the Melilla coastal buoy (Fig. 1b) during 2011–2022 was conducted not only to put the former into a broader historical context but also to disentangle their common driving mechanisms (i.e. the predominant atmospheric conditions on a synoptic scale). The return

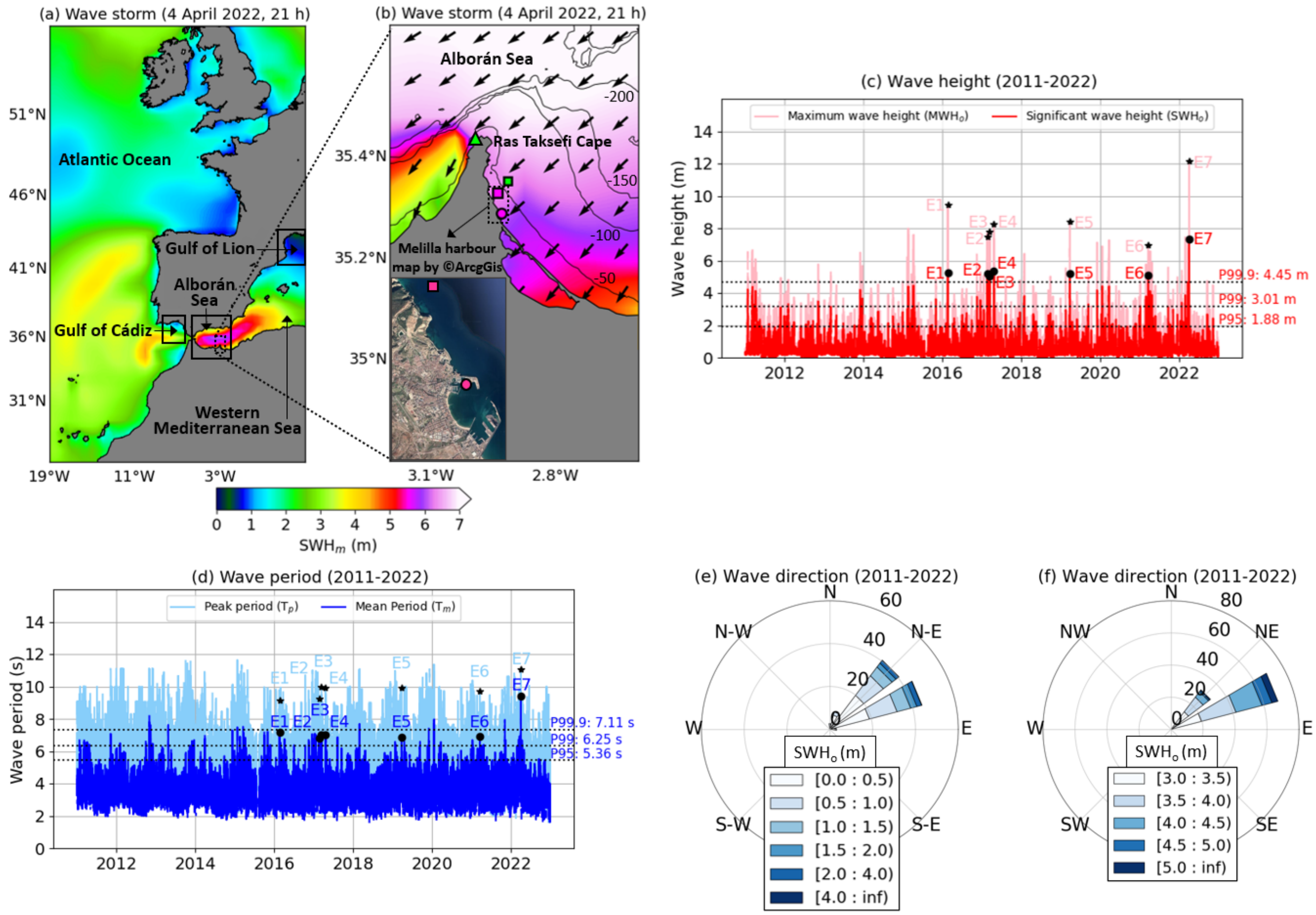

Figure 1. Wave storm in the SW Mediterranean Sea. **(a)** Hourly map (4 April 2022, 21:00 local time) of $\mathrm{SWH_m}$ on a synoptic scale during the peak storm as derived from ERA5 reanalysis (product ref. no. 3 in Table 1). **(b)** Hourly map of $\mathrm{SWH_m}$ and $\mathrm{MWD_m}$ on a coastal scale during the peak storm as derived from MED reanalysis (product ref. no. 4 in Table 1). Isobath depths are labelled every 50 m. The magenta dot and the magenta square represent the Melilla tide gauge and coastal buoy location, respectively. The green triangle and the green square indicate the location of the Ras Taksefi cape and the grid point of MED reanalysis closest to the Melilla coastal buoy, respectively. In the lower-left corner is the Melilla harbour configuration: map by © ArcGis. **(c)** Hourly time series of SWH_o and MWH_o recorded at the Melilla coastal buoy for 2011–2022 (product ref. no. 1 in Table 1). Black dots and stars indicate the seven extreme events examined, labelled from E1 to E7. The 99.9th (P99.9), 99th (P99), and 95th (P95) percentiles are represented by horizontal dotted black lines. **(d)** Hourly time series of T_m and T_p for 2011–2022 (product ref. no. 1 in Table 1). **(e)** Wave rose illustrating the main incoming directions (MWD_o) during 2011–2022 – product ref. no. 1 (Table 1). **(f)** Wave rose showing the MWD_o associated with SWH_o values above P99 (3.01 m) during 2011–2022.

period associated with these extreme wave episodes, which is defined as the average time interval between two consecutive events exceeding a specific wave height value, was also calculated. This concept is often used in marine engineering for the design of port facilities and the identification of dangerous events, providing a means for rational decision-making and risk assessment (Salvadori et al., 2013). For instance, harbour breakwaters are commonly designed to withstand 100-year-return-period metocean conditions without significant damage while having service lifetimes of similar durations (Todd et al., 2012; Gutiérrez-Serret et al., 2009).

Additionally, following the approach of Pérez-Gómez et al. (2021) for Storm Gloria (2020), high-frequency (2 Hz) sea level data and agitation observations provided by the Melilla tide gauge (Fig. 1b) during 2011–2022 were used to investigate the relationship between offshore energetic conditions and the sea state within the harbour. Precise estimations of agitation (i.e. oscillations within the port due to wind waves) are essential for downtime analysis and efficient port management (Romano-Moreno et al., 2022). Equally, infragravity (IG) waves with periods between 30 and 300 s (Bellafont, 2019; Elgar et al., 1992; Munk, 1950) were examined, since their presence in semi-closed ports of small to intermediate size (where the surface water area and depth are about 1–10 km^2 and 5–10 m, respectively) may cause excessive ship motions at berth and unacceptable forces on mooring lines and fenders that could result in ship collisions and significant damage to vessels and port facilities (Costas et al., 2022;

Bellotti and Franco, 2011). Under adverse circumstances, IG waves can be highly amplified by the basin geometry due to resonant processes (commonly referred to as seiches), resulting in large water level fluctuations and strong horizontal currents that disturb port operations (unsafe and inefficient cargo activities) and negatively impact cost–time efficiency (López and Iglesias, 2014; Okihiro et al., 1993).

Finally, a 30-year (1993–2022) regional wave reanalysis product developed in the framework of the Copernicus Marine Service for the Mediterranean Sea was analysed to characterise the spatiotemporal variability in the long-term extreme wave climate along the Alborán Sea. The intra-annual variability in the 99th percentile (P99 hereinafter) for the significant wave height was examined over this subregion on a monthly timescale to identify potential trends, thereby complementing similar studies previously focused on the intra-seasonal (Barbariol el al., 2021) or the inter-annual (Zacharioudaki et al., 2022; Morales-Márquez et al., 2020) climate variability in extreme waves in the entire Mediterranean Basin.

This work is structured as follows: Sect. 2 outlines the observational and modelled data sources. Section 3 describes the methodology adopted. Results are presented and discussed in Sect. 4. Finally, principal conclusions are drawn in Sect. 5.

2 Data

All the observational and modelled datasets used in this study are briefly described below. Complementary information about them is gathered in Tables 1 and 2.

2.1 In situ observational data

Although the two in situ instruments used in this work were deployed before 2009, the time span for the observational datasets was standardised to 2011–2022 for consistency reasons, as the collection of directional wave data started on April 2010 (Table 2).

2.1.1 Melilla coastal buoy

A Datawell scalar buoy was moored at 15 m depth in April 2008, close to Melilla harbour (Fig. 1b). It was replaced in April 2010 by a TRIAXYS buoy able to provide directional information. This in situ device, operated by Puertos del Estado, collects hourly averaged estimations of diverse wave parameters (product ref. no. 1 in Table 1), encompassing the significant wave height (SWH_o), maximum wave height (MWH_o), mean period (T_m), peak period (T_p), and incoming mean wave direction (MWD_o). The quality control applied to data time series, defined by the Copernicus Marine In situ Team (Copernicus Marine In Situ Team, 2020), consisted of a battery of automatic checks performed to flag and filter inconsistent values. For the Mediterranean Sea, the spike test was based on the difference between sequential measurements of SWH_o, T_m, and T_p so they were discarded, respectively, when the difference exceeded 3 m, 4 s, and 10 s. Occasional gaps (not larger than 6 h) were linearly interpolated to ensure the continuity of the records.

2.1.2 Melilla port tide gauge

A radar tide gauge, manufactured by Miros and operated by Puertos del Estado as part of its REDMAR network (Pérez-Gómez et al., 2008 and 2014), was deployed inside of Melilla harbour in October 2007 (Fig. 1b). Quality-controlled 2 Hz sea level data (product ref. no. 2 in Table 1) contain information on sea level oscillations with periods above 1 s, capturing all sea surface height variability including waves, high-frequency sea level oscillations (HFSLOs), and tides. Sea level oscillations with periods over 1 h were extracted using a 10th-order Chebyshev low-pass filter with a cut frequency of $1/3600$, whereas wave agitation (with periods below 30 s) was obtained using an 8th-order Butterworth high-pass digital filter with a cut frequency of $1/30$. HFSLOs (with periods between 30 s and 1 h) were obtained by subtracting the two previous time series from the raw 2 Hz data signal. Then, a simplified four-band energy spectrum was also calculated to facilitate the understanding of the energy distribution in the HFSLO band: (i) the period between 30 s and 5 min (IG waves), (ii) the period between 5 and 15 min, (iii) the period between 15 and 30 min, and (iv) the period between 30 min and 1 h. For further details about the frequency domain analysis (used to describe how energy is distributed among all frequencies and to determine the most energetic frequency on an hourly basis) and time domain analysis (used to determine the hourly amplitudes of the HFSLO, where the maximum is denoted by $\mathrm{HFSLO}_\mathrm{max}$ and the average of the highest-third heights is denoted by HFSLO_{13}), the reader is referred to García-Valdecasas et al. (2021). Finally, 20 min estimations of $\mathrm{HFSLO}_\mathrm{max}$, HFSLO_{13}, IG wave energy (IGE), and agitation were subsampled at hourly intervals (Table 2) and examined to assess the impact of extreme wave storms inside the harbour. Likewise, hourly estimations of total water fluctuations, astronomical tides, and storm surge component were qualitatively analysed to infer any potential sea level rise that could take place simultaneously (or in close sequence) with the extreme wave storms.

2.2 Modelled data

The time span for the modelled datasets was standardised to 1993–2022 for consistency reasons (Table 2).

2.2.1 ERA5 reanalysis

ERA5 reanalysis (product ref. no. 3 in Table 1), which is generated by the European Centre for Medium-Range Weather Forecasts (ECMWF), provides hourly estimates from 1940

Table 2. Complementary information about the data sources used in this study.

Source (product ref.)	Type	Location (coverage)	Variable (unit)	Temporal resolution	Time span used	Spatial resolution
In situ sensor (1)	Buoy	Coastal location (2.94° W–35.33° N)	SWH_o (m) MWH_o (m) T_m (s) T_p (s) MWD_o (°)	Hourly	2011–2022	Point-wise location
In situ sensor (2)	Tide gauge	Port location (2.93° W–35.29° N)	Agitation (m) $HFSLO_{13}$ (m) $HFSLO_{max}$ (m) IGE (m^2 s)	Hourly	2011–2022	Point-wise location
Numerical model (3)	ERA5 reanalysis	Regional domain (19° W–5° E 26–56° N)	SLP (Pa) W10 ($m\,s^{-1}$) SWH_m (m)	Hourly	1993–2022	0.25° 0.25° 0.5°
Numerical model (4)	MED reanalysis	Subregional domain (6–1° W 35–37° N)	SWH_m (m) MWD_m (°)	Hourly	1993–2022	1/24°

onwards for a large number of atmospheric and oceanic parameters which are regridded, respectively, to a 0.25 and 0.5° regular grid. In this work, hourly maps of modelled sea level pressure (SLP), wind at 10 m height (W10), and significant wave height (SWH_m) were analysed on a synoptic scale (26–56° N, 19° W–5° E) for the 1993–2022 period (Table 2) in order to disentangle the common atmospheric configurations that drove the most extreme wave events registered by the Melilla buoy.

2.2.2 Multi-year wave product

The multi-year wave product of the Mediterranean Sea Waves forecasting system (product ref. no. 4 in Table 1) is based on a Wave Model (WAM) suite that predicts hourly wave parameters at a 1/24° horizontal grid resolution. The atmospheric wind forcing used in WAM consists of hourly 0.25° horizontal-resolution ERA5 reanalysis from the ECMWF. The multi-year product consists of a reanalysis dataset (MED reanalysis hereinafter), which spans 1 January 1993 to 31 December 2022, and an interim dataset covering the period after the reanalysis until 1 month before the present. In the present work, only the MED reanalysis was used: hourly SWH_m estimations were examined for the selected 30-year period (Table 2) to characterise the spatiotemporal variability in the long-term extreme wave climate affecting the Alborán Sea in general and specifically the Melilla harbour area. Equally, hourly maps of propagation direction (MWD_m) were depicted to assess the prevalent wave directionality during the extreme events.

3 Methodology

As not all extreme metocean hazards necessarily have destructive impacts on coastal areas, there is not a worldwide consensus on the protocol for their categorisation (Radovic and Iglesias, 2018). In this work, the 99.9th percentile (P99.9 hereinafter) of SWH_o for the 12-year time series (2011–2022) provided by the Melilla coastal buoy was used as a threshold to select and chronologically tag a manageable number of extreme wave events that previously occurred. Once shortlisted, these episodes were characterised in terms of intensity (magnitude of diverse wave parameters) and duration (hours above the P99 of SWH_o), placing the focus on the joint occurrence of interconnected extremes that might exacerbate the coastal impact compared to individual hazards occurring in isolation. Complementarily, hourly maps of SWH_m were depicted to explore if the extreme wave events shared similar synoptic features in terms of severity and spatial distribution.

In order to elucidate the potential existence of a common driving mechanism, the predominant atmospheric conditions (in terms of SLP and W10) on a synoptic scale that led to the record-breaking storm were retrospectively compared to those giving rise to previous extreme wave events. Additionally, the temporal distribution of extreme hourly wave data (above P99) affecting the Melilla area was derived from the 12-year observational time series of SWH_o and T_m to elucidate if they showed a relevant preference for a specific stage of the year. The annual cycle was split into six evenly spaced 50 d intervals and a longer 65 d summertime interval that did not negatively impact the consistency of the percentages of occurrence obtained, as extreme wave events during summer remained marginal regardless of the interval length selected.

The return period associated with these extreme wave episodes was derived from hourly time series of SWH_o for two different periods: 2011–2021 (before the record-breaking storm) and 2011–2022 (including the storm). For this purpose, we assumed the following:

i. An exceedance threshold based on the 95th percentile (P95) value of the dataset following the approach proposed by Harley (2017) and Fanti et al. (2023) for coastal storm analysis.

ii. A distance of 5 d between two independent storms. Although there is some subjectivity in how a time series is partitioned into separate storms, the broadly accepted criteria state that the independence between consecutive events is achieved by imposing the separation of storm peaks by a time period longer than 3 d, which is the average lifetime of extra-tropical cyclones (Trigo et al., 1999). For instance, the most intense activity period of Storm Gloria in the western Mediterranean Sea was between 20 and 23 January 2020 (Amores et al., 2020; Lorente et al., 2021). Since adjacent peaks separated by 5 d will correspond to waves generated from different low-pressure systems, meteorologically independent events were identified by applying a moving time window of 5 d length between consecutive storms, in accordance with Mackay and Johanning (2018a and b).

The long-term extreme sea state was characterised by using the Peaks-Over-Threshold (POT) method (Goda, 1988) with the fitting of a three-parameter Weibull probability distribution to the SWH_o observations. The POT method is based on extracting, from the recorded time series, those individual storms which surpass the aforementioned exceedance threshold of SWH_o at the peak of the storm and are not dependent upon another one due to their proximity in time. The three-parameter Weibull distribution was computed following the approach proposed by de Alfonso et al. (2021) to obtain the return period for the maximum SWH_o registered during the selected extreme wave events.

Furthermore, the relationship between offshore sea states and IG waves within Melilla harbour was investigated. Here we focused on the most common type of IG waves: those induced by the non-linear interactions between incident wind short waves (Belloti and Franco, 2011). While IG waves tend to elude human perception in deep waters (heights of the order of a few centimetres), they can abruptly increase near the coastline and even exceed 1 m (Aucan and Ardhuin, 2013), contributing significantly to nearshore processes (beach erosion) and affecting coastal structures (Okihiro et al., 1993). Significant efforts have previously been devoted to analysing the connection between offshore wave parameters and IGE, either at the shore (in the form of run-up) or in the nearshore area (surf zone). While Guza and Thornton (1982) found that the IG component of wave run-up increased linearly with increasing offshore SWH_o, Stockdon et al. (2006) concluded that the IG component scaled better with $\mathrm{SWH}_o \cdot L$ (where L represents the deep-water wavelength) and was actually independent of the foreshore slope. In the same vein, Senechal et al. (2011) reported that IG wave run-up during extreme storm conditions was significantly less scattered when correlated with $\mathrm{SWH}_o \cdot L$ than with SWH_o only. By contrast, Inch et al. (2017) reported that nearshore IG waves were best predicted using an offshore forcing parameter that is proportional to $\mathrm{SWH}_o^2 \cdot T_\mathrm{p}$. These contradictory findings reveal that further research on the subject is required and suggest that nearshore IGE is unlikely to be a function of any single environmental factor (Lashley et al., 2020).

While the four aforementioned field studies focused on low-sloping to mildly sloping sandy beaches, the present work attempts to relate IGE measured within a harbour with offshore wave parameters. To this aim, a rough approximation approach (based on three simplifications) was adopted:

i. Local slope effects were not included, similarly to Stockdon et al. (2006).

ii. IGE registered at the Melilla tide gauge was scaled with SWH_o^2, $\mathrm{SWH}_o \cdot L$, and $\mathrm{SWH}_o^2 \cdot T_\mathrm{p}$ despite the fact that IGE is affected by wave–structure interaction processes (diffraction and reflection, to name the main ones) which are not so relevant on open sandy beaches.

iii. Although the Melilla coastal buoy is moored at 15 m depth (d), the deep-water approximation is broadly accepted since the relative depth (defined as d/L) is above 0.5 for 78 % of the time during 2011–2022 (not shown). Therefore, the wavelength can be defined as $L = (g \cdot T_\mathrm{m}^2)/2\pi$, where the gravity acceleration g is $9.8\,\mathrm{m\,s^{-2}}$. As a consequence, we can derive from point (ii) that IGE was scaled with SWH_o^2, $\mathrm{SWH}_o \cdot T_\mathrm{m}^2$, and $\mathrm{SWH}_o^2 \cdot T_\mathrm{p}$.

Additionally, HFSLO (with periods between 30 s and 1 h) and harbour agitation (with periods below 30 s) data recorded by the Melilla tide gauge during 2011–2022 were thoroughly examined. On the one hand, HFSLO heights observed during the selected extreme events were categorised based on specific IG wave thresholds which are universally common to all locations (McComb et al., 2020; McComb, 2011). This approach is valid since spectra of the 2 Hz data (not shown), generated to identify energetic sea level variability inside the port, were dominated by energy in the IG band during these storms. On the other hand, total seawater levels were examined to disentangle if they exerted a relevant role in the sharp increase in harbour agitation during the extreme wave events and if astronomical tides were thereby enhanced by storm surge effects. In this context, connected extremes are of particular concern for harbour operability, as their individual effects may interact synergistically and cause more damage in port structures than isolated extreme events do (Velpuri et al., 2023).

Finally, potential long-term changes in the extreme sea state climate during the 30-year period analysed (1993–2022) were assessed over the Alborán Sea. As a preliminary step, the accuracy of MED reanalysis was evaluated at the grid point 35.354° N, 2.916° W (denoted by a green rectangle in Fig. 1b) closest to the Melilla coastal buoy and located at a distance of 3450 m. Concurrent estimations of hourly SWH_o and SWH_m were compared for the period 2011–2022, and the best linear fit of the scatter plot was computed. The statistical metrics used in the present study to compare two datasets included the mean, the standard deviation, and the Pearson correlation coefficient (Emery and Thompson, 2001). Afterwards, maps of linear trend for the P99 of SWH_m were obtained over the entire Alborán Sea on a monthly timescale. The attention was particularly focused on the intra-annual variability in order to complement prior research dealing with intra-seasonal and inter-annual variability in extreme waves in the entire Mediterranean Basin (Amarouche et al., 2022a; Barbariol el al., 2021; Zacharioudaki et al., 2022; Morales-Márquez et al., 2020). The presence of temporal trends in the P99 of SWH_m time series was evaluated with two well-known non-parametric tests, which have been recently documented as the most used for trend detection in the Mediterranean Sea (De Leo et al., 2023).

i. Trends were calculated using the Sen's slope estimator of P99 because it is not subject to the influence of extreme values (outliers); therefore, it is more consistent than simple linear regression methods (Sen, 1968). Although P95 is also commonly used (Fanti et al., 2023), P99 was selected as the reference percentile for the most extreme wave events affecting the Melilla area, in agreement with previous approaches reported in the literature (Zacharioudaki et al., 2022; Barbariol et al., 2021).

ii. The statistical significance at the 90 % confidence interval was assessed at each grid point with the Mann–Kendall test (Mann, 1945; Kendall, 1962), in accordance with similar works previously published (Caloiero and Aristodemo, 2021; Barbariol et al., 2021). Afterwards, a specific subdomain (35.02–35.48° N, 2.70–3.00° W) in the vicinity of Melilla harbour was selected, and the statistical significance was spatially averaged to infer if this area is affected by meaningful trends.

4 Results

4.1 Extreme events analysis

The P99.9 of SWH_o (set to 4.45 m and derived from the 12-year time series provided by the Melilla coastal buoy) was used as a threshold to detect the most extreme wave events (Fig. 1c). A total of seven storms were identified and tagged chronologically from E1 to E7. They presented values ranging from 5.05 (E3) to 7.32 m (E7), as shown in Table 3. The associated T_m values, which ranged from 6.83 (E2) to 9.42 s (E7), surpassed the P99 (set to 6.25 s; Fig. 1d). The seven episodes also showed concurrent high values of MWH_o and T_p, emerging in the ranges 6.83–12.11 m and 9.13–10.75 s, respectively (Table 3). The storm that hit Melilla harbour during 4–5 April 2022 (E7) exhibited unprecedented values for each wave parameter: the peak of SWH_o (7.32 m) was coincident with the greatest values of MWH_o (12.11 m) and T_m (9.42 s), jointly beating all previous historical records (Fig. 1c–d). In terms of storm duration (Table 3), defined as the number of consecutive hours above the P99 of SWH_o (set to 3.01 m), E1 and E6 were significantly shorter (<20 h) than the long-lasting E2 and E4 events (>50 h). The duration of the E3 and E5 (27–31 h) events can be considered similar to E7 (37 h). From a directional perspective, the prevailing incoming wave directions during 2011–2022 were NE (41 %) and NE–E (43 %), with an overall associated mean value of 58° ± 37° (Fig. 1e). These are the most common origins of waves recorded at the Melilla coastal buoy due to its particular emplacement, sheltered to the east of the Ras Taksefi cape (Fig. 1b). As a result, the shadow effect of this coastal promontory prevents the angular spreading of the storms coming from the westernmost sector. For extreme wave events with SWH_o above P99 (3.01 m), the predominant incoming wave direction was NE–E with 72 % of occurrence, whereas the remaining 28 % corresponded to the NE sector (Fig. 1f).

Hourly maps of SWH_m for E1–E6 events (Fig. A1) and E7 (Fig. 1a) shared common synoptic features such as the peak of SWH_m (above 4.5 m) over the entire Alborán Sea. A secondary peak could be found over the Gulf of Cádiz for the E1, E2, E4, E5, and E7 episodes, while E3 barely showed it. In the case of the E6 event, the peak of SWH_m over the easternmost part of the Alborán Sea was not so high (around 4 m) but affected broader areas of the SW Mediterranean Sea. The spatial patterns of SWH_m and MWD_m, zoomed in on the areas surrounding Melilla harbour (small maps in the lower-right corner of each panel in Fig. A1), revealed a similar visual resemblance for SWH_m and a uniform MWD_m field from the NE. The record-breaking E7 event stood out from the rest due to the severity of the storm, with SWH_m above 5.5 m over the entire Alborán Sea (Fig. 1a) but also in the vicinity of Melilla harbour (Fig. 1b).

4.2 Return period analysis

For the period 2011–2021, the entire hourly time series of SWH_o was fitted to a three-parameter Weibull distribution, leading to return periods of 3.25–4.51 years for the extreme wave events E1 to E6 (Table 4). However, the E7 event was associated with a 53-year return period which highlights the extraordinary magnitude of this twice-in-a-century high-impact episode. For the period 2011–2022, which already included the record-breaking E7 storm (April 2022), a new fitting of the three-parameter Weibull probability distribution to the SWH_o observations was performed, and the associated Weibull parameters (threshold, scale, and shape) were updated (Table 4). Results revealed that the return period related to the E1 to E6 events decreased by 17 %–22 % to

Table 3. Characterisation of the seven most extreme wave events registered by the Melilla coastal buoy during the 12-year period analysed (2011–2022).

Event	Date YYYY-MM-DD (hh:mm)	SWH_o (m)	Time above P99 (h)*	MWH_o (m)	Mean period (s)	Peak period (s)	Mean direction (°)
E1	2016-02-21 (00:00)	5.25	16	9.46	7.15	9.13	63
E2	2017-02-21 (01:00)	5.21	57	7.22	6.83	9.25	66
E3	2017-03-15 (01:00)	5.05	27	7.79	6.99	9.98	51
E4	2017-04-21 (15:00)	5.36	58	6.97	7.03	9.34	69
E5	2019-03-27 (00:00)	5.21	31	8.03	6.88	9.91	69
E6	2021-03-20 (21:00)	5.09	14	6.83	6.91	9.69	55
E7	2022-04-04 (21:00)	7.32	37	12.11	9.42	10.75	55

* Consecutive hours above the 99th percentile of SWH_o.

2.69–3.51 years, while the updated E7 return period dropped by 53 % from 53 years to 25 years. These relevant outcomes should be applicable in the design and construction of new facilities at Melilla harbour and also integrated into the port operations planning and day-to-day logistics activities.

4.3 Driving atmospheric conditions

The prevailing atmospheric conditions on a synoptic scale during the seven extreme wave storms were inferred from the ERA5 reanalysis of SLP and W10. The SLP map for the E7 event (Fig. 2a) exhibited the so-called hybrid Rex block (Sousa et al., 2021; Lupo, 2021; Rex, 1950), a large-scale blocking pattern characterised by two adjacent (northwestern) high- and (southeastern) low-pressure systems. This type of blocking is usual during the transition phase from an omega block (midlatitude high-pressure centre surrounded by two low-pressure systems on its western and eastern flanks) to a pure Rex shape (a north–south dipole pattern of SLP). Blocking episodes in Europe have long been acknowledged as persistent atmospheric disturbances that can lead to weather extremes (Kautz et al., 2022). As a consequence, this dipole was visible for the whole investigation period, whereas it followed a clockwise rotation. The derived pressure gradient (above $2\,\mathrm{Pa\,km^{-1}}$) gave rise to very strong northeasterly winds (above $20\,\mathrm{m\,s^{-1}}$) that affected broad areas of the SW Mediterranean and Alborán seas, while extremely intense easterlies were channelled through the Strait of Gibraltar due to its specific geometric configuration (Fig. 2b). In the Gulf of Cádiz (denoted in Fig. 1a), the wind field exhibited an anticlockwise rotation around the low-pressure core.

The analysis of the six previous extreme events revealed that all of them shared very similar meteorological conditions: (i) a northwestern–southeastern hybrid Rex pattern of SLP anomalies (Fig. A2), in contrast to the climatological mean (Fig. 2c) that shows two well-known semi-permanent pressure systems (i.e. the Azores High at middle latitudes and the Icelandic Low at subpolar latitudes), and (ii) a peak of wind speed ($>15\,\mathrm{m\,s^{-1}}$) over the entire Alborán Sea, where easterlies blew strongly along both sides of the Strait of Gibraltar (Fig. A3). Only the event E6 showed a slightly different structure (Fig. A3f), with moderately strong winds (13–$15\,\mathrm{m\,s^{-1}}$) blowing from the NE and massively affecting the entire western Mediterranean Sea. In terms of persistence, intense winds steadily affected the study area for 1–2.5 d, except in the case of the E1 and E6 events where the duration was shorter (14–16 h), as derived indirectly from the time that the SWH_o consecutively exceeded the P99 (Table 3).

The primary factors that jointly triggered the record-breaking E7 wave storm were the short distance (1400 km) between the two main pressure systems and the relatively deep (below 1000 hPa) system of low pressures over the Gulf of Cádiz (Fig. 2a). The resulting SLP gradient was anomalously powerful (above $2\,\mathrm{Pa\,km^{-1}}$), leading to very strong easterlies (up to $20\,\mathrm{m\,s^{-1}}$, as shown in Fig. 2b) that ultimately induced high (~ 6 m) waves over the entire Alborán Sea (Fig. 1a).

The previous six episodes also presented intense (albeit 25 %–50 % weaker) SLP gradients, ranging from $1.01\,\mathrm{Pa\,km^{-1}}$ (E4; Fig. A2d) to $1.48\,\mathrm{Pa\,km^{-1}}$ (E6; Fig. A2f), due to the usually longer distances (ranging from 1900 to 3000 km) between the two pressure systems (Fig. A2). Although the E1 event exhibited SLP cores with similar separation (1438 km, shown in Fig. A2a), the low-pressure system was not so deep (1016 hPa), in contrast to the E7 event where minimum SLP values dropped below 1000 hPa (Fig. 2a).

Finally, it should be noted that the seven extreme episodes took place during the same stage of the year, a 50 d period between late February and early April (Fig. 2d and Table 3). Therefore, it might be deduced that large-scale atmospheric blocks leading to severe sea states (above the P99 of SWH_o and T_m) in Melilla tend to be more probable during the winter-to-spring transition period, in agreement with previous blocking climatologies for the eastern North Atlantic (Kautz et al., 2022; Barriopedro et al., 2006).

Table 4. Return period computed for two different periods, as derived from hourly in situ observations from the Melilla coastal buoy. The long-term extreme sea state was characterised by using the POT method with the fitting of a three-parameter Weibull probability distribution to the observed significant wave height (SWH_o).

Parameter	2011–2021	2011–2022	Decrease
Weibull parameter: threshold (or location)	1.82	1.88	–
Weibull parameter: scale	1.19	1.10	–
Weibull parameter: shape (or Weibull slope)	1.20	1.07	–
Return period for events with $\mathrm{SWH}_o = 3\,\mathrm{m}$	1.02 years	1.02 years	0.00 %
Return period for events with $\mathrm{SWH}_o = 4\,\mathrm{m}$	1.38 years	1.34 years	2.89 %
Return period for events with $\mathrm{SWH}_o = 5\,\mathrm{m}$	3.09 years	2.59 years	16.18 %
Return period for E1 extreme event ($\mathrm{SWH}_o = 5.25\,\mathrm{m}$)	4.00 years	3.19 years	20.25 %
Return period for E2 extreme event ($\mathrm{SWH}_o = 5.21\,\mathrm{m}$)	3.83 years	3.08 years	19.58 %
Return period for E3 extreme event ($\mathrm{SWH}_o = 5.05\,\mathrm{m}$)	3.25 years	2.69 years	17.23 %
Return period for E4 extreme event ($\mathrm{SWH}_o = 5.36\,\mathrm{m}$)	4.51 years	3.51 years	22.17 %
Return period for E5 extreme event ($\mathrm{SWH}_o = 5.21\,\mathrm{m}$)	3.83 years	3.08 years	19.58 %
Return period for E6 extreme event ($\mathrm{SWH}_o = 5.09\,\mathrm{m}$)	3.38 years	2.78 years	17.75 %
Return period for E7 extreme event ($\mathrm{SWH}_o = 7.32\,\mathrm{m}$)	53.06 years	24.91 years	53.23 %

4.4 Sea state within the port

An accurate estimation of the historical harbour wave agitation is fundamental for many practical applications such as port downtime analysis (Romano-Moreno et al., 2022). The analysis of hourly time series of agitation provided by the Melilla tide gauge revealed that there was a record-breaking value during the E7 event (1.41 m; Fig. 2e), while the six previous events also exceeded the P99.9 threshold (0.56 m; Fig. 3a). The agitation response is usually determined by wave penetration into the harbour arising from the combination of diverse parameters: SWH_o, T_m, MWD_o, astronomical tide, and storm surge outside the port (Camus et al., 2018). As shown in Figs. 2e and A4, the impact of the last two elements on harbour agitation during the seven extreme events was negligible due to a number of factors: (i) Melilla harbour waters are characterised by a maximum tidal range of 0.40 m; (ii) for each extreme event, the evolution of harbour agitation was independent from the tidal phase as the peak of agitation was not coincident with high tides; (iii) during E7, the low-pressure core ($\sim 1000\,\mathrm{hPa}$) was located in the Gulf of Cádiz (western side of the Strait of Gibraltar; Fig. 2a), so the storm surge affecting Melilla harbour was small ($\sim 5\,\mathrm{cm}$; Fig. 2e); and (iv) during the previous six extreme events (E1–E6), the meteorological residual was even negative (Fig. A4), ranging from -2 (E3) to $-14\,\mathrm{cm}$ (E2).

Hourly scatter plots evidenced the strong relationship between the agitation inside the port and the wave conditions outside the port registered by the Melilla coastal buoy (Fig. 3b–d). The best linear fit of the scatter plot between the agitation and SWH_o revealed a significantly high correlation coefficient (0.87). During the 12-year period analysed (2011–2022), there were 967 hourly agitation values above the P99 threshold (0.36 m): 89 % of them were associated with waves coming from the predominant sector between 50 and 70° (clockwise from true north), while 6 % of them were related to incoming waves with angles emerging from 70 to 90° (Fig. 3b). The remaining 5 % were assigned to waves with an angular spread ranging from 30 to 50°. Therefore, the overall agitation is direction-dependent due to the harbour orientation (Fig. 1b) and its inherent structural design (mouth width, port layout configuration, etc.). Additionally, harbour agitation was also importantly modulated by offshore period, as shown in Fig. 3c–d. Agitation values above the P99 were generally observed when T_m and T_p values were above 4 and 6 s, respectively. Equally, the highest values of agitation (above 1 m height) were associated with T_m and T_p values above 7 and 10 s, respectively. It seems reasonable to deduce that the record-breaking harbour agitation (1.41 m) registered during the E7 event was caused by the combined effect of unprecedented values of SWH_o (7.32 m), MWH_o (12.11 m), and T_m (9.42 s) in tandem with a very high value of T_p (10.75 s) and a MWD_o (55°) within the predominant angular sector (50–70°) previously mentioned.

Operational thresholds in the IG band, which are common to all locations, have been historically proposed for safe conditions during port operations (McComb et al., 2020; McComb, 2011). Since the spectra of 2 Hz sea level oscillations measured inside the harbour by the Melilla tide gauge (not shown) revealed a high energy content in the IG band during the seven storms, HFSLO_{13} values registered during the seven extreme events (which contained not only the predominant contribution of oscillations in the IG band but also of oscillations with periods between 5 min–1 h) were categorised according to this methodology (Fig. 3e). The exploration of hourly time series of HFSLO_{13} showed that the E1 and E6 events surpassed the 0.15 m threshold (denoted as “extreme caution” in Fig. 3e), while the remaining five events also exceeded the “danger” threshold (0.20 m), with an unprecedented value of 0.31 m during the E7 episode. Likewise,

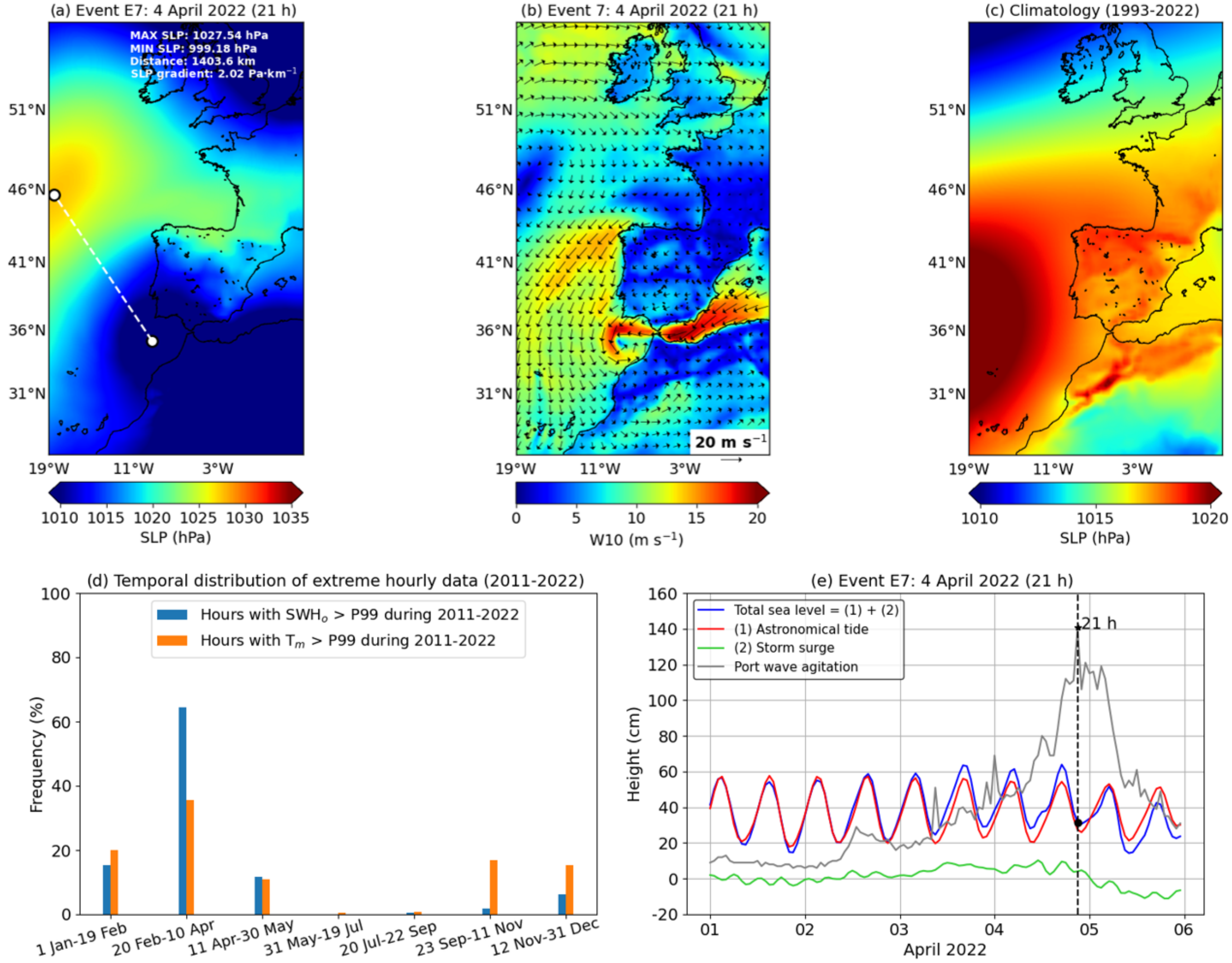

Figure 2. **(a–b)** Hourly synoptic patterns of sea level pressure (SLP) and wind at 10 m height (W10) during the extreme event E7. **(c)** Climatology (1993–2022) of SLP. Maps derived from ERA5 reanalysis (product ref. no. 3 in Table 1). **(d)** Bar diagram with the temporal distribution of hourly data (significant wave height, SWH_o, and mean wave period, T_m) above the 99th percentile (P99) derived from the 12-year time series (2011–2022) provided by the Melilla coastal buoy (product ref. no. 1 in Table 1). The annual time span was divided into seven 50 d periods, except period 5 (20 July–22 September), which is composed of 65 d. **(e)** Time series of total sea level height (blue line) and port agitation (black line) observations during the E7 extreme event as provided by the Melilla tide gauge (product ref. no. 2 in Table 1). Astronomical tides and storm surge component (meteorological residuals) are represented by the red and green lines, respectively. The vertical dashed black line indicates the peak of E7 wave storm.

hourly values of $HFSLO_{max}$ clearly went beyond 0.35 m during the extreme episodes, reaching the record-breaking value of 0.58 m during the E7 event. Furthermore, IGE was scaled with SWH_o^2, $SWH_o \cdot T_m^2$, and $SWH_o^2 \cdot T_p$ (Fig. 3f–h). The best linear fit of each scatter plot showed very high correlations: 0.94, 0.93, and 0.96, respectively. Therefore, IGE was best predicted using an offshore forcing parameter that is proportional to $SWH_o^2 \cdot T_p$, in accordance with Inch et al. (2017). As expected, the highest IGE values (above 1500 m^2 s) were observed for energetic swell waves with SWH_o and T_p above 5 m and 10 s, respectively.

4.5 Trends in extreme wave climate

The evolution of the extreme wave conditions over the Alborán Sea during the 30-year period analysed (1993–2022) was assessed. As a preliminary step, SWH_m estimations from MED reanalysis were compared with hourly in situ SWH_o observations provided by the Melilla coastal buoy during the concurrent 12-year period (2011–2022). To this aim, the MED reanalysis grid point (35.354° N, 2.916° W) closest to the moored buoy (located at a distance of 3450 m) was selected, and both time series were compared. A significantly high correlation coefficient (0.96) for a set of 77 100 hourly

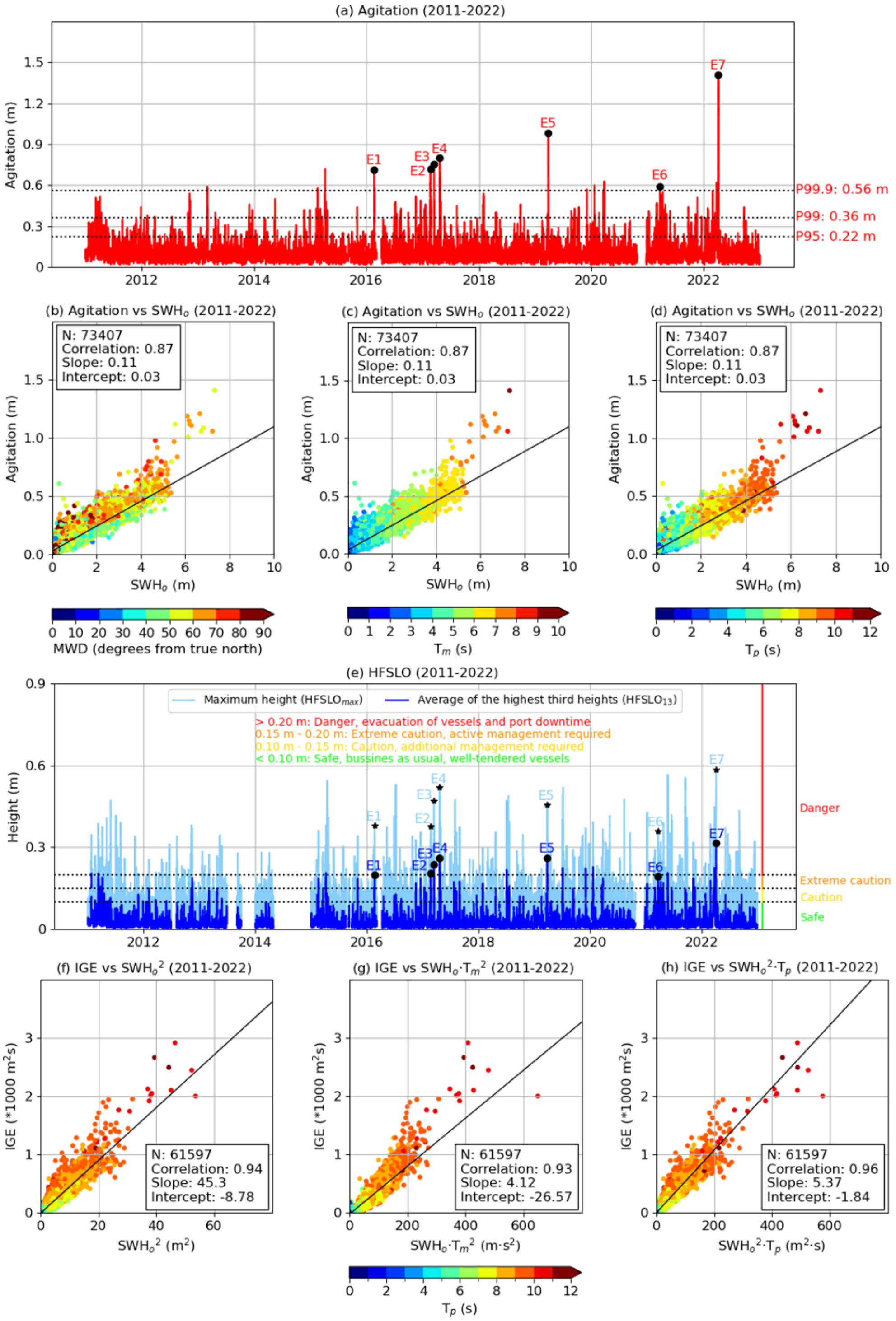

Figure 3. **(a)** Hourly time series of agitation inside the harbour for the period 2011–2022 (product ref. no. 2 in Table 1) as provided by the Melilla tide gauge. **(b–d)** Best linear fit (solid black line) of scatter plots of the harbour agitation against SWH_o observations provided by the Melilla coastal buoy. Statistical metrics are presented in the white box, where N represents the number of hourly observations. **(e)** Hourly time series of high-frequency sea level oscillations (HFSLO) with periods between 30 s and 1 h: maximum height (cyan line) and average of the highest-third heights (blue line) for the period 2011–2022 (product ref. no. 2 in Table 1), as registered by the Melilla tide gauge. The seven extreme events analysed in this work are denoted by black stars and dots. Thresholds for port management, which are universally common to all locations (McComb et al., 2020; McComb, 2011), are indicated with horizontal dotted lines. **(f–h)** Best linear fit (solid black line) of scatter plots of the energy in the IG band (IGE) against offshore wave observations from the Melilla coastal buoy.

data was derived from the best linear fit of the scatter plot (Fig. A5a). Equally, the slope and intercept values were close to 1 (0.85) and moderately low (0.15), respectively.

These results revealed that MED reanalysis, albeit accurate in the Melilla region, seems to underestimate SWH_o, especially for extreme waves. Such systematic underestimation has been previously reported for the entire domain (Fanti et al., 2023; Zacharioudaki et al., 2022), since shallow water processes cannot properly be captured by global and regional reanalysis, because (i) the coastline and the bottom topography are not well resolved as the grid mesh is too coarse, (ii) there are fetch limitations, and (iii) there are inherent uncertainties in the wind field used to force the wave model. These limitations are even more pronounced in regions with complex coastal configurations (sheltered by islands, headlands, and reefs) and in port-approach areas where sharp topo-bathymetric gradients pose special difficulties for accurate local predictions (Sánchez-Arcilla et al., 2016a). Nevertheless, according to Zacharioudaki et al. (2022), the reanalysis skill can be considered robust and good enough to conduct further investigations into the wave climate affecting the Melilla area and the related intra-annual variability in the Alborán Sea.

Thus, the monthly P50 and P99 of $\mathrm{SWH_m}$ were computed over the entire Alborán Sea for the 1993–2022 period (Fig. A5b–e). In particular, we selected only April and July as representative months of the stormy and calm seasons, respectively. According to homogeneous spatial patterns of P50, the mean wave climate is rather similar for April and July, only differing in the magnitude: while April is characterised by a P50 slightly above 1.1 m over Alborán open waters (Fig. A5b), P50 is around 0.7–0.8 m in July (Fig. A5c). By contrast, significant differences can be found in the most energetic sea states (Fig. A5d–e). In April, the P99 values around Melilla are up to 3 m, while they reach 4 m offshore (Fig. A5d). Peaks of 4.3 m are attained in the easternmost sub-basin, probably as a consequence of strong easterly winds. On the contrary, during July the largest P99 barely reaches 3 m in the central part of Alborán Sea, while the spatial distribution of P99 generally remains uniformly below 2 m in the rest of the spatial domain, including littoral areas and nearby regions of Melilla harbour (Fig. A5e).

The climate variability over the Alborán Sea was assessed by analysing the intra-annual variations in the extreme $\mathrm{SWH_m}$ conditions (Fig. 4). Monthly trend maps of P99 were calculated for the period 1993–2022, revealing statistically significant changes in the vicinity of Melilla harbour for a few specific months: while an increase of $2\,\mathrm{cm\,year^{-1}}$ was observed for April (Fig. 4a), a downward P99 trend of 1.5–$2\,\mathrm{cm\,year^{-1}}$ was detected for June (Fig. 4b) and October (Fig. 4c). The temporal trends for each month (Fig. 4d–f), computed over the subdomain surrounding Melilla harbour (black box in Fig. 4a–c), visually supported the previous statement: the trends were statistically significant at the 90 % confidence interval for April, June, and October. By contrast, during both the second part of summer (July–September) and the transitional season (November–February), monthly maps of P99 trends (not shown) did not exhibit statistically significant values over the entire Alborán Sea. The trend map of P99 for March and May (not shown) showed large areas with positive trends and negative trends, respectively, but delimited over the easternmost part (2–1° W) of the Alborán basin.

The long-term changes detected in the extreme wave climate over Melilla are, to a certain extent, comparable to those previously exposed by Barbariol et al. (2021). Although the wave reanalysis used and its associated temporal coverage (1980–2019) were different, this previous work reported both an upward trend for the P99 of $\mathrm{SWH_m}$ (about 0.8–$1.2\,\mathrm{cm\,year^{-1}}$) and a non-significant trend in the vicinity of Melilla harbour for the extended winter (defined as NDJFM) and for summer (defined as JJA), respectively. From a broader perspective focused on the entire western Mediterranean Sea, Barbariol et al. (2021) also documented a relevant positive trend ($1.2\,\mathrm{cm\,year^{-1}}$) during winter in the Gulf of Lion (denoted in Fig. 1a) due to strong northwesterly mistral winds. By contrast, Amarouche et al. (2022b) examined a 41-year (1979–2020) hindcast database and determined that the west coast of the Gulf of Lion was affected by a significant upward trend for all seasons, with a considerable annual increase ($4\,\mathrm{cm\,year^{-1}}$) in maximum values of $\mathrm{SWH_m}$. Complementarily, Amarouche et al. (2022a) demonstrated significant decadal increases in wave storm intensity and duration not only over the eastern part of the Alborán Sea but also in the Balearic basin. All these findings highlighted both the existence of an inter-seasonal variability in P99 of $\mathrm{SWH_m}$ and the importance of multi-temporal scale analysis.

5 Conclusions

Gaining a deeper, holistic understanding of extreme weather events and the related driving mechanisms has been identified as one of the World Climate Research Programme's Grand Challenges (WCRP website, 2024) due to their detrimental impact on ecosystem health and societal assets (Hochman et al., 2022). Concerning the latter, climate-driven extreme coastal hazards have long been recognised as imposing heavy socio-economic tolls, particularly aggravated in vulnerable semi-enclosed regions like the Mediterranean Sea and in exposed sectors like harbour systems (Verschuur et al., 2023).

As port downtime leads to a reduction in safety levels and wide trade losses through maritime transport and global supply-chain networks (Verschuur et al., 2022), the accurate monitoring of violent weather-related episodes is a deciding factor in adopting prevention strategies (i.e. wise design of safe port infrastructures) and mitigation measures that should eventually result in the enhancement of coastal communities' resilience.

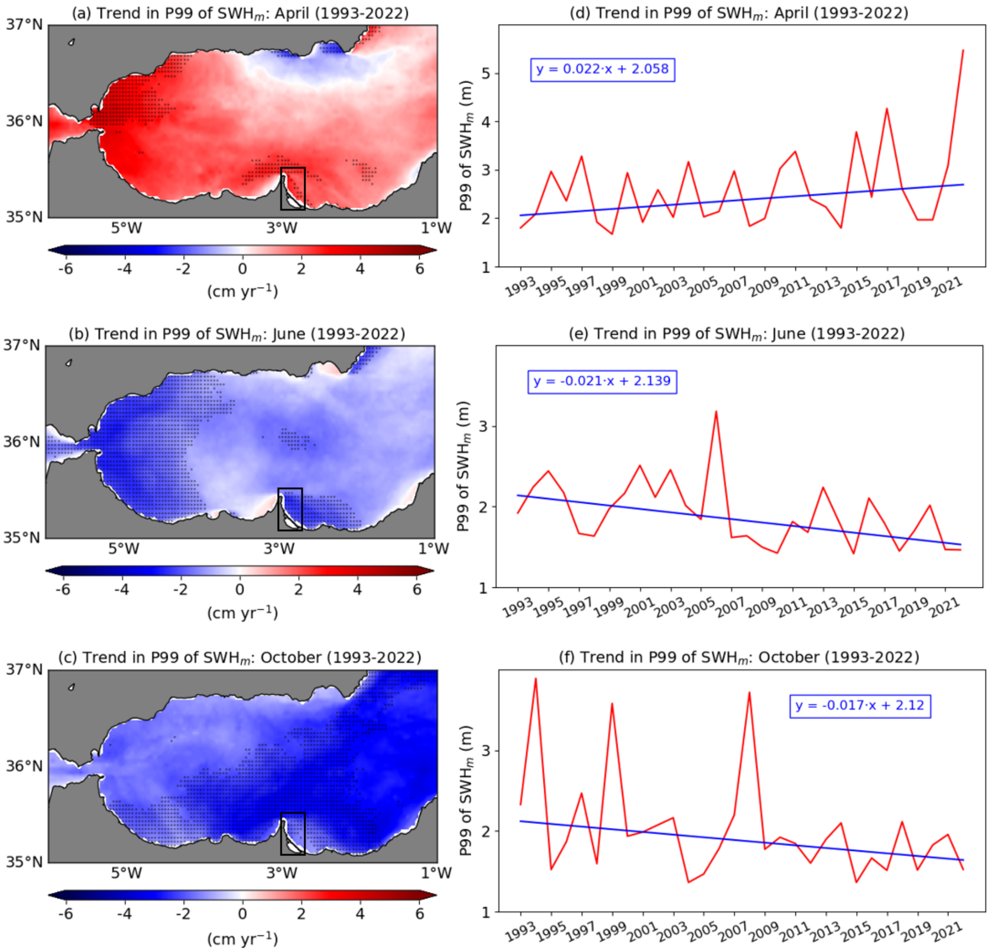

Figure 4. **(a, b, c)** Monthly trend maps of the 99th percentile (P99) of significant wave height (SWH$_\mathrm{m}$) over the Alborán Sea for the 1993–2022 period as derived from MED reanalysis (product ref. no. 4 in Table 1). Areas with statistically significant trends at the 90 % confidence intervals are denoted by black dots. **(d, e, f)** Temporal trends computed over the Melilla subdomain (represented by a black box on the associated maps).

In the present work, the attention is focused on the unprecedented storm that hit Melilla harbour (Alborán Sea; Fig. 1a) during 4–5 April 2022 with heavy rainfall and strong easterly winds, which induced extremely high waves (above 7 m) with associated long mean periods (above 9 s) that simultaneously beat previous historical records (Fig. 1c–d). The return period associated with this extreme wave event decreased from 53 years to 25 years. These outcomes are essential for the safe design of future facilities at Melilla port (Naseef et al., 2019). Conversely, it is worth pointing out that the port is also subjected to a constant geometric modification (in the docks, basins, bathymetry, breakwaters, etc.) which in turn can induce additional variations in the port response to extreme wave events that should be further assessed.

The analysis of hourly time series of SWH$_o$ (2011–2022) revealed that there were seven episodes that exceeded the P99.9 threshold (4.45 m), denoted chronologically from E1 to E7 in Fig. 1c. The retrospective comparison of the record-breaking E7 event with six previous extreme wave episodes (E1 to E6) revealed that all of them were connected with similar large-scale atmospheric blocks: a dipole-like SLP pattern, characterised by two adjacent (northwestern) high- and (southeastern) low-pressure systems, induced strong easterly winds channelled over the entire Alborán Sea (Figs. 2a–b, A2, and A3). Furthermore, this common atmospheric configuration seems to predominantly feature during the same stage of the year, a 50 d period between late February and early April (Fig. 2d). These findings contrast with other Spanish harbours (i.e. NW Iberian Peninsula) where the storm season typically spans from November to March (Ribeiro et al., 2023), highlighting the strong need to conduct a tailored assessment for each specific port and oceanographic region. Therefore, it might be deduced that large-scale atmospheric blocks leading to severe sea states in Melilla tend to be more probable during the winter-to-spring transition period. This outcome is in line with prior blocking climatologies for the eastern North Atlantic (Kautz et al., 2022; Barriopedro et al., 2006). In this context, previous works have also explored the dynamical links between blocking patterns and the North Atlantic Oscillation (NAO), which is the leading mode of atmospheric circulation variability over the Euro-Atlantic sector and is characterised by a seesaw of atmospheric mass between the Iceland Low and the Azores High (e.g. Hurrell and Deser 2009). The NAO appeared as the leading variability pattern during winter, accounting for 45 % of the blocking frequency variance (Barriopedro et al., 2006).

High-frequency (2 Hz) sea level and agitation observations during the 2011–2022 period, provided by the Melilla tide gauge, were used to investigate the relationship between offshore energetic waves and the sea state inside of the harbour (Fig. 3). A record-breaking value of harbour agitation (1.41 m) was recorded during the E7 event (Fig. 3a). The highest agitation records (above 1 m) were registered for incident high waves coming predominantly from the sector between 50 and 70° (clockwise from true north) with T_m and T_p values above 7 and 10 s, respectively (Fig. 3b–d). Extreme sea level oscillations (30 s to 1 h), which also reached record heights (up to 0.58 m), were linked to the highest values in the IG energy band (Fig. 3e). The seven extreme events in the Alborán Sea led to harsh sea conditions within the port: the energy in the IG band was significantly correlated (0.96) with an offshore parameter proportional to $\mathrm{SWH}_o \cdot T_\mathrm{p}^2$, with energetic swell being responsible for the highest energies (above $2000\,\mathrm{m}^2\,\mathrm{s}$), as shown in Fig. 3f–h. Therefore, the IG waves related to energetic swell commonly observed on the NW Iberian coast can also be present during extreme wave events on the Mediterranean coast, as previously reported for Storm Gloria (2020) by Pérez-Gómez et al. (2021) and Álvarez-Fanjul et al. (2022).

Additionally, MED reanalysis was used to characterise the long-term mean (Fig. A5) and extreme (Fig. 4) wave climate over the Alborán Sea for the period 1993–2022. The intra-annual variability in the P99 of SWH_m was examined on a monthly timescale to identify the existence of potential trends. Results seem to suggest that the intensity of extreme wave events impacting Melilla harbour increased for April (Fig. 4a and d), while observed trends indicate a significant decrease in P99 for the SWH_m during June (Fig. 4b and e) or October (Fig. 4c and f). Such alterations of outer-harbour wave climate conditions might impact in-port wave agitation response as the amount of energy penetrating into the harbour would be different, as previously indicated by Sierra et al. (2015).

Still, it should be noted that the present work does not focus on the duration of extreme wave events over the SW Mediterranean Sea, so future endeavours should address this relevant aspect to complement the results presented here. Moreover, long-term historical changes in wave period and directionality are receiving increasing attention and should be further analysed to assess their specific impact on the operability of harbours (Erikson et al., 2022; Casas-Prat and Sierra, 2012). Permanent modifications in the wave direction might result in enhanced wave penetration into the harbour and thereby larger agitation, as port protective structures were originally designed to dampen wind and short waves coming from a predetermined sector (Casas-Prat and Sierra, 2012). Likewise, the offshore wave period also plays a primary role in the modulation of harbour agitation, as derived from Fig. 3c–d. As a consequence, any sharp increase in both wave period and SWH_o could lead to severe sea states within the port. Regardless of the reported limitations of global and regional reanalyses (inherent to their coarse spatial resolution) when used on coastal and port scales (Fanti et al., 2023; Zacharioudaki et al., 2022), the MED reanalysis used in this work can be considered a robust first-guess estimator for the present intra-annual variability assessment of extreme waves in Melilla. This statement is supported not only by the comprehensive Quality Information Document (Zacharioudaki et al., 2023) but also by the 12-year skill assessment conducted against in situ hourly observations from the Melilla coastal buoy (Fig. A5a). The comparison yielded a correlation coefficient of 0.96 and revealed a slight underestimation of extreme SWH_o values. To overcome such a drawback, future works should include the implementation of a dynamical downscaling methodology to improve wave reanalysis accuracy on finer coastal scales (Vannucchi et al., 2021). Of course, this would necessarily require finding the right trade-off between adequate spatial resolutions and the available in-house computational resources. Complementarily, additional efforts should be devoted to assessing the dominant modes of extreme wave variability and their relationship with the most important climatic indices since this could enhance the prognostic skills of extreme wave events and benefit the adaptation plans in the entire Spanish harbour system.

Finally, it is worth mentioning that most of the outcomes derived from this work could not only feed the incoming climate change observatory for the Spanish ports (which should be fully operational by 2025) but also be integrated into tailored multi-hazard early warning systems. They would act as a key component of robust capacity analysis frameworks, covering a wide range of dimensions, such as legislative, planning, infrastructure, technical, scientific, and institutional partnerships (Haigh et al., 2018). Special attention should be focused on the thorough revision of security protocols and the implementation of mitigation plans within the harbour territory based on the updated return periods presented in this work. The design lifetime risk should be recalculated accordingly, as coastal structures in the vicinity of the harbour must resist growing stresses during their lifespan and operations, such as wave overtopping, flooding, or resonance, to name a few. While the current port layout configuration must be adapted to the increasing frequency and magnitude of these stressors, future maritime facilities at Melilla harbour should be wisely designed and constructed taking into account these outcomes in order to withstand extreme wave regimes imposed by the changing marine environment (Vanem et al., 2019). Albeit methodologically robust, the return periods exposed in this work are based on a short (12-year) time series of quality-controlled in situ wave observations. Therefore, they should be further complemented by return periods computed by means of longer modelled time series from very-high-resolution wave reanalysis.

Appendix A

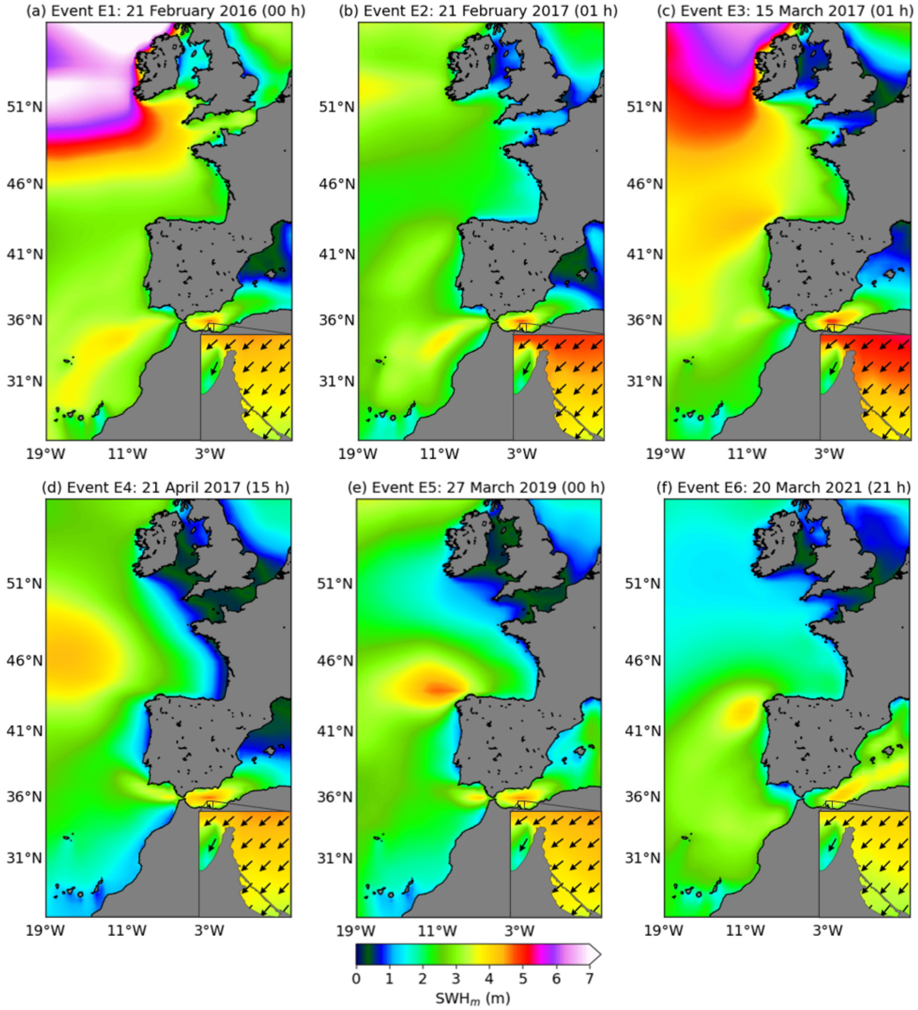

Figure A1. Hourly maps of significant wave height (SWH$_\mathrm{m}$), derived from ERA5 reanalysis (product ref. no. 3 in Table 1), corresponding to six extreme wave events (E1–E6) affecting the Melilla area. Small maps in the bottom-right corner of each panel represent the hourly SWH$_\mathrm{m}$ and wave propagation direction in the vicinity of Melilla harbour as derived from MED reanalysis (product ref. no. 4 in Table 1). The hour represents local time.

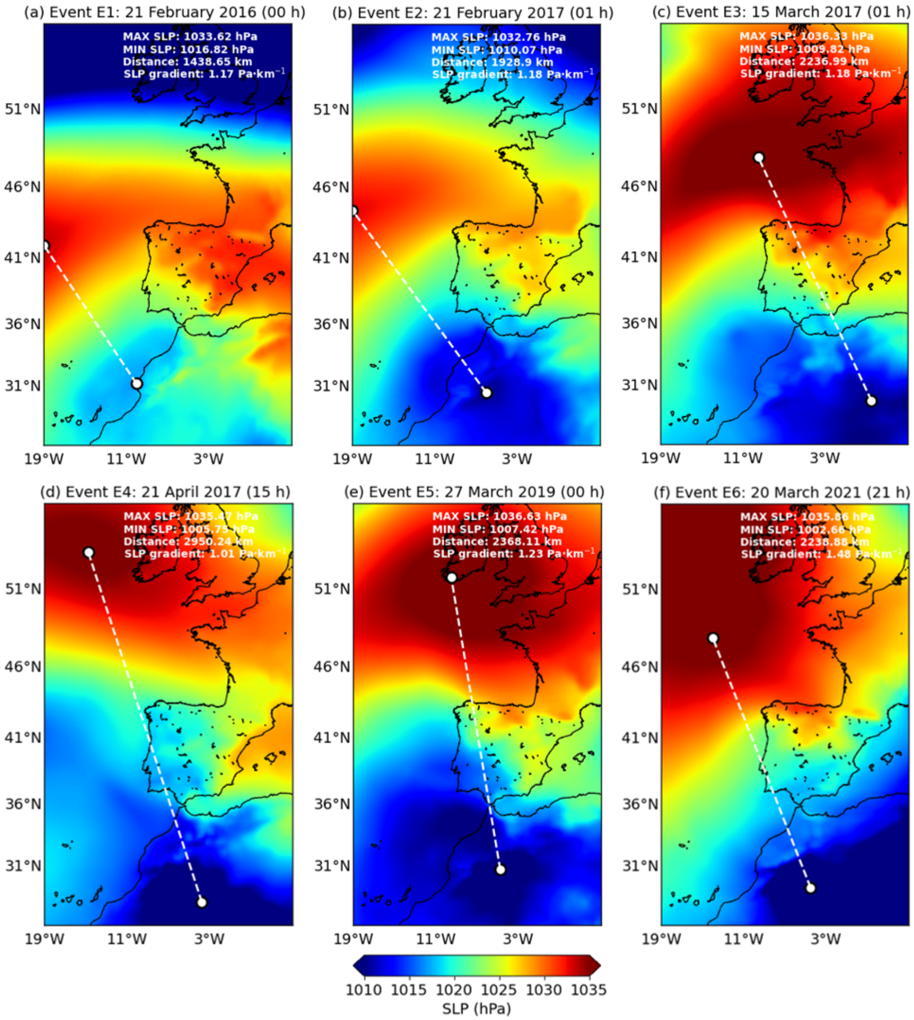

Figure A2. Hourly maps of sea level pressure (SLP), derived from ERA5 reanalysis (product ref. no. 3 in Table 1), corresponding to six extreme wave events (E1–E6) affecting the Melilla area. Maximum and minimum values of SLP are marked with white dots and linked with a dashed white line. The distance between the two pressure centres and the related SLP gradient are indicated in the upper-right corner. The hour represents local time.

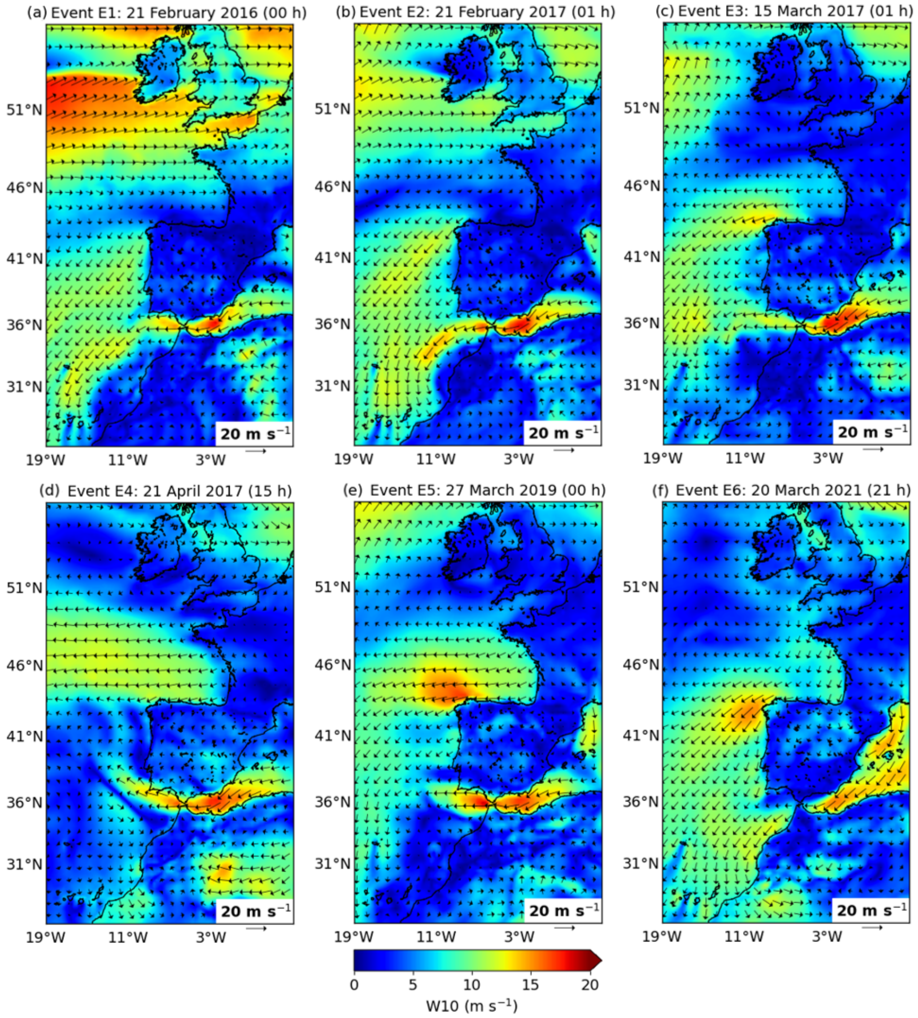

Figure A3. Hourly maps of wind at 10 m height (W10), derived from ERA5 reanalysis (product ref. no. 3 in Table 1), corresponding to six extreme wave events (E1–E6) affecting the Melilla area. The hour represents local time.

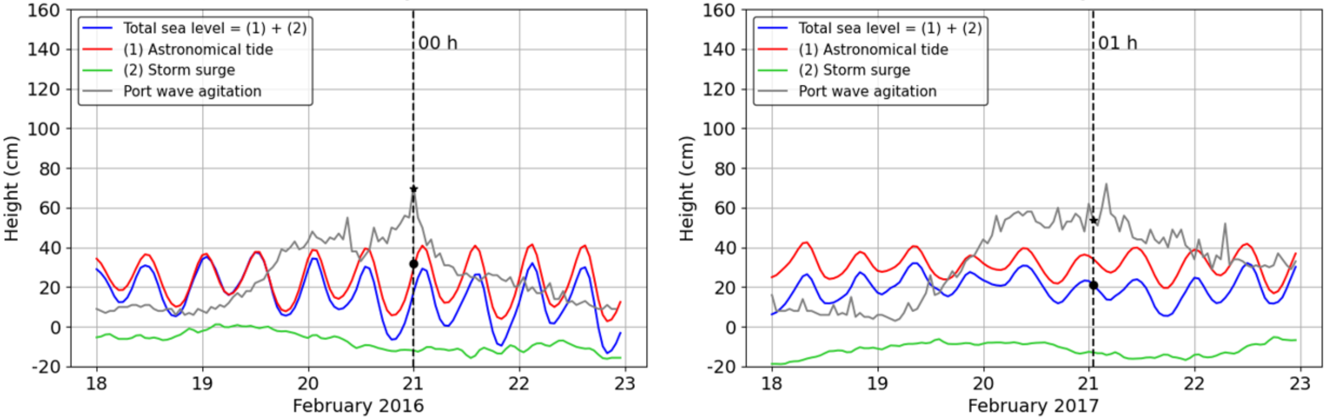
(a) Event E1: 21 February 2016 (00 h)

(b) Event E2: 21 February 2017 (01 h)

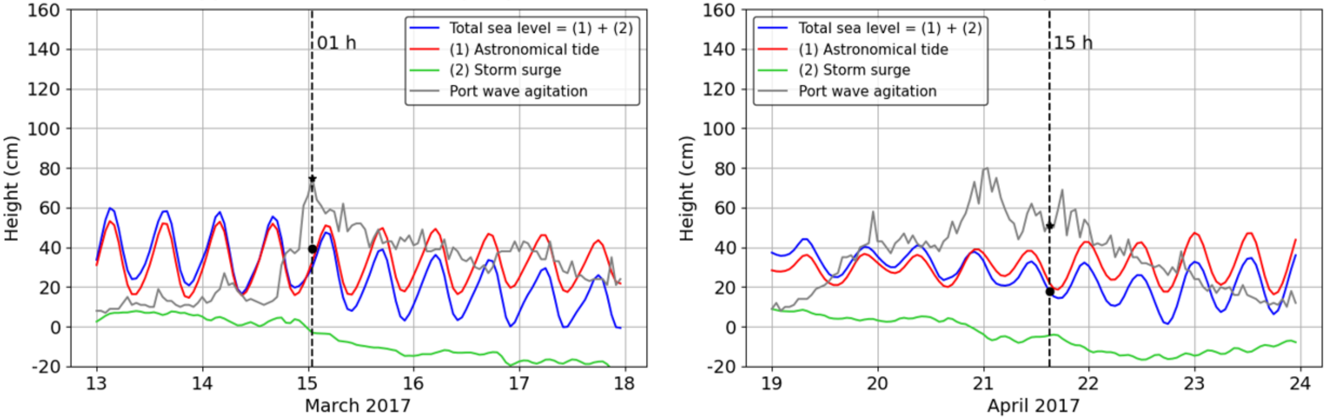
(c) Event E3: 15 March 2017 (01 h)

(d) Event E4: 21 April 2017 (15 h)

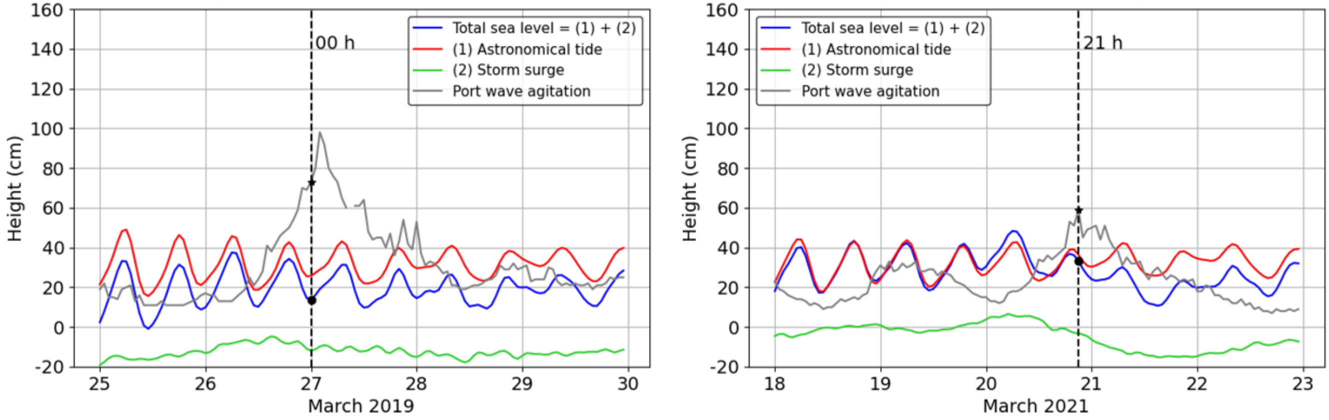
(e) Event E5: 27 March 2019 (00 h)

(f) Event E6: 20 March 2021 (21 h)

Figure A4. Hourly time series of sea level height (blue line) and port agitation (grey line) observations corresponding to the six extreme wave events detected before the study case and labelled in Fig. 1d. Observations provided by the Melilla tide gauge (product ref. no. 2 in Table 1). Astronomical tides and meteorological residuals are represented by the red and green lines, respectively. The vertical dashed black line indicates the peak of the wave storm for each of the six events analysed.

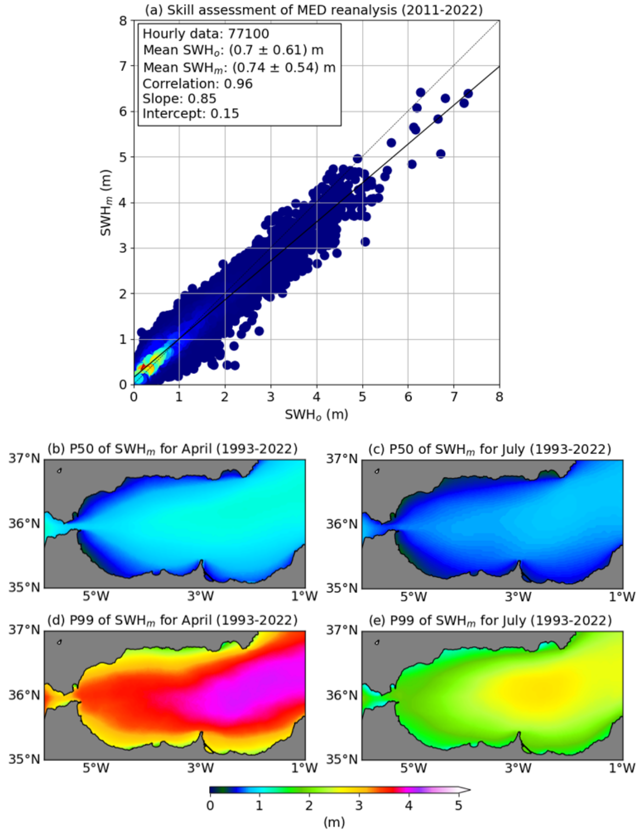

Figure A5. **(a)** Skill assessment of MED reanalysis (product ref. no. 4 in Table 1) at the grid point closest to the Melilla coastal buoy (product ref. no. 1 in Table 1): best linear fit (solid black line) of the scatter plot between hourly estimations of modelled ($\mathrm{SWH_m}$) and observed (SWH_o) significant wave height for the concurrent 12-year period (2011–2022). The dotted black line represents the result of perfect agreement with slope 1.0 and intercept 0. Statistical metrics are presented in the white box. Spatial distribution of the 50th (P50) **(b, c)** and 99th (P99) **(d, e)** percentiles of $\mathrm{SWH_m}$ over the Alborán Sea for April **(b, d)** and July **(c, e)**, as derived from MED reanalysis for the 1993–2022 period.

Data availability. The model and observation products used in this study from both the Copernicus Marine Service and other sources are listed in Table 1.

Author contributions. PL, MdA, FM, BPG, and SPR conducted the pilot study through fruitful discussions in the framework of working team meetings. PL designed the experiment, analysed the long-term wave trends, created the figures, and prepared successive versions of the draft with inputs from several co-authors. MdA conducted a bibliographic revision of extreme metocean events previously occurring in the Mediterranean Sea. PG computed the return period before and after the record-breaking event. FM extracted time series from the Puertos del Estado internal database and prepared diverse in situ sensor datasets. BPG proposed the agitation and infragravity band study in the port and analysed the corresponding tide gauge records. SPR provided a tailored coastline for Melilla harbour and analysed the atmospheric driving mechanisms during the event. MIR applied a quality control for historical time series of wave parameters from Melilla coastal buoy. Finally, several authors participated in successive iterations and in the draft and revision of the article.

Competing interests. The contact author has declared that none of the authors has any competing interests.

Acknowledgements. The authors are grateful to the Copernicus Marine Service for the data provision.

Review statement. This paper was edited by Marta Marcos and reviewed by two anonymous referees.

References

Álvarez-Fanjul, E., Pérez Gómez, B., de Alfonso Alonso-Muñoyerro, M., Lorente, P., García Sotillo, M., Lin-Ye, J., Aznar Lecocq, R., Ruíz Gil de la Serna, M., Pérez Rubio, S., Clementi, E., Coppini, G., García-León, M., Fernandes, M., García Valdecasas, J., García Valdecasas, J.M., Santos Muñoz, D., Luna Rico, M.Y., Mestres, M., Molina, R., Tintoré, J., Mourre, B., Masina, S., Mosso, C., Reyes, E., and Santana, A.: Western Mediterranean record-breaking storm Gloria: An integrated assessment based on models and observations, J. Oper. Oceanogr., 15, 1–220, https://doi.org/10.1080/1755876X.2022.2095169, 2022.

Amarouche, K., Akpınar, A., and Semedo, A.: Wave storm events in the Western Mediterranean Sea over four decades, Ocean Model., 170, 101933, https://doi.org/10.1016/j.ocemod.2021.101933, 2022a.

Amarouche, K., Bingölbali, B., and Akpinar, A.: New wind-wave climate records in the Western Mediterranean Sea, Clim. Dynam., 58, 1899–1922, https://doi.org/10.1007/s00382-021-05997-1, 2022b.

Amores, A., Marcos, M., Carrió, D. S., and Gómez-Pujol, L.: Coastal impacts of Storm Gloria (January 2020) over the north-western Mediterranean, Nat. Hazards Earth Syst. Sci., 20, 1955–1968, https://doi.org/10.5194/nhess-20-1955-2020, 2020.

Aucan, J. and Ardhuin, F.: Infragravity waves in the deep ocean: an upward revision, Geophys. Res. Lett., 40, 3435–3439, https://doi.org/10.1002/grl.50321, 2013.

Barbariol, F., Davison, S., Falcieri, F.M., Ferretti, R., Ricchi, A., Sclavo, M. and Benetazzo, A.: Wind Waves in the Mediterranean Sea: An ERA5 Reanalysis Wind-Based Climatology, Front. Mar.

Sci., 8, 760614, https://doi.org/10.3389/fmars.2021.760614, 2021.

Barriopedro, D., García-Herrera, R., Lupo, A. R., and Hernández, E.: A climatology of Northern Hemisphere blocking, J. Climate, 19, 1042–1063, https://doi.org/10.1175/JCLI3678.1, 2006.

Bellafont, F.: Role of infragravity waves on port agitation during storm events, Civil Engineering, PhD thesis, Université de Pau et des Pays de l'Adour, France, 202 pp., 2019.

Bellotti, G. and Franco, L.: Measurement of long waves at the harbor of Marina di Carrara, Italy, Ocean Dynam., 61, 2051–2059, https://doi.org/10.1007/s10236-011-0468-6, 2011.

Bensoussan, N., Chiggiato, J., Nardelli, B. B., Pisano, A., and Garrabou, J.: Insights on 2017 Marine Heat Waves in the Mediterranean Sea, J. Oper. Oceanogr., 12, 101–108, https://doi.org/10.1080/1755876X.2019.1633075, 2019.

Berta, M., Corgnati, L., Magaldi, M., Griffa, A., Mantovani, C. Rubio, A. Reyes, E., and Mader, J.: Small scale ocean weather during an extreme wind event in the Ligurian Sea, J. Oper. Oceanogr., 13, 149–154, https://doi.org/10.1080/1755876X.2020.1785097, 2020.

Caloiero, T. and Aristodemo, F.: Trend Detection of Wave Parameters along the Italian Seas, Water, 13, 1634, https://doi.org/10.3390/w13121634, 2021.

Camus, P., Tomás, A., Izaguirre, C., Rodríguez, B., Díaz-Hernández, G., and Losada, I.: Probabilistic assessment of port operability under climate change, Coastal Engineering Proceedings, 1, 54, https://doi.org/10.9753/icce.v36.risk.54, 2018.

Casas-Prat, M. and Sierra, J. P.: Trend analysis of wave direction and associated impacts on the Catalan coast, Climatic Change, 115, 667–691, https://doi.org/10.1007/s10584-012-0466-9, 2012.

Cavaleri, L., Bertotti, L., Torrisi, L., Bitner-Gregersen, E., Serio, M., and Onorato, M.: Rogue waves in crossing seas: The Louis Majesty accident, J. Geophys. Res., 117, C00J10, https://doi.org/10.1029/2012JC007923, 2012.

Chiggiato, J., Artale, V., de Madron, X. D., Schroeder, K., Taupier-Letage, I., Velaoras, D., and Vargas-Yáñez, M.: Recent changes in the Mediterranean Sea, in: Oceanography of the Mediterranean Sea, An introductory guide, Elsevier, 289–334, https://doi.org/10.1016/B978-0-12-823692-5.00008-X, 2023.

Clementi, E., Korres, G., Cossarini, G., Ravdas, M., Federico, I., Goglio, A.C., Salon, S., Zacharioudaki, A., Pattanaro, M., and Coppini, G.: The September 2020 Medicane Ianos predicted by the Mediterranean Forecasting systems, Ocean State Report Issue 6, J. Oper. Oceanogr., 15, 185–192, https://doi.org/10.1080/1755876X.2022.2095169, 2022.

Copernicus Marine In Situ Team: Copernicus In Situ TAC, Real Time Quality Control for WAVES. CMEMS-INS-WAVES-RTQC, https://doi.org/10.13155/46607, 2020.

Costas, R., Figuero, A., Sande, J., Peña, E., and Guerra, A.: The influence of infragravity waves, wind, and basin resonance on vessel movements and related downtime at the Outer Port of Punta Langosteira, Spain, Appl. Ocean Res., 129, 103370, https://doi.org/10.1016/j.apor.2022.103370, 2022.

Dayan, H., McAdam, R., Juza, M., Masina, S., and Speich, S.: Marine heat waves in the Mediterranean Sea: An assessment from the surface to the subsurface to meet national needs, Front. Mar. Sci., 10, 1045138, https://doi.org/10.3389/fmars.2023.1045138, 2023.

de Alfonso, M., García-Valdecasas, J. M., Aznar, R., Pérez-Gómez, B., Rodríguez, P., de los Santos, F. J., and Álvarez-Fanjul, E.: Record wave storm in the Gulf of Cadiz over the past 20 years and its impact on harbours, Copernicus Marine Service Ocean State Report, Issue 4, J. Oper. Oceanogr., 13, 137–144, https://doi.org/10.1080/1755876X.2020.1785097, 2020.

de Alfonso, M., Lin-Ye, J., García-Valdecasas, J. M., Pérez-Rubio, S., Luna, M. Y., Santos-Muñoz, D., Ruiz, M. I., Pérez-Gómez, B., and Álvarez-Fanjul, E.: Storm Gloria: sea state evolution based on in situ measurements and modelled data and its impact on extreme values, Front. Mar. Sci., 8, 1–17, https://doi.org/10.3389/fmars.2021.646873, 2021.

De Leo, F., Briganti, R., and Besio, G.: Trends in ocean waves climate within the Mediterranean Sea: a review, Clim. Dynam., 62, 1555–1566, https://doi.org/10.1007/s00382-023-06984-4, 2023.

Denaxa, D., Korres, G., Sotiropoulou, M., and Lecci, R.: EU Copernicus Marine Service Product User Manual for the Mediterranean Sea Waves Reanalysis, MEDSEA_MULTIYEAR_WAV_006_012, Issue: 2.3, Mercator Ocean International, https://catalogue.marine.copernicus.eu/documents/PUM/CMEMS-MED-PUM-006-012.pdf (last access: 1 March 2024), 2023.

ECCLIPSE website: Homepage, https://ecclipse.eu/, last access: 11 January 2024.

Emery, W. J. and Thompson, R. E.: Data Analysis Methods in Physical Oceanography, Elsevier Science, Amsterdam, 654 pp., ISBN 9780080477008, 2001.

EU Copernicus Marine Service Product: Atlantic Iberian Biscay Irish Ocean- In-Situ Near Real Time Observations, Mercator Ocean International [data set], https://doi.org/10.48670/moi-00043, 2023a.

EU Copernicus Marine Service Product: Mediterranean Sea Waves Reanalysis, Mercator Ocean International [data set], https://doi.org/10.25423/cmcc/medsea_multiyear_wav_006_012, 2023b.

Elgar, S., Herbers, T. H. C., Okihiro, M., Oltman-Shay, J., and Guza, R. T.: Observations of infragravity waves, J. Geophys. Res., 97, 15573–15577, 1992.

Erikson, L., Morim, J., Hemer, M., Young, I., Wang, X. L., Mentaschi, L., Mori, N., Semedo, A., Stopa, J., Grigorieva, V., Gulev, S., Aarnes, O., Bidlot, J.-R., Breivik, Ø., Bricheno, L., Shimura, T., Menendez, M., Markina, M., Sharmar, V., Trenham, C., Wolf, J., Appendini, C., Caires, S., Groll, N., and Webb, A.: Global Ocean wave fields show consistent regional trends between 1980 and 2014 in a multi-product ensemble, Commun. Earth Environ., 3, 320, https://doi.org/10.1038/s43247-022-00654-9, 2022.

Eyring, V., Gillett, N. P., Achuta Rao, K. M., Barimalala, R., Barreiro Parrillo, M., Bellouin, N., Cassou, C., Durack, P. J., Kosaka, Y., McGregor, S., Min, S., Morgenstern, O., and Sun, Y.: Human Influence on the Climate System, In Climate Change 2021: The Physical Science Basis. Contribution of Working Group I to the Sixth Assessment Report of the Intergovernmental Panel on Climate Change, edited by: Masson-Delmotte, V., Zhai, P., Pirani, A., Connors, S. L., Péan, C., Berger, S., Caud, N., Chen, Y., Goldfarb, L., Gomis, M. I., Huang, M., Leitzell, K., Lonnoy, E., Matthews, J. B. R., Maycock, T. K., Waterfield, T., Yelekçi, O., Yu, R., and Zhou, B., Cambridge University Press, Cambridge, United Kingdom and New York, NY, USA, 423–552, https://doi.org/10.1017/9781009157896.005, 2021.

Fanti, V., Ferreira, Ó., Kümmerer, V., and Loureiro, C.: Improved estimates of extreme wave conditions in coastal areas from calibrated global reanalyses, Commun. Earth Environ., 4, 151, https://doi.org/10.1038/s43247-023-00819-0, 2023.

García-Valdecasas, J., Pérez Gómez, B., Molina, R., Rodríguez, A., Rodríguez, D., Pérez, S., Campos, A., Rodríguez-Rubio, P., Gracia, S., Ripollés, L., Terrés Nicoli, J. M., de los Santos, F. J., and Álvarez-Fanjul, E.: Operational tool for characterizing high-frequency sea level oscillations, Nat. Hazards, 106, 1149–1167, https://doi.org/10.1007/s11069-020-04316-x, 2021.

Garrabou, J., Gómez-Gras, D., Medrano, A., Cerrano, C., Ponti, M., Schlegel, R., Bensoussan, N., Turicchia, E., Sini, M., Gerovasileiou, V., Teixido, N., Mirasole, A., Tamburello, L., and Cebrian, E.: Marine heatwaves drive recurrent mass mortalities in the Mediterranean Sea, Glob. Change Biol., 28, 5708–5725, https://doi.org/10.1111/gcb.16301, 2022.

Giesen, R., Clementi, E., Bajo, M., Federico, I., Stoffelen, A., and Santoleri, R.: The November 2019 record high water levels in Venice, Italy, J. Oper. Oceanogr., 14, 156–162, https://doi.org/10.1080/1755876X.2021.1946240, 2021.

Goda, Y.: On the methodology of selecting design wave height, in: Proceedings 21st Coastal Engineering Conference, ASCE, New York, 20–25 June 1988, 899–913, https://doi.org/10.9753/icce.v21.67, 1988.

Gutiérrez-Serret, R., Grassa, J. M., and Grau, J. I.: Breakwater development in Spain, The last ten years, Proceeding presented at Coasts, Marine Structures and Breakwaters: Adapting to Change, 9th International Conference organised by the Institution of Civil Engineers, Edinburgh, Scotland, UK, 16–18 September 2009, https://doi.org/10.1680/cmsb.41301.0004, 2009.

Guza, R. T. and Thornton, E. B.: Swash oscillations on a natural beach, J. Geophys. Res.-Oceans, 87, 483–491, 1982.

Haigh, R., Amaratunga, D., and Hemachandra, K.: A capacity analysis framework for multi-hazard early warning in coastal communities, Procedia Engineer., 212, 1139–1146, https://doi.org/10.1016/j.proeng.2018.01.147, 2018.

Harley, M.: Coastal storm definition, in: Coastal storms: processes and impacts, John Wiley & Sons, 1–21, https://doi.org/10.1002/9781118937099.ch1, 2017.

Hersbach, H., Bell, B., Berrisford, P., Biavati, G., Horányi, A., Muñoz Sabater, J., Nicolas, J., Peubey, C., Radu, R., Rozum, I., Schepers, D., Simmons, A., Soci, C., Dee, D., and Thépaut, J.-N.: ERA5 hourly data on single levels from 1940 to present, Copernicus Climate Change Service (C3S) Climate Data Store (CDS) [data set], https://doi.org/10.24381/cds.adbb2d47, 2023.

Hochman, A., Marra, F., Messori, G., Pinto, J. G., Raveh-Rubin, S., Yosef, Y., and Zittis, G.: Extreme weather and societal impacts in the eastern Mediterranean, Earth Syst. Dynam., 13, 749–777, https://doi.org/10.5194/esd-13-749-2022, 2022.

Hurrell, J. W. and Deser, C.: North Atlantic climate variability: The role of the North Atlantic Oscillation, J. Mar. Syst., 78, 28–41, https://doi.org/10.1016/j.jmarsys.2009.11.002, 2009.

Inch, K., Davidson, M., Masselink, G., and Russell, P.: Observations of nearshore infragravity wave dynamics under high energy swell and wind-wave conditions, Cont. Shelf Res., 138, 19–31, https://doi.org/10.1016/j.csr.2017.02.010, 2017.

In Situ TAC partners: EU Copernicus Marine Service Product User Manual for the Atlantic Iberian Biscay Irish Ocean- In- Situ Near Real Time Observations, INSITU_IBI_PHYBGCWAV_DISCRETE_MYNRT_013_033, Issue: 2.0, Mercator Ocean International, https://catalogue.marine.copernicus.eu/documents/PUM/CMEMS-INS-PUM-013-030-036.pdf (last access: 1 March 2024), 2023.

Intergovernmental Panel on Climate Change (IPCC): The Ocean and Cryosphere in a Changing Climate: Special Report of the Intergovernmental Panel on Climate Change, Cambridge University Press, Cambridge, https://doi.org/10.1017/9781009157964, 2022.

Izaguirre, C., Losada, I. J., Camus, P., Vigh, J. L., and Stenek, V.: Climate change risk to global port operations, Nat. Clim. Change, 11, 14–20, https://doi.org/10.1038/s41558-020-00937-z, 2021.

Juza, M. and Tintoré, J.: Multivariate Sub-Regional Ocean Indicators in the Mediterranean Sea: From Event Detection to Climate Change Estimations, Front. Mar. Sci., 8, 610589, https://doi.org/10.3389/fmars.2021.610589, 2021.

Kautz, L.-A., Martius, O., Pfahl, S., Pinto, J. G., Ramos, A. M., Sousa, P. M., and Woollings, T.: Atmospheric blocking and weather extremes over the Euro-Atlantic sector – a review, Weather Clim. Dynam., 3, 305–336, https://doi.org/10.5194/wcd-3-305-2022, 2022.

Kendall, M. G.: Rank Correlation Methods; Hafner Publishing Company, New York, NY, USA, ISBN B008089IDY, 1962.

Kokkini, Z. and Notarstefano, G.: Unusual salinity pattern in the South Adriatic Sea in 2016, Copernicus Marine Service Ocean State Report, J. Oper. Oceanogr., 11, 130–131, https://doi.org/10.1080/1755876X.2018.1489208, 2018.

Konisky, D. M., Hughes, L., and Kaylor, C.H.: Extreme weather events and climate change concern, Climatic Change, 134, 533–547, https://doi.org/10.1007/s10584-015-1555-3, 2015.

Lashley, C. H., Bricker, J. D., Van der Meer, J., Altomare, C., and Suzuki, T.: Relative Magnitude of Infragravity Waves at Coastal Dikes with Shallow Foreshores: A Prediction Tool, J. Waterw. Port C., 146, 1–17, https://doi.org/10.1061/(ASCE)WW.1943-5460.0000576, 2020.

Linnenluecke, M. K., Griffiths, A., and Winn, M.: Extreme weather events and the critical importance of anticipatory adaptation and organizational resilience in responding to impacts, Bus. Strat. Environ., 21, 17–32, https://doi.org/10.1002/bse.708, 2012.

López, M. and Iglesias, G.: Long wave effects on a vessel at berth, Appl. Ocean Res., 47, 63–72, https://doi.org/10.1016/j.apor.2014.03.008, 2014.

Lorente, P., Lin-Ye, J., García-León, M., Reyes, E., Fernandes, M., Sotillo, M. G., Espino, M., Ruiz, M. I., Gracia, V., Pérez, S., Aznar, R., Alonso-Martirena, A., and Álvarez-Fanjul, E.: On the Performance of High Frequency Radar in the Western Mediterranean During the Record-Breaking Storm Gloria, Front. Mar. Sci., 8, 645762, https://doi.org/10.3389/fmars.2021.645762, 2021.

Lupo, A. R.: Atmospheric blocking events: a review, Ann. N. Y. Acad. Sci., 1504, 5–24, https://doi.org/10.1111/nyas.14557, 2021.

Mackay, E. and Johanning, L.: Long-term distributions of individual wave and crest heights, Ocean Eng., 165, 164–183, https://doi.org/10.1016/j.oceaneng.2018.07.047, 2018a.

Mackay, E. and Johanning, L.: A generalised equivalent storm model for long-term statistics of ocean waves, Coast. Eng., 140, 411–428, https://doi.org/10.1016/j.coastaleng.2018.06.001, 2018b.

Mann, H. B. Nonparametric tests against trend, Econometrica, 13, 245–259, 1945.

McComb, J.: Modelling long wave generation and propagation around and within ports, Proc. 2011 Coasts and Ports Conf. Perth, Australia, 28–30 September 2011.

McComb, P., Zyngfogel, R., and Pérez-Gomez, B.: Predicting infragravity waves in harbours – an evaluation of published equations and their use in forecasting operational thresholds, Coastal Engineering Proceedings, 36v, waves.7, https://doi.org/10.9753/icce.v36v.waves.7, 2020.

Milglietta, M. M. and Rotunno, R.: Development mechanisms for Mediterranean tropical-like cyclones (medicanes), Q. J. Roy. Meteor. Soc., 145, 1444–1460, 2019.

Morales-Márquez, V., Orfila, A., Simarro, G., and Marcos, M.: Extreme waves and climatic patterns of variability in the eastern North Atlantic and Mediterranean basins, Ocean Sci., 16, 1385–1398, https://doi.org/10.5194/os-16-1385-2020, 2020.

Naseef, T. M., Kumar, V. S., Joseph, J., and Jena, B. K.: Uncertainties of the 50-year wave height estimation using generalized extreme value and generalized Pareto distributions in the Indian Shelf seas, Nat. Hazards, 97, 1231–1251, https://doi.org/10.1007/s11069-019-03701-5, 2019.

Munk, W. H.: On the wind-driven ocean circulation, J. Atmos. Sci., 7, 80–93, https://doi.org/10.1175/1520-0469(1950)007<0080:OTWDOC>2.0.CO;2, 1950.

Notarstefano, G., Menna, M., and Legeais, J. F.: Reversal of the Northern Ionian circulation in 2017, Ocean State Report, 3, J. Oper. Oceanogr., 12, 108–111, https://doi.org/10.1080/1755876X.2019.1633075, 2019.

Okihiro, M., Guza, R. T., and Seymour, R. J.: Excitation of seiche observed in a small harbor, J. Geophys. Res., 98, 18.201–18.211, 1993.

Pérez, B., Payo, A., López, D., Woodworth, P. L., and Alvarez Fanjul, E.: Overlapping sea level time series measured using different technologies: an example from the REDMAR Spanish network, Nat. Hazards Earth Syst. Sci., 14, 589–610, https://doi.org/10.5194/nhess-14-589-2014, 2014.

Pérez-Gómez, B., Vela, J., and Alvarez-Fanjul, E.: A new concept of multi-purpose sea level station: example of implementation in the REDMAR network, in: Proceedings of the Fifth International Conference on EuroGOOS, 20–22 May 2008: Coastal to global operational oceanography: achievements and challenges, Exeter, 2008.

Pérez-Gómez, B., García-León, M., García-Valdecasas, J., Clementi, E., Mösso Aranda, C., Pérez-Rubio, S., Masina, S., Coppini, G., Molina-Sánchez, R., Muñoz-Cubillo, A., García Fletcher, A., Sánchez González, J. F., Sánchez-Arcilla, A., and Álvarez-Fanjul, E.: Understanding Sea Level Processes During Western Mediterranean Storm Gloria, Front. Mar. Sci. 8, 647437, https://doi.org/10.3389/fmars.2021.647437, 2021.

Portillo Juan, N., Negro Valdecantos, V., and del Campo, J. M.: Review of the Impacts of Climate Change on Ports and Harbours and Their Adaptation in Spain, Sustainability, 14, 7507, https://doi.org/10.3390/su14127507, 2022.

Radovic, V. and Iglesias, I.: Extreme Weather Events: Definition, Classification and Guidelines towards Vulnerability Reduction and Adaptation Management, in: Climate Action. Encyclopedia of the UN Sustainable Development Goals, edited by: Leal Filho, W., Azul, A., Brandli, L., Özuyar, P., and Wall, T., Springer, Cham. https://doi.org/10.1007/978-3-319-71063-1_68-1, 2018.

Ramirez-Llodra, E., De Mol, B., Company, J. B., Coll, M., and Sardà, F.: Effects of natural and anthropogenic processes in the distribution of marine litter in the deep Mediterranean Sea, Prog. Oceanogr., 118, 273–287, https://doi.org/10.1016/j.pocean.2013.07.027, 2013.

Rex, D. F.: Blocking action in the middle troposphere and its effect upon regional climate, Tellus, 2, 275–301, https://doi.org/10.1111/j.2153-3490.1950.tb00339.x, 1950.

Ribeiro, A. S., Lopes, C. L., Sousa, M. C., Gómez-Gesteira, M., Vaz, N., and Dias, J. M.: Reporting Climate Change Impacts on Coastal Ports (NW Iberian Peninsula): A Review of Flooding Extent, J. Mar. Sci. Eng., 11, 477, https://doi.org/10.3390/jmse11030477, 2023.

Romano-Moreno, E., Diaz-Hernandez, G., Lara, J. L. Tomás, A., and Jaime, F. F.: Wave downscaling strategies for practical wave agitation studies in harbours, Coast. Eng., 175, 104140, https://doi.org/10.1016/j.coastaleng.2022.104140, 2022.

Salvadori, G., Durante, F., and De Michele, C.: Multivariate return period calculation via survival functions, Water Resour. Res., 49, 2308–2311, https://doi.org/10.1002/wrcr.20204, 2013.

Sánchez-Arcilla, A., García-León, M., Gracia, V., Devoy, R., Stanica, A., and Gault, J.: Managing coastal environments under climate change: Pathways to adaptation, Sci. Total Environ., 572, 1336–1352, https://doi.org/10.1016/j.scitotenv.2016.01.124, 2016a.

Sánchez-Arcilla, A., Sierra, J. P., Brown, S., Casas-Prat, M., Nicholls, R. J., Lionello, P., and Conte, D.: A review of potential physical impacts on harbours in the Mediterranean Sea under climate change, Reg. Environ. Change, 16, 2471–2484, https://doi.org/10.1007/s10113-016-0972-9, 2016b.

Scicchitano, G., Scardino, G., Monaco, C., Piscitelli, A., Milella, M., De Giosa, F., and Mastronuzzi, G.: Comparing impact effects of common storms and Medicanes along the coast of south-eastern Sicily, Mar. Geol., 439, 106556, https://doi.org/10.1016/j.margeo.2021.106556, 2021.

Sen, P. K.: Estimates of the regression coefficient based on Kendall’s tau, J. Am. Stat. Assoc., 63, 1379–1389, 1968.

Senechal, N., Coco, G., Bryan, K. R., and Holman, R. A.: Wave runup during extreme storm conditions, J. Geophys. Res., 116, C07032, https://doi.org/10.1029/2010JC006819, 2011.

Sierra, J. P., Casas-Prat, M., Virgili, M., Mösso, C., and Sánchez-Arcilla, A.: Impacts on wave-driven harbour agitation due to climate change in Catalan ports, Nat. Hazards Earth Syst. Sci., 15, 1695–1709, https://doi.org/10.5194/nhess-15-1695-2015, 2015.

Sierra, J. P., Genius, A. Lionello, P. Mestres, M., Mösso, C., and Marzo, L.: Modelling the impact of climate change on harbour operability: The Barcelona port case study, Ocean Eng., 141, 64–78, https://doi.org/10.1016/j.oceaneng.2017.06.002, 2017.

Sotillo, M. G., Mourre, B., Mestres, M., Lorente, P., Aznar, R., García-León, M., Liste, M., Santana, A., Espino, M., and Álvarez, E.: Evaluation of the Operational CMEMS and Coastal Downstream Ocean Forecasting Services During the Storm Gloria (January 2020), Front. Mar. Sci., 8, 644525, https://doi.org/10.3389/fmars.2021.644525, 2021.

Sousa, P. M., Barriopedro, D., García-Herrera, R., Woollings, T., and Trigo, R. M.: A New Combined Detection Algorithm for

Blocking and Subtropical Ridges, J. Climate, 34, 7735–7758, https://doi.org/10.1175/JCLI-D-20-0658.1, 2021.

Soussi, A., Bersani, C., Sacile, R., Bouchta, D., El Amarti, A., Seghiouer, H., Nachite, D., and Al Miys, J.: Coastal Risk Modelling for Oil Spill in The Mediterranean Sea, Advances in Science, Technol. Eng. Syst. J., 5, 273–286, 2020.

Stockdon, H. F., Holman, R. A., Howd, P. A., and Sallenger Jr., A. H.: Empirical parameterization of setup, swash and runup, Coast. Eng., 53, 573–588, 2006.

Todd, D., Blanksby, A., and Schepis, J.: Verification of design life exposure and performance of a berm breakwater, Coast. Eng. Proceedings, 1, structures.72, https://doi.org/10.9753/icce.v33.structures.72, 2012.

Trigo, I. F., Davies, T. D., and Bigg, G. R. Objective climatology of cyclones in the Mediterranean region, J. Climate, 12, 1685–1696, https://doi.org/10.1175/1520-0442(1999)012<1685:OCOCIT>2.0.CO;2, 1999.

Tuel, A. and Eltahir, E. A. B.: Why Is the Mediterranean a Climate Change Hot Spot?, J. Climate, 33, 5829–5843, https://doi.org/10.1175/JCLI-D-19-0910.1, 2020.

Vanem, E., Fazeres-Ferradosa, T., Rosa-Santos, P., and Taveira-Pinto, F.: Statistical description and modelling of extreme ocean wave conditions, Proceedings of the Institution of Civil Engineers – Maritime Engineering, 172, 124–132, 2019.

Vannucchi, V., Taddei, S., Capecchi, V., Bendoni, M., and Brandini, C.: Dynamical Downscaling of ERA5 Data on the North-Western Mediterranean Sea: From Atmosphere to High-Resolution Coastal Wave Climate, Journal of Marine Science and Engineering, 9, 208, https://doi.org/10.3390/jmse9020208, 2021.

Velpuri, M., Das, J., and Umamahesh, N. V.: Spatio-temporal compounding of connected extreme events: Projection and hotspot identification, Environ. Res., 235, 116615, https://doi.org/10.1016/j.envres.2023.116615, 2023.

Verschuur, J., Koks, E. E., and Hall, J. W.: Ports' criticality in international trade and global supply-chains, Nat. Commun., 13, 4351, https://doi.org/10.1038/s41467-022-32070-0, 2022.

Verschuur, J., Koks, E. E., Li, S., and Hall, J. W.: Multi-hazard risk to global port infrastructure and resulting trade and logistics losses, Commun. Earth Environ., 4, 5, https://doi.org/10.1038/s43247-022-00656-7, 2023.

WCRP website: Homepage, https://www.wcrp-climate.org/gc-extreme-events, last access: 11 January 2024.

Wehde, H., Schuckmann, K. V., Pouliquen, S., Grouazel, A., Bartolome, T., Tintore, J., De Alfonso Alonso-Muñoyerro, M., Carval, T., Racapé, V., and the INSTAC team: EU Copernicus Marine Service Quality Information Document for the Atlantic Iberian Biscay Irish Ocean- In-Situ Near Real Time Observations, INSITU_IBI_PHYBGCWAV_DISCRETE_MYNRT_013_033, Issue 2.3, Mercator Ocean International, https://catalogue.marine.copernicus.eu/documents/QUID/CMEMS-INS-QUID-013-030-036.pdf (last access: 1 March 2024), 2023.

Wolff, C., Vafeidis, A. T., Muis, S., Lincke, D., Satta, A., Lionello, P., Jimenez, J. A., Conte, D., and Hinkel, J. A.: Mediterranean coastal database for assessing the impacts of sea-level rise and associated hazards, Sci. Data, 5, 180044, https://doi.org/10.1038/sdata.2018.44, 2018.

Zacharioudaki, A., Ravdas, M., and Korres, G.: Wave climate extremes in the Mediterranean Sea obtained from a wave reanalysis for the period 1993–2020. In: Copernicus Ocean State Report, Issue 6, J. Oper. Oceanogr., 15, s119–s126, https://doi.org/10.1080/1755876X.2022.2095169, 2022.

Zacharioudaki, A., Ravdas, M., Korres, G., and Goglio, A. C.: EU Copernicus Marine Service Quality Information Document for the Mediterranean Sea Waves Reanalysis. MEDSEA_MULTIYEAR_WAV_006_012, Issue: 2.3, Mercator Ocean 765 International, https://catalogue.marine.copernicus.eu/documents/QUID/CMEMS-MED-QUID-006-012.pdf (last access: 1 March 2024), 2023.

Table of contents

Copernicus Ocean State Report | OSR8 | 2024

Chapter 1: The state of the ocean

1.1 The state of the global ocean. K. von Schuckmann et al.

1.2 The state of the ocean in the northeastern Atlantic and adjacent seas. K. von Schuckmann et al.

Chapter 2: Updated and new pathways in ocean science

2.1 Monitoring global ocean heat content from space geodetic observations to estimate the Earth energy imbalance. F. Marti et al.

2.2 Changes in the Gulf Stream path over the last 3 decades. A. Sánchez-Román et al.

2.3 Monitoring main ocean currents of the Iberia–Biscay–Ireland region. Á de Pascual Collar et al.

2.4 Statistical analysis of global ocean significant wave heights from satellite altimetry over the past 2 decades. A. Laloue et al.

2.5 Characteristics and trends of marine heatwaves in the northwest European Shelf and the impacts on density stratification. W. Chen and J. Staneva

2.6 Surface and bottom marine heatwave characteristics in the Barents Sea: a model study. V. S. Lien et al.

Chapter 3: Ocean state and change for relevance to society

3.1 Oceanographic preconditions for planning seawater heat pumps in the Baltic Sea – an example from the Tallinn Bay, Gulf of Finland. J. Elken et al.

3.2 Event-based wave statistics for the Baltic Sea. J.-V. Björkqvist et al.

3.3 The role of air–sea heat flux for marine heatwaves in the Mediterranean Sea. D. Denaxa et al.

3.4 Variability in manometric sea level from reanalyses and observation-based products over the Arctic and North Atlantic oceans and the Mediterranean Sea. A. Storto et al.

Chapter 4: Specific events in the ocean in 2022

4.1 Forecasting the Mediterranean Sea marine heatwave of summer 2022. R. McAdam et al.

4.2 Coastal ocean response during the unprecedented marine heatwaves in the western Mediterranean in 2022. M. Juza et al.

4.3 Anomalous 2022 deep-water formation and intense phytoplankton bloom in the Cretan area. A. Teruzzi et al.

4.4 Baltic Sea surface temperature analysis 2022: a study of marine heatwaves and overall high seasonal temperatures. A. Lindenthal et al.

4.5 Characterization of marine heat waves in the Iberia–Biscay–Ireland (IBI) region in 2022. L. Castrillo-Acuña et al.

4.6 Subsurface warming derived from Argo floats during the 2022 Mediterranean marine heat wave. A. Pirro et al.

4.7 Monitoring the record-breaking wave event in Melilla harbour (SW Mediterranean Sea). P. Lorente et al.

https://sp.copernicus.org/articles/4-osr8

eISSN 2752-0706